Searches for charged lepton flavour violation involving final states with an electron / muon pair in pp collisions at the CMS detector

Der Fakultät für Mathematik, Informatik und Naturwissenschaften
der RWTH Aachen University vorgelegte Dissertation
zur Erlangung des akademischen Grades eines
Doktors der Naturwissenschaften

von

Diplom-Physiker Andreas Güth

aus Wilhelmshaven

Zusammenfassung

Die Entdeckung der Leptonflavourzahlverletzung im Neutrinosektor motiviert verstärkte Anstrengungen bei der Suche nach entsprechenden Wechselwirkungen zwischen geladenen Leptonen (cLFV Wechselwirkungen), deren experimenteller Nachweis einen klaren Beweis für Physik jenseits des Standardmodells der Teilchenphysik (SM) liefern würde. In dieser Arbeit werden mehrere direkte Suchen nach cLFV Wechselwirkungen in Proton-Proton (pp) Kollisionen am Large Hadron Collider (LHC) präsentiert. Der LHC liefert unterschiedliche partonische Anfangszustände bei einer zuvor unerreichten Schwerpunktsenergie und eignet sich daher besonders für die Suche nach noch unbekannten, schweren Teilchen an der TeV-Skala.
Die präsentierten Suchen basieren auf Datensätzen, welche in pp Kollisionen mit einer Schwerpunktsenergie von $\sqrt{s} = 8$ TeV im Jahr 2012 mit dem Compact Muon Solenoid (CMS) Detektor am LHC aufgezeichnet worden sind und einer integrierten Luminosität von 19.7 fb^{-1} entsprechen. In Kollisionsereignissen mit einem Elektron-Myon (eμ) Paar wird in zwei unterschiedlichen Analysen nach Hinweisen auf cLFV Wechselwirkungen gesucht: In der ersten Analyse wird im aufgezeichnete Spektrum der invarianten Masse des eμ Leptonpaares nach Peaks und einem Überschuss an Ereignissen mit Massen im TeV-Bereich gesucht. Entsprechende Signaturen würden als Hinweise auf neue Physik mit cLFV zwischen der ersten und zweiten Leptonenfamilie dienen. In der zweiten Analyse werden die Daten nach Anzeichen für die resonante Produktion eines $\mu\tau$ Paares mit leptonischem Zerfall des Tauons in ein Elektron und Neutrinos untersucht. Diese Suche testet zwar andere Modelle neuer Physik als die Analyse des eμ Massenspektrums, lässt sich aber ohne großen Mehraufwand als Erweiterung der eμ Suche formulieren. Die Untergrundbeiträge diverser Standardmodellprozesse werden anhand von Simulationen und datengestützten Methoden ermittelt. Besonderes Augenmerk wird auf die Auswertung der systematischen Unsicherheiten auf die Untergrundabschätzung gelegt. Im Rahmen der für die Abgrenzung von Signal- und Untergrundbeiträgen wichtigen Studie der Detektorauflösung der Masse des eμ Paares wird eine Messung der Transversalimpulsauflösung von Myonen mit Hilfe atmosphärischer Myonen vorgestellt. Die Ereignisselektion und Formulierung der statistischen Analyse sind möglichst modellunabhängig gestaltet, um eine Umdeutung der Ergebnisse mit Hinblick auf hier nicht berücksichtigte Modelle neuer Physik zu erleichtern.
In keiner der zwei Analysen wird eine signifikante Abweichung der Daten von der Untergrunderwartung beobachtet und Ausschlussgrenzen auf Parameter in diversen Modellen neuer Physik mit cLFV Wechselwirkungen werden bestimmt. Diese reichen von R-Parität verletzender (RPV) Supersymmetrie (SUSY) über Modelle für die Produktion von mikroskopischen schwarzen Löchern in Theorien mit Extradimensionen bis hin zu Modellen mit schweren Partnern des SM Higgs-Bosons. Die Produktion eines Tau-Sneutrinos als leichtestes supersymmetrisches Teilchen (LSP) in RPV SUSY mit einer Masse unterhalb von 1.28 TeV wird für die Kopplungen $\lambda'_{311} = \lambda_{312} = \lambda_{321} = 0.01$ bei einem Konfidenzintervall von 95% ausgeschlossen. Die Ausschlussgrenzen für die Mindestmasse mikroskopischer schwarzer Löcher fallen in den multi-TeV Bereich. In einem durch das ADD (Arkani-Hamed, Dimopoulos, Dvali) Modell großer Extradimensionen motivierten Szenario mit $n = 6$ Extradimensionen werden Massen der schwarzen Löcher unterhalb von 3.63 TeV ausgeschlossen. Diese Resultate werden im Kontext der Ergebnisse diverser indirekter Suchen nach cLFV Wechselwirkungen eingeordnet. In der $\mu\tau$ Suche werden Tau-Sneutrino LSPs mit Massen unterhalb von 1.42 TeV für die Kopplungsparameter $\lambda'_{311} = \lambda_{323} = 0.05$ ausgeschlossen. Die entsprechenden Ausschlussgrenzen auf den Wirkungsquerschnitt für die resonante Produktion einer $\mu\tau$ Resonanz kurzer Lebensdauer werden in Form eines Modells für die Produktion eines schweren Higgs-Bosons umgedeutet. Die in der $\mu\tau$ Suche erzielten Ausschlussgrenzen sind die restriktivsten aller Suchen nach entsprechenden cLFV Effekten.

Abstract

The observation of lepton flavour violation in the neutrino sector heightens the interest in searches for charged lepton flavour violating (cLFV) interactions whose observation would constitute proof of physics beyond the Standard Model (SM). In this thesis, direct searches for heavy particles that may mediate such cLFV interactions are presented. As a proton-proton (pp) collider that provides a range of different partonic initial states with unprecedented centre-of-mass energy, the Large Hadron Collider (LHC) is a powerful tool to explore the landscape of new physics models. The presented searches utilize datasets that have been recorded in pp collisions at a centre-of-mass energy of $\sqrt{s} = 8$ TeV with the CMS detector in 2012 at the LHC and correspond to an integrated luminosity of 19.7 fb^{-1}. Event samples including an electron / muon (eμ) pair are investigated in two different searches for cLFV interactions: In the first analysis, the invariant mass spectrum of selected events with an eμ pair is tested for peaks and extended high-mass tails that may point to new physics involving cLFV between the first and second generation of leptons. In the second analysis, the data are investigated for the resonant production of a $\mu\tau$ pair with subsequent decay of the τ lepton to an electron and neutrinos. This search probes a different type of cLFV interaction, but is formulated as a straightforward extension of the eμ search. The background expectation from SM processes is evaluated using both simulated event samples and data-driven background estimates. A focus is put on the study of the systematic uncertainties affecting the background contributions. A measurement of the muon transverse momentum resolution is performed in the context of the study of the dilepton mass resolution of eμ pairs, that is crucial for the discrimination between signal and background. From the choice of selection cuts to the statistical interpretation of the measurement, an effort is made to formulate the searches in a model-unspecific fashion that is suitable for reinterpretation in terms of various models of physics beyond the SM.

No significant excess above the SM expectation is observed in either of the two searches and exclusion limits are set on various models of new physics with cLFV. These range from R-parity violating (RPV) Supersymmetry (SUSY) to quantum black hole (QBH) production in theories with extra dimensions and cLFV decays of heavy scalar bosons in models with extended Higgs sectors. In the eμ search, an RPV SUSY model in which the τ sneutrino is the lightest supersymmetric particle (LSP) is excluded for sneutrino masses below 1.28 TeV for Yukawa couplings $\lambda'_{311} = \lambda_{312} = \lambda_{321} = 0.01$ at 95% CL. The limits on the threshold mass for the production of QBHs fall in the multi-TeV region for all considered models; in a scenario inspired by the ADD (Arkani-Hamed, Dimopoulos, Dvali) model of large extra dimensions with $n = 6$ extra dimensions, threshold masses below 3.63 TeV are excluded. These results are compared to those obtained from various indirect searches for cLFV phenomena. In the $\mu\tau$ search, a tau sneutrino LSP is excluded for masses below 1.42 TeV for Yukawa couplings $\lambda'_{311} = \lambda_{323} = 0.05$. The corresponding cross section limits for the production of a narrow $\mu\tau$ resonance are recast in terms of a model with a heavy Higgs boson with cLFV decays that is produced via a top-quark loop. The limits obtained for the resonant production of a $\mu\tau$ pair are the most stringent to date.

Contents

Introduction

In the Standard Model (SM) of particle physics with vanishing neutrino masses, the three lepton flavour numbers are conserved, although the theory lacks an underlying principle that would enforce this conservation. Lepton flavor violation (LFV) has been firmly established in the neutrino sector in the contexts of neutrino oscillations [1, 2] and the solution of the solar neutrino problem [3][1] by various experiments since 1998 (for a review see Ref. [5]). This milestone in the history of particle physics can be regarded as the first observation of physics beyond the SM in its original formulation. Even if the SM is extended to account for neutrino oscillations by adding non-zero neutrino masses and mixing parameters, several questions remain. One of them is the starting point for the analyses of data recorded in 2012 with the CMS detector [6] in pp collision delivered by the CERN Large Hadron Collider (LHC) [7] at a centre-of-mass energy of $\sqrt{s} = 8$ TeV that are presented in this thesis:

Is the conservation of lepton flavour violated in interactions involving charged leptons?

There are two main routes for the experimental physicist to address this question concerning the existence of *charged lepton flavour violation* (cLFV)[2] when designing a corresponding search at the LHC. One approach is to look for decays of known particles, such as mesons, the Z boson, and the (not yet as well experimentally studied) Higgs boson h^0 into a pair of charged leptons that carry different flavour. Its advantage is that the search strategy is well-defined in this case; in particular, the experimental signatures and the masses of the particles participating in the process are known. However, if such decays were observed, one might still expect some physics beyond the SM (BSM) at a higher energy scale to be the underlying cause of cLFV. The second approach sets out for searching for this hypothetical new physics directly between the electroweak scale and the multi-TeV scale by exploiting the high centre-of-mass energy of the LHC that is unprecedented (in a laboratory). This second path towards searches for cLFV interactions is taken in this thesis. Various models of BSM physics incorporate, or at least allow for, cLFV interactions (a comprehensive review is presented in Ref. [8]). Examples are R-parity violating supersymmetry; models with extended Higgs sectors, such as multi-Higgs doublet models or Higgs triplet models; or certain models for quantum black hole production and decay at the LHC. Some of these models provide very different experimental signatures that are most promising for a discovery of cLFV at the LHC depending on unknown parameters. Again, the experimentalist faces a choice concerning the analysis strategy: Either a specific signal model is chosen, such that the setup of the analysis can be guided by the corresponding experimental signatures, cross section calculations, and constraints on the model obtained from other experiments (*model-specific search*); or a *key signature* can be identified that covers most of the models of interest and is robust against variations of model parameters (*signature-based search*). Both approaches are pursued in this thesis. First, a signature-based search for structures in the mass spectrum of selected electron/muon pairs is presented that starts from a very inclusive event selection. Its is referred to as *the eμ search* in the following. After interpreting the experimental findings in terms of

---

[1] The distinction between neutrino oscillations and non-oscillatory adiabatic flavor conversions -the *MSW effect* that is now understood as the driving force behind the observed flavor conversion of solar neutrinos- is explained in Ref. [4].

[2] The abbreviation cLFV is used for both the terms *charged lepton flavour violation* and *charged lepton flavour violating* in the following, depending on the context.

specific models of new physics, the analysis is extended by a search for the resonant production of heavy particles that decay into a $\mu\tau$ pair. In this more model-specific approach, event selection cuts are tightened in order to improve the sensitivity of the search for the chosen signal model and challenge the sensitivity of existing searches by other experiments. Its is referred to as *the* $\mu\tau$ *search* or *the* $\mu\tau_{\mathrm{e}}$ *search* in the following.

Two interesting aspects of searches for cLFV are the complementarity of very different experimental approaches and the wide range of suggested models of BSM physics. This work tries to do justice to both. First, the experimental findings in two different final states ($\mathrm{e}\mu$ and $\mu\tau$) obtained with the CMS detector at the LHC are interpreted in terms of BSM signals ranging from resonant sneutrino production in quark/antiquark annihilation in R-parity violating supersymmetry to quantum black hole production in theories with extra dimensions and top-loop-induced production of heavy scalars in two-Higgs-doublet models with cLFV. Secondly, the results obtained in this work are compared to those from other searches at the LHC, from searches at B-factories, and also from analyses of processes at significantly lower energies, such as searches for muon-to-electron conversion in heavy nuclei.

The rest of this introduction is dedicated to a more formal introduction to some important topics that have been mentioned without explanation or the quotation of references in the motivational outline given above. Furthermore, the structure of this thesis and a summary of contributions of the author to publications by the CMS collaboration related to this thesis are presented.

Lepton flavour violation in the neutrino sector

The following introduction to LFV in the neutrino sector and in interactions between charged leptons is partly based on Ref. [9].
The Lagrangian of the SM is invariant under global $U(1)_e \times U(1)_\mu \times U(1)_\tau$ transformations of the lepton fields if neutrinos are assumed to be massless. As a result, the three additive lepton flavour quantum numbers L_ℓ ($\ell \in \{e,\, \mu,\, \tau\}$), that are assigned the value $L_\ell = +1$ for the charged leptons and neutrinos of the respective flavour and the value $L_\ell = -1$ for the corresponding antiparticles, are conserved individually. The conservation of lepton number $L = L_e + L_\mu + L_\tau$ follows. In contrast to the conservation of electric charge for example, this invariance is not a direct result of a more fundamental underlying principle of the SM but an accidental symmetry of the SM Lagrangian.

The assumption that the individual lepton flavour numbers L_f are conserved passed decades of experimental tests successfully until neutrino experiments [1–3] established that L_f conservation is violated, whereas there is still no conclusive evidence for the violation of lepton number L. The wealth of information gathered on neutrino oscillations since their discovery can be explained in an extension of the aforementioned Lagrangian of the SM, in which some of the three known neutrinos have non-zero and different masses, and the flavour eigenstates of the neutrinos are non-trivial superpositions of the mass eigenstates. These superpositions are described by a unitary mixing matrix and neutrino oscillations are a mixing phenomenon that results from the non-trivial relation between the flavour eigenstates of the neutrinos that take part in the weak interactions and the mass eigenstates that determine the propagation of neutrinos in vacuum. This theoretical description does not explain the observed values of the parameters in the mixing matrix, nor does it provide an explanation for the origin of neutrino masses, their smallness, and the resulting violation of L_f conservation. Furthermore, the Lorentz structure of neutrino mass terms in the Lagrangian of the (extended) SM remains unknown; studies are ongoing to determine whether neutrinos are Dirac or Majorana fermions. The answer to this question is related to total lepton number conservation, which would be violated in case neutrinos are Majorana fermions.

In summary, the former paradigm of lepton flavour conservation (LFC) encoded in the Lagrangian of the SM is in contradiction with the observation of *lepton flavour violation* (LFV) in the neutrino sector and as a result searches for other LFV processes have become increasingly interesting.

Charged lepton flavour violation

In this thesis, searches for signals of physics beyond the SM that involve LFV in interactions of charged leptons, rather than in the neutrino sector, are considered. The corresponding field of study is that of *charged lepton flavour violation*, comprising the theoretical description and experimental searches for processes involving charged leptons that violate the individual lepton flavour numbers L_f. Reviews of theoretical aspects of cLFV include Refs. [8–10]. The status and prospects of experiments searching for cLFV are summarized in Refs. [11, 12]. Different types of processes are relevant for the study of cLFV, among them the flavour-changing neutral current (FCNC) interactions: $\ell \to \ell'\gamma$, $\ell \to \ell'\ell''\bar{\ell}'''$, $\ell + X \to \ell' + X$, $X \to \ell\bar{\ell}'\,(+Y)$, where $\ell'^{(\cdots)}$ denotes a charged lepton of different flavour than ℓ and both X and Y represent states that do not carry lepton number[3] [9]. They are examined in different types of experiments [11, 12]: LFV muon decays are searched for by dedicated experiments [13, 14], whereas detectors at B-factories are particularly suited to probe LFV decays of the τ lepton [15–18]; searches for muon-to-electron conversion in heavy nuclei [19] and various searches for LFV meson [20, 21] or Z boson [22, 23] decays are examples of processes involving non-leptonic probes.

The presence of LFV in the neutrino sector raises the question of SM contributions to the aforementioned cLFV processes via loops involving neutrinos. Such contributions are found to be extremely small as a result of generalizations of the GIM mechanism [24] from the quark sector to the neutrino sector: First, the contributions from massless virtual neutrinos or from mass-degenerate neutrinos vanish because of the unitarity of the neutrino mixing matrix. Secondly, the non-vanishing amplitude induced by non-zero neutrino mass differences is tiny due to their smallness in relation to the electroweak scale. Two examples are the SM branching fractions of the LFV decays of the Z boson, $\mathcal{B}(\mathrm{Z} \to \ell\bar{\ell}') \lesssim 10^{-54}$ [25], and the expected SM branching fraction for muon decays into an electron and a photon $\mathcal{B}(\mu \to \mathrm{e}\gamma) \lesssim 10^{-54}$ [9]. No conceivable, realistic experiment is capable of detecting these tiny SM contributions. Searches for cLFV signatures are therefore searches for physics beyond the SM. For most cLFV processes, the particles associated with hypothetical new physics inducing measurable cLFV rates are expected to have masses close to an energy scale Λ_{NP} that is much larger than the typical momentum transfer characterizing the interaction. An exception is the signature $X \to \ell\bar{\ell}'$, if the state X is a hitherto unknown particle of mass $M_X \sim \Lambda_{\mathrm{NP}}$.

Searches for cLFV at the LHC

Searches for cLFV at the LHC focus on signatures of the type $X \to \ell\bar{\ell}'\,(+Y)$, where the state X represents a meson [21], a neutral boson with a mass somewhat below the electroweak scale $v \approx 246$ GeV (Z, h^0) [22, 23, 26–29], or a hypothetical heavy new particle with mass $M_X \gtrsim v$ [30–32][4]. An exception are searches for the decay $\tau^\pm \to \mu^\pm\mu^+\mu^-$ [33, 34] that are challenging in the LHC environment but have shown the potential to compete with the corresponding searches at B-factories (in the case of the result in Ref. [33]).

Direct searches for cLFV pursued in this thesis

In this thesis, processes of the type $X \to \ell\bar{\ell}'$ are considered, where X corresponds to a heavy state ($M_X \gtrsim v$) with a short lifetime. In the models of new physics under study, the cLFV interactions are encoded in the classical Lagrangian, in contrast to the mentioned SM contributions to cLFV processes that arise at the quantum level. In this sense, the analyses described in the following are *direct searches* for physics beyond the SM with cLFV. Such searches are complementary to the abovementioned *indirect searches* for new physics, that look for the signatures of cLFV processes

---

[3] If X also carries lepton number, then the interaction $X \to \ell\bar{\ell}'$ does not only violate L_f but also lepton number L. This is the case for one of the signal models for new physics considered in this work, the RPV $\tilde{\nu}_\tau$ model introduced in Sec. 1.1.2.

[4] The references provided in this section only contain examples of the different types of searches. This list of references does not cover all publications on searches for cLFV processes by the LHC experiments.

at energy scales well below the expected energy scale of the underlying BSM physics.

In the eμ search, interactions between the first and the second generation of leptons, $X \to \mathrm{e}\mu$, are considered, whereas the second analysis, the $\mu\tau$ search, is designed to find signals for cLFV between the second and third generation, $X \to \mu\tau$. Both searches are performed in experimental final states involving an electron/muon pair, i.e. only the leptonic decay of the τ lepton $\tau^- \to \mathrm{e}^-\nu_\tau\bar{\nu}_e$ is considered in the search for the process $X \to \mu\tau$. From an experimentalist's point of view this $\mu\tau_\mathrm{e}$ search can be regarded as an extension or reformulation of the eμ search, whereas from a theorist's perspective the two searches probe very different types of BSM physics that are subject to different types of constraints from indirect searches for cLFV.

So far, the BSM physics behind the state X has not been specified apart from the requirement that X mediates an interaction between charged leptons of different flavour. In particular, the quantum numbers of X, its production mechanism in pp collisions, and the full experimental signature

$$\mathrm{pp} \to X + Y \to \ell\bar{\ell}' + Y \;, \tag{1}$$

that may involve additional particles Y, have not been chosen. The range of signatures that the searches are designed to cover is different in the eμ and $\mu\tau$ cases. They are chosen based on arguments related to the detection of the final state leptons.

Analysis strategy of the eμ search

In the eμ search, all leptons in the final state can be reconstructed with high efficiency as long as they fall into the geometrical acceptance of the detector. Furthermore, the four-momentum vectors of electrons and muons can be inferred from the measured detector signals with high precision, such that a four-momentum vector can be assigned to X as $p_X = p_\mathrm{e} + p_\mu$. The corresponding invariant mass $M_{\mathrm{e}\mu}$ is chosen as the key observable of the search. The presence of additional particles in the final state does not spoil the reconstruction of X as long as the effects of finite detector granularity and resolution are neglected. Additional particles Y may arise for example if X is produced in a decay chain rather than directly in an interaction with constituents of the protons in the initial state, or if it is produced in association with a second particle. Therefore, a very *inclusive* set of selection cuts is chosen by just requiring a reconstructed electron and a reconstructed muon in the event, while leaving the kinematics of the dilepton system largely unrestricted and including events with complex topologies. The design of the eμ search thus aims at a high selection efficiency for a large range of models of BSM physics and associated signatures and does not optimize the cuts in order to achieve maximal sensitivity to a specific model that would involve a customized background rejection. However, every attempt at formulating a *model-independent* search strategy for BSM physics at hadron colliders has shortcomings. The conditions that must be fulfilled by a given signal model including the signature $X \to \mathrm{e}\mu$ in order to be covered by the presented eμ search are summarized before the presentation of the event selection in Sec. 4.

Analysis strategy of the $\mu\tau$ search

The final state in the $\mu\tau_\mathrm{e}$ search contains a neutrino and an antineutrino from the decay of the τ lepton that cannot be detected by the CMS detector. Only the missing transverse momentum can be inferred from the measured particle momenta by invoking momentum conservation. If additional neutrinos or other weakly interacting particles are present in the final state, the missing transverse momentum cannot be assigned to the neutrinos from the τ decay. This motivates the focus of the search on the resonant production of particle X in pp collisions, that is reflected in an event selection with corresponding cuts on the kinematics of the $\mu\tau_\mathrm{e}$ system. Since the τ lepton receives a large Lorentz boost in the resonant production of a $\mu\tau$ pair with $M_{\mu\tau} \gtrsim v \gg m_\tau$, its four-momentum vector can be approximated from the measured missing transverse energy and the direction of the electron momentum vector using the so-called *collinear approximation* of the

τ decay. With the four-momentum vector from this pseudo-τ-lepton reconstruction in hand, the *collinear mass* $M_{\mu\tau}^{\text{coll}}$ of the $\mu\tau_{\text{e}}$ pair can be defined. It is the key observable in the $\mu\tau$ search.

Structure of this thesis

The thesis is divided into three parts. The first one contains information about the BSM models under study, hadron collider physics, the LHC and the CMS detector. It ought to be regarded as an overview of the essential ingredients needed for the two physics analyses described in the second and third part. The searches for new physics outlined in the second and third part of the thesis have been devised, planned, and executed by the author based on data taken with the CMS detector, a software framework written by others in the CMS collaboration, and knowledge shared by other physicists inside and outside of the CMS collaboration.

The three different parts of the thesis are structured as follows.

- *Part I: Aspects of BSM physics and experimentation at the LHC*
  - In Chapter 1, models of BSM physics are introduced that are used in the interpretation of the experimental results.
  - In Chapter 2, the LHC is briefly described with a focus on its design parameters and operation in the year 2012. Basics of high-p_{T} physics at hadron colliders are summarized and the corresponding nomenclature is introduced. Finally, the physics environment in which the CMS detector performs measurements is presented and the detector itself is described. The chapter is concluded with an overview of CMS data taking in 2012 and a summary of the datasets utilized in the eμ and $\mu\tau$ searches.
  - In Chapter 3, the reconstruction of physics objects that are used in the analyses described in this thesis, and the performance of the associated reconstruction algorithms are outlined. This includes a description of the utilized trigger algorithms.
- *Part II: A search for decays of heavy resonances and quantum black holes into an eμ pair in pp collisions at $\sqrt{s}$ =8 TeV*
  - In Chapter 4, the event selection of the eμ search is presented in detail and the choice of selection cuts is justified.
  - In Chapter 5, properties of the BSM signals introduced in Chapter 2, that are of particular importance to the eμ search, are presented with the aid of simulated Monte Carlo (MC) samples. The $M_{\text{e}\mu}$ spectra expected from signal contributions, the signal selection efficiency, and the $M_{\text{e}\mu}$ mass resolution obtained from simulated samples are discussed. The chapter concludes with a measurement of the muon p_{T} resolution in cosmic ray events detected with the CMS detector.
  - In Chapter 6, the SM background processes that are relevant in the eμ search (and later in the $\mu\tau_{\text{e}}$ search) are discussed. The corresponding cross sections at the LHC are given together with details about the production of simulated background samples. Data-driven methods that are used to obtain background estimates for processes involving jets that are misidentified as leptons are presented.
  - In Chapter 7, the background expectation for events passing the eμ event selection is compared to the observed data in control distributions of variables relevant to the eμ search.
  - In Chapter 8, the systematic uncertainties affecting the background and signal estimates are presented with focus on their impact on the respective $M_{\text{e}\mu}$ spectra.
  - In Chapter 9, the observable of interest in the eμ search, $M_{\text{e}\mu}$, is discussed in detail. To this end, the observed and expected $M_{\text{e}\mu}$ spectra are compared for different subsets of selected events. Finally, the $M_{\text{e}\mu}$ spectrum of all selected events is described.

  - Chapter 10 contains the interpretation of the experimental findings and is divided into two parts. In the first one, the utilized methods of statistical inference are introduced. Based on them, the agreement between the observed $M_{\mathrm{e}\mu}$ spectrum and the background expectation is quantified. The results are then interpreted in terms of the models of BSM physics introduced in Chapters 4 and 5 and compared to the results from other experiments.

- *Part III: A search for decays of heavy resonances into a $\mu\tau$ pair in pp collisions at $\sqrt{s}$ =8 TeV*

  - In Chapter 11, the transformation of the inclusive eμ search into a search for a heavy particle decaying into a $\mu\tau$ pair in the final state containing an electron, a muon, and missing transverse energy is described. Ingredients of the analysis such as the definition of the key observable of the search $M_{\mu\tau}^{\mathrm{coll}}$, data-driven cross checks of individual background components, and the signal selection efficiency are concisely introduced with recourse to the eμ search.
  - In Chapter 12, the background expectation for events passing the $\mu\tau_{\mathrm{e}}$ event selection are confronted with the data in distributions of various variables. The agreement between data and expectation in the $M_{\mu\tau}^{\mathrm{coll}}$ spectrum is discussed. The chapter concludes with the presentation of the systematic uncertainties affecting the background and signal estimates with focus on their impact on the respective $M_{\mu\tau}^{\mathrm{coll}}$ spectra.
  - Chapter 13 contains the statistical interpretation of the experimental findings and its implications for two different models of BSM physics with resonant production of $\mu\tau$ pairs in different initial states. Both the production via quark/antiquark annihilation and in the gluon-gluon initial state via a top-quark loop (heavy Higgs boson production) are considered. A model of BSM physics involving a heavy Higgs boson with cLFV decay to a $\mu\tau$ pair is introduced. Including this additional signal model connects this thesis to studies of extended Higgs sectors, that are of particular interest in the light of the discovery of a Higgs boson by the CMS and ATLAS [35] collaborations at the LHC in 2012 [36, 37].

Finally, the results obtained in this thesis are summarized and set in the wider context of searches for cLFV in the concluding remarks.

Contributions to CMS publications related to this thesis

The results of the eμ search presented in this work have partly been published before in a journal paper [30] and a *Physics Analysis Summary* (PAS) [38] by the CMS collaboration.

- CMS Collaboration,

  Search for lepton flavour violating decays of heavy resonances and quantum black holes to an eμ pair in proton-proton collisions at $\sqrt{s} = 8$ TeV,

  Eur. Phys. J. C 76 (2016) 317

- CMS Collaboration,

  Search for lepton flavour violating decays of heavy resonances and quantum black holes to eμ pairs in pp collisions at $\sqrt{s} = 8$ TeV,

  CMS-PAS-EXO-13-002 (2015)

In both instances, the author of this thesis has been the leading author of the publication. The Figures 9.3, 10.2 (left), and 10.9, as well as Table 9.1 have been originally produced by the author and are adopted here from the journal publication [30] with only minor modifications. For the same reason, several figures in this thesis are similar to those included in the CMS-internal documentation of the analysis in the form of an *Analysis Note* (AN) [39].

The results of the eμ search and other CMS searches for BSM physics in two-particle final states have been presented by the author in talks at international conferences on behalf of the CMS collaboration on three occasions.

- Phenomenology 2015 Symposium, Pittsburgh (USA)

  Searches for new physics in final states with an electron/muon pair at CMS

- 20th International Conference on Particles and Nuclei, Hamburg

  Searches for heavy resonances in two-particle final states with leptons, jets and photons at CMS

  Proceedings: *Searches for heavy resonances in two-particle final states with leptons, jets and photons at CMS*, CMS-CR-2014-281(2014)

- Phenomenology 2014 Symposium, Pittsburgh (USA)

  Search for massive resonances decaying to charged lepton pairs at CMS

Part I

Aspects of BSM physics and experimentation at the LHC

Chapter 1

Beyond the Standard Model

1.1 R-parity violating Supersymmetry and charged lepton flavour violation

1.1.1 Introduction

In supersymmetric models, an additional symmetry relating fermions and bosons is added to the Poincaré group. The generators of this symmetry satisfy a specific algebra of anticommutation relations, the supersymmetry algebra. In supersymmetric extensions of the SM, a *superpartner* is assigned to each SM degree of freedom. If Supersymmetry (SUSY) were unbroken, the SM particles and their superpartners would have the same mass. Despite the extensive experimental effort devoted to searches for superpartners, none have been found to date. If SUSY is realized in nature, it must therefore be a spontaneously broken symmetry. Introductions to SUSY and examples for the construction of supersymmetric models are presented for example in Refs. [40–42]. Supersymmetry[1] is regarded as one of the most promising theories of physics beyond the SM due to its implications for the so-called hierarchy problem [43–46], the unification of gauge couplings [47–49] and because it can provide dark matter candidates [50]. The most general renormalizable superpotential introduces interactions between scalar sparticles and ordinary quarks and leptons which violate both baryon number B and/or lepton number L. In many supersymmetric models these terms, many (combinations) of which are tightly constrained by experiment[2], are removed from the Lagrangian by asking for an additional $\mathbb{Z}_2$ symmetry, called R-parity. The multiplicative quantum number R assigned to ordinary particles and their supersymmetric counterparts, which is conserved by this symmetry, is given by [52]

$$\mathrm{R} = (-1)^{2S} (-1)^{3B+L} \quad , \tag{1.1}$$

where S denotes the particle spin. In particular, the requirement of R-parity conservation prohibits the combination of baryon and lepton number violating terms, that would lead to rapid proton decay[3].

In the following, the conservation of R-parity is not assumed and it will be replaced by a different discrete symmetry to prevent rapid proton decay. Allowing for R-parity violation (RPV) leads to a rich collider phenomenology that incorporates several signatures that are absent in SUSY model with R-parity conservation. Many aspects of RPV SUSY are covered in detail in Ref. [51], on which the following short introduction is based. The full set of R-parity violating (RPV) terms of

---

[1] The term *Supersymmetry* is used in the following for both the symmetry itself and the class of theories based on it.

[2] For a comprehensive review see [51]. Updated limits on lepton number violating couplings and their combinations that are relevant for the signal model under study are summarized in Sec. 1.1.3.

[3] R-parity conservation removes the lepton and baryon number violating terms from the renormalizable Lagrangian. However, it allows for dimension-five proton decay operators [53]. These dangerous operators can be cancelled by replacing R-parity, which is commonly used, with the proton-hexality symmetry [54].

the superpotential, W_{RPV} is given by [51]

$$W_{RPV} = \epsilon_{ab} \left[\frac{1}{2} \lambda_{ijk} L_i^a L_j^b \bar{E}_k + \lambda'_{ijk} L_i^a Q_j^{xb} \bar{D}_{kx} \right] - \epsilon_{ab}\ \kappa^i L_i^a H_u^b + \frac{1}{2} \epsilon_{xyz}\ \lambda''_{ijk} \bar{U}_i^x \bar{D}_j^y \bar{D}_k^z, \qquad (1.2)$$

where $i, j, k \in \{1, 2, 3\}$ are generation indices, $a, b \in \{1, 2\}$ are $SU(2)_L$ weak isospin indices and $x, y, z \in \{1, 2, 3\}$ denote the $SU(3)_C$ colour indices; L and Q are the $SU(2)_L$ doublet superfields of the lepton and quark, and $\bar{E}$, $\bar{U}$ and $\bar{D}$ denote the $SU(2)_L$ singlet superfields of the charged lepton, up- and down-like quark, respectively. H_u is one of two Higgs superfields, the one that provides mass to the u-type quarks. Summation over the generation and gauge indices in Eqn. 1.2 is implied.

The Yukawa couplings λ and λ' lead to interactions violating both lepton flavour and lepton number, whereas baryon number violation is introduced by the couplings λ''. The bilinear term with parameters κ_i mixes the lepton and Higgs superfields and violates lepton number. As a consequence of gauge invariance, the couplings λ_{ijk} and λ''_{ijk} are antisymmetric in the first and last two indices, respectively, and the corresponding terms in the superpotential introduce 9 free parameters each. The λ' terms come with 27 parameters and the three couplings κ_i complete the set of $2 \times 9 + 27 + 3 = 48$ parameters associated with the RPV superpotential in Eqn. 1.2. These parameters are a priori complex [51] but they are assumed to be real in the context of the simplified RPV SUSY signal model described below. Due to this large number of additional interactions and parameters, it is customary to adopt the dominant coupling scheme, i.e. assuming the couplings relevant for the analysis at hand are finite and all other couplings equal zero.

In order to account for the tight constraints from the measured lower limit on the proton lifetime on models with both lepton and baryon number violation, at least one of the sets of couplings leading to lepton or baryon number violation must only contain couplings that are extremely small. Therefore, the introduction of additional symmetries is motivated for the model building and study of the phenomenology. Apart from R-parity, other discrete symmetries are well motivated and have been studied in the literature. In this work, the baryon triality symmetry B_3 [54, 55] that cancels the baryon number violating terms with couplings λ'' is considered.

In Sec. 1.1.2, the superpotential Eqn. 1.2 is used to construct a signal model for resonant production of an $e\mu$ pair in proton-proton (pp) collisions. Similar models for the $\mu\tau$ and $e\tau$ final states are discussed in Sec. 1.1.4.

1.1.2 RPV SUSY signal model with resonant eμ production

The relevant aspects of RPV SUSY for the production of a resonance decaying into an electron/muon pair at hadron colliders are:

1. The single production of sparticles is allowed. In particular, sparticles can be produced resonantly.

2. The couplings λ'_{ijk} allow for the lepton number violating resonant production of a sneutrino $\tilde{\nu}_{iL}$ through the annihilation of a down-type quark d_j with generation index j and an antiquark $\overline{\mathrm{d}}_k$, and the production of an anti-sneutrino $\tilde{\nu}^*_{iL}$ in $\mathrm{d}_k\overline{\mathrm{d}}_j$ annihilation in hadron-hadron collisions.

3. The couplings λ_{i12} and λ_{i21} lead to a lepton number violating decay of a sneutrino into an eμ pair.

The simplified RPV signal model that is used as a benchmark model for the resonant production of an eμ pair in this work has the following parameters.

1. The tau sneutrino $\tilde{\nu}_{\tau L}$ (often abbreviated to $\tilde{\nu}_\tau$ in the following) is chosen as the resonantly produced slepton. It is a viable LSP candidate [56] and is assumed to be the LSP for

the simplified signal model[4]. In this case, only decays into SM particles are kinematically allowed. The corresponding model parameter is the tau sneutrino mass $M_{\tilde{\nu}_\tau}$.

2. The coupling λ'_{311} leads to the production of the tau sneutrino and the tau anti-sneutrino in $\mathrm{d\bar{d}}$ annihilation. In the following, the term tau sneutrino production (or tau sneutrino cross section $\sigma(\mathrm{pp} \to \tilde{\nu}_\tau)$) implies the sum of the tau sneutrino and tau anti-sneutrino production, unless explicitly stated otherwise. The $\tilde{\nu}_\tau$ production cross section for a given value of λ'_{3ii} at a pp collider is largest for the coupling to the first generation because of the PDF of the proton. According to 1.2, sneutrinos couple to the down-type quark/antiquark pairs only. Tau sneutrinos and tau anti-sneutrinos are produced with equal rates in $\mathrm{d\bar{d}}$ annihilation at pp colliders.

3. In order to obtain the $e\mu$ final state from the decay of the tau sneutrino, $\lambda_{312} = -\lambda_{132}$ and $\lambda_{321} = -\lambda_{231}$ are chosen as the two additional, independent couplings that are assumed to be non-zero. For simplicity, $\lambda_{312} = \lambda_{321}$ is assumed.

The thus defined simplified SUSY model with the parameters $M_{\tilde{\nu}_\tau}$, λ'_{311}, and $\lambda_{312} = \lambda_{321}$ is referred to as the *RPV $\tilde{\nu}_\tau$ model* in the following. The part of the Lagrangian that describes the RPV interactions of the $\tilde{\nu}_\tau$ with SM fermions in Dirac notation is given by [5]

$$\mathcal{L}^{\mathrm{LLE}}_{\mathrm{model}} \supset \quad -\frac{1}{2}\left(\lambda_{312}\; \tilde{\nu}_{\tau L}\bar{\mu}_R e_L + \lambda^*_{312}\; \bar{e}_L \mu_R \tilde{\nu}^*_{\tau L} - \lambda_{132}\; \tilde{\nu}_{\tau L}\bar{\mu}_R e_L - \lambda^*_{132}\; \bar{e}_L \mu_R \tilde{\nu}^*_{\tau L}\right) \tag{1.3}$$

$$-\frac{1}{2}\left(\lambda_{321}\; \tilde{\nu}_{\tau L}\bar{e}_R \mu_L + \lambda^*_{321}\; \bar{\mu}_L e_R \tilde{\nu}^*_{\tau L} - \lambda_{231}\; \tilde{\nu}_{\tau L}\bar{e}_R \mu_L - \lambda^*_{231}\; \bar{\mu}_L e_R \tilde{\nu}^*_{\tau L}\right) \tag{1.4}$$

$$\underset{\mathrm{Im}(\lambda)=0}{\overset{\lambda_{ijk}=-\lambda_{jik}}{=}} -\lambda_{312}\left(\tilde{\nu}_{\tau L}\bar{\mu}_R e_L + \bar{e}_L \mu_R \tilde{\nu}^*_{\tau L}\right) - \lambda_{321}\left(\tilde{\nu}_{\tau L}\bar{e}_R \mu_L + \bar{\mu}_L e_R \tilde{\nu}^*_{\tau L}\right) \tag{1.5}$$

$$\mathcal{L}^{\mathrm{LQD}}_{\mathrm{model}} \underset{\mathrm{Im}(\lambda')=0}{\supset} -\lambda'_{311}\left(\tilde{\nu}_{\tau L}\bar{d}_R d_L + \bar{d}_L d_R \tilde{\nu}^*_{\tau L}\right) \;, \tag{1.6}$$

where the superscript * denotes the complex conjugate of a complex scalar field, the $SU(3)_C$ gauge indices are suppressed, and the subscripts L and R on the fermion spinors imply application of the projection operators $\bar{e}_L \mu_R = \bar{e}\frac{1}{2}(1+\gamma_5)\mu$. In the simplified model defined above, the tau sneutrino can decay either into the final state under study, an $e^+\mu^-$ pair via the coupling λ_{312}, or an $e^-\mu^+$ pair via the Yukawa coupling λ_{321}; or into a $\mathrm{d\bar{d}}$ pair via the coupling λ'_{311}. The resulting relative decay width evaluated at leading order (LO) reads

$$\frac{\Gamma_{\tilde{\nu}_\tau}}{M_{\tilde{\nu}_\tau}} \underset{N_C=3}{=} \frac{1}{16\pi} \cdot \left(3(\lambda'_{311})^2 + (\lambda_{312})^2 + (\lambda_{321})^2\right) \;. \tag{1.7}$$

For couplings $\lambda'_{311}, \lambda_{312}, \lambda_{321} \lesssim 0.1$, the tau sneutrino decay width is more than two orders of magnitude smaller than its mass and off-shell production of the $\mathrm{e}\mu$ pair is small. The impact of finite-width effects on the signal cross section and their treatment in the $\mathrm{e}\mu$ search are described in Sec. 5.1.1. In the narrow width approximation, the dependence of the RPV $\tilde{\nu}_\tau$ signal cross

---

[4] The term LSP refers here to the lightest supersymmetric particle among those in the minimal supersymmetric extension of the SM (MSSM). This LSP is not stable in RPV SUSY and therefore no dark matter candidate. Additional sparticles such as the axino are still viable options.

[5] The derivation of the Lagrangian from the superpotential in Eqn. 1.2 is sketched in App. A.

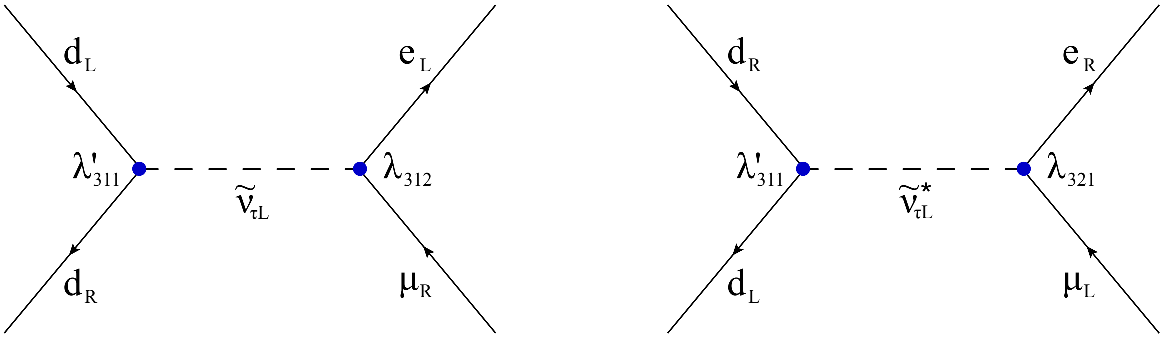

(a) $\tilde{\nu}_\tau$ production and decay into an $e^-\mu^+$ pair via the coupling λ_{312}.

(b) $\tilde{\nu}^*_\tau$ production and decay into an $e^-\mu^+$ pair via the coupling λ_{321}.

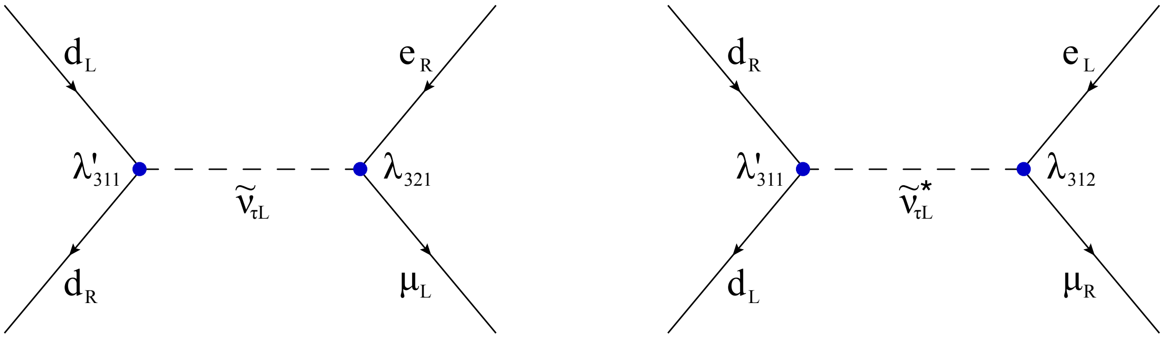

(c) $\tilde{\nu}_\tau$ production and decay into an $e^+\mu^-$ pair via the coupling λ_{321}.

(d) $\tilde{\nu}^*_\tau$ production and decay into an $e^+\mu^-$ pair via the coupling λ_{312}.

Figure 1.1: Amplitudes contributing to resonant tau sneutrino and anti-sneutrino production in $d\bar{d}$ annihilation and subsequent decay into an $e^\pm\mu^\mp$ pair.

section on the Yukawa couplings is given by the formula

$$\sigma(\mathrm{pp} \to \tilde{\nu}_\tau) \cdot \mathrm{BR}(\tilde{\nu}_\tau \to \mathrm{e}^\pm\mu^\mp) = \sigma(\mathrm{pp} \to \tilde{\nu}_\tau) \cdot \frac{(\lambda_{312})^2 + (\lambda_{321})^2}{3\left(\lambda'_{311}\right)^2 + (\lambda_{312})^2 + (\lambda_{321})^2} \tag{1.8}$$

$$\sim \left(\lambda'_{311}\right)^2 \frac{(\lambda_{312})^2 + (\lambda_{321})^2}{3\left(\lambda'_{311}\right)^2 + (\lambda_{312})^2 + (\lambda_{321})^2} \, . \tag{1.9}$$

The coupling pairs (λ'_{311}, λ_{312}) and (λ'_{311}, λ_{321}) each lead to the final states $e^+\mu^-$ and $e^-\mu^+$ with equal rates. Allowing only one of the two independent couplings λ_{312}, λ_{321} to be non-zero would not alter the analysis except for a reduction of the signal cross section according to Eqn. 1.8. For $\lambda'_{311} \gg \lambda_{312} = \lambda_{321}$, the dependence on λ'_{311} vanishes and an increase of this coupling does not result in an increased sensitivity to the signal. The production cross section increases but so does the branching ratio into the $\mathrm{d}\bar{\mathrm{d}}$ (dijet) final state which is not the subject of this analysis. For $\lambda'_{311} \ll \lambda_{312}$, the branching fraction of the $\tilde{\nu}_\tau$ decay into the $e\mu$ final state is close to unity and the sensitivity of the search only depends on the production cross section and λ'_{311}.

Tau sneutrino production cross section at next-to-leading order in perturbative QCD

The tau sneutrino production cross section $\sigma(\mathrm{pp} \to \tilde{\nu}_\tau)$ in Eqn. 1.8 is evaluated at next-to-leading order (NLO) in perturbative QCD (pQCD) for a centre-of-mass energy of $\sqrt{s} = 8$ TeV, based on calculations carried out in Ref. [57]. The NLO SUSY-QCD corrections are not taken into account, because their application would introduce an additional model dependence on the masses of the contributing squarks and gluinos. Effectively, the omission of the higher-order SUSY-QCD correction means that these masses are assumed to be very heavy. The NLO cross sections in Fig. 1.2 are obtained with the coupling fixed to $\lambda'_{311} = 0.01$ at all scales; the running of the renormalized Yukawa coupling at order α_s is not taken into account. Figure 1.2 also contains the ratio of the NLO to LO cross section for $\tilde{\nu}_\tau$ production, referred to as the LO-to-NLO *k-factor*. The PDF set CTEQ6M is used in the determination of the NLO cross section, whereas the LO cross section is calculated using the CTEQ6L1 set [58].

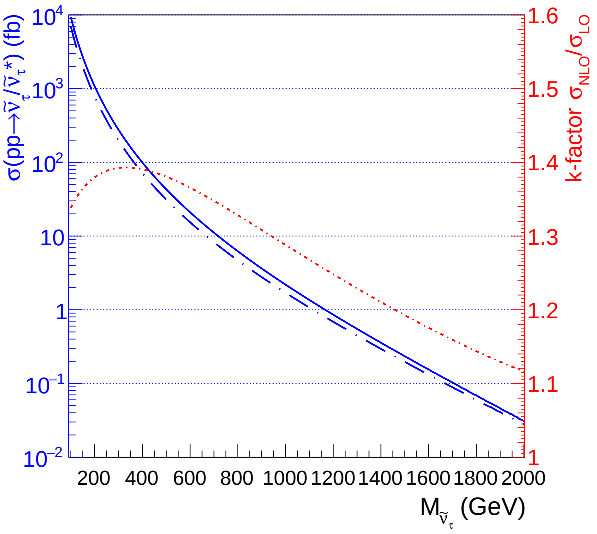

Figure 1.2: Blue: Sum of the $\tilde{\nu}_\tau$ and $\tilde{\nu}_\tau^*$ production cross sections in pp collisions at $\sqrt{s} = 8$ TeV evaluated at LO (blue, dashed) and at NLO in pQCD (blue, solid) as a function of $M_{\tilde{\nu}_\tau}$ for the production coupling $\lambda'_{311} = 0.01$. Red: Corresponding ratio of the NLO cross section to the LO cross section, called the k-factor.

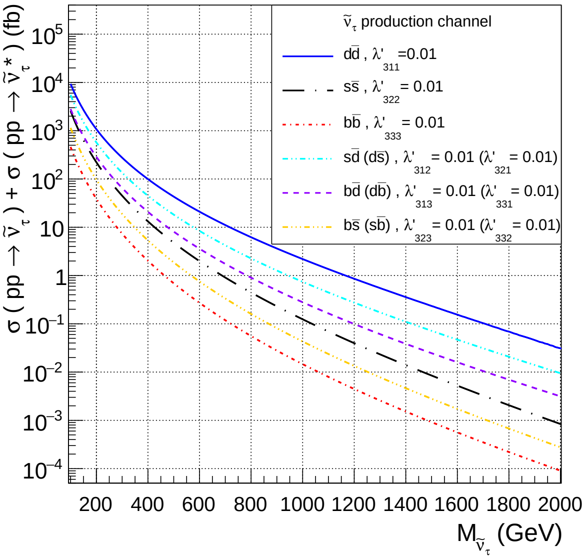

Figure 1.3: Sum of the $\tilde{\nu}_\tau$ and $\tilde{\nu}_\tau^*$ production cross sections in pp collisions at $\sqrt{s} = 8$ TeV at NLO in pQCD as a function of $M_{\tilde{\nu}_\tau}$ for different quark/antiquark initial states. The corresponding RPV production couplings λ'_{3jk} are set to 0.01.

The benchmark RPV $\tilde{\nu}_\tau$ model with its $\mathrm{d}\overline{\mathrm{d}}$ initial state and $\tilde{\nu}_\tau$ production coupling λ'_{311} can be varied by considering a different initial state $\mathrm{d}_k\overline{\mathrm{d}}_j$ with a corresponding non-zero Yukawa coupling λ'_{3jk}. The dependence of the $\tilde{\nu}_\tau$ production cross section in pp collisions at $\sqrt{s} = 8$ TeV on the quark flavour in the initial state is shown in Fig. 1.3 for $\lambda'_{3jk} = 0.01$. The large difference in the cross sections for different initial states reflects the difference in the respective parton luminosities. All cross sections in Fig. 1.3 will be used in the context of a recast of the eμ search with the RPV $\tilde{\nu}_\tau$ benchmark model, that is presented in Sec. 10.2.2.

1.1.3 Bounds on the RPV signal model with $e\mu$ final state from existing searches

Direct searches at high-energy colliders

This summary of exclusion limits on the RPV $\tilde{\nu}_\tau$ benchmark model from searches at hadron colliders presents the status at the time of the publication of parts of this work in Refs. [30, 38]. Direct searches for $\tilde{\nu}_\tau$ production with subsequent decay into the $e\mu$ final state have been carried out by the CDF [59] and D0 [60] collaborations in proton-antiproton collisions at $\sqrt{s} = 1.96$ TeV at the Tevatron, using datasets with integrated luminosities of 1.0 fb^{-1} and 5.3 fb^{-1}, respectively. For $M_{\tilde{\nu}_\tau} = 100$ GeV and $\lambda_{312} = \lambda_{321} = 0.07$, the search by D0 excludes couplings $\lambda'_{311} > 6.2 \cdot 10^{-4}$ at 95% confidence level (CL). At the LHC, the ATLAS collaboration has carried out searches for resonances in the $e\mu$ invariant mass spectrum in pp collisions at both $\sqrt{s} = 7$ TeV [61–63] and $\sqrt{s} = 8$ TeV [31]. The most stringent bounds from direct searches at high-energy colliders for sneutrino masses $M_{\tilde{\nu}_\tau} \gtrsim 500$ GeV stem from the ATLAS search at $\sqrt{s} = 8$ TeV with a dataset corresponding to an integrated luminosity of 20.3 fb^{-1}. For couplings $\lambda'_{311} = 0.11$ and $\lambda_{312} = \lambda_{321} = 0.07$[6], tau sneutrino masses $M_{\tilde{\nu}_\tau} < 2.0$ TeV are excluded at 95% CL.

Indirect constraints from low-energy experiments

Searches for lepton flavour violating muon-to-electron conversion in muonic atoms are sensitive to new particles that mediate between the charged leptons of the first and second generation and couple to quarks. Muons that stop in matter form muonic atoms in excited states, which decay electromagnetically into the ground state. The process under study is the conversion

$$\mu^- N(A, Z) \rightarrow e^- N(A, Z) \ , \tag{1.10}$$

where A denotes the mass number and Z is the atomic number of the used nucleus N. The experimental signature of this process would be a delayed electron, which is emitted at the kinematical endpoint for bound muon decay, that depends on the target material. The most stringent bounds on the branching ratio for the ground state transition defined as

$$\mathcal{B}\left(\mu^- N \rightarrow e^- N\right) = \frac{\Gamma\left(\mu^- N \rightarrow e^- N\right)}{\Gamma\left(\mu^- N \text{ capture}\right)} \tag{1.11}$$

have been obtained with the SINDRUM II spectrometer at PSI for the target materials titanium [64] (and references therein) and gold [19]. At 90% CL these limits are given by

$$\mathcal{B}\left(\mu^- \mathrm{Ti} \rightarrow e^- \mathrm{Ti}\right) \ < \ 6.1 \cdot 10^{-13} \tag{1.12}$$

$$\mathcal{B}\left(\mu^- \mathrm{Au} \rightarrow e^- \mathrm{Au}\right) \ < \ 7.0 \cdot 10^{-13} \ . \tag{1.13}$$

The RPV $\tilde{\nu}_\tau$ model defined above involves tree-level contributions to the process 1.10 mediated by the tau sneutrino and the bounds 1.12 and 1.13 can thus be translated into its parameter space.

---

[6] The ATLAS paper [31] states the exclusion limits for the benchmark couplings $\lambda'_{311} = 0.11$ and $\lambda_{312} = 0.07$. The author of this work can reproduce the reported signal cross section times branching ratio for $\lambda'_{311} = 0.11$ and $\lambda_{312} = \lambda_{321} = 0.07$.

Based on the SINDRUM II limit on $\mathcal{B}\left(\mu^{-}\mathrm{Au} \to e^{-}\mathrm{Au}\right)$, coupling products $|\lambda'_{311}\lambda_{312}| < 3.3 \cdot 10^{-7}(M_{\tilde{\nu}_\tau}/\mathrm{TeV})^2$ are excluded at 90% CL [65], and the bound on $\mathcal{B}\left(\mu^{-}\mathrm{Ti} \to e^{-}\mathrm{Ti}\right)$ yields $|\lambda'_{311}\lambda_{312}| < 8.2 \cdot 10^{-9}$ for slepton and squark masses of 100 GeV [64] [7]. As pointed out in [64], the contribution of the strange quark sea of the nucleon is comparable to the valence quarks, and the muon conversion searches thus also constrain the coupling product $|\lambda'_{322}\lambda_{312}|$. In Ref. [66], the interpretation is extended further to b-quark mediated muon-to-electron conversion, yielding bounds on the coupling product $|\lambda'_{333}\lambda_{312}|$.
The upper limits on products of RPV couplings $|\lambda'_{3ii}\lambda_{312}|$ derived from the non-observation of muon-to-electron conversion in muonic atoms are summarized in Tab. 1.1.

coupling product	upper bound in units of $(M_{\tilde{\nu}_\tau}/\mathrm{TeV})^2$
$\lvert\lambda'_{311}\lambda_{312}\rvert$	$3.3 \cdot 10^{-7}$ [65]
$\lvert\lambda'_{322}\lambda_{312}\rvert$	$1.5 \cdot 10^{-6}$ [64]
$\lvert\lambda'_{333}\lambda_{312}\rvert$	$1.7 \cdot 10^{-4}$ [66]

Table 1.1: Summary of upper bounds on the RPV coupling products $|\lambda'_{3ii}\lambda_{312}|$ at 90% CL. The same bounds apply to the couplings $|\lambda'_{3ii}\lambda_{321}|$.

As outlined in Refs. [67, 68], constraints from muonium conversion arise when both RPV couplings λ_{312} and λ_{321} are non-zero. In this case, the electromagnetic bound state muonium $M \equiv \mu^{+}e^{-}$ can convert into antimuonium $\overline{M} \equiv \mu^{-}e^{+}$ via $\tilde{\nu}_\tau$ exchange. Using the most restrictive bounds on the coupling $G_{M\overline{M}}$ in the effective four-lepton Lagrangian given in Ref. [69], and the formula relating it to the RPV couplings from Ref. [68]

$$\frac{G_{M\overline{M}}}{\sqrt{2}} = \frac{|\lambda_{312}\lambda_{321}|}{8M^2_{\tilde{\nu}_\tau}}\ , \tag{1.14}$$

an upper limit of $|\lambda_{312}\lambda_{321}| < 2.3 \cdot 10^{-1}(M_{\tilde{\nu}_\tau}/\mathrm{TeV})^2$ at 90% CL is derived[8].

Apart from the mentioned bounds from dedicated searches for cLFV between leptons of the first and second generation, limits on various RPV coupling products $|\lambda'_{3jk}\lambda_{312}|$ and $|\lambda'_{3jk}\lambda_{321}|$ have been obtained from searches for cLFV meson decays. These are included in the context of the reinterpretation of the eμ search with the RPV $\tilde{\nu}_\tau$ benchmark model, that is presented in Sec. 10.2.2.

1.1.4 RPV SUSY signal models with $\mu\tau$ or $e\tau$ final states

By changing the non-zero couplings involved in the leptonic decay of the $\tilde{\nu}_\tau$, the signal model described in Sec. 1.1.2 can be adapted to cover final states with resonantly produced lepton pairs other than the eμ final state discussed above. In the context of cLFV interactions two additional experimental signatures are of interest: the $\mu\tau$ and $e\tau$ final states. The former is induced by a non-zero coupling $\lambda_{323} = -\lambda_{233}$ and the latter by a non-zero value of $\lambda_{313} = -\lambda_{133}$. Note that in both cases only two RPV λ couplings are involved (one independent coupling), in contrast to a total of four couplings in the $e\mu$ signal model (two independent couplings). This difference can be traced back to gauge invariance under $SU(2)_L$, enforcing $\lambda_{332} = \lambda_{331} = 0$, as shown in App. A.

---

[7] The bounds in the Ref. [64–66] have been multiplied with a factor 2 in order to match the form of the LLE term in the RPV superpotential in [64, 65] to Eqn. 1.2.

[8] In Ref. [69], a bound of $|\lambda_{312}\lambda_{321}| < 3 \cdot 10^{-4}$ at 90% CL is given for superpartner masses of 100 GeV without a definition of the model or superpotential used and referring to a private communication. Ref. [68], which examines the signal model used in this work, quotes a limit of $|\lambda_{312}\lambda_{321}| < 6.3 \cdot 10^{-1}(M_{\tilde{\nu}_\tau}/\mathrm{TeV})^2$ at 90% CL based on a different measurement.

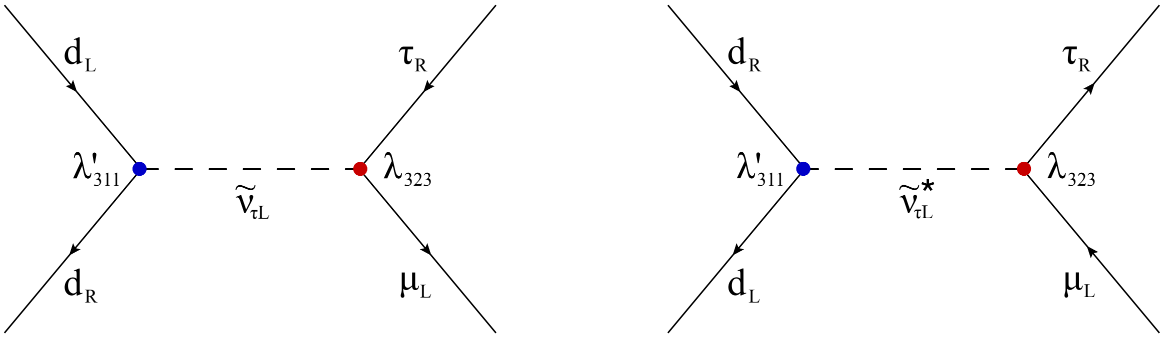

(a) $\tilde{\nu}_\tau$ production and decay into an $\mu^-\tau^+$ pair via the coupling λ_{323}.

(b) $\tilde{\nu}^*_\tau$ production and decay into an $\mu^+\tau^-$ pair via the coupling λ_{323}.

Figure 1.4: Amplitudes contributing to resonant tau sneutrino production in $d\bar{d}$ *annihilation and subsequent decay into a* $\mu^\mp\tau^\pm$ *pair.*

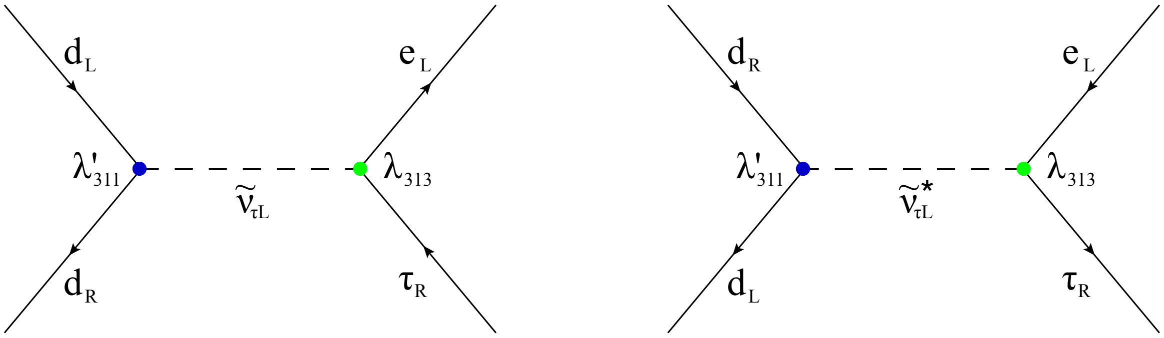

(a) $\tilde{\nu}_\tau$ production and decay into an $e^-\tau^+$ pair via the coupling λ_{313}.

(b) $\tilde{\nu}^*_\tau$ production and decay into an $e^+\tau^-$ pair via the coupling λ_{313}.

Figure 1.5: Amplitudes contributing to resonant tau sneutrino production in $d\bar{d}$ *annihilation and subsequent decay into a* $e^\mp\tau^\pm$ *pair.*

The processes contributing to the $\mu\tau$ and $e\tau$ final states are depicted in Figures 1.4 and 1.5, respectively. The total decay width of the $\tilde{\nu}_\tau$ and its production cross section times branching fraction depend on the non-zero RPV couplings as

$$\frac{\Gamma_{\tilde{\nu}_\tau}}{M_{\tilde{\nu}_\tau}} = \frac{1}{16\pi} \cdot \left(3(\lambda'_{311})^2 + (\lambda_{3j3})^2\right) \tag{1.15}$$

$$\sigma(\mathrm{pp} \to \tilde{\nu}_\tau) \cdot \mathrm{BR}(\tilde{\nu}_\tau \to \ell_j^\mp \tau^\pm) \sim \left(\lambda'_{311}\right)^2 \frac{(\lambda_{3j3})^2}{3\left(\lambda'_{311}\right)^2 + (\lambda_{3j3})^2}\,, \tag{1.16}$$

with $j = 2$ in the $\mu\tau$ signal model and $j = 1$ in the $e\tau$ case. Since the $\tilde{\nu}_\tau$ production mechanism is the same as in the $e\mu$ model and narrow resonances are considered, the NLO/LO k-factors for the signal cross section derived in Sec. 1.1.2 apply to the $\mu\tau$ and $e\tau$ signal models as well.

1.1.5 Bounds on the RPV signal model with $\mu\tau$ or $e\tau$ final state from existing searches

Direct searches at high-energy colliders

Searches for $\mu\tau$ and eτ resonances in proton-antiproton collisions at $\sqrt{s} = 1.96$ TeV have been reported by the CDF collaboration in Ref. [59] based on a dataset corresponding to an integrated luminosity of 1.0 fb^{-1}. For the coupling parameters $\lambda'_{311} = 0.1$ and $\lambda_{323} = 0.05$ ($\lambda_{313} = 0.05$), lower limits of $M_{\tilde{\nu}_\tau} = 441$ GeV ($M_{\tilde{\nu}_\tau} = 442$ GeV) are set in the $\mu\tau$ (eτ) channel at 95% CL. The ATLAS collaboration has carried out searches for resonances in the $\mu\tau$ and eτ mass spectra in pp collisions at both $\sqrt{s} = 7$ TeV [63] and $\sqrt{s} = 8$ TeV [31]. The most stringent bounds from direct searches at high-energy colliders for sneutrino masses $M_{\tilde{\nu}_\tau} \gtrsim 500$ GeV stem from the ATLAS search at $\sqrt{s} = 8$ TeV with a dataset corresponding to an integrated luminosity of 20.3 fb^{-1}. For couplings $\lambda'_{311} = 0.11$ and $\lambda_{323} = 0.07$ ($\lambda_{313} = 0.07$), the lower bound on the tau sneutrino mass in the $\mu\tau$ (eτ) channel reads $M_{\tilde{\nu}_\tau} = 1.7$ TeV ($M_{\tilde{\nu}_\tau} = 1.7$ TeV) at 95% CL.

Indirect constraints from low-energy experiments

The very stringent bounds on products of RPV couplings from muon conversion in heavy nuclei discussed in Sec. 1.1.3, which are relevant for cLFV between the first and second generation, do not apply to the $\mu\tau$ and $e\tau$ signal models. In these cases, the indirect bounds to consider arise from searches for cLFV, semileptonic τ decays. As reported in Ref. [68], the tightest limits on the coupling products $|\lambda'_{3ii}\lambda_{323}|$ and $|\lambda'_{3ii}\lambda_{313}|$ ($i \in \{1, 2\}$) are obtained from bounds on the branching fractions of the processes $\tau \to \mu\eta$ and $\tau \to e\eta$, respectively, that have been obtained at B-factories. As summarized in Ref. [70], both the BaBar [71] and Belle [72] collaborations have published bounds on the branching ratios of these τ decay modes based on ditau event candidates in datasets of about 400 fb^{-1} each, recorded around the $\Upsilon(4S)$ resonance. The Belle analysis has been updated to a dataset of about 900 fb^{-1} [70]. The resulting bounds on the $\tau \to \mu\eta$ and $\tau \to e\eta$ branching fractions are summarized in Tab. 1.2. Using these latest experimental bounds, the limits on the coupling products $|\lambda'_{3ii}\lambda_{323}|$ and $|\lambda'_{3ii}\lambda_{313}|$ ($i \in \{1, 2\}$) are recalculated for this work, based on formulae derived in Ref. [68]. The results are given in Tab. 1.2. The branching ratios of the two τ decays under study are related to the RPV couplings and $M_{\tilde{\nu}_\tau}$ by

$$\mathcal{B}(\tau \to \mu\eta) = \frac{1}{32\pi}\frac{M_\tau}{\Gamma_\tau}\left(\frac{f_\pi M_\eta^2}{4\sqrt{3}M_d}\right)^2\left(\frac{|\lambda'_{311}\lambda_{323}|}{M_{\tilde{\nu}_\tau}^2}\right)^2 \quad , \quad \Big(\text{for } \lambda'_{322} = 0\Big) \tag{1.17}$$

$$\Rightarrow |\lambda'_{311}\lambda_{323}| \approx 13.5 \cdot \sqrt{\mathcal{B}(\tau \to \mu\eta)}\left(\frac{M_{\tilde{\nu}_\tau}}{\text{TeV}}\right)^2 \tag{1.18}$$

$$\mathcal{B}(\tau \to \mu\eta) = \frac{1}{32\pi}\frac{M_\tau}{\Gamma_\tau}\left(\frac{2f_\pi M_\eta^2}{4\sqrt{3}M_s}\right)^2\left(\frac{|\lambda'_{322}\lambda_{323}|}{M_{\tilde{\nu}_\tau}^2}\right)^2 \quad , \quad \Big(\text{for } \lambda'_{311} = 0\Big) \tag{1.19}$$

$$\mathcal{B}(\tau \to e\eta) = \frac{1}{32\pi}\frac{M_\tau}{\Gamma_\tau}\left(\frac{f_\pi M_\eta^2}{4\sqrt{3}M_d}\right)^2\left(\frac{|\lambda'_{311}\lambda_{313}|}{M_{\tilde{\nu}_\tau}^2}\right)^2 \quad , \quad \Big(\text{for } \lambda'_{322} = 0\Big) \tag{1.20}$$

$$\mathcal{B}(\tau \to e\eta) = \frac{1}{32\pi}\frac{M_\tau}{\Gamma_\tau}\left(\frac{2f_\pi M_\eta^2}{4\sqrt{3}M_s}\right)^2\left(\frac{|\lambda'_{322}\lambda_{313}|}{M_{\tilde{\nu}_\tau}^2}\right)^2 \quad , \quad \Big(\text{for } \lambda'_{311} = 0\Big) \tag{1.21}$$

where M_τ and Γ_τ denote the measured τ mass and decay width; f_π is the pseudo scalar meson decay constant; M_η is the mass of the η meson; and M_d, M_s are the current-quark masses of the d- and s-quark, respectively[9].

---

[9] In this calculation, the parameters $M_\tau = 1.77682 \pm 0.00016$ GeV ; $\tau_\tau = (290.3 \pm 0.5) \times 10^{-15}$ s ; $M_\eta = 547.862 \pm 0.018$ MeV ; $M_d = 4.8^{+0.5}_{-0.3}$ MeV and $M_s = 95 \pm 5$ MeV are taken from Ref. [5], and $f_\pi = 93$ MeV is extracted from Ref. [68]. The values for the current-quark masses used here differ significantly from those used in Ref. [68] (from 1997), $M_d = 10$ MeV and $M_s = 200$ MeV. Ref. [73] from 1996 contains $M_d = 5 - 15$ MeV and $M_s = 100 - 300$ MeV.

search	channel	upper limit BR ($\times 10^{-8}$)	upper limit RPV couplings in units of $(M_{\tilde{\nu}_\tau}/\mathrm{TeV})^2$
BABAR 2007 [71]	$\tau \to \mu\eta$	15	$\lvert\lambda'_{311}\lambda_{323}\rvert < 5.2 \cdot 10^{-3}$
			$\lvert\lambda'_{322}\lambda_{323}\rvert < 5.2 \cdot 10^{-2}$
	$\tau \to e\eta$	16	$\lvert\lambda'_{311}\lambda_{313}\rvert < 5.4 \cdot 10^{-3}$
			$\lvert\lambda'_{322}\lambda_{313}\rvert < 5.3 \cdot 10^{-2}$
BELLE 2007 [72]	$\tau \to \mu\eta$	6.5	$\lvert\lambda'_{311}\lambda_{323}\rvert < 3.4 \cdot 10^{-3}$
			$\lvert\lambda'_{322}\lambda_{323}\rvert < 3.4 \cdot 10^{-2}$
	$\tau \to e\eta$	9.2	$\lvert\lambda'_{311}\lambda_{313}\rvert < 4.1 \cdot 10^{-3}$
			$\lvert\lambda'_{322}\lambda_{313}\rvert < 4.0 \cdot 10^{-2}$
BELLE 2010 [70]	$\tau \to \mu\eta$	2.3	$\lvert\lambda'_{311}\lambda_{323}\rvert < 2.0 \cdot 10^{-3}$
			$\lvert\lambda'_{322}\lambda_{323}\rvert < 2.0 \cdot 10^{-2}$
	$\tau \to e\eta$	4.4	$\lvert\lambda'_{311}\lambda_{313}\rvert < 2.8 \cdot 10^{-3}$
			$\lvert\lambda'_{322}\lambda_{313}\rvert < 2.8 \cdot 10^{-2}$

Table 1.2: Summary of searches for cLFV, semileptonic tau decays at B-factories. The bounds on the branching ratios are defined at 90% CL and translated into upper limits on the RPV couplings using Eqns. 1.17-1.21 based on Ref. [68].

1.2 Quantum black hole production at the LHC

1.2.1 Introduction

This summary of physics beyond the SM involving black hole production at the LHC is based on the following journal papers and review articles: The possibility of producing microscopic black holes at high-energy colliders at the TeV scale was first studied in Refs. [74–76]. The main references used for this outline are Refs. [5, 77, 78], the underlying frameworks with gravity at the TeV scale are described in Refs. [79–83], and details about quantum black hole production at the LHC are covered in Refs. [84–86].

Models of new physics with a fundamental Planck scale M_D around one TeV can provide solutions to the hierarchy problem, or at least reformulate it. Such theoretical frameworks typically require the introduction of one or more additional spatial dimensions and involve effects of quantum gravity that might be observable at the LHC, such as the production of microscopic black holes. In the *transplanckian regime*, $\sqrt{s} \gg M_\mathrm{D}$, predictions can be based on a semiclassical description [5]: Black holes form when the impact parameter in a collision is smaller than the Schwarzschild radius r_S, and the cross section for black hole production is estimated to be of the order of $\sigma \sim \pi r_S^2$. The semiclassical black holes thus produced are thermal objects and their decays are described by Hawking radiation. Searches for thermal black hole decays into multiparticle final states have been carried out at the LHC by the CMS [87, 88] and ATLAS [89, 90] collaborations, setting limits on M_D in the multi-TeV range. Given that their production requires a momentum transfer of the order of several fundamental Planck scales M_D, it is unlikely that thermal black holes will occur at the LHC in large numbers if M_D is of order several TeV [77].

Quantum black holes (QBHs) differ from their semiclassical counterparts in several aspects: They are expected to be produced at center-of-mass energies close to the fundamental Planck scale and decay into a few particles, in particular two-particle final states [85]. In the following, the cross section for QBH production is extrapolated from the semiclassical case[10], and the mass spectrum of QBHs is assumed to be continuous, with a threshold mass for QBH production M_th [11]. It is further assumed that the entire fraction of the center-of-mass energy carried by the two incoming partons, $\sqrt{\hat{s}}$, is available in the formation of the black hole. The effects of possible inelasticity described in [77] are neglected. A QBH with mass $M_\mathrm{QBH} = \sqrt{\hat{s}}$ can then form for $M_\mathrm{QBH} \geq M_\mathrm{th}$ and the partonic cross section for QBH production in interactions of the incoming partons i and j is given by

$$\hat{\sigma}^{ij}_\mathrm{QBH}\left(\sqrt{\hat{s}} = \sqrt{x_i x_j}\sqrt{s}, n, M_\mathrm{D}, M_\mathrm{th}\right) = \pi r_s^2\left(\sqrt{\hat{s}}, n, M_\mathrm{D}\right) \cdot \theta\left(\sqrt{\hat{s}} - M_\mathrm{th}\right) , \qquad (1.22)$$

where x_i and x_j denote the momentum fractions carried by the respective partons, and n is the number of spatial extra dimensions in the underlying model of TeV-scale quantum gravity. Basic aspects of some of these models are discussed next. Since the details of quantum black hole formation are not known, the chosen signal models may be regarded as benchmarks that provide different cross sections for QBH production. The following short introductions to the different models aim at a complete definition of the respective QBH production cross sections and the parameters involved therein, rather than introductions to the underlying frameworks, their purpose, or collider phenomenology.

1.2.2 Theoretical frameworks with quantum gravity in the TeV regime

Three different models of physics beyond the SM with a fundamental Planck scale in the TeV range are considered in the following, each of which is associated with a different number or range

---

[10] Note that in the regime $\sqrt{s} \sim M_\mathrm{D}$, semiclassical predictions can receive large modifications due to the details of quantum gravity, which are not yet known.

[11] It has been argued that the mass spectrum of non-thermal black holes might be quantized in terms of the Planck scale M_D [84]. The experimental signature of such QBHs decaying into the eμ final state would be given by several well-separated peaks in the eμ mass distribution smeared out by the detector resolution. This signature is covered by the search for narrow eμ resonances described in Secs. 4-10.

of spatial extra dimensions n.

1. **$n = 0$: Renormalization of Newton's constant from a large hidden sector**

   The running of Newton's constant $G(\mu)$ with the energy scale μ can receive large contributions from a hidden sector with many light degrees of freedom that couple to the SM only gravitationally [79]. Newton's constant $G = M_{Pl}^{-2}$ is measured in low-energy experiments, probing the laws of gravity down to distance scales of $\sim 100\ \mu$m [91] that correspond to an energy of $\mathcal{O}(10^{-3}$ eV). In this domaine, the effective Planck mass is known to be of order $M_{Pl}(\mu \lesssim 10^{-3}\text{ eV}) \sim 10^{19}$ GeV. In a scenario with a hidden sector including N light scalars or Weyl fermions that contribute to the running of G, the measured value $G(\mu = 0)$ can be related to Newton's constant at higher energy scales, $G(\mu)$ [79] according to

   $$\frac{1}{G(\mu)} = \frac{1}{G(0)} - N\frac{\mu^2}{12\pi} \tag{1.23}$$

   $$\Rightarrow M_{Pl}^2(\mu) = M_{Pl}^2(0) - N\frac{\mu^2}{12\pi}\ . \tag{1.24}$$

   A Planck scale in the TeV range, $M_{Pl}(\mu = 1\text{ TeV}) \sim 1$ TeV, can thus be obtained for $N \sim 10^{33}$ light degrees of freedom in the hidden sector, without requiring extra dimensions. QBHs may then be produced in the flat Minkowski space-time of this framework with Schwarzschild radius [92]

   $$r_s = \frac{1}{4\pi}\frac{M_{\text{QBH}}}{M_{Pl}^2(\mu)}\ . \tag{1.25}$$

2. **$n = 1$: The RS model with a warped extra dimension**

   In the Randall-Sundrum (RS1) model [80, 81] with a single compact extra dimension, the metric

   $$ds^2 = e^{-2kr_c|\phi|}\eta_{\mu\nu}dx^\mu dx^\nu + r_c^2 d\phi^2 \tag{1.26}$$

   is considered, that describes a five-dimensional anti-deSitter (AdS$_5$) space-time and provides solutions to the field equations of general relativity. In the metric Eqn. 1.26, $0 \leq \phi \leq \pi$ denotes the coordinate along the compact, warped dimension with radius r_c and k is related to the AdS$_5$ curvature. The apparent weakness of gravity is explained by considering two branes, 3+1-dimensional subspaces of the five-dimensional AdS$_5$ space-time, separated along the compact dimension: Gravity originates on the Planck brane at $\phi = 0$ and the wave function of the graviton falls off exponentially along the fifth dimension towards the TeV brane at $\phi = \pi$. The SM fields are confined to this TeV brane. The Planck scale on the TeV brane in the higher-dimensional theory, $M_5 \sim \overline{M}_{Pl} = M_{Pl}/\sqrt{8\pi}$, is related to the scale of physical masses $\tilde{M}$ by an exponential warp factor:

   $$\tilde{M} = e^{-kr_c\pi}M_5\ . \tag{1.27}$$

   $\tilde{M}$ sets the mass scale for Kaluza-Klein (KK) modes of the graviton and their couplings to SM particles of order $1/\tilde{M}$, as well as the mass scale for the production of QBHs. Requiring $kr_c \approx 12$ bridges the gap of 15 orders of magnitude between one TeV and the reduced Planck scale $\overline{M}_{Pl}$, without introducing new large hierarchies between the model parameters.

   In contrast to black holes in flat Minkowski space-time, the warping of the extra dimension in the RS1 case allows for different types of solutions for black holes, depending on the relation between the Schwarzschild radius and the curvature parameter k. In the following the case $r_s \ll 1/(ke^{-kr_c})$ is considered that involves black holes which can be treated approximately as their counterparts in flat five-dimensional space-time with Schwarzschild radius [77]

   $$r_s = \frac{1}{\sqrt{3}\pi}\left(\frac{M_{\text{QBH}}}{\tilde{M}^3}\right)^{\frac{1}{2}}\ . \tag{1.28}$$

The RS1 model allows for the production of both black holes and KK resonances. These two sectors of the model's phenomenology are related. In particular, the five-dimensional Planck scale multiplied with the warp factor, $\tilde{M}$, that enters the QBH Schwarzschild radius (Eqn. 1.28) is related to the mass of the first KK excitation of the graviton, M_1, via [77]:

$$\tilde{M} = \frac{M_1}{3.83 \cdot \left(k/\overline{M}_{Pl}\right)^{\frac{2}{3}}} \ . \tag{1.29}$$

3. **$n \geq 2$: The ADD model of large extra dimensions**

The Arkani-Hamed–Dimopoulos–Dvali (ADD) framework [82, 83] features a fundamental scale for gravity in the TeV range by means of compactified extra spatial dimensions, which are required to be large with a compactification radius $r_c \gg 1/M_{Pl} \sim 10^{-35}$ m . The SM fields are confined to a four-dimensional brane, whereas the graviton can propagate in the entire $4+n$-dimensional bulk space. The wave function of the graviton is spread out over the volume V_n of the n-dimensional compact manifold and the strength of the gravitational interaction on the brane is thereby diluted. Under the assumption that all extra dimensions have the same compactification radius and are compactified on a torus, the fundamental $4+n$-dimensional Planck scale M_D is related to the apparent Planck scale $M_{Pl} = 1/\sqrt{G}$ measured by an observer on the brane for distances $r \gg r_c$ by

$$M_{Pl}^2 = V_n M_D^{n+2} = 8\pi r_c^n M_D^{n+2} \ . \tag{1.30}$$

Requiring $M_D = 1$ TeV yields $r_c = 10^{12}$ m for $n = 1$, which is excluded by the observation of a $1/r$ gravitational potential in our solar system, $n = 2$ leads to $r_c = 10^{-4}$ m and is strongly disfavored by measurements of the gravitational potential down to distance scales of $\mathcal{O}(100\ \mu\text{m})$ [91], whereas for $n = 6$ with $r_c = 10^{-14}$ m it is up to experiments at high-energy colliders to probe the ADD model.

In the ADD framework $4+n$-dimensional black holes may be produced in high-energy collisions for energies $\sqrt{\hat{s}} \gtrsim M_D$. Small black holes with a Schwarzschild radius much smaller than the compactification radius can be described by the Schwarzschild solution in $4+n$-dimensional flat Minkowski space-time [78] with the Schwarzschild radius given by [92]

$$r_s = \frac{1}{M_D}\left(\frac{2^n \pi^{(n-3)/2}}{n+2}\Gamma\left(\frac{n+3}{2}\right)\frac{M_{\text{QBH}}}{M_D}\right)^{\frac{1}{n+1}} \ , \tag{1.31}$$

where Γ denotes the gamma function. The dependence of the partonic cross section as defined in Eqn. 1.22 on the model parameters is then given by

$$\hat{\sigma}^{ij}_{\text{QBH}}\left(M_{\text{QBH}}, n, M_{\text{D}}, M_{\text{th}}\right) = \frac{\pi}{M_D^2}\left(\frac{2^n \pi^{(n-3)/2}}{n+2}\Gamma\left(\frac{n+3}{2}\right)\frac{M_{\text{QBH}}}{M_D}\right)^{\frac{2}{n+1}} \theta\left(M_{\text{QBH}} - M_{\text{th}}\right) \ . \tag{1.32}$$

1.2.3 The quantum black hole signal model

Due to our lack of knowledge of quantum gravity, the symmetries governing the interactions of QBHs are not known and one has to rely on the semiclassical extrapolation for the cross section calculation. Given these unknowns, the simplified model proposed in Ref. [93] is adopted, which considers the production of electrically neutral and scalar QBHs in quark/antiquark annihilation. In this approach, the production of fermion pairs at the LHC via the formation of a QBH is described by a four-fermion contact interaction with the generic Lagrangian

$$\mathcal{L}_{\text{cont}} = \frac{g_{\text{cont}}}{\Lambda^2}\bar{\psi}_a \psi_b \bar{\psi}_i \psi_j \ . \tag{1.33}$$

The indices a and b denote the incoming quark flavours, i and j stand for the fermions in the final state, g_{cont} is a dimensionless coupling constant and Λ the energy scale of the interaction. Assuming that gravitational interactions become strong ($g_{\text{cont}} = 1$) at the fundamental Planck scale ($\Lambda = M_D$) this Lagrangian reproduces the semiclassical cross section of QBH production for $n = 0$. The dependence on the number of extra dimensions in the RS and ADD frameworks can be introduced by a simple form factor given in Ref. [93]. This model neglects the formation of a QBH in initial states involving gluons, in particular the process gg $\rightarrow$ QBH $\rightarrow \ell^+\ell^-$. This omission is motivated because the parton luminosities of the quark-antiquark initial states are higher than that of the gluon-gluon initial state for $\sqrt{\hat{s}} \sim \mathcal{O}(\text{TeV})$ at the $\sqrt{s} = 8$ TeV LHC, which is the most promising energy regime for the QBH search in the light of existing constraints.

In the considered signal model, the gauge symmetries of the SM are assumed to be conserved but quark flavour violation and LFV are allowed. The quantum number B–L is assumed to be conserved. Therefore, quark-antiquark initial states with different quark flavour contribute to the QBH production, and the QBH can decay into all flavour permutations of the $q_a\bar{q}_b$, $\ell_i^+\ell_j^-$ and $\nu_i\bar{\nu}_j$ final states. The total number of final states, $N_{\text{dof}}^{\text{QBH}}$, is

$$N_{\text{dof}}^{\text{QBH}} = 3 \cdot \left(N_C^2 N_{\text{F}}^{\text{quarks}} + N_{\text{F}}^{\text{leptons}}\right) = 3 \cdot 6 \cdot \left(N_C^2 + 1\right) = 180 \ . \tag{1.34}$$

For QBH masses well above twice the top quark mass, the branching fraction of the QBH decay into the $\mathrm{e}^{\pm}\mu^{\mp}$ final state is $N_{\text{dof}}^{\text{QBH}}(\text{QBH} \rightarrow \mathrm{e}^{\pm}\mu^{\mp})/N_{\text{dof}}^{\text{QBH}} = 2/180 \approx 1.1\%$, twice that of the e^+e^- or $\mu^+\mu^-$ final states, making it the most promising leptonic decay channel for QBH searches.

1.2.4 Bounds from quantum black hole searches at high-energy colliders

Since the symmetries governing the QBH interaction are not known, searches for QBH production make different assumptions in the definition of the signal models and QBH production cross sections. This complicates the comparison of their results, which is particularly relevant for the search presented in this work with the uncommon requirement of LFV.

There have been direct searches of QBHs decaying hadronically by the CMS [94–96] and ATLAS [97,98] collaborations. As in the discussion of the existing bounds on the RPV $\tilde{\nu}_\tau$ model, this summary presents the status of limits on QBH models at the time of the publication of parts of this work in Refs. [30,38]. CMS sets limits on the threshold mass M_{th} in the dijet final state for a fixed fundamental Planck scale $M_D = 1$–5 TeV and fixed number of extra dimensions $n = 1$–6. For $n = 6$ and $M_D = 5$ TeV a lower bound of $M_{\text{th}} = 5.8$ TeV is obtained at 95% CL [95]. The corresponding ATLAS search assumes $M_{\text{th}} = M_D$ and sets a lower limit of $M_{\text{th}} = 5.66$ TeV [97]. The ATLAS collaboration has also searched for QBH production in pp collisions in the photon plus jet, lepton plus jet, dimuon and dielectron final states [99–102]. In the analysis of high-mass lepton plus jet events, a lower bound of $M_{\text{th}} = M_D = 5.3$ TeV for $n = 6$ is obtained [101].

Regarding the QBH search in the eμ final state, which is part of this thesis, the ATLAS search at $\sqrt{s} = 8$ TeV in the dilepton final state is of particular interest. The model considered in the ATLAS paper assumes conservation of both lepton and quark flavour. The combination of the $\mu\mu$ and ee final states analyzed then leads to a lower mass limit of $M_{\text{th}} = \tilde{M} = 2.24$ TeV for the RS case with $n = 1$, and $M_{\text{th}} = M_D = 3.65$ TeV for ADD-type QBHs with $n = 6$.

Chapter 2

The CMS detector at the LHC

2.1 Physics at hadron colliders and the LHC

This section serves two purposes. First, the Large Hadron Collider (LHC) is introduced as a proton-proton (pp) accelerator and collider in Sec. 2.1.1 with focus on the key physics parameters and the performance of the collider in the year 2012. Second, basics of hadron collider physics are summarized in Sec. 2.1.2. The combination of these two topics leads to the description of the physics environment in which the high-luminosity detectors at the LHC perform measurements, that is given in Sec. 2.1.3. The stage is then set for the description of the CMS detector in Sec. 2.2.

2.1.1 The LHC at CERN

The LHC is a superconducting hadron collider that accelerates protons or lead ions in two rings. It is situated in a 26.7 km long tunnel and provides collisions to the ALICE [103], ATLAS [35], CMS [6], and LHCb [104] detectors at four interaction points. The two rings of the accelerator are housed in a single ring of superconducting magnets with twin-bore design[1]. The LHC is described in Ref. [7] and in more detail in Refs [105–107]. Since the beginning of its operation in November 2009, it has delivered proton-proton, lead-lead, and proton-lead collisions at different centre-of-mass energies $\sqrt{s}$. The LHC has been designed to reach a nominal beam energy of 7 TeV for protons (2.76 TeV per nucleon for lead ions) and a corresponding centre-of-mass energy of $\sqrt{s} = 14$ TeV for pp collisions. The nominal peak instantaneous luminosity (the instantaneous luminosity reached at the beginning of data taking during a fill of the LHC, before the beam intensity slowly decreases[2]) for pp operation is $\mathcal{L} = 10^{34}\mathrm{cm}^{-2}\mathrm{s}^{-1}$.

The LHC accelerator is the final stage of a chain of accelerators. It includes a linear accelerator at the first stage, followed by the four rings of the Proton Synchrotron Booster (PSB), and the Proton Synchrotron (PS) from which proton bunches are ejected at an energy of 25 GeV into the Super Proton Synchrotron (SPS). The protons are then accelerated to an energy of 450 GeV before injection into the LHC. The maximum beam energy achievable at the final acceleration stage in the LHC rings depends mainly on the magnetic field of the LHC superconducting dipole magnets and on the distance along which the beam is exposed to it. Therefore, the dipole magnets are briefly described in the following paragraph. Other crucial parts of the LHC such as the multipole magnets; the 400 MHz RF system used for acceleration; or the vacuum, cryogenic, or powering systems are not covered here. Instead, a focus is put on the resulting LHC performance parameters that are presented in Tab. 2.1 in the context of the discussion of the LHC luminosity.

---

[1] Not all superconducting LHC magnets have two bores, but the vast majority of them does.

[2] The luminosity lifetime in *stable beams* is studied for LHC fills in 2012 in Ref. [108]. Therein, the luminosity lifetime is found to be dominated by intensity losses to luminosity and collimation rather than emittance growth.

LHC beam energy and superconducting dipole magnets

The LHC is equipped with 1232 dipole magnets with a length of about 15 m each, corresponding to a total length of more than two thirds of the tunnel's circumference. Inside the two bores of the dipole magnets, uniform magnetic fields with a nominal maximum magnetic flux density of 8.33 T are provided by dipoles made of Rutherford-style cables with Niobium-Titanium (NbTi) acting as the superconductor. The two poles around each bore consist of coils wound in two layers.

The beam energy is ramped up after injection from 450 GeV to the nominal 7 TeV by increasing the electric current from about 0.76 kA (resulting in a magnetic field of 0.54 T) to 11.7 kA. The two bores and the coils are surrounded by rigid, non-magnetic collars that provide mechanical stability. Outside this structure, the magnetic field lines are returned in an iron yoke. This entire structure forms the 27.5 t cold mass of a dipole magnet and is cooled down to a temperature of 1.9 K using superfluid helium. The orientation of the magnetic field lines inside a dipole in the plane perpendicular to the directions of the two beams are shown in Fig. 2.1 [105].

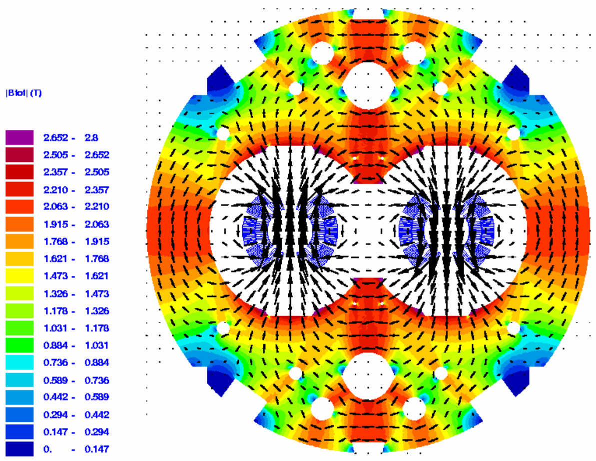

Figure 2.1: Cross section of the magnetic field inside of an LHC dipole magnet in the plane perpendicular to the directions of the two beams: Absolute value of the magnetic flux density $|B|$ inside the iron yoke of the dipole (colour code), and the orientation of the magnetic field lines in the dipole cold mass (arrows). The figure is taken from Ref. [105].

LHC luminosity

Under the assumptions of round beams in the plane perpendicular to the beams and equal values of the amplitude function β for both beams, the instantaneous luminosity per interaction point is given by [7]

$$\mathcal{L} = \frac{N_{\mathrm{b}}^{2} k_{\mathrm{b}} f_{\mathrm{rev}} \gamma_{\mathrm{p}}}{4\pi \epsilon_{\mathrm{n}} \beta^{*}} F\left(\theta_{\mathrm{c}}\right) \ , \tag{2.1}$$

where N_{b} is the number of protons per bunch (the bunch intensity), k_{b} is the number of colliding bunches per beam, f_{rev} is the revolution frequency, γ_{p} is the ratio of beam energy and proton mass, $\epsilon_{\mathrm{n}} = \beta_{\mathrm{p}}\gamma_{\mathrm{p}}\epsilon$ denotes the normalized transverse emittance, and β^{*} denotes the value of the amplitude function β at the interaction point (IP). The factor $F(\theta_{\mathrm{c}})$ equals unity if the two beams collide head-on, and accounts for the reduction of the luminosity caused by a finite crossing angle of the two beams θ_{c} at the IP, otherwise. The nominal values of these parameters are given in Tab. 2.1. They have been set in the context of the LHC design as long-term goals to be achieved after a few years of operation of the accelerator.

Table 2.1: Comparison of the nominal LHC parameters [7, 109, 110] to those used for pp operation of the collider in 2012. The latter have been used in LHC fill 3347, for which the highest instantaneous luminosity of any fill in 2012 with stable beams has been measured. The values have been taken from Ref. [111] and apply to the CMS interaction point.

LHC parameter	Nominal value	Value reference fill 3347 2012 LHC pp operation
Beam (proton) energy (TeV)	7	4
Current dipole magnets (kA)	11.7	6.7
Number of bunches n_b	2808	1374
Colliding bunch pairs k_b	-	1368
Bunch intensity N_b ($\times 10^{11}$)	1.15	1.6
Bunch spacing (ns)	25	50
Normalized emittance ϵ_n at beginning of fill (mm × mrad)	3.75	2.56
β^* (m)	0.55	0.6
Crossing angle θ_c (μrad)	285	290
Peak instantaneous luminosity ($\times 10^{34}$ cm^{-2}s^{-1})	1.0	0.77
Stored beam energy (MJ)	362	141

LHC operation in the year 2012

This summary of the LHC operation in 2012 is based on Ref. [109]. In the description of the LHC presented above, the targeted (nominal) performance has been used as a benchmark. The year 2012 has been the first year that saw luminosity production as the main goal of LHC operation, after 2010 and 2011 had been largely devoted to commissioning, ensuring the readiness of the machine protection system, and then slowly improving the performance of the collider. Hence, the key LHC performance parameters that have been achieved in 2012 differ from the nominal LHC parameters; the two sets are compared in Tab 2.1, where the settings of the LHC fill number 3347, that provided the highest instantaneous luminosity [111], are used as the benchmark for operation in 2012.

In 2012, the proton beam energy is 4 TeV, corresponding to a pp centre-of-mass energy of 8 TeV. According to Eqn. 2.1, this smaller than nominal proton energy implies a smaller than nominal luminosity via the factor γ_p that is related to the larger emittance ϵ at lower energies. Furthermore, the number of bunches per beam for 2012 operation is 1374, about half of the nominal 2808, with a bunch spacing of 50 ns instead of 25 ns. The reduction in luminosity caused by these choices is largely compensated by the larger than nominal (140%) bunch intensities, due to the N_b^2-dependence of the luminosity. Furthermore, the nominal emittance ϵ_n is smaller than anticipated by about 30%. A main reason for these improvements over the anticipated performance is the high beam quality of the accelerator chain prior to injection into the LHC [109]. At the IPs of the high-luminosity experiments CMS and ATLAS, the beams are collimated to a β^* of 0.6 m with a crossing angle close to the nominal value. As a result, a peak instantaneous luminosity of 0.77×10^{34} cm^{-2}s^{-1} is achieved although the total energy stored per beam is smaller than the nominal value by more than a factor of two. The downside of the high bunch intensities is a larger number of pp collisions per bunch crossing (*pileup*), as will be explained in the following sections.

About 200 days of LHC operation have been dedicated to pp physics in 2012. *Stable beams* that allow the experiments at the IPs to run safely and take high-quality data have been provided by the LHC during 36% of this time. The resulting integrated luminosity $L_{\mathrm{int}} = \int \mathcal{L}\mathrm{d}t$ for pp collisions at $\sqrt{s} = 8$ TeV delivered to the IP of the CMS experiment amounts to 23.3 fb^{-1} [112].

2.1.2 Fundamentals of hadron collider physics

This summary of fundamental hadron collider physics is based on Refs. [113–117]. The covered topics are chosen in order to briefly introduce some concepts and terminology that are used without further explanation throughout this work.

Hadrons are bound states of the strong interaction, which is described by quantum chromodynamics (QCD) in terms of a relativistic quantum field theory. The substructure of hadrons results in features of hadronic collisions that differ from those of collisions at lepton colliders. At a momentum transfer Q well above the QCD confinement scale $\Lambda_{\mathrm{QCD}} \approx 200$ MeV, the strong coupling constant α_S is in the perturbative regime and the substructure of the hadrons can be resolved; meaning that interactions can be divided into a *hard interaction* between one constituent (or *parton*) per colliding hadron, and the *underlying event* that consists of the processes involving the hadron remnants. Most physics analyses at hadron colliders discuss a certain class of hard interactions between two partons in the initial state. Some key properties of the hard interaction in hadronic collisions at colliders like the LHC are summarized in the following.

- Various combinations of two partons are possible in the initial state. Both fermions (quarks and antiquarks of five flavours) and bosons (gluons, photons) are present.
- The partonic centre-of-mass energy $\sqrt{\hat{s}}$ is smaller than the centre-of-mass energy of the hadronic collision, and varies from event to event. Hence, hadron colliders provide a broad-band (parton) energy distribution in the hard interaction.
- The centre-of-mass of the colliding-hadron system and the laboratory frame of reference at the interaction point coincide, whereas the centre-of-mass of the colliding-parton system can exhibit a significant boost relative to the laboratory frame of reference along the beam axis. This is reflected in the set of coordinates that is chosen to parameterize single-particle phase space, and in further kinematic variables used in the physics analyses.

All of these features of hadronic collisions inform choices made in the presented search for *narrow* dilepton resonances in a *wide* range of dilepton *invariant mass*. Such resonances arise in various theoretical models of physics beyond the SM that suggest *different initial states* for the process under study.

Phase space and coordinates at hadron colliders

To motivate and introduce the most common choice of coordinates in hadron collider physics, the behaviour of the four elements of a particle's four-momentum vector $p^\nu = (E, p_x, p_y, p_z)$ under a Lorentz boost along the beam axis $\hat{z}$ is considered. Using these coordinates, the Lorentz-invariant single-particle phase space volume $\mathrm{d}\tau$ reads:

$$\mathrm{d}\tau = \frac{\mathrm{d}^3 p}{2(2\pi)^3 E} = \frac{\mathrm{d}p_x \mathrm{d}p_y \mathrm{d}p_z}{2(2\pi)^3 E} \ . \tag{2.2}$$

The coordinates p_x and p_y are invariant under a Lorentz boost along $\hat{z}$, whereas the non-trivial behaviour of p_z and E under such transformations masks the Lorentz-invariance of $\mathrm{d}\tau$. It is therefore convenient to choose a different set of coordinates that leads to a manifestly invariant expression of single-particle phase space volume. The set $\{m, p_\mathrm{T}, \phi, y\}$ with the Lorentz-invariant particle mass m; two coordinates that are defined in the $x-y$ plane perpendicular to the beam (the so-called *transverse plane*), the transverse momentum p_T and azimuthal angle ϕ; and the rapidity $y \equiv \frac{1}{2}\ln\frac{E+p_z}{E-p_z}$ fulfills this requirement. Under a Lorentz boost γ_b along $\hat{z}$, the rapidity receives an additional constant contribution $y \to y + \ln(\gamma_\mathrm{b}(1+\beta_\mathrm{b}))$, such that the rapidity difference $\mathrm{d}y$ is invariant, as is the phase space volume [114]

$$\mathrm{d}\tau = \frac{\mathrm{d}^3 p}{2(2\pi)^3 E} = \frac{p_\mathrm{T}\mathrm{d}p_\mathrm{T}\mathrm{d}\phi\mathrm{d}y}{2(2\pi)^3} \; . \tag{2.3}$$

According to this parameterization of single-particle phase space, final state particles are uniformly distributed in rapidity as long as the dependence of the matrix element on the rapidity is small. This leads to the so-called *rapidity plateau* in the differential cross section $\mathrm{d}\sigma/\mathrm{d}y$ at large polar angle θ that is measured relative to the beam axis $\hat{z}$.

A particle's rapidity depends both on its velocity β and polar angle θ. The pseudorapidity η defined as $\eta \equiv -\ln\tan(\theta/2)$ does not depend on β and is therefore frequently used in experimental particle physics, where particle velocities are often not measured. In the massless limit $\beta \to 1$, the pseudorapidity and rapidity values are equal. A commonly used measure of the distance between two particle trajectories is $\Delta R = \sqrt{(\Delta\eta)^2 + (\Delta\phi)^2}$. Cones in $\eta - \phi$ space of size R are used below to define particle isolation criteria; the scalar p_T sum of other particles that fall in the isolation cone around the particle of interest ($\Delta R \leq R$) must not exceed a predefined value or the particle is regarded as non-isolated.

By analogy with the transverse momentum, the transverse energy E_T is defined as the projection of the momentum vector onto the transverse plane, scaled by the ratio of measured energy to momentum E/p. Another important quantity at hadron colliders is the so-called *missing transverse energy* $\not{E}_\mathrm{T}$. The transverse momentum of the protons in the initial state is close to zero. Therefore, the transverse component of the vector sum of all particle momenta in the final state has to be zero according to conservation of momentum. Particles that are not detected in the LHC experiments, such as neutrinos, carry off unmeasured transverse momentum. The resulting imbalance in the transverse momenta, $\vec{\not{E}}_\mathrm{T} \equiv -\sum \vec{p}_\mathrm{T}$ with absolute value $|\vec{\not{E}}_\mathrm{T}|$, can be used to infer the presence of one or several such particles in the final state. In contrast to the other quantities introduced in this paragraph, which are defined for each particle, the missing transverse energy is assigned to an entire event that may consist of several pp collisions.

Hadronic cross sections and parton distribution functions

The relation between the hadronic cross section for a given process at a pp collider $\sigma(\sqrt{s})$ and the short-distance cross section $\hat{\sigma}(\sqrt{\hat{s}})$ of the hard interaction[3] is discussed next. The two partons in the initial state, denoted i and j, carry momentum fractions x_1 and x_2 of the colliding protons with momenta P_1 and P_2 along the beam axis (the beam energy). The resulting partonic centre-of-mass energy is $\sqrt{\hat{s}} = \sqrt{x_1 x_2 s}$.

In the following, a pp collision with the production of a certain final state Y in the hard interaction between two partons is considered, $\mathrm{p} + \mathrm{p} \to Y + X$. Here, X stands for the additional particles in the final state, including the proton remnants. The differential pp cross section can be factorized [118, 119] into a short-distance part, that corresponds in the parton model to the hard interaction ($Q \gg \Lambda_\mathrm{QCD}$) between the partons, and a long-distance part, that incorporates the information about the proton substructure via the *parton distribution functions* (PDFs) of the proton $f_k(x, \mu_\mathrm{F}^2)$ for the individual partons [113]:

---

[3] At leading order, the short-distance cross section of the hard cross section is equal to the corresponding partonic cross section [113].

$$\begin{aligned}\sigma\left(\mathrm{p}(P_1)+\mathrm{p}(P_2)\to Y+X\right) &= \int_0^1 \mathrm{d}x_1 \int_0^1 \mathrm{d}x_2 \sum_{(i,j)} f_i\left(x_1,\mu_\mathrm{F}^2\right) f_j\left(x_2,\mu_\mathrm{F}^2\right) \times \\ &\qquad \hat{\sigma}_{(i,j)}\left(i(x_1P_1)+j(x_2P_2)\to Y;\ \alpha_S(\mu_\mathrm{R}^2),\ \frac{Q^2}{\mu_\mathrm{F}^2},\ \frac{Q^2}{\mu_\mathrm{R}^2}\right) .\end{aligned} \tag{2.4}$$

The sum on the right hand side of Eqn. 2.4 runs over all partonic initial states (i,j) that contribute to the cross section. The energies μ_F and μ_R denote the factorization scale and the renormalization scale, respectively. Only the short-distance interaction can be calculated in perturbative QCD (pQCD). The dependence of the PDFs on the factorization scale μ_F can be determined via the DGLAP equations [120–122], but the dependence on the parton momentum fraction x has to be obtained from data. How the current understanding of QCD and experimental efforts are combined to yield proton PDFs is reviewed in Ref. [117], that includes a short description of the most commonly used PDF sets. In the following, aspects of the proton PDFs are discussed only for partons with color charge. The proton structure functions for photons are covered in Ref. [123], but they are not important to the analysis presented in this work. The extension of the concept of proton PDFs to the electroweak gauge bosons W and Z is not relevant at the LHC, where these bosons can be regarded as heavy particles, but it would be relevant at future pp colliders with higher centre-of-mass energy [124].

The quantity $xf_k(x,\mu_\mathrm{F}^2)$ obtained from the MSTW 2008 NLO [125] proton PDF set is shown in Fig. 2.2 (left) as a function of x at a fixed factorization scale $\mu_\mathrm{F}=100$ GeV, corresponding roughly to the electroweak scale. At values of the parton momentum fraction $x\lesssim 0.05$, the gluon PDF dominates (it is scaled down by a factor 0.1 in the figure), and the valence quarks q_V that determine the quantum numbers of the proton yield the largest contributions for $x\gtrsim 0.1$. At pp colliders such as the LHC, hadronic cross sections are in general not invariant under the transformation $q_\mathrm{V}\leftrightarrow\bar{q}_\mathrm{V}$. Apart from the top quark, all quark flavours contribute to the set of initial state configurations at the LHC. For pp colliders with even higher energy $\sqrt{\hat{s}}\sim 100$ TeV, the introduction of a proton PDF for the top quark is being considered [124].

It is instructive to introduce the differential parton luminosity $\mathrm{d}^2L_{ij}/\mathrm{d}\hat{s}\mathrm{d}y$ in the master formula for the hadronic cross section Eqn. 2.4 by using the relation $\mathrm{d}x_1\mathrm{d}x_2=\mathrm{d}\hat{s}\mathrm{d}y/s$:

$$\begin{aligned}\sigma(s) &= \sum_{(i,j)}\int \mathrm{d}\hat{s}\int \mathrm{d}y\left(\frac{\mathrm{d}^2L_{ij}}{\mathrm{d}\hat{s}\mathrm{d}y}\right)\hat{\sigma}_{(i,j)}(\hat{s})\ , \qquad \text{with} \\ \frac{\mathrm{d}^2L_{ij}}{\mathrm{d}\hat{s}\mathrm{d}y} &= \frac{1}{s(1+\delta_{ij})}\left(f_i(x_1,\mu_\mathrm{F}^2)f_j(x_2,\mu_\mathrm{F}^2)+(1\to 2)\right)\ ,\end{aligned} \tag{2.5}$$

and its integral with respect to the rapidity of the partonic subprocess $y=\frac{1}{2}\ln(x_1/x_2)$, the *parton luminosity* $\mathrm{d}L_{ij}/\mathrm{d}\hat{s}$. The parton luminosity yields the hadronic cross section for the production of a particle Y with mass M_Y in the s-channel, if the short-distance cross section corresponds to the trivial case $\hat{\sigma}(\hat{s})=\delta(\hat{s}-M_Y^2)$. It is helpful for the comparison of hadronic cross sections of processes that have a similar structure of the partonic cross section but different initial states (see Fig. 1.3). The comparison of the parton luminosities for gg and $q\bar{q}$ initial states in Fig. 2.2 (right) exemplifies the importance of initial states with gluons at the LHC. For $\sqrt{s}=8$ TeV, the parton luminosity of the gg initial state exceeds that of the $q\bar{q}$ initial states by at least one order of magnitude for final state masses up to about twice the mass of the top quark, $M_Y\lesssim 2m_\mathrm{t}$. Due to the dominance of the valence quark PDFs at high x, the sum of the parton luminosities for $q\bar{q}$ initial states surpasses that for the gg case at $M_Y\sim 1$ TeV. The gq initial states are not included in Fig. 2.2 because they are not as relevant for the signal and leading background processes in this work. However, it is noted that they yield the largest parton luminosities of any parton combination over a wide mass range at the LHC.

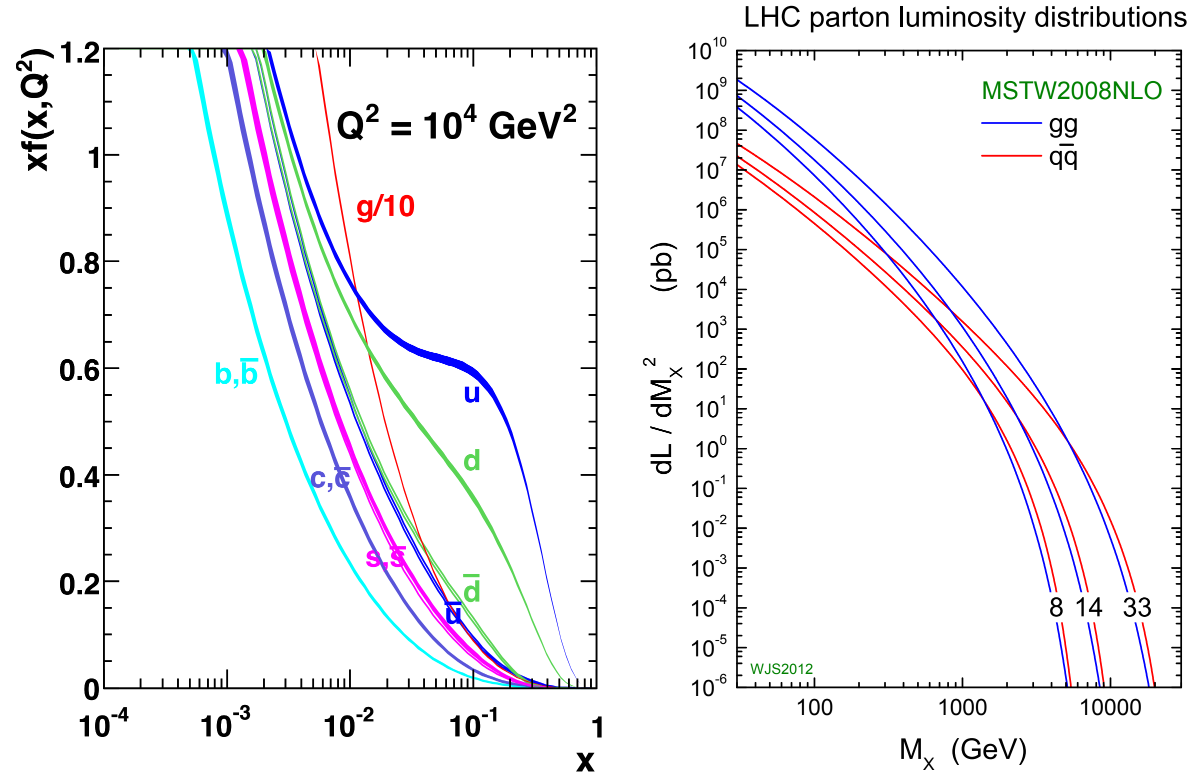

Figure 2.2: Left: The product of the parton momentum fraction and the corresponding value of the parton distribution functions, $xf_k(x,Q^2)$, evaluated at a factorization scale of 100 *GeV for the proton constituents with colour charge. The figure is taken from Ref. [125]. Right: Parton luminosities for pp colliders with centre-of-mass energies of $\sqrt{s} = 8$ TeV,* 14 *TeV, and* 33 *TeV. The notation $q\bar{q}$ stands for the sum over all quark/antiquark combinations, see Eqn. 2.5. The figure is taken from Ref. [126]. The MSTW 2008 NLO PDF set [125] has been used to obtain both figures.*

The 2 → 2 process with a heavy mediator in the *s*-channel

The resonant production of a heavy particle Y with $M_Y \gtrsim 100$ GeV in pp collisions is of great importance for the study carried out in this thesis. Two basic properties of the associated kinematics are the following [116].

- The particle Y is produced with a maximum rapidity $|y_Y^{\max}| = \frac{1}{2}\ln(s/M_Y^2)$. The rapidity range in which the heavy particle and its decay products are produced shrinks logarithmically with increasing M_Y.
- If the resonantly produced particle decays into two particles in the final state, the p_{T} distributions of the latter exhibit a peak close to $p_{\mathrm{T}}^f = M_Y/2$, followed by a steep decrease. This *Jacobian peak* is manifest in the differential cross section after a coordinate transformation

$$\frac{\mathrm{d}\sigma}{\mathrm{d}p_{\mathrm{T}}^f} = \frac{\mathrm{d}\cos\hat{\theta}}{\mathrm{d}p_{\mathrm{T}}^f}\,\frac{\mathrm{d}\sigma}{\mathrm{d}\cos\hat{\theta}} \sim \frac{p_{\mathrm{T}}^f}{M_Y\sqrt{\left(\frac{M_Y}{2}\right)^2 - \left(p_{\mathrm{T}}^f\right)^2}}\,\frac{\mathrm{d}\sigma}{\mathrm{d}\cos\hat{\theta}}\ , \tag{2.6}$$

where $\hat{\theta}$ denotes the θ coordinate of the final state particle f in the rest frame of particle Y. In a full calculation of this differential cross section, the edge at $p_{\mathrm{T}}^f = M_Y/2$ is washed out by the decay width Γ_Y and the non-zero transverse momentum of particle Y.

Cross sections for dijet production and key SM processes

The most common type of hard interaction at pp colliders is the parton-parton scattering mediated by the strong force. The two partons in the final state hadronise and yield two hadronic jets.

The partonic cross section for dijet production evaluated at leading order in pQCD diverges for vanishing p_{T} of the two particles c_1 and c_2 in the final state as $\mathrm{d}\hat{\sigma}/\mathrm{d}\hat{t} \sim p_{\mathrm{T}}^{-4}$, where $\hat{t}$ denotes the Mandelstam variable t in the centre-of-mass of the two-parton system. The differential hadronic cross section [116]

$$\frac{\mathrm{d}^3\sigma}{\mathrm{d}p_{\mathrm{T}}\mathrm{d}\eta_{c_1}\mathrm{d}\eta_{c_2}} = 2p_{\mathrm{T}}x_1x_2 \sum_{(i_1,i_2)} f_{i_1}(x_1)f_{i_1}(x_2)\frac{\mathrm{d}\sigma}{\mathrm{d}\hat{t}}\,(i_1+i_2 \to c_1+c_2) \tag{2.7}$$

diverges faster than p_{T}^{-3} for vanishing p_{T} and fixed pseudorapidities because the PDFs grow faster than x^{-1} for vanishing parton momentum fractions and $x \sim p_{\mathrm{T}}/\sqrt{s}$. This divergency in the perturbative calculation is regulated once the condition $p_{\mathrm{T}} \gg \Lambda_{\mathrm{QCD}}$ does not hold anymore and the non-perturbative regime is reached. Most interactions at pp colliders such as the LHC occur in the non-perturbative regime and the total cross section for pp collisions can therefore be roughly estimated to be

$$\sigma_{\mathrm{tot}} \sim \frac{4\pi}{\Lambda^2_{\mathrm{QCD}}} \sim 100\ \mathrm{mb}\ . \tag{2.8}$$

This estimate can be compared to the more accurate numbers [5] that are included in Fig. 2.3 [126], where cross sections for various process at proton-antiproton (for $\sqrt{s} \leq 4$ TeV) and proton-proton colliders (for $\sqrt{s} > 4$ TeV) are shown. At the 8 TeV LHC, the total pp cross section has been determined to $\sigma_{\mathrm{tot}} = 101.7 \pm 2.9$ mb by the TOTEM collaboration [127]. The corresponding results for the inelastic and the elastic cross sections read $\sigma_{\mathrm{inel}} = 74.7 \pm 1.7$ mb and $\sigma_{\mathrm{el}} = 27.1 \pm 1.4$ mb, respectively.

As shown in Fig. 2.3 [126], the hadronic cross section for processes of interest at the LHC, such as the production of W and Z bosons, top pairs, or SM Higgs bosons, are smaller than the total pp cross section by six to ten orders of magnitude. In contrast to the total cross section, these cross sections rise significantly with increasing centre-of-mass energy of the collider because the typical parton momentum fraction $x = \sqrt{x_1x_2} = M/\sqrt{s}$ needed to reach the relevant mass scale of the process, M, decreases.

2.1.3 The physics environment at an LHC interaction point

The total and inelastic cross sections for proton-(anti)proton colliders at the energy frontier vary only slightly with the hadronic centre-of-mass energy, as shown in Fig. 2.3. The physics environment in which the detectors at the LHC perform measurements is more challenging than at earlier hadron colliders mainly because of the high luminosity per bunch crossing and the high bunch crossing frequency.

At the LHC design luminosity of $\mathcal{L} = 10^{34}\mathrm{cm}^{-2}\mathrm{s}^{-1}$, bunches collide at the IPs of the high-luminosity experiments ATLAS and CMS with a bunch spacing of 25 ns and a peak luminosity per bunch crossing of $\mathcal{L}/(k_{\mathrm{b}}f_{\mathrm{rev}}) \approx 320\ \mathrm{b}^{-1}$, corresponding to an average number of about $\langle N_{\mathrm{inel}}\rangle = 25$ inelastic collisions per bunch crossing. For pp operation of the LHC at $\sqrt{s} = 8$ TeV with higher than nominal bunch intensities in 2012, the peak luminosity per bunch crossing increases up to $\mathcal{L}/(k_{\mathrm{b}}f_{\mathrm{rev}}) \approx 500\ \mathrm{b}^{-1}$ for the LHC fill with the highest instantaneous luminosity, albeit at a bunch spacing of 50 ns. This corresponds to almost 40 inelastic collisions per bunch crossing at the beginning of the fill. The following paragraph gives a brief description of some characteristics of a typical pp collision at the LHC.

The typical pp bunch crossing at the LHC - minimum bias events

The most common events in pp collisions are referred to as minimum bias events. They account for most of the total cross section and are selected starting from a very mild trigger requirement that biases the selection as little as possible. At the CMS IP, the two tracking telescopes of the TOTEM experiment [128], one at each side of the IP along the beam direction, provide a minimum bias trigger that requires a track candidate in the polar angle range $3-10$ mrad, corresponding

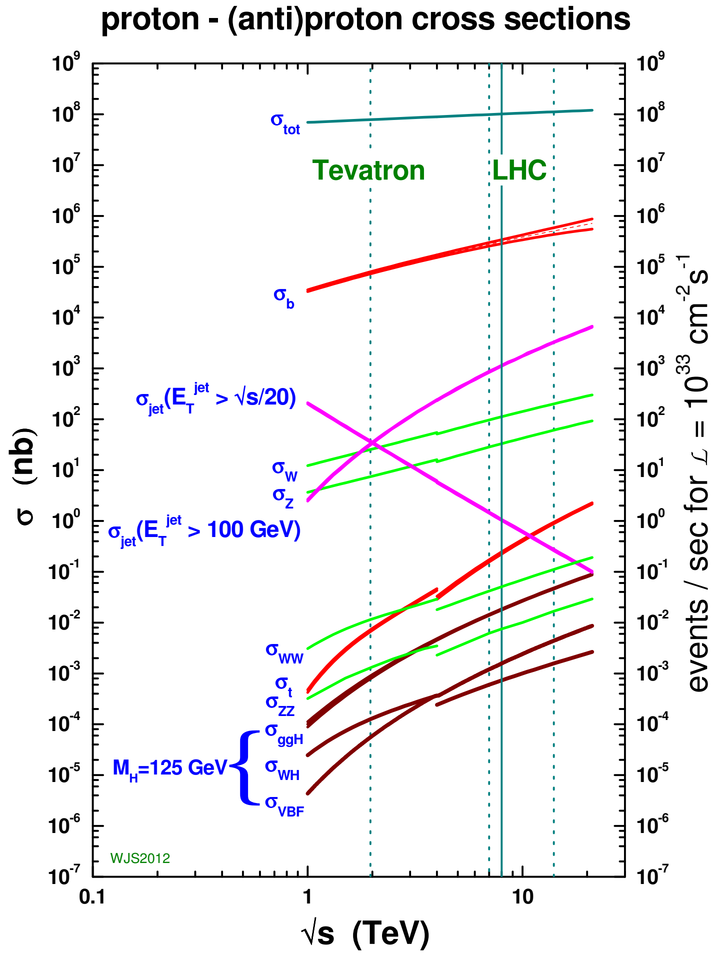

Figure 2.3: The total pp cross section and cross sections of various processes at proton-(anti)proton colliders as a function of hadronic centre-of-mass energy $\sqrt{s}$. The individual curves are valid for proton-antiproton colliders for $\sqrt{s} \leq 4$ TeV, and for proton-proton colliders for $\sqrt{s} > 4$ TeV. Cross sections have been evaluated at NLO or NNLO accuracy in pQCD with the MSTW 2008 NLO PDF set, except for the total pp cross section that is taken from Ref. [5]. The figure is taken from Ref. [126].

to $5.3 < |\eta| < 6.5$. The pseudorapidity distribution of charged hadrons (tracks) $\mathrm{d}N_{\mathrm{ch}}/\mathrm{d}\eta$ in minimum bias events obtained from pp collisions at $\sqrt{s} = 8$ TeV [129] is shown in Fig. 2.4 (left) for the two pseudorapidity ranges $|\eta| < 2.2$ (CMS tracker) and $5.3 < |\eta| < 6.5$ (TOTEM). These data have been obtained in an LHC fill with comparably low luminosity, and events with more than one reconstructed vertex are removed, such that the $\mathrm{d}N_{\mathrm{ch}}/\mathrm{d}\eta$ distribution corresponds in good approximation to that of events with a single pp collision. In the central region $|\eta| < 2.2$, the number of charged hadrons per unit in pseudorapidity is about six, with only a small η dependence (rapidity plateau). It falls to a value of about three at $|\eta| \approx 6$. However, the number of tracks per solid angle increases significantly in the forward region because the covered solid angle $\mathrm{d}\Omega = \mathrm{d}(\cos\theta)\mathrm{d}\phi$ per unit in pseudorapidity decreases fast at small θ.

The average transverse momentum of charged hadrons $\langle p_{\mathrm{T}} \rangle$ measured by various experiments at pp and p$\overline{\mathrm{p}}$ colliders with different centre-of-mass energies is presented in Fig 2.4 (right) [130]. The CMS measurement uses a dataset of pp events obtained at $\sqrt{s} = 7$ TeV and yields an average transverse momentum of $\langle p_{\mathrm{T}} \rangle = 0.545 \pm 0.005$ (stat) $\pm\, 0.015$ (syst) GeV for charged hadrons with $p_{\mathrm{T}} > 0.1$ GeV within the pseudorapidity range $|\eta| < 2.4$.

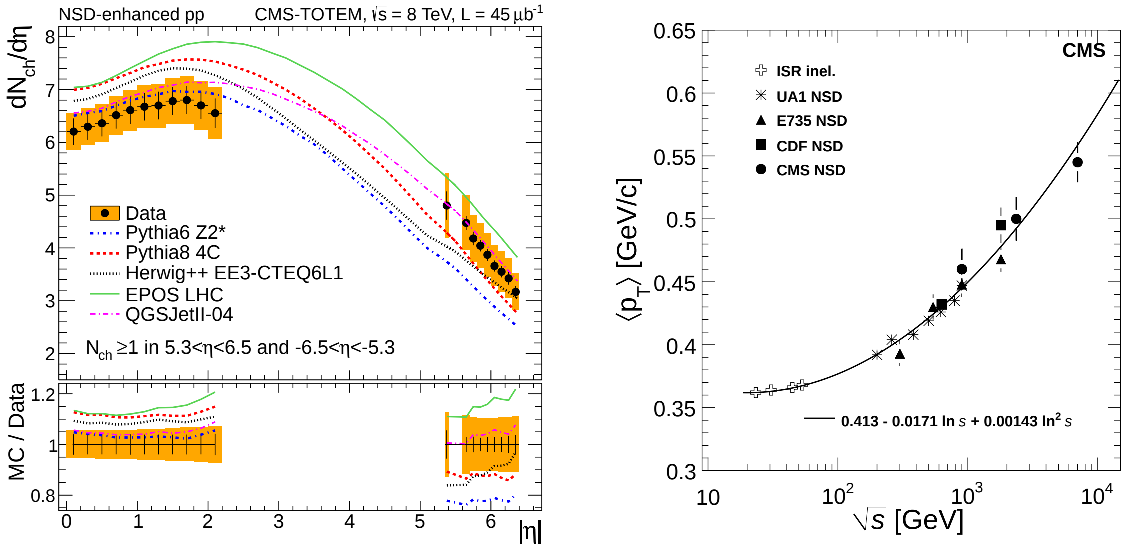

(a) The distribution of charged hadrons per unit in pseudorapidity $\mathrm{d}N_{\mathrm{ch}}/\mathrm{d}\eta$ measured in pp collisions at $\sqrt{s} = 8$ TeV for the pseudorapidity ranges $|\eta| < 2.2$ and $5.3 < |\eta| < 6.4$. The figure is taken from Ref. [129].

(b) The average transverse momentum $\langle p_{\mathrm{T}} \rangle$ measured at various pp and p$\bar{\mathrm{p}}$ colliders with different $\sqrt{s}$. The figure is taken from Ref. [130]; a short description of the different measurements is given therein.

Figure 2.4: Basic quantities of minimum bias events in pp (p$\bar{p}$) collisions: The distribution of charged hadrons per unit in pseudorapidity $\mathrm{d}N_{\mathrm{ch}}/\mathrm{d}\eta$ *(left) and the average transverse momentum* $\langle p_{\mathrm{T}} \rangle$ *(right).*

So far, only the charged hadrons in minimum bias events have been considered. Under the simplifying assumptions that the hadrons in the final state of a typical pp collision are pions, and that the three pion species π^+, π^-, π^0 occur in equal numbers, half as many neutral hadrons as charged hadrons are produced.

In summary, a typical pp bunch crossing at the CMS IP at the 8 TeV LHC contains up to 40 overlapping pp collisions that each yield 55 particles in the central part of the detector, $|\eta| < 3$, corresponding to a transverse kinetic energy per pp collision of $\sum_{i=1}^{55} p_{\mathrm{T}}^{i} \approx 55 \times \langle p_{\mathrm{T}} \rangle \approx 30$ GeV. Hence, a total transverse kinetic energy in excess of 1 TeV is deposited in the central part of the detector every 50 ns. The CMS detector is designed to operate in these challenging conditions, select events that contain hard interactions of interest from the plethora of pp collisions, and measure the different particles in these events with high precision.

2.2 The CMS detector

The main references that have been used to compile this description of the CMS detector are Refs. [6, 131]. Very detailed descriptions of subsystems of the CMS detectors are presented in Technical Design Reports (TDRs); the corresponding references are given within the text.

Before considering the details of the detector design and individual subdetectors, basic features of a multi-purpose detector at the LHC such as CMS are summarized. The required coverage of the detector in pseudorapidity and the detector segmentation can be motivated by considering a few benchmark processes with different kinematics that reflect larger classes of interesting processes at the LHC. As dictated by the proton PDFs and the high pp centre-of-mass energy, gluon-gluon scattering gg → gg is a defining process at the LHC. The pseudorapidity distribution of the gluon jets in the final state exhibits a rapidity plateau with a width of $\pm(2.5 - 3)$ and falls off towards higher $|\eta|$ [115]. Almost the entire transverse momentum of the produced particles is retained in the detector volume if it extends from $\eta = 0$ to $|\eta| = 5$, such that the missing transverse momentum $\not{E}_{\mathrm{T}}$ can be determined accurately. Moreover, a meaningful determination of $\not{E}_{\mathrm{T}}$ requires the detector volume to be instrumented hermetically, such that (almost) no particles other than neutrinos and hitherto unknown, weakly-interacting ones escape detection.

Another benchmark process that calls for a large η coverage of the detector is the fusion of two vector bosons radiated off an incoming quark/antiquark pair (the vector boson fusion or VBF process) that is of particular importance for the study of vector boson scattering at the LHC and Higgs physics [132, 133]. Its signature features two jets in the forward direction with large $\Delta\eta$.

While a large coverage of the detector is always favourable and a prerequisite for the $\not{E}_{\mathrm{T}}$ measurement, it is not a necessity for the study of all theoretically anticipated signatures of new physics. For example, resonant pair-production of SM particles at high $\sqrt{\hat{s}}$, that constitute one of the key signatures of new physics at the TeV scale, fall into the central part of the detector. This is described in some detail by means of the signal processes for the $\mathrm{e}\mu$ resonance search in Sec. 5.1.3.

The increase of the radiation field towards the forward direction necessitates the use of different choices of detector technology in different ranges of pseudorapidity: Precision detectors that allow for particle identification and an exact reconstruction of particle momenta/energies are installed in the central detector region with coverage up to $|\eta| \sim 2.5 - 3$, whereas the very forward region is equipped with calorimetry that is very radiation-hard. The detector components in the central region of the detector are subdivided further into a *barrel* and an *endcap* section, with the former extending from $\eta = 0$ to $|\eta| \sim 1.5$.

2.2.1 The CMS coordinate system

The coordinates that are used in the following have been defined in Sec. 2.1.2, but the orientation of the CMS coordinate system [6] has not yet been specified. Its center $\vec{x} = (0, 0, 0)$ is placed at the nominal interaction point. The x-, y-, and z- axes form a right-handed cartesian coordinate system: The z-axis is oriented along the anticlockwise beam direction, the y-axis points vertically upward, and the x-axis points inward towards the centre of the LHC ring. The polar angle θ is measured from the z-axis. The $x - y$ plane corresponds to the transverse plane parameterized by the radial coordinate r, that denotes the distance to the centre in the transverse plane, and the azimuthal angle ϕ that is measured from the x-axis.

2.2.2 Solenoid magnet and steel return yoke

Most aspects of the CMS detector design are informed by the decision to place a superconducting solenoid magnet [134] around the beamline with a uniform axial magnetic field of $B_0 = 3.8$ T, a free bore of 3.15 m radius, and a length of 12.5 m, that yields an unprecedented stored energy of 2.6 GJ. The utilized conductor is NbTi that is incorporated in Rutherford-style cables. The windings of the magnet coil comprise four cable layers in a support structure made of aluminium alloy that can cope with the strain generated by the large magnetic pressure ($P_{\mathrm{mag}} \sim B_0^2$). At a temperature of 4.45 K and a current of 18 kA, the magnet is operated in the superconducting regime of NbTi. The coil has a radial extension of about 31 cm and adds 3.9 radiation lengths (X_0) to the material budget. Therefore, the calorimetry has to be contained within the magnet coil. The cold mass of the magnet amounts to 220 t.

The large magnetic flux inside the magnet coil is directed outside of it by a 10 kt magnetic flux return yoke made of construction steel. It consist of a barrel part and two endcap sections, as indicated in Fig. 2.5. The barrel section of the yoke weighs 6 kt and is segmented into five *wheels* (numbered as wheels -2 to 2) along the z coordinate. Each wheel is formed by connected steel plates that form three cylinders around the beamline. Both endcap sections weigh 2 kt and are composed of three steel disks.

A map of the magnetic flux density in CMS obtained from a 3D model of the detector is shown in Fig. 2.5 [135]. Measurements of the magnetic flux density inside the coil have been

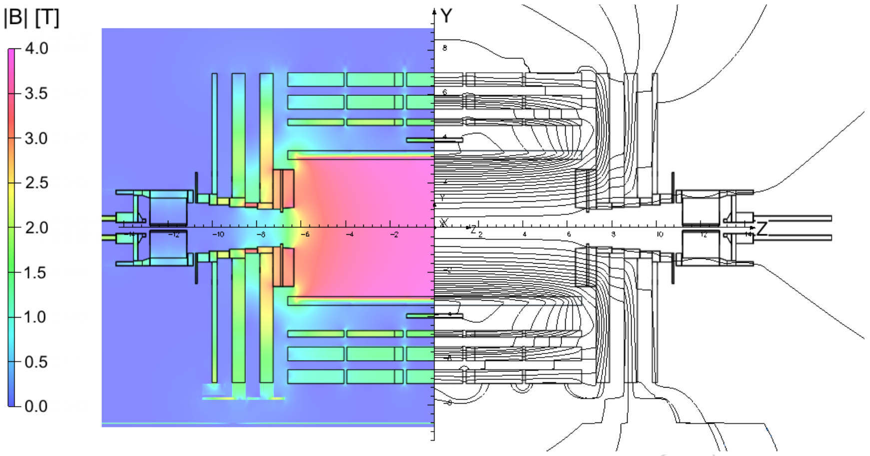

Figure 2.5: Left: Map of the absolute value of the magnetic flux density in the CMS detector in the $z - y$ *plane. Right: Orientation of the magnetic field lines. These are results obtained from a model of the magnetic field in CMS with a central magnetic flux density of* $B_0 = 3.8$ T*. The figure is taken from Ref. [135].*

performed prior to the assembly of the CMS detector with an accuracy better than 0.1% and agreement with the model is found [136]. The magnetic field in the barrel section of the steel return yoke has further been mapped for the assembled detector using muons from cosmic ray events [135]. Furthermore, the magnetic flux density in the yoke has been measured via installed flux loops [137].

2.2.3 Inner all-silicon tracking system

The inner tracking system of CMS is described in detail in Refs. [138, 139]. Its layout is sketched in Fig. 2.6. With about 25 pp collisions per bunch crossing at design luminosity (25 ns bunch spacing), and a pileup of up to 40 reached during the $\sqrt{s} = 8$ TeV data taking period in 2012 (50 ns bunch spacing), $750 - 1200$ tracks per bunch crossing are produced in the acceptance of a tracking detector covering the region $|\eta| < 2.5$. In order to meet the requirements of precise measurements for SM physics and sensitivity to new physics at the multi-TeV scale, this large number of tracks has to be reconstructed unambiguously and efficiently with an impact parameter resolution well below 100 μm, and a p_{T} resolution of better than 1% for muon tracks from W and Z boson decays and about 10% for muon tracks with $p_{\mathrm{T}} \sim 1$ TeV that fall into the central region $|\eta| \lesssim 1$ of the detector.

The choice of detector technology for the inner tracking system is driven by the following considerations.

- A high granularity of the detector with a correspondingly large number of readout channels is needed for robust pattern recognition and the reconstruction of the individual tracks.
- A spatial resolution of ~ 100 μm for single hits or better is needed to achieve the envisaged momentum resolution.
- Due to the high flux of charged particles in this innermost part of the detector, the sensors and readout electronics have to be very fast in order to assign the reconstructed tracks to the right bunch crossing.
- Both the sensors and the readout electronics have to tolerate the strong radiation field close to the beam pipe with a lifetime of about 10 years (expect for the innermost detector layers).
- The p_{T} resolution requirements call for a large outer radius of the tracker but the material budget must not exceed about one radiation length X_0 in order to keep energy losses due to

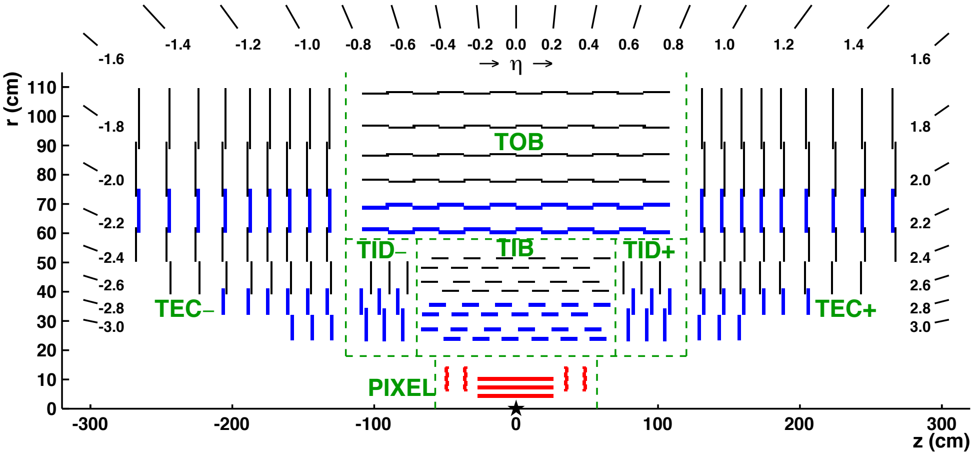

Figure 2.6: Cross section of the upper half of the inner tracking detectors in the $r-z$ plane. The numbers at the edges of the figure denote values of the η coordinate. The figure is taken from Ref. [140].

bremsstrahlung (for electrons), multiple scattering, and nuclear interactions of the copiously produced pions at an acceptable level.

The experience gained before construction of the LHC detectors with silicon-based tracking devices at LEP and the Tevatron, and the further progress made during the development of the CMS tracker, led to the choice of an all-silicon inner tracking system for CMS. The goal of resolving the individual tracks is achieved by measurements with high position resolution in a limited number of sensor layers, rather than by relying on a large number of measurements along the track.

Pixel detector

The innermost layers of the tracking detectors play a crucial role in the reconstruction of individual vertices and they provide seeds for track reconstruction. The necessary impact parameter resolution of below 100 μm is set by the lifetimes of the τ lepton, c hadrons (D^0, $\mathrm{D}^\pm$), and b hadrons that correspond to distances between the production vertex and the secondary decay vertex of $\ell_i = \gamma_i c\tau_i$ with $c\tau_\tau = 87$ μm, $c\tau_c \sim 120$ μm, and $c\tau_b \sim 500$ μm, respectively. This in turn requires a position resolution in both $|\mathrm{d_z}|$ and $r\,\mathrm{d}\phi$ well below 100 μm and a small extrapolation uncertainty from the innermost tracking layer to the vertex. The latter receives an important, inevitable contribution from multiple scattering in the beam pipe and grows with the distance to the inner tracking layers. Therefore, a balance must be found between the requirement of a small distance in r from the beamline to the first tracking layer and the requirement to avoid the high particle flux close to the beamline. An unambiguous reconstruction of track seeds furthermore demands a fine segmentation of the vertex detector with a low occupancy of individual channels.

These requirements point to silicon pixels as the detector technology of choice. The employed sensors have a thickness of about 300 μm that together with a Lorentz angle (for electrons, not the holes of the induced electron-hole pairs) of about 25° fixes the size of the pixels along the ϕ direction to $\Delta s_\phi \equiv r\Delta\phi = 100$ μm. The Lorentz drift is induced by the solenoid magnetic field in the pixels in the barrel section of the pixel detector. With an analog readout of the pulse-height information for each pixel, the Lorentz drift of the electrons released by the ionizing particle crossing the silicon allows for an improved position resolution by using the charge-sharing between neighbouring pixels. This improves the position resolution from $100\ \mu\mathrm{m}/\sqrt{12} \approx 30\ \mu$m to $10-15$ μm. For the purpose of vertex reconstruction and track seeding, good position resolution is needed not only in the ϕ direction, but also along z. A similar size of the pixel in the z dimension is therefore chosen and the pixel area is given by $100\ \mu\mathrm{m}(r\phi) \times 150\ \mu\mathrm{m}(z)$. Assuming a pileup of 25 events and the associated charged track density of order $10^{-2}/\mathrm{mm}^2$ per bunch crossing at the innermost layer of the pixel detector for $\eta = 0$, this corresponds to a pixel occupation probability of $\mathcal{O}(10^{-4})$ per bunch crossing.

The barrel pixel detector is organized in three layers that form cylinders around the beam pipe with radii of $r_1 = 4.4$ cm, $r_2 = 7.3$ cm, and $r_3 = 10.2$ cm, respectively, and with a length along the z direction of 2×28 cm. These layers are accompanied by two endcap sections on each side at $z = \pm 34.5$ cm and $z = \pm 46.5$ cm with an inner radius of 6 cm. A total of 66 million pixels corresponds to an active area of about 1 m^2. This detector layout extends to $|\eta| = 2.5$, provides three pixel hits for the majority of central tracks, and a high probability for at least two hits for tracks close to the edge of the acceptance. In order to induce a Lorentz drift also in the endcaps, that are oriented perpendicular to the solenoid field, the sensors there are tilted with respect to the $r - \phi$ plane and a position resolution similar to the barrel section of the pixel detector is obtained.

The transverse impact parameter resolution obtained with the complete silicon tracker (including the silicon-strip tracker described below) for muon tracks ranges from about 100 μm for $p_\mathrm{T} = 1$ GeV to 10 μm for $p_\mathrm{T} = 100$ GeV with a modest dependence on η. The longitudinal impact parameter resolution exhibits a stronger η dependence and is inferior to the impact parameter resolution in the transverse plane by a factor two to five.

Silicon-strip tracker

The outer radius of the strip tracker is set by the desired transverse momentum resolution that calls for a long lever arm $L \sim 1$ m in the direction perpendicular to the $B = 3.8$ T solenoid magnetic field. The 10 sensor layers in the barrel region of the silicon-strip tracker are mounted at radii from 20 cm to 116 cm, at an approximately constant distance between adjacent layers. This defines the bending power BL^2 of the CMS tracker. The barrel detector extends to $|\eta| \sim 1$ and is followed by endcap discs that provide coverage up to $|\eta| = 2.5$, as shown in Fig. 2.6. Above $|\eta| \sim 1.6$, the lever arm is reduced with increasing pseudorapidity of the track.

The resulting sagitta of tracks in the barrel part of the detector is of order 200 μm for a muon track with $p_\mathrm{T} \sim 1$ TeV. A resolution of 10% for such high transverse momenta requires a single hit position resolution of about 25 μm along the ϕ direction if twelve hits along the track in the pixel and silicon-strip detectors are assumed [4]. Silicon sensors with a pitch of about 80 μm yield this digital position resolution. With an analog readout and the utilization of charge sharing on neighbouring strips the position resolution is improved further; it varies between $\sigma_\mathrm{pos}^{s_\phi} \approx 20$ μm in the inner layers of the silicon-strip detector with a pitch of 80 μm and $\sigma_\mathrm{pos}^{s_\phi} \approx 40$ μm in the outer layers with a pitch of 180 μm. The presented values for the position resolution are valid for the position along the ϕ coordinate measured with strips in the barrel part of the detector oriented along the z direction in parallel with the magnetic field. The requirement on the position resolution in the non-bending plane is less strict, $\sigma_\mathrm{pos}^{z} \sim 1$ mm. The angular resolution has to provide an unambiguous matching to track seeds in the pixel detector and a precision in the extrapolation to the inner surface of the ECAL better than the size of a single crystal. The position measurement in the non-bending plane is obtained from sensors with a strip orientation at a stereo angle of 100 mrad.

The unambiguous identification of tracks with high efficiency calls for high granularity of the detector and a small cell size with a target cell occupancy of order 1%. Assuming a pileup of 20 events, the (primary) track density per bunch crossing at $\eta = 0$ falls from about $10^{-3}/\mathrm{mm}^2$ at $r = 20$ cm to $10^{-5}/\mathrm{mm}^2$ at $r = 100$ cm. Its reduction with radius is faster than $1/r^2$ because of the small average p_T of charged tracks $\langle p_\mathrm{T} \rangle \approx 0.9$ GeV and the strong magnetic field that forces low-p_T charged particles on a helix trajectory (*loopers*) within the tracker volume. The cell sizes

---

[4] The relation between the single hit position resolution along the ϕ direction, $\sigma(s_\phi)$, and the p_T resolution can be approximated for large track p_T and a large number of measurements along the track, $N \gtrsim 10$, by using a quadratic fit to the hit positions in the transverse plane; the result reads $\sigma(s_\phi) \approx 0.3\ B[\mathrm{T}]L[m]\ L \times \sqrt{(N+4)/(720)} \times (\delta p_\mathrm{T}/p_\mathrm{T})/p_\mathrm{T}[\mathrm{GeV}]$ [141]. For $\delta p_\mathrm{T}/p_\mathrm{T} = 0.1$, $p_\mathrm{T} = 1$ TeV, $N = 12$, and the bending power of the CMS tracker, this formula yields the quoted position resolution of about 25 μm.

are given by the length of the strip and the sensor thickness of order 300 μm ($r < 60$ cm) and 500 μm ($r \geq 60$ cm). In the inner layers of the barrel, a strip length of 10 cm yields a cell cross section of order 30 mm^2 and is thus small enough to meet the occupancy target; the effective strip lengths increases in the outer layers of the tracker to 20 cm. A total of 9.3 million strips (channels) forms an active silicon area of 198 m^2.

This sensitive part only contributes a fraction of the total material budget of the tracker. The readout electronics for the high number of channels and in particular the cabling yield other important contributions. Finally, the silicon sensors require cooling down to -10°C. The cooling system and structure needed for the mechanical stability of the large tracker add to the material budget. It varies between 0.3 X_0 and 0.4 X_0 close to $\eta = 0$ and a maximum of about 2 X_0 at $|\eta| \approx 1.4$; a region, where low-mass cooling and electrical connections are connected to the outside of the tracker via robust pipes and cables.

The material within the tracking volume degrades the p_{T} resolution due to multiple scattering and is therefore linked to another important requirement for the tracking performance of CMS; the resolution of the Z boson decay width Γ_{Z} when combining the four-momenta of the two charged tracks from muonic Z decays. This calls for a p_{T} resolution of
$\sigma(p_{\mathrm{T}})/p_{\mathrm{T}} \sim \Gamma_{\mathrm{Z}}/(2\sqrt{2\ln 2} \times M_{\mathrm{Z}}) \approx 1.2\%$ [5] at $p_{\mathrm{T}} \sim 50$ GeV. The impact of the multiple scattering depends on the pseudorapidity due to the increasing material budget. For $|\eta| \lesssim 0.5$, it contributes 0.7% to 0.8% to the p_{T} resolution of muon tracks and a total p_{T} resolution of about 1% can be achieved. At $|\eta| \sim 1.4$, the multiple scattering contribution to the p_{T} resolution alone reaches 1.5% and for larger $|\eta|$ the lever arm of the tracker decreases such that the resolution degrades further. However, a p_{T} resolution for muon tracks with $p_{\mathrm{T}} = 100$ GeV better than 10% is still achieved at the edge of the tracker acceptance $|\eta| \sim 2.5$.

2.2.4 Electromagnetic calorimeter

The ECAL [142,143] is central to the precise reconstruction of the energy and position of photons, electrons, and the electromagnetic component of hadronic jets ($\pi^0 \to \gamma\gamma$). The precise study of physics at the electroweak scale calls for an energy resolution of the ECAL of 1% for photons and electrons with energies of 50 GeV in the central part of the calorimeter. Use cases for such an energy resolution are measurements and searches involving Z bosons with decays into electron/positron pairs and the Higgs boson search in the decay channel $h^0 \to \gamma\gamma$. The latter benefits from a good energy resolution because the decay width of the SM Higgs boson is expected to be $\lesssim 10$ MeV for Higgs masses with a sizeable diphoton branching fraction (4 MeV for $M_{h^0} = 125$ GeV) [144], such that the width of a signal peak in the diphoton mass spectrum on top of the irreducible background from the direct production of photon pairs is determined by the energy resolution of the ECAL.

The radial extension of the ECAL between the large tracker and the HCAL in the solenoid coil is strictly limited in CMS; this necessitates the choice of an active material with high density and small radiation length X_0. With a radiation length of 0.89 cm, lead tungstate $\mathrm{PbWO_4}$ fulfills this requirement and its small Molière radius of $r_{\mathrm{M}} = 2.2$ cm allows for a small lateral segmentation and high granularity of the ECAL. The scintillation decay time of $\mathrm{PbWO_4}$ is similar to the design bunch crossing interval of 25 ns. Details of the scintillation mechanism in $\mathrm{PbWO_4}$ are presented in Ref. [145]. Sufficient radiation hardness in the LHC environment is achieved by reducing the density of point structure defects in the $\mathrm{PbWO_4}$ crystals and by doping them with specified impurities.

The mentioned basic properties of $\mathrm{PbWO_4}$ and developments in the context of the work towards the CMS ECAL, ranging from the process of growing the crystals to the mechanical processing of their surfaces, allow for the construction of a hermetic, homogeneous, compact crystal ECAL. It consists of a cylindrical barrel part with an inner radius of $r_{\mathrm{ECAL}} = 129$ cm extending up to

---

[5] A factor $1/(2\sqrt{2\ln 2})$ is introduced in order to compare the *full width at half maximum* (FWHM) value of the Gaussian distribution with standard deviation $\sigma(p_{\mathrm{T}})$ to the FWHM of the Breit-Wigner distribution, Γ_{Z}, that characterizes the Z resonance.

$|\eta| = 1.479$ and two endcap regions that provide coverage up to $|\eta| = 3.0$. The layout of the CMS ECAL is shown in Fig. 2.7. In the barrel, the $PbWO_4$ crystals are 23 cm long, corresponding to 25.8 X_0; the lossless containment of electromagnetic showers is a prerequisite for the desired energy resolution. The crystals have a tapered shape and a quadratic front face area of 2.2×2.2 cm^2 defined by the Molière radius. In the barrel, they are arranged in a quasi-projective $\eta - \phi$ geometry with a 3° angle of the crystal axes with respect to the nominal interaction point and a granularity of $\Delta\eta = \Delta\phi/\mathrm{rad} \approx r_{\mathrm{M}}/r_{\mathrm{ECAL}} = 0.0174$. The shape of the crystals in the endcaps is similar, they are however mounted in a rectangular $x - y$ grid. This difference in detector geometry between ECAL barrel and endcap is the reason for the usage of different shower shape identification criteria in the electron selection covered in Sec. 4.3.1. A preshower detector is placed in front of the ECAL endcap disks in the region $1.653 < |\eta| < 2.6$ in order to provide additional separation power between single photons and collimated diphoton pairs from boosted π^0 decays. It consisting of a first layer of lead absorber (1 X_0) and two silicon planes of silicon strip detectors that are separated by another layer of lead absorber (1 X_0).

A disadvantages of $PbWO_4$ compared to other materials used in crystal calorimeters is the relatively low light yield. It calls for photodetectors with high quantum efficiency, gain, and insensitivity to traversing ionizing particles. In the endcap region, phototubes (vacuum phototriodes) can be used, while silicon avalanche photodiodes (APDs) have to be employed in the barrel with the strong magnetic field perpendicular to the crystal axes. The photodetectors are mounted on the rear face of the crystals, followed by the readout electronics. The ECAL provides no longitudinal segmentation. The response along each crystal must be very uniform because of fluctuations of the longitudinal shower profile that would otherwise lead to a large constant term in the energy resolution.

Both the light yield of the crystals and the APD gain exhibit a temperature dependence of $-2\%/^\circ$C [146], and the desired energy resolution requires a regulation of the operating temperature, 18°C, with a precision better than 0.05°C in the barrel and 0.1°C in the endcap. A detailed description of the ECAL cooling system can be found in Ref. [147]. Irradiation of the crystals leads to a loss of transparency of the $PbWO_4$ and a changed response of the ECAL. The changes of the detector response are monitored crystal-by-crystal by means of a laser-based light-monitoring system [148, 149], such that response corrections can be derived.

With these measures and a low-noise electronic readout the following energy resolution (decomposed into stochastic term, noise term, and constant term) can be achieved [6]:

$$\left(\frac{\sigma_E}{E}\right)^2 = \left(\frac{2.8\%}{\sqrt{E/\mathrm{GeV}}}\right)^2 + \left(\frac{12\%}{E/\mathrm{GeV}}\right)^2 + (0.3\%)^2 \ . \tag{2.9}$$

This result is obtained from measurements in an electron test beam under the conditions defined in Ref [150]. It underlines that the ECAL meets the design requirements and as a detector in its own right achieves an energy resolution of 0.6% for electrons with an energy of 50 GeV. However, the formula Eqn. 2.9 does not yield the energy resolution for electrons and photons under CMS operation in the LHC environment as pointed out for example in Refs. [146, 151].

The most energetic electrons produced in pp collisions at the LHC can saturate the readout electronics attached to individual ECAL crystals. Readout saturation in the ECAL occurs for energy deposits in a single crystal of about 1.7 TeV and 3 TeV in the barrel and endcap, respectively. It has been shown for the energy reconstruction of electron and photon ECAL clusters that the full energy deposited in the *hottest* crystal with saturated readout can be approximated by using the lateral shower profile information provided by the surrounding crystals [152].

The ECAL material contributes the first 1.1 nuclear interaction lengths (λ_{I}) that hadrons are exposed to before reaching the hadronic calorimeter (HCAL) that is described next.

2.2.5 Hadronic calorimetry

The HCAL [153] is central to the reconstruction of the energy and position of hadrons and hadronic jets, and with its hadron forward (HF) section it provides coverage up to $|\eta| = 5.2$ which is crucial

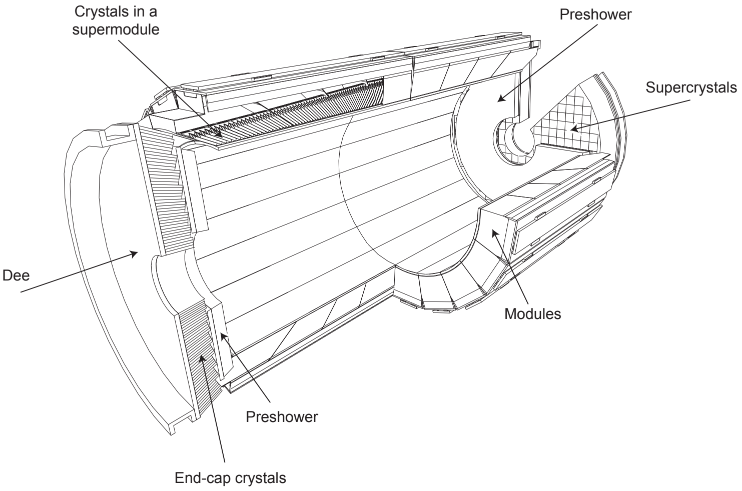

Figure 2.7: Detector design of the ECAL with the cylindrical barrel detector, the two endcaps, and upstream preshower detectors. The figure is taken from Ref. [6].

for a meaningful determination of $\not{E}_{\mathrm{T}}$.

Since the number of hadrons produced in a hadronic shower is much smaller than the corresponding number of particles in electromagnetic showers, the stochastic term in the energy resolution for the HCAL is much larger than the 2.8% achieved for the ECAL. The requirement on the constant term of better than 5% is less strict than for the crystal calorimeter and a leakage of the shower energy through the rear face of the HCAL at the 1% level is acceptable. The granularity of the device should suffice to resolve dijet systems from boosted W and Z decays up to a relativistic boost of $\gamma_{\mathrm{W/Z}} = E_{\mathrm{W/Z}}/M_{\mathrm{W/Z}} \sim 5-6$; this is desired for example in searches for heavy Higgs bosons with $M_{H^0} \lesssim 1$ TeV [115].

The very restricted space behind the ECAL inside the coil of the magnet ($1.8\text{ m} \lesssim r \lesssim 3.0\text{ m}$) calls for a sampling calorimeter with thick absorber plates followed by thin layers of active medium. Brass plates with a nuclear interaction length of $\lambda_{\mathrm{I}} = 16.42$ cm and varying thickness of $5-8$ cm are used as absorbers and $4-9$ mm thin tiles of plastic scintillator are used as the active medium. As indicated in Fig. 2.8, the HCAL consists of a barrel part (HB) extending up to $|\eta| = 1.3$ that is complemented by a tail-catcher (hadron outer, HO) outside the magnet coil; an endcap region (HE) providing coverage to $|\eta| = 3$; and a forward calorimeter (HF) based on Cherenkov-radiating quartz fiber technology that is located outside the central part of the CMS detector and extends up to $|\eta| = 5.2$. In the barrel, the calorimeter is segmented into towers of size $\Delta\eta \times \Delta\phi/\mathrm{rad} \approx 0.087 \times 0.087$, corresponding to a 5×5 array of crystals in the ECAL. At the inner HB surface at $r = 1.8$ m, this granularity corresponds to the lateral extension of a hadronic shower of roughly $\lambda_{\mathrm{I}} \sim 16$ cm and suffices to achieve the desired angular resolution for boosted dijet systems mentioned above. The material in the HB provides a thickness of 5.82 λ_{I} at $\eta = 0$ and 10.6 λ_{I} at $|\eta| = 1.3$. With the HO extension and the magnet coil in front of it acting as an absorber, the absorber thickness is increased; most noticeably at $\eta = 0$, where the resulting total absorber thickness (including the ECAL) reaches more than 10 λ_{I}. The light from the plastic scintillator tiles is collected with wavelength-shifting fibers and guided by clear fibers to photodetectors outside of the HCAL volume but still inside the magnetic volume. The light from scintillator tiles in the same calorimeter tower is merged, such that there is no information about the longitudinal shower development within a tower (in the HB). The need for a photodetector with a quantum efficiency above 10% in the 500 nm region, a gain of at least 10^3, and the ability to operate in a strong magnetic field led to the choice of hybrid photodiodes (HPDs).

The detector technology employed in the endcap section HE is the same as in the barrel. The total absorber thickness provided by the calorimetry in the endcap is about 10 λ_{I}. About 70000 scintillator tiles are installed in the HCAL and the collected light contributes to 2592 channels for

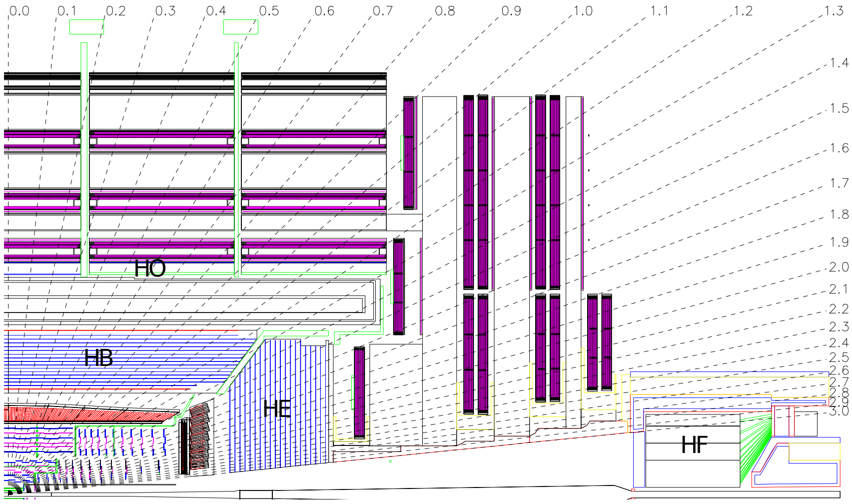

Figure 2.8: Cross section of one quadrant of the CMS detector in the $r - z$ plane with the four HCAL detector sections HB, HO, HE, and HF. The numbers at the upper and the right edge of the figure denote values of the η coordinate. The figure taken from Ref. [6] is slightly modified to represent the actual layout of the CMS muon system during 2012 data taking.

the HB, the same number for the HE, and 2160 channels for the HO [154].

The energy resolution in a pion beam has been measured in a test beam with an HB segment and upstream ECAL segment in the energy range $E_\pi = 20 - 300$ GeV [154]. The result reads:

$$\left(\frac{\sigma_E}{E}\right)^2 = \left(\frac{115\%}{\sqrt{E/\mathrm{GeV}}}\right)^2 + (5.5\%)^2 \ . \tag{2.10}$$

This result does not represent the energy resolution obtained for hadronic jets with the full CMS detector [155]. The HO tail-catcher is not present in the test beam setup. In a jet of a given energy, the momentum is shared between several (primary) particles, not carried by a single one. Furthermore, the jet reconstruction uses tracker information as described in Sec. 3.4.2.

The HF calorimeter that covers the forward region $3.0 < |\eta| < 5.2$ uses very radiation-hard quartz fibers as the active material. It measures both the electromagnetic and the hadronic component of the particle flux and provides separation power between the two. The HF calorimeter is described in detail in Ref. [6].

2.2.6 Muon system

As shown in Fig. 2.9, the CMS muon system [156] is situated inside and around the iron return yoke, outside the magnet coil or downstream the calorimetry in the barrel and endcap sections of the detector, respectively. Its main purposes are to provide a muon trigger, muon identification and a *standalone* muon track reconstruction, an improved p_T resolution and reduced charge misidentification probability for muons with $p_\mathrm{T} \gtrsim 200$ GeV. The latter requirement applies to muon tracks that include information from the inner silicon tracker, while the first two demands have to be fulfilled by the muon system alone. The approach to track reconstruction in the muon system is different to that adopted in the silicon tracker because the large amount of material in the iron return yoke calls for a large number of detector layers and redundant measurements.

Key requirements for the muon trigger are a time resolution well below 25 ns and a p_T resolution of $20 - 30\%$ for muons in the p_T range $10 - 50$ GeV already at the first, fast trigger level. This requires fast pattern-recognition circuits that yield a *(trigger) position resolution* per muon chamber of $1 - 2$ mm [6, 131]. This accuracy is indispensable because the p_T spectrum of singly produced muons from b and c hadron decays falls steeply in the central detector region

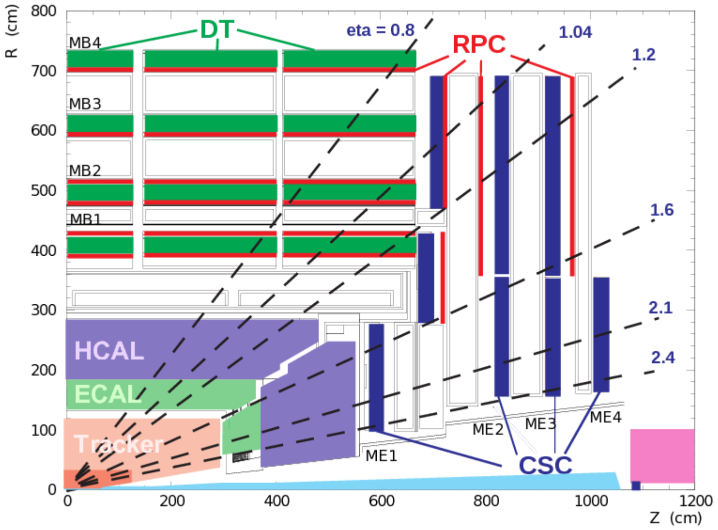

Figure 2.9: Cross section of one quadrant of the CMS detector in the $r-z$ plane with the DT chambers, CSCs, and RPCs. The numbers at the upper and the right edge of the figure denote values of the η coordinate. The figure is taken from Ref. [157].

($\mathrm{d}\sigma/\mathrm{d}p_\mathrm{T} \sim p_\mathrm{T}^{-4}$) [131], such that the migration of lower p_T muons above the trigger threshold has to be controlled tightly.

The p_T resolution in the muon system is limited by multiple scattering at low transverse momenta, where the inner tracking system alone provides an excellent accuracy. The *(off-line) position resolution* requirement that the muon detectors have to meet is thus dictated by the goals set for the muon p_T resolution at high p_T, $\delta p_\mathrm{T}/p_\mathrm{T} \sim 5-10\%$ for muons with a p_T of 1 TeV in the central region of the detector. With the measurements provided by the inner tracker and the sizeable additional lever arm provided by the muon system (the tracker only covers about one third of the inner radius of the magnet coil), this p_T resolution can be achieved with a position resolution of the chambers in the muon system of about 100 μm in the bending plane. According to the magnetic field orientation (Fig. 2.5), the position measurement along the ϕ coordinate is the relevant one for the p_T determination both in the barrel section of the iron return yoke and in its endcap disks. The position resolution requirement for single detector cells is loosened by utilizing a high number of $6-8$ tracking layers per chamber that measure the ϕ coordinate [131].

The CMS muon system employs three different types of gaseous muon detectors. Two types of multiwire proportional chambers cover all tasks of the muon system mentioned above.

- Chambers with **drift tubes (DT)** are utilized in the barrel part of the detector, $|\eta| < 1.2$. The magnetic field there is relatively uniform and mostly contained in the layers of the iron return yoke, and the rates of muons and *punch-through* (particles other than muons that reach the muon system) are low. As shown in Fig. 2.9, the DT chambers are mounted in four *stations* downstream, in between, and upstream the layers of the iron return yoke and form cylinders around the beamline. The inner three stations contain 60 chambers and the outermost cylinder is made of 70 chambers.

- **Cathode-strip chambers (CSCs)** are installed in the endcap region, covering the pseudorapidity range $0.9 < |\eta| < 2.4$. They yield shorter drift times than DTs and are suited for the operation in a stronger, non-uniform magnetic field. Furthermore, they can process the particle rate in the endcaps that exceeds the one in the barrel by orders of magnitude. The CSCs are placed in four stations behind the HCAL endcap and in between the three disks of the iron return yoke. A total of 2×234 chambers with trapezoidal shape are arranged in rings in the $r-\phi$ plane.

These muon detectors are described further below. They are accompanied by **resistive plate chambers (RPCs)** providing fast pattern recognition that supports the trigger decision and resolves ambiguities in the tracking. The RPCs are described in detail in Refs. [6].

Drift tubes in the barrel muon system

The smallest unit of the DTs are drift cells with a cross section of 13×42 mm^2 perpendicular to the anode wire that has a diameter of 50 μm. The electrical setup involves the anode wire at a voltage of 3.6 kV, the cathode at -1.2 kV, and two field-forming electrodes at 1.8 kV. The cells are filled with a gas mixture of 85% Ar/15% CO_2 that yields a drift velocity of 55 μm/ns and a sufficiently linear space-drift-time relation. The resulting maximal drift time of 380 ns is significantly larger than the 25(50) ns between two bunch crossings. The position resolution provided by a single cell is about 250 μm. Four layers of drift cells with the same orientation of the wires form a *superlayer*. The cells in consecutive layers are displaced by half the width of a cell. This layout yields a time resolution of the superlayer of a few nanoseconds by means of meantimer circuits, such that an efficient bunch crossing assignment is possible. The DT chambers in the three inner muon stations contain two superlayers with wires along the z direction that provide measurements of the ϕ coordinate and one superlayer that provides measurements of the z coordinate. In order to optimize the angular resolution in the bending plane, the two ϕ superlayers are placed at the inner and outer planes of a chamber with the z superlayer and a spacer between them. Chambers in the outermost station only contain two superlayers that both measure the ϕ coordinate. The eight measurements in the bending plane per chamber suffice to achieve the desired position resolution per chamber of 100 μm, while the z superlayers add precise enough directional information for the matching of track segments in different chambers and the matching to the muon track in the inner silicon tracker. The total number of channels (wires) of the DT system is about 172000.

CSCs in the endcap muon system

With the coverage of the endcap muon system up to $|\eta| < 2.4$, trajectories that pass the CSCs closest to the beamline are not exposed to the full bending power provided inside the magnet coil. Therefore, the off-line position resolution per chamber required to achieve the desired overall p_T resolution of 10% for muons with $p_T = 1$ TeV varies between 75 μm for chambers at high values of $|\eta|$ and 150 μm for the others. Furthermore, sizeable differences in the strength and orientation of the magnetic field within the chambers have to be taken into account. This results in slightly different designs of the CSCs in different locations.

In the CSCs, the cathode strips are oriented radially and have a fixed size $\Delta\phi$. The ϕ coordinate is determined by interpolating the charge induced on adjacent strips. The anode wires run along the ϕ direction and measure the radial coordinate r. A typical chamber contains six tracking layers that are defined by a gas gap with a width of 9.5 mm between the two planes of cathode strips that contains an anode wire. Both the signals of induced charges from the cathode strips and from the wires are read out. The former provides the better position resolution and is hence used to measure the coordinate in the bending plane, while the wire yields the faster signal and is used for timing purposes. The nominal gas mixture is 40% Ar/50% CO_2/10% CF_4. There are 220000 cathode strip readout channels and 180000 anode wire readout channels.

2.2.7 Trigger system and data acquisition

This section describes the general layout of the CMS trigger and data acquisition system and its basic features for CMS operations in pp collision mode, without including details of the trigger requirements and reconstruction algorithms. More information is presented for the physics objects most relevant to this work in Sec. 3.

The CMS trigger and data acquisition (DAQ) systems are described in Refs. [158, 159]. The performance of the trigger system during Run 1 (2009-2012) of the LHC is reported in Ref. [160].

This summary is also based on Refs. [131, 161].

The trigger and DAQ system is built to serve the crucial task of reducing the event rate from the bunch crossing rate of 40 MHz and corresponding inelastic pp interaction rate of almost 1 GHz (at the design performance of the LHC) to several 100 Hz for storage and data analysis, while retaining the events of interest for a broad physics program ranging from studies of soft QCD to the physics of B meson decays and searches for physics beyond the SM at the multi-TeV scale. It consists of the front-end readout systems of the individual subdetectors, the trigger system, and a global readout system that collects the data fragments and builds a single event. The detector front ends are synchronized with the LHC clock and temporarily store their data in a buffer for each bunch crossing. These front-end pipelines allow for a trigger latency below 4 μs [160] of the first, crucial stage of the two-stage trigger system, the L1 trigger. Within this time, the L1 trigger system has to form a decision on whether to further process or discard the event, and this information has to be communicated back to the detector front-end readout systems. Only data from the calorimeters and the muon system inform the L1 trigger decision. The L1 trigger system reduces the event rate by almost three orders of magnitude to a maximum of 100 kHz. Upon reception of a positive L1 trigger decision, the front-end pipelines are read out and the data are forwarded to the event building network of the DAQ. The assembled events are then filtered in the second stage of the trigger system, the high-level trigger (HLT), that makes a trigger decision based on refined reconstruction algorithms for physics objects that include information from all subdetectors. The HLT reduces the event rate to the desired several 100 Hz that are stored offline.

The L1 trigger

The L1 trigger system is implemented in customized hardware. The short bunch spacing at the LHC requires a very short L1 trigger latency and excludes extensive usage of commercial hardware. At the L1 trigger stage, events are selected with detector signals that are consistent with those expected from muons, electrons, photons, tau leptons, jets, or missing transverse energy. The front-ends of the calorimeters and the muon systems provide trigger primitives that are processed further in several steps, yielding a global muon trigger (GMT) and a global calorimeter trigger (GCT). The combination of the trigger information from these two pillars of the L1 trigger architecture informs the trigger decision of the global L1 trigger. Up to 128 selection algorithms can be applied by the global L1 trigger. These algorithms can be adjusted to changing LHC conditions and include in particular flexible p_{T} and E_{T} thresholds, and prescale values. The L1 decision of the global L1 trigger is processed by a trigger control system that forwards it to the front ends of all subdetectors and their pipelined data of the triggered bunch crossing are read out. Data fragments with a nominal size of 2 kB from roughly 700 front-end drivers (FEDs) are then fed into the DAQ system.

Data acquisition and high-level trigger

The data acquisition system has to combine all the information from the detector front ends, reduce the data rate by means of the HLT, and write the events to storage elements for further analysis. With a maximum L1 trigger rate of 100 kHz and an event size of order 1 MB, the DAQ has to process a total data rate of up to 0.1 TB/s. In contrast to the L1 trigger, the DAQ system is largely based on commodity technologies, such as networking technology for telecommunication and CPUs for PCs.

The event building is implemented in two stages. At the first stage, the output of eight FRLs is merged into an event superfragment. The full events are then built from superfragments in builder/filter unit PCs that also run the HLT software. The DAQ system is organized in eight independent slices that can process a L1 trigger rate of 12.5 kHz, each.

The HLT is implemented in software and uses reconstruction and particle identification algorithms similar to those for offline analysis of fully reconstructed events. The HLT trigger is organized in several so-called *HLT paths* that denote sequences of reconstruction and selection steps that are executed in a fixed order. As in the case of the L1 trigger, trigger prescales can be assigned to a given HLT path to keep its rate at the desired level without changing the selection thresholds. Events that pass the HLT are first stored in a storage network with a capacity of several 100 TB at the CMS site before their transfer to the Tier-0 computing center at the main CERN site and distribution via the Worldwide LHC Computing Grid [162].

2.2.8 Processing CMS data

The collection of software for the processing and analysis of CMS data is called *CMSSW* and is publicly available [163, 164]. All the software is integrated in a common modular framework and uses a common model for the event content, the *Event Data Model* (EDM). Thus, from software run at the HLT stage to offline reconstruction and analysis codes, the used software is based on an equal footing. In the EDM, a collision event is a `c++` object container for the raw detector data (RAW), assembled by the DAQ and trigger system, and the reconstructed data (physics objects) derived from it. The event data is structured in different layers. The HLT system creates the raw data events that provide the foundation of the EDM architecture. These raw data are then digitized and reconstructed using reconstruction software, that uses input from alignment and calibration services, resulting in the second layer of the EDM, the reconstructed data (RECO). The RAW and RECO data form the full event data, based on which further layers of the EDM can be derived by reducing the event content to those data needed by a specific analysis. The *Analysis Object Data* (AOD) event data is such a reduced event data format and constitutes the starting point for the analyses described in this thesis. The main CMSSW release for this work is version 5_3_X.

In most analyses, the event data collected with the detector is compared to the expectation from simulations. The software for the CMS detector simulation is also part of CMSSW. For simulated events, that start from event generators and parton shower programs which provide the particles in the event, the passage of the generated particles through the detector and the resulting detector signals that result in the RAW data have to be simulated. Two approaches are maintained by CMS for the detector simulation; a full simulation of the entire detector based on `GEANT4` [165], referred to as *FullSim*, and the simulation of a simplified detector geometry with infinitely thin material layers and simplified descriptions of energy loss in materials, referred to as *FastSim* [166, 167]. The latter reduces the processing time of the simulation step by about two orders of magnitude compared to the former, at the price of a less precise approximation of the detector response. Both approaches to the CMS detector simulation are utilized in simulated samples of signal events that have been produced by the author and are described further below.

2.2.9 CMS data taking in 2012

The integrated luminosities delivered by the LHC to the CMS IP and recorded by the detector in 2012 are shown in Fig. 2.10 [112]. In total, pp data corresponding to an integrated luminosity of 21.8 fb^{-1} have been recorded by the CMS detector. About 90.5% [168] of the recorded data have been cleared for physics analysis using all subdetectors after analysis of the data quality. This yields a dataset of pp collisions with an integrated luminosity of 19.7 fb^{-1} that is used in this work.

The peak instantaneous luminosity per day depicted in Fig 2.11 (left) exemplifies that the LHC operation in 2012 has been devoted to luminosity production; peak luminosities in excess of 6×10^{33} $\text{cm}^{-2}\text{s}^{-1}$ have been delivered on a regular basis and there has been no prolonged build-up of the instantaneous luminosity over the year. Fills of the LHC that delivered pp collisions to the experiments for several hours have been common, such that the instantaneous luminosity has often varied significantly over one fill. This is reflected in the broad distribution of the average number of pileup events in Fig. 2.11 (right) with a mean of 21 inelastic events per bunch crossing [112]. The maximum recorded integrated luminosity per fill in 2012 has been 239 pb^{-1} for LHC fill number 2692 that delivered stable beams for a record 22.74 h [169].

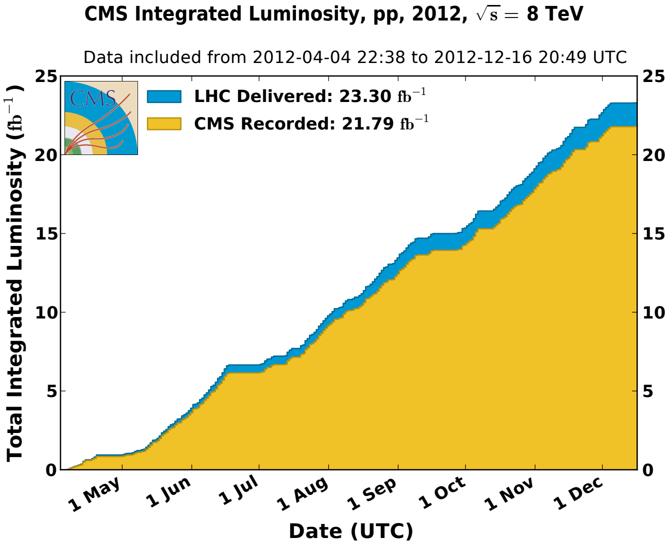

Figure 2.10: Build-up of the integrated luminosity delivered to (blue) and recorded by (orange) the CMS detector in the year 2012. The figure is taken from Ref. [112].

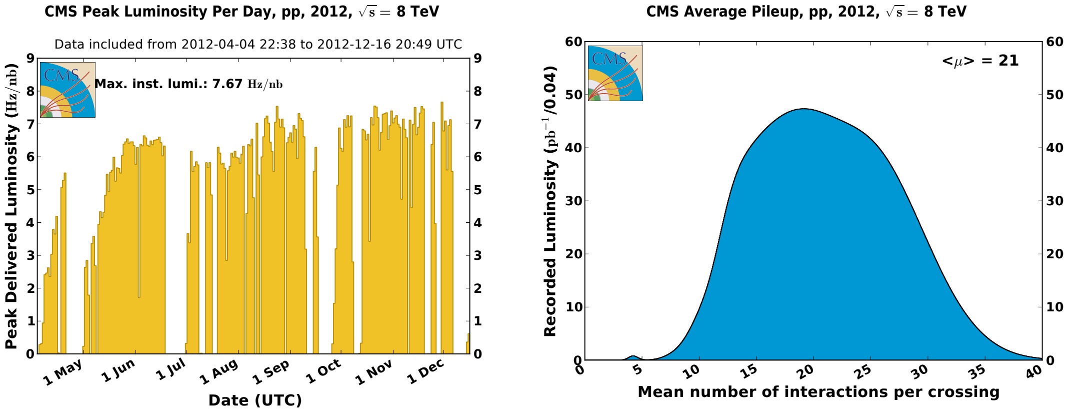

(a) Peak instantaneous luminosity delivered to the CMS detector by the LHC in 2012 per day.

(b) Integrated luminosity of the pp dataset recorded by CMS in 2012 as a function of the mean number of inelastic pp collisions per bunch crossing.

Figure 2.11: Quantities related to the instantaneous luminosity delivered to the CMS detector by the LHC in the year 2012. Both figures are obtained from Ref. [112].

A typical average L1 trigger rate at the end of 2012 data taking has been 56.5 kHz, well below the 100 kHz limit of the DAQ system, and an average HLT event rate of 400 Hz has been written to storage [160].

2.3 Utilized datasets

The eμ resonance search is based on an unprescaled single-muon HLT path that writes to the *SingleMu* primary dataset for offline analysis. The $\mu\tau_{\mathrm{e}}$ resonance search utilizes a different HLT path that requires both a reconstructed muon and a supercluster in the ECAL, writes to the *MuEG* primary dataset, and is also unprescaled. Both HLT paths are described in more detail in Sec. 3.3. The sample names of the used datasets in the CMS data aggregation system (DAS) [170] are summarized in Tab. B.1 in App. B together with the corresponding integrated luminosities.

Chapter 3

Reconstruction of physics objects in CMS

In this chapter, basic information about the trigger criteria as well as the reconstruction of physics objects that are used in the presented analyses are given. A focus is put on the reconstruction of electron and muon candidates that are most important to this work, but other physics objects that play a rôle in the event selections of the $e\mu$ and $\mu\tau_e$ resonance searches are briefly introduced, too. A more detailed description of the utilized set of cuts for muon and electron identification is included in the description of the event selection for the $e\mu$ resonance search in Sec. 4.

3.1 Track reconstruction in the inner tracking system

Both muons and electrons leave tracks in the inner tracking system. The standard sequence for the reconstruction of tracks in the CMS tracker is outlined in this section, based on Ref. [140], before the specifics of muon and electron track reconstruction are presented in the following sections.

In the uniform magnetic field in the tracker volume, charged particle trajectories follow a helix (or section of a helix). The latter is defined by five parameters in the CMS coordinate system. The five track parameters are summarized in a *state vector* that is evaluated at a reference surface (for example a tracking layer) or a reference point. The set of parameters adopted to describe a track in the CMS tracking software is given by $\{|\mathrm{d_{xy}}|, |\mathrm{d_z}|, \phi, \cot\theta, p_\mathrm{T}\}$ [140], where $|\mathrm{d_{xy}}|$ and $|\mathrm{d_z}|$ denote the distances between the reference point and the point of closest approach of the track to this reference point in the transverse plane and along the z direction, respectively. In most analyses, the track parameters evaluated at the point of closest approach to the beam axis or the assigned interaction vertex are the ones of primary interest, but the extrapolation of tracks to other detector surfaces, such as the inner surface of the ECAL, is also important for the matching of detector signals produced by charged particles in different subdetectors.

The algorithm used in the standard reconstruction of tracks in the inner tracking system is an adaption of the combinatorial Kalman filter [171], which is in turn a generalization of the Kalman filter [172], a recursive tracking algorithm. The tracks are the result of an iterative tracking process that comprises several track reconstruction sequences. Each of the iterations consists of the following steps:

- Track seeding: Initial track candidates are formed in the inner layers of the tracking system from only three 3D hits, or two 3D hits plus information from a fast vertex reconstruction using only hits in the pixel detector. The 3D hits are either pixel hits or so-called matched strip hits in the silicon strip tracker that are built from a pair of hits in a strip that measures the position in the $r-\phi$ plane and in the corresponding adjacent strip that is mounted at 100 mrad stereo angle. The seeds provide an initial estimate of the trajectory parameters. Track seeding can be performed by the inner tracking system alone. For the reconstruction of electron tracks, the algorithms selecting track seeds use the position and energy of ECAL superclusters for reasons given in Sec. 3.2.2.

- Track finding: Track finding in the standard CMS track reconstruction is based on the Kalman filter approach. Starting from the seed and the first estimate of the track parameters, compatible hits from adjacent detector layers are added. The state vector and the associated uncertainties are updated at each layer. The necessary inputs to the algorithm are the uncertainties in the hit positions and a model of the material crossed by the particle from which the expected energy loss and multiple scattering can be inferred. Multiple versions of the track are considered at each layer and propagated to the next one.

- Track fitting: The track finding stage concludes with a list of hits for a given track. These are used as input for further iterations of the Kalman filter, one progressing inside-out and the other outside-in. The track parameters at each surface with an associated hit are then obtained from the weighted average of these two iterations. Following this procedure, the association of hits with the track is re-evaluated on the basis of a χ^2 requirement.

- Track selection: The selection of reconstructed tracks is based on the χ^2/N_{dof} value of the track fit, the number of layers with associated hits, the number of missing hits in detector layers on the trajectory, and the (loose) compatibility of the track with primary interaction vertices.

The requirements defining a seed, the configuration of the Kalman filters, and the track selection criteria vary for the different iterations of the described reconstruction sequence.

According to simulations, the tracking efficiency of the described standard (inner) track reconstruction for isolated muons with $p_{\mathrm{T}} > 1$ GeV exceeds 99% in the full geometrical acceptance of the tracker [140]. The tracking efficiencies for isolated pions and electrons are smaller and show a pronounced dependence on the pseudorapidity. In contrast to muons, charged hadrons are subject to nuclear interactions and electrons are affected by sizeable energy loss due to bremsstrahlung. A Gaussian-sum filter is employed in the final stage of electron track reconstruction and the electron tracking efficiency is thereby improved, as described in Sec. 3.2.2.

3.2 Reconstruction of muon and electron candidates

Fundamentals of muon and electron reconstruction in CMS are introduced in this section before turning to the corresponding triggers in the following one. These topics are presented in this order because complex (offline) reconstruction algorithms are used already at the (online) HLT trigger stage.

3.2.1 Muon reconstruction

The standard algorithms for the reconstruction of muon tracks are described in detail in Ref. [152]. Information on specialized muon track fits that are intended for high-p_{T} muons and yield an improved p_{T} resolution for $p_{\mathrm{T}} \gtrsim 200$ GeV is included in Ref. [173].

Muons with $p_{\mathrm{T}} > 5$ GeV typically produce hits not only in the inner tracking system but also in the muon system. The track in the muon system is crucial for the muon trigger and the identification of muon tracks. Reconstruction of muon tracks starts from the separate reconstruction of the *inner* muon track in the all-silicon tracking system and of the *standalone* muon track in the muon system. Reconstruction of the inner muon track proceeds as described above in Sec. 3.1; the standalone muon reconstruction is presented in the following paragraph. The two individual tracks are then combined in a *global* muon track fit.

Standalone muon reconstruction

The reconstruction of muon tracks in the muon system starts from track segments in the innermost chambers. The associated estimate of the track parameters is used to initialize a Kalman filter that works as a track finder from the inner to the outer stations of the muon system. The measurements that are used as input to the Kalman filter at each tracking layer are the track segments reconstructed in the DT chambers or 3D hits in the CSC system, respectively. Hits in the RPC chambers are included in the track reconstruction as well. After a second Kalman filter is run that performs a reconstruction from the outer to the inner muon stations, a final track fit with a beamspot constraint (for hadron collision data) yields the final standalone muon track.

Global muon reconstruction

In the global muon reconstruction, standalone muon tracks are propagated from the innermost layer of the muon system to the silicon-strip detector, where their track parameters are compared to those of tracker tracks evaluated at a common detector surface. If a match is found, a new track fit (Kalman filter) that spans the entire detector hemisphere is performed, based on the hits of both the inner and outer tracks.

Track refits for high-p_T muons

The muon critical energy in iron is about 350 GeV [174]. Therefore, the trajectory in the muon system of muons with momenta of several 100 GeV can be affected by significant radiative energy loss. The measured track parameters may thus differ substantially from those at the interaction vertex. Furthermore, electromagnetic showers can induce additional hits in the muon chambers that degrade the accuracy of the track reconstruction. As a result, additional algorithms for the reconstruction of the global muon track, that differ from the standard reconstruction in the treatment of the information from hits in the muon system, have been developed in CMS [173]. The *Tracker-Plus-First-Muon-Station (TPFMS)* track fit includes only muon hits in the first muon station and rejects those in the subsequent stations that are more likely affected by radiation. The *Picky* track fit includes information about the hit occupancy in the chambers traversed by the muon trajectory and rejects hits in chambers that appear to contain showers, based on a χ^2 criterion.

With several track fits available for muon trajectories, an algorithm is needed to evaluate which track fit and associated set of track parameters to choose for a given muon candidate. In the analyses presented in this work, an updated version of the *Tune P* algorithm described in Ref. [173] is utilized. It choses for each muon candidate between a maximum of four muon track fits; the inner track in the silicon tracking detectors, the global muon track, the TPFMS track, and the Picky track. This choice is based on the logarithmic tail probabilities of the corresponding track fits, $-\log(P(\chi^2_\mathrm{track}, N^\mathrm{track}_\mathrm{dof}))$, and a cutoff on the relative uncertainties in the p_T assignments of $\delta p_\mathrm{T}/p_\mathrm{T} < 0.25$. The track parameters of the inner muon track are used if either the selected track fit or the inner muon track yield a p_T below 200 GeV because additional information from the muon system does not improve the p_T resolution in this region (the muon system is however necessary for the triggering and muon identification).

The uncertainty in the muon scale has been determined to about 0.2% at $p_\mathrm{T} \approx 50$ GeV using muons at the Z peak and to 5% for muons with $p_\mathrm{T} \approx 1$ TeV using muons from cosmic rays [173].

The transverse momentum resolution achieved by the Tune P algorithm is compared to that obtained from the standard global muon reconstruction for muons from cosmic rays that fall in the barrel region of the CMS muon system equipped with DTs in Ref. [173]. For muon transverse momenta above 200 GeV, the Tune P p_T assignment is found to improve the momentum resolution of the global muon fit. The results of a transverse momentum resolution study with cosmic muons, that reflects the performance of the 2012 configuration of the CMS detector, are presented in Sec. 5.4.2. The transverse momentum resolution for isolated muons within $|\eta| \lesssim 0.9$ is found to range from just below 1% at $p_\mathrm{T} = 10$ GeV to about 5% at $p_\mathrm{T} = 500$ GeV. The angular resolution for muon tracks in the barrel provided by the inner tracking system is $\mathcal{O}(10^{-1}$ mrad) in the ϕ coordinate and $\mathcal{O}(10^{-4})$ in $\cot(\theta)$ for $p_\mathrm{T} > 50$ GeV [140].

3.2.2 Electron reconstruction

One of the most important challenges of electron reconstruction in CMS arises from the combination of the sizeable material budget of the all-silicon tracking system ($0.4 - 2.0\ X_0$) upstream of the ECAL with the strong solenoid magnetic field that bends the electron trajectory. Since electrons lose on average between 33% ($\eta \approx 0$) and 86% ($|\eta| \approx 1.4$) of their energy via the emission of bremsstrahlung photons whose trajectories are not affected by the magnetic field, the distribution of energy deposits in the ECAL crystals (ECAL cluster) associated with an electron can be extended significantly along the ϕ direction. Furthermore, the energy loss distribution of the bremsstrahlung process is not described well by a Gaussian distribution and thus poses a challenge to the tracking algorithm.

In the following, the reconstruction of electron tracks in the inner tracking system and the reconstruction of ECAL clusters resulting from electrons are described. The main references that have been used are Refs. [140, 175, 176] for the track reconstruction and Ref. [151, 177] for the reconstruction of the ECAL cluster.

Reconstruction of electron energy in the ECAL

The collection of ECAL clusters from bremsstrahlung photons in addition to the reconstruction of the energy deposited in the ECAL by the electron itself is crucial to the reconstruction of the original electron energy at the interaction vertex. Therefore, the clustering algorithms employed in the CMS reconstruction of the electron (and photon) energy select an extended cluster of energy deposits, the so-called *supercluster* (SC). Two different clustering algorithms are employed to collect the energy deposited by electrons in the barrel and endcap sections of the ECAL. Different algorithms are needed because the $PbWO_4$ crystals are arranged in different patterns; a $\eta - \phi$ geometry is used in the barrel, whereas the crystals are placed in a $x - y$ pattern in the two endcaps.

In the barrel, the clustering algorithm starts from a single seed crystal (the one with the highest E_T value in any region considered for ECAL SC reconstruction) that must have a transverse energy above 1 GeV. Strips of 5×1 crystals in $\eta \times \phi$ are added around the seed crystal in both directions along ϕ within an interval $\Delta\phi \approx \pm 0.3$ rad if the energy contained in the strips exceeds 100 MeV. Sets of connected 5×1 crystal arrays are then merged into individual clusters. A supercluster is the set of nearby clusters which contain at least one strip of 5×1 crystals with an energy above 350 MeV. The electron (or photon) energy is obtained from the supercluster.

In the endcap, the clustering algorithm starts from 5×5 arrays of crystals around seed crystals. These clusters may overlap. They are sorted according to the E_T of their seed crystal and SCs are formed by merging clusters with an E_T above 1 GeV. The energy-weighted positions of the individual clusters in an SC are then associated with energy deposits in the preshower detector and the sum of the energies in the ECAL crystals and the preshower yields the SC energy.

The SC position is given by the energy-weighted mean of the position of its individual cluster, as described in detail in Ref. [152].

Reconstruction of electron tracks in the inner tracking system

The Kalman filter used for the reconstruction of muon tracks is the optimal choice for the estimation of the track parameters if -among other conditions- the random variables describing the disturbance of the track at a measurement layer are Gaussian-distributed [172]. It is therefore the tracking algorithm of choice if the energy loss distribution describing the particle's passage through matter follows a Gaussian distribution. However, a single Gaussian distribution yields a poor description of the probability density function for the energy loss of electrons due to bremsstrahlung. The model of energy loss that informs the reconstruction algorithm for electron tracks used in CMS is the Bethe-Heitler model of bremsstrahlung [178]. Its energy loss distributions are approximated for various values of the traversed thickness of material by Gaussian mixtures (weighted sums of Gaussian distributions) with up to six components [179]. With this approximation, the new tracking algorithm is obtained as a generalization of the Kalman filter by replacing the single Gaussian distributions describing the energy loss with Gaussian mixtures. The resulting algorithm can be thought of as several Kalman filters running in parallel, with one Kalman filter per component of the mixture. It is referred to as a *Gaussian-sum filter* (GSF) [175] and the resulting tracks are called *GSF tracks*. The improvement in the momentum resolution for electron tracks that is achieved by replacing the Kalman filter with the GSF track reconstruction is quantified in Refs. [140, 175].

Since the GSF track fit is very CPU-time consuming, it is not applied to all tracks that start from the standard track seeds. Instead, two dedicated selections of track seeds are carried out for electrons [151]. They both use the information from the superclusters reconstructed in the ECAL. The ECAL-based seeding uses the SC position and energy to estimate two electron trajectories (one for each electric charge) and find corresponding candidates for track seeds in the inner layers of the tracking system. This outside-in approach to electron track seed finding is complemented by an inside-out procedure that starts from the tracks from the standard CMS track reconstruction, extrapolates them to the inner ECAL surface, and tries to identify a matching SC. If a match is found, the initial track seed is used to start the reconstruction of a GSF track. The track seeding efficiency for electrons in simulated $\mathrm{Z} \to \mathrm{ee}$ events is larger than 95% when both approaches are combined. The corresponding efficiency for the ECAL-based seeding alone is about 92% [151].

Uncertainties in the electron energy scale of 0.2% (barrel) and 0.3% (endcap) have been estimated using electrons from Z decays [151].

The additional challenges in the reconstruction of electron tracks compared to that of muon tracks are reflected in the different momentum resolutions achieved by the respective tracking algorithms: The effective p_T resolution[1] for muon tracks with $p_\mathrm{T} = 100$ GeV is $2-3\%$ in the pseudorapidity range $|\eta| \lesssim 1.5$. In contrast, the effective transverse momentum resolution of simulated GSF electron tracks that are generated within $|\eta| < 1$ with $p_\mathrm{T} = 100$ GeV lies between 10% and 20% [140].

For electron energies above 15 GeV, the energy resolution for electron superclusters is smaller than the momentum resolution from the GSF track, as shown in Fig. 3.1 [151]. The large difference in these two resolutions for high electron p_T is important to the choice of the electron identification criteria used in this work, that are introduced in Sec. 4.1.

3.3 Triggering on muons and ECAL clusters

This summary of the utilized trigger algorithms is based on Ref. [160]. The $\mathrm{e}\mu$ resonance search utilizes a single-muon trigger (`HLT_Mu40_eta2p1`), whereas the $\mu\tau_\mathrm{e}$ search starts from a two-object trigger that calls for a muon candidate and an ECAL cluster (photon or electron candidate) already at the L1 trigger level (`HLT_Mu22_Photon22_CaloIdL`).

3.3.1 Level 1 muon trigger

In the DT and CSC muon systems, the front-end trigger electronics use the hit information from the multiple tracking layers within a single chamber to identify track segments. In a second step, collected track segments are forwarded to regional track finders that combine information from more than one station to identify muon candidates with pattern recognition algorithms. This stage also includes a first p_T assignment, computation of the azimuthal and longitudinal coordinates of the track, and the assignment of a track quality measure. In the RPC muon system, the hits are directly transmitted to trigger electronics that perform pattern recognition to select track candidates. The regional track finders of the three muon systems forward a maximum of four

---

[1] The so-called effective momentum resolution is defined as half of the smallest interval around the peak position of the $\delta p/p$ distribution that contains 68.3% of the entries. Note that the definition of the momentum and energy resolutions in the description of the CMS detector and in Secs 5.4 and 11.3.2 are different; they represent the standard deviation of a Gaussian fit to the core of the corresponding distributions.

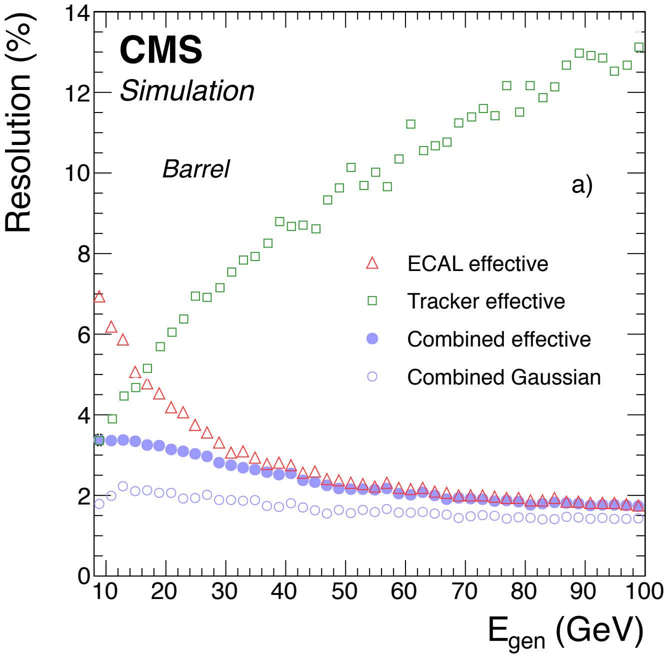

Figure 3.1: The effective energy (momentum) resolutions for electron superclusters (GSF tracks) and their combination as a function of the generated electron energy. The numbers are obtained from a simulated MC sample of electrons generated with uniform distributions in η and p_T. The open circles indicate the Gaussian core resolution for the combination of supercluster and track information. The figure is taken from Ref. [151].

sorted candidates (DT, CSC systems) or eight candidates (RPC system) to the global muon trigger (GMT) for each bunch crossing. Track segments from the different muon systems that can be associated with a single muon are merged at the GMT level, and the p_T assignment and track quality are re-assessed before the information is transmitted to the global L1 trigger for the trigger decision.

The single-muon L1 trigger efficiency is commonly defined with respect to muons that pass tight muon identification criteria offline and determined via a *tag-and-probe* method [173]. For p_T values of the probe muon well above the L1 p_T threshold (above the *trigger turn-on* stemming from the limited p_T resolution at the L1 stage), the single-muon L1 trigger efficiency is approximately constant at about 95% up to $p_T = 100$ GeV [160]. The L1 trigger that seeds the single-muon HLT path utilized in the eμ resonance search is not prescaled and requires $|\eta| < 2.1$ and $p_T > 16$ GeV. For this L1 p_T threshold, the efficiency plateau is reached at an offline muon p_T of 20 GeV. The rate of this single-muon L1 trigger as implemented in typical L1 trigger menus used for data taking in 2012 is about 4 kHz for an instantaneous luminosity of $5 \times 10^{33}\text{cm}^{-2}\text{s}^{-1}$ [160]. The restriction of the muon pseudorapidity to $|\eta| < 2.1$ reduces the rate by about 50% and allows the trigger to remain unprescaled for the entire 2012 data taking period.

3.3.2 Muon high-level trigger

The muon HLT involves two main sequences of track reconstruction and event filtering, referred to as L2 and L3. In the first (L2) reconstruction step, only information from the muon systems is used. Pairs of muon track segments in DT chambers and CSCs provide seeds for a muon track reconstruction in the muon system using the Kalman filtering technique. The muon p_T resolution is improved by using the IP position as a constraint in the determination of the track parameters. The event filter decision after the L2 reconstruction depends on the number of reconstructed muons, the associated p_T values, and the number of measurements in the muon system associated with a track. In the second (L3) reconstruction step, tracks in the muon system that pass the first (L2) filter serve as seeds for track reconstruction in the inner, all-silicon tracking system. Due to this seeding, the full reconstruction of all tracks in the event does not have to be carried out for the muon reconstruction at HLT level. The inner muon track reconstruction employs a Kalman filter, again. The tracks reconstructed in the inner tracking system are matched to L2 muon tracks in the muon system and the hits associated with identified track pairs are used as input to a refit of the muon track spanning both the inner and muon tracking systems. The result is the L3 muon track that informs the final HLT filter decision. The p_{T} resolution at the L3 stage is close to that achieved by the offline muon track reconstruction.

The single-muon HLT path utilized in the eμ resonance search requires $p_{\mathrm{T}} > 16$ GeV at the L2 stage and $p_{\mathrm{T}} > 40$ GeV at the L3 stage. In addition to the pseudorapidity requirement of $|\eta| < 2.1$, the L3 track is also required to yield a $\chi^2/N_{\mathrm{dof}} < 20$ and a transverse impact parameter with respect to the beamspot below 0.1 cm.

3.3.3 Muon plus ECAL cluster trigger

In addition to a muon candidate, the two-object trigger utilized in the $\mu\tau_{\mathrm{e}}$ resonance search requires the presence of an ECAL cluster in the event. The L1 calorimeter trigger is described in detail in Ref. [160]. It processes input from both the ECAL and HCAL. The L1 triggers for photons and electrons start from trigger towers that combine the energy deposits from several ECAL crystals. The preshower information is not used in the L1 trigger. Starting from 2012, crystal transparency corrections to the trigger tower energy have been applied at the L1 trigger stage. For electrons or photons with transverse energies below about 60 GeV, a L1 E_{T} resolution better than 10% is achieved in the pseudorapidity range $|\eta| < 2.5$. For electrons/photons with transverse energies well above the L1 trigger threshold, the L1 trigger efficiency is close to 100%. At the HLT stage, superclusters are reconstructed using the standard offline algorithm described above.

In the $\mu\tau_{\mathrm{e}}$ search, the trigger requirement at the L1 stage includes a muon with $p_{\mathrm{T}} > 3.5$ GeV (without a restriction of the muon pseudorapidity) and an ECAL cluster with $E_{\mathrm{T}} > 12$ GeV. Demanding the presence of two objects allows for significantly reduced trigger p_{T} thresholds while keeping the rate at an acceptable level; for an instantaneous luminosity of $5 \times 10^{33}\mathrm{cm}^{-2}\mathrm{s}^{-1}$ the rate of this L1 seed is about 2 kHz [160]. At the HLT stage, the muon p_{T} and the E_{T} of the ECAL supercluster are required to exceed 22 GeV. In addition, loose cuts on the cluster shape in the ECAL are applied and the sum of energy deposits in the HCAL around the ECAL supercluster, H/E, has to be smaller than 0.10 (0.15) in the barrel (endcap) region of the ECAL. No tracker information is used in the selection of the ECAL cluster at HLT level. Therefore, the HLT path `HLT_Mu22_Photon22_CaloIdL` can be used in searches with a photon/muon pair in the final state of interest or with an eμ pair, as in the case of the $\mu\tau_{\mathrm{e}}$ resonance search.

3.4 Jet reconstruction and missing transverse energy

Jets, the experimental signatures of energetic gluons and quarks, and the missing transverse energy $\not{E}_{\mathrm{T}}$ do not play a central role in the eμ resonance search but yield important control distributions. In the $\mu\tau_{\mathrm{e}}$ search, a veto against b-tagged jets is applied and the key observable, the mass of the $\mu\tau$ system, involves $\not{E}_{\mathrm{T}}$ that arises from the neutrinos in the τ decay. Both the utilized jet reconstruction and $\not{E}_{\mathrm{T}}$ definition are based on the particle-flow event reconstruction employed by CMS. It is therefore introduced in Sec. 3.4.1 before the jet reconstruction and the definition of $\not{E}_{\mathrm{T}}$ are covered in Secs. 3.4.2 and 3.4.3, respectively.

3.4.1 The CMS particle-flow algorithm

The design of the CMS detector calls for the combination of information from different subdetectors in the reconstruction of all physics objects. For example, jet reconstruction from the energy deposits in the calorimeters alone yields a comparatively poor performance because charged particles in the central region of the detector are trapped in the tracker volume for $p_{\mathrm{T}} \lesssim 0.7$ GeV (loopers) and the momentum resolution of the tracks of charged hadrons is much better than the energy resolution in the HCAL over a wide range of momenta.

The CMS particle-flow (PF) event reconstruction [180, 181] organizes the signals from all subdetectors (tracks and energy clusters) in a list of individual particles: muons, electrons, charged hadrons, photons, and neutral hadrons. This mapping of detector signals to stable particles (*PF candidates*) mitigates the problem of double-counting particle momenta when combining information from different subdetectors, allows for a momentum/energy assignment that is optimized for the individual particle species, and permits a corresponding customized energy calibration. The high resolution and granularity of both the all-silicon tracking system and the ECAL are particularly important for this mapping. How detector signals are linked and how the PF algorithm organizes the set of linked detector signals into a list of particles is sketched in Ref. [180]. Rather than building complex physics objects such as jets and event variables like $\not\!\!E_{\mathrm{T}}$ directly from detector signals, these are reconstructed from the list of reconstructed PF candidates.

3.4.2 Particle-flow jets

The jets used in this work are reconstructed from the four-momenta of PF candidates with the anti-k_{T} algorithm [182] with a distance parameter R = 0.5 for cones in the space spanned by rapidity y and azimuthal angle ϕ. Jet energy corrections (JEC), that are provided by the CMS JetMET group, are applied to jet momenta in experimental data and to those from Monte Carlo (MC) simulations in a consecutive, factorized approach [183]:

$$p^{\mu}_{\mathrm{corr}} = \mathcal{C}_{\mathrm{JEC}} \times p^{\mu}_{\mathrm{raw}} \tag{3.1}$$

$$\mathcal{C}_{\mathrm{JEC}} = \mathcal{C}_{\mathrm{PU}} \times \mathcal{C}_{\mathrm{MC}}(p'_{\mathrm{T}},\, \eta) \times \mathcal{C}_{\mathrm{rel}}(\eta) \times \mathcal{C}_{\mathrm{abs}}(p''_{\mathrm{T}}) \;, \tag{3.2}$$

where p^{μ}_{raw} and p^{μ}_{corr} denote one component of the originally measured and the corrected jet four-momenta, respectively; and p'_{T}, p''_{T} denote consecutively corrected jet p_{T} values. In a first step ($\mathcal{C}_{\mathrm{PU}}$), the contributions of pileup events and electronic noise to the jet energy and momentum are removed. In a second step ($\mathcal{C}_{\mathrm{MC}}(p'_{\mathrm{T}},\, \eta)$), the measured jet energy is corrected to the particle level based on the expected response of the detector to particle-level jets that is obtained from simulations. This correction to the particle level takes into account the nonuniformity of the energy response of the calorimetry in jet pseudorapidity and the nonlinearity in jet p_{T}. In a third step, jets in data are further corrected for residual differences in the jet energy response in data and simulation with the so-called relative ($\mathcal{C}_{\mathrm{rel}}(\eta)$) and absolute ($\mathcal{C}_{\mathrm{abs}}(p''_{\mathrm{T}})$) corrections. This complex procedure is described in detail in Ref. [155]. After the application of the JEC, the jet energy scale uncertainty is smaller than 3% for jets with $p_{\mathrm{T}} > 30$ GeV over the full HCAL/HF coverage ($|\eta| < 5$).

Only PF jets with $p_{\mathrm{T}} > 35$ GeV in the geometrical acceptance of the tracker, $|\eta| < 2.4$, are considered in this work. The PF jet reconstruction yields a straightforward definition of jet identification criteria such as the number of constituents and various energy fractions because it starts from a list of reconstructed physics objects. The set of loose jet identification criteria summarized in Tab. 3.1 is applied in order to reject detector noise or detector signals by cosmic muons that are reconstructed as jets. They retain more than 99% of genuine jets according to simulations [155, 184].

For jets in the barrel region of the detector, the jet energy resolution is 15−20% at $p_{\mathrm{T}} = 35$ GeV, depending on pileup; typical values at $p_{\mathrm{T}} = 100$ GeV and $p_{\mathrm{T}} = 1$ TeV are 10% and 5%, respectively [155].

B-tagging

The identification of jets that are initiated by a b quark is of interest in the eμ and $\mu\tau_{\mathrm{e}}$ resonance searches because the production of top quark pairs constitutes the most important background

Table 3.1: The identification criteria applied to PF jets within $|\eta| < 2.4$.

Jet identification variable	Selection cut
Number of constituents	≥ 2
Number of charged particles	≥ 1
Energy fractions	
Charged hadrons	≥ 1
Electrons	< 0.99
Muons	< 0.8
Neutral hadrons	< 0.99
Photons	< 0.99

in both cases. Different algorithms for b jet identification are employed by CMS as described in Ref. [185]. The performance of b-tagging in pp collisions at $\sqrt{s} = 8$ TeV is studied in Ref. [186].

The b-tagging algorithms employed by CMS use information from impact parameters of tracks with respect to primary vertices and/or information from reconstructed decay vertices within jets, so-called *secondary vertices*. Secondary vertex candidates are built from tracks passing track selection requirements that are tightened compared to the standard track selection and reconstructed by applying an adaptive vertex fit [187]. The resulting vertex candidates have to pass a selection; in particular, they are rejected if more than 65% of the associated tracks are also associated to the primary vertex from which the jet originates and the information from the distance vector connecting the primary and secondary vertex is used to define further selection criteria [185]. The *Combined Secondary Vertex* (CSV) algorithm, that is used for the identification of b jets in this work, combines information from secondary vertices and track-based lifetime information into a likelihood estimator with discrimination power between b jets and light jets (u, d, s, g), as well as between b jets and c jets. Up to nine observables are used in the definition of the CSV discriminator, depending on whether a secondary vertex is found or only track-based information is available for the studied jet.

In this work, jets are assigned a b tag if the CSV discriminator is required to be larger than 0.679. This value defines the so-called medium operating point for b-tagging with the CSV algorithm that is chosen such that the misidentification probability of a light jet as a b-tagged jet is of order 1%. As a function of the light jet p_{T}, this mistag probability increases from 1% at $p_{\mathrm{T}} = 50$ GeV to about 4% at $p_{\mathrm{T}} = 1$ TeV. An average b-tagging efficiency of 67% has been measured for this discriminator in $\mathrm{t\bar{t}}$ events in the lepton+jets channel with an average p_{T} of the b jets of about 80 GeV [186].

3.4.3 Adding it all up - missing transverse energy

The main reference for the reconstruction of $\not{E}_{\mathrm{T}}$ in pp collisions at $\sqrt{s} = 8$ TeV with the CMS detector is Ref. [188]. The PF missing transverse energy, in short PF $\not{E}_{\mathrm{T}}$, that is the $\not{E}_{\mathrm{T}}$ assignment of choice in this work, is defined as the negative of the vectorial sum of the momenta of all PF objects in the event. Several corrections are applied to the thus defined uncorrected PF $\not{E}_{\mathrm{T}}$ in an additive fashion:

$$\vec{\not\!\!E}_{\mathrm{T}}^{\mathrm{raw}} \equiv -\sum_{i} \vec{p}_{\mathrm{T,\,i}} \,, \tag{3.3}$$

$$\vec{\not\!\!E}_{\mathrm{T}}^{\mathrm{corr}} = \vec{\not\!\!E}_{\mathrm{T}}^{\mathrm{raw}} - \vec{\Delta}_{\mathrm{jets}} - \vec{\Delta}_{\mathrm{PU}} - \vec{\Delta}_{\phi} - \vec{\Delta}_{\mathrm{p}_{\mathrm{T}}^{\mu}} \,, \tag{3.4}$$

where the index i runs over all PF objects and the symbols $\vec{\Delta}_X$ stand for various corrections that are described in the following.

PF $\not\!\!E_{\mathrm{T}}$ corrections

- *JEC-related correction* $\vec{\Delta}_{\mathrm{jets}}$

  The JEC described in Sec. 3.4.2 are partially propagated to PF $\not\!\!E_{\mathrm{T}}$. To this end, the PF objects are grouped into three categories: Jets with $p_{\mathrm{T}} > 10$ GeV (*clustered energy*), jets with $p_{\mathrm{T}} < 10$ GeV, and unclustered particles. The jet p_{T} cut separating the former two categories is applied after the application of JEC to the jet. In the propagation of the JEC to PF $\not\!\!E_{\mathrm{T}}$, only the clustered energy is corrected. This is done by replacing the vector sum of the (uncorrected) transverse momenta of PF particles clustered in a jet with the corresponding corrected jet momenta. The pileup correction in the JEC ($\mathcal{C}_{\mathrm{PU}}$ in Eqn. 3.2) is removed in the JEC propagation because pileup effects are accounted for separately in the $\not\!\!E_{\mathrm{T}}$ reconstruction as described below. The result is the so-called *type-I-corrected* PF $\not\!\!E_{\mathrm{T}}$ [155, 188] that can be expressed as:

$$\vec{\not\!\!E}_{\mathrm{T}}^{\mathrm{type-I}} = \vec{\not\!\!E}_{\mathrm{T}}^{\mathrm{raw}} - \vec{\Delta}_{\mathrm{jets}} \tag{3.5}$$

$$= \left[- \sum_{\substack{i \,\in\, \mathrm{jets} \\ p_{\mathrm{T}} \geq 10\ \mathrm{GeV}}} \vec{p}_{\mathrm{T,\,i}}^{\mathrm{\,raw}} - \sum_{\substack{j \,\in\, \mathrm{jets} \\ p_{\mathrm{T}} < 10\ \mathrm{GeV}}} \vec{p}_{\mathrm{T,\,j}}^{\mathrm{\,raw}} - \sum_{k \,\notin\, \mathrm{jets}} \vec{p}_{\mathrm{T,\,k}} \right] - \sum_{\substack{i \,\in\, \mathrm{jets} \\ p_{\mathrm{T}} \geq 10\ \mathrm{GeV}}} \left(\vec{p}_{\mathrm{T,\,i}}^{\mathrm{\,corr}} - \vec{p}_{\mathrm{T,\,i}}^{\mathrm{\,PU}} \right) \,, \tag{3.6}$$

  where the sums run over the PF objects satisfying the indicated requirements, $\vec{p}_{\mathrm{T,\,i}}^{\mathrm{\,corr}}$ denotes the transverse jet momentum after all JEC are applied, and $\vec{p}_{\mathrm{T,\,i}}^{\mathrm{\,PU}}$ denotes the transverse jet momentum after only the pileup correction is applied.

- *Pileup correction* $\vec{\Delta}_{\mathrm{PU}}$

  The correction of the measured missing transverse energy for pileup effects is based on the assumption that the vectorial sum of the transverse momenta of charged particles (tracks) associated with vertices from pileup interactions and the corresponding sum from neutral particles almost cancel each other. This assumption is justified because the probability for the production of neutrinos with considerable energy, i.e. genuine $\not\!\!E_{\mathrm{T}}$, in minimum bias interactions is small. However, the nonlinearity of the energy response and the minimum energy thresholds in the calorimeters bias the measured transverse energy contribution from neutral particles and thus spoil the cancellation of the pileup contributions of charged and neutral particles to $\vec{\not\!\!E}_{\mathrm{T}}$. The needed pileup correction (referred to as the *type-0 correction*) uses the information from tracks that can be associated with pileup vertices according to the ansatz [188]:

$$\vec{\not\!\!E}_{\mathrm{T}}^{\mathrm{type-0}} = \vec{\not\!\!E}_{\mathrm{T}}^{\mathrm{raw}} - \vec{\Delta}_{\mathrm{PU}} \tag{3.7}$$

$$= \vec{\not\!\!E}_{\mathrm{T}}^{\mathrm{raw}} - \sum_{i \,\in\, \mathrm{PUvertices}} \left[-\alpha \left(1 - F(\vec{P}_{\mathrm{T,\,ch}}^{i}) \right) \vec{P}_{\mathrm{T,\,ch}}^{i} \right] \,, \tag{3.8}$$

where $\vec{P}^{i}_{\mathrm{T,ch}}$ stands for the vector sum of the transverse momenta of charged particles associated with a given pileup vertex i. The function $F(\vec{P}^{i}_{\mathrm{T,ch}})$ satisfies the relation $0 \leq F(\vec{P}^{i}_{\mathrm{T,ch}}) < 1$ and converges to unity as $\vec{P}^{i}_{\mathrm{T,ch}}$ increases. It is given in Ref. [188] together with the parameter $\alpha = 0.71$.

- *Correction of ϕ modulation $\vec{\Delta}_{\phi}$*

  Since particles are on average produced uniformly in ϕ, the corresponding distribution for $\vec{\not\!\!E}_{\mathrm{T}}$ should be uniform. However, both simulated events and events in data exhibit a slight sinusoidal modulation in the $\vec{\not\!\!E}_{\mathrm{T}}$ ϕ distribution that has been found to be caused by a combination of several detector effects [188]. These effects result in different shifts of the $\vec{\not\!\!E}_{\mathrm{T}}$ components along the x and y directions. On average, these shifts increase approximately linearly with the number of reconstructed vertices N_{vtx} and can be parameterized as

  $$\vec{\Delta}_{\phi} = \begin{pmatrix} c_{x_0} + c_{x_s} \times N_{\mathrm{vtx}} \\ c_{y_0} + c_{y_s} \times N_{\mathrm{vtx}} \end{pmatrix} . \tag{3.9}$$

  The four parameters c_{x_0}, c_{x_s} c_{y_0}, c_{y_s} are of order 0.1 GeV and are determined separately for simulated events and events in data using the $\mathrm{Z} \to \mu^{+}\mu^{-}$ process. Their exact values are documented in Ref. [188].

- *Correction for different muon p_{T} assignments $\vec{\Delta}_{\mathrm{p}^{\mu}_{\mathrm{T}}}$*

  The Tune P algorithm, that is used in this work to choose the muon track fit for high-p_{T} muons, is not used in the reconstruction of the muon momenta in the PF algorithm. Therefore, the PF $\not\!\!E_{\mathrm{T}}$ is corrected for the difference in the two momentum assignments for the leading muon (the muon with the largest p_{T}) via the term

  $$\vec{\Delta}_{\mathrm{p}^{\mu}_{\mathrm{T}}} = \vec{p}^{\,\mu}_{\mathrm{T}}(\mathrm{Tune\,P}) - \vec{p}^{\,\mu}_{\mathrm{T}}(\mathrm{PF}) . \tag{3.10}$$

$\not\!\!E_{\mathrm{T}}$ filters

Various sources of anomalous contributions to $\not\!\!E_{\mathrm{T}}$ from instrumental effects and shortcomings of the reconstruction have been identified by the JetMET POG [188, 189]. Event filters have been developed in order to identify events that are affected by such non-genuine $\not\!\!E_{\mathrm{T}}$ contributions. In the $\mu\tau_{\mathrm{e}}$ resonance search, that involves $\not\!\!E_{\mathrm{T}}$ in the definition of the key observable, events that do not pass the filters listed below are rejected both in data and simulated samples. No such filtering is applied in the eμ resonance search, in which no cuts on $\not\!\!E_{\mathrm{T}}$ are applied and the $\not\!\!E_{\mathrm{T}}$ distribution of selected events merely serves as a control distribution.

The list of event filters that are included in the $\mu\tau_{\mathrm{e}}$ resonance search reads:

- *HCAL anomalous noise filter*

  This filter rejects events with large noise contributions in the HCAL barrel and HCAL endcap regions that are associated with the HPDs and readout boxes. These noise contributions are a result of instrumentation problems and can be separated from the normal electronics (pedestal) noise.

- *HCAL laser filter*

  Events in which the laser used for calibration of the HCAL has fired during the bunch crossing are removed.

- *ECAL laser energy calibration filter*

  A few ECAL crystals have been found to receive unreasonably large corrections to the crystal energy from the laser-based calibration system. Events with large crystal energies that receive correction factors in excess of 3(8) in the ECAL barrel(endcap) are rejected.

- *ECAL dead cell filter*

  Significant amounts of energy can escape undetected if they are deposited in noisy ECAL crystals that are masked in the standard reconstruction, yielding a large contribution to $\not\!\!E_{\mathrm{T}}$. The event filter that identifies such cases uses trigger-level information that is not included in the standard reconstruction of ECAL cluster energies.

- *ECAL endcap bad supercrystal filter*

  Arrays of 5 × 5 ECAL crystals that occasionally yield large anomalous signals have been identified in the endcap region. Events with such signals are rejected.

- *Tracking failure filter*

  Events with a typical activity in the calorimetry but unreasonably few associated tracks are rejected.

- *CSC beam halo filter*

  Beam halo particles that are produced by interactions of the beam with gas inside the LHC vacuum chamber or by interactions with apertures occasionally cross the CMS detector in coincidence with a bunch crossing. They are identified using information from the CSCs and the corresponding events are rejected.

The fraction of events that pass all $\not\!\!E_{\mathrm{T}}$ filters depends strongly on the selection cuts applied prior to the $\not\!\!E_{\mathrm{T}}$ filtering step. In the $\mu\tau_{\mathrm{e}}$ search, seven per mille of the events passing the initial selection of an eμ pair are rejected because they fire at least one of the $\not\!\!E_{\mathrm{T}}$ filters listed above (about half of the rejected events fire the CSC beam halo filter, see Sec. 12.1.1).

Performance of the $\not\!\!E_{\mathrm{T}}$ reconstruction

The performance of the PF $\not\!\!E_{\mathrm{T}}$ reconstruction is assessed in Ref. [188] by analyzing the *hadronic recoil* $\vec{u}_{\mathrm{T}}$ in $\mathrm{Z} \to \mu^+\mu^-$, $\mathrm{Z} \to \mathrm{e}^+\mathrm{e}^-$, and $\gamma + \text{jets}$ events, that typically involve little genuine $\not\!\!E_{\mathrm{T}}$ (neutrinos). The bosons are used in these types of events as well reconstructed probes, to which the additional activity in the event can be compared. The hadronic recoil is inferred from the measured transverse momentum of the participating boson $\vec{q}_{\mathrm{T}}$ and the measured PF $\vec{\not\!\!E}_{\mathrm{T}}$ by using momentum conservation in the transverse plane: $\vec{u}_{\mathrm{T}} + \vec{q}_{\mathrm{T}} + \vec{\not\!\!E}_{\mathrm{T}} = 0$. Under the assumption that the contribution from genuine $\not\!\!E_{\mathrm{T}}$ is small, the projection of the hadronic recoil onto the axis defined by the boson momentum, $u_{||}$, can be used to define the $\not\!\!E_{\mathrm{T}}$ response as $-\langle u_{||}\rangle/q_{\mathrm{T}}$. The $\not\!\!E_{\mathrm{T}}$ response is found to deviate from unity by only a few percent for $q_{\mathrm{T}} \gtrsim 40$ GeV. At such transverse momenta of the boson, the recoiling hadronic activity is typically clustered in a jet that receives JEC, such that all objects in the event are calibrated well. For smaller values of q_{T}, the $\not\!\!E_{\mathrm{T}}$ response is about 70 – 90% due to the bias in the hadronic energy scale that propagates to the measured $\not\!\!E_{\mathrm{T}}$ [188].

The resolution of the two $\vec{\not\!\!E}_{\mathrm{T}}$ components $\not\!\!E_{\mathrm{x}}$ and $\not\!\!E_{\mathrm{y}}$ in the processes mentioned above can be described as a linear function of the quantity $\sqrt{\sum E_{\mathrm{T}}}$, where $\sum E_{\mathrm{T}}$ is the scalar E_{T} sum of all reconstructed PF particles except for those associated with the participating boson [188]:

$$\sigma(\not\!\!E_{\mathrm{x}}, \not\!\!E_{\mathrm{y}}) = \sigma_0 + \sigma_s\sqrt{\sum E_{\mathrm{T}}}\ , \tag{3.11}$$

where σ_0 is $\mathcal{O}(1\ \text{GeV})$ and σ_s is about $0.6 \times \sqrt{\text{GeV}}$.

Importantly for the $\mu\tau_{\mathrm{e}}$ analysis in this work, both the measured $\not\!\!E_{\mathrm{T}}$ response and the $\not\!\!E_{\mathrm{T}}$ resolution are found to be reproduced well by the detector simulation.

Part II

A search for decays of heavy resonances and quantum black holes into an eμ pair in pp collisions at $\sqrt{s} = 8$ TeV

Chapter 4

Analysis strategy and event selection

The aim of the presented search for eμ resonances is to cover as many signal hypotheses as possible. The models of new physics with eμ signatures introduced in Sec. 1 are only used as benchmarks for the interpretation of the results, i.e. the selection is not tailored to yield the most sensitive search possible assuming the lepton kinematics and event topology of a specific model. In particular, the selection is meant to cover other signal models in which a heavy particle X that can decay into an eμ pair is pair-produced or arises in a decay chain together with additional particles. The intention behind this analysis strategy is not to miss out on theoretically-unanticipated new physics at the LHC. This inclusive approach to the wide landscape of BSM physics is reasonable for high-mass searches of prompt eμ resonances because the signal efficiencies for the eμ final state are high (Sec. 5.3); the background expectation is relatively low (Sec. 7), compared for example to SM Drell-Yan production of same-flavour dilepton pairs in searches for new heavy vector bosons; and the observable under study, the invariant mass of the eμ system from the decay of particle X is invariant under Lorentz transformations.

Instead of a specific signal model, the following set of criteria informs the choices made in the event selection and defines the boundaries of the region in BSM theory space that is probed by the presented search:

1. The focus of the eμ resonance search is put on the high-mass region $M_X \geq 200$ GeV, with an emphasis on the almost background-free tail of the $M_{\mathrm{e}\mu}$ spectrum above 1 TeV. This informs the choices of the lepton p_{T} cuts and the lepton identification criteria. In particular, this requirement excludes all models of new physics, in which known particles at the electroweak scale decay into an eμ pair. Dedicated searches for LFV decays of Z and h^0(125 GeV) bosons have been carried out by the ATLAS and CMS collaborations and are reported in Refs. [22, 23, 26–29].

2. The particle X is required to have a short lifetime $\tau_X \lesssim 10^{-12}$s . Therefore, the eμ pair from the decay is produced *promptly* at the primary vertex of the bunch crossing close to the interaction point in the center of the CMS detector ($c\tau_X \lesssim 0.1$ cm). This requirement constrains the class of signals than can be probed to those with large enough coupling strengths. In the RPV model for example, the RPV Yukawa couplings must satisfy $\lambda \gtrsim 10^{-8}$ for $M_{\tilde{\nu}_\tau} = 100$ GeV; this requirement does not constrain the region of parameter space with signal cross sections that would lead to an observable signal at the LHC. Searches for events with an electron and a muon that have large transverse impact parameters up to $\mathcal{O}$(10 cm) have been presented by the CMS collaboration in Refs. [190, 191].

3. The leptons are required to be isolated in order to reduce the background from leptons from hadron decays within jets. The basic isolation cuts that are utilized reject strongly boosted eμ pairs from the decay of particle X, in which the leptons would fall in each other's isolation cones. The requirement on $M_X \geq 200$ GeV (1.) already disfavours this boosted topology.

4.1 Summary of selection criteria

The selection of muons and electrons is based on sets of identification criteria (commonly abbreviated to *IDs*) that have been provided by the corresponding POGs in the CMS collaboration, the so-called *HEEP (High-Energy Electron Pair) electron* and *high-p_T muon* IDs. Both IDs have been developed in the context of the $\mathrm{Z}' \to \mathrm{ee}$ and $\mathrm{Z}' \to \mu\mu$ searches documented in Ref. [192] with lepton momenta at the TeV scale in mind. The HEEP electron ID is discussed in Ref. [151]. Before turning to the details of the lepton identification, the isolation requirements, and the utilized trigger in Secs. 4.2 and 4.3, the selection criteria of the $\mathrm{e}\mu$ resonance search are briefly summarized in the following overview.

Selection of events with an $\mathrm{e}\mu$ pair

1. The event selection starts from an unprescaled single-muon trigger with a p_T threshold of 40 GeV and a pseudorapidity requirement of $|\eta| < 2.1$.

2. The event must contain a reconstructed pp collision vertex with at least four associated tracks. The vertex must lie within a cylindrical volume around the centre of the detector defined by a circle of radius 2 cm in the transverse plane and a length of 48 cm along the beam direction, such that its two circular end faces are located at $z = \pm 24$ cm. The selected vertex with the largest sum of squared transverse momenta of its associated tracks is chosen as the primary vertex.

3. The event must contain at least one isolated muon with $p_\mathrm{T} > 45$ GeV that falls into the acceptance of the trigger, $|\eta| < 2.1$, and passes the high-p_T muon ID.

4. The event must contain at least one isolated electron with $E_\mathrm{T} > 35$ GeV that falls into the acceptance of the all-silicon inner tracking system $|\eta| < 2.5$ and passes the HEEP electron ID. Electrons in the overlap region of the barrel and endcap sections of the ECAL ($1.442 \leq |\eta^{\mathrm{SC}}| \leq 1.56$) are not selected. Electrons passing these selection criteria are not considered if a global muon with $p_\mathrm{T} > 5$ GeV is present within a cone of size $R = 0.1$ around the electron. This requirement is imposed in order to reject misidentified electrons from energy radiated off highly energetic muons. This *fake electron veto* is motivated in Sec. 4.4.

5. If more than one electron and one muon are present in the event, the $\mathrm{e}\mu$ combination with the highest invariant mass $M_{\mathrm{e}\mu}$ is chosen as the selected $\mathrm{e}\mu$ pair.

Note that no requirement is imposed on the product of the electric charges of the two selected leptons. This is done for two reasons: First, the omission of an opposite-sign (OS) electric charge selection follows the model-unspecific approach of the search. Sensitivity to less-discussed BSM scenarios such as LFV decays of heavy, doubly-charged Higgs bosons $H^{\pm\pm}$ to same-sign (SS) $\mathrm{e}\mu$ pairs in Higgs triplet models [193, 194] is thereby retained. Second, even if the search were restricted to the OS $\mathrm{e}^{\pm}\mu^{\mp}$ final states of the RPV $\tilde{\nu}_\tau$ and QBH signals, a selection of the electric charges would be disfavoured; the charge misidentification probability for electrons with $p_\mathrm{T} \gtrsim 500$ GeV would lead to a reduced signal efficiency for resonance masses in the (multi-)TeV range.

4.2 Muon selection

As outlined in Sec. 3.2.1, several track (re-)fits are carried out for each muon candidate, each with its own estimate of the track parameters p_T, η, and ϕ that are used to define the muon momentum vector. In the $\mathrm{e}\mu$ analysis, these track parameters are obtained from the *Tune P* algorithm described in Sec. 3.2.1.

4.2.1 Single-muon trigger

The used single-muon trigger path, named `HLT_Mu40_eta2p1`, has been described in detail in Sec. 3.3. At the L3 stage, a p_{T} cut of 40 GeV is applied and the acceptance in pseudorapidity of the trigger path is restricted to $|\eta| < 2.1$ in order to reduce its trigger rate and allow it to remain unprescaled. No isolation requirement is imposed on the muon track at trigger level [160].

4.2.2 Muon identification criteria

The high-p_{T} muon ID consists of a similar set of muon selection criteria as the so-called *tight muon ID* that is commonly used in CMS for the selection of prompt, isolated muons from W and Z boson decays at intermediate transverse momenta $p_{\mathrm{T}} \gtrsim 20$ GeV [173, 195, 196]. The changes with respect to the tight muon ID can be attributed either to the treatment of highly energetic muons that shower in the iron return yoke of the detector, or to the intended independence of the particle-flow event description. The full set of high-p_{T} muon identification criteria reads:

- The muon candidate must be reconstructed in both the inner silicon detector and the muon system and the global track fit that spans the entire detector must be successful.
- At least one valid hit in the muon system must be associated with the global muon track. Note that the global track fit is a refit of the initial list of hits in the inner tracker and the muon system and hits can be removed from the list of track-associated hits in the process of building the global track [152].
- Track segments in at least two muon stations must be matched to the track in the inner tracking detectors. This requirement is in line with the muon trigger that relies on track segments in at least two muon stations to provide a reliable estimate of the muon p_{T}.
- The inner muon track must have at least one associated hit in the pixel detector and hits in at least six layers of the silicon-strip tracker.
- The transverse impact parameter of the Tune P track with respect to the primary vertex $|\mathrm{d}_{\mathrm{xy}}|$ must be smaller than 0.2 cm. This is a very loose requirement for prompt muons and retains a large fraction of muons from decays of b and c hadrons. It is however effective against muons from hadrons with only light valence quarks and against muons from air showers of cosmic rays.
  The longitudinal impact parameter of the Tune P track with respect to the primary vertex $|\mathrm{d}_{\mathrm{z}}|$ must be smaller than 0.5 cm. In addition to its rejection power against muons from decays-in-flight and cosmic rays, this cut is effective against muons from pileup interactions.
- The relative uncertainty in the p_{T} measurement of the Tune P track $\delta p_{\mathrm{T}}/p_{\mathrm{T}}$ must be smaller than 0.3.

4.2.3 Muon isolation

The utilized relative muon isolation requirement relies solely on information from the inner tracking detectors. The scalar sum of the transverse momenta of additional tracks within a cone of size $R = 0.3$ around the inner muon track must be smaller than 10% of its p_{T}. Only tracks with $|\mathrm{d}_{\mathrm{z}}| < 0.2$ cm with respect to the muon track are included in the sum. Hence, the impact from pileup interactions is reduced and no further corrections of the isolation variable for tracks and energy deposits by additional pp interactions in the same bunch crossing are needed.

4.3 Electron selection

The HEEP electron ID [151,192] differs from other electron IDs used in CMS for the identification of prompt, isolated leptons at intermediate p_{T} values [151] in several ways. An important conceptual difference lies in the focus of the HEEP electron selection on the measurement of the electron supercluster in the ECAL and a reduced reliance on information from the electron track in the inner tracking detectors. This choice is motivated by the emphasis on highly energetic electrons with $E_{\mathrm{T}} \gtrsim 100$ GeV, for which the relative E_{T} resolution is dominated by the constant term of the ECAL and remains at the 1% level for electrons in the barrel (see Sec. 5.4, Fig. 5.10), whereas the relative p_{T} resolution increases to several per cent. The transverse energy of the supercluster $E_{\mathrm{T}}^{\mathrm{SC}}$ is used in the definition of the electron four-momentum vector in the analysis rather than a weighted combination of the p_{T} and energy measurements in the tracker and ECAL, respectively. Furthermore, no matching of the track momentum p and supercluster energy E^{SC} is required in the HEEP electron identification in order to avoid any inefficiency of the selection that might arise from gross mismeasurements of the transverse momentum of high-p_{T} GSF tracks with sizeable radiative losses due to bremsstrahlung and subsequent photon conversions. Information from the electron track is however used in the reconstruction of the η and ϕ coordinates of the electron and also enters the determination of $E_{\mathrm{T}}^{\mathrm{SC}}$ from the measured supercluster energy E^{SC}. Electrons that produce a supercluster in the overlap region of the barrel and endcap sections of the ECAL ($1.442 \leq |\eta^{\mathrm{SC}}| \leq 1.56$) are rejected.

4.3.1 Electron identification criteria

The HEEP electron selection differs for electrons in the barrel with $|\eta^{\mathrm{SC}}| < 1.442$ and electrons in the endcaps of the ECAL with $|\eta^{\mathrm{SC}}| > 1.56$. The electron identification variables are explained below and the cut values for the two cases are collected in Tab. 4.1.

- **Seeding:** The ECAL-based track seeding must have been successful for HEEP electron candidates. It is one of two approaches to finding the two or three hits in the first layers of the tracker that initiate the GSF track reconstruction, and starts from the supercluster energy and position (*outside-in* seeding).

- **Supercluster-to-track matching:** The electron GSF track and the supercluster in the ECAL that initiated the track seed must fulfill geometrical matching criteria in η and ϕ. For this matching, the track is extrapolated from the innermost track position and direction to the point of closest approach to the supercluster, where its η and ϕ coordinates are evaluated [151]. Cuts are then applied to the differences in the coordinates $|\Delta\eta| = |\eta^{\mathrm{SC}} - \eta_{\mathrm{extrap}}^{\mathrm{track}}|$ and $|\Delta\phi| = |\phi^{\mathrm{SC}} - \phi_{\mathrm{extrap}}^{\mathrm{track}}|$.

- **Energy in HCAL and ECAL:** The ratio of the energy deposited in the HCAL around the direction of the electron to the energy of the electron supercluster in the ECAL, denoted H/E^{SC}, must be smaller than 0.05. The former is defined as the sum of energy deposits (clusters) in the HCAL in a cone of size $R = 0.15$ around the position of the electron in the ECAL.

- **Lateral shower shape in the ECAL:** Different lateral shower shape variables are used for the HEEP electron selection in the barrel and endcap. They discriminate between electromagnetic and hadronic showers in the ECAL because the former are more concentrated along η. The extension of the shower along the ϕ direction is not an equally powerful discriminant because of energy losses due to bremsstrahlung and the curvature of the electron track in the magnetic field. Both shower shape variables start from a 5×5 matrix of crystals around the crystal with the highest E_{T} in the electron supercluster. In the endcap section of the ECAL, an energy-weighted spread of the 25 crystal positions η_i is used, defined as $(\sigma_{i\eta i\eta})^2 = \sum_i^{5\times5}(\eta_i - \langle\eta\rangle_{5\times5})^2 w_i / \sum_i^{5\times5} w_i$. The weights w_i depend logarithmically on the energy contained in the crystals. In the barrel region of the ECAL with its $\eta - \phi$ geometry, the energy fractions contained in adjacent rows of 5 crystals along ϕ (1×5 rows in $\eta - \phi$ coordinates) that include the crystal with the highest E_{T}, $E^{1\times5}/E^{5\times5}$ and $E^{2\times5}/E^{5\times5}$, are used as the shower shape variables, instead.

- **Track-related cuts:** With the exception of one allowed missing hit, the electron track must have associated hits in all layers of the pixel detector that it passes. In addition, a cut on the transverse impact parameter of the electron track is applied. These cuts are aimed at selecting prompt electrons and remove electrons from photon conversions.

Table 4.1: The HEEP ID selection cuts on electron identification variables for electrons with superclusters in the barrel and endcap sections of the ECAL.

Electron identification variable	Cut value Barrel	 Endcap
ECAL-based seed	✓	✓
$\|\Delta\eta\|$	< 0.005	< 0.007
$\|\Delta\phi\|$	< 0.06 rad	< 0.06 rad
$\sigma_{i\eta i\eta}$	-	< 0.03
$E^{2\times5}/E^{5\times5}$ or $(E^{1\times5}/E^{5\times5})$	> 0.94 or (> 0.83)	-
H/E^{SC}	< 0.05	< 0.05
Missing pixel hits	≤ 1	≤ 1
$\|\mathrm{d_{xy}}\|$	< 0.02 cm	< 0.05 cm

4.3.2 Electron isolation

As in the case of the muon isolation, the utilized definition of the electron isolation does not rely on the particle-flow algorithm. It consist of two separate isolation criteria that use information from the calorimeters and the tracker, respectively.

The calorimeter isolation is the scalar sum of the transverse energy deposits in the ECAL and in the HCAL in two cones of size $R = 0.3$ around the position of the electron in the calorimeter. Different inner veto cones are defined to remove the contribution of the electron itself in the two calorimeters. The average energy density in the event due to pileup interactions is subtracted from the calorimeter isolation as described in Ref. [197]. The resulting measure of the transverse energy surrounding the electron in the calorimeter is required to be smaller than about 3% of the transverse energy of the supercluster $E_{\mathrm{T}}^{\mathrm{SC}}$; the exact cut values are given in Tab. 4.2. A more detailed definition of the calorimeter isolation is given in Ref. [198].

The tracker isolation is defined as the scalar sum of the transverse momenta of additional tracks within a cone of size $R = 0.3$ around the inner electron track and must be smaller than 5 GeV. Only tracks with $|\mathrm{d_z}| < 0.2$ cm with respect to the electron track are included in the sum.

4.4 Muons faking electrons

Highly-energetic muons as those expected in the signal signature of the eμ resonance search do occasionally lose significant amounts of energy due to radiative effects before reaching the HCAL. In such cases, the combination of the corresponding supercluster in the ECAL and the close-by muon track can lead to an accidental cluster-to-track match in $|\Delta\eta|$ and $|\Delta\phi|$. This can result in a reconstructed electron because no matching between the electron track momentum

Table 4.2: The HEEP isolation cuts for electrons with superclusters in the barrel and endcap sections of the ECAL. The definitions of the two isolation variables for the calorimetry and the tracker are given in the text.

Isolation	Cut value barrel	Cut value endcap
Calorimeter	$< 2\ \text{GeV} + 0.03 \times E_{\text{T}}^{\text{SC}}$	$< 2.5\ \text{GeV} + 0.03 \times (E_{\text{T}}^{\text{SC}} - 50\ \text{GeV})$ for $E_{\text{T}}^{\text{SC}} \geq 50\ \text{GeV}$ $< 2.5\ \text{GeV}$ for $E_{\text{T}}^{\text{SC}} < 50\ \text{GeV}$
Tracker	$< 5\ \text{GeV}$	$< 5\ \text{GeV}$

and supercluster energy is required in the utilized electron ID for reasons discussed above. Key aspects concerning the energy loss of muons in the PbWO_4 crystals of the ECAL are summarized in the following paragraph.

The muon stopping power $\langle -dE/dx \rangle$ in PbWO_4 has been measured by the CMS collaboration in cosmic ray events for muon momenta p ranging from 5 GeV to 1 TeV [199]. One aspect of this result is the first measurement of muon critical energy $E_{\text{c}}^{\mu}(\text{PbWO}_4) = 160^{+5}_{-6}\ (\text{stat}) \pm 8\ (\text{syst})\ \text{GeV}$, in agreement with calculations that yield $E_{\text{c}}^{\mu}(\text{PbWO}_4) = 170\ \text{GeV}$ [200]. The energy loss in the ECAL of the muons of interest in the eμ resonance search with momenta between several 100 GeV and a few TeV is dominated by radiative losses. With the density of PbWO_4 of 8.3 gcm^{-3} and a muon path length in the ECAL of approximately 23 cm (one crystal length), the thickness Δx of the traversed PbWO_4 is about 190 gcm^{-2}. Combining this value with the measured (mean) muon stopping powers for muon momenta of 100 GeV and 1 TeV yields mean energy losses of about 0.5 GeV and 2 GeV, respectively. Hence, the average muon in this momentum range does not deposit enough energy in the ECAL to produce a supercluster that passes the E_{T} requirement of the electron selection of 35 GeV. As pointed out in Ref. [199] however, the tail of the pdf of (radiation-dominated) energy loss for single events extends to values much higher than its mean. A non-negligible fraction of muons with energies in the TeV regime produces hard radiation that results in ECAL clusters with transverse energies above the selection threshold. This fraction is evaluated based on simulated signal samples for the eμ resonance search that are described below in Sec. 5.2. At generator level, the simulated events include a muon and an electron in the final state that arise from the decay of a heavy object with mass M. For $M = 200$ GeV and a corresponding average muon momentum of order 100 GeV, below 0.1% of the selected muons are accompanied by a HEEP electron within $\Delta R < 0.1$. This fraction increases to 3% for $M = 4$ TeV and muon momenta of about 2 TeV.

Figure 4.1 (left) shows the angular distance ΔR between the muon with the highest p_{T} and all selected HEEP electrons in simulated eμ events with $M = 4$ TeV. The eμ pairs are grouped into two categories; in the first category, the electron in the eμ pair passes the fake electron veto and in the second it fails the requirement. In the eμ pairs with vetoed electrons, the two lepton are separated by less than $\Delta R = 0.02$. The ratio of supercluster energy to track momentum E/p peaks significantly below unity for the vetoed electrons, and the ratio of the two p_{T} values obtained from the electron track and the muon track is close to unity, as shown in Figs. 4.1 (middle, right). These features point to the muon as the origin of the reconstructed electron in these events.

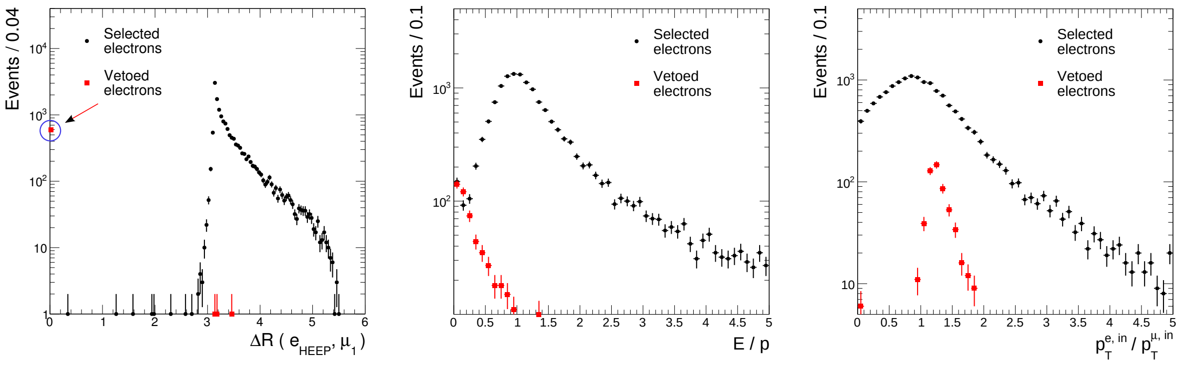

(a) ΔR between HEEP electrons and the selected muon with the highest p_T in the event (μ_1).

(b) Ratio of the supercluster energy to the track momentum of HEEP electrons.

(c) Ratio of the p_T of the electrons's inner GSF track to the p_T of the muon's inner track.

Figure 4.1: Three distributions for electrons passing the HEEP electron selection in high-mass eμ events with a reconstructed muon that fulfills the muon selection. The events are obtained from simulated signal samples for the eμ resonance search that are described below in Sec. 5.2. The muons have a momentum of about 2 TeV.

4.5 Muon and electron selection efficiencies

The single-muon trigger efficiency and the efficiencies of the muon and electron selections described above have been measured by the Muon and EGM POGs in samples of dilepton events dominated by the contribution from the $\mathrm{Z} \to \ell^+\ell^-$ process via *tag-and-probe* methods. These methods are described in Refs. [151, 195, 201]. In the following the results of these measurements are summarized.

Selection efficiencies for muons

The identification efficiency for muons is defined in the following as the fraction of muon tracks reconstructed in the all-silicon tracking system that pass the high-p_T muon ID including the isolation cut. The efficiencies are obtained from Ref. [202] and depicted in Fig. 4.2, where the results derived from measured events passing a $\mathrm{Z} \to \mu^+\mu^-$ selection ($70\ \mathrm{GeV} \leq M(\mu^{\mathrm{tag}}, \mu^{\mathrm{probe}}) \leq 130\ \mathrm{GeV}$) are compared to the efficiencies in simulated Drell-Yan events. For muons in the barrel region of the muon system ($|\eta| < 0.9$) with transverse momenta above 45 GeV (the cut value in the event selection of the eμ resonance search), the identification efficiency is constant within the statistical uncertainties at about 95% up to $p_\mathrm{T} \sim 300\ \mathrm{GeV}$[1], the highest muon p_T values considered in the efficiency measurement. The η-dependence of the identification efficiency is more pronounced with values varying between 87% and 98% as shown in Fig. 4.2 (right). Statistically significant dips in the trigger efficiency occur close to the transition between wheel 0 and wheels ± 1 at $|\eta| \approx 0.25$. These are related to the two so-called *chimneys* that pass through the steel return yoke and house the massive cryogenic lines for the solenoid magnet. Both this η-dependence and the evolution of the muon identification efficiency are described well by the simulation; the measured and simulated efficiency values agree typically within 1-2%, even the two dips that are visible in the measured efficiency in Fig. 4.2 (right) are reproduced well by the simulation.

---

[1] For a note on CMS measurements involving muons with even higher p_T values, see the paragraph *Dimuon and dielectron events at high invariant mass $M_{\ell\ell}$* below.

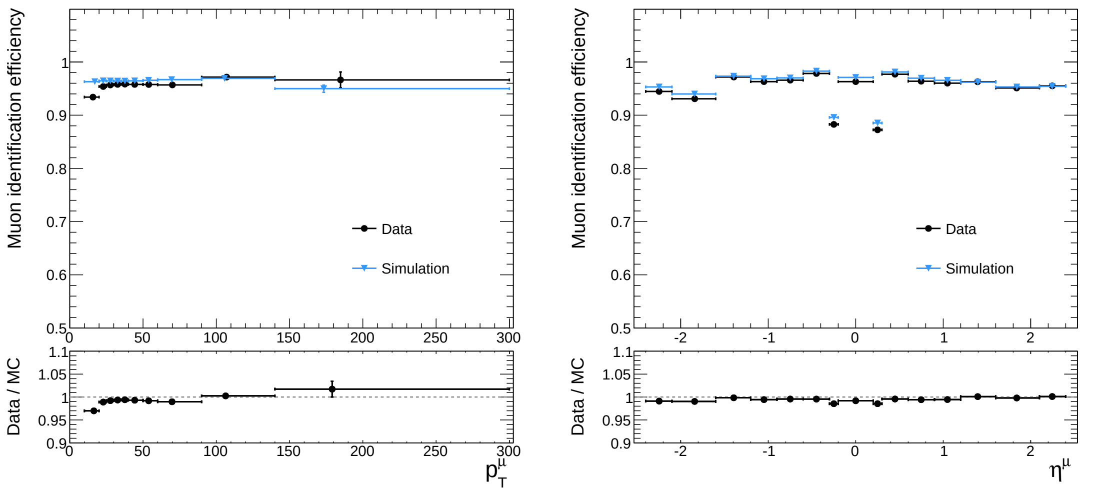

(a) Efficiency of the high-p_T muon ID for muons in the barrel section of the muon system ($|\eta| < 0.9$) in bins of muon p_T.

(b) Efficiency of the high-p_T muon ID for muons with $p_\mathrm{T} > 20$ GeV in bins of muon η.

Figure 4.2: The muon identification efficiency for the high-p_T muon selection including the isolation criterion. The ratio plots on the bottom show the data-to-simulation scale factors. The figures show efficiencies provided by the MUON POG in Ref. [202].

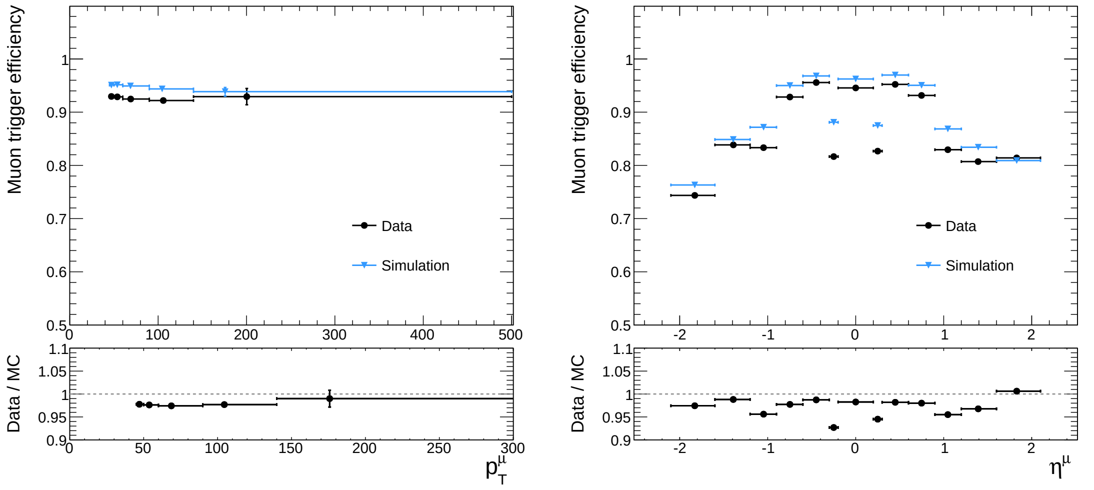

(a) Trigger efficiency for muons in the barrel section of the muon system ($|\eta| < 0.9$) in bins of muon p_T.

(b) Trigger efficiency for muons with $p_\mathrm{T} > 45$ GeV in bins of muon η.

Figure 4.3: The single-muon trigger efficiency of the HLT path `HLT_Mu40_eta2p1`*, evaluated with respect to muons passing the high-p_T muon selection including the isolation criterion. The ratio plots on the bottom show the data-to-simulation scale factors. The figures show efficiencies provided by the MUON POG in Ref. [202].*

Single-muon trigger efficiencies

The trigger efficiency of the single-muon HLT path `HLT_Mu40_eta2p1` is defined here as the fraction of reconstructed muons passing the high-p_T muon ID with the isolation cut that can be matched to a corresponding trigger object. The efficiencies are presented as a function of muon p_T and η in Fig. 4.3. As in the case of the muon identification efficiency, the trigger efficiency is approximately constant in the probed p_{T} range. However, the η-dependence of the trigger efficiency is much stronger than that of the identification efficiency, as shown in Fig. 4.3 (right), with efficiencies ranging from 75% at $\eta \approx -2$ in the CSCs to 95% for $|\eta| < 0.9$ in the DTs. Two features stand out: First, the trigger efficiency drops by almost 10% in the CSC/DT overlap region $0.9 < |\eta| < 1.2$ compared to the efficiency in the barrel part of the muon system that is only equipped with DTs. Secondly, statistically significant dips in the trigger efficiency occur close to the transition between wheel 0 and wheels ±1 at $|\eta| \approx 0.25$. These efficiency dips are present in both data and MC but their modelling in the simulation is imperfect, resulting in deviations between measured and expected efficiencies of up to 7%. For other values of η, the measured and simulated trigger efficiencies differ by typically 2-3%.

Selection efficiencies for electrons

The electron identification efficiencies presented in Fig. 4.4 have been measured in dielectron events as described in Ref. [151]. The electron identification efficiency is defined here as the fraction of reconstructed GSF electrons that pass the HEEP ID including the isolation requirement. This definition implies a factorization of the electron selection efficiency into a reconstruction and an identification efficiency: $\epsilon_{\mathrm{Sel}}^{\mathrm{HEEP}} = \epsilon_{\mathrm{Reco}}^{\mathrm{GSF}} \times \epsilon_{\mathrm{ID}}^{\mathrm{HEEP}}$. The reconstruction efficiency is documented in Ref. [151] and larger than 95% for electrons with $E_{\mathrm{T}} \geq 35$ GeV.

The identification efficiency in the barrel section of the ECAL, Fig. 4.4 (left), and the ECAL endcaps, Fig. 4.4 (right), both exhibit a turn-on between 35 GeV and 50 GeV. The efficiency values vary from 85% to 95% in the ECAL barrel and from 80% to 95% in the endcaps.

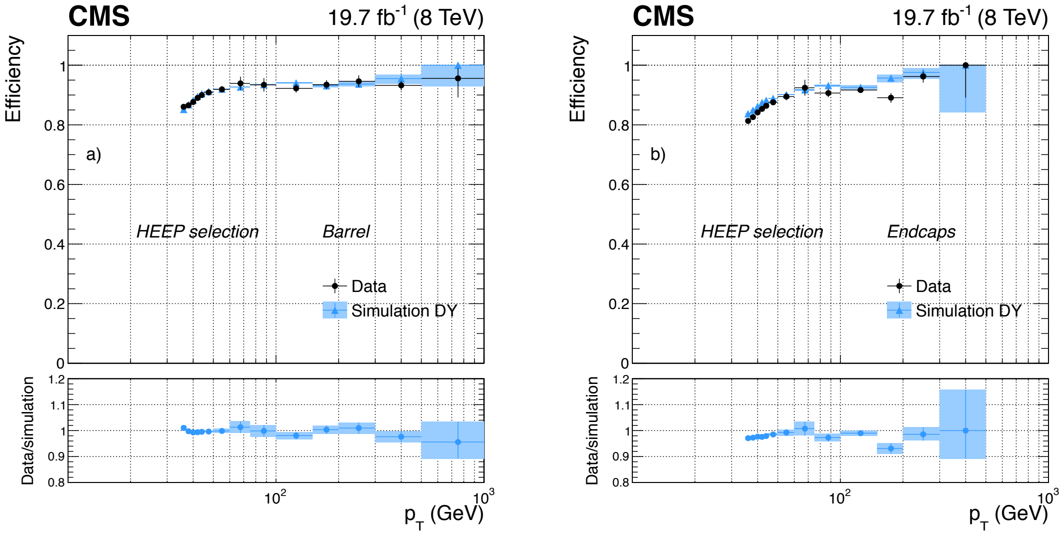

(a) HEEP ID efficiency in the ECAL barrel.
(b) HEEP ID efficiency in the ECAL endcaps.

Figure 4.4: The efficiency of the HEEP electron ID as a function of the electron p_{T} in the barrel region of the ECAL (barrel) and the endcap regions (right). The ratio plots on the bottom show the data-to-simulation scale factors. The figures are taken from Ref. [151].

Dimuon and dielectron events at high invariant mass $M_{\ell\ell}$

The presented measurement of the muon reconstruction and identification efficiencies does not extend beyond $p_{\mathrm{T}}^{\mu} = 300$ GeV, which is too low to claim that these efficiencies have been measured for muons from the decay of a heavy particle with mass $M \gtrsim 1$ TeV, that have transverse momenta of $p_{\mathrm{T}} \sim M/2$. However, searches for dimuon and dielectron pairs of high invariant mass at $\sqrt{s} = 8$ TeV indicate no drop in the muon or electron efficiencies in the mass range $M_{\ell\ell} \lesssim 2$ TeV [192]; 10 events with $M_{\ell\ell} > 1.3$ TeV are observed in the dimuon channel with 7 ± 1 (syst) events expected and 4 events are observed in the dielectron channel in the same mass range, in agreement with the expectation of 6 ± 0.5 (syst) events. The capability of the CMS detector to precisely reconstruct muons with $p_\mathrm{T} \sim 1$ TeV has been established in the early days of the detector commissioning using muons from cosmic ray events [215].

Corrections to lepton selection efficiencies in simulated events

As shown in the figures above, the measured muon and electron efficiencies are overall described well by the detector simulation. It is therefore reasonable to correct for the remaining imperfections in simulated efficiencies rather than trying to identify all their sources and re-run the detector simulation. This efficiency correction is achieved by assigning a weight w_SF to each simulated event according to:

$$w_\mathrm{SF} = \prod_i \prod_j \frac{\epsilon_{i,j}^\mathrm{Data}}{\epsilon_{i,j}^\mathrm{MC}} \left(p_{\mathrm{T},i},\, \eta_i\right) \equiv \prod_i \prod_j \mathrm{SF}_{i,j} \left(p_{\mathrm{T},i},\, \eta_i\right) \ , \tag{4.1}$$

where the first product runs over all participating muons and electrons i and the second runs over all (uncorrelated) single-lepton selection efficiencies j. Since only single-lepton efficiencies are involved in the eμ analysis, the efficiency correction factorizes. The efficiency ratios in Eqn. 4.1 are referred to as *data-to-simulation scale factors* SF and are evaluated as functions of lepton p_T and η. Examples of such scale factors are given in the ratio plots of Figs. 4.2, 4.3, and 4.4.

Chapter 5

Signal simulation and properties

5.1 Signal event generation and signal kinematics

The generation of signal events at parton level has been carried out at LO in pQCD with the `CALCHEP` event generator (v. 3.4.1) [203] for both the RPV $\tilde{\nu}_\tau$ and QBH signals. The `CALCHEP` event generator produces output according to the Les Houches Accord [204] in so-called Les Houches Event (LHE) files. These can be used as standardized input for parton shower programs.

5.1.1 RPV $\tilde{\nu}_\tau$ signal model

The implementation of the RPV $\tilde{\nu}_\tau$ signal in `CALCHEP` is a simplified version of a more complete RPV SUSY model covering all vertices associated with the trilinear LFV terms in the superpotential Eqn. 1.2. The latter is publicly available from HEPMDB [205][1].

In the simplified CalcHEP model, only the vertices relevant for the resonant production and the decay of the $\tilde{\nu}_\tau$ have been included. The most important parameters and settings that have been used for the event generation are summarized below.

- As described in Sec. 1.1, the RPV $\tilde{\nu}_\tau$ model has four parameters, $M_{\tilde{\nu}_\tau}$, λ_{312}, λ_{321}, and λ'_{311}, that can be set independently in the model implementation.
- Proton-proton collisions with proton momenta $p_\mathrm{z} = 4$ TeV and an $\mathrm{e}^{\pm}\mu^{\mp}$ final state are generated.
- The renormalization scale (μ_R) and factorization scale (μ_F) are set to the mass of the outgoing particles $M_{e\mu}$, i.e. the centre-of-mass energy in the resonant $\tilde{\nu}_\tau$ exchange, $\sqrt{\hat{s}}$.
- The PDF set used is CTEQ6L [58]. The hard scattering cross sections and splitting functions that enter the CTEQ6L PDF fit are evaluated at LO in pQCD, whereas the running of the strong coupling constant $\alpha_s(Q)$ is evaluated at NLO in pQCD.
- The strong coupling at the Z boson mass is set to $\alpha_S(M_\mathrm{Z}) = 0.1172$.
- No kinematic cuts are applied to the generated lepton pair.

While the generated RPV $\tilde{\nu}_\tau$ signal samples are obtained using a LO event generator, the signal cross section is taken from a calculation at NLO in pQCD as described in Sec. 1.1.2. As a cross check, the cross sections from `CALCHEP` are compared to the LO results obtained from the code that is also capable of the higher-order calculation. Agreement is found at the level of a few per mille.

---

[1] The RPV SUSY model in `CALCHEP` has been implemented by Alexander Belyaev and Christoph Charles, the corresponding HEPMDB model ID is hepmdb:0512.0068 . Initial checks of the model and a comparison to an earlier implementation in the `HERWIG` generator [206,207] have been carried out by Lars Sonnenschein and the author. The reduced version of the model used in this work has been derived by the author.

The aim in the eμ resonance search is to design it in a model-independent fashion and to allow for a reinterpretation of the results in terms of different signal models that share the common signature $X \to \mathrm{e}\mu$, with the mass of the particle X at the electroweak scale or above. A narrow peak in the $M_{\mathrm{e}\mu}$ spectrum on top of a smoothly falling background is a generic signal shape that allows for a (largely) model-independent approach. In the following, a subset of possible signal models is considered: the resonant (s-channel) production in pp collisions of the heavy particle X that decays into the eμ final state. The aim is to study the impact of the size of the coupling parameters involved in the resonant production and the decay of particle X and to extend the validity of the search to signals with an eμ resonance that feature sizeable values of the coupling parameters and a cross section that deviates from the narrow width approximation.

A narrow peak in the eμ mass spectrum is obtained in models with an eμ resonance for which the narrow width approximation (NWA) is a good approximation, meaning that the phase space can be factorized and the Breit-Wigner function in the propagator of particle X can be integrated out (see Ref. [208] for a detailed discussion). This way the production and decay processes can be treated independently and the cross section of the process factorizes into production cross section of the exchanged particle times branching ratio into the desired final state, $\sigma_{\mathrm{NWA}} = \sigma_{\mathrm{prod}} \times \mathcal{B}$. In the following, the RPV $\tilde{\nu}_\tau$ model with resonant production of an eμ pair is used as a benchmark processes to study the impact of finite width effects that are not covered in the NWA. The aim is to restore the model independence of the search in the case of sizeable coupling values and decay widths by restricting the search region in the $M_{\mathrm{e}\mu}$ spectrum to the vicinity of the peak at M_{res}. Before turning to the definition of this search region, the conditions for the validity of the NWA are briefly reviewed [209]:

1. The total width of the exchanged particle is small compared to its mass, $\Gamma_{\mathrm{res}} \ll M_{\mathrm{res}}$.

2. The particles produced in the decay are much lighter than M_{res}.

3. The pp centre-of-mass energy is much larger than M_{res}.

4. There is no significant interference with other processes.

In contrast to Drell–Yan dimuon or dielectron production, there is no process in the SM that would cause an interference with the amplitude of signals with resonant eμ production. The kinematics of the RPV $\tilde{\nu}_\tau$ signal can therefore be studied independently of the SM backgrounds discussed later. Conditions 2 and 3 are satisfied for signal masses 100 GeV $\lesssim M_{\mathrm{res}} \lesssim$ 2.5 TeV, which is the relevant range in the resonance search for coupling values $\lambda \lesssim 0.1$, given the fast decrease in parton luminosity for $\sqrt{\hat{s}} \to \sqrt{s} = 8$ TeV. The impact of the size of the relative decay width $\Gamma_{\mathrm{res}}/M_{\mathrm{res}}$ is discussed in the following.

A non-negligible relative decay width $\Gamma_{\mathrm{res}}/M_{\mathrm{res}}$ leads to off-shell production of eμ pairs with invariant mass $M_{\mathrm{e}\mu} \ll M_{\mathrm{res}}$. Since the parton luminosities fall off sharply in the $\sqrt{\hat{s}} \gtrsim 1$ TeV regime, the off-shell production can receive a strong enhancement relative to the peak around M_{res}. Finite width effects are included in the `CALCHEP` event generator and the resulting off-shell production can be considerable, as shown in the $M_{\mathrm{e}\mu}$ distributions of selected points in parameter space of the RPV $\tilde{\nu}_\tau$ model in Fig. 5.1. The fraction of events produced with an invariant mass significantly lower than the resonance mass increases with $\Gamma_{\mathrm{res}}/M_{\mathrm{res}}$, or the size of the couplings involved (Fig. 5.1 left). It furthermore increases with M_{res} for a fixed value of the couplings (Fig. 5.1 right). An analysis approach that is as independent of the coupling values as possible can be formulated by restricting the search region in the invariant mass distribution, $|M_{\mathrm{e}\mu} - M_{\mathrm{res}}| \leq \Delta M$, such that the total cross section for the process including finite width effects, σ_{FW}, times the fraction of events falling into this search region, $f_{\Delta M}$, matches the cross section in the NWA, σ_{NWA}. As pointed out in Ref. [210] in the context of Z$'$ searches with dimuon and dielectron decays, the choice $\Delta M \approx 5\% \times \sqrt{s}$ fulfills this requirement for a wide range of decay widths Γ_{res}. In the case $M_{\mathrm{res}} < \Delta M$, the lower boundary of the invariant mass window is set to zero. The validity of this approach is checked for the eμ resonance signal by comparing the CalcHEP cross

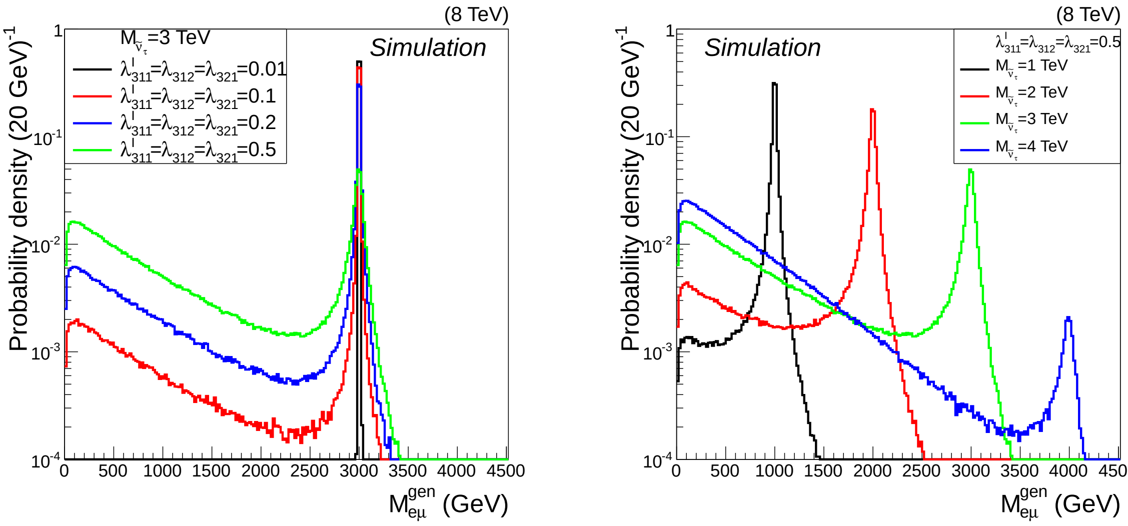

(a) The $M_{e\mu}$ spectra of generated pp $\rightarrow \tilde{\nu}_\tau \rightarrow$ eμ events for samples with $M_{\tilde{\nu}_\tau} = 3$ TeV and different values of the Yukawa couplings.

(b) The $M_{e\mu}$ spectra of generated pp $\rightarrow \tilde{\nu}_\tau \rightarrow$ eμ events for samples with the RPV Yukawa couplings $\lambda'_{311} = \lambda_{312} = \lambda_{321} = 0.5$ and different $\tilde{\nu}_\tau$ masses.

Figure 5.1: Comparison of on-shell and off-shell production of an $e\mu$ *pair in* $\tilde{\nu}_\tau$ *decays.*

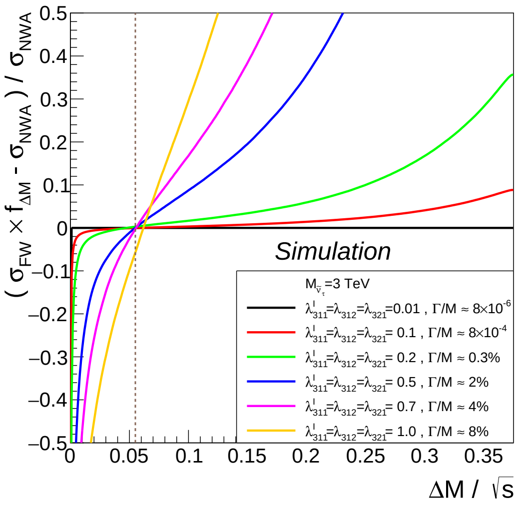

Figure 5.2: The relative difference between the cross section for the process $pp \rightarrow \tilde{\nu}_\tau \rightarrow e\mu$ *including finite width effects times the fraction of events falling into this search region,* $\sigma_{\mathrm{FW}} \times f_{\Delta M}$*, and the NWA cross section evaluated at LO in pQCD as a function of the width of the search region,* $\Delta M/\sqrt{s}$*. The curves correspond to RPV* $\tilde{\nu}_\tau$ *signal samples with* $M_{\tilde{\nu}_\tau} = 3$ *TeV and different values of the Yukawa couplings* $\lambda'_{311} = \lambda_{312} = \lambda_{321}$ *ranging from 0.01 to 1.0. The corresponding relative decay widths* $\Gamma_{\tilde{\nu}_\tau}/M_{\tilde{\nu}_\tau}$ *are between* $8 \cdot 10^{-6}$ *and 8% . The dashed vertical line indicates the resulting choice for the width of the search region,* $\Delta M = 5.5\% \times \sqrt{s}$ *.*

section for the RPV $\tilde{\nu}_\tau$ signal process multiplied by $f_{\Delta M}$ with the corresponding LO NWA calculation as a function of $\Delta M/\sqrt{s}$ and the result is given in Fig. 5.2. When restricted to the invariant mass range $|M_{e\mu} - M_{\mathrm{res}}| \leq \Delta M = 5.5\% \times \sqrt{s}$, the two cross sections $\sigma_{\mathrm{FW}} \times f_{\Delta M}$ and σ_{NWA} agree within about 1% for relative decay widths up to $\Gamma_{\mathrm{res}}/M_{\mathrm{res}} = 2\%$ and resonance masses up to 3 TeV. The key figures for this comparison are given in Tab. 5.1 for resonance masses between 200 GeV

λ	$\Gamma_{\tilde{\nu}_\tau}/M_{\tilde{\nu}_\tau}$	$M_{\tilde{\nu}_\tau}$ (TeV)	$f_{\Delta M}$	$\frac{\sigma_{\mathrm{FW}}\times f_{\Delta M}-\sigma_{\mathrm{NWA}}}{\sigma_{\mathrm{NWA}}}$ (%)	$M_{\tilde{\nu}_\tau}$ (TeV)	$f_{\Delta M}$	$\frac{\sigma_{\mathrm{FW}}\times f_{\Delta M}-\sigma_{\mathrm{NWA}}}{\sigma_{\mathrm{NWA}}}$ (%)
0.01	$8.0 \cdot 10^{-6}$	0.2	1.00	0.0	3	1.00	0.0
0.1	$8.0 \cdot 10^{-4}$	0.2	1.00	0.0	3	0.92	0.0
0.2	$3.2 \cdot 10^{-3}$	0.2	1.00	0.0	3	0.74	0.3
0.5	$2.0 \cdot 10^{-2}$	0.2	1.00	0.0	3	0.31	0.0
0.7	$3.9 \cdot 10^{-2}$	0.2	1.00	-0.1	3	0.19	-0.3
1.0	$8.0 \cdot 10^{-2}$	0.2	1.00	-0.4	3	0.097	-5.7
0.01	$8.0 \cdot 10^{-6}$	1	1.00	0.0	4	0.98	0.0
0.1	$8.0 \cdot 10^{-4}$	1	1.00	-0.1	4	0.30	0.1
0.2	$3.2 \cdot 10^{-3}$	1	0.99	-0.2	4	0.097	1.6
0.5	$2.0 \cdot 10^{-2}$	1	0.97	-0.6	4	0.018	7.4
0.7	$3.9 \cdot 10^{-2}$	1	0.93	-1.2	4	0.009	6.8
1.0	$8.0 \cdot 10^{-2}$	1	0.88	-2.7	4	0.004	0.9

Table 5.1: Summary of the difference between the cross sections $\sigma_{\mathrm{FW}} \times f_{\Delta M}$ and σ_{NWA} for the process $pp \to \tilde{\nu}_\tau \to e\mu$ at $\sqrt{s} = 8$ TeV for several signal masses and couplings in the RPV $\tilde{\nu}_\tau$ model. The mass window is fixed to $\Delta M = 5.5\% \times \sqrt{s} = 440$ GeV. The placeholder λ stands for $\lambda'_{311} = \lambda_{312} = \lambda_{321}$. In the case $M_{\tilde{\nu}_\tau} < \Delta M$, the lower boundary of the mass window is set to zero.

and 4 TeV. In order to allow for well-defined reinterpretations of the results of the eμ resonance search, events entering the statistical interpretation of the observed invariant mass spectrum in eμ events are therefore required to fall within $M_{\mathrm{res}} \pm \Delta M$, with $\Delta M = 5.5\% \times \sqrt{s} = 440$ GeV, of the resonance mass hypothesis tested.

5.1.2 QBH signal model

The QBH model and its implementation in `CALCHEP` are described in Ref. [93]. It is publicly available at HEPMDB[2].

The generator settings are the same as for the RPV $\tilde{\nu}_\tau$ model described above. The adjustable model parameters are the number of extra dimensions n and the fundamental Planck mass, M_{D}. The threshold mass for QBH production, M_{th}, is fixed to M_{D}. Events can be generated with the fundamental Planck scale evaluated either in the PDG or RS convention introduced in Sec. 1.2. Invariant mass spectra of eμ pairs from QBH decays normalized to unit area are shown in Fig. 5.3 (left) for different threshold masses M_{th} and a fixed number of extra dimensions $n = 6$ with the Planck scale in the PDG definition. The shape of the distribution shows two characteristic features: A sharp edge at the production threshold and an extended tail that falls off monotonously towards higher masses. According to Eqn. 1.32, the partonic cross section for a fixed fundamental Planck scale increases with the QBH mass $M_{\mathrm{QBH}} = \sqrt{\hat{s}}$ as

$$\hat{\sigma}_{\mathrm{QBH}} = \pi r_s^2 \left(M_{\mathrm{QBH}}, n\right) \sim \left(M_{\mathrm{QBH}}\right)^{\frac{2}{n+1}} \quad . \tag{5.1}$$

This rise in the partonic cross section is however more than compensated by the falling proton PDF. In contrast to the eμ resonance signal model with its localized peak around M_{res}, the thresh-

---

[2] The model has been implemented by Alexander Belyaev and Xavier Calmet, the HEPMDB model ID is hepmdb:1113.0146 .

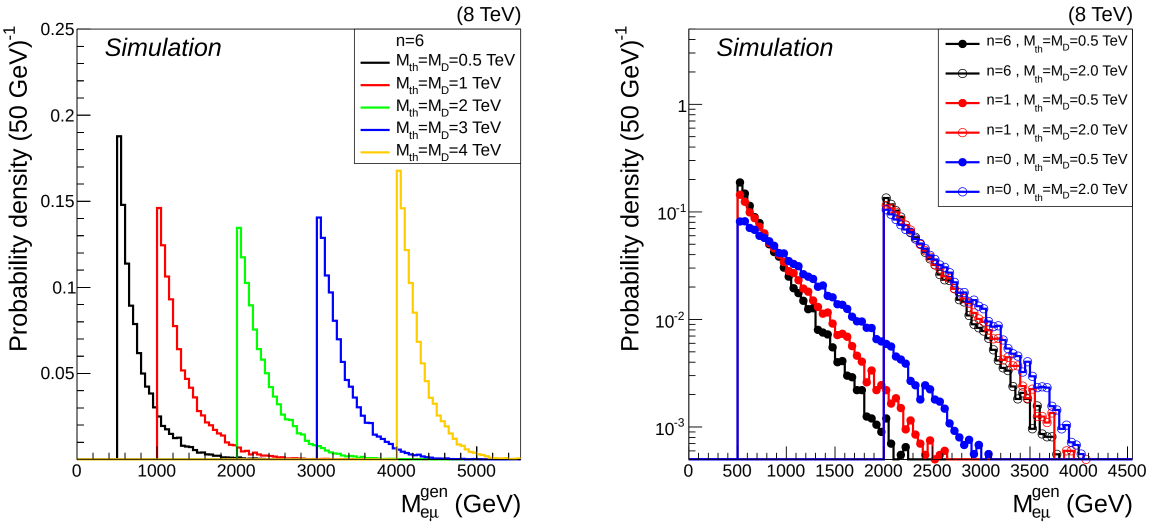

(a) The $M_{e\mu}$ distribution normalized to unity, obtained from QBH signal samples with $n = 6$ extra dimensions and threshold mass M_{th} between 0.5 TeV and 4 TeV.

(b) The dependence of the $M_{e\mu}$ distribution obtained from QBH signal samples on the number of extra dimensions, n, for two signal masses $M_{\mathrm{th}} = 0.5$ TeV and $M_{\mathrm{th}} = 2$ TeV.

Figure 5.3: Invariant mass distributions of eμ pairs from generated QBH signal samples.

old mass differs significantly from the median of the corresponding $M_{e\mu}$ distribution; for $n = 0$ and $M_{\mathrm{th}} = 500$ GeV the median lies at about 880 GeV. The impact of the number of extra dimensions on the shape of the invariant mass distribution from QBH decays is depicted in Fig. 5.3 (right) for two different QBH threshold masses. For $M_{\mathrm{th}} = 0.5$ TeV, the dependence of the shape on the number of extra dimensions is more pronounced than for $M_{\mathrm{th}} = 2$ TeV because at lower signal mass the n-dependent evolution of the partonic cross section with the QBH mass has a larger influence relative to the n-independent impact of the proton PDF.

5.1.3 Comparison of lepton kinematics in RPV $\tilde{\nu}_\tau$ and QBH signal events

This paragraph summarizes the differences in the signal cross sections and kinematics of generated RPV $\tilde{\nu}_\tau$ and QBH signal events. Due to the absence of small coupling parameters in the QBH signal cross section, Eqn. 1.32, the QBH model gives rise to cross sections of several fb at $\sqrt{s} = 8$ TeV even for threshold masses M_{th} as high as 2 TeV. If QBH production were possible in the $M_{\mathrm{th}} \sim 100$ GeV regime, it would already have been discovered at the Tevatron. The search for events from QBH decays in the eμ invariant mass spectrum therefore focuses on the multi-TeV region. For the RPV $\tilde{\nu}_\tau$ model with its potentially small Yukawa couplings, searches in the $M_{\tilde{\nu}_\tau} \sim 100$ GeV range are still relevant.

The differences in the shape of the invariant mass distributions have been described above. While the resonance in the RPV $\tilde{\nu}_\tau$ model constitutes a generic signal shape and encourages a model-independent analysis strategy, the invariant mass distribution of the QBH decay products has a very model-specific shape. In the following, the focus is put on the comparison of the final-state lepton kinematics and it is shown that the common event selection applied in the searches for both signal models is appropriate.

Both the $\tilde{\nu}_\tau$ and QBH considered in this work are scalar objects, and it is verified in the signal event samples generated with `CALCHEP` that the distributions of ϕ^*_ℓ and $\cos(\theta^*_\ell)$, the angular variables of the leptons in the rest frame of the eμ dilepton system, are flat. The p_{T} and η distributions of generated muons from the two different signals are compared in Fig. 5.4. In the signal models

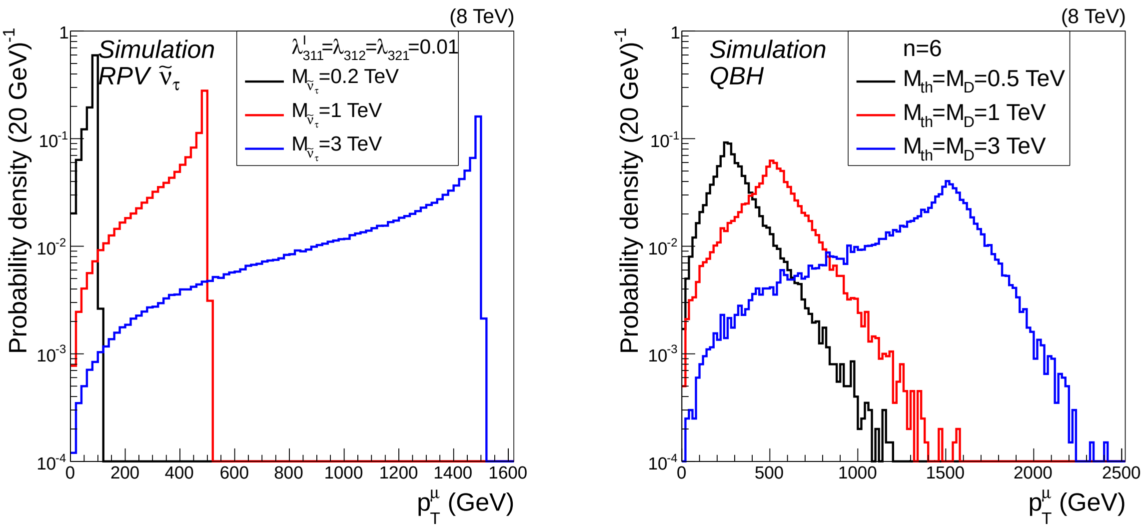

(a) Muon p_T distribution in generated RPV $\tilde{\nu}_\tau$ signal events.

(b) Muon p_T distribution in generated QBH signal events.

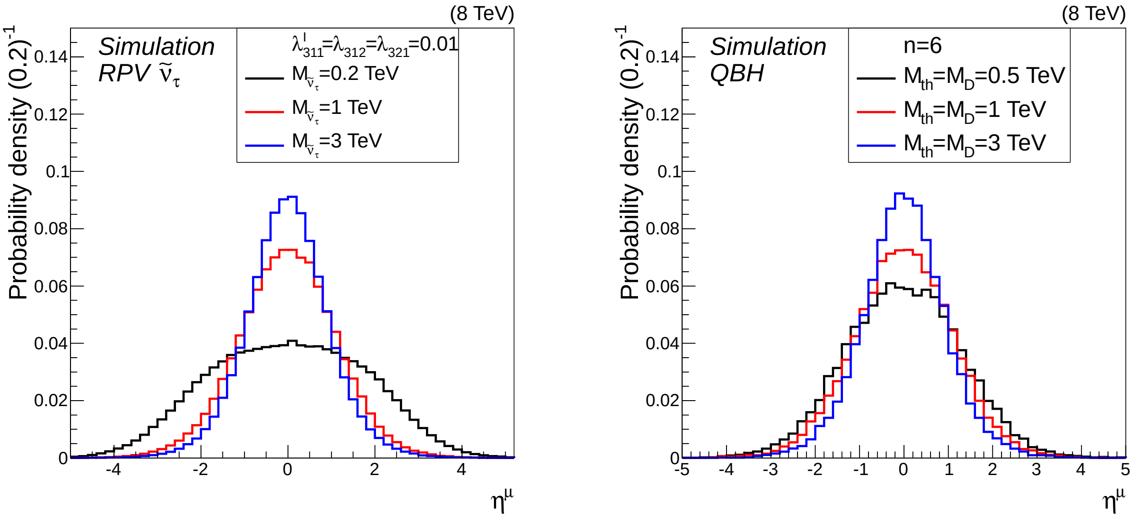

(c) Muon η distribution in generated RPV $\tilde{\nu}_\tau$ signal events.

(d) Muon η distribution in generated QBH signal events.

Figure 5.4: Transverse momentum and pseudorapidity distributions of muons in $e\mu$ pairs from generated RPV $\tilde{\nu}_\tau$ (left) and QBH (right) signal samples.

considered here, the muon and electron kinematics at generator level coincide. While the RPV $\tilde{\nu}_\tau$ signal exhibits the Jacobian peak with a maximum just below $p_\mathrm{T}^\ell = M_{\tilde{\nu}_\tau}/2$ followed by a sharp edge characteristic for resonant production, the p_T^ℓ spectrum from QBH mediated decays is more symmetrically distributed around $p_\mathrm{T}^\ell = M_\mathrm{th}/2$ with pronounced tails extending to both lower and higher transverse momenta. The η distributions of generated muons from the two different signals both become more central with increasing signal mass as expected due to smaller relativistic boost factors β_z along the beamline (the rapidity plateau shrinks). Accordingly, the geometrical signal acceptance, that is given by the fraction of generated signal events falling into the solid angle defined by the η selection cuts on the leptons, increases.

The impact of finite width effects on the signal acceptance in the RPV $\tilde{\nu}_\tau$ model is described in the next section. The detailed discussion of the signal selection efficiencies in the RPV $\tilde{\nu}_\tau$ and QBH models follows in Sec. 5.3.

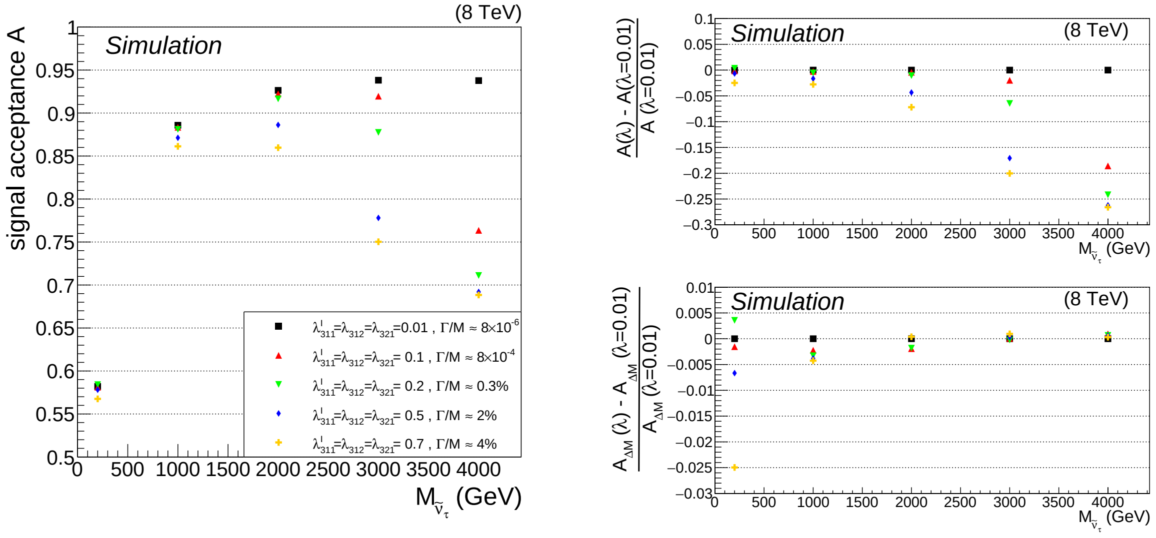

(a) The signal acceptance A (Eqn. 5.2) of scalar spin-0 resonances defined by the selection cuts on p_{T} and η applied on the leptons as a function of resonance mass for different decay widths Γ.

(b) Difference between the signal acceptance of the RPV signal model for couplings $\lambda = \lambda'_{311} = \lambda_{312} = \lambda_{321}$ and for $\lambda'_{311} = \lambda_{312} = \lambda_{321} = 0.01$, illustrating a narrow resonance with negligible influence of finite width effects. In the upper panel, the acceptance definition A (Eqn. 5.2) is used. The lower panel shows the results for the acceptance definition $A_{\Delta M}$ (Eqn. 5.3). Note that the scales on the ordinates of the two plots differ by a factor ten.

Figure 5.5: Impact of finite width effects on the acceptance of signal models with a spin-0 resonance, exemplified by the RPV signal model. The different acceptances A and $A_{\Delta M}$ are defined in the text. The term λ is used as a placeholder for $\lambda'_{311} = \lambda_{312} = \lambda_{321}$.

5.1.4 Signal acceptance studies

The dependence of the signal acceptance on the decay width Γ for a spin-0 resonance is studied based on generated RPV $\tilde{\nu}_\tau$ signal samples produced with `CALCHEP` with very large event counts. It is shown that the restriction of the signal events to the invariant mass window $M_{\mathrm{res}} \pm \Delta M$ introduced in Sec. 5.1.1 reduces the impact of finite with effects, and thus the coupling-dependence of the search strategy, significantly.

In what follows two different definitions of the signal acceptance, denoted A and $A_{\Delta M}$, are used:

$$A = \frac{\text{Number of events with leptons passing } p_{\mathrm{T}} \text{ and } \eta \text{ cuts}}{\text{Number of generated events}} \tag{5.2}$$

$$A_{\Delta M} = \frac{\text{Number of events within } M_{\mathrm{res}} \pm \Delta M \text{ with leptons passing } p_{\mathrm{T}} \text{ and } \eta \text{ cuts}}{\text{Number of generated events within } M_{\mathrm{res}} \pm \Delta M} . \tag{5.3}$$

As shown in Fig. 5.5 (left), the signal acceptance A exhibits a strong dependence on the decay width. At $M_{\mathrm{res}} = 200$ GeV, the relative difference in A between a narrow resonance with a relative decay width of order 10^{-5} and a resonance with a relative decay width of 4% amounts to 2.5%, Fig. 5.5 (right, upper panel). This relative difference increases to about 25% at $M_{\mathrm{res}} = 4$ TeV. The strong dependence of the acceptance on the decay width at high resonance mass is removed when restricting the signal events to the invariant mass window $M_{\mathrm{res}} \pm \Delta M$ as presented in Fig. 5.5 (right, lower panel). For $M_{\mathrm{res}} = 4$ TeV, the relative difference in the acceptances $A_{\Delta M}$ of the resonant signals with relative decay widths 10^{-5} and 4% is reduced to the sub-percent level.

5.2 Simulation of signal events

For the simulation of RPV and QBH signal events, the parton-level events produced with the `CALCHEP` generator using the CTEQ6L PDF set are forwarded to `PYTHIA` (v. 6.426) [211] for showering and hadronization with the underlying event tune Z2*, and are processed through a full simulation of the CMS detector based on `GEANT4` (v. 9.4) [165]. The `PYTHIA` tune Z2* is derived from the Z1 tune described in Ref. [212], but uses a different PDF set, CTEQ6L.

Further information on the signal simulation is given in App. C. The parameter points for which samples have been produced are listed there in Tabs. C.2 and C.3 for the RPV $\tilde{\nu}_\tau$ signal and in Tab. C.1 for the QBH signal.

5.3 Signal efficiency of the event selection

In this section, the impact of the event selection outlined in Sec. 4 on the signal events is studied. The terms *full selection efficiency* and *acceptance times efficiency*, $A \times \epsilon$, are used interchangeably in the following. The investigation starts from the simulated signal samples described above and the resulting simulated selection efficiencies. The latter are then corrected to the efficiency values measured in data by the so-called data-to-simulation scale factors, SF, introduced in Sec. 4.5 that are determined binned in lepton p_{T} and η. For this correction, the same factorization of efficiencies as in the efficiency measurement is used, i.e. in ascending order of the efficiencies determined relative to one another:

$$A \times \varepsilon = A \times \varepsilon^{e} \times \varepsilon^{\mu} = A \times (\varepsilon^{e}_{\mathrm{Reco}}\ \varepsilon^{e}_{\mathrm{Id}}) \times \left(\varepsilon^{\mu}_{\mathrm{Id}}\ \varepsilon^{\mu}_{\mathrm{trigger}}\right) \ . \tag{5.4}$$

The efficiency correction via SFs is introduced on an event-by-event basis by assigning an event weight w_{SF} equal to the product of the corresponding four efficiency scale factors evaluated for the p_{T} (E_{T}) and η values of the selected muon (electron) in the event:

$$A \times \varepsilon = \frac{\sum_{j=1}^{N_{\mathrm{pass}}} w_{\mathrm{SF}}\,(j)}{N_{\mathrm{tot}}} = \frac{\sum_{j=1}^{N_{\mathrm{pass}}} w_{\mathrm{SF}}\,(j)}{N_{\mathrm{pass}}} \times A \times \varepsilon_{\mathrm{MC}} \ , \tag{5.5}$$

where j is an index running over the events passing the selection, N_{tot} denotes the number of simulated events for the signal sample under study and N_{pass} stands for the number of events in the sample passing the event selection. The acceptance is defined by kinematic cuts on the leptons at generator level after final state radiation of $p^{e}_{\mathrm{T}} \geq 35$, $|\eta^{e}| \leq 1.442$ or $1.56 \leq |\eta^{e}| \leq 2.5$ for the electron; and $p^{\mu}_{\mathrm{T}} \geq 45$, $|\eta^{\mu}| \leq 2.1$ for the muon.

5.3.1 RPV $\tilde{\nu}_\tau$ signal model

As shown in Sec. 5.1.4, the signal acceptance of the spin-0 resonance search becomes in good approximation independent of the resonance decay width when the search is restricted to a suitable invariant mass range around the resonance peak. Therefore the discussion of the signal acceptance and selection efficiency for the RPV $\tilde{\nu}_\tau$ signal can be restricted to the narrow resonance case with $\lambda'_{311} = \lambda_{312} = \lambda_{321} = 0.01$. In Fig. 5.6 (left) the acceptance A defined in Eqn. 5.2 is presented. Up to $M_{\tilde{\nu}_\tau} = 500$ GeV, it exhibits a steep increase to 79.5% from 23.5% at $M_{\tilde{\nu}_\tau} = 100$ GeV, where the loss in acceptance is still driven by the p_{T} requirements removing events close to the Jacobian peak shown in Fig. 5.4 (left). For signal masses above 500 GeV, the impact of the p_{T} cuts on the signal acceptance is negligible and the further increase in acceptance towards higher masses is a result of the shrinking rapidity plateau. As the η distributions of the leptons become more and more central, the slope of the acceptance curve falls steadily but remains positive. From $M_{\tilde{\nu}_\tau} = 1$ TeV to $M_{\tilde{\nu}_\tau} = 2.6$ TeV it rises from 89.0% to 93.2%.

The shape of the full selection efficiency in Fig. 5.6 (left) displays the same key characteristics as the acceptance: After a rise from 15.0% at $M_{\tilde{\nu}_\tau} = 100$ GeV to 64.5% at $M_{\tilde{\nu}_\tau} = 1$ TeV it reaches a

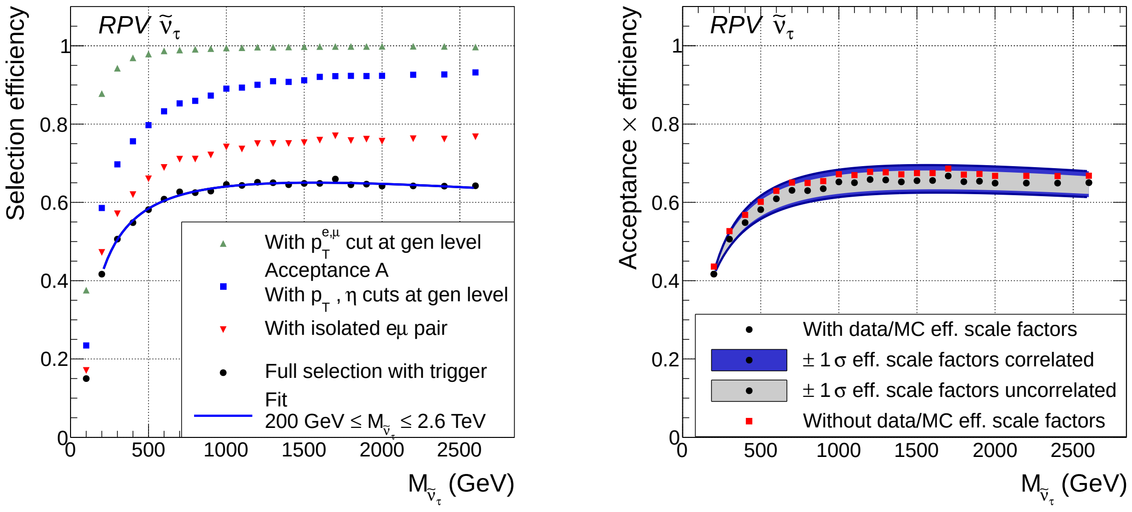

(a) Evolution of the RPV $\tilde{\nu}_\tau$ selection efficiency from the signal acceptance to the efficiency after all cuts as a function of signal mass $M_{\tilde{\nu}_\tau}$ based on simulated signal samples. The selection efficiency of the reconstructed isolated $e\mu$ pair (red triangles) and full selection efficiency, that also contains the trigger requirement (black dots), are both corrected to account for the efficiencies measured in data. The solid blue curve is the result of the fit to the full acceptance times efficiency.

(b) Uncertainty in the acceptance times efficiency of the RPV $\tilde{\nu}_\tau$ signal obtained by treating the uncertainties in the data-to-simulation scale factors of the individual efficiencies as uncorrelated (inner light blue band) and fully correlated (outer dark blue band). For comparison, the full selection efficiency obtained from the simulation (red squares) without data-driven corrections to the efficiencies is shown.

Figure 5.6: Signal acceptance and selection efficiencies for the RPV $\tilde{\nu}_\tau$ model as a function of $M_{\tilde{\nu}_\tau}$. All efficiencies shown are defined as the fraction of events passing the indicated selection requirements relative to the total number of simulated events in the corresponding MC sample.

plateau, varying within ±1.5% for higher masses. In contrast to the acceptance however, the total acceptance times efficiency does exhibit a small negative slope at signal masses above 1.5 TeV due to the decline of the single-muon trigger efficiency for muon momenta in the TeV range.

In the following, the efficiencies of the individual steps of the selection obtained from the simulated signal samples are discussed. The efficiency measurements based on the tag-and-probe method at the Z peak, that are described in Sec. 4.5, only extend to $p_T^\ell = 300$ GeV. For lower transverse momenta, the simulation has been found to be in good agreement with the measured efficiency values. Given that the transverse momenta of most leptons from the resonance decay fall in the vicinity of the Jacobian peak at $M_{\tilde{\nu}_\tau}/2$, one has to rely on the simulation for the description of the individual selection efficiencies for resonance masses $M_{\tilde{\nu}_\tau} \gtrsim 600$ GeV. Starting from the information at parton level in the simulated events, the efficiencies are defined relative to each other starting from the lepton reconstruction to the lepton identification and the trigger efficiency.

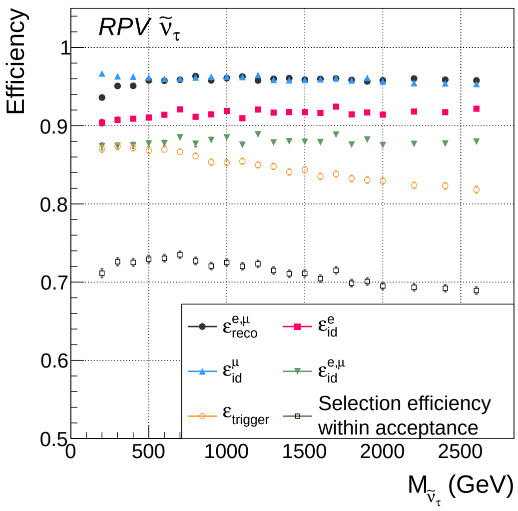

Figure 5.7: Dependence of reconstruction, lepton identification, and trigger efficiencies on the signal mass $M_{\tilde{\nu}_\tau}$. The efficiencies are defined in the text. The combined efficiency for signal events with an $e\mu$ pair in the acceptance is also shown. The efficiencies are obtained directly from simulated signal samples without applying corrections to account for the efficiencies measured in data. The uncertainty bars represent the binomial statistical uncertainty that results from the limited number of simulated events.

1. **Lepton reconstruction efficiency $\varepsilon_{\mathbf{reco}}$**
   For the lepton reconstruction efficiencies, a match within $\Delta R = 0.1$ between a generated lepton from the resonance decay in the acceptance and a corresponding muon candidate in the RECO muon collection or an electron candidate in the GSF electron collection is required. The efficiency is then defined as the fraction of generated electrons or muons in the acceptance with a matching reconstructed lepton candidate.

2. **Lepton identification efficiency $\varepsilon_{\mathbf{id}}$**
   The lepton identification efficiencies are defined as the fraction of reconstructed lepton candidates selected in the step above that pass the full lepton selection including the isolation requirement.

3. **Trigger efficiency $\varepsilon_{\mathbf{trigger}}$**
   The trigger efficiency is the fraction of selected muons that fire the single-muon trigger.

4. **Selection efficiency $\varepsilon_{\mathbf{sel}}$**
   Total selection efficiency for events falling into the acceptance.

The reconstruction and identification efficiencies of the dilepton system are shown together with the trigger efficiency and the total selection efficiency of events falling into the acceptance as a function of the signal mass $M_{\tilde{\nu}_\tau}$ in Fig. 5.7. While the variation with signal mass of the dilepton reconstruction and identification efficiencies above $M_{\tilde{\nu}_\tau} = 300$ GeV does not exceed 1%, the trigger efficiency falls off steadily towards higher masses from 87% at $M_{\tilde{\nu}_\tau} = 300$ GeV to 82% at $M_{\tilde{\nu}_\tau} = 2.4$ TeV. The single-muon (L1) trigger efficiency is affected by electromagnetic showers within the muon system, which can result from radiative processes off high-p_{T} muons in the iron return yoke. The emission probability of hard bremsstrahlung off a muon rises with increasing muon p_{T} and is responsible for the decline of the total selection efficiency $\varepsilon_{\mathrm{sel}}$ from 73% at $M_{\tilde{\nu}_\tau} = 500$ GeV to 69% at $M_{\tilde{\nu}_\tau} = 2.4$ TeV, that is visible in Fig. 5.7. As pointed out above, the effect of this moderate decline of the efficiency $\varepsilon_{\mathrm{sel}}$ on the total acceptance times efficiency is eased

by an increase in signal acceptance towards higher masses.
Given that the evolution of the efficiency towards signal masses in the multi-TeV range is taken from MC simulations, the assigned systematic uncertainty is supposed to cover the full variation in $\varepsilon_{\mathrm{sel}}$ of 4% found for $M_{\tilde{\nu}_\tau} \geq 500$ GeV (Fig. 5.7, grey open squares). As shown in Fig. 5.6 (right), the propagation of the uncertainties in the data-to-simulation scale factors, which are large for high lepton p_{T}, to the selection efficiency fulfills this requirement. This uncertainty in $A \times \epsilon$ covers the difference between the values obtained directly from the simulation and the result after the application of the data-to-simulation scale factors; i.e. the combined scale factor is compatible with unity within the uncertainties for high signal masses.

In the narrow resonance search it is crucial to scan the invariant mass spectrum with a fine spacing of the probed signal hypotheses that is smaller than the detector resolution. Producing simulated signal samples for each of these masses is resource- and time-consuming, and unnecessary given the generic signal shape. The acceptance times efficiency is thus fitted with a phenomenological function to obtain a parameterization that can be evaluated for each desired signal mass. The fit range starts at the lower bound of the search region in invariant mass, $M_{\tilde{\nu}_\tau} = 200$ GeV, and extends up to the highest signal mass for which a simulated sample has been produced, $M_{\tilde{\nu}_\tau} = 2.6$ TeV. The chosen parameterization with the resulting fit parameters reads

$$A \times \epsilon \left(M_{\tilde{\nu}_\tau}\right) = 0.76 - 86.9/\left(61.4 + M_{\tilde{\nu}_\tau}/\mathrm{GeV}\right) - 3.3 \times 10^{-5}\ M_{\tilde{\nu}_\tau}/\mathrm{GeV}\ , \tag{5.6}$$

and is compared to the mass points included in the fit in Fig. 5.6 (left). The fit is carried out using the implementation of `MINUIT` in `ROOT` [213], taking into account the statistical uncertainties in the acceptance times efficiency and yields $\chi^2/\mathrm{ndf} = 19.6/18$. The same functional form is used in the fits that define the envelope of the systematic uncertainty in the efficiency in Fig. 5.6 (right).

5.3.2 QBH signal model

In contrast to the resonance search, the QBH signal has a pronounced tail towards higher masses and the invariant mass spectrum does not have to be scanned with very small step sizes. Thus, no parameterization of the acceptance times efficiency or the signal shape is carried out for this signal and these informations are directly obtained from the simulated samples after applying the corrections to the efficiencies described above. The signal mass dependence of the acceptance and full selection efficiency is presented in Fig. 5.8 for the QBH signal with $n = 0$. The key features are similar to those of the acceptance for the RPV $\tilde{\nu}_\tau$ signal, namely the rise in acceptance towards higher masses and the slight decline in the overall selection efficiency due to the loss in trigger efficiency. Due to the dependence of the kinematics of the final state leptons on the number of extra dimensions, the acceptance times efficiency can vary by about 1% for a given signal mass M_{th} when different numbers of extra dimensions are considered. The acceptance and full selection efficiencies are compared for $n = 0$ and $n = 6$ in Tab. 5.2.

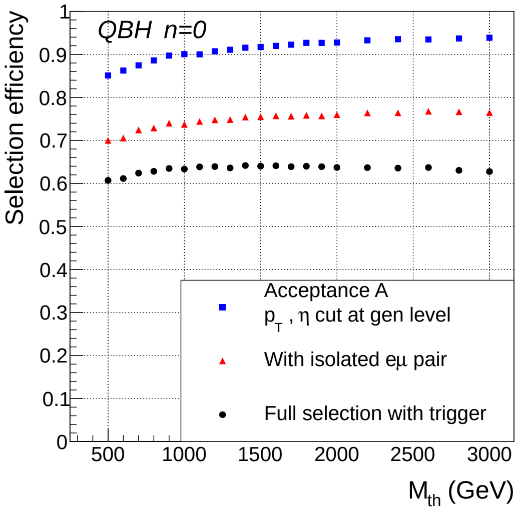

Figure 5.8: Evolution of the QBH selection efficiency for $n = 0$ *from the signal acceptance to the efficiency after all cuts as a function of threshold mass* M_{th} *based on simulated signal samples. The definition of the shown efficiencies is the same as in Fig. 5.6 (left).*

Table 5.2: Comparison of the acceptance A *as defined in Eqn. 5.2 and the full selection efficiency* $A \times \epsilon$ *for various QBH threshold masses. The values are given for QBH signals with* $n = 0$ *(left set of columns) and* $n = 6$ *(right set of columns).*

QBH $n = 0$	A	$A \times \epsilon$	QBH $n = 6$	A	$A \times \epsilon$
$M_{\mathrm{th}} = 0.5$ TeV	0.85	0.61	$M_{\mathrm{th}} = 0.5$ TeV	0.82	0.60
$M_{\mathrm{th}} = 1.0$ TeV	0.90	0.63	$M_{\mathrm{th}} = 1.0$ TeV	0.89	0.64
$M_{\mathrm{th}} = 2.0$ TeV	0.93	0.64	$M_{\mathrm{th}} = 2.0$ TeV	0.93	0.65
$M_{\mathrm{th}} = 3.0$ TeV	0.94	0.63	$M_{\mathrm{th}} = 3.0$ TeV	0.94	0.64
			$M_{\mathrm{th}} = 3.5$ TeV	0.94	0.63
			$M_{\mathrm{th}} = 4.0$ TeV	0.94	0.63

5.4 Invariant mass resolution

The invariant mass resolution is one of the key numbers for shape-based searches for new physics in mass spectra. Among the two signal models considered in this work, an appropriate modelling of the detector resolution is most important in the narrow resonance search, where the signal line shape, i.e. the width of the peak around the resonance mass and the extend of the tails further away from it, is dominated by the detector effects. In contrast, the wide tail above the threshold mass of the QBH signal on display in Fig. 5.3 is mainly defined by the interplay between the mass dependence of the partonic cross section and the proton PDFs, and the detector resolution plays a subleading rôle. The following discussion therefore focusses on the narrow resonance line shape. In this context, the eμ invariant mass resolution and its systematic uncertainty are discussed and these general results are also used in the QBH search.

The eμ invariant mass resolution is obtained from the signal simulation. Since the most critical component in the eμ invariant mass resolution is the muon p_{T} resolution, the focus is put on the muon in the eμ pair in the following rather than on the electron. One aspect of the signal simulation that is of particular importance for the muon p_{T} resolution is the assumed (mis)alignment scenario for the tracker and the muon system. The scenario used in the simulated signal samples, referred to as the *baseline* misalignment[3], is based on an alignment obtained from cosmic ray muon data collected during the *Cosmic Run At Four Tesla* (CRAFT) [214]. The muon $M_{\mathrm{e}\mu}$ resolution obtained from simulations with this muon misalignment is compared to that from simulated samples using a different alignment scenario, which is closer to an ideally aligned detector, in Sec. 5.4.1.

A data-driven study of the muon p_{T} resolution at high muon momenta is carried out using cosmic ray data recorded with the CMS detector in the 2012 data-taking period in Sec. 5.4.2. Within the uncertainties, agreement between this measurement and the expectation from simulated samples is found up to the highest muon momenta probed and the usage of the signal MC for the extraction of the signal shape is thus supported.

To the end of extracting the eμ relative invariant mass resolution from simulated samples, the relative residual $R_{\mathrm{res}} = (M_{e\mu}^{\mathrm{reco}} - M_{e\mu}^{\mathrm{gen}})/M_{e\mu}^{\mathrm{gen}}$ is fitted, where $M_{e\mu}^{\mathrm{gen}}$ is the generated eμ mass and $M_{e\mu}^{\mathrm{reco}}$ the corresponding value after reconstruction of the leptons. The distributions of this residual are shown for simulated samples with $M_{\tilde{\nu}_\tau} = 200$ GeV and $M_{\tilde{\nu}_\tau} = 1.5$ TeV in Fig. 5.9. Two different fit functions are used to illustrate the key features of the relative invariant mass resolution; a Gaussian fit with a constrained fit range and a double-sided Crystal ball (CB) fit. For the Gaussian fit, a first fit iteration is carried out in the wide fit range $R_{\mathrm{res}} \in [-0.5, 0.5]$ and the resulting width σ_{full} is used to constrain the fit range in the second iteration of the Gaussian fit to $R_{\mathrm{res}} \in [-2\sigma_{\mathrm{full}}, 2\sigma_{\mathrm{full}}]$. As shown in Fig. 5.9, the width σ of the constrained Gaussian fit is a good measure of the core resolution, whereas this fit significantly underestimates the tails of the R_{res} distribution. Therefore, the piecewise-defined, two-sided CB function, f_{CB}, is used to model both the Gaussian core resolution and the tails at lower and higher values of R_{res}. It is given by

$$f_{\mathrm{CB}}\left(R_{\mathrm{res}}\right) = \begin{cases} A_0 \times \exp\left(-\frac{\left(R_{\mathrm{res}}-R_{\mathrm{res}}^0\right)^2}{2\sigma_{\mathrm{CB}}^2}\right) & , \quad -|\alpha_L| < \frac{R_{\mathrm{res}}-R_{\mathrm{res}}^0}{\sigma_{\mathrm{CB}}} < |\alpha_R| \\ A_0 \times B_L\left(C_L - \frac{R_{\mathrm{res}}-R_{\mathrm{res}}^0}{\sigma_{\mathrm{CB}}}\right)^{-n_L} & , \quad \frac{R_{\mathrm{res}}-R_{\mathrm{res}}^0}{\sigma_{\mathrm{CB}}} \leq -|\alpha_L| \\ A_0 \times B_R\left(C_R + \frac{R_{\mathrm{res}}-R_{\mathrm{res}}^0}{\sigma_{\mathrm{CB}}}\right)^{-n_R} & , \quad \frac{R_{\mathrm{res}}-R_{\mathrm{res}}^0}{\sigma_{\mathrm{CB}}} \geq |\alpha_R| \end{cases} \tag{5.7}$$

$$\text{where} \quad B_x = \left(\frac{n_x}{|\alpha_x|}\right)^{n_x} \exp\left(-|\alpha_x|^2/2\right) \quad \text{and} \quad C_x = \frac{n_x}{|\alpha_x|} - |\alpha_x| \quad , \quad x \in \{L, R\} \quad ,$$

with one normalization parameter A_0 and six parameters defining the shape, namely the width of the central Gaussian σ_{CB} and its central value R_{res}^0, plus two parameters describing each tail; the values $\alpha_{L,R}$ marking the transitions from core to tail and the exponents $n_{L,R}$. The double-sided CB fit to the signal MC is carried out in the fit range $R_{\mathrm{res}} \in [-0.5, 0.4]$ and describes the tails of the R_{res} distribution well within the statistical uncertainties in the simulated event yields, as shown in the ratio plots in Fig. 5.9, and expressed by the χ^2/ndf of the fits, 79/80 and 117/121, for $M_{\tilde{\nu}_\tau} = 200$ GeV and $M_{\tilde{\nu}_\tau} = 1.5$ TeV, respectively.

The resulting core resolution σ_{CB} is presented as a function of resonance mass in Fig. 5.10 (left). It is compared to the width of the constrained Gaussian fit to illustrated the impact of the choice of fit function. The relative invariant mass resolution increases from 1.4% at $M_{\tilde{\nu}_\tau} = 200$ GeV to 5.7% at $M_{\tilde{\nu}_\tau} = 3$ TeV, driven by the rising relative resolution of the muon track's curvature. In order to parameterize the signal shape, the resolution σ_{CB} is fitted in the range $M_{\tilde{\nu}_\tau} \in [0.2\ \mathrm{TeV}, 3\ \mathrm{TeV}]$ with a second-degree polynomial. The result reads

$$\sigma_{\mathrm{CB}}(M_{\tilde{\nu}_\tau}) = 9.6 \times 10^{-3} + 2.1 \times 10^{-5}\left(M_{\tilde{\nu}_\tau}/\mathrm{GeV}\right) - 1.8 \times 10^{-9}\left(M_{\tilde{\nu}_\tau}/\mathrm{GeV}\right)^2 \quad . \tag{5.8}$$

The resolution of the inverse muon p_{T} and the electron E_{T}, derived in an analogous manner as the invariant mass resolution, is given in Fig. 5.10 (right). This comparison underlines the importance

---

[3] More information about the slightly different muon misalignment scenarios used in the production of the signal samples is given in App. C.

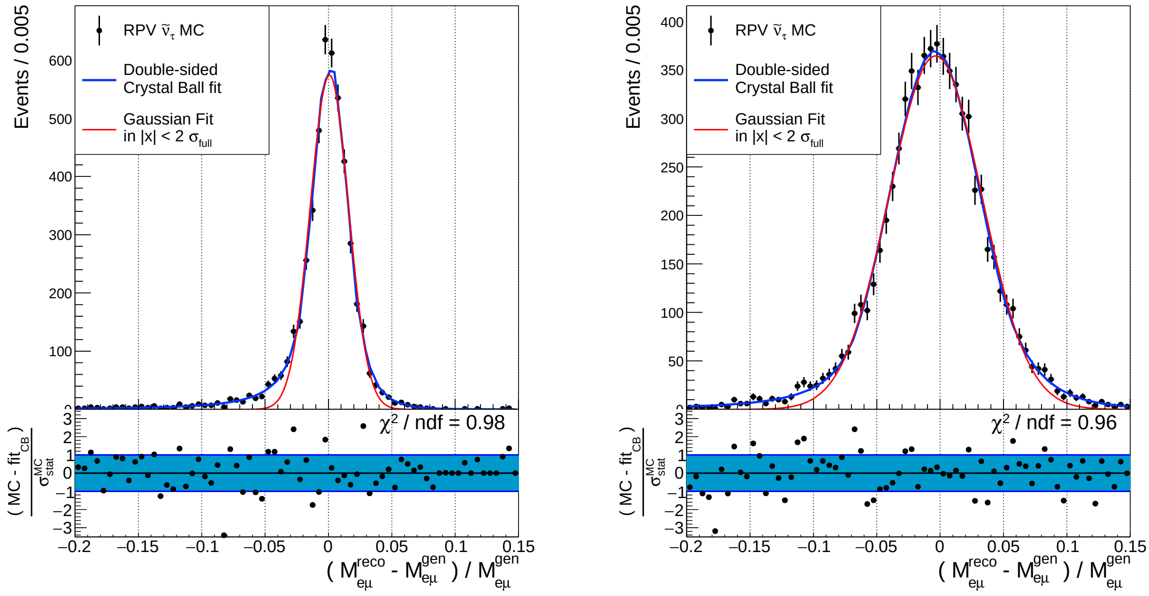

(a) Relative residual R_{res} for the RPV $\tilde{\nu}_\tau$ signal sample with $M_{\tilde{\nu}_\tau} = 200$ GeV.

(b) Relative residual R_{res} for the RPV $\tilde{\nu}_\tau$ signal sample with $M_{\tilde{\nu}_\tau} = 1.5$ TeV.

Figure 5.9: Distributions of the relative residual R_{res} *obtained from signal simulations with* $M_{\tilde{\nu}_\tau} = 200$ *GeV (left) and* $M_{\tilde{\nu}_\tau} = 1.5$ *TeV (right). Two different fits to the simulated distributions are compared; the double-sided CB fit and the Gaussian fit with restricted fit range. The uncertainty bars represent the statistical uncertainty in the simulated event yields, which are taken into account in the fits.*

of the muon p_{T} resolution, which is expected to rise approximately proportional with the muon p_{T} in contrast to the electron E_{T} resolution that is dominated by the constant term of the ECAL at high electron energy. The linear evolution of the muon p_{T} resolution is obscured by the choice of the simulated samples from which the curve in Fig. 5.10 is obtained. It represents the resolution averaged over the η values of the muons in each p_{T} bin. However, the muon p_{T} resolution varies significantly between the endcap and the barrel part of the muon system. In the signal kinematics, lower p_{T} values correspond to a lower signal mass and therefore a wider η distribution. The p_{T} dependence of the muon p_{T} resolution is closer to the expected linear behaviour when only muons in the barrel part of the muon system are considered.

5.4.1 Impact of the alignment on the muon p_{T} resolution

The $M_{\text{e}\mu}$ resolution in Eqn. 5.8 is derived from simulations using a CRAFT-based muon alignment (the so-called C1 misalignment). This alignment is assumed to lead to a conservative estimate of the muon p_{T} resolution because the understanding of the detector alignment has improved after studies using pp collision data from the 2011 data taking period. In order to test how an improved alignment would impact the $M_{\text{e}\mu}$ resolution, simulated eμ resonance samples have been produced with an alignment that assumes the detector components to be randomly displaced from their positions in an ideally aligned detector within the statistical uncertainties in the alignment parameters obtained from the studies including 2011 collision data. The corresponding misalignment scenario is referred to as the optimistic misalignment (or C2 misalignment). Simulated samples for the resonant production of eμ pairs with this optimistic misalignment scenario have been produced by Thomas Reis and the resulting $M_{\text{e}\mu}$ resolution is documented in Ref. [39]. The relative difference in the mass resolution obtained with the C1 and C2 misalignment scenarios, $(\sigma_M^{\text{C1}} - \sigma_M^{\text{C2}})/\sigma_M^{\text{C1}} \equiv \Delta\sigma_{\text{align}}/\sigma_M^{\text{C1}}$, varies from 2% at a resonance mass of 500 GeV to about 25% at

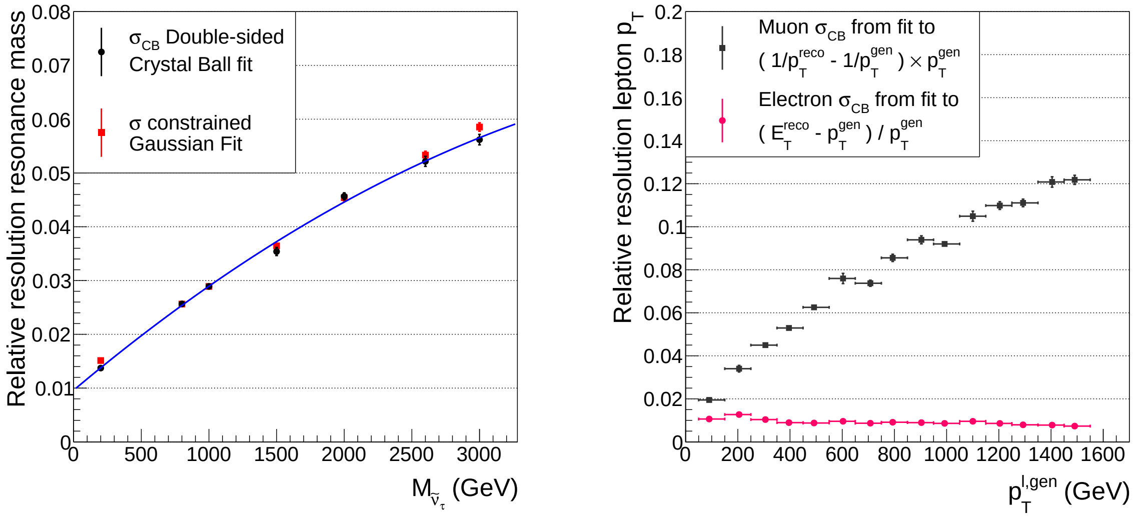

(a) Relative eμ invariant mass resolution as a function of resonance mass $M_{\tilde{\nu}_\tau}$. The resolution is obtained from fits with two different fit functions, constrained Gaussian fits (red) and double-sided CB fits (black). The results from the CB model are used to determine the parameterization of the invariant mass resolution (blue curve).

(b) Relative lepton p_{T} resolution obtained from CB fits. For the muon, the relative difference in the inverse transverse momentum distribution, $(1/p_{\mathrm{T}}^{\mathrm{reco}} - 1/p_{\mathrm{T}}^{\mathrm{gen}})/(1/p_{\mathrm{T}}^{\mathrm{gen}})$, is fitted, whereas the relative resolution of the electron E_{T} measured in the ECAL, $(E_{\mathrm{T}}^{\mathrm{reco}} - p_{\mathrm{T}}^{\mathrm{gen}})/p_{\mathrm{T}}^{\mathrm{gen}}$, is considered for the electron. The horizontal bars indicate the used binning in generated lepton p_{T}. The position of the data points on the abscissa indicates the mean value of the p_{T} distribution in each bin.

Figure 5.10: Relative resolution of the eμ invariant mass (left) and lepton p_{T} (right) derived from double-sided CB fits to simulated signal samples. The vertical uncertainty bars represent the uncertainty in the fit parameter σ_{CB} obtained from the fit.

2 TeV and 45% at 4 TeV. This difference is used as an estimate of the systematic uncertainty in the width of the signal shape (peak in $M_{\mathrm{e}\mu}$) in the statistical interpretation of the eμ resonance search that is reported in Sec. 10.

The impact on the selection efficiency (Sec. 5.3) of simulating the signal events with the different muon misalignment scenarios is much smaller than that on the muon p_{T} and $M_{\mathrm{e}\mu}$ resolutions; differences do not exceed the 1% level and are covered within the uncertainties shown in Fig. 5.6 (right).

5.4.2 Intermezzo: Muon p_{T} resolution from cosmic ray muons

Muons from cosmic ray air showers that traverse the CMS detector have been used for detector alignment and to assess the performance of the CMS muon reconstruction, including the muon p_{T} resolution, once the detector was assembled in 2008 [215]. Such studies ought to be repeated each time the detector is opened for interventions and reassembled. For the 2012 data taking period, the study of the muon p_{T} resolution presented in this paragraph has been carried out by Matthias Endres and the author using the methods developed earlier by others in the CMS collaboration, and in particular codes written by Jordan M. Tucker [216].

The aim of this study is twofold, as dictated by the expectation from the resonance signal shape described above: First, it is intended to verify that the detector simulation correctly describes the Gaussian core resolution. Secondly, it has to be confirmed that the distribution of the measure of the muon p_{T} resolution ($R(q/p_{\mathrm{T}})$ defined below) exhibits no unexpectedly large tails, that would result from gross mismeasurement of the track curvature and may indicate imperfections in the track reconstruction.

In order to work with reconstructed muon tracks similar to those from pp collisions, which originate from the beamspot, only cosmic ray muons that traverse the silicon pixel detector are considered in the analysis. The great majority of these cosmic ray muons pass through the central barrel part of the muon systems which is equipped with DT chambers and RPCs. Therefore, this study of the muon p_T resolution is restricted to the central part of the detector $|\eta^\mu| \lesssim 1$, and cosmic muon trajectories with hits in the CSC chambers are rejected. To the end of checking the signal simulation, this angular constraint is acceptable because the BSM signal models considered here produce central high-p_T muons (Fig. 5.4). The data samples used have been collected during the commissioning and the inter-fill periods of the LHC in the 2012 data-taking period and are summarized in App. D together with the list of simulated cosmic muon MC samples, which invoke the CMSCGEN generator [217, 218]. In the used data samples, the inner tracking detectors and the DT chambers are required to be fully operational (declared *good* by the CMS data quality monitoring). Data have been collected with two different operation modes of the tracker front-end electronics, the *peak* and *deconvolution* modes [219]. For the TuneP muon p_T assignment, similar resolutions are obtained for both datasets and only the results based on the *peak* mode dataset, which includes the higher number of recorded events, are presented in the following. In order to reduce the size of the initial datasets and MC samples, a preselection is applied which requires the events to contain so-called *superpointing* muons that pass a cylindrical volume around the nominal beamspot defined by $z = \pm 50$ cm and $R_{xy} = 10$ cm.

To the end of measuring the resolution, the hits of the cosmic muon track traversing the entire detector are divided into two sets, one in the upper hemisphere of the detector, the other in the lower hemisphere, and a global muon track reconstruction is applied to both sets, yielding an upper track with transverse momentum $p_\mathrm{T}^\mathrm{upper}$ and a lower track with $p_\mathrm{T}^\mathrm{lower}$. The resolution is then obtained from the distribution of the relative residual [215]

$$R(q/p_\mathrm{T}) = \frac{(q/p_\mathrm{T}^\mathrm{upper}) - (q/p_\mathrm{T}^\mathrm{lower})}{\sqrt{2}\,(q/p_\mathrm{T}^\mathrm{lower})} \tag{5.9}$$

in bins of $p_\mathrm{T}^\mathrm{lower}$. The factor $\sqrt{2}$ in the denominator reflects the assumption that the two reconstructed tracks are independent. The following muon identification criteria are applied to both tracks in selected events:

- The track segments in the inner tracking detector and the muon system can be matched to form a global muon.
- The track traverses at least one pixel layer.
- The track traverses at least eight layers of the silicon strip tracker.
- At least one valid hit in the muon system remains in the global track fit.
- All refits of the muon tracks intended for high-p_T muons are successful (see Sec. 3.2.1).

To ensure that the two tracks originate from one muon, they are required to fall within $|\Delta\theta| < 0.05$ and $|\Delta\phi| < 0.1$. After this selection, 16188 events remain, 56 of which contain a muon with $p_\mathrm{T}^\mathrm{lower} \geq 500$ GeV. The requirement of a pixel hit in each track reduces the number of selected events by about a factor 5, and restricts the longitudinal impact parameter with respect to the nominal beamspot, $|\mathrm{d}_z|$, to about 25 cm as presented in Fig. 5.11 (right). The distribution exhibits the expected sharp edge at the boundary of the barrel pixel detector and two peaks close to the position of the two pixel endcap disks at $z = \pm 34.5$ cm and $z = \pm 46.5$ cm. Figure 5.11 (left) shows the comparison of the ϕ distributions of the track reconstructed in the lower half of the detector in cosmic data and the MC simulation. The symmetry of the ϕ distribution around $\phi = -\pi/2$ is broken by the charge asymmetry of atmospheric muons, with more muons carrying positive than negative electric charge [220].

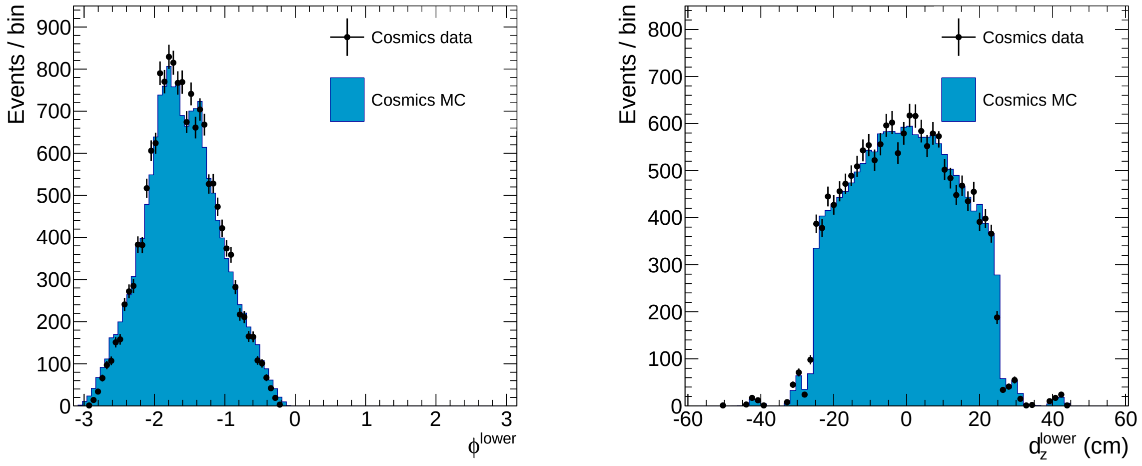

(a) The ϕ distribution of the lower global muon track in selected cosmic ray events.

(b) Distribution of the longitudinal impact parameter d_z with respect to the nominal beamspot of the lower global muon track in selected cosmic ray events.

Figure 5.11: Comparison between data and simulation of track variables of muon tracks from cosmic ray events reconstructed in the lower half of the CMS detector. The areas of the histograms obtained from simulated events are scaled to those of the histograms representing the measured data.

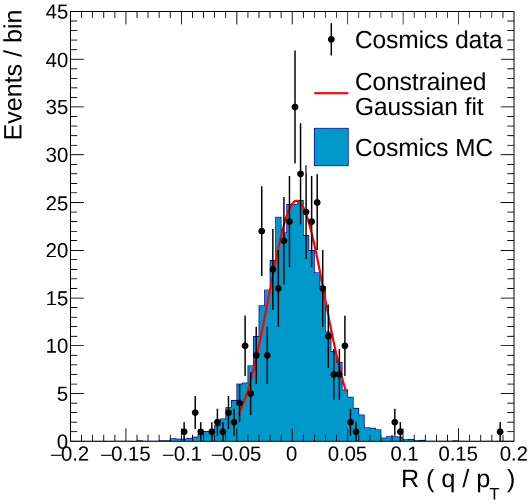

Figure 5.12: Distribution of the relative residual $R(q/p_\mathrm{T})$ for selected cosmic ray events in the muon p_T bin 200 GeV $\leq p_\mathrm{T}^\mathrm{lower} \leq 350$ GeV. The area of the histogram obtained from simulated events is scaled to that of the histogram representing the measured data. The fit curve shows the constrained Gaussian fit to the data.

Two measures of the muon p_T resolution are considered: the RMS of the residuals $R(q/p_\mathrm{T})$ and the Gaussian core resolution from constrained Gaussian fits to $R(q/p_\mathrm{T})$ distributions, both evaluated in bins of $p_\mathrm{T}^\mathrm{lower}$. The constrained Gauss fits are carried out as explained in Sec. 5.4. To give an example, the $R(q/p_\mathrm{T})$ distributions obtained from MC and from data in the muon p_T bin 200 GeV $\leq p_\mathrm{T}^\mathrm{lower} \leq 350$ GeV are compared in Fig. 5.12. The results for the muon p_T resolution as a function of $p_\mathrm{T}^\mathrm{lower}$ are presented in Fig. 5.13. The RMS of the residuals $R(q/p_\mathrm{T})$ in Fig. 5.13 (left) is sensitive to the tails of the distribution. In the region below $p_\mathrm{T}^\mathrm{lower} \lesssim 350$ GeV, with high event

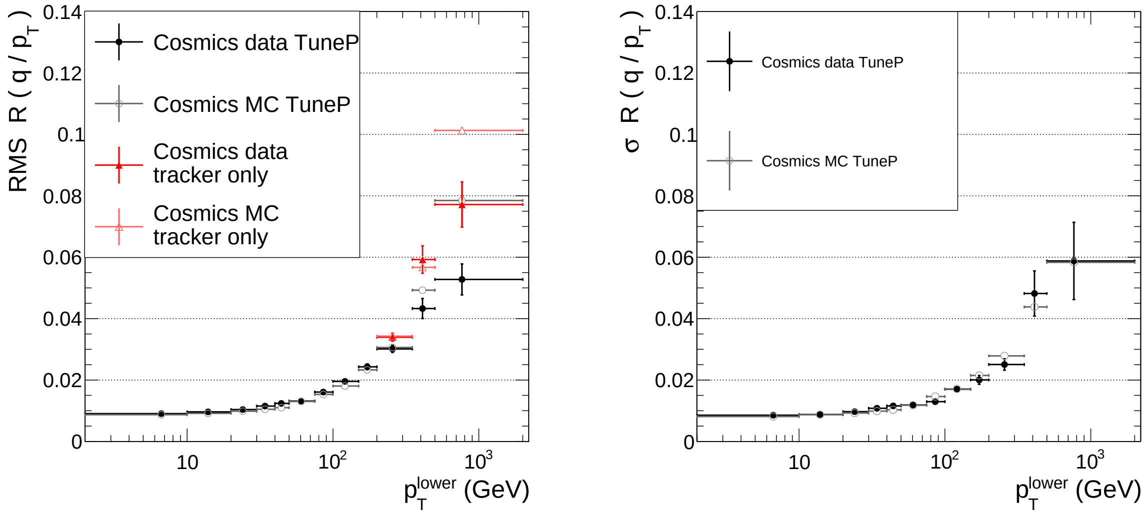

(a) The RMS of the $R(q/p_{\mathrm{T}})$ distribution evaluated in bins of $p_{\mathrm{T}}^{\mathrm{lower}}$. The vertical bars indicate the statistical uncertainty.

(b) The standard deviations obtained from constrained Gaussian fits to the $R(q/p_{\mathrm{T}})$ distribution evaluated in bins of $p_{\mathrm{T}}^{\mathrm{lower}}$. The vertical bars indicate the uncertainty obtained from the fit.

Figure 5.13: Comparison between cosmic ray data and MC for two measures of the resolution in the relative residual $R(q/p_{\mathrm{T}})$ defined in Eqn. 5.9, evaluated in bins of $p_{\mathrm{T}}^{\mathrm{lower}}$. The position of the data points on the abscissa indicates the mean value of the $p_{\mathrm{T}}^{\mathrm{lower}}$ distribution in the bin according to the simulation and the horizontal bars indicate the bin width.

yields observed in data, agreement is observed between data and simulation. For higher muon transverse momenta, data and simulation do not agree within the statistical uncertainty, but the observed RMS values are below the expectation, and there is no indication of unexpectedly large tails. The *Tune P* muon p_{T} assignment is used and in addition the p_{T} of the inner track is shown above $p_{\mathrm{T}}^{\mathrm{lower}} = 200$ GeV. As predicated by the simulation, the tails of the $R(q/p_{\mathrm{T}})$ distribution are wider when the information from the track segments in the muon system is not included at such high transverse momenta. Figure 5.13 (right) shows the standard deviations obtained from constrained Gaussian fits to the $R(q/p_{\mathrm{T}})$ distributions binned in $p_{\mathrm{T}}^{\mathrm{lower}}$. For this measure of the core resolution, agreement between the observation and the simulation is obtained within the uncertainties. The measured resolution ranges from about 1.5% at $p_{\mathrm{T}}^{\mathrm{lower}} = 100$ GeV to about 6% at $p_{\mathrm{T}}^{\mathrm{lower}} = 770$ GeV.

In conclusion, no evidence for an underestimate of the tails of the muon p_{T} resolution in the MC simulation is found in this measurement and the detector simulation reproduces the core resolution observed in data. This supports the modeling of the signal shape from simulated samples described in Sec. 5.4, for which a correct description of the muon p_{T} resolution is essential.

Modelling of narrow eμ resonances in the invariant mass spectrum

In the statistical interpretation of the eμ resonance search that is the subject of Sec. 10.2, the signal shape is approximated by a Gaussian distribution with width σ_{CB} from Eqn. 5.8. The bias introduced by this approximation in the obtained significances and exclusion limits is found to be negligible when using the results obtained with the invariant mass distribution from simulated signal samples as the reference.

Chapter 6

Description of SM background processes

6.1 Backgrounds involving a prompt eμ pair

This chapter serves two purposes: First, basic aspects of the dominant SM background processes that involve prompt eμ pairs are introduced. The background estimates for these processes are obtained from simulated samples. Second, some information is presented about the event generation for the individual background components and the event simulation. The top pair production and W boson pair production are treated in more detail than the other backgrounds because they constitute the most important background contributions and because simulated samples have been produced in the context of this work to extend the background estimate at large values of $M_{\mathrm{e}\mu}$ for these two processes.

The simulated background samples are produced with different event generators, at different accuracy in perturbation theory, utilizing different PDF sets. This information is given in Tabs. C.5, C.6, and C.7 in App. C that list the background samples, including their names in the CMS data aggregation system (DAS) [170]. All utilized background samples use `PYTHIA` (v. 6.426) for showering and hadronization with the underlying event tune Z2* and are processed through a full simulation of the CMS detector based on `GEANT4` (v. 9.4). If not stated otherwise, the background samples have been produced *centrally* by others in the CMS collaboration.

6.1.1 Backgrounds involving top quarks

Parts of this summary are inspired by a review article on top physics studied at the LHC in pp collisions at $\sqrt{s} = 7$ TeV [221].

Top quark pair production

Top quark/antiquark pairs are produced via the strong interaction at the LHC. The diagrams contributing to top pair ($\mathrm{t\bar{t}}$) production in pp collisions at tree level are summarized in Fig. 6.1. For $\sqrt{s} = 8$ TeV, about 80% of the LO $\mathcal{O}(\alpha_S^2)$ cross section stem from the gluon-gluon initiated subprocess and quark-antiquark annihilation accounts for 20%. The LO cross section receives sizeable higher-order corrections that have been calculated up to exact NNLO $\mathcal{O}(\alpha_S^4)$ accuracy in fixed order [222]; additionally soft-gluon resummation is included to NNLL accuracy [222,223]. An evaluation of the $\sqrt{s} = 8$ TeV top pair production cross section with the `Top++` program [224] using the MSTW2008NNLO(68cl) PDF set [125,225] yields fixed order cross sections of 145 pb (LO), 214 pb (NLO), and 239 pb (NNLO) for $m_{\mathrm{t}} = 173.3$ GeV and the renormalization and factorization scale choice $\mu_{\mathrm{ren}} = \mu_{\mathrm{fac}} = m_{\mathrm{t}}$. At NNLO+NNLL accuracy, the result reads [222]

$$\sigma_{\mathrm{t\bar{t}}} = 245.8\ ^{+2.5\%}_{-3.4\%}\ (\mathrm{scales})\ ^{+2.5\%}_{-2.6\%}\ (\mathrm{PDF})\ \mathrm{pb}\ . \tag{6.1}$$

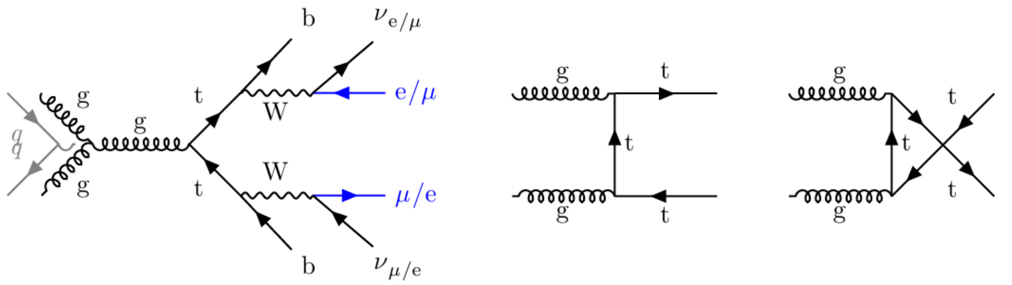

(a) Gluon-gluon fusion (black) and quark-antiquark annihilation (gray) with subsequent decay into a final state containing a prompt eμ pair.

(b) Gluon-gluon production via t-channel exchange.

(c) Gluon-gluon production via u-channel exchange.

Figure 6.1: Leading order diagrams for top pair production in pp collisions.

These numbers do not include electroweak corrections. A brief summary of the electroweak corrections is given in the following, all values are presented as relative corrections to the LO $\mathcal{O}(\alpha_S^2)$ cross section. The QED corrections at NLO including interference terms with QCD amplitudes (mixed QCD-QED corrections $\mathcal{O}(\alpha_S^2\alpha)$) have been studied in Ref. [226] prior to LHC data taking for pp collisions at $\sqrt{s} = 14$ TeV. Their effect on the integrated cross section is small, at the 1% level. A suppression by 5% is found in the tail of the differential cross section $\mathrm{d}\sigma/\mathrm{d}p_\mathrm{T}^\mathrm{t}$ at $p_\mathrm{T}^\mathrm{t} = 2.5$ TeV, but the QED corrections remain at the 1% level when the $\sqrt{\hat{s}}$ dependence of the $\mathrm{t\bar{t}}$ cross section is considered. The non-photonic mixed QCD-weak corrections $\mathcal{O}(\alpha_S^2\alpha)$, calculated for example in Refs. [227, 228] ($\sqrt{s} = 14$ TeV LHC) and Ref. [229] ($\sqrt{s} = 8$ TeV LHC), are larger. Again, the impact on the integrated cross section is just a reduction of about 2% [229] because most $\mathrm{t\bar{t}}$ events are produced close to threshold where the electroweak corrections are small. However, the negative contribution to the cross section by large Sudakov logarithms at high p_T^t and $M_\mathrm{t\bar{t}}$ leads to a sizeable suppression in the tails of the corresponding differential cross sections. For the cross section $\mathrm{d}\sigma/\mathrm{d}p_\mathrm{T}^\mathrm{t}$, the electroweak corrections read -7% at $p_\mathrm{T}^\mathrm{t} = 500$ GeV and -13% at $p_\mathrm{T}^\mathrm{t} = 1$ TeV. The cross section as a function of $M_\mathrm{t\bar{t}}$ receives corrections of -4% at $M_\mathrm{t\bar{t}} = 1$ TeV and -7% at $M_\mathrm{t\bar{t}} = 2$ TeV [229].

In this work, the $\mathrm{t\bar{t}}$ background simulation is not corrected for the mentioned electroweak effects. It is emphasized however that the expected size of the electroweak effects from a few percent on the integrated cross section to the 10% ballpark in the tails of differential distributions is covered comfortably by the uncertainties applied to the $\mathrm{t\bar{t}}$ background estimate, see Sec. 8.1.3.

Top quarks decay almost exclusively into a W boson and a b quark. The reason is twofold: First, the large mass of the top quark leads to a fast weak decay with a lifetime $\tau_\mathrm{t} \approx 5 \times 10^{-25}$ s. This is about one order of magnitude smaller than the timescale of hadronization $1/\Lambda_\mathrm{QCD}$, such that the top quark decays as a bare quark. Second, the CKM matrix element $|V_\mathrm{tb}|$ is close to unity, $|V_\mathrm{tb}|^2 \gg |V_\mathrm{td}|^2$, $|V_\mathrm{ts}|^2$.

Top pair production results in final states with a high-p_T electron and muon primarily via leptonic decays of the two W bosons that carry opposite electric charge, as depicted in Fig. 6.1 (left). A further source of charged leptons are the decays of B hadrons within the b jets from the top quark decays. These result in non-prompt leptons with softer p_T spectra than the prompt leptons from W boson decays.

The simulation of the $\mathrm{t\bar{t}}$ background at NLO in pQCD that is used in this work is based on event generation with the `POWHEG` method. A short description of this approach is in order because it is used for the dominant background contributions obtained from simulated samples ($\mathrm{t\bar{t}}$, WW, single top tW production). The `POWHEG` method [230, 231] is a prescription for the combination of the total rate from a full NLO calculation with the emission of one additional parton at LO by parton showering (PS) programs (NLO+PS approach). To this end, the $\mathcal{O}(\alpha_S)$ contribution from the shower has to be removed from the NLO matrix element. The `POWHEG-BOX` [232] is a software framework that, starting from a NLO cross section calculation as input, provides this subtraction according to the `POWHEG` method. In the following, the term *generated with* `POWHEG` is used to describe the production of parton level events provided in LHE format by the `POWHEG-BOX` that are ready to be processed by parton shower programs in the CMSSW framework. If a version number is provided, it indicates the used version of the `POWHEG-BOX` and if a citation is added, it indicates the publication associated with the implemented NLO cross section calculation.

The $\mathrm{t\bar{t}}$ background samples used in this work are based on event generation with `POWHEG` (v. 1.0) [233] and the CT10 [234] NLO PDF set. The corresponding cross section obtained without applying cuts at parton level is 211 pb in good agreement with the NLO result obtained from `Top++`. Since the full NNLO cross section is however more than 10% larger than that obtained at NLO, it is used for the scaling of the simulated $\mathrm{t\bar{t}}$ background yield to luminosity. Apart from the $\mathrm{t\bar{t}}$ *bulk sample* that does not involve cuts on the final state particles, two background samples with cuts at parton level of 700 GeV $< M_{\mathrm{t\bar{t}}} <$ 1 TeV and $M_{\mathrm{t\bar{t}}} >$ 1 TeV, respectively, are used to enrich the tail of the $M_{\mathrm{t\bar{t}}}$ distribution with simulated events. The samples are combined by applying the corresponding cuts to the generated $\mathrm{t\bar{t}}$ pair and scaling the `POWHEG` cross sections of the $M_{\mathrm{t\bar{t}}}$-binned samples up by the ratio of the full NNLO cross section to the NLO $\mathrm{t\bar{t}}$ cross section. An additional $\mathrm{t\bar{t}}$ background sample is produced in the context of this work in order to improve the number of simulated events at high $M_{\mathrm{e}\mu}$. It uses the settings of the other `POWHEG` $\mathrm{t\bar{t}}$ samples with one exception: the decays of the $\mathrm{W^+W^-}$ pair are forced to result in an $\mathrm{e}^{\pm}\mu^{\mp}$ final state. LHE files with a total of 40 million $\mathrm{t\bar{t}} \to \mathrm{b\bar{b}}\,\mathrm{e}^{\pm}\mu^{\mp}\bar{\nu}\nu$ events are produced and filtered by requiring the cut $M_{\mathrm{e}\mu} >$ 600 GeV. About 35000 events remain and are processed through hadronization and the full detector simulation. The cross section for the scaling of this $\mathrm{t\bar{t}}$ high-mass *tail sample* is 5 fb. The tail sample is matched to the other $\mathrm{t\bar{t}}$ samples by removing events with $M_{\mathrm{e}\mu} >$ 600 GeV at generator level from the latter. The reduction in the statistical uncertainty of the background expectation at high $M_{\mathrm{e}\mu}$ is visible in Fig. 6.2. From $M_{\mathrm{e}\mu} =$ 100 GeV to $M_{\mathrm{e}\mu} =$ 1 TeV, the differential cross section $\mathrm{d}\sigma_{\mathrm{t\bar{t}}}/\mathrm{d}M_{\mathrm{e}\mu}$ drops by almost five orders of magnitude.

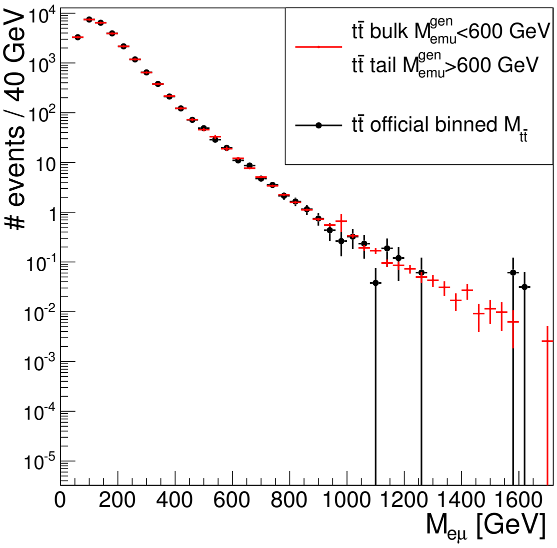

Figure 6.2: Comparison of the $M_{\mathrm{e}\mu}$ *spectra of reconstructed* eμ *pairs after the event selection that have been obtained from the* $t\bar{t}$ *bulk sample only (black) and from the combination of all* $t\bar{t}$ *background samples (red). The distributions are scaled to an integrated luminosity of* 19.7 fb^{-1}. *The vertical bars on the data points represent the statistical uncertainty.*

The p_{T} and η distributions of prompt muons from W boson decays in $\mathrm{t\bar{t}}$ events are shown in Fig. 6.3 for an inclusive $\mathrm{t\bar{t}}$ sample and the tail sample with its cut on $M_{\mathrm{e}\mu}$. The prompt leptons in $\mathrm{t\bar{t}}$ events are typically produced centrally in the detector and the η distribution peaks

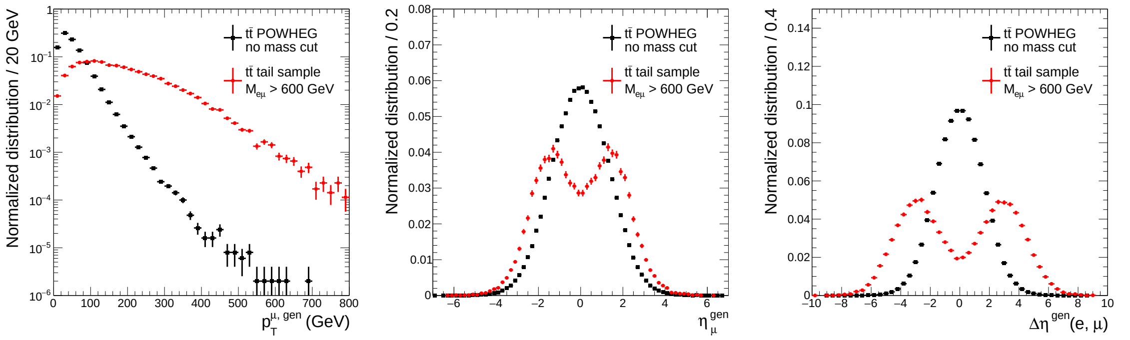

(a) The p_{T}^{μ} distribution.

(b) The η^{μ} distribution.

(c) The pseudorapidity difference $\Delta\eta(e, \mu)$.

Figure 6.3: Normalized distributions of kinematic variables of leptons in generated $t\bar{t}$ events without p_{T} and η cuts applied to the leptons at parton level. The inclusive sample is shown in black and the tail sample with a cut of $M_{e\mu} > 600$ GeV is shown in red.

at zero. When requiring high $M_{e\mu}$, more leptons are produced in the forward direction and the η distribution develops two maxima while the region around $\eta = 0$ is depleted. The mass cut enhances decay topologies in which the two lepton momenta exhibit a back-to-back orientation, resulting in a growing pseudorapidity gap as shown in Fig. 6.3 (right). The efficiency of the pseudorapidity cuts on the leptons thus decreases with increasing eμ mass. This behaviour is opposite to that observed for signal events for which the η distributions become more central with increasing signal mass and corresponding higher $M_{e\mu}$. The lepton p_{T} spectrum from $\mathrm{t\bar{t}}$ events (Fig. 6.3 (left)) is much harder after the $M_{e\mu}$ cut is applied and its maximum is shifted from about 30 GeV to above 100 GeV, well above the cuts on the transverse momenta of the leptons.

Single-top production

The production of single top quarks proceeds via the electroweak interaction and the vertex Wtb with CKM matrix element V_{tb}. The amplitudes contributing to single top production can be sorted into three different production channels, the $t-$, $s-$, and tW$-$channels. While the $t-$channel exchange comes with the largest cross section at the LHC (56 pb for t and 31 pb for $\bar{\mathrm{t}}$ production [235]), the focus is put on the tW channel in the following because it is the most relevant for the eμ analysis. In the *massless* or *5-flavour scheme*, in which the b and $\bar{\mathrm{b}}$ quarks in the initial state are treated as originating from the proton sea, the LO $\mathcal{O}(\alpha\alpha_S)$ contributions to the cross section of tW production are represented by the Feynman diagrams in Fig. 6.4, that also include the decays of the W bosons that lead to the final state of interest.

Due to the $\mathrm{b(\bar{b})g}$ initial state, the cross sections for $\mathrm{tW^-}$ and $\mathrm{\bar{t}W^+}$ in pp collisions are the same and for $\sqrt{s} = 8$ TeV they read at NLO+NNLL accuracy in pQCD [235]:

$$\sigma_{\mathrm{tW^-}} = \sigma_{\mathrm{\bar{t}W^+}} = 11.1 \pm 0.3 \text{ (scales)} \pm 0.7 \text{ (PDF) pb} , \tag{6.2}$$

for $m_{\mathrm{t}} = 173$ GeV. The single top tW process can lead to a prompt eμ pair in the final state when both W bosons decay leptonically as depicted in Fig. 6.4.

The simulated background samples for $\mathrm{tW^-}$ and $\mathrm{\bar{t}W^+}$ production are based on events generated with `POWHEG` (v. 1.0) [236] at NLO in pQCD using the CTEQ6M [58] PDF set. Next-to-leading order real corrections to single-top $\mathrm{tW^-}$ production $\mathcal{O}(\alpha\alpha_S^2)$ interfere with $\mathrm{t\bar{t}}$ production at LO with subsequent decay of the top antiquark [237]. Therefore, a separation of the two processes (here: into two background samples) at NLO accuracy is non-trivial. Two schemes to remove contributions in the NLO calculation of the tW process have been developed [238] and both are

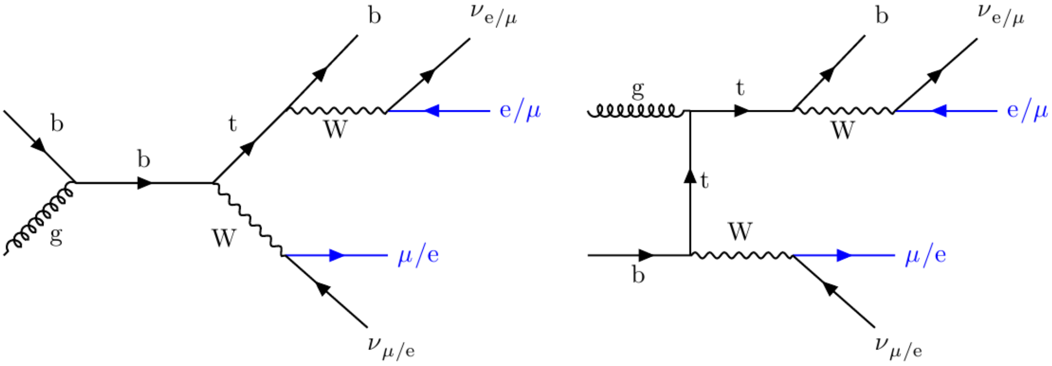

(a) Fermion in s-channel. (b) Fermion in t-channel.

Figure 6.4: Leading order diagrams for single-top tW production and subsequent decay into a final state containing a prompt eμ pair.

implemented in `POWHEG` [236]. In the *diagram removal* (DR) scheme, all *doubly-resonant* diagrams are excluded from the amplitude, whereas $\mathrm{t\bar{t}}$ contributions are removed at the cross section level in the *diagram subtraction* (DS) scheme. The tW background samples used in this analysis employ the DR scheme. Only events with leptonic decays of the two W bosons in the final state are produced. The resulting cross section for the $\mathrm{tW^- \to W^+W^-\,b} \to \ell^+\nu_\ell\,\ell'^-\bar{\nu}_{\ell'}\,\mathrm{b}$ sample reads 1.12 pb, in $\mathcal{O}(5\%)$ agreement with the resummed cross section (Eqn. 6.2) after correcting for the branching fraction of the fully leptonic process (1.12 pb / $[9 \times \mathcal{B}(\mathrm{W^-} \to \ell^-\bar{\nu})^2]$). For comparison, the cross section in the DS scheme calculated using the `POWHEG` implementation is 1.08 pb.

6.1.2 Pair production of pairs of massive gauge bosons

W boson pair production

A $\mathrm{W^+W^-}$ pair can be produced in pp collisions at leading order in perturbation theory $\mathcal{O}(\alpha^2)$ via quark/antiquark initial states. The tree LO Feynman diagrams for $q\bar{q} \to WW$ production at the LHC are depicted in Fig. 6.5. Beyond LO in pQCD, the definition of the WW cross section is complicated by the interference with single-top tW production (at NLO $\mathcal{O}(\alpha^2\alpha_S)$) and, more importantly, $\mathrm{t\bar{t}}$ production (at NNLO $\mathcal{O}(\alpha^2\alpha_S^2)$). The methods to overcome these conceptual challenges are discussed for example in Ref. [239]. Calculations of the full NNLO QCD corrections to the WW cross section have become available after the end of Run 1 of the LHC [239, 240].

In this work, the cross section is treated at NLO accuracy in pQCD, such that the sizeable increase from LO to NLO of more than 30% [239] is covered. The only included contribution beyond $\mathcal{O}(\alpha^2\alpha_S)$ is the gluon-gluon production channel that arises from the loop-induced diagram depicted in Fig. 6.6 (left). As a $\mathcal{O}(\alpha^2\alpha_S^2)$ process it is part of the NNLO calculation but it had already been studied as a separate contribution to the WW cross section [241, 242] before full NNLO results became available. The gluon box contribution adds about 3% to the NLO cross section. Gluon-induced W pair production is included in the cross section calculation with `MCFM` (v. 6.6) [242–244] that is used for the scaling of the simulated background sample. The `MCFM` cross section at NLO+gg accuracy for WW production reads [245]:

$$\begin{aligned} \sigma_{\mathrm{W^+W^-} \to\, \mu^+\mathrm{e}^-\nu_\mu\bar{\nu}_\mathrm{e}} &= 0.65 \pm 0.02 \text{ (scales)} \pm 0.03 \text{ (PDF) pb} \\ \sigma_{\mathrm{WW}} &= 54.9 \pm 2.0 \text{ (scales)} \pm 2.3 \text{ (PDF) pb}\,, \end{aligned} \tag{6.3}$$

where the integrated cross section value has been obtained by a simple rescaling with the leptonic decay branching fraction of the W boson. The result in Eqn. 6.3 agrees with the NLO+gg result in Ref. [239] at the 1% level. It is noteworthy that the genuine NNLO corrections exceed the gg box contribution by almost a factor two as pointed out in Ref. [239]. According to this reference, the

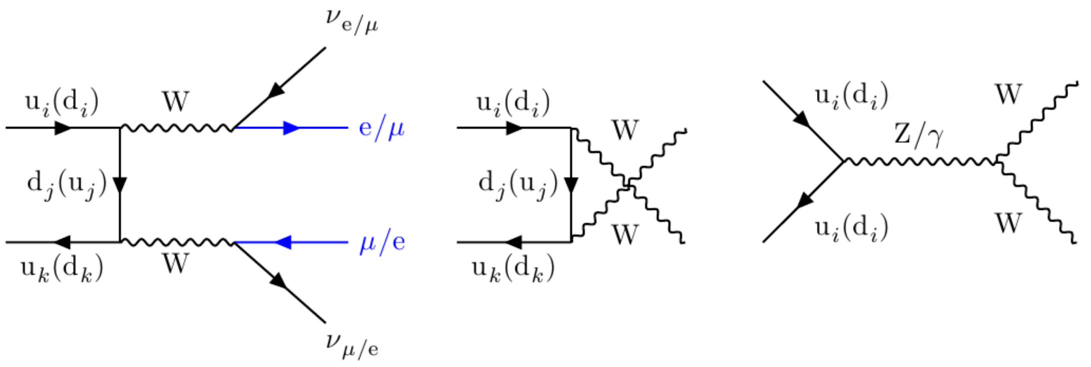

(a) T-channel diagram. (b) U-channel diagram. (c) S-channel diagram.

Figure 6.5: The tree level diagrams for the process $q\bar{q} \rightarrow WW$*.*

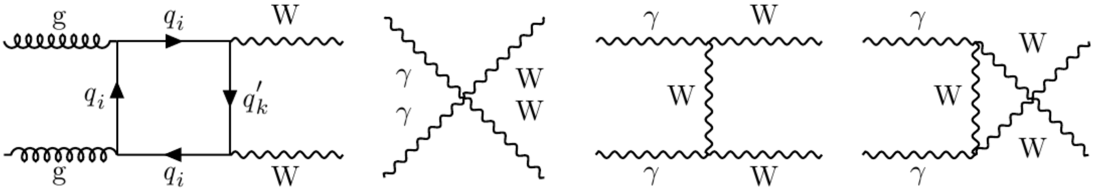

(a) Digluon box. (b) $\gamma\gamma$ fusion. (c) $\gamma\gamma$ t-channel. (d) $\gamma\gamma$ u-channel.

Figure 6.6: The box diagram for the processes $gg \rightarrow WW$ *and the LO diagrams for the process* $\gamma\gamma \rightarrow WW$*.*

additional correction to the NLO+gg result when taking into account the full NNLO corrections is about +5%. This additional increase in the integrated WW cross section is not accounted for in this work but it is covered within the systematic uncertainties in the WW cross section that are discussed in Sec. 8.1.4.

Electroweak corrections to the WW cross section are available at NLO $\mathcal{O}(\alpha)$ [246, 247] and change the integrated LO cross section at the per cent level. Their impact on differential cross sections grows towards larger values of $p_{\mathrm{T}}^{\mathrm{W}}$ and M_{WW}. At $M_{\mathrm{WW}} \sim 1$ TeV, the EWK corrections decrease the cross section by about 15% in pp collisions at $\sqrt{s} = 8$ TeV. A sizeable fraction of this reduction in the differential cross section $\mathrm{d}\sigma_{\mathrm{WW}}/\mathrm{d}M_{\mathrm{WW}}$ is compensated by the photon-photon induced W boson pair production depicted in Fig. 6.6 and by the photon-quark induced processes that add to the cross section [246, 247]. In this analysis, it is assumed that the total effect of higher-order EWK contributions to the differential WW cross section $d\sigma_{WW}/dM_{\mathrm{e}\mu}$ does not exceed the 10% level at $M_{\mathrm{e}\mu} \sim 1$ TeV and is thus covered within the assigned uncertainties discussed in Sec. 8.1.4.

In accord with the simulation of the $\mathrm{t\bar{t}}$ and tW backgrounds, the event generation for the WW background is carried out with `POWHEG` (v. 1.0) [248] using the CT10 PDF set. The implemented calculation does not include the gg box contribution. Only the leptonic decays of the two W bosons have been simulated. The `POWHEG` cross section reads $\sigma_{\mathrm{WW}} = 51$ pb when corrected for the branching fractions. For the normalization of the WW samples, an additional k-factor of 1.07 is applied in order to reproduce the cross section calculated with `MCFM`.

As in the case of the $\mathrm{t\bar{t}}$ background, a high-mass sample with a cut of $M_{\mathrm{e}\mu} > 600$ GeV has been produced for the WW background in the context of this work. It uses the same settings in `POWHEG` as in the case of the bulk sample and consists of 52000 $\mathrm{W^+W^-} \rightarrow \mu^{\pm}\mathrm{e}^{\mp}\nu\bar{\nu}$ events after applying the high-mass filter on the LHE events. These events are processed through hadronization and the full detector simulation. The resulting $M_{e\mu}$ distribution at parton level without acceptance cuts on the leptons is compared to that of the bulk sample in Fig. 6.7. The differential cross section $\mathrm{d}\sigma_W W/\mathrm{d}M_{e\mu}$ falls by a factor 5×10^{-4} between $M_{e\mu} = 100$ GeV and $M_{e\mu} = 1$ TeV. It thus falls off slower than the $\mathrm{t\bar{t}}$ background.

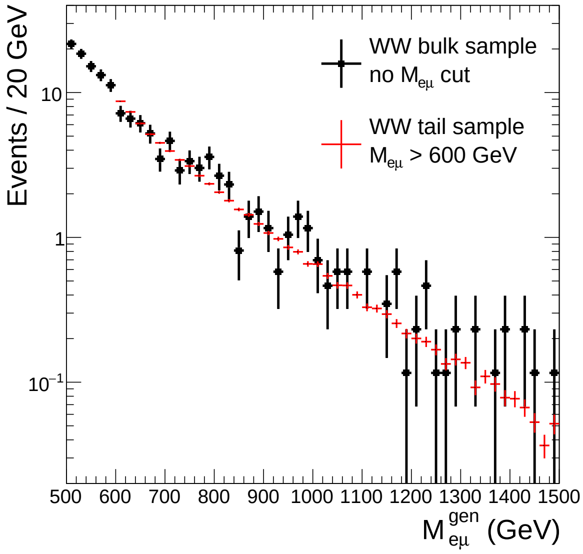

Figure 6.7: Comparison of the $M_{e\mu}$ spectra of generated eμ pairs in the W W bulk sample only (black) and from the tail sample with the mass cut $M_{e\mu} > 600$ GeV (red). The distributions are scaled to an integrated luminosity of 19.7 fb^{-1}. The vertical bars on the data points represent the statistical uncertainty.

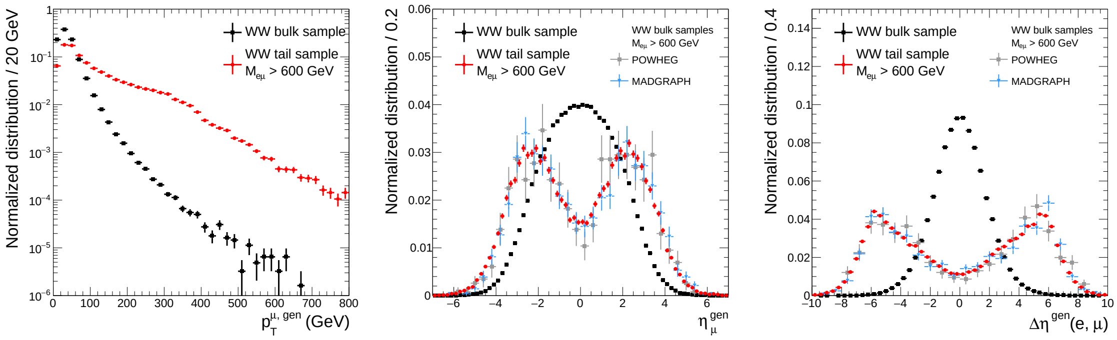

(a) The p_T^{μ} distribution.

(b) The η^{μ} distribution.

(c) The pseudorapidity difference $\Delta\eta(e, \mu)$ distribution.

Figure 6.8: Normalized distributions of kinematic variables of leptons in generated W W events without p_T and η cuts on the leptons at parton level. The inclusive sample is shown in black and the tail sample with a cut of $M_{e\mu} > 600$ GeV is shown in red. The W W tail sample is compared to the events from the W W bulk samples produced with `POWHEG` *and* `MadGraph` *that involve eμ pairs with an eμ mass above 600 GeV.*

The evolution of basic kinematical quantities of the charged leptons in the process $\mathrm{W^+W^-} \to \mu^{\pm}\mathrm{e}^{\mp}\nu\bar{\nu}$ with increasing $M_{e\mu}$ is sketched in Fig. 6.8. Similar to what is observed for the $\mathrm{t\bar{t}}$ process, a cut of $M_{e\mu} > 600$ GeV results in increased forward production of the leptons. The pseudorapidity gap between the two leptons is more pronounced than in the case of $\mathrm{t\bar{t}}$

production, owing to the importance of the t-channel exchange depicted in Fig. 6.5 (left). The shape of the muon η distribution for WW events with $M_{\mathrm{e}\mu} > 600$ GeV obtained with `POWHEG` is confirmed when utilizing the `MadGraph` generator instead, as shown in Fig. 6.8 (middle, right). The enhanced forward production of the leptons for high $M_{\mathrm{e}\mu}$ is also reflected in the muon p_{T} spectrum in Fig. 6.8 (left); although the spectrum is much harder with the mass cut applied, the position of its maximum is only shifted from about 30 GeV to 40 GeV.

WZ and ZZ diboson production

The production of WZ and ZZ pairs is less important than the WW process in the eμ resonance search. One reason is the factor three between the branching fractions of the leptonic decays of the W and Z bosons. An evaluation of the cross section for the process $\mathrm{pp} \to \mathrm{W}^{\pm}(\mathrm{W}^{\pm} \to \ell_i^{\pm}\nu) \;+\; \mathrm{Z}/\gamma^*(\mathrm{Z}/\gamma^* \to \ell_j^+\ell_j^-)$ with `MCFM` (v. 6.6) yields 1.1 pb for $M_{\ell_j\ell_j}$ above 12 GeV. This is more than a factor five smaller than the cross section for WW production with subsequent leptonic decays of the W boson. The cross section for Z pair production with a final state involving four charged leptons is about 0.2 pb.

The simulation of the WZ and ZZ backgrounds starts from the `MadGraph` (v. 5.1.3.30) generator and includes a cut on the mass of the dilepton pairs from the Z/γ^* legs of 12 GeV.

6.2 Backgrounds involving misidentified or non-prompt leptons

6.2.1 Drell-Yan production of a charged lepton pair

The prompt production of opposite-sign, same-flavour lepton pairs via the Drell-Yan (DY) process $\mathrm{pp} \to \mathrm{Z}/\gamma^* \to \ell^+\ell^-$ leads to final states with a high-p_{T} electron and muon mainly through the production of a $\tau\tau$ pair with subsequent leptonic τ decays; one τ lepton provides a non-prompt electron and the other τ provides a non-prompt muon. This process is referred to as $\tau_{\mathrm{e}}\tau_{\mu}$ production in the following. Apart from $\tau_{\mathrm{e}}\tau_{\mu}$ production, Drell-Yan dielectron and dimuon final states that include an additional hard jet can result in an eμ pair; this is the case if the jet contains a lepton from hadron decays or if it is misreconstructed as a lepton.

The Drell-Yan background is obtained from a simulated sample using the `MadGraph` (v. 5.1.3.30) generator with a dilepton mass cut of 50 GeV. The emission of additional hard jets (that may be misidentified as leptons) is included in the event generation at LO up to $N_{\mathrm{jets}} = 4$. The cross section used for the scaling of the DY background sample to luminosity is obtained from `FEWZ` (v. 3.1) [249, 250] at NNLO accuracy in pQCD and reads [245]:

$$\sigma(\mathrm{pp} \to \mathrm{Z}/\gamma^* \to \ell^+\ell^-) = 3530\,^{+18}_{-11}\ (\mathrm{scales}) \pm 120\ (\mathrm{PDF})\ \mathrm{pb} \quad \text{for} \quad M_{\ell^+\ell^-} > 50\ \mathrm{GeV}\ . \tag{6.4}$$

6.2.2 Wγ diboson production

The production of a W boson in association with a high-p_{T} photon can result in a reconstructed eμ pair that passes the event selection. The dominant mechanisms are photon conversion and the misidentification of the hard photon as an electron by accidentally matching its ECAL supercluster with a track of a charged hadron in the inner silicon detector while the W boson decay yields a prompt muon. This subleading background is obtained from simulated samples that utilize the `MadGraph` (v. 5.1.3.30) generator. Three samples are produced for different bins of the generated photon p_{T}, starting from $p_{\mathrm{T}}^{\gamma} > 30$ GeV, the pseudorapidity of the generated photon is restricted to $|\eta| < 3.5$, and the momenta of the charged lepton and hard photon in the final state have to be separated by $\Delta R(\ell,\gamma) > 0.5$. The cross section provided by `MadGraph` + `PYTHIA` for the process $\mathrm{pp} \to \mathrm{W}^{\pm}(\mathrm{W}^{\pm} \to \ell_i^{\pm}\nu) \;+\; \gamma$ with these cuts on the photon reads 24 pb after correcting for the efficiency of the matching of matrix element and shower contributions. This falls between the cross sections at LO and NLO accuracy in pQCD obtained from `MCFM` (v. 6.6) of 19 pb and 30 pb, respectively.

6.2.3 W + jet and QCD multijet backgrounds

The background contribution from W + jet and QCD multijet production is derived from data. In order to pass the event selection of the eμ search, both processes require that at least one of the high-p_T leptons in the eμ final state is produced by a jet. The two main mechanisms relevant in the following are the misidentification of a jet as an electron (a fake electron, for example from π^0/charged hadron overlap) and the production of (isolated) leptons within jets, particularly from heavy-flavour hadron decays and photon conversions. For simplicity, both of these mechanisms of non-prompt lepton production are bundled under the term *jet-to-lepton misidentification*.

As will be shown below, W + jet production dominates QCD multijet production when the eμ selection is applied, although the W production cross section is much smaller than that for dijet production. The reason is that leptonic decays of the W boson yield one high-p_T prompt lepton and only its partner in the selected dilepton pair has to arise from a jet. The magnitude of the muon p_T and electron E_T cuts of 45 GeV and 35 GeV, respectively, is relevant in this context because the cross section for dijet production that involves isolated leptons decreases steeply as the transverse momentum cuts on the leptons are tightened.

Monte Carlo samples for the W + jet and QCD multijet processes are used to study the production of an eμ pair at generator level and to provide a point of reference for the results of the data-driven approach. W + jet production is simulated with `MadGraph` at LO accuracy in pQCD with up to 4 additional jets. Four samples covering different ranges of W boson transverse momentum are employed. The subleading QCD multijet background sample is obtained from `PYTHIA` (v. 6.426) with the requirement that one muon with p_T above 15 GeV be present in the events. Details are given in Tab. C.7 in App. C. According to these simulations, the most important subprocess for the production of an eμ pair with jet misidentification is pp $\rightarrow$ W+jet $\rightarrow$ $\mu\nu$+jet(e), where the isolated electron arises from the jet; among the simulated W events that lead to an eμ pair, about 85% involve a prompt muon from the W decay, with the remaining 15% shared equally between the leptonic decay modes with electrons and τ leptons. Therefore, the data-driven method explained in the following is based on a measured jet-to-electron misidentification rate.

Jet-to-electron misidentification rate

The jet-to-(HEEP)electron misidentification rate has not been measured by the author of this work but by others in the context of Ref. [192]. The following is a short summary of how it is obtained. Further details can be found in Ref. [251].

The sample from which the jet-to-electron misidentification rate is obtained is based on prescaled single-photon triggers that require a cluster in the ECAL with different E_T requirements (corresponding to different prescales) at the HLT level ranging from 30 GeV to 150 GeV. Events are reweighted by the prescale of the fired trigger with the lowest prescale. Events in the sample are required to contain electron candidates that fulfill a reduced set of identification criteria that are less strict than those imposed in the HEEP electron identification. This *loose* electron selection starts from an ECAL cluster and a corresponding ECAL-seeded GSF track. A minimum E_T of the supercluster of 35 GeV is required as in the case of the HEEP electron selection and the same definition is used for the electron pseudorapidity and the separation into barrel and endcap electrons for both selections. The identification criteria of the loose electron selection differ in the barrel and endcap regions of the ECAL and are summarized in Tab. 6.1.

The sample obtained after the selection of a loose electron candidate contains mainly events with a jet that passes the loose selection rather than a real electron or photon. The fraction of such events that also pass the HEEP electron selection is the sought-after jet-to-electron misidentification rate (MR). Contaminations of the jet sample arising from real electrons and photons have to be subtracted. Otherwise, they would bias the MR measurement towards higher values. The contamination of Drell-Yan dielectron production is reduced by removing events with an additional electron with $E_\mathrm{T} > 10$ GeV. The contribution from other processes with real electrons and photons, that is dominated by W + jet (W $\rightarrow$ eν) and γ + jet production, are removed by a

Table 6.1: The identification criteria for loose electron candidates.

Electron identification variable	Cut value Barrel	 Endcap
$\sigma_{i\eta i\eta}$	< 0.013	< 0.034
H/E	< 0.15	< 0.10
Number of missing hits	≤ 1	≤ 1
$\lvert\mathrm{d}_{xy}\rvert$	< 0.02 cm	< 0.05 cm

subtraction based on simulations. After this cleaning, the MR is given by the ratio of the number of electron candidates passing the HEEP selection and the number of electrons passing the loose selection in the sample. It is evaluated separately in the barrel and endcap regions of the ECAL for different (loose) electron E_{T} ranges as shown in Tab. 6.2. An uncertainty of 30% is assigned to these values.

Table 6.2: The parameterization of the jet-to-electron misidentification rate derived in the context of Ref. [192] and documented in Ref. [251].

ECAL region	$E_{\mathrm{T}}^{\mathrm{e}}$ range	Misidentification rate (%) Functional form
Barrel $\lvert\eta^{\mathrm{e}}\rvert < 1.442$	$35 \leq E_{\mathrm{T}}^{\mathrm{e}}$ / GeV ≤ 98	$2.3 - 1.5 \times 10^{-2} \times (E_{\mathrm{T}}^{\mathrm{e}}$ / GeV$)$
	$98 < E_{\mathrm{T}}^{\mathrm{e}}$ / GeV ≤ 192	$1.2 - 4.0 \times 10^{-3} \times (E_{\mathrm{T}}^{\mathrm{e}}$ / GeV$)$
	$E_{\mathrm{T}}^{\mathrm{e}}$ / GeV > 192	0.38
Endcap $1.56 < \lvert\eta^{\mathrm{e}}\rvert < 2.5$	$35 \leq E_{\mathrm{T}}^{\mathrm{e}}$ / GeV ≤ 90	$8.2 - 5.2 \times 10^{-2} \times (E_{\mathrm{T}}^{\mathrm{e}}$ / GeV$) + (\lvert\eta^{\mathrm{e}}\rvert - 1.9) \times 6.5$
	$90 < E_{\mathrm{T}}^{\mathrm{e}}$ / GeV ≤ 166	$4.0 - 5.5 \times 10^{-3} \times (E_{\mathrm{T}}^{\mathrm{e}}$ / GeV$) + (\lvert\eta^{\mathrm{e}}\rvert - 1.9) \times 6.5$
	$E_{\mathrm{T}}^{\mathrm{e}}$ / GeV > 166	$2.9 + 1.3 \times 10^{-3} \times (E_{\mathrm{T}}^{\mathrm{e}}$ / GeV$) + (\lvert\eta^{\mathrm{e}}\rvert - 1.9) \times 6.5$

The misidentification rate in the barrel is approximately independent of η^{e} and falls from 1.8% at $E_{\mathrm{T}}^{\mathrm{e}} = 35$ GeV to a constant value below five per mille for $E_{\mathrm{T}}^{\mathrm{e}} \gtrsim 200$ GeV. In the endcaps, where the cuts of the loose electron selection are different, the misidentification rate is larger than in the barrel and exhibits a non-negligible η^{e} dependence. For electrons with $E_{\mathrm{T}}^{\mathrm{e}} \sim 500$ GeV that fall into the very forward region ($\lvert\eta^{\mathrm{e}}\rvert > 2.2$), the misidentification rate amounts to more than five per cent.

Application of the misidentification rate

The jet-to-electron misidentification rate is applied to the sample of events selected in data that satisfy the following selection criteria:

- The event passes the single-muon trigger and the muon selection criteria required in the baseline eμ event selection. It is required to contain exactly one muon.
- The event contains exactly one loose electron candidate as defined in the measurement of the misidentification rate.
- The event contains no HEEP electron. This means that the selected sample of events and that defined by the baseline eμ selection cuts are mutually exclusive.
- The event contains no b-tagged PF jet with $p_{\mathrm{T}}^{\mathrm{jet}} > 35$ GeV and $|\eta^{\mathrm{jet}}| < 2.5$ that is separated from the two lepton candidates by $\Delta R > 0.5$.

This set of selection criteria is referred to as the *muon+loose electron* selection or *loose* selection in the following. The veto against additional b-tagged jets that are separated from the selected leptons is applied in order to reduce the contribution from $\mathrm{t\bar{t}}$ events. According to the simulation, the impact of this cut on the background estimate for the W + jet and QCD multijet processes is negligible; less than 3% of such events are rejected by the veto. Importantly, the selection of a loose electron and veto against HEEP electrons renders this selection very inefficient when considering the signals in the eμ resonance search, such that a possible signal contamination to the resulting background estimate would be negligible.

The distributions of the transverse energy and pseudorapidity of the loose electron candidate in events passing this selection are compared to the simulation in Fig. 6.9. The simulated samples are normalized to luminosity using the cross sections reported in App. C, Tabs. C.5-C.7. Agreement between observation and expectation is observed for both kinematic variables. A total of 90562 events are selected in data and 89300 ± 1000 (stat) are expected. According to the simulation, the composition of the sample by individual SM process reads: 63% W + jet, 15% QCD multijet, 13% Drell-Yan, and 5% $\mathrm{t\bar{t}}$, with the remaining 4% shared among other processes. The dominant W+jet contribution is split in Fig. 6.9 into four subsamples that correspond to different $p_{\mathrm{T}}^{\mathrm{W}}$ ranges. Among them, the subsample of events with $p_{\mathrm{T}}^{\mathrm{W}} > 100$ GeV yields the largest contribution, although the differential cross section for W production at the LHC $\mathrm{d}\sigma_W/\mathrm{d}p_{\mathrm{T}}^{\mathrm{W}}$ drops steeply from a maximum at $p_{\mathrm{T}}^{\mathrm{W}} \approx 5$ GeV. The enhancement of events with high $p_{\mathrm{T}}^{\mathrm{W}}$ is explained by the additional high-p_{T} jet needed to yield the loose electron candidate with $E_{\mathrm{T}}^{\mathrm{e}} \geq 35$ GeV that recoils against the transverse momentum of the W boson.

In order to separate the contributions from W + jet production and QCD multijet production, it is instructive to turn to the transverse mass distribution of the selected muon and $\not\!\!E_{\mathrm{T}}$. The transverse mass M_{T} of the two objects is defined as:

$$M_{\mathrm{T}}(\mu, \not\!\!E_{\mathrm{T}}) = \sqrt{p_{\mathrm{T}}^{\mu}\ \not\!\!E_{\mathrm{T}}\,(1 - \cos(\Delta\phi(\mu, \not\!\!E_{\mathrm{T}})))}\ . \tag{6.5}$$

Its distribution in events passing the muon+loose electron selection is depicted in Fig. 6.10. While the QCD multijet contribution peaks at very low M_{T}, the W + jet process exhibits a Jacobian peak at $M_{\mathrm{T}} \approx M_{\mathrm{W}}$. This structure is found in data and reproduced well by the simulation.

After this successful cross check of the sample's composition, the sample is corrected for the presence of contributions from other processes than the sought-after W + jet and QCD multijet processes. This is not achieved by a subtraction of the corresponding histograms because of unwanted effects from the low number of simulated events in the tails of distributions, such as negative event yields in some bins. Instead, the simulated $E_{\mathrm{T}}^{\mathrm{e}}$ distribution (Fig. 6.9 (left)) is divided into bins of variable size. For each bin, the fraction of W + jet and QCD multijet events $N_{\mathrm{W+QCD}}^{\mathrm{bin}}/N_{\mathrm{tot}}^{\mathrm{bin}}$ is determined. The selected data events are then reweighted by using this ratio as an event weight. Within the statistical uncertainties in the ratios that range from 3% for the

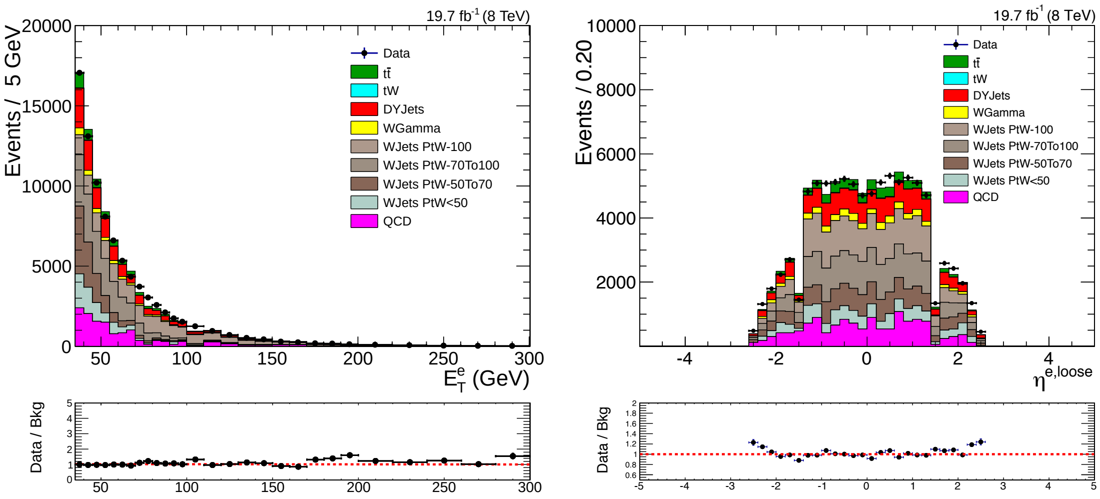

(a) The E_T^e distribution. (b) The η^e distribution.

Figure 6.9: Kinematics of the loose electron candidate in events passing the loose selection including the veto against b-tagged jets. The data is compared to the expectation obtained from simulated samples. The dominant W + jet contribution is split into four samples corresponding to different p_T^W ranges.

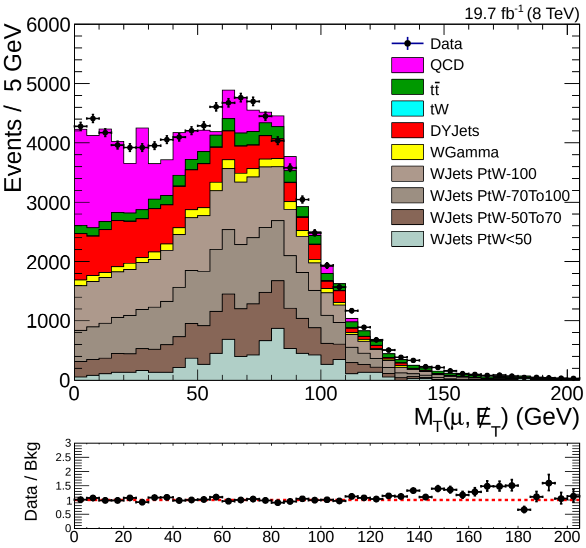

Figure 6.10: The distribution of the transverse mass between the muon and $\not{E}_\mathrm{T}$, $M_\mathrm{T}(\mu, \not{E}_\mathrm{T})$ in events passing the loose selection including the veto against b-tagged jets. The vertical bars in both the upper and lower plots represent the statistical uncertainties in the event yields.

bin 35 GeV $\leq E_\mathrm{T}^\mathrm{e} \leq$ 40 GeV to 15% for the highest-E_T^e bin 260 GeV $\leq E_\mathrm{T}^\mathrm{e} \leq$ 340 GeV, the event weights show no significant dependence on the electron candidate's E_T. The average weight is 78%. The ratio $N_\mathrm{W+QCD}/N_\mathrm{tot}$ is extrapolated beyond $E_\mathrm{T}^\mathrm{e} = 340$ GeV, where the simulation runs out of events. This event-by-event correction based on the electron E_T is applied for the W + jet and QCD multijet estimate in all distributions shown in the following, except for the crucial $M_{\mathrm{e}\mu}$ distribution; there the same approach is used but the event weights are determined as a function of $M_{\mathrm{e}\mu}$.

The final step towards the data-driven estimate of the sum of the W + jet and QCD multijet contributions is the application of the misidentification rate. It is carried out by applying another event weight w_{MR} to the data events passing the muon+loose electron selection as a function of electron E_{T} and η. The event weight is defined as

$$w_{\mathrm{MR}}(E_{\mathrm{T}}^{\mathrm{e}}, \eta^{\mathrm{e}}) = \frac{\mathrm{MR}(E_{\mathrm{T}}^{\mathrm{e}}, \eta^{\mathrm{e}})}{1 - \mathrm{MR}(E_{\mathrm{T}}^{\mathrm{e}}, \eta^{\mathrm{e}})} , \tag{6.6}$$

where $\mathrm{MR}(E_{\mathrm{T}}^{\mathrm{e}}, \eta^{\mathrm{e}})$ denotes the misidentification rate shown in Tab. 6.2. The denominator in Eqn. 6.6 takes into account that a fraction MR of the W +jet and QCD multijet events under study does not pass the loose selection but the *tight, signal-like* eμ event selection. Further corrections to this formula, that arise because the HEEP electron identification efficiency is smaller than unity, are not applied. Their effect on the resulting background yield is estimated to be 3% to 5% and therefore much smaller than that of a variation of the misidentification rate within its uncertainty of 30%.

Data-driven W + jet and QCD multijet background estimate

The $M_{\mathrm{e}\mu}$ distribution of the data-driven W +jet and QCD multijet background estimate is shown in Fig. 6.11. A total of 1570 ± 470 (syst) events is obtained compared to an event yield of 1000 ± 170 (stat) from simulated samples. The statistical uncertainty in the data-driven background estimate is small (about 3 per mille on the total yield) due to the large number of events passing the loose selection to which the misidentification rate is applied. For the same reason, the background prediction extends to masses of the eμ pair in the 1 TeV range.

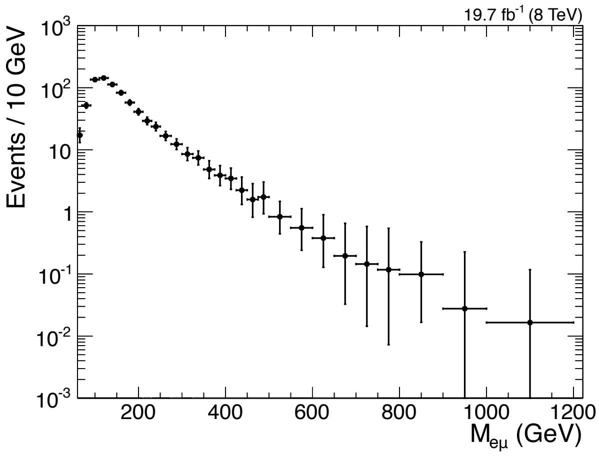

Figure 6.11: The $M_{e\mu}$ distribution of the data-driven estimate for W + jet and QCD multijet background events passing the full eμ event selection. The vertical bars represent the statistical uncertainty.

The eμ events from W + jet and QCD multijet production feature a higher ratio of same-charge ($\mathrm{e}^{\pm}\mu^{\pm}$) to opposite charge ($\mathrm{e}^{\pm}\mu^{\mp}$) dilepton pairs than the overall dominant backgrounds that involve a pair of a prompt electron and prompt muon from leptonic decays of a $\mathrm{W}^{+}\mathrm{W}^{-}$ pair. The comparison of the $M_{\mathrm{e}\mu}$ spectrum of same-charge eμ pairs in data and the background expectation is therefore used as a cross-check of the W + jet and QCD multijet background estimate. It is presented in Sec. 9.

Chapter 7

Events passing the eμ event selection

In this chapter, the level of agreement between observed events that pass the eμ event selection and the background expectation is discussed. It is structured as follows: First, corrections applied to the simulated background samples are introduced in Sec. 7.1. The total event yield and the expected background composition are presented in Sec. 7.2. Finally, data and expectation are compared in various distributions with a focus on the lepton kinematics in Sec. 7.3 and an emphasis on the event topology in Sec. 7.4.

Systematic uncertainties are already included in the discussion of the total event yield after selection and the contribution of the individual backgrounds. They are evaluated below in Sec. 8 with a focus on their dependence on the eμ mass. The $M_{\mathrm{e}\mu}$ spectrum is covered in a separate chapter, Sec. 9, because it is of paramount importance for the eμ resonance search.

7.1 Pileup reweighting and efficiency corrections

Before comparing the background expectation to the eμ sample selected in data, corrections related to the number of pileup interactions and the selection efficiencies of leptons are applied to the MC samples via reweighting of simulated events.

The simulation of pileup interactions on top of the pp collision with the hard interaction of interest starts from a carefully engineered distribution of the mean number of interactions per bunch crossing $\langle N_{\mathrm{inter}}\rangle$(MC), from which one value is drawn and stored per simulated event. This distribution is related to the assumed distribution of average per-bunch instantaneous luminosities per-lumi section [252] delivered by the LHC via the total inelastic cross section. The latter has been measured by the TOTEM collaboration for pp collisions at $\sqrt{s} = 7$ TeV [253] and $\sqrt{s} = 8$ TeV [127]. The CMS collaboration has provided measurements of inelastic cross sections at $\sqrt{s} = 7$ TeV in Refs. [254, 255]. The total inelastic cross section has been set to 69.4 mb for the reweighting procedure described in the following. For each lumi section in the analyzed dataset the measured average per-bunch instantaneous luminosity per-lumi section is stored. With the inelastic cross section, the distribution of these luminosities is translated into a distribution of $\langle N_{\mathrm{inter}}\rangle$(Data). From the comparison of the distributions of the mean number of interactions per bunch crossing in MC and data, event weights are obtained for each value of $\langle N_{\mathrm{inter}}\rangle$(MC). The distributions of the number of reconstructed vertices N_{vtx} obtained from data and the simulation after this pileup reweighting are compared in Fig. 7.1. Good agreement is observed apart from the region $N_{\mathrm{vtx}} < 5$ that contains about 1% of all observed events.

The simulated efficiencies for the triggering of muons, and the reconstruction and identification of electrons and muons are corrected to the measured values via the application of event weights as outlined in the context of the discussion of the signal efficiency in Sec. 5.3.

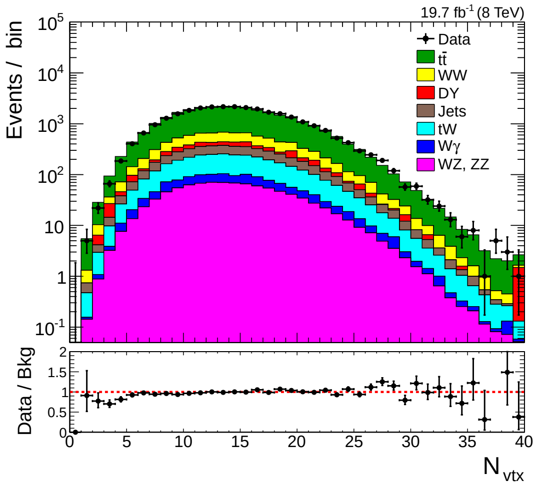

Figure 7.1: The number of reconstructed vertices per event. The simulation is reweighted to the measured luminosity profile.

7.2 Background composition

In total 28925 observed events pass the event selection. This is compared to the background expectation in Tab. 7.1 which also contains the individual contributions from the dominant SM processes. The total background yield reads 29200 events. Processes that involve prompt eμ production from decays of a pair of W bosons make up about 86% of the total background estimate. Among these, $\mathrm{t\bar{t}}$ production is the most important background with 69%, followed by direct WW production with 11% and the single-top tW process with 7%. The second-most important class of background consists of processes with non-prompt or misidentified leptons: W + jet and QCD multijet production (estimated from data and referred to by the label *Jets* in figures and tables), Drell-Yan production of lepton pairs, and a non-negligible contamination from Wγ events (note that the HEEP electron ID does not require the track momentum to match the energy of the supercluster). Together these processes contribute about 10% of the total background. Another 3% arise from WZ and ZZ diboson production.

	Data	Total bkg	Background process						
			$\mathrm{t\bar{t}}$	WW	tW	Jets	DY	WZ/ZZ	Wγ
Number of selected events	28925	29200 ±2300	20100 ±1800	3150 ±260	2000 ±160	1570 ±470	960 ±100	940 ±80	480 ±240

Table 7.1: Comparison of observed and expected event yields after the eμ selection. The systematic uncertainty in the total background expectation does exceed the quadratic sum of the uncertainties in the individual background contributions due to correlations.

7.3 Lepton kinematics

The p_T (E_T), η, and ϕ distributions of the muons and electrons in the selected eμ pairs are presented in Fig. 7.2. The observed electron E_T and muon p_T spectra follow the background expectation. However, a discrepancy is observed in the tail of the muon p_{T} distribution; above $p_{\mathrm{T}}^{\mu} = 400$ GeV 4 events are observed and 10 events are expected. In contrast, 11 events are observed in the tail of the electron E_{T} distribution above $E_{\mathrm{T}}^{\mathrm{e}} = 400$ GeV where 10 events are expected. The poisson probability of observing 4 events when the expectation value is 10 events is 1.9%, i.e. the deficit observed in the tail of the muon p_{T} spectrum is not statistically significant. However, the efficient triggering and reconstruction of high-p_{T} muons are of vital importance to this analysis and therefore some arguments that support the assumption of a statistical fluctuation are briefly mentioned. First, the CMS searches at $\sqrt{s} = 8$ TeV for new heavy vector bosons that decay into final states with muons, $\mathrm{Z}' \to \mu^{+}\mu^{-}$ [192] and $\mathrm{W}' \to \mu\nu$ [256], both utilize the same trigger and muon identification criteria. They observe (insignificant) excesses, rather than deficits, at high $M_{\mu\mu}$ and $M_{\mathrm{T}}(\mu, \nu)$, respectively. Second, a cross check is carried out in the context of this work based on the single-electron trigger `HLT_Ele80_CaloIdVT_GsfTrkIdT_vX` that is unprescaled and involves a cut on the electron E_{T} of 80 GeV at HLT level. No additional events are found in the region of phase space defined by the cuts $E_{\mathrm{T}}^{\mathrm{e}} > 100$ GeV and $p_{\mathrm{T}}^{\mu} > 400$ GeV when the single-muon trigger of the baseline selection is replaced by this single-electron trigger. Therefore, there is no indication that the observed deficit at high muon p_{T} is caused by the single-muon trigger. In addition to this cross-check of the utilized trigger, the impact of removing the individual muon identification criteria one by one is investigated. The distributions of muon identification variables to which selection cuts are applied are shown in App. E.4, Fig. E.5 for eμ events with a muon that satisfies $p_{\mathrm{T}}^{\mu} > 200$ GeV, fires the single-muon trigger, and passes all muon identification criteria except for the requirement on the plotted variable (the so-called $N - 1$ distributions for the muon selection). The observed $N - 1$ distributions are all described well by the background simulation. Removing a single muon identification requirement does not add a single selected event with $p_{\mathrm{T}}^{\mu} > 400$ GeV. Hence, this test shows no indication of a problem with the muon trigger or muon identification cuts (or their implementation in the analysis software) that might cause the observed deficit of high-p_{T} muons in Fig. 7.2 (top, right).

Most of the selected muons and electrons fall into the barrel region of the detector as shown in the pseudorapidity distributions in Fig. 7.2. The electron η distribution exhibits pronounced dips in the overlap region of the barrel and endcap sections of the ECAL. These are a result of the acceptance cuts on the pseudorapidity of the electron supercluster, $|\eta_{\mathrm{SC}}^{\mathrm{e}}| < 1.442$ and $|\eta_{\mathrm{SC}}^{\mathrm{e}}| > 1.56$. The pseudorapidity η^{e} that is plotted above is evaluated at the interaction vertex. The most prominent features in the pseudorapidity distribution of the muons are the two dips at $0.2 \lesssim |\eta^{\mu}| \lesssim 0.3$ mentioned in Sec. 4.5 which are caused by the gaps for cryogenic and electrical connections (chimneys) close to the transitions between wheel 0 and wheels ±1 of the segmented barrel muon system.

The $\mathrm{W} + \mathrm{jet}$ and $\mathrm{W}\gamma$ processes are the only backgrounds for which a pronounced difference between the shape of the η distributions for electrons and muons is expected. In both cases, the muons arise typically from W boson decays and are produced more centrally than the non-prompt or misidentified electrons. This is already visible in the two η distributions of these processes in Fig. 7.2 but it becomes more apparent in the corresponding distributions from the subsample of selected same-sign eμ pairs in App. E.1, Fig. E.1.

7.4 Event topology

In addition to the distributions of kinematical distributions of the individual leptons, the background description is found to describe the kinematics of the eμ system. Examples are the p_{T} of the dilepton pair, the differences in the ϕ and η coordinates, and the muon p_{T} to electron E_{T} ratio in Fig. 7.3. In a typical background event the electron and the muon are separated in the ϕ coordinate by more than 90° and carry similar transverse momentum. There is no pronounced pseudorapidity gap between the leptons in contrast to eμ events with high $M_{\mathrm{e}\mu}$ (see App. E.5). This is the case for all the individual background processes, such that the comparison of data and expectation in these distributions is no powerful test of the assumed background composition.

This is different for the distributions of the number of jets and b-tagged jets in eμ events shown in Fig. 7.4 that separate backgrounds with top quarks, in particular the leading $\mathrm{t\bar{t}}$ background, from the other background contributions. The jet reconstruction, identification, and kinematical selection is defined by the following criteria:

- The jets are clustered from objects that are reconstructed by the particle-flow algorithm.
- The jet clustering is carried out using the anti-k_T clustering algorithm [182] with a distance parameter R of 0.5 for cones in the space spanned by rapidity y and azimuth ϕ.
- The jets have to satisfy the loose particle-flow jet identification criteria presented in Sec. 3.4.2.
- Selected jets fall within $|\eta| < 2.4$, such that information from the inner silicon tracking system is available, and have a transverse momentum above 35 GeV.
- In order to avoid double-counting of the selected leptons that are not obtained from the particle-flow reconstruction, the jets have to be separated from both leptons in the selected eμ pair by $\Delta R = \sqrt{(\eta^{\mathrm{jet}} - \eta^{\ell})^2 + (\phi^{\mathrm{jet}} - \phi^{\ell})^2} > 0.5$.

The b-tagging of selected jets is based on the CSV algorithm [185] introduced in Sec. 3.4.2. In all plots that present information related to b-tagged jets (and only these plots), the b-tagging efficiencies and misidentification probabilities from simulations are corrected to the values measured in data as a function of jet p_T and η. This is achieved by the application of event weights to simulated events according to the recommendations by the BTV POG [257]. The input for the calculation of the event weights w_{btag} consists of the b-tagging probabilities for three different jet categories (b jets, c jets, light jets) obtained from the simulated background samples, and corresponding efficiency scale factors $\mathrm{SF}_{\mathrm{btag}} = \epsilon^{\mathrm{Data}}_{\mathrm{btag}}/\epsilon^{\mathrm{MC}}_{\mathrm{btag}}$. The latter have been determined by members of the BTV POG on an inclusive multijet sample [186, 257]. Information on b-tagging efficiencies obtained from $\mathrm{t\bar{t}}$-selected samples is not included. With these inputs, the b-tagging event weight is defined as the ratio of the probability for obtaining the observed subset of b-tagged jets from the observed set of selected PF jets with the measured b-tagging efficiencies $\epsilon^{\mathrm{Data}}_{\mathrm{btag}} = \mathrm{SF}_{\mathrm{btag}}\epsilon^{\mathrm{MC}}_{\mathrm{btag}}$ to the corresponding probability obtained when using the b-tagging efficiencies from simulations $\epsilon^{\mathrm{MC}}_{\mathrm{btag}}$.

$$\begin{aligned}
P\left(\epsilon^{\mathrm{MC}}_{\mathrm{btag}}\right) &= \prod_{\substack{\mathrm{j}_i\in\\ \text{b$-$tagged jets}}} \epsilon^{\mathrm{MC}}_{\mathrm{btag}}(\mathrm{j}_i) \quad \times \\
&\quad \prod_{\substack{\mathrm{j}_k\in\\ \text{untagged jets}}} \left(1-\epsilon^{\mathrm{MC}}_{\mathrm{btag}}(\mathrm{j}_k)\right) \\
P\left(\epsilon^{\mathrm{Data}}_{\mathrm{btag}} = \mathrm{SF}_{\mathrm{btag}}\ \epsilon^{\mathrm{MC}}_{\mathrm{btag}}\right) &= \prod_{\substack{\mathrm{j}_i\in\\ \text{b$-$tagged jets}}} \mathrm{SF}_{\mathrm{btag}}(\mathrm{j}_i)\ \epsilon^{\mathrm{MC}}_{\mathrm{btag}}(\mathrm{j}_i) \quad \times \\
&\quad \prod_{\substack{\mathrm{j}_k\in\\ \text{untagged jets}}} \left(1-\mathrm{SF}_{\mathrm{btag}}(\mathrm{j}_k)\ \epsilon^{\mathrm{MC}}_{\mathrm{btag}}(\mathrm{j}_k)\right) \\
w_{\mathrm{btag}} &= \frac{P(\epsilon^{\mathrm{Data}}_{\mathrm{btag}})}{P(\epsilon^{\mathrm{MC}}_{\mathrm{btag}})} \quad , \qquad (7.1) \\
\text{with} \quad \epsilon^{\mathrm{MC}}_{\mathrm{btag}}(\mathrm{j}) &= \epsilon^{\mathrm{MC}}_{\mathrm{btag}}\ (\ \text{jet type(j)};\ p_\mathrm{T}(\mathrm{j}),\ \eta(\mathrm{j})\ ) \\
\text{and} \quad \mathrm{SF}_{\mathrm{btag}}(\mathrm{j}) &= \mathrm{SF}_{\mathrm{btag}}\ (\ \text{jet type(j)};\ p_\mathrm{T}(\mathrm{j}),\ \eta(\mathrm{j})\ )\ .
\end{aligned}$$

The distributions of the number of selected PF jets and b-tagged jets in eμ events presented in Fig. 7.4 show agreement between data and expectation within the statistical uncertainties. In particular, the expected and observed numbers of events without a selected jet match. Direct W pair production, the overall second largest background, is the main contributor to this subsample of events and is separated from the dominant $\mathrm{t\bar{t}}$ process in the N_{jet} and N_{bjet} distributions. These distributions thus constitute an important check of the assumed background composition of the selected $\mathrm{e}\mu$ sample.

In addition to the N_{jet} and N_{bjet} distributions, the corresponding jet p_{T} spectra exhibit satisfactory agreement between data and expectation. They are included in App. E.2, Fig. E.3 together with the $\not{E}_{\mathrm{T}}$ spectrum in Fig. E.2.

With understanding of the main control distributions for both the lepton kinematics and the event topology established, the focus is shifted towards the $M_{\mathrm{e}\mu}$ spectrum in the following, starting with the discussion of the systematic uncertainties in the background estimate as a function of $M_{\mathrm{e}\mu}$.

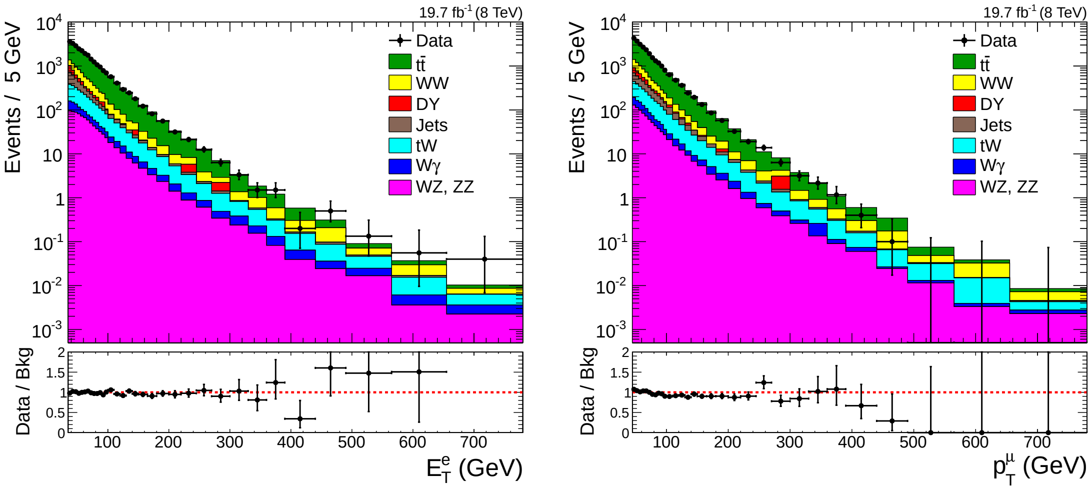

(a) The electron E_T distribution.

(b) The muon p_T distribution.

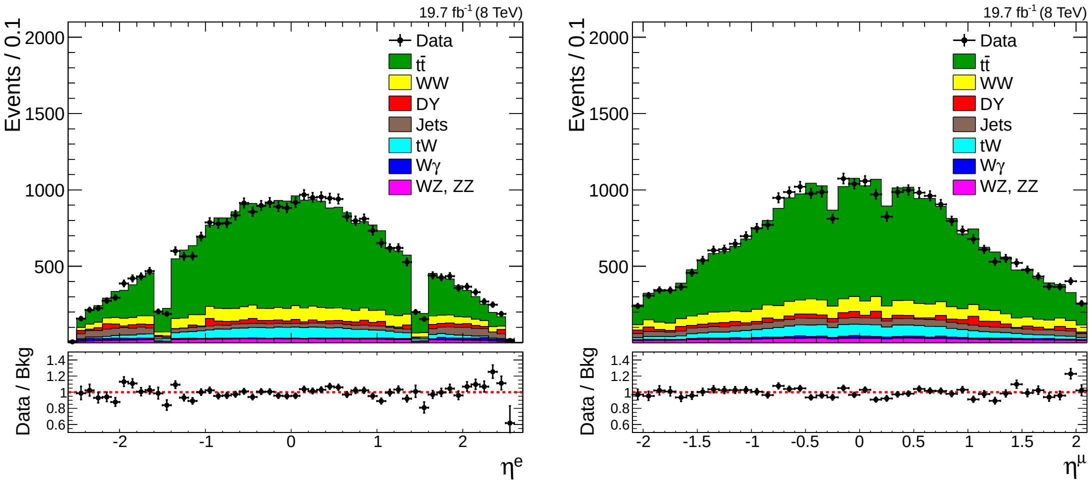

(c) The electron η distribution.

(d) The muon η distribution.

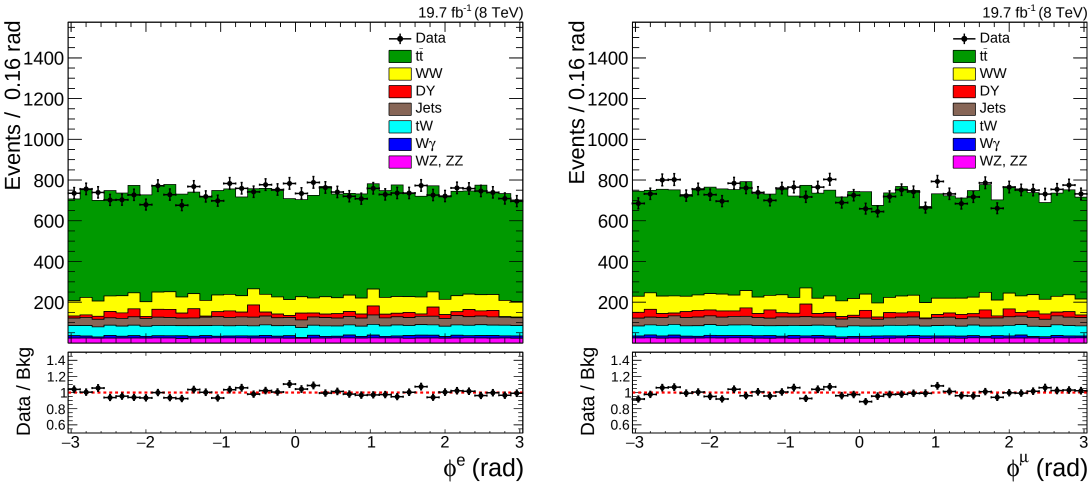

(e) The electron ϕ distribution.

(f) The muon ϕ distribution.

Figure 7.2: Distributions of variables describing the basic kinematics of the leptons in events that pass the selection of an eμ pair. Left: The E_T, η, and ϕ distributions of the electron. Right: The p_T, η, and ϕ distributions of the muon. For the sake of readability, the distributions are not binned according to the detector resolution.

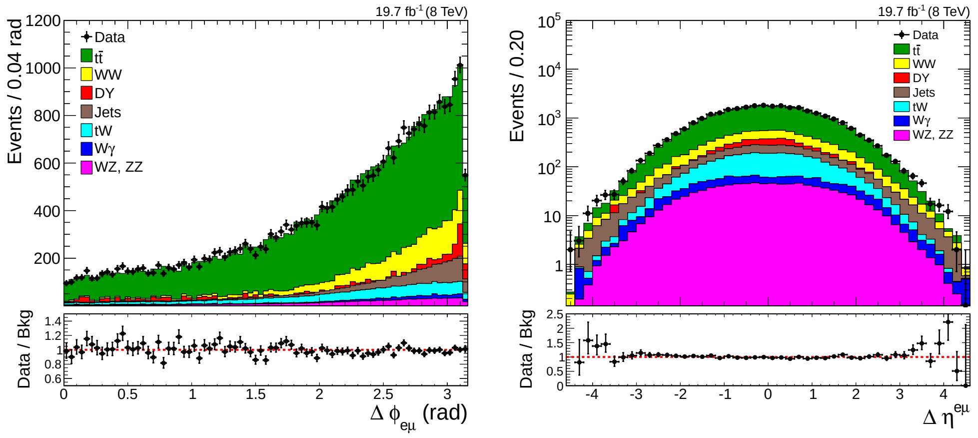

(a) The absolute value of the difference in azimuthal angle of the leptons $\Delta\phi_{e\mu}$.

(b) The difference of the pseudorapidities of the leptons $\Delta\eta_{e\mu}$.

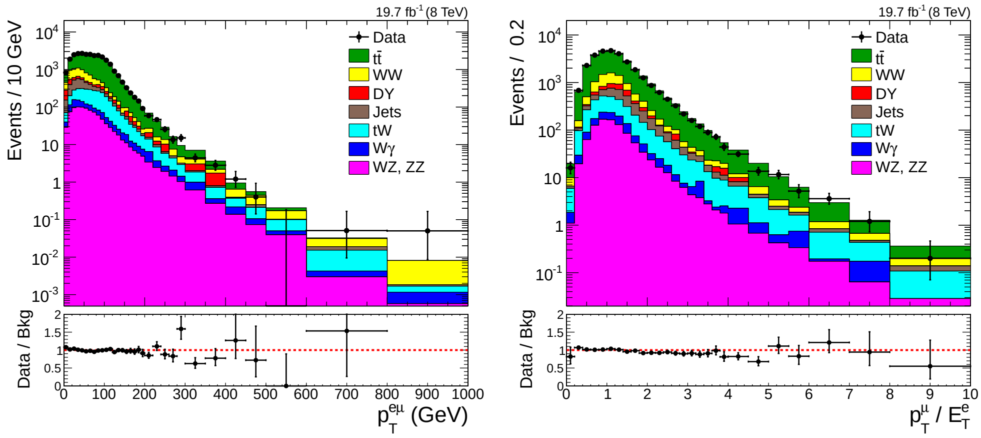

(c) The p_{T} of the eμ dilepton system.

(d) The ratio of muon p_{T} to electron E_{T}.

Figure 7.3: Distributions of variables describing the kinematics of the eμ system. The agreement between data and expectation in plots (c) and (d) improves further when the top-p_{T} reweighting described in Sec. 8.1.3 is applied to the $t\bar{t}$ simulation.

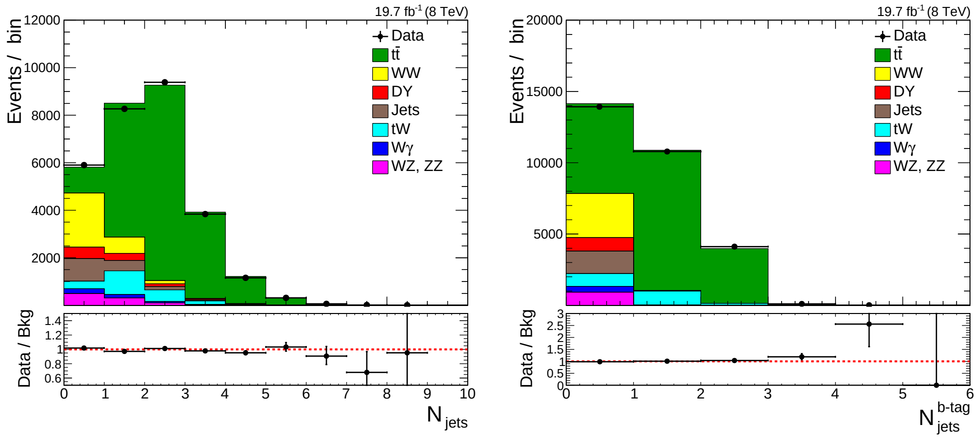

(a) The number of selected jets.

(b) The number of selected jets with a b-tag.

Figure 7.4: Distributions of the number of jets in selected eμ events. The jet selection is explained in the text.

Chapter 8

Systematic uncertainties

8.1 Uncertainties in the background prediction

The description of the systematic uncertainties in the background estimate is divided into three parts. First, uncertainties affecting all background estimates from simulations are briefly presented in Sec. 8.1.1. The uncertainties affecting background processes involving non-prompt leptons are given separately in Sec. 8.1.2. Second, the uncertainties in the cross sections of the dominant backgrounds, $\mathrm{t\bar{t}}$ and WW production, are discussed in some detail in Secs. 8.1.3 and 8.1.4, and the PDF uncertainty in the total background estimate is evaluated in Sec. 8.1.5. Finally, the impact of the individual uncertainties in the background estimate is given and they are combined into a total background uncertainty for different $M_{\mathrm{e}\mu}$ ranges in Sec. 8.1.6.

8.1.1 Common uncertainties in the scaling of simulated background yields to luminosity

- uncertainties in backgrounds obtained from simulations
  - **Efficiency of the eμ pair selection**

    The uncertainty in the selection efficiency of the eμ pair depends on the lepton kinematics, in particular on the transverse momenta and the pseudorapidities of the electron and muon. Rather than evaluating the impact of uncertainties in the lepton efficiencies as a function of these kinematic variables for each background individually, a flat relative uncertainty of 5% in the selection efficiency of the eμ pair is applied. This number is based on the impact of the uncertainties in the electron and muon efficiencies on the selection efficiency of the resonance signal, that has been studied in Sec. 5.3.1, Fig. 5.6 (right). At $M_{\mathrm{e}\mu} = 1$ TeV, a fully correlated variation of the uncertainties in the electron and muon efficiencies yields uncertainties in the selection efficiency of $\epsilon = 0.65^{+0.03}_{-0.04}$, i.e. a relative uncertainty of about 5%. At $M_{\mathrm{e}\mu} = 300$ GeV, this uncertainty is reduced to about 4% and at $M_{\mathrm{e}\mu} = 200$ GeV the assigned flat uncertainty covers the relative difference of 5% between the selection efficiency from MC simulations and the one after corrections to the measured lepton efficiencies are applied.
  - **Luminosity**

    An uncertainty in the luminosity of 2.6% is assigned. This number has been derived in Ref. [252].
  - **Background cross sections**

    The uncertainties in the background cross sections that are used to normalize the event yields from simulated background samples to the measured luminosity are treated differently for the leading contributions from $\mathrm{t\bar{t}}$ and WW production and the other backgrounds. A mass-dependent uncertainty is derived in the first case (Secs. 8.1.3 and

8.1.4), while the $M_{e\mu}$ dependence of the uncertainty is neglected for the subleading contributions. The PDF uncertainty in the background is treated separately in Sec. 8.1.5, such that the following numbers represent scale uncertainties associated with the total cross sections, only.

The cross sections for the diboson production processes WZ and ZZ and their scale uncertainties are obtained from Ref. [245] where `MCFM` (v. 6.6) has been utilized. The scale uncertainties read 4% and 3% for WZ and ZZ production, respectively. For the single top tW process, the scale uncertainty of 3% from Ref. [258] is used. An uncertainty of 5% is assigned to the normalization of the DY background that is obtained at LO using `MadGraph` but scaled to a cross section calculation with NNLO accuracy in pQCD from `FEWZ` (v. 3.1) [249, 250].

- Uncertainties associated with charged leptons
  - **Muon p_T scale**

    The muon p_T scale uncertainty is taken to be 5% per TeV as suggested by the MUON POG for high-p_T ($p_T > 200$ GeV) muons that fall into the barrel part of the detector [259]. This number has been obtained from studies of cosmic muons collected with the CMS detector by applying the so-called *cosmic endpoint* method described in Ref. [173]. It is propagated to the simulated samples by shifting the muon p_T on an event-by-event basis by $p_T \rightarrow p_T \times (\ 1 \pm 0.05 \times p_T/\text{TeV}\ )$.

  - **Muon p_T resolution**

    A relative uncertainty of 30% is assigned to the muon p_T resolution. For example, the relative muon p_T resolution and its uncertainties at $p_T^\mu \approx 500$ GeV read $6.0 \pm 1.8\%$. This uncertainty covers the differences observed between data and simulation at high muon p_T in the measurement of the p_T resolution with cosmic muons presented in Sec. 5.4.2 (Fig. 5.13). It furthermore reproduces the uncertainty in the resolution for $p_T^\mu < 100$ GeV: For muons from Z decays that fall into the barrel part of the CMS detector, a muon p_T resolution of about $1.5 \pm 0.5\%$ has been obtained [173].

    The impact of this uncertainty in the muon resolution on the $M_{e\mu}$ spectrum of selected background events is determined by randomly displacing the inverse muon p_T in the simulated background samples for each event by $1/p_T \rightarrow 1/p_T \times (1 + \Delta(\sigma(p_T)/p_T))$. The smearing $\Delta(\sigma(p_T)/p_T)$ is obtained from a Gaussian pdf with mean zero and width $w(p_T^\mu) = 0.3 \times \sigma(p_T^\mu)/p_T^\mu$, where the simulated muon p_T resolution $\sigma(p_T^\mu)/p_T^\mu$ is obtained from a fit to the corresponding graph in Fig. 5.10 (right).

  - **Electron energy scale**

    Uncertainties in the electron energy scale of 0.6% (barrel) and 1.5% (endcap) are applied to the electron E_T by shifting the transverse energy,
    $E_T \rightarrow E_T \times (\,1 \pm 0.006(0.015)\,)$. These uncertainties correspond to the variation of the electron momentum scale obtained from fits to the Z peak in $Z \rightarrow e^+e^-$ events in different electron p_T ranges [151].

8.1.2 Uncertainties in backgrounds with misidentified and non-prompt leptons

- **Uncertainty in the misidentification rate**

  An uncertainty of 40% is taken into account in the jet-to-electron misidentification rate, as suggested in Ref. [192] from which it is obtained.

- **Uncertainty in the Wγ cross section**

  The Wγ background estimate is obtained from a simulation at LO in pQCD that utilizes the `MadGraph` generator. Its contribution to the $e\mu$ final state under study stems from the process $pp \to W\gamma \to \mu\nu\ \gamma$, where the photon is misidentified as an electron. A large systematic uncertainty of 50% is assigned to the resulting event yield because higher-order corrections to the cross section are not applied and the photon-to-electron misidentification rate is taken directly from the simulation and is not determined from data.

8.1.3 Uncertainties in the $t\bar{t}$ background

The background yield from the dominant $t\bar{t}$ contribution is obtained from simulated samples. This approach is chosen over a data-driven background estimate for two reasons. First, the analysis aims at signal model-independence, i.e. as many signatures as possible that involve an $e\mu$ resonance, possibly among many other particles, shall be covered. This approach calls for a reduced set of selection cuts that only target the $e\mu$ pair in the final state. A data-driven approach to obtain the $t\bar{t}$ background would involve additional cuts on the event topology, like the veto of events with b-tagged jets, to define suitable control regions. Second, this search puts a strong focus on the high-mass region, $M_{e\mu} \sim 1$ TeV, where SM backgrounds yield few events. A data-driven approach to the $M_{e\mu}$ spectrum from $t\bar{t}$ production would involve large statistical uncertainties in this mass region.

The uncertainties that are assigned to the $t\bar{t}$ background yield from simulation arise from different sources. One are corrections to the simulated kinematics of $t\bar{t}$ production derived from the comparison of differential $t\bar{t}$ cross section measurements and predictions from simulation. Such a procedure will be discussed in the next paragraph. Its application is only justified in regions of phase space in which a sufficient number of events has been accumulated in data to allow for a meaningful comparison between measurement and prediction. In order to extend the evaluation of the $t\bar{t}$ background uncertainty beyond the region probed by the $t\bar{t}$ cross section measurements, the impact of higher-order corrections to differential $t\bar{t}$ cross sections on the simulated $M_{e\mu}$ spectrum is estimated. The resulting uncertainty estimate from the two approaches is then tested by comparing the simulated $t\bar{t}$ background estimate with its uncertainty to data in a $t\bar{t}$ background-enriched subset of selected $e\mu$ events.

Impact of reweighting the simulated top p_T spectrum to measurement

In general, good agreement between the data and predictions from simulated samples has been observed for different event generators in cross section measurements and other dedicated studies of $t\bar{t}$ production in pp collisions at $\sqrt{s} = 7,\ 8$, and 13 TeV by the CMS TOP PAG [260, 261]. However, measurements of the differential top pair production cross sections by CMS have pointed to imperfections in the modelling of the top p_T spectrum in various combinations of event generators and parton showers. Discrepancies between the prediction for the differential cross section $d\sigma/dp_T^t$ and unfolded data such as those depicted in Fig. 8.1 (left, ratio plot) have been found for different $t\bar{t}$ decay channels and pp centre-of-mass energies [260–262].

Based on these measurements, a prescription to reweight the p_T^t spectrum of the `POWHEG+PYTHIA` $t\bar{t}$ background sample used in this analysis is provided by the TOP PAG [262]. In a first step, an event weight w_i is assigned as a function of the top and antitop p_T values at parton level

$$w_i = \sqrt{e^{a+b\times p_T^t} e^{a+b\times p_T^{\bar{t}}}}\ , \tag{8.1}$$

with the parameters $a = 0.159$ and $b = -0.00141/\text{GeV}$ obtained from events collected in pp collisions at $\sqrt{s} = 8$ TeV that pass the $t\bar{t}$ selection in the $e/\mu +$ jets channel [262]. This reweighting changes both the shape and normalization of the simulated p_T^t spectrum. In a second step, the original normalization is restored by scaling the cross section of the sample with the inverse of the mean of the weight distribution $1/\langle w_i \rangle$.

This reweighting procedure is used to obtain an uncertainty in the $M_{e\mu}$ spectrum from the $t\bar{t}$ background simulation. The suppression of the tail in the p_T^t distribution corresponds to a

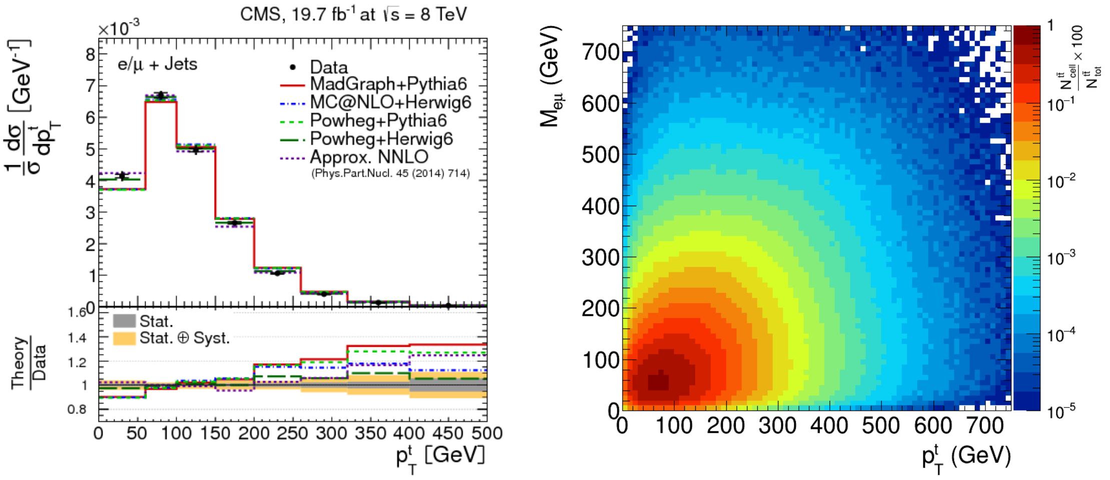

(a) Measurement of the differential $t\bar{t}$ production cross section $d\sigma/dp_T^t$ in pp collisions at $\sqrt{s} = 8$ TeV by the CMS collaboration. The measurement is compared to several theoretical predictions, including that by the `POWHEG` generator interfaced with `PYTHIA` 6 for parton showering. This latter combination of tools for event generation is used for the $t\bar{t}$ background estimate in this work. The figure has been taken from Ref. [261].

(b) Scatter plot of the kinematic variables $M_{e\mu}$ and p_T^t obtained at parton level from a sample of $t\bar{t}$ events generated with the `POWHEG` generator. No selection cuts are applied to the leptons.

Figure 8.1: The top pair production cross section as a function of p_T^t (left). Correlation between p_T^t and $M_{e\mu}$ in $t\bar{t}$ events (right).

suppression of the high-mass tail in the $M_{e\mu}$ spectrum because the two observables p_T^t and $M_{e\mu}$ exhibit a positive correlation. The reweighting thus leads to a one-sided shape uncertainty (-1σ) in $M_{e\mu}$. The correlation between $M_{e\mu}$ and p_T^t is shown in Fig. 8.1 (right) that is obtained from four million $pp \to t\bar{t} \to b\bar{b}\, e^{\pm}\mu^{\mp}\bar{\nu}\nu$ events generated with the `POWHEG` event generator.

The p_T^t reweighting comes with two caveats that are important when considering its impact on the $M_{e\mu}$ spectrum from the $t\bar{t}$ simulation. First, the reweighting procedure is based on measurements of the differential top pair production cross section up to $p_T^t = 400$ GeV. As shown in Fig. 8.1 (right), a significant fraction of the $t\bar{t}$ events with $M_{e\mu} \gtrsim 500$ GeV features values of p_T^t that exceed 400 GeV. Secondly, reweighting the p_T^t spectrum in the $t\bar{t}$ background simulation to the measurement does not necessarily improve the agreement between data and expectation for the observable of interest, $M_{e\mu}$.

Impact of higher-order corrections to the top p_T spectrum

Higher-order corrections to the differential $t\bar{t}$ cross section $d\sigma/dp_T^t$ in pp collisions at $\sqrt{s} = 8$ TeV have been calculated in the literature. Approximate NNLO and NNNLO calculations in pQCD based on soft-gluon resummation are presented in Refs. [263, 264] and the full NNLO calculation is given in Ref [265]. In the following, the results from the resummed cross section calculation are used because they are presented in Ref. [264] up to $p_T^t = 1$ TeV, including the ratio of the differential cross sections $d\sigma/dp_T^t$ obtained at aNNNLO and from a full NLO calculation. The cross section is evaluated using fixed renormalization and factorization scales $\mu^2 = m_t^2$. The high-p_T^t behaviour of the differential cross section ratio (inset plot in Fig. 3 in Ref. [264]) can be

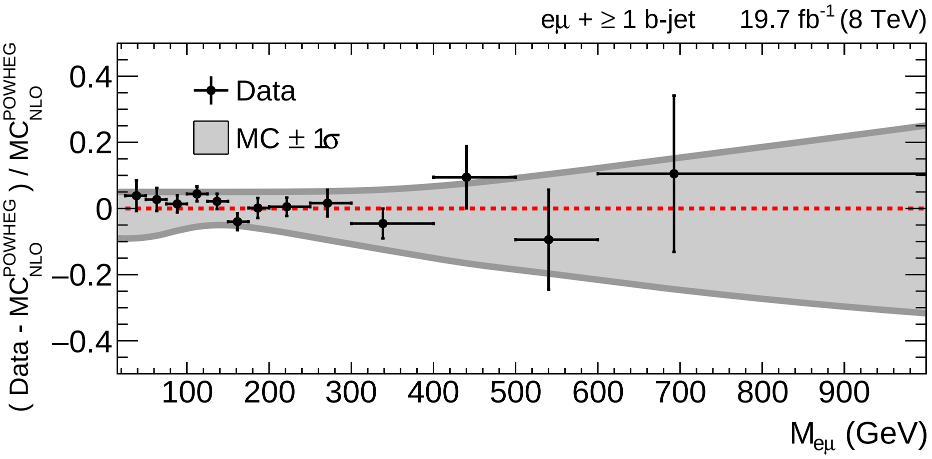

Figure 8.2: The ratio of event yields in data to the background expectation in events with an $e\mu$ *pair and at least one b-tagged jet as a function of* $M_{e\mu}$*. The grey band represents the* 1σ *uncertainty envelope. The vertical bars on the data points represent the statistical uncertainty and the horizontal bars represent the bin width. The mean value of the simulated* $M_{e\mu}$ *distribution in each mass bin is chosen as the* x *coordinate of the corresponding data point.*

approximated by a linear function:

$$\frac{(\mathrm{d}\sigma/\mathrm{d}p_\mathrm{T}^\mathrm{t})_\mathrm{aNNNLO}}{(\mathrm{d}\sigma/\mathrm{d}p_\mathrm{T}^\mathrm{t})_\mathrm{NLO}} = 1 + 1.2 \times \frac{p_\mathrm{T}^\mathrm{t} - 300\ \mathrm{GeV}}{700\ \mathrm{GeV}} \qquad \text{for} \quad p_\mathrm{T}^\mathrm{t} \geq 300\ \mathrm{GeV}\ . \tag{8.2}$$

In order to estimate the impact of higher order corrections to the top pair cross section on the $M_{e\mu}$ spectrum from the NLO $\mathrm{t\bar{t}}$ sample generated with `POWHEG`, event weights given by Eqn. 8.2 are applied to the simulation as a function of p_T^t evaluated at parton level. This reweighting procedure enhances the tail of the $M_{e\mu}$ distribution from simulated $\mathrm{t\bar{t}}$ events by about 10% at $M_{e\mu} = 500$ GeV and by 25% at $M_{e\mu} = 1$ TeV. The difference between the reweighted $M_{e\mu}$ distribution and the nominal spectrum obtained from the `POWHEG` sample is used as a one-sided shape uncertainty ($+1\sigma$) in $M_{e\mu}$.

Cross-check of the uncertainty estimate for the $\mathrm{t\bar{t}}$ background

Since the $\mathrm{t\bar{t}}$ process constitutes the dominant background process in the search for new physics in the $M_{e\mu}$ spectrum it has to be ensured that the uncertainty assigned to the $\mathrm{t\bar{t}}$ background estimate is appropriate. This is achieved by comparing data and background estimate in the subset of selected $e\mu$ events with at least one b-tagged jet, that is strongly $\mathrm{t\bar{t}}$-enriched. In data 15007 events fall into this subset and the simulation yields 14800 events, with the $\mathrm{t\bar{t}}$ process contributing more than 90% of this background estimate. The ratio between data and observation as a function of $M_{e\mu}$ is depicted in Fig. 8.2 together with the 1σ uncertainty band obtained from adding the uncertainty in the inclusive $\mathrm{t\bar{t}}$ cross section of 5% (scale uncertainties and PDF uncertainties added in quadrature [266]) and the mass-dependent, one-sided uncertainties from the two p_T^t reweighting procedures described above. The bin size in $M_{e\mu}$ is chosen such that it is not smaller than ten times the invariant mass resolution for this cross-check that is not intended to reveal any sought-after structures in the $M_{e\mu}$ spectrum. There is no indication for an underestimate of the uncertainty in the $\mathrm{t\bar{t}}$ background, nor for a substantial overestimate.

8.1.4 Uncertainties in the WW background cross section

The uncertainty in the WW background yield that is obtained from simulated samples using the `POWHEG` generator is estimated by studying the renormalization and factorization scale uncertainties in the cross section of the process $\mathrm{pp} \to \mathrm{W}^+\mathrm{W}^- \to \mathrm{e}^\pm\mu^\mp + \nu + \bar{\nu}$. The scale uncertainties are determined as a function of the observable of interest, the mass of the generated eμ pair in the final state $M_{\mathrm{e}\mu}$. Their evaluation is based on three samples of LHE events produced with the `POWHEG` (v. 1.0) event generator. The generator settings are the same as for the fully simulated WW background sample but only one of the three LHE samples uses the same choice for the renormalization and factorization scales

$$\mu^2 = \mu_R^2 = \mu_F^2 = M_{\mathrm{WW}}^2 \ . \tag{8.3}$$

This scale choice is referred to as the nominal scale choice μ^2_{nom} in this paragraph. For the other two samples, the scale choices are varied up and down in a fully correlated way as

$$\mu_R^{2,\mathrm{up}} = \mu_F^{2,\mathrm{up}} = 4 \times \mu^2_{\mathrm{nom}} \qquad \text{and} \qquad \mu_R^{2,\mathrm{down}} = \mu_F^{2,\mathrm{down}} = 0.25 \times \mu^2_{\mathrm{nom}} \ . \tag{8.4}$$

Each LHE sample contains ten million leptonic $\mathrm{W}^+\mathrm{W}^-$ events and the W decays are forced to result in an $\mathrm{e}^\pm\mu^\mp$ pair in the final state. The scale uncertainty in the total WW production cross section obtained from the three cross section values provided by the `POWHEG` generator is 3.7%. It is in good agreement with the scale uncertainties of 3.6% evaluated in Ref. [245] using the same scale variations (Eqn. 8.4) but the `MCFM` (v. 6.6) [242] NLO cross section calculator.

No kinematic cuts are applied to the lepton pair in the final state for this study of scale uncertainties in the differential WW production cross section $\mathrm{d}\sigma_{\mathrm{WW}}/\mathrm{d}M_{\mathrm{e}\mu}$. The symmetrized scale uncertainty defined as

$$\frac{\left|\left(\mathrm{d}\sigma_{\mathrm{WW}}/\mathrm{d}M_{\mathrm{e}\mu}\right)\left(\mu^2 = 0.25 \times \mu^2_{\mathrm{nom}}\right) - \left(\mathrm{d}\sigma_{\mathrm{WW}}/\mathrm{d}M_{\mathrm{e}\mu}\right)\left(\mu^2 = 4 \times \mu^2_{\mathrm{nom}}\right)\right|}{2\,\left(\mathrm{d}\sigma_{\mathrm{WW}}/\mathrm{d}M_{\mathrm{e}\mu}\right)\left(\mu^2 = \mu^2_{\mathrm{nom}}\right)} \tag{8.5}$$

is depicted in Fig. 8.3. It ranges from 3.5% at $M_{\mathrm{e}\mu} = 100$ GeV to about 17% at $M_{\mathrm{e}\mu} = 1.5$ TeV. Since the increase in uncertainty in this mass range is approximately linear in $M_{\mathrm{e}\mu}$, the mass-dependent uncertainty in the WW background yield that is used in this analysis is obtained from a linear fit to the data points in Fig. 8.3 in the range 100 GeV $\leq M_{\mathrm{e}\mu} \leq$ 1.6 TeV.

The study of the WW production cross section at the LHC in Ref. [246] goes beyond the determination of scale uncertainties at NLO in pQCD by explicitly evaluating additional contributions; corrections to the LO cross section for $q\bar{q} \to \mathrm{WW}$ that arise due to the processes $\mathrm{gg} \to \mathrm{WW}$ and $\gamma\gamma \to \mathrm{WW}$; as well as electroweak and QCD corrections are given as a function of the cut value on the WW mass, M_{WW}^{cut}. These results are shown in Fig. 8.4. The electroweak corrections to the cross section are negative and sizeable for high WW mass, but most of this correction is cancelled by the contribution from $\gamma\gamma$-induced WW production (for pp collisions at $\sqrt{s} = 8$ TeV). Therefore, no additional uncertainty associated with these effects is included in the following. This argument neglects the potentially sizeable uncertainties in the $\gamma\gamma$-induced WW cross section stemming from the uncertainties in the photon PDF of the proton.

8.1.5 PDF uncertainties

The evaluation of PDF uncertainties is based on the PDF4LHC recommendations [267,268]. The PDF uncertainty in the background yield is evaluated as a function of $M_{\mathrm{e}\mu}$ based on three NLO PDF sets by different groups; the CT10 [269], MSTW 2008 NLO [125], and NNPDF2.3 NLO [270] PDF sets. The PDF uncertainties for each set, that arise from the uncertainties in the measurements used as input to the PDF fits, are evaluated at 68% CL according to the prescriptions of the individual PDF sets. In addition, the uncertainty associated with the variation of α_S is evaluated. For simplicity, the combination of these two uncertainties is referred to as the PDF uncertainty in the following, rather than using the term 'PDF+α_S uncertainty' throughout the entire text. The 1σ uncertainty contours obtained for each of the three PDF sets are then combined as suggested in the PDF4LHC recommendation.

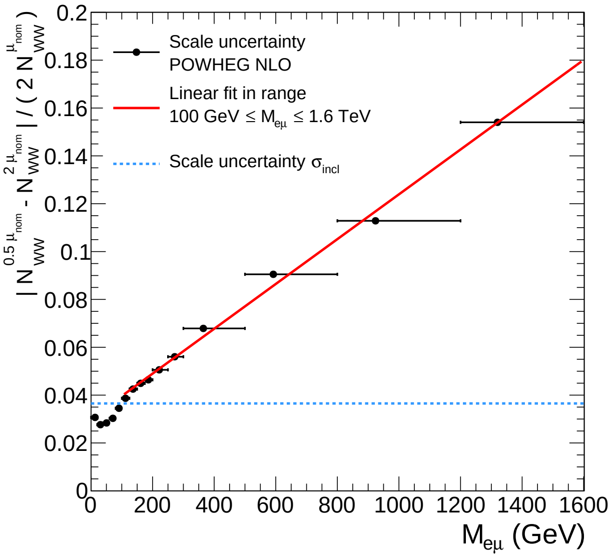

Figure 8.3: The symmetrized scale uncertainty in the WW production cross section as a function of $M_{e\mu}$. It is evaluated at NLO in pQCD using LHE samples produced with `POWHEG`*. The black vertical lines indicate the bin width. The mean values of the WW $M_{e\mu}$ spectrum (for the nominal scale choice) in the chosen mass bins are used as the x-coordinates of the data points. The red line indicates a linear fit to these data points in the range 100 GeV $\leq M_{e\mu} \leq 1.6$ TeV. The dashed blue line represents the symmetrized scale uncertainty in the total cross section obtained from the generator.*

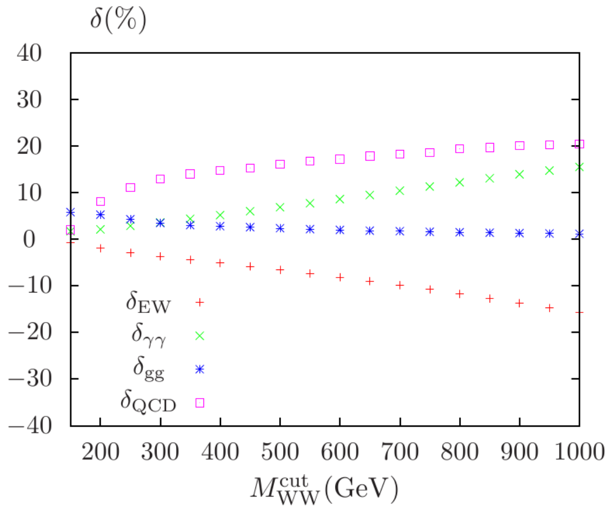

Figure 8.4: Corrections δ to the $q\bar{q} \to WW$ LO cross section due to the processes $gg \to WW$ and $\gamma\gamma \to WW$, as well as electroweak and QCD higher-order corrections for the $\sqrt{s} = 8$ TeV LHC. The corrections δ are defined by $\sigma_{q\bar{q}\oplus X} = (1 + \delta_X) \times \sigma_{q\bar{q}}$. Note that δ is not plotted as a function of the mass of the W boson pair M_{WW} but as a function of the lower mass threshold M_{WW}^{cut}. The figure is obtained from Ref. [246].

The PDF uncertainty only affects the background contribution obtained from simulations and the data-driven estimate of the W + jet and QCD multijet contributions is therefore excluded from the definition of the background yield $N_{\text{bkg}}^{\text{MC}}$ in the following. The dominant remaining backgrounds $\text{t}\bar{\text{t}}$, WW, and single-top tW production, that constitute more than 90% of the

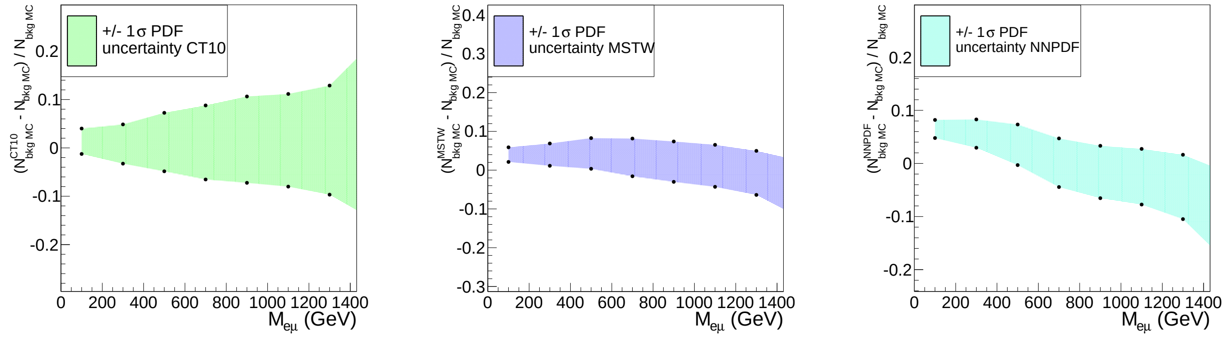

(a) PDF uncertainty obtained from the CT10 PDF set.

(b) PDF uncertainty obtained from the MSTW2008nlo68cl PDF set.

(c) PDF uncertainty obtained from the NNPDF23 NLO PDF set.

Figure 8.5: The relative uncertainty in the background event yield in seven invariant mass bins represented by 1σ contours obtained for the individual PDF sets in the PDF4LHC [267, 268] recommendation.

total background estimate $N^{\mathrm{MC}}_{\mathrm{bkg}}$, are all produced with NLO PDF sets provided by the CTEQ collaboration (CT10 [269] for $\mathrm{t\bar{t}}$ and WW production, CTEQ6M [58] for the single-top process). Therefore, the reweighting of the simulated background events to other PDFs is simplified by choosing the CT10 central PDF as the baseline PDF for all background samples and processing the entire background expectation obtained from simulations in a single step. The 1σ contours illustrating the relative PDF uncertainties in the background yield $N^{\mathrm{MC}}_{\mathrm{bkg}}$ for the three individual PDF sets are depicted in Fig. 8.5. These contours are defined by the upper and lower relative PDF uncertainties in the number of background events in 200 GeV-wide mass bins $\Delta M^{i}_{\mathrm{e}\mu}$. The upper and lower relative PDF uncertainties are given by:

$$\Delta^{+}_{\mathrm{PDF}}(\Delta M^{i}_{\mathrm{e}\mu}) = \frac{N^{\mathrm{PDF},\ \sigma_{+}}_{\mathrm{bkg}}(\Delta M^{i}_{\mathrm{e}\mu}) - N^{\mathrm{MC}}_{\mathrm{bkg}}(\Delta M^{i}_{\mathrm{e}\mu})}{N^{\mathrm{MC}}_{\mathrm{bkg}}(\Delta M^{i}_{\mathrm{e}\mu})} \tag{8.6}$$

$$\Delta^{-}_{\mathrm{PDF}}(\Delta M^{i}_{\mathrm{e}\mu}) = \frac{N^{\mathrm{PDF},\ \sigma_{-}}_{\mathrm{bkg}}(\Delta M^{i}_{\mathrm{e}\mu}) - N^{\mathrm{MC}}_{\mathrm{bkg}}(\Delta M^{i}_{\mathrm{e}\mu})}{N^{\mathrm{MC}}_{\mathrm{bkg}}(\Delta M^{i}_{\mathrm{e}\mu})}, \tag{8.7}$$

where $N^{\mathrm{MC}}_{\mathrm{bkg}}(\Delta M^{i}_{\mathrm{e}\mu})$ is the number of background events in mass bin $\Delta M^{i}_{\mathrm{e}\mu}$ using the baseline PDF choice for the background samples and $N^{\mathrm{PDF},\ \sigma_{+}}_{\mathrm{bkg}}$, $N^{\mathrm{PDF},\ \sigma_{-}}_{\mathrm{bkg}}$ are the corresponding event yields obtained when following the recommendations for the evaluation of the PDF uncertainties for the individual PDF sets.

Among the three PDF uncertainty contours in Fig. 8.5, the one obtained for the CT10 PDF set (left) shows the most symmetric behaviour around zero. This is expected because the MC samples of the dominant background processes are produced with the central PDF member of the CT10 set. In contrast to the CT10 uncertainty contour, the 1σ bands of the MSTW2008 and NNPDF2.3 PDF sets exhibit an offset with respect to the CT10 values at low $M_{\mathrm{e}\mu}$, i.e. these PDF sets yield a larger value for the sum of the involved background cross sections. The area of the uncertainty contour is largest for the CT10 PDF set. In the mass bin $M_{\mathrm{e}\mu} \in [1.2\ \mathrm{TeV}, 1.4\ \mathrm{TeV}]$, the symmetrized PDF uncertainty $|\Delta^{+}_{\mathrm{PDF}} - \Delta^{-}_{\mathrm{PDF}}|/2$ reaches about 11% for CT10. At these high masses, the uncertainties from this individual PDF set define the size of the overall envelope obtained from the combination of the three different PDF sets according to the PDF4LHC recipe, as depicted in Fig. 8.6 (left). At lower masses, the differences in the central values obtained for the three sets also contributes to the envelope.

The treatment of the PDF uncertainty in the statistical interpretation of the experimental results is simplified by using the symmetrized LHC4PDF uncertainty envelope

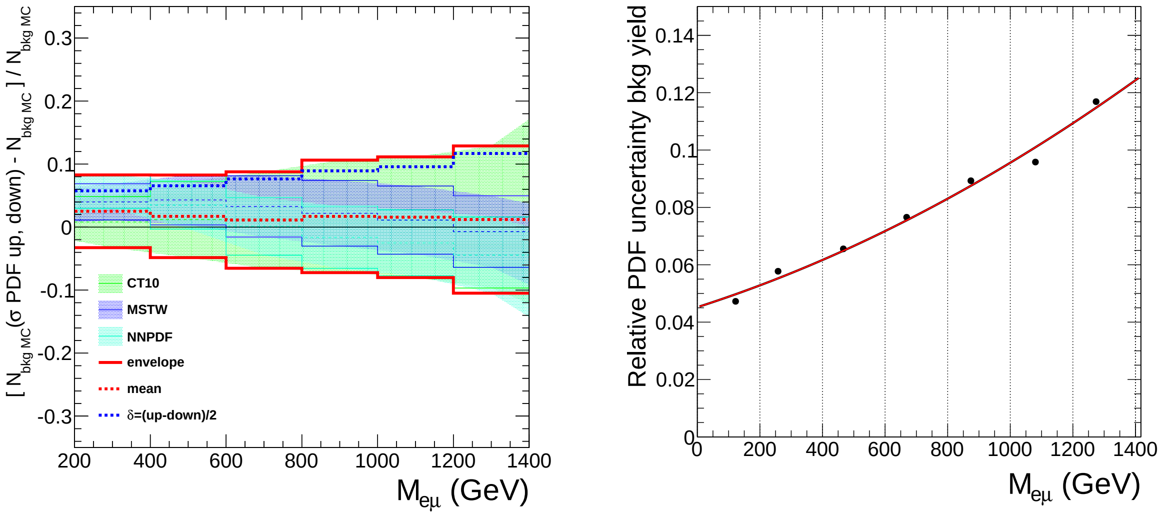

(a) The PDF4LHC uncertainty envelope (solid red lines) and δ_{PDF} (dashed blue line).

(b) Fit of a second-order polynomial to $\delta_{\mathrm{PDF}}(M_{e\mu})$.

Figure 8.6: The PDF4LHC uncertainty envelope constructed from the three individual PDF uncertainty contours in Fig. 8.5 and the fit to its symmetrized form δ_{PDF} *as a function of* $M_{e\mu}$.

$\delta_{\mathrm{PDF}} \equiv |\Delta^{+}_{\mathrm{comb}} - \Delta^{-}_{\mathrm{comb}}|/2$ (plotted in Fig. 8.6 as a dashed blue line), and fitting the resulting PDF uncertainty values $\delta_{\mathrm{PDF}}(\Delta M^{i}_{\mathrm{e}\mu})$ with a second-order polynomial. To this end, the eμ mass values on the abscissa are chosen as the mean of the $M_{\mathrm{e}\mu}$ background spectrum in the interval $\Delta M^{i}_{\mathrm{e}\mu}$. The result of the fit, that is used to obtain the relative PDF uncertainty in the event yield from simulated background processes, is depicted in Fig. 8.6 (right) and reads:

$$\delta_{\mathrm{PDF}}(M_{\mathrm{e}\mu}) = 4.5 \times 10^{-2} + 3.5 \times 10^{-5} \left(\frac{M_{\mathrm{e}\mu}}{\mathrm{GeV}}\right) + 1.5 \times 10^{-8} \left(\frac{M_{\mathrm{e}\mu}}{\mathrm{GeV}}\right)^{2} . \tag{8.8}$$

8.1.6 Summary of the impact of systematic uncertainties in the background $M_{\mathrm{e}\mu}$ spectrum

After introducing the considered sources of systematic uncertainty, their impact on the background $M_{\mathrm{e}\mu}$ spectrum is considered next[1]. The uncertainties in the background yield in various bins of $M_{\mathrm{e}\mu}$ are depicted in Fig. 8.7. The plot includes neither the uncertainty stemming from the muon resolution because they lie well below 1% over the entire mass range nor the uncertainty associated with the electron energy scale that has a similar impact as that associated with the muon scale. All uncertainties are symmetrized for this graphical representation, i.e. the absolute value of half the difference between the $\pm 1\sigma$ variations is shown in the case of asymmetric uncertainties. The presented total systematic uncertainty is the quadratic sum of the individual contributions and does not include the statistical uncertainty in the background estimate which arises from the finite number of events in the background samples. This statistical uncertainty is shown separately in the plot.

The total systematic uncertainty ranges from about 9% at the lower edge of the search region to 18% at $M_{\mathrm{e}\mu} = 1$ TeV. At $M_{\mathrm{e}\mu} = 200$ GeV, there is no single dominant uncertainty and several uncertainties contribute significantly: Both the uncertainty in the selection efficiency and

---

[1] In this paragraph, the uncertainties in the total background yield (comprising both the background yields obtained from simulations and data-driven background estimates) are discussed. Note that the uncertainties in the event yield from simulated background processes, such as the PDF uncertainty in Eqn. 8.8, do not affect the data-driven estimate of the W + jet and QCD multijet contributions, such that their impact on the total background yield is reduced.

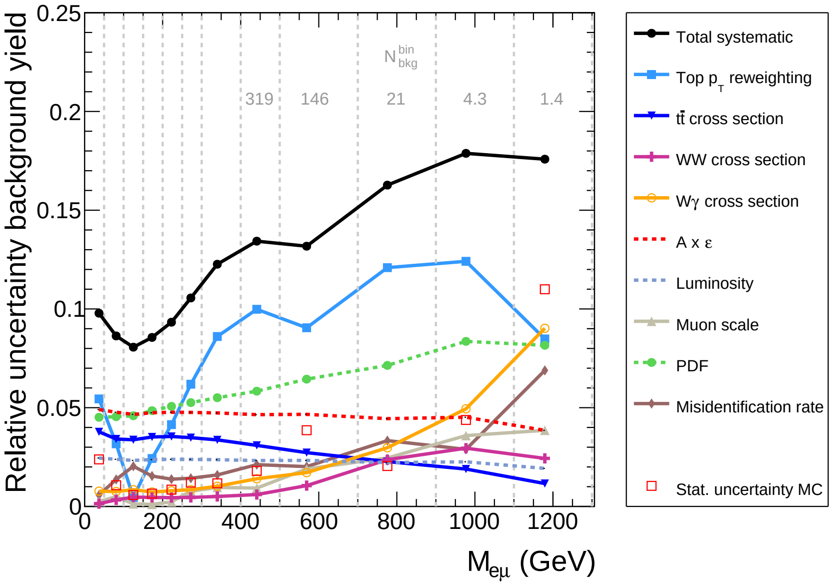

Figure 8.7: The most important uncertainties in the total background yield in bins of $M_{e\mu}$. The long dashed vertical lines indicate the bin width and the x−coordinate of the data points is evaluated at the mean of the $M_{e\mu}$ background spectrum in each bin. The numbers in the upper part of the plot indicate the expected number of background events in the five bins of highest eμ mass. The empty red squares denote the statistical uncertainty in the background expectation from the finite number of events in the background samples.

PDF yield 5% and those in the scaling and shape of the $t\bar{t}$ background contribute 4%, each. The uncertainty in the $t\bar{t}$ shape from the reweighting of the p_T^t distribution is the largest single contribution to the systematic uncertainty in the total background yield in the mass range from 300 GeV to 1 TeV. Note that this is not due to a rising background fraction of the $t\bar{t}$ processes that does in fact fall towards higher masses. The uncertainty from the inclusive $t\bar{t}$ cross section used for the scaling of the background yield to luminosity fades as $M_{e\mu}$ is increased and diboson production as well as background processes involving misidentified or non-prompt leptons become more important. For masses above 1 TeV, the large uncertainties in the misidentification rates that affect the W + jet, QCD multijet, and Wγ backgrounds contribute significantly to the total systematic uncertainty. Finally, the statistical uncertainty in the expected background yield reaches 11% in the $M_{e\mu}$ range from 1.1 TeV to 1.3 TeV and surpasses all individual sources of systematic uncertainty. Given that the number of expected background events in this mass range is 1.4, this statistical uncertainty is acceptable and does not affect the statistical interpretation of the results significantly.

8.2 Uncertainties in the signal contribution

The uncertainties in the signal contribution are separated into an uncertainty in the total number of expected signal events and an uncertainty in the signal pdf. The number of expected signal events is given by $N_{\text{sig}} = \sigma_{\text{sig}} \cdot (A \times \varepsilon)_{\text{sig}} \cdot \mathcal{L}$. Among the three quantities that influence it, the product of acceptance and efficiency, $A \times \varepsilon$, as well as the luminosity are directly related to the measurement, whereas the signal cross section can be regarded as an external parameter affected by theory uncertainties such as renormalization and factorization scale uncertainties and PDF uncertainties in the inclusive signal cross section. Only the uncertainties in the product of acceptance and efficiency and on the luminosity are included as uncertainties related to the signal normalization in the statistical interpretation of the experimental findings (the calculation of cross

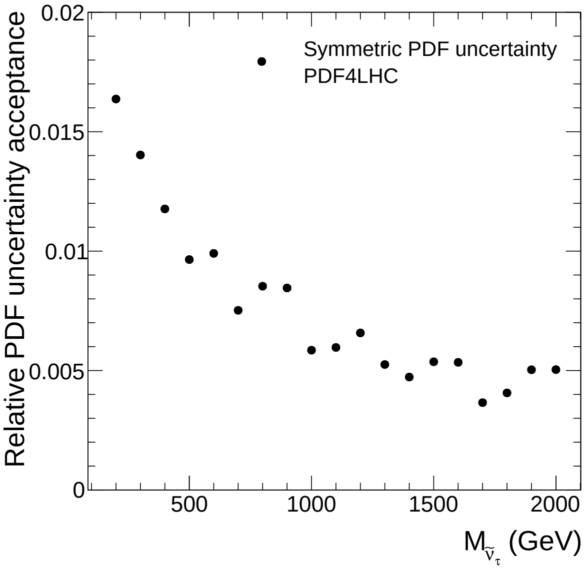

Figure 8.8: The relative PDF uncertainty in the $\tilde{\nu}_\tau$ signal acceptance as a function of $M_{\tilde{\nu}_\tau}$, given by the combination of the 1σ contours from the CT10, MSTW2008, and NNPDF2.3 PDF sets.

section limits and of the significances of observed excesses).

PDF uncertainty in the signal acceptance

In the results section, Sec. 10, exclusion limits will be provided on the product of inclusive signal production cross section times branching fraction of the decay into the eμ final state. In order to transform the experimental bound on the number of signal events in the detector into a limit on an inclusive cross section, a theoretical prediction for the signal acceptance and its uncertainty are necessary. Thereby, the PDF uncertainty in the signal acceptance, which is a theoretical uncertainty unrelated to the measurement that is only possible within part of the total phase space, enters the result. The relative PDF uncertainty in the signal acceptance is again evaluated for the CT10, MSTW 2008 NLO, and NNPDF2.3 NLO PDF sets, individually. The final result is obtained from a combination of these results according to the PDF4LHC recommendations and depicted in Fig. 8.8 for the RPV $\tilde{\nu}_\tau$ signal. It drops from 1.6% at $M_{\tilde{\nu}_\tau} = 200$ GeV to 1% at $M_{\tilde{\nu}_\tau} = 500$ GeV and 0.5% at $M_{\tilde{\nu}_\tau} = 1.5$ TeV. This decline in the uncertainty in the acceptance is explained by the shrinking of the plateau in the leptons' η distributions as $M_{\tilde{\nu}_\tau}$ rises and the eμ pair is produced ever more centrally in the detector. The $\tilde{\nu}_\tau$ is produced via annihilation of a same-flavour valence quark/sea antiquark pair; similar to, albeit not exactly as a Z boson. The relative uncertainty in the acceptance of 1.6% at $M_{\tilde{\nu}_\tau} = 200$ GeV lies in the ballpark of the corresponding values of 1-2% [2] that have been obtained by the CMS collaboration in the Z boson cross section measurement in pp collisions at $\sqrt{s} = 8$ TeV using lepton pairs [196, 271].

Uncertainty in the signal selection efficiency

The uncertainty in the acceptance decreases with increasing signal mass, whereas the uncertainty in the trigger and lepton identification efficiencies increase. The treatment of the systematic uncertainty in the total signal selection efficiency $A \times \epsilon$ is simplified by assigning a constant relative uncertainty; based on the uncertainty band in Fig. 5.6 (right) for high mass values, a relative uncertainty of 5% is assigned.

---

[2] The different values for the uncertainty given in Ref. [271] correspond to different choices of the PDF set and analyzed Z boson decay channel (dimuon and dielectron channels with slightly different kinematic cuts).

Uncertainty in the luminosity

An uncertainty in the luminosity of 2.5% is assigned. This number has been derived in Ref. [252].

Uncertainty in the signal shape

In the RPV eμ resonance search, the signal shape is a peak in the $M_{\mathrm{e}\mu}$ distribution that is modelled with a Gaussian pdf. The uncertainty in the signal shape is obtained by varying the width σ from the default value obtained for each signal mass hypothesis from Eqn. 5.8 by the difference $\Delta\sigma_{\mathrm{align}}$ found when using different alignment scenarios in the simulation, as described in Sec. 5.4.1. The uncertainty is parameterized as

$$\begin{aligned}\frac{\Delta\sigma_{\mathrm{align}}}{\sigma} &= 0.018 &&, \text{ for } M_{\mathrm{res}} \leq 700\ \mathrm{GeV} \\ &= -0.12 + 0.21 \times \left(\frac{M_{\mathrm{res}}}{\mathrm{TeV}}\right) - 0.018 \times \left(\frac{M_{\mathrm{res}}}{\mathrm{TeV}}\right)^2 &&, \text{ for } M_{\mathrm{res}} > 700\ \mathrm{GeV}\ .\end{aligned} \tag{8.9}$$

In the eμ search for QBHs, a relative uncertainty in the muon p_{T} resolution of 30% is propagated to $M_{\mathrm{e}\mu}$ by smearing the default p_{T} value of the muon, as described in the treatment of this uncertainty for background processes in Sec. 8.1.1.

Chapter 9

Invariant mass of selected eμ pairs

Before turning to the key distribution of the eμ resonance search, the $M_{\mathrm{e}\mu}$ spectrum binned according to the $M_{\mathrm{e}\mu}$ resolution of resonantly produced eμ pairs, further cross checks of the background estimate are presented. To this end, the selected events are divided into subsamples that allow to disentangle different background processes and thus test whether the data reflects the expected background composition.

9.1 Invariant mass spectra split by charge and b-jet multiplicity

Since the $\mathrm{t\bar{t}}$ process yields the dominant background contribution, it is instructive to check the agreement between data and expectation for both the $M_{\mathrm{e}\mu}$ spectrum of selected events with a veto against b-tagged jets, and that of events containing at least one b-tagged jet. Furthermore, the main source of eμ pairs from SM processes, opposite-sign (OS), prompt dilepton ($\mathrm{e}^{\pm}\mu^{\mp}$) production via leptonic decays of a $\mathrm{W}^{+}\mathrm{W}^{-}$ pair, is strongly suppressed when the selected electron and muon are required to carry the same electric charge. Same-sign (SS) $\mathrm{e}^{\pm}\mu^{\pm}$ pairs are produced predominantly in processes with non-prompt or misidentified leptons. Therefore, the mass distribution of SS eμ pairs can be used to test the data-driven estimate of the sum of the W + jet and QCD multijet backgrounds that has been discussed in Sec. 6.2.3.

The eμ mass distributions of the four subsamples (OS with veto against b-tagged jets, OS with b-tagged jet, SS with veto against b-tagged jets, SS with b-tagged jet) are presented in Fig. 9.1 and discussed in the following. Since the focus in this section is put on cross checks of the background rather than the visualization of the peak from a possible resonant signal contribution, the binning of the $M_{\mathrm{e}\mu}$ spectra exceeds the mass resolution by at least a factor 2.5. The $M_{\mathrm{e}\mu}$ dependence of the fraction $N_{\mathrm{SS}}^{\mathrm{e}\mu}/N_{\mathrm{tot}}^{\mathrm{e}\mu}$ is evaluated in Sec. 9.1.3 as a byproduct of the described cross checks. Note that all results shown in this section that involve a selection of lepton charge represent cross checks of the background estimate for the baseline eμ selection without charge requirement. They do not represent complete measurements in their own right, ready for interpretation in terms of searches for new physics. This would require a careful evaluation of the charge misidentification probability for high-p_{T} electrons that is not included in this work.

9.1.1 Opposite-charge eμ pairs

Among all selected events observed in data 26840 involve an eμ pair with opposite electric charge and the background expectation yields 27300 ± 2200 (syst) events. The $M_{\mathrm{e}\mu}$ spectrum of OS eμ pairs with at least one b-tagged jet is depicted in Fig. 9.1 (top right). The background expectation for this subsample of eμ events is dominated by the $\mathrm{t\bar{t}}$ process with an additional 7% contribution of single-top tW production. As shown in the ratio plot, there is no evidence of a systematic shift in the shapes of the distributions obtained from data and simulation, up to the highest eμ masses where events are observed. There is also no indication for a flaw in the normalization of the background samples; the difference of 1.5% in the number of expected and observed events is covered within the 5% uncertainty in the $\mathrm{t\bar{t}}$ cross section (scale variations and PDF uncertainty) used for the scaling of the simulated $\mathrm{t\bar{t}}$ sample to luminosity, only.

In the $M_{\mathrm{e}\mu}$ spectrum of OS eμ pairs with a veto against b-tagged jets shown in Fig. 9.1 (top left), the $\mathrm{t\bar{t}}$ background still yields the largest contribution of any single background process. However, the contribution from other background processes is enhanced and contributes half of the events in this subsample. The WW background yields a fraction of 25%. Again, the difference in the number of expected and observed events of 3.5% is accommodated within the systematic uncertainties in the background cross sections. The ratio plot exhibits only a modest slope between $M_{\mathrm{e}\mu} = 60$ GeV and $M_{\mathrm{e}\mu} = 400$ GeV of about $-2.5 \pm 1.1\,(\mathrm{stat})\%$ per 100 GeV, that is not significant within the statistical uncertainties.

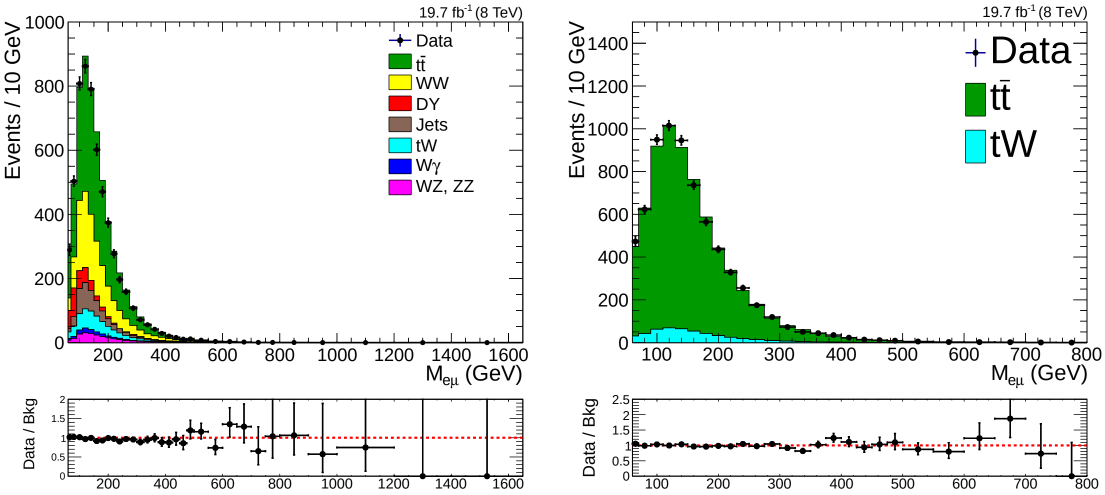

(a) OS eμ pairs, veto against b-tagged jets. (b) OS eμ pairs, ≥ 1 b-tagged jets.

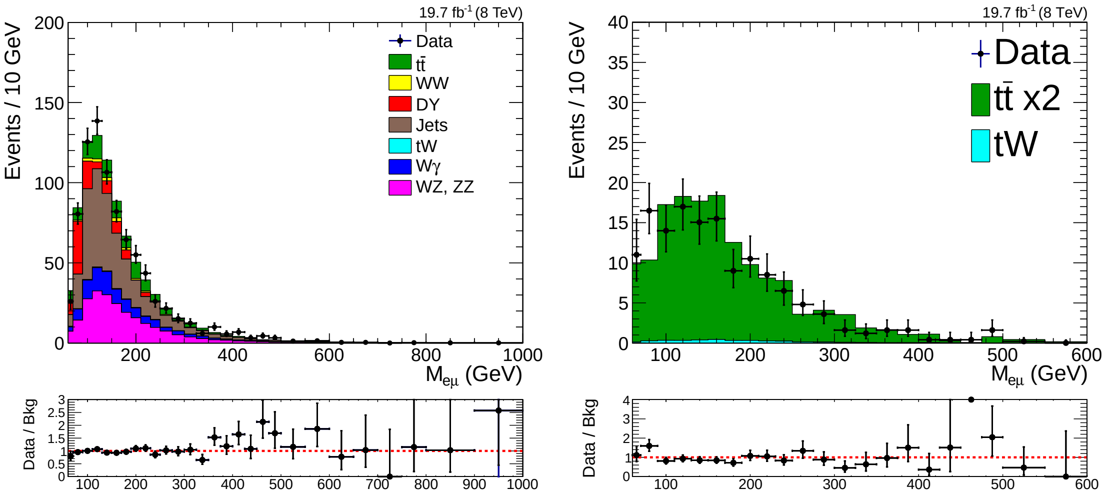

(c) SS eμ pairs, veto against b-tagged jets. (d) SS eμ pairs, ≥ 1 b-tagged jets.

Figure 9.1: The invariant mass of selected opposite charge (top) and same-charge (bottom) eμ pairs with b-jet veto (left) and selection of at least one b-jet (right). The $\mathrm{t\bar{t}}$ contribution to the same-charge spectrum obtained from simulation is enhanced by a factor of two as explained in the text.

9.1.2 Same-charge eμ pairs

The selected data sample of SS eμ pairs comprises 2085 events. Among those, 1782 pass the veto against b-tagged jets. The $M_{\mathrm{e}\mu}$ spectrum of these events is compared to the background expectation in Fig. 9.1 (bottom left). According to the background expectation, the dominant contribution to SS eμ events arises from the data-driven estimate of the W + jet and QCD multijet backgrounds (38%), followed by WZ and ZZ diboson production (26%), and the processes $\mathrm{t\bar{t}}$, Wγ, and Drell-Yan dilepton production (about 11%, each). The total expected background yield amounts to 1800 ± 300 (syst) events. Overall, data and background expectation are found to be in good agreement when considering that the dominant background process involves non-prompt or misidentified leptons and comes with sizeable systematic uncertainties. The ratio plot reveals an excess of the data over the background in a broad mass range from $M_{\mathrm{e}\mu} = 400$ GeV to 600 GeV. In this interval, 57 events are observed with 37 ± 10 (syst) expected.

The agreement between observation and expectation in the SS sample with b-jet veto is not reproduced when same-sign eμ pairs including at least one b-tagged jet are selected. According to simulations, this class of events is again dominated by $\mathrm{t\bar{t}}$ with negligible contributions from other processes. However, the expected background yield from $\mathrm{t\bar{t}}$ production only accounts for about half of the 303 observed events. Apart from charge misidentification in promptly produced eμ pairs, SS dilepton pairs arise in $\mathrm{t\bar{t}}$ events when electrons and muons from decays of B hadrons are selected. This imposes additional challenges on the background simulation compared to other background processes. When the $\mathrm{t\bar{t}}$ background sample is scaled up to match the observed number of events in this subsample, the distributions for event variables, such as $\not{E}_{\mathrm{T}}$, N_{jet}, and $N_{\mathrm{b-jet}}$ show good agreement between the $\mathrm{t\bar{t}}$ simulation and the data. The initial discrepancy in the event yield is therefore interpreted as an under-prediction by the $\mathrm{t\bar{t}}$ background simulation and compensated for by including an additional factor of two in the normalization of the $\mathrm{t\bar{t}}$ background sample in the same-sign subsamples. Importantly, this correction is only relevant for the evaluation of the same-sign fraction $N_{\mathrm{SS}}/N_{\mathrm{tot}}$ of selected eμ events, that is discussed in the following paragraph. It does not effect the result of the eμ resonance search significantly, where no selection of lepton charge is applied and the application of the additional scaling factor for $\mathrm{t\bar{t}}$ same-sign events increases the total background prediction by only one per cent. Therefore, no correction of the $\mathrm{t\bar{t}}$ same-sign event yield is included for the final estimate of the full $\mathrm{t\bar{t}}$ background contribution from simulation. The additional scaling factor of two is however applied in Figs. 9.1 (bottom, left and right) and 9.2.

9.1.3 Same-charge fraction of selected eμ pairs

The fraction of same-sign eμ events $N_{\mathrm{SS}}/N_{\mathrm{tot}}$ as a function of $M_{\mathrm{e}\mu}$ can be used to check whether the share of background processes that contribute to the selected eμ sample mainly via events with mis-identified or non-prompt leptons is correctly reproduced by the background estimate. This is particularly important at high $M_{\mathrm{e}\mu}$, where these backgrounds contribute up to one third of the total background estimate. The most relevant processes with non-prompt leptons are W + jet, Wγ, and QCD multijet, all of which come with sizeable uncertainties.

The fraction $N_{\mathrm{SS}}/N_{\mathrm{tot}}$ is shown in Fig. 9.2 (left) as a function of $M_{\mathrm{e}\mu}$ for the jet background estimate (W + jet and QCD multijet), Wγ production, and the two overall most important backgrounds, $\mathrm{t\bar{t}}$ and WW production. For the Wγ process, the same-sign fraction is compatible with 50% within the statistical uncertainties from the limited number of simulated events. In this case, an equal amount of OS and SS eμ pairs is expected because the selected electron arises from photon conversion or photon/charged hadron overlap - in both cases the charge associated with the selected track is independent of the muon's charge. In W + jet and QCD multijet events, the electric charges of the particles that result in the reconstructed leptons of the eμ pair are partly correlated, enhancing OS eμ production (for example $\mathrm{g}q$-initiated W + jet production or strong production of a $\mathrm{b\bar{b}}$ pair). Therefore, the same-sign fraction falls below 50%. This is visible in Fig. 9.2 for the jet background estimate that yields a same-sign fraction of about 42%.

The fraction of same-sign events is much smaller for $\mathrm{t\bar{t}}$ (2-3%) and WW production (1%). The comparison of the same-sign fractions obtained from data and simulation is shown in Fig. 9.2 (right). The observed value increases from 4% at $M_{\mathrm{e}\mu} \approx 50$ GeV to 14% in the mass region $M_{\mathrm{e}\mu} \geq 400$ GeV, where a total of 72 same-sign events is observed. This is expected because the contribution of the

W+jet and Wγ processes rises compared to that from other backgrounds as $M_{e\mu}$ is increased. For $M_{e\mu} \lesssim M_Z$, the same-sign fraction exhibits a bump. According to simulations, this effect is caused by $Z \to \mu^+\mu^-$ events, where one of the muons results in a reconstructed electron. No significant deviations between the measured same-sign fraction and the expectation are observed. There is no indication that the contribution of backgrounds that yield mainly eμ pairs with misidentified or non-prompt leptons differs significantly from the expectation.

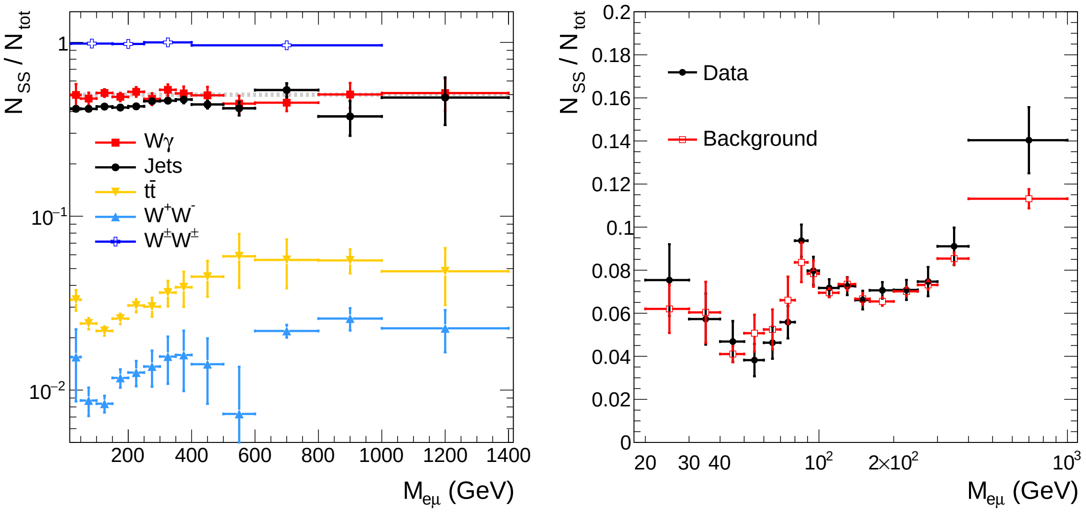

(a) Same-sign fraction of individual backgrounds.

(b) Observed and expected same-sign fraction.

Figure 9.2: The fraction of same-charge eμ pairs N_{SS}/N_{tot} for different backgrounds (left) and the comparison between data and the full background estimate (right). The vertical bars on the data points indicate the statistical uncertainty. The $t\bar{t}$ contribution to the same-charge spectrum obtained from simulation is enhanced by a factor of two as explained in the text.

9.2 Invariant mass spectrum of all selected events

The $M_{e\mu}$ spectrum of all 28925 selected events is shown for different binnings in Figs. 9.3 (left) and 9.4. The latter plot is binned according to the invariant mass resolution of resonantly produced eμ pairs that is discussed in Sec. 5.4, as is evident from the resolved signal peaks of the RPV $\tilde{\nu}_\tau$ signal for different $M_{\tilde{\nu}_\tau}$.

The comparison of observed event yields in different $M_{e\mu}$ ranges and the corresponding background expectation per process are shown in Tab. 9.1. The background composition depends considerably on $M_{e\mu}$: The $t\bar{t}$ contribution to the total background estimate drops from 69% in the mass region $M_{e\mu} < 200$ GeV to 25% for masses above 1 TeV. The overall second largest contribution arises from WW production and increases from 10% below 200 GeV to 25% above 1 TeV. In the same mass interval the relative contribution from backgrounds involving non-prompt or misidentified leptons (the data-driven jet background estimate and Wγ production) increases from 7% to 34%.

The $M_{e\mu}$ spectrum in Fig. 9.3 (left) and the corresponding cumulative distribution (right) exhibit two readily visible discrepancies between the data and background expectation for masses above 500 GeV. Between $M_{e\mu} = 600$ GeV and $M_{e\mu} = 700$ GeV, a slight excess over the background expectation is observed with 49 data events and 36 ± 5 (syst) expected events. Above $M_{e\mu} = 700$ GeV, however, the number of observed events is smaller than the expected event yield, as can be seen in the cumulative $M_{e\mu}$ distribution Fig. 9.3 (right); in total 17 events are observed and 27±4 (syst) are expected. When both systematic and statistical uncertainties are considered, the local significances of these discrepancies are below 2σ. Figures that focus on the high-mass region of the $M_{e\mu}$ distribution with systematic uncertainty bands are included in App. E.3, Fig. E.4.

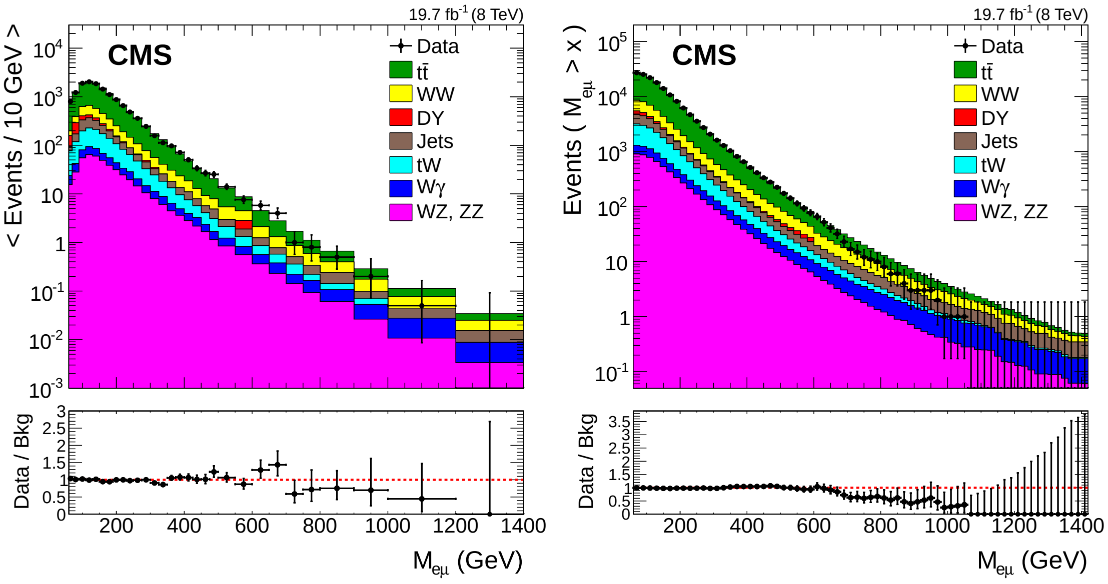

(a) The $M_{e\mu}$ spectrum.

(b) The cumulative $M_{e\mu}$ distribution.

Figure 9.3: Left: The $M_{e\mu}$ distribution of events passing the full event selection not binned according to the mass resolution. In the lower ratio plot, the black dots with vertical uncertainty bars indicate the data to background ratio and its statistical uncertainty. Right: The cumulative $M_{e\mu}$ distribution, where all events above the $M_{e\mu}$ value on the abscissa are summed. These figures are also included in Ref. [30].

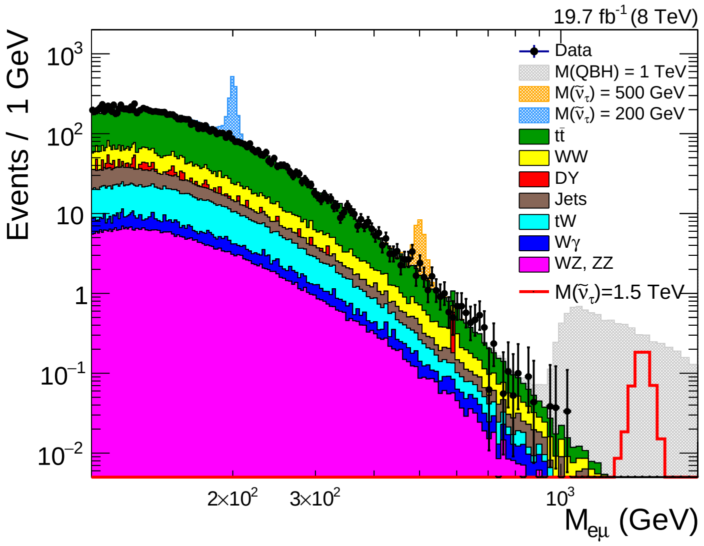

Figure 9.4: The $M_{e\mu}$ distribution of selected $e\mu$ pairs, binned according to the mass resolution for a resonantly produced $e\mu$ pair. Hypothetical contributions from the RPV $\tilde{\nu}_\tau$ signal are represented by three signal peaks for the points in parameter space $M_{\tilde{\nu}_\tau} = 200$ GeV, $\lambda = 0.01$; $M_{\tilde{\nu}_\tau} = 500$ GeV, $\lambda = 0.01$; and $M_{\tilde{\nu}_\tau} = 1.5$ TeV, $\lambda = 0.05$, where λ is a placeholder for $\lambda'_{311} = \lambda_{312} = \lambda_{321}$. The QBH signal is shown for the parameters $M_{\rm th} = 1$ TeV and $n = 0$.

The highest observed $M_{\mathrm{e}\mu}$ value is $1046 \pm 20\,(\delta p_{\mathrm{T}}^{\mu})$ GeV[1]. Inspecting the plot of the $M_{\mathrm{e}\mu}$ spectrum in Fig. 9.4 visually does not allow for a meaningful assessment of observed excesses above the background expectation. Significance scans of the $M_{\mathrm{e}\mu}$ distribution are obtained by algorithms that are based on the methods of statistical inference presented next.

		$M_{\mathrm{e}\mu}$ ranges in units of GeV				
	Total	< 200	200–400	400–600	600–1000	> 1000
$\mathrm{t\bar{t}}$	$20\,100 \pm 1800$	$15\,800 \pm 1400$	4050 ± 450	260 ± 44	30 ± 7	0.9 ± 0.4
WW	3150 ± 260	2400 ± 200	670 ± 64	68 ± 8	13 ± 2	0.9 ± 0.2
tW	2000 ± 160	1550 ± 120	430 ± 40	30 ± 3	4 ± 0.5	< 0.2
Jets	1570 ± 470	1250 ± 400	280 ± 83	30 ± 9	5 ± 2	0.6 ± 0.3
DY	960 ± 100	910 ± 100	40 ± 15	5 ± 5	< 1	< 0.1
WZ/ZZ	940 ± 80	670 ± 60	240 ± 20	27 ± 3	5 ± 0.6	0.3 ± 0.1
Wγ	480 ± 240	360 ± 180	100 ± 50	12 ± 6	3 ± 1.5	0.6 ± 0.3
Total bkg	$29\,200 \pm 2300$	$22\,900 \pm 1800$	5800 ± 560	430 ± 53	60 ± 9	3.5 ± 0.6
Data	28 925	22 736	5675	448	65	1

Table 9.1: Comparison of observed and expected event yields in five eμ mass ranges and the entire $M_{\mathrm{e}\mu}$ spectrum. The systematic uncertainty in the total background expectation can exceed the quadratic sum of the uncertainties in the individual background contributions due to correlations. This table is also included in Ref. [30].

---

[1] The uncertainty that is assigned to the measured $M_{\mathrm{e}\mu}$ value is obtained by propagating the uncertainty in the muon p_{T} from the muon track fit ($\delta p_{\mathrm{T}}^{\mu}/p_{\mathrm{T}}^{\mu} \approx 4\%$) to the mass of the e$\mu$ pair. This uncertainty is specific for this event and denoted by the symbol ($\delta p_{\mathrm{T}}^{\mu}$).

Chapter 10

Results of the search for new physics in the $e\mu$ mass spectrum

This section presents the statistical analysis of the measured $M_{\mathrm{e}\mu}$ spectrum and the resulting conclusions concerning the signal models under study. This encompasses the following steps:

1. Quantify the significance of observed excesses over the SM background expectation based on a statistical model for the signal (eμ resonance, peak in the $M_{\mathrm{e}\mu}$ spectrum) and background contributions.

2. If a significant excess is found, quantify its compatibility with different signal hypotheses.

3. In the absence of significant deviations, determine limits on the signal model parameters[1].

The employed methods of statistical inference are introduced in Sec. 10.1. The results of the statistical interpretation of the experimental findings in terms of the RPV $\tilde{\nu}_\tau$ model (scalar eμ resonance) are presented in Sec. 10.2 and those for the QBH model are given in Sec. 10.3.

10.1 Methods of statistical inference

This section outlines the statistical methods used in the interpretation of the experimental results. Since this work deals with searches for physics beyond the SM, the task at hand is that of testing the data $\boldsymbol{x}$ (the measured invariant mass spectrum $\mathrm{d}N/\mathrm{d}M$) against two hypotheses for the underlying theoretical model. The first model hypothesis is the SM or background-only hypothesis, referred to as H_{bkg} in the following. The second model hypothesis is the SM plus a signal contribution, with the signal either an eμ resonance as in the RPV $\tilde{\nu}_\tau$ model or the QBH signal. It is referred to as H_{sig}.

The significances and cross section limits presented below are calculated using software tools developed by others in CMS in the context of searches for the SM Higgs boson, that are based on the `RooStats` toolkit [272]. The latter uses several tools provided by the `RooFit` package, for example for the generation of pseudo-data or the determination of maximum likelihood parameter estimates via `MINUIT` [213]. Some technical detail on the implemented procedure for the computation of exclusion limits and a brief overview of different statistical approaches to the quantification of the significance of an excess are provided in Ref. [273]. Among the other references used to compile the summary of statistical methods in this section, Refs. [5, 274, 275] have been particularly helpful.

---

[1] Limits on model parameters may also be set if a significant excess is found (item (2)) but priority would be given to the interpretation of the excess in this case.

10.1.1 Signal models and likelihood

The data and both model hypotheses enter the statistical interpretation as binned mass spectra $\mathrm{d}N/\mathrm{d}M$ with a binning that is smaller than the mass resolution. The data is represented by the set of event counts $\boldsymbol{x} = \{x_i\}$, with i denoting the corresponding mass bin. Neglecting the impact of nuisance parameters for the moment, the signal and background contributions are modelled as follows:

- **Signal models**

  Both the resonance and QBH signal hypotheses are functions of two parameters; an assumed mass parameter M_{sig} and the observable signal event yield $s = \sigma_{\text{sig}} \cdot (A \times \epsilon) \cdot \mathcal{L}$.
  In the RPV $\tilde{\nu}_\tau$ model, the mass parameter is given by $M_{\text{sig}} = M_{\tilde{\nu}_\tau}$. The signal shape in the mass spectrum is a peak at the resonance mass that is modelled as a Gaussian distribution with a fixed width $\sigma_{\mathrm{e}\mu}(M_{\text{sig}})$ that is set to the mass resolution determined in Sec. 5.4. This model for the signal shape implies that the searched for resonance is narrow, $\Gamma_{\text{res}}(M_{\text{sig}}) \ll \sigma_{\mathrm{e}\mu}(M_{\text{sig}})$.
  In the search for QBHs, the signal shape is obtained as the $\mathrm{d}N/\mathrm{d}M$ spectrum from simulated samples and the threshold mass for QBH production is chosen as the signal mass parameter, $M_{\text{sig}} = M_{\text{th}}$.
  Since the shapes of the signal contributions to the mass spectrum are fixed for a given mass hypothesis M_{sig}, the hypothesis for the signal yield s fixes the signal event yields in mass bin i, s_i.

- **Background model**

  The background model is obtained directly from the sum of background contributions that are described in Sec. 6 and depicted (with a broader binning than used in the limit setting) in Fig. 9.4. The fixed number of expected background events in mass bin i is referred to as b_i.

The chosen parameter of interest in the statistical analysis is not the observable total signal event yield s but the so-called *signal strength modifier* μ that modifies the chosen signal cross section σ_{sig} such that the expected number of events per bin reads

$$n_i(\mu) = \mu s_i + b_i \ . \tag{10.1}$$

Likelihood

Both the expected signal contribution and the background expectation are affected by uncertainties and therefore the event yields per bin are functions of corresponding nuisance parameters $\boldsymbol{\nu} = \{\nu_1, ..., \nu_m\}$. With these definitions the likelihood function for the observation $\boldsymbol{x}$ assuming H_{sig} is given by

$$L(\boldsymbol{x}|\mu, \boldsymbol{\nu}) = \prod_{\substack{i \in \text{bins} \\ \text{search region}}} \frac{n_i\,(\mu,\, \boldsymbol{\nu})^{x_i}}{x_i!} \exp\left(-n_i(\mu,\, \boldsymbol{\nu})\right) \ , \tag{10.2}$$

where the product runs over all mass bins in the search region and the pdfs for the nuisance parameters that are introduced below in Eqn. 10.5 are suppressed. The corresponding likelihood for the background-only hypothesis H_{bkg} is obtained for $\mu = 0$. The search region is a function of the signal mass hypothesis M_{sig} and is defined differently in the eμ resonance and QBH searches.

Search regions

For the resonant signal, the considered mass range is

$$M_{\mathrm{e}\mu} \in \begin{cases} [0,\, M_{\mathrm{sig}} + 440\ \mathrm{GeV}] & \text{for } M_{\mathrm{sig}} \leq 440\ \mathrm{GeV} \\ [M_{\mathrm{sig}} \pm 440\ \mathrm{GeV}] & \text{for } M_{\mathrm{sig}} > 440\ \mathrm{GeV},\ 6 \times \sigma_{\mathrm{e}\mu}(M_{\mathrm{sig}}) < 440\ \mathrm{GeV} \\ [M_{\mathrm{sig}} \pm 6 \times \sigma_{\mathrm{e}\mu}(M_{\mathrm{sig}})] & \text{for } 6 \times \sigma_{\mathrm{e}\mu}(M_{\mathrm{sig}}) \geq 440\ \mathrm{GeV} \end{cases} , \tag{10.3}$$

where $\sigma_{\mathrm{e}\mu}$ denotes the $M_{\mathrm{e}\mu}$ resolution. The size of the search region of $\Delta M = 440$ GeV is motivated in Sec. 5.1.1 with a definition of the signal cross section in mind that does not depend strongly on finite-width effects. This argument does not take into account the detector resolution as an additional limiting factor; restricting the size of the search region to values below $\mathcal{O}(5)$ times the $M_{\mathrm{e}\mu}$ resolution would introduce an additional acceptance cut affecting the signal selection efficiency and is unreasonable. Therefore, the definition of the search region is changed for high signal masses from the theory-inspired choice of $\Delta M = 440$ GeV to the detector-inspired criterion $\Delta M(M_{\mathrm{sig}}) = 6 \times \sigma_{\mathrm{e}\mu}(M_{\mathrm{sig}})$. Since the relative $M_{\mathrm{e}\mu}$ resolution is small (less than 5% for signal masses below 2 TeV), the change in the definition of the search region occurs at high signal masses, $M_{\mathrm{sig}} \approx 1.8$ TeV.

In the QBH search, the search region is defined by a one-sided cut below the threshold mass M_{th} as

$$M_{\mathrm{e}\mu} \in \left[M_{\mathrm{th}} - 6 \times \sigma_{\mathrm{e}\mu},\, \sqrt{s} = 8\ \mathrm{TeV}\right] . \tag{10.4}$$

10.1.2 Bayesian limit setting

Exclusion limits are calculated based on the Bayesian approach described in Refs. [5, 273]. The *posterior probability* distribution for the parameter of interest μ and nuisance parameters $\boldsymbol{\nu}$ given the measurement $\boldsymbol{x}$, $P_\nu(\mu, \boldsymbol{\nu}|\boldsymbol{x})$, is given by the likelihood (Eqn. 10.2), the *prior probability distribution* for the signal strength parameter, $\pi_\mu(\mu)$, and the combined pdf for the nuisance parameters $\rho_{\mathrm{comb}}(\boldsymbol{\nu})$ as

$$P_\nu(\mu, \boldsymbol{\nu}|\boldsymbol{x}) = \frac{L(\boldsymbol{x}|\mu, \boldsymbol{\nu}) \times \rho_{\mathrm{comb}}(\boldsymbol{\nu}) \times \pi_\mu(\mu)}{\int \mathrm{d}\mu' \int \mathrm{d}\boldsymbol{\nu}' L(\boldsymbol{x}|\mu', \boldsymbol{\nu}') \times \rho_{\mathrm{comb}}(\boldsymbol{\nu}') \times \pi_\mu(\mu')} . \tag{10.5}$$

The different sources of uncertainties represented by the nuisance parameters are assumed to be uncorrelated, such that the combined prior function factorizes, $\rho_{\mathrm{comb}}(\boldsymbol{\nu}) = \prod_j \rho_j(\nu_j)$. The prior probability distribution for the signal strength is taken to be uniform for $\mu \geq 0$ and zero otherwise. The treatment of the systematic uncertainties and the assigned pdfs $\rho_j(\nu_j)$ are described separately in the following section. Once they are specified, the posterior probability distribution for the parameter of interest μ given the measurement $\boldsymbol{x}$, $P(\mu|\boldsymbol{x})$, is obtained by integrating over the nuisance parameters [273]

$$P(\mu|\boldsymbol{x}) = \int \prod_j \mathrm{d}\nu_j P_\nu(\mu, \boldsymbol{\nu}|\boldsymbol{x}) . \tag{10.6}$$

This integration is carried out using Markov Chain Monte Carlo techniques (Metropolis-Hastings algorithm) [276, 277]. The upper bound on the signal strength modifier $\mu_{\mathrm{up}}^{\mathrm{CL}}$ at confidence level (CL) $1 - \alpha$ is then obtained by solving the equation

$$\int_0^{\mu_{\mathrm{up}}^{\mathrm{CL}}} \mathrm{d}\mu\, P(\mu|\boldsymbol{x}) = 1 - \alpha = 0.95\,(0.90) , \tag{10.7}$$

where the values on the right define the 95% (90%) CLs that are used in the following (the 90% CL is evaluated in order to be able to compare to results from indirect searches).

Treatment of systematic uncertainties

The pdfs $\rho_j(\nu_j)$ in Eqn. 10.5 constrain the nuisance parameters. In this work, these distributions are not obtained from auxiliary measurements and rather represent models for the description of systematic uncertainties.

As described in the context of the estimation of systematic uncertainties in Sec. 8, two types of uncertainties are distinguished from one another, depending on whether they are assumed to affect the event yields in all bins in the mass spectrum $\mathrm{d}N/\mathrm{d}M$ via the same factor (*scaling uncertainties*) or in a mass-dependent way (*shape uncertainties*)[2].

The pdfs of nuisance parameters associated with scaling uncertainties are modelled with a log-normal pdf as described in Ref. [273]. An example is the uncertainty in the luminosity that affects the background estimates obtained from simulations and the expected signal event yield by 2.5%, irrespective of the mass value.

The pdfs of nuisance parameters associated with spectral uncertainties are obtained by a *vertical template morphing* technique, see Refs. [278, 279].

Expected exclusion limits

Expected limits are obtained by generating toy Monte Carlo pseudo-data for the background-only hypothesis ($\mu = 0$). For each set of pseudo-data $\boldsymbol{x}_k^{\mathrm{toy}}$, the exclusion limit $\mu_{\mathrm{up}}^{\mathrm{CL}}$ is evaluated according to Eqns. 10.5-10.7. The *expected limit* is defined in the following as the median of the resulting sampling distribution of $\mu_{\mathrm{up}}^{\mathrm{CL}}$. In addition, the values of $\mu_{\mathrm{up}}^{\mathrm{CL}}$ corresponding to the 68% and 95% quantiles of the sampling distribution are evaluated.

10.1.3 The profile likelihood ratio and the quantification of an excess

In contrast to the limit setting that is based on Bayesian inference, the quantification of excesses over the background expectation is carried out in a frequentist context, using the *profile likelihood* approach. Again, the calculations are carried out with software tools developed within the CMS collaboration in the context of searches for the SM Higgs boson. This summary of the underlying statistical methods is largely based on Ref. [275], in which the formulae for likelihood-based test statistics are derived that are used in the scan of the $M_{\mathrm{e}\mu}$ spectrum for signs of localized peaks.

P-value for H_{bkg} and the significance of an excess

The characterization of an observed deviation from the expected background starts with the evaluation of the probability to obtain data with equal or greater incompatibility with the background expectation under the background-only hypothesis H_{bkg}. This *p-value* for H_{bkg} is denoted p_0 and obtained by evaluating the observed value of a suitable test statistic q_0 defined below with pdf $f(q_0|H_{\mathrm{bkg}})$

$$p_0 = \int_{q_0^{\mathrm{obs}}}^{\infty} \mathrm{d}q_0 \, f(q_0|H_{\mathrm{bkg}}) \ . \tag{10.8}$$

Only observed excesses, in contrast to deficits, are regarded as evidence against H_{bkg} in the following because in the case at hand there is no interference term between the SM background and the eμ signal processes that may lead to cancellations in the total cross section. The *significance* Z_0 (or *z-score*) of the excess is then defined by interpreting p_0 as the one-sided tail probability of the normal distribution and solving

$$p_0 = \int_{Z_0}^{\infty} \mathrm{d}x \, \frac{1}{\sqrt{2\pi}} \exp(-x^2/2) \ \Rightarrow \ Z_0 = \Phi^{-1}(1 - p_0) \ , \tag{10.9}$$

where Φ^{-1} is the inverse of the cumulative distribution of the standard Gaussian. In high-energy physics, values of the significance of $Z_0 = 3$ (3σ level) and $Z_0 = 5$ (5σ level) are typically chosen

---

[2] The term shape uncertainties is used here for any uncertainty that leads to distortions of the shape of the mass spectrum $1/N_{\mathrm{tot}} \times \mathrm{d}N/\mathrm{d}M$. These distortions may also change the total event yield N_{tot}.

as a necessary condition to claim *evidence* for and the *discovery* of a new phenomenon beyond the SM (H_{bkg}), respectively[3].

The profile likelihood test statistic q_0

The profile likelihood ratio used to obtain the significance is defined as

$$\lambda(\mu) = \frac{L(\boldsymbol{x}|\mu, \hat{\hat{\boldsymbol{\nu}}})}{L(\boldsymbol{x}|\hat{\mu}, \hat{\boldsymbol{\nu}})} \ , \tag{10.10}$$

where $\hat{\hat{\boldsymbol{\nu}}}$ denotes the set of nuisance parameters that maximizes the likelihood under the assumption of the signal strength μ and $\{\hat{\mu}, \hat{\boldsymbol{\nu}}\}$ is the set of parameters that maximizes the likelihood when both the parameter of interest and the nuisance parameters are varied. Based on the definition of the likelihood ratio in Eqn. 10.10 the test statistic q_0 for the discovery of a signal with positive event yield is chosen as [275]

$$q_0 = \begin{cases} -2\ln\lambda(0) & \hat{\mu} \geq 0 \\ 0 & \hat{\mu} < 0 \end{cases} \ . \tag{10.11}$$

Setting q_0 to zero for a negative maximum likelihood estimator of the signal strength $\hat{\mu}$ reflects the assumption that the signal contribution to the event yield is positive; only positive values of $\hat{\mu}$ are regarded as evidence against H_{bkg}.

In the limit of large sample size $N \to \infty$ (asymptotic limit), the pdf for q_0 under the assumption of H_{bkg}, $f(q_0|H_{\mathrm{bkg}})$, is found to be a *half chi-square distribution* for one degree of freedom [275] by using the Wald approximation [281]

$$f(q_0|H_{\mathrm{bkg}}) = \frac{1}{2}\delta(q_0) + \frac{1}{2}\frac{1}{\sqrt{2\pi}}\frac{1}{\sqrt{q_0}}\exp(-q_0/2) \ . \tag{10.12}$$

The p-value for H_{bkg} evaluated according to Eqn. 10.8 is then given by [275]

$$p_0 = 1 - \Phi\left(\sqrt{q_0}\right) \tag{10.13}$$

and the significance (Eqn. 10.9) takes on the simple form

$$Z_0 = \sqrt{q_0} \ . \tag{10.14}$$

The formula for the significance is obtained in the large sample limit but has been shown to provide satisfactory results in the case of small event counts as well [273]. This is important for the significance scan in the eμ resonance search presented in the following because event yields at high $M_{\mathrm{e}\mu}$ are low.

---

[3] These arbitrary thresholds depend on the exact definition of the significance and the search being performed. In the case of the eμ resonance search, that is performed over a large range of hypothetical signal masses, the significance should certainly be corrected for the *look-elsewhere-effect* [280] for a 3σ deviation to be considered as evidence for a signal.

10.2 Search for narrow resonances

The presentation of the results starts in Sec. 10.2.1 with a significance scan of the $M_{e\mu}$ spectrum. The assumed signal shape is a Gaussian peak at mass M_{res} (corresponding to an eμ resonance model). The signal shape is generic in this case, but the resulting significances may be interpreted in terms of the RPV $\tilde{\nu}_\tau$ signal model.
In a second step, exclusion limits are set on the signal cross section of the RPV $\tilde{\nu}_\tau$ model as a function of the signal mass hypothesis $M_{\tilde{\nu}_\tau}$ in Sec. 10.2.2. These limits are specific to the $\tilde{\nu}_\tau$ model with production coupling λ'_{311} and the corresponding $\mathrm{d}\overline{\mathrm{d}}$ initial state. Finally, mentioned cross section bounds are re-interpreted in terms of other RPV $\tilde{\nu}_\tau$ models that also involve an eμ resonance in the final state but different RPV Yukawa couplings λ'_{3jk} for its production and, correspondingly, different initial states.

10.2.1 Local significance for narrow eμ resonance signal model

The significance of excesses over the background expectation evaluated with the likelihood for the RPV $\tilde{\nu}_\tau$ signal model as a function of $M_{\tilde{\nu}_\tau}$ is shown in Fig. 10.1. The hypothetical resonance mass is incremented in this significance scan in steps that are smaller than the $M_{e\mu}$ resolution evaluated at $M_{\tilde{\nu}_\tau}$. The maximum significance found over the entire probed mass range is about 2.2σ at $M_{\tilde{\nu}_\tau} = 278$ GeV. This value represents the *local significance*, i.e. it is not corrected for the trial factor that would account for the fact that several signal mass hypotheses with non-overlapping signal pdfs have been probed when scanning the $M_{e\mu}$ spectrum (for details about this so-called *look elsewhere effect* see Ref. [280]). Given that the observed maximum local significance does not indicate evidence for a signal, the significances are not recalculated including the trial factor.

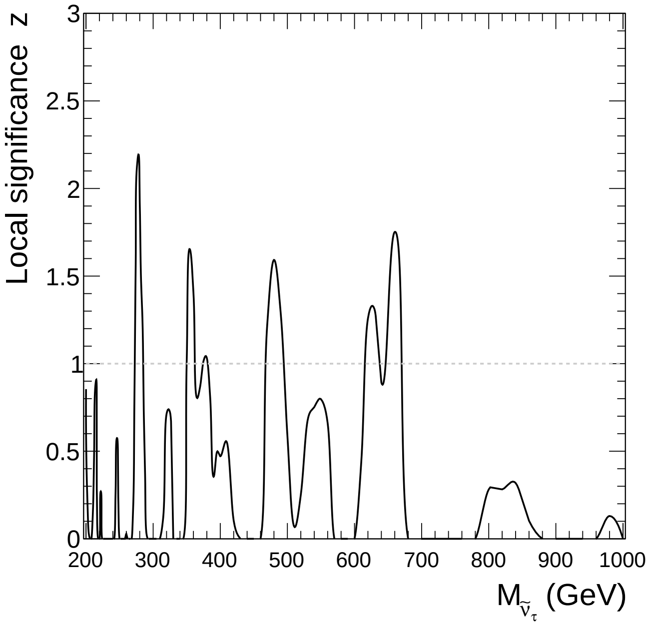

Figure 10.1: The significance, or z-score, of excesses over the background expectation observed in data as a function of the resonance mass hypothesis. These are the local significance values that are not corrected for the look-elsewhere effect.

10.2.2 Exclusion limits

With no significant excess observed in data with respect to the background expectation, exclusion limits are set on the product of signal cross section and branching fraction of the decay into the eμ final state and exclusion boundaries in the parameter spaces of the considered models of new physics are derived. The presentation of the results is structured as follows:

First, the cross section limits for narrow scalar resonances are shown in the following paragraph. These are then translated into bounds in the parameter space of the RPV $\tilde{\nu}_\tau$ model with the non-zero Yukawa couplings λ'_{311} and $\lambda_{312} = \lambda_{321}$. Finally, the impact of the experimental findings on RPV $\tilde{\nu}_\tau$ models with a different production mode of the resonance, i.e. a different choice for the non-zero production coupling λ'_{3jk}, is discussed. All these results are put into context by comparing them to the outcome of other searches for cLFV involving electrons and muons both at high-energy colliders and lower-energy facilities.

Before turning to the presentation of the exclusion limits, a clarification concerning the treatment of theoretical uncertainties in the inclusive signal cross sections is in order: As described in the context of the discussion of the systematic uncertainties in the signal contribution in Sec. 8.2, the theoretical uncertainties (PDF, renormalization and factorization scale uncertainties) in the inclusive signal cross section are not included in the calculation of the cross section limits and they are not included in the cross section curves in figures such as Fig. 10.2, either. These uncertainties do not affect the excluded signal cross section but merely the translation of cross section limits into exclusion bounds in the parameter space of a given signal model. This additional uncertainty in the derivation of the exclusion limits on model parameters is neglected in the following; the bounds on parameters such as the signal mass presented in the following are obtained assuming the (exact) cross sections calculated as outlined in Secs. 1.1 and 1.2 and documented for various choices of model parameters in App. C.

Cross section limits

The observed limits on the product of the narrow resonance signal cross section and the branching fraction of the decay into the eμ final state at 95% CL are given in Fig. 10.2 (left) in the signal mass range from 200 GeV to 2 TeV together with the median expected limit and its 1σ and 2σ uncertainty bands.

The observed upper limits on the signal cross section range from 13 fb at $M_{\tilde{\nu}_\tau} = 200$ GeV to 0.24 fb at $M_{\tilde{\nu}_\tau} = 1.2$ TeV. The corresponding median expected limits read 9.0 fb and 0.30 fb, respectively. For $M_{\tilde{\nu}_\tau} \geq 1.2$ TeV, the cross section limit varies only very slowly with the slightly falling signal efficiency towards higher masses, that is discussed in Sec. 5.3. The signal efficiency is the key parameter in the cross section limit calculation in this high-mass region because the background expectation in the mass region $M_{\tilde{\nu}_\tau} \geq 1.2$ TeV is very small (below one event) and no event is observed in data. The variation of the observed cross section limit as a function of the probed signal mass is more pronounced at lower masses, where the number of expected and observed events is sizeable and the detector resolution, that determines the width of the peak of the hypothetical narrow resonance signal, is small. As the signal mass and with it the $M_{\mathrm{e}\mu}$ resolution increase, the number of local extrema of the observed limit curve per mass interval decreases. A zoom into the low-mass region of the limit plot between $M_{\tilde{\nu}_\tau} = 200$ GeV and $M_{\tilde{\nu}_\tau} = 400$ GeV is shown in Fig. 10.2 (right) in order to illustrate the variations of the observed cross section limit in this region. The observed limit curve is almost fully contained within the 2σ band around the median expected limit. A comprehensive compilation of the observed and expected cross section limits in the signal mass range from $M_{\tilde{\nu}_\tau} = 200$ GeV to $M_{\tilde{\nu}_\tau} = 2$ TeV evaluated at both 95% CL and 90% CL is given in Tab. E.1 App. E. These cross section bounds obtained at $\sqrt{s} = 8$ TeV can be compared directly to the limits from the ATLAS search for LFV resonances at the same centre-of-mass energy, reported in Ref. [31]. The signal cross section for the RPV $\tilde{\nu}_\tau$ model is included in Fig 10.2 (left) for $\lambda'_{311} = \lambda_{312} = \lambda_{321} = 0.01$, yielding a lower bound on $M_{\tilde{\nu}_\tau}$ of 1.28 TeV at

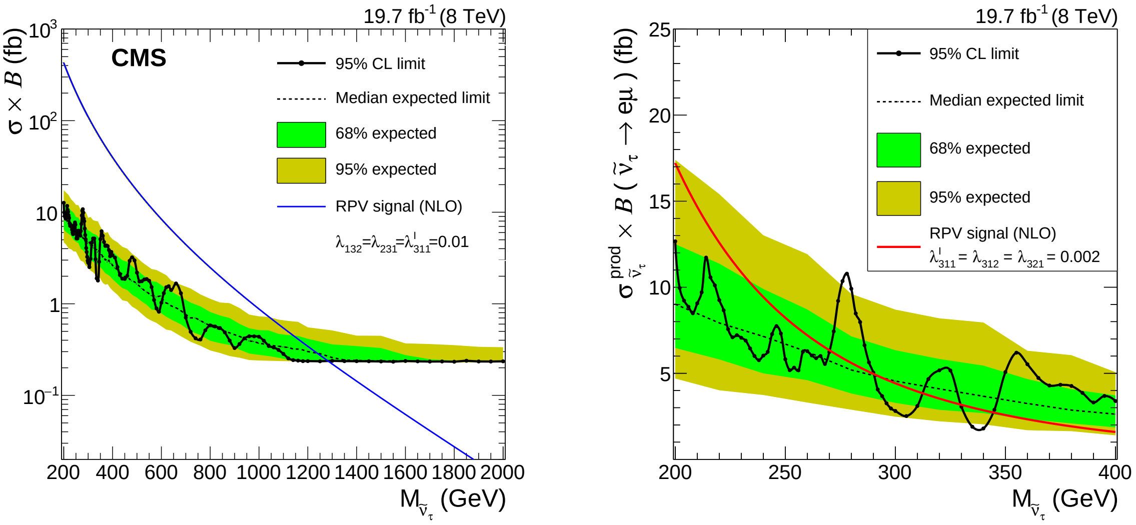

(a) Cross section limits in the mass range 200 GeV $\leq M_{\tilde{\nu}_\tau} \leq$ 2 TeV. A curve representing the signal cross section is shown for the RPV couplings $\lambda'_{311} = \lambda_{312} = \lambda_{321} = 0.01$. This figure is also included in Ref. [30].

(b) Zoom of the cross section limit plot in the range 200 GeV $\leq M_{\tilde{\nu}_\tau} \leq$ 400 GeV. A curve representing the signal cross section is shown for the RPV couplings $\lambda'_{311} = \lambda_{312} = \lambda_{321} = 0.002$.

Figure 10.2: The observed and expected 95% CL exclusion limits on the product of $\tilde{\nu}_\tau$ production cross section and the branching fraction of its decay into the $e\mu$ final state as a function of the signal mass hypothesis.

95% CL. For the Yukawa couplings $\lambda'_{311} = 0.11$ and $\lambda_{312} = \lambda_{321} = 0.07$, the observed mass limit reaches 2.30 TeV and the search by the ATLAS collaboration at $\sqrt{s} = 8$ TeV reports a bound of 2.0 TeV. Lower bounds on $M_{\tilde{\nu}_\tau}$ are set for further values of the involved RPV Yukawa couplings and documented in Tab. 10.1. A mass limit of 270 GeV, close to the lower edge of the probed resonance mass interval, is obtained for the coupling choice $\lambda'_{311} = \lambda_{312} = \lambda_{321} = 0.002$. The total decay width of the $\tilde{\nu}_\tau$ for these model parameters is about 0.1 MeV, such that the eμ pair in the final state is still produced promptly.

Apart from considering the uncertainty in the expected limit, it is instructive to quantify the impact of the systematic uncertainties in the observed limit. To this end, the observed limit is recalculated without the systematic uncertainties in the background and signal contributions and compared to the full limit calculation in Fig. 10.3. The importance of including the systematic uncertainties is illustrated by the signal cross section curve for the couplings $\lambda'_{311} = \lambda_{312} = \lambda_{321} = 0.003$; the mass limit obtained for these parameters lies 100 GeV above the actual value if the systematic uncertainties are ignored.

Table 10.1: The 95% CL lower limits on $M_{\tilde{\nu}_\tau}$ for seven choices of the RPV couplings λ'_{311} and $\lambda_{312} = \lambda_{321}$. The median expected limit is shown together with the boundaries of the corresponding 1σ uncertainty band.

RPV coupling strengths	95% CL lower limits on $M_{\tilde{\nu}_\tau}$ (TeV) Observed	 Median expected	 $+1\sigma$	 -1σ
$\lambda'_{311} = \lambda_{312} = \lambda_{321} = 0.002$	0.27	0.29	0.35	0.23
$\lambda'_{311} = \lambda_{312} = \lambda_{321} = 0.005$	0.65	0.83	0.93	0.71
$\lambda'_{311} = \lambda_{312} = \lambda_{321} = 0.01$	1.28	1.24	1.28	1.14
$\lambda'_{311} = \lambda_{312} = \lambda_{321} = 0.02$	1.61	1.61	1.62	1.56
$\lambda'_{311} = \lambda_{312} = \lambda_{321} = 0.05$	2.07	2.07	2.07	2.06
$\lambda'_{311} = 0.1$, $\lambda_{312} = \lambda_{321} = 0.05$	2.16	2.16	2.16	2.15
$\lambda'_{311} = 0.11$, $\lambda_{312} = \lambda_{321} = 0.07$	2.30	2.30	2.30	2.30
$\lambda'_{311} = \lambda_{312} = \lambda_{321} = 0.1$	2.42	2.42	2.42	2.41

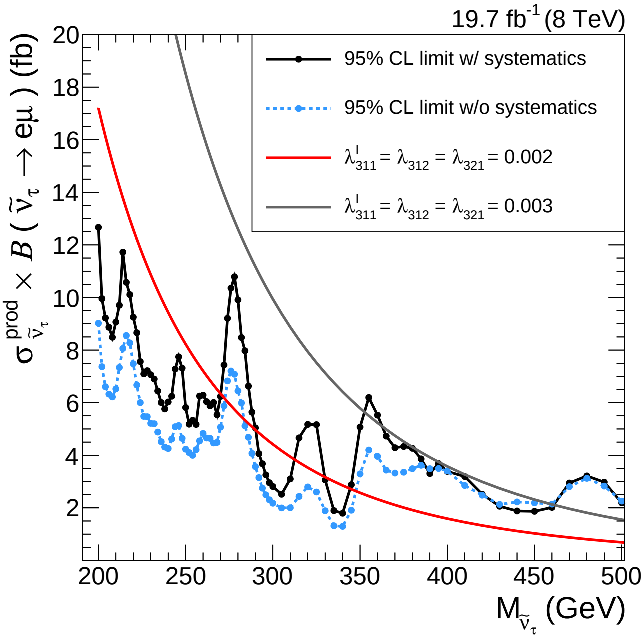

Figure 10.3: The observed 95% CL exclusion limits on the product of $\tilde{\nu}_\tau$ production cross section and the branching fraction of its decay into the $e\mu$ final state calculated with (black solid line) and without (light blue dashed line) systematic uncertainties.

Exclusion boundaries in the parameter space of the RPV $\tilde{\nu}_\tau$ model

Using the narrow width approximation formula of the RPV signal cross section, the cross section limit is translated into exclusion bounds in the $(M_{\tilde{\nu}_\tau}, \lambda'_{311})$ plane of the parameter space of the RPV model for fixed values of the couplings responsible for the $\tilde{\nu}_\tau$ decay into an eμ pair, $\lambda_{312}^{\text{fix}} = \lambda_{321}^{\text{fix}}$. As discussed in Sec. 1.1.2, the NWA of the signal cross section can be factorized into a term that only depends on the $\tilde{\nu}_\tau$ mass and a term that reflects the dependence on the coupling parameters:

$$(\sigma \cdot \mathcal{B})_{\text{NWA}} \quad = \quad k(M_{\tilde{\nu}_\tau}) \frac{\left(\lambda'_{311}\right)^2 \left[\left(\lambda_{312}^{\text{fix}}\right)^2 + \left(\lambda_{321}^{\text{fix}}\right)^2\right]}{3\left(\lambda'_{311}\right)^2 + \left[\left(\lambda_{312}^{\text{fix}}\right)^2 + \left(\lambda_{321}^{\text{fix}}\right)^2\right]} \tag{10.15}$$

$$\underset{\lambda_{312}^{\text{fix}}=\lambda_{321}^{\text{fix}}}{=} \quad k(M_{\tilde{\nu}_\tau}) \frac{2\left(\lambda'_{311}\right)^2 \left(\lambda_{312}^{\text{fix}}\right)^2}{3\left(\lambda'_{311}\right)^2 + 2\left(\lambda_{312}^{\text{fix}}\right)^2} \tag{10.16}$$

$$\underset{\lambda'_{311}\gg\lambda_{312}^{\text{fix}}}{\rightarrow} \quad 2\,k(M_{\tilde{\nu}_\tau})\left(\lambda_{312}^{\text{fix}}\right)^2 / \,3 \equiv \ (\sigma \cdot \mathcal{B})_{\max}\left(M_{\tilde{\nu}_\tau}, \lambda_{312}^{\text{fix}}\right). \tag{10.17}$$

If the observed cross section limit $(\sigma \cdot \mathcal{B})_{\text{obs}}$ lies above the cross section $(\sigma \cdot \mathcal{B})_{\max}$ for a given parameter pair $(M_{\tilde{\nu}_\tau}, \lambda_{312}^{\text{fix}})$, no limit on λ'_{311} can be set for that point in parameter space. Otherwise, the observed limit on λ'_{311} is given by

$$\lambda'_{311} = \sqrt{\frac{2\,(\sigma \cdot \mathcal{B})_{\text{obs}}\left(\lambda_{312}^{\text{fix}}\right)^2}{2\,k(M_{\tilde{\nu}_\tau})\left(\lambda_{312}^{\text{fix}}\right)^2 - 3\,(\sigma \cdot \mathcal{B})_{\text{obs}}}}\,, \tag{10.18}$$

according to Eqn. 10.16. The resulting 95% CL exclusion boundaries in the $(M_{\tilde{\nu}_\tau}, \lambda'_{311})$ plane are shown in Fig. 10.4 with a comparison to the corresponding limits from CMS dijet searches. The dijet signal in the chosen RPV $\tilde{\nu}_\tau$ model is represented by the Feynman diagram in Fig. 10.5 that, in contrast to the eμ signal, only involves the Yukawa coupling λ'_{311}. The other non-zero couplings in the model, λ_{312} and λ_{321}, enter the dijet cross section of the $\tilde{\nu}_\tau$ model via the total decay width of the $\tilde{\nu}_\tau$. Replacing the branching fraction $\mathcal{B}(\tilde{\nu}_\tau \to \text{e}\mu)$ in Eqn. 10.15 with the branching fraction of the $\tilde{\nu}_\tau$ decay into the dijet final state yields the dijet cross section in the narrow width approximation:

$$(\sigma \cdot \mathcal{B})_{\text{NWA}}^{\text{dijet}} = k(M_{\tilde{\nu}_\tau}) \frac{3\left(\lambda'_{311}\right)^4}{3\left(\lambda'_{311}\right)^2 + \left[\left(\lambda_{312}^{\text{fix}}\right)^2 + \left(\lambda_{321}^{\text{fix}}\right)^2\right]}\,. \tag{10.19}$$

The searches for dijet resonances carried out with the CMS experiment at the LHC at $\sqrt{s} = 8$ TeV [95,282] and $\sqrt{s} = 13$ TeV [96] in the running periods in 2012 and 2015, respectively, do not include an interpretation in terms of the RPV model discussed here. The results are however presented with a level of detail that allows for a reinterpretation in terms of other models. The following reinterpretation is based on the two searches at $\sqrt{s} = 8$ TeV; the baseline search for dijet resonances using the full CMS data format and focussing on high dijet masses ($M_{\text{res}} \geq 1.2$ TeV) [95], and a search extending to lower masses ($M_{\text{res}} \geq 0.5$ TeV) by utilizing the technique of data scouting [282]. The cross section exclusion limits are given in both cases at 95% CL on $\sigma \times \mathcal{B} \times A$, the product of resonance production cross section, branching fraction into the dijet final state, and acceptance of the dijet pair at parton level. They are furthermore provided for different two-parton final states, and, in the case of the high-mass search, for different decay widths of the resonance. In the following, the limits for narrow quark-(anti)quark resonances are used. In order to compare them to the limits derived above on $\sigma \times \mathcal{B}$, the acceptance A of the RPV $\tilde{\nu}_\tau$ model in the dijet search is estimated by applying the dijet selection cuts to the two final state leptons

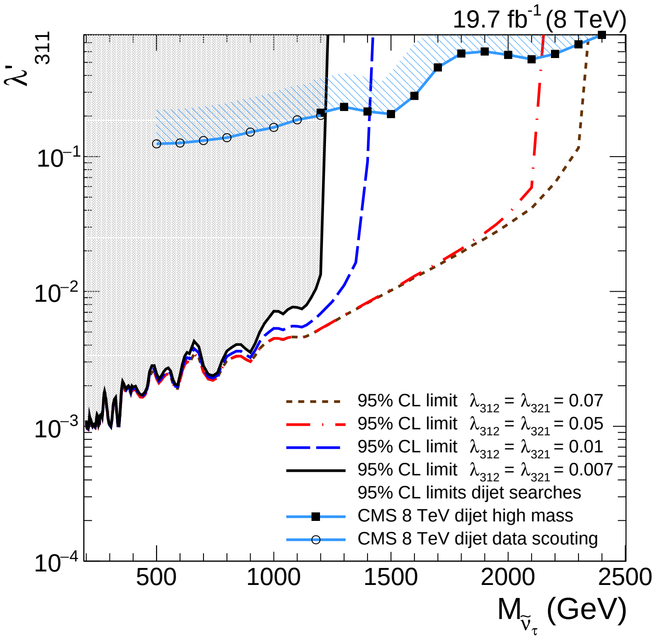

Figure 10.4: The 95% observed limit boundaries in the $(M_{\tilde{\nu}_\tau}, \lambda'_{311})$ plane of the RPV model for four fixed values of the third parameter $\lambda_{312} = \lambda_{321}$: 0.007, 0.01, 0.05, and 0.07. These bounds are compared to the results from a reinterpretation of dijet searches by the CMS collaboration [95, 282] that are represented by the two curves with markers. The areas in parameter space above the curves are excluded, as exemplified by the shaded regions.

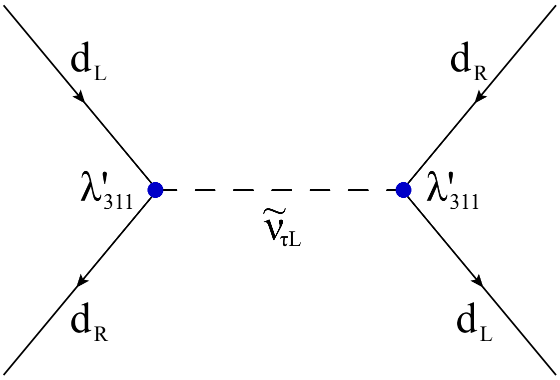

Figure 10.5: Feynman graph for resonant tau sneutrino production in $d\,\bar{d}$ annihilation and subsequent decay into a $d\,\bar{d}$ pair.

in the eμ resonance signal samples at parton level. The following cuts are applied: In both dijet searches, the two jets in the final state are required to have a pseudorapidity of $|\eta| < 2.5$ and a transverse momentum of $p_{\mathrm{T}} > 30$ GeV. The separation in pseudorapidity of the two jets $|\Delta\eta_{jj}|$ has to be less than 1.3 in both cases. According to Ref. [282], the effect of the cut on the dijet mass at 390 GeV is already taken into account in the limits provided by the search with data scouting, and is therefore not included when calculating the corresponding acceptance. In the case of the high-mass search, the mass cut at 890 GeV is included in the acceptance calculation. The resulting acceptances range from 56% at $M_{\tilde{\nu}_\tau} = 0.5$ TeV to 57% at $M_{\tilde{\nu}_\tau} = 1.2$ TeV for the low-mass search, and remain at 57% for masses above $M_{\tilde{\nu}_\tau} = 1.2$ TeV for the high-mass search. These numbers are in satisfactory agreement with an acceptance of about 60% that is stated for isotropic decays of resonances, such as in the case of the scalar $\tilde{\nu}_\tau$ in the model under study, in Ref. [95]. With these acceptances, the limits from the dijet searches on the product of cross section and branching ratio, $(\sigma \cdot \mathcal{B})^{\text{dijet}}_{\text{obs}}$, are obtained and the bound on λ'_{311} is calculated using Eqn. 10.19 as:

$$\lambda'_{311} = \sqrt{\left(\frac{2\,(\sigma \cdot \mathcal{B})^{\text{dijet}}_{\text{obs}}}{3k(M_{\tilde{\nu}_\tau})}\left(\lambda^{\text{fix}}_{312}\right)^2 + \left(\frac{(\sigma \cdot \mathcal{B})^{\text{dijet}}_{\text{obs}}}{2k(M_{\tilde{\nu}_\tau})}\right)^2\right)^{\frac{1}{2}} + \frac{(\sigma \cdot \mathcal{B})^{\text{dijet}}_{\text{obs}}}{2k(M_{\tilde{\nu}_\tau})}}\,. \tag{10.20}$$

As is apparent from this formula, the dependence of the dijet exclusion boundary in the $(M_{\tilde{\nu}_\tau}, \lambda'_{311})$ plane on the coupling $\lambda^{\text{fix}}_{312}$ is small for $\lambda^{\text{fix}}_{312} \ll 1$. For the exclusion curve in Fig. 10.4 the value $\lambda^{\text{fix}}_{312} = 0.007$ is chosen, but it is accurate for all choices of $\lambda^{\text{fix}}_{312}$ in the legend and for vanishing $\lambda^{\text{fix}}_{312}$. In the mass range 500 GeV $\leq M_{\tilde{\nu}_\tau} \leq$ 2.2 TeV the 95% CL upper bounds on λ'_{311} obtained from the reinterpretation of the dijet search lie between 0.12 and 0.60. Under the condition $\lambda'_{311} \gg \lambda_{312}$, these coupling values correspond to a relative decay with $\Gamma_{\tilde{\nu}_\tau}/M_{\tilde{\nu}_\tau}$ of $9 \cdot 10^{-4}$ and $2 \cdot 10^{-2}$, respectively. Since the latter case does not represent a narrow resonance anymore, the coupling limit is recalculated for $M_{\tilde{\nu}_\tau} = 2$ TeV with the cross section limit for quark-(anti)quark resonances with a decay width of 1.5% given in Ref. [95]. The result differs by only about 4% from the coupling bound obtained in the narrow resonance case that is shown in Fig. 10.4.

The comparison of the limit boundaries obtained in the eμ search and from the reinterpretation of the dijet search in Fig. 10.4 exemplifies the importance of dilepton resonance searches with their relatively small background contamination in the LHC environment. While the dijet search does not constrain the RPV $\tilde{\nu}_\tau$ model for resonance masses below 500 GeV or couplings below $\lambda' \sim 0.1$, couplings in the per mille range are probed in the eμ search for $M_{\tilde{\nu}_\tau} \lesssim 500$ GeV.

After the comparison of the obtained limits in the parameter space of the $\tilde{\nu}_\tau$ model with the results of other direct resonance searches at the LHC, the bounds from indirect searches for cLFV effects of new physics at the TeV scale at lower-energy facilities are considered. Some of these indirect searches have been introduced in Sec. 1.1.3. For $M_{\tilde{\nu}_\tau} = 1$ TeV, the exclusion boundary of the eμ resonance search in the $(\lambda'_{311}\ ,\ \lambda_{312} = \lambda_{321})$ plane is compared to the limits obtained from searches for μ-e conversion in heavy nuclei and for muonium conversion in Fig. 10.6.

The direct search for the $\tilde{\nu}_\tau$ sets more restrictive limits than the search for muonium conversion as long as the coupling of the production vertex λ'_{311} is larger than $4.5 \cdot 10^{-3}$. It does not improve the bounds obtained from μ-e conversion searches but it confirms this indirect search at a lower energy scale by probing the TeV scale directly for eμ resonances. Under the assumption $\lambda'_{311} = \lambda_{312} = \lambda_{321}$ and for $M_{\tilde{\nu}_\tau} = 1$ TeV, the bound on the coupling product at 90% CL obtained in the eμ resonance search reads $|\lambda'_{311}\lambda_{312}| < 4.1 \cdot 10^{-5}$. This can be compared to the bound of $|\lambda'_{311}\lambda_{312}| < 3.3 \cdot 10^{-7}$ [65] from the search for μ-e conversion with the SINDRUM II experiment. Note that signal models of new physics with an eμ resonance signature that do evade the μ-e conversion searches but might be detected at the LHC can be constructed, as discussed for example in Ref. [283]. Direct searches for eμ resonances at the LHC are valuable because they provide a complementary approach to indirect searches for cLFV effects between the first and second generation of leptons. For example, results of searches for resonant production of an eμ pair at the LHC (with high integrated luminosity) would be valuable to differentiate between BSM physics scenarios if evidence for cLFV between the first and second generation were discovered at the next generation of μ-e conversion experiments, as pointed out in Ref. [65].

Probing different Yukawa couplings for $\tilde{\nu}_\tau$ production

The cross section bounds for a narrow scalar eμ resonance produced via $\mathrm{d\bar{d}}$ annihilation presented in Sec. 10.2.2 can be reinterpreted in terms of different $\tilde{\nu}_\tau$ signal models with a different production mode of the $\tilde{\nu}_\tau$. These models can be obtained from the reference model with its three non-zero,

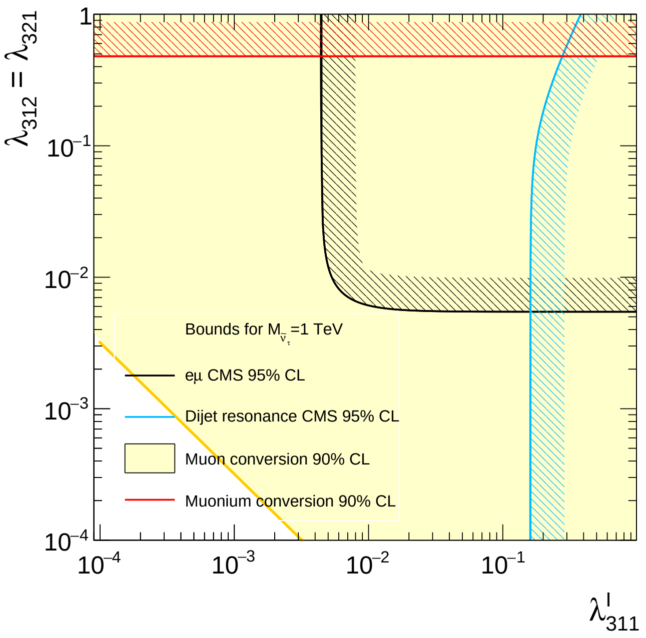

Figure 10.6: The exclusion boundaries in the (λ'_{311} , $\lambda_{312} = \lambda_{321}$) *plane of the parameter space of the* $\tilde{\nu}_\tau$ *model obtained for* $M_{\tilde{\nu}_\tau} = 1$ *TeV at 90% CL from the* $e\mu$ *resonance search (black line). They are compared to those derived from searches for* μ*-e conversion [65] (90% CL, yellow area), from searches for muonium conversion [69] (90% CL, red line), and from the CMS search for dijet resonances using data scouting [282] (95% CL, blue line). Which area in parameter space is excluded is indicated by the shaded regions.*

independent coupling parameters λ'_{311}, λ_{312}, and λ_{321} by setting λ'_{311} to zero and assigning a finite value to one of the other 8 production couplings λ'_{3jk}. For the purpose of interpreting the eμ resonance search, the models defined by the production couplings λ'_{3jk} and λ'_{3kj} with $k \neq j$ are equivalent. Therefore, five additional signal models are discussed in the following that share the decay couplings λ_{312} and λ_{321} with the reference model but involve one of the non-zero couplings λ'_{322}, λ'_{333}, λ'_{312}, λ'_{313}, or λ'_{323}. These couplings correspond to the $\tilde{\nu}_\tau$ ($\tilde{\nu}^*_\tau$) production modes via s$\overline{\text{s}}$ (s$\overline{\text{s}}$), b$\overline{\text{b}}$ (b$\overline{\text{b}}$), s$\overline{\text{d}}$ (d$\overline{\text{s}}$), b$\overline{\text{d}}$ (d$\overline{\text{b}}$), and b$\overline{\text{s}}$ (s$\overline{\text{b}}$) annihilation, respectively. As above, the assumption $\lambda_{312} = \lambda_{321}$ is made in the derivation of all the presented results in order to simplify the parameter space. For convenience, the different models are referred to according to the involved λ'_{3jk} coupling in the following, e.g. the reference model is also called the λ'_{311} model.

The experimental signature of these different $\tilde{\nu}_\tau$ resonance models is a narrow peak in the eμ mass spectrum, irrespective of the chosen production coupling. However, there are two major differences due to the different production modes. First, the inclusive cross section for $\tilde{\nu}_\tau/\tilde{\nu}^*_\tau$ production can differ by orders of magnitude as shown in Fig. 1.3 in Sec. 1.1.2 because of the different parton luminosities for the different quark-antiquark combinations. Second, the kinematics of the processes differ depending on the balance of fractional proton momenta between the two partons in the initial state. In particular, this leads to different boosts of the dilepton pair in the final state along the beam axis and thus different η and p_{T} distributions of the produced leptons. Since the inclusive signal cross sections have been evaluated above, the focus is put in the following on the effect of the differences in the kinematics on the signal efficiency that directly enters the cross section limits.

To the end of comparing the signal selection efficiencies of the $\tilde{\nu}_\tau$ models with different partonic initial states, LHE events are generated for the five additional $\tilde{\nu}_\tau$ models using the CalcHEP event generator (v. 3.6.23) with the inputs and settings described in Sec. 5.1.1. The CTEQ6L [58] central PDF set is used in the event generation. Per initial state, 19 samples are generated for

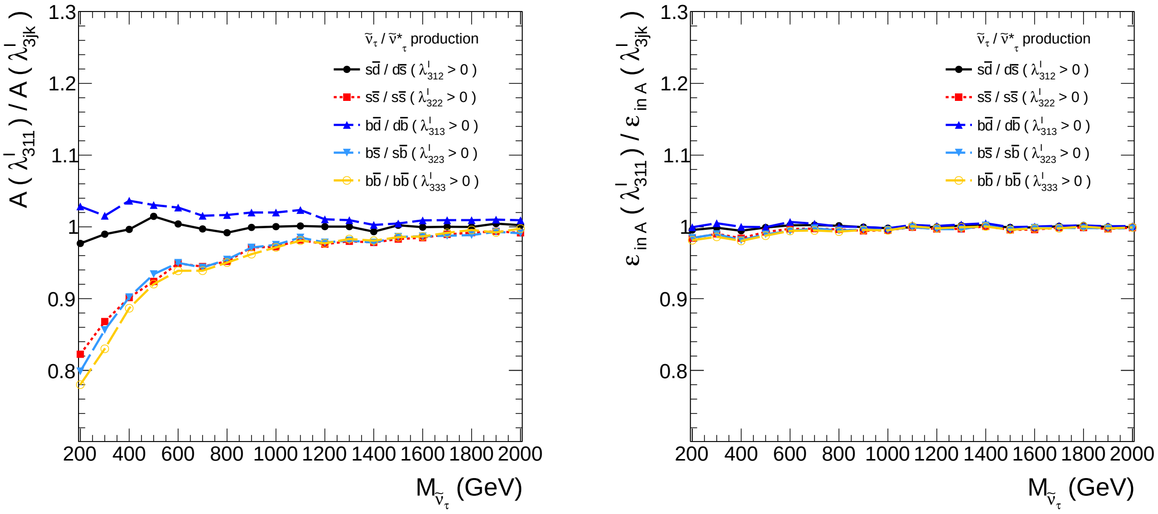

(a) The ratio of the signal acceptances obtained for the $\tilde{\nu}_\tau$ model with production coupling λ'_{311} and for different production couplings λ'_{3jk}.

(b) The ratio of the signal efficiencies within the acceptance obtained for the $\tilde{\nu}_\tau$ model with production coupling λ'_{311} and for different production couplings λ'_{3jk}.

Figure 10.7: Ratios of acceptances (left) and efficiencies (right) obtained for the $\tilde{\nu}_\tau$ model with production coupling λ'_{311} and for different production couplings λ'_{3jk}. In the references model with a non-zero value of λ'_{311}, the $\tilde{\nu}_\tau$ is produced via $d\bar{d}$ annihilation, while other choices of the production coupling correspond to the initial states indicated in the legend.

masses ranging from $M_{\tilde{\nu}_\tau} = 200$ GeV to $M_{\tilde{\nu}_\tau} = 2$ TeV with 20000 events, each. The generated events allow for the determination of the signal acceptance at parton level of the different $\tilde{\nu}_\tau$ models, denoted $A_{\lambda'_{3jk}}$. This acceptance is defined as before as the fraction of events passing the cuts on η and p_{T} of the two leptons in the final state. The resulting ratios $A_{\lambda'_{311}}/A_{\lambda'_{3jk}}$ are depicted in Fig. 10.7 (left). The $\tilde{\nu}_\tau$ signals can be grouped according to two different kinematic scenarios, depending on whether the initial state for $\tilde{\nu}_\tau/\tilde{\nu}^*_\tau$ production contains a down quark or not. If this is the case, then either the $\tilde{\nu}_\tau$ or the $\tilde{\nu}^*_\tau$ is predominantly produced in the annihilation of a valence down quark with a sea antiquark. If not, both the quark and the antiquark originate from the sea. On average, the fractions of the proton momenta carried by the quark and antiquark are more balanced in the second case, resulting in a more central production of the dilepton pair in the detector and higher acceptances. The reference model with its production coupling λ'_{311} contains a down quark in the initial state and falls in the category with smaller acceptance together with the λ'_{312} and λ'_{313} models. The difference in acceptance between the two kinematic scenarios falls with increasing signal mass from about 20% at $M_{\tilde{\nu}_\tau} = 200$ GeV to below 1% at $M_{\tilde{\nu}_\tau} = 2$ TeV. This is explained by the shrinking of the rapidity plateau in the η distributions of the produced leptons with increasing $\sqrt{\hat{s}}$ that results in acceptances close to one for signal masses in the multi-TeV range in both cases. Note that while the signal acceptances of the λ'_{311} and λ'_{322} models for example become more similar with increasing signal mass, the corresponding inclusive signal cross section grow further apart; they differ by roughly a factor five at $M_{\tilde{\nu}_\tau} = 200$ GeV but by more than a factor 30 at $M_{\tilde{\nu}_\tau} = 2$ TeV.

In addition to the differences in the signal acceptances of the λ'_{3jk} models, the impact of the different signal kinematics on the selection efficiency of signal events falling into the acceptance is evaluated. This is achieved by reweighting the generated events according to the muon trigger, muon identification, and electron identification efficiencies that have been measured by the corresponding POGs in CMS and have been presented in Sec. 4.5. A one-dimensional parameterization is chosen for the muon efficiencies $\epsilon^{\mu}_{\text{trig}}(\eta^{\mu})$ and $\epsilon^{\mu}_{\text{ID}}(\eta^{\mu})$, that captures the η dependence of these efficiencies. The electron identification efficiency is included as a function of electron p_{T} for electrons in the barrel part of the detector and electrons in the endcaps, separately, because the electron identification criteria differ between these two regions. The resulting ratios of the selection efficiencies for the λ'_{311} model and other models λ'_{3jk} are shown in Fig. 10.7 (right) and range from 0.98 to 1.01. As expected, the differences between the λ'_{3jk} models in the selection efficiency of events falling into the acceptance are much smaller than the differences in the acceptance itself.

For simplicity, only the acceptance ratios in Fig. 10.7 (left) are considered for the translation of the eμ resonance cross section limits of the λ'_{311} $\tilde{\nu}_{\tau}$ model in Fig. 10.2 into the corresponding limits of the λ'_{3jk} models. Parameterizations of the acceptances of the individual models as a function of $M_{\tilde{\nu}_{\tau}}$, $A_{\lambda'_{3jk}}(M_{\tilde{\nu}_{\tau}})$, are obtained by applying fits, as described in detail for the λ'_{311} signal model in Sec. 5.3.1. The upper cross section limit for the λ'_{3jk} model as a function of the signal mass hypothesis, $(\sigma \times \mathcal{B})^{\text{limit}}_{\lambda'_{3jk}}(M_{\tilde{\nu}_{\tau}})$, is then obtained as

$$(\sigma \times \mathcal{B})^{\text{limit}}_{\lambda'_{3jk}}(M_{\tilde{\nu}_{\tau}}) = \frac{A_{\lambda'_{311}}(M_{\tilde{\nu}_{\tau}})}{A_{\lambda'_{3jk}}(M_{\tilde{\nu}_{\tau}})}(\sigma \times \mathcal{B})^{\text{limit}}_{\lambda'_{311}}(M_{\tilde{\nu}_{\tau}}) \ . \tag{10.21}$$

They are translated into limits in the parameter spaces of the different $\tilde{\nu}_{\tau}$ models by replacing the production coupling ($\lambda'_{311} \rightarrow \lambda'_{3jk}$), the cross section limit (Eqn. 10.21), and the coupling-independent factor entering the signal cross section in Eqn. 10.18 ($k(M_{\tilde{\nu}_{\tau}}) \rightarrow k_{\lambda'_{3jk}}(M_{\tilde{\nu}_{\tau}})$), accordingly. The factors $k_{\lambda'_{3jk}}(M_{\tilde{\nu}_{\tau}})$ contain the convolution of the PDFs for the quark/antiquark pair in the initial state and they thus differ significantly for the different considered production couplings. The resulting 95% CL exclusion boundaries in the $(M_{\tilde{\nu}_{\tau}}, \lambda'_{3jk})$ planes in these different parameter spaces for decay couplings $\lambda_{312} = \lambda_{321} = 0.05$ are overlayed in Fig. 10.8. The size of the excluded area in the parameter planes increases with the signal cross section of the corresponding λ'_{3jk} model. It is largest for the λ'_{311} coupling with its d$\overline{\text{d}}$ initial state and decreases with the parton luminosities of the other initial states for $\tilde{\nu}_{\tau}$ ($\tilde{\nu}^{*}_{\tau}$) production in the order: s$\overline{\text{d}}$ (d$\overline{\text{s}}$), b$\overline{\text{d}}$ (d$\overline{\text{b}}$), s$\overline{\text{s}}$ (s$\overline{\text{s}}$), b$\overline{\text{s}}$ (s$\overline{\text{b}}$), and b$\overline{\text{b}}$ (b$\overline{\text{b}}$).

Two types of indirect searches for BSM physics are relevant for the comparison of the obtained bounds in RPV parameter space with the existing bounds in the literature. On the one hand, there are limits from the aforementioned searches for μ-e conversion in heavy nuclei, on the other hand searches for LFV decays of neutral mesons into an eμ pair play an important role. These results from searches for processes at lower energy scales that are forbidden or extremely rare in the SM are typically presented as limits on coupling products $|\lambda'_{3jk}\lambda_{312}|$ at 90% CL. All RPV SUSY-induced contributions to the rates of rare processes that are considered in the following occur at tree level and therefore the dependence of the coupling bounds on $M_{\tilde{\nu}_{\tau}}$ is given by $|\lambda'_{3jk}\lambda_{312}| \sim (M_{\tilde{\nu}_{\tau}}/1\ \text{TeV})^2$ at LO.

The comparison of the limits obtained in the eμ resonance search to the existing bounds is simplified by assuming $M_{\tilde{\nu}_{\tau}} = 1$ TeV and $\lambda'_{3jk} = \lambda_{312} = \lambda_{321}$. With these choices, the 90% CL cross section limits from Tab. E.1 and Eqn. 10.21 can be translated into a bound on $|\lambda'_{3jk}\lambda_{312}|$:

$$|\lambda'_{3jk}\lambda_{312}|^{\text{limit}} = \frac{5}{2} \times \frac{(\sigma \times \mathcal{B})^{\text{limit}}_{\lambda'_{3jk}}\left(M_{\tilde{\nu}_{\tau}} = 1\ \text{TeV}\right)}{k_{\lambda'_{3jk}}\left(M_{\tilde{\nu}_{\tau}} = 1\ \text{TeV}\right)} \ . \tag{10.22}$$

The results are compared to the existing bounds in Tab. 10.2. Since the published bounds on $|\lambda'_{3jj}\lambda_{312}|$ that stem from the interpretation of searches for μ-e conversion are stronger than those obtained in this work, the discussion will focus on the bounds on $|\lambda'_{3jk}\lambda_{312}|$ ($j \neq k$) from searches for exotic meson decays in the following. Details about their calculation are summarized in App. E.7. The indirect bounds on $|\lambda'_{312}\lambda_{312}|$ from searches for the rare kaon decay $\text{K}^0_{\text{L}} \rightarrow \text{e}\mu$ with the BNL E871 experiment [20] are very constraining and surpass the limit obtained in this work

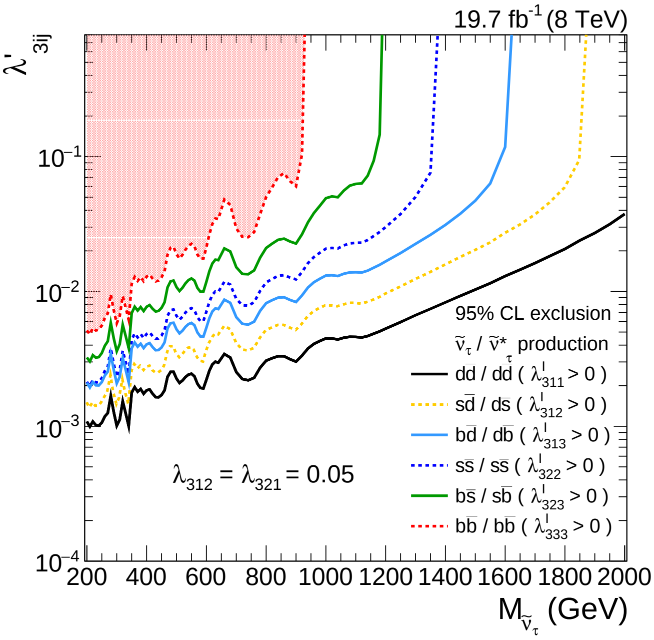

Figure 10.8: Exclusion boundaries in the $(M_{\tilde{\nu}_\tau}, \lambda'_{3jk})$ plane of the RPV model at 95% CL for different choices of the production coupling λ'_{3jk}. In all cases, the value of the decay couplings is $\lambda_{312} = \lambda_{321} = 0.05$. The areas in parameter space above the curves are excluded, as exemplified by the shaded region above the 95% CL exclusion boundary for the $b\bar{b}$ initial state.

by more than two orders of magnitude. However, the direct limits are much more competitive for the λ'_{313} and λ'_{323} models where the $\tilde{\nu}_\tau$ is produced via annihilation of a light quark and a b-quark. The corresponding coupling products $|\lambda'_{313}\lambda_{312}|$ and $|\lambda'_{323}\lambda_{312}|$ are constrained by searches for the decays $\mathrm{B}^0_\mathrm{d} \to \mathrm{e}^\pm\mu^\mp$ and $\mathrm{B}^0_\mathrm{s} \to \mathrm{e}^\pm\mu^\mp$ at hadron colliders. The previously strongest upper bounds on the branching ratios of these decays set by the CDF collaboration [284] have been improved by about a factor 20 by the LHCb collaboration [21] in 2013 based on 1.0 fb^{-1} of data collected in pp collisions at $\sqrt{s} = 7$ TeV, yielding $\mathcal{B}(\mathrm{B}^0_\mathrm{d} \to \mathrm{e}^\pm\mu^\mp) < 2.8 \times 10^{-9}$ and $\mathcal{B}(\mathrm{B}^0_\mathrm{s} \to \mathrm{e}^\pm\mu^\mp) < 1.1 \times 10^{-8}$ at 90% CL. For $M_{\tilde{\nu}_\tau} = 1$ TeV, the limit on $|\lambda'_{313}\lambda_{312}|$ from the interpretation of the LHCb search (App. E.7) is more restrictive than the limits from the direct search obtained in this work by about a factor two. However, the direct limit is stronger than the bound set by the CDF collaboration. The limits on $|\lambda'_{323}\lambda_{312}|$ for $M_{\tilde{\nu}_\tau} = 1$ TeV from the direct search and the LHCb search differ by almost an order of magnitude.

The results reported in Tab. 10.2 are the most stringent bounds on the individual $\tilde{\nu}_\tau$ models from direct searches at high-energy colliders at the time of writing.

In summary, the λ'_{313} model with its $\mathrm{b\bar{d}}$ ($\mathrm{d\bar{b}}$) initial state for $\tilde{\nu}_\tau$ ($\tilde{\nu}^*_\tau$) production has been identified as the eμ resonance $\tilde{\nu}_\tau$ model for which the direct search is most competitive compared to existing indirect constraints. For every probed combination of RPV couplings an indirect search has been identified that sets a more stringent limit than the direct search for eμ resonances carried out in this work. Still, the results in Tab. 10.2 and Fig. 10.8 illustrate the power of direct searches at the LHC with its range of partonic initial states and broadband coverage of partonic centre-of-mass energy: A wealth of models of new physics can be probed directly over a wide range of possible BSM mass scales with a single signature in the detector, a narrow peak in the mass spectrum of selected eμ pairs.

Table 10.2: The 90% CL upper bounds on the coupling products $|\lambda'_{3jk}\lambda_{312}|$ *evaluated for* $M_{\tilde{\nu}_\tau} = 1$ *TeV and* $\lambda'_{3jk} = \lambda_{312} = \lambda_{321}$*. Each bound corresponds to an individual model with its own production mode of the* $\tilde{\nu}_\tau$ *in pp collisions that is given in the first column. The results from the e*μ *resonance search are compared to indirect limits reported in the literature.*

Initital state $\tilde{\nu}_\tau$ $(\tilde{\nu}^*_\tau)$ prod.	Coupling product	Upper bound CMS (90% CL)	Upper bound literature (90% CL)	Experiment	Probed process
$\mathrm{d\bar{d}}$ $(\mathrm{d\bar{d}})$	$\lvert\lambda'_{311}\lambda_{312}\rvert$	$4.1 \cdot 10^{-5}$	$3.3 \cdot 10^{-7}$ [65]		μ-e
$\mathrm{s\bar{s}}$ $(\mathrm{s\bar{s}})$	$\lvert\lambda'_{322}\lambda_{312}\rvert$	$7.0 \cdot 10^{-4}$	$6.3 \cdot 10^{-7}$ [64]	SINDRUM II [19]	conversion
$\mathrm{b\bar{b}}$ $(\mathrm{b\bar{b}})$	$\lvert\lambda'_{333}\lambda_{312}\rvert$	$5.9 \cdot 10^{-3}$	$8.5 \cdot 10^{-5}$ [66]		in nuclei
$\mathrm{s\bar{d}}$ $(\mathrm{d\bar{s}})$	$\lvert\lambda'_{312}\lambda_{312}\rvert$	$1.2 \cdot 10^{-4}$	$4.2 \cdot 10^{-7}$	BNL E871 [20]	$\mathrm{K^0_L} \to \mathrm{e}^{\pm}\mu^{\mp}$
$\mathrm{b\bar{d}}$ $(\mathrm{d\bar{b}})$	$\lvert\lambda'_{313}\lambda_{312}\rvert$	$3.2 \cdot 10^{-4}$	$1.4 \cdot 10^{-4}$ $6.9 \cdot 10^{-4}$	LHCb [21] CDF [284]	$\mathrm{B^0_d} \to \mathrm{e}^{\pm}\mu^{\mp}$
$\mathrm{b\bar{s}}$ $(\mathrm{s\bar{b}})$	$\lvert\lambda'_{323}\lambda_{312}\rvert$	$2.0 \cdot 10^{-3}$	$2.9 \cdot 10^{-4}$ $1.2 \cdot 10^{-3}$	LHCb [21] CDF [284]	$\mathrm{B^0_s} \to \mathrm{e}^{\pm}\mu^{\mp}$

10.3 Search for quantum black holes

The $M_{\mathrm{e}\mu}$ distribution of the QBH signal is not as localized as that of the RPV $\tilde{\nu}_\tau$ narrow resonance signal, as has been shown in Fig. 5.3. Therefore, the $M_{\mathrm{e}\mu}$ signal shape is not parameterized as a function of the signal mass but obtained directly from the simulated MC samples with a spacing of 100 GeV in the threshold mass parameter M_{th}. The signal selection efficiency is also obtained from simulation. Since all QBH $M_{\mathrm{e}\mu}$ distributions share the feature of a sharp turn-on at M_{th} and a long tail towards higher masses, events entering the likelihood function for statistical interpretation are required to fall within the search region $M_{\mathrm{e}\mu} \in [M_{\mathrm{th}} - 6\sigma_M, \infty)$, where σ_M denotes the $M_{\mathrm{e}\mu}$ resolution. Except for the different $M_{\mathrm{e}\mu}$ signal shape and the changed definition of the search region, the limit setting procedure and treatment of the systematic uncertainties is the same as in the narrow resonance search.

The 95% CL limit on the product of QBH signal cross section and branching fraction into the eμ final state, that are obtained using the QBH $M_{\mathrm{e}\mu}$ distributions for the model without extra dimensions ($n = 0$), are displayed in Fig. 10.9. The observed cross section limit falls slightly from 0.55 fb at $M_{\mathrm{th}} = 500$ GeV to 0.24 fb at $M_{\mathrm{th}} = 1.2$ TeV and remains approximately constant towards higher signal masses.

It is instructive to compare the QBH cross section limits with those for the narrow resonance signal in Fig. 10.2. Both limit plots share the almost constant value of 0.24 fb at high signal masses where the background expectation is negligible and no event is observed in data. This is due to the acceptances and selection efficiencies of the two signals being very similar at high mass; the relative difference for signal masses of 2 TeV is one to two per cent. At lower masses, however, the shape of the signals' eμ mass spectra is relevant for the discrimination against the sizeable background, and two obvious differences arise in the limit plots for the QBH and the narrow resonance signals. First, for $M_{\mathrm{th}} = M_{\tilde{\nu}_\tau}$ the QBH cross section limits are smaller than the resonance limits. This is explained by the long tail of the QBH eμ mass distribution extending towards masses well above the mass threshold M_{th} where the backgrounds are lower than at $M_{\mathrm{th}} = M_{\tilde{\nu}_\tau}$. To illustrate this difference, the QBH cross section bounds are shown in Fig. 10.10 (left) as a function of different definitions of the QBH signal mass; the threshold mass M_{th}, the mean of the QBH $M_{\mathrm{e}\mu}$ distribution, and its 25% and 50% quantiles. Each point on the graphs in different shades of red

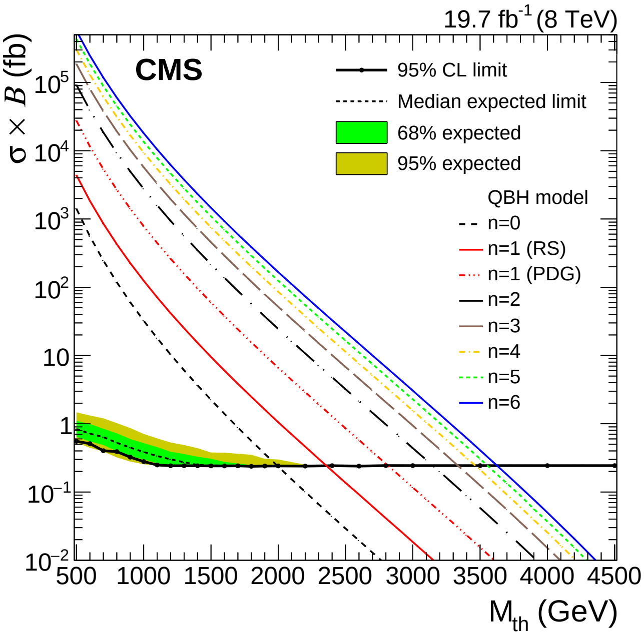

Figure 10.9: The observed and expected 95% CL exclusion limits on the product of the QBH production cross section and the branching fraction of its decay into the eμ final state as a function of the threshold mass. The signal cross sections are shown in the PDG convention for $n = 0$ to $n = 6$ extra dimensions and in the RS convention for $n = 1$. This figure is also included in Ref. [30].

corresponds to one QBH signal generated for the parameters M_{th} and $n = 0$, which is assigned one cross section limit. For $n = 0$, the median of the QBH eμ mass distributions lies hundreds of GeV above M_{th}. For comparison, the cross section limits for the narrow resonance signal are also shown. Furthermore, the observed limit lies always below the median expected limit for the QBH signal, between the 1σ and 2σ uncertainty band around the expectation, while for the narrow resonance signal it oscillates around the median expected limit (see Figs. 10.9 and 10.2). The latter behaviour is expected due to statistical fluctuations. The behaviour of the observed cross section limit of the QBH signal is again explained by its tail towards high masses: For the threshold masses M_{th} between 500 GeV and about 1.3 TeV, a significant fraction of the QBH signal events falls in the $M_{\text{e}\mu}$ range between 700 GeV and 1.3 TeV, where a deficit is observed in data with respect to the background expectation, as shown in Figs. 9.3 (right) and E.4. These expected signal events at higher masses where backgrounds are lower have a large impact on the cross section limit, such that the observed bound falls below the expectation.

The curves in Fig. 10.9 represent the product of QBH signal cross section and branching fraction for different numbers of extra dimensions. All cross sections are given in the PDG convention, only for $n = 1$ both the PDG convention and the RS case are considered. The lower bounds on $M_{\text{th}} = M_{\text{D}}$ fall in the multi-TeV range for all n and are summarized in Tab. 10.3. Note that in contrast to the RPV $\tilde{\nu}_\tau$ signal there are no potentially small coupling parameters present in the QBH cross section formula Eqn. 1.32, yielding comparatively large cross sections. Moreover, all quark-antiquark combinations, including quark flavour violating ones, couple to the QBH with equal strength in the model considered here. The background yield in the mass region where the different types of QBHs (different n) are excluded is negligible and the signal efficiencies are very similar, as shown in Tab. 5.2. Therefore, only the observed and expected limit curves calculated for the $n = 0$ QBH signal are included in Fig. 10.9. For threshold masses below 1 TeV however, the different shapes of the $M_{\text{e}\mu}$ distributions obtained for QBH signals with different n lead to different cross section limits. This is shown in Fig. 10.10 (right). The QBH signal is most localized

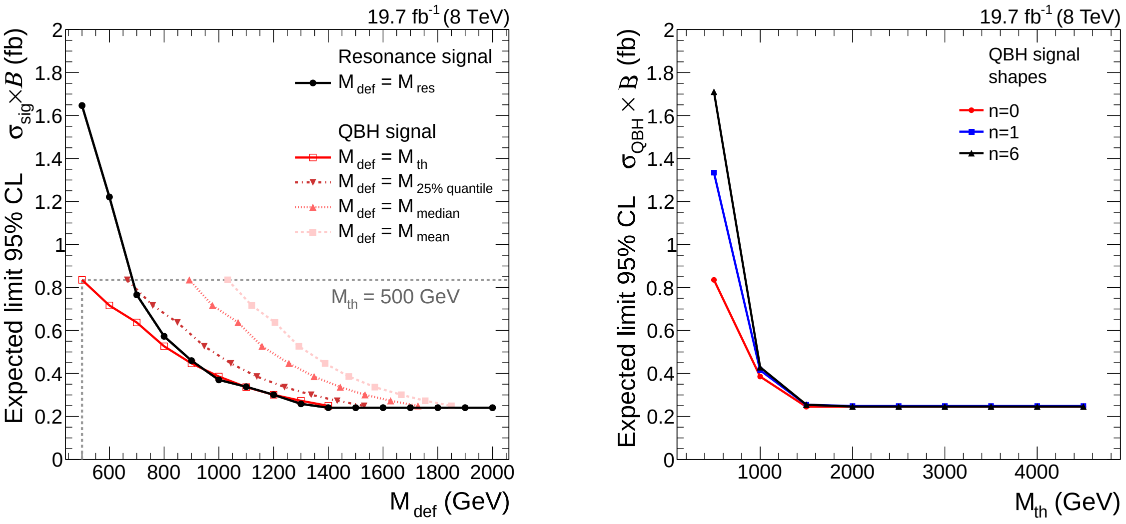

(a) The limit for the QBH signal with $n = 0$ for different definitions of the signal mass: the threshold mass M_{th}, and the mean and different quantiles of the reconstructed $M_{e\mu}$ spectrum from QBH decays.

(b) The limit for the QBH signal for different n.

Figure 10.10: The expected 95% CL exclusion limits on the product of signal production cross section and branching fraction of the decay into the $e\mu$ *final state for different number of extra dimensions* n *and different mass definitions* M_{def}.

at M_{th}, and thus most similar to a resonance peak at $M_{\text{res}} = M_{\text{th}}$, for high n (Fig. 5.3). This is reflected in the cross section limits in Fig. 10.10; the bound obtained with the $M_{e\mu}$ signal shape of the QBH model with $n = 6$ is close to that obtained for the narrow resonance signal.

The results in Tab. 10.3 were the first bounds on QBHs decaying to an eμ pair when published in Ref. [30, 38]. They have been surpassed after the arrival of the first few fb^{-1} of data recorded in pp collisions at $\sqrt{s} = 13$ TeV at the LHC in 2015 as documented in Refs. [32, 285].

Table 10.3: The 95% CL lower limits on the QBH threshold mass $M_{\text{th}} = M_{\text{D}}$ *in the PDG convention for different choices of the number of extra dimensions* n. *For* $n = 1$ *the results are given in both the PDG and RS conventions.*

n	95% CL lower limits on M_{th} (TeV) Observed	 Median expected
0	1.99	1.99
1 (PDG)	2.36	2.36
1 (RS)	2.81	2.81
2	3.15	3.15
3	3.34	3.34
4	3.46	3.46
5	3.55	3.55
6	3.63	3.63

In contrast to the RPV $\tilde{\nu}_\tau$ search, more stringent bounds from direct searches in other final states exists in the case of the QBH signal. Quantum black holes are expected to couple to lepton and quark pairs with the same strength. There are however more flavor combinations that lead to quark/(anti)quark final states and they come with additional color factors. Therefore the branching fraction of the QBH decay into a dijet pair is much higher than that of the decay into an eμ pair in typical QBH models (see Ref. [84] for an overview). For example, the search for QBHs in the dijet mass spectrum obtained from 15.7 fb^{-1} of pp collision data at $\sqrt{s} = 13$ TeV by the ATLAS [286] collaboration excludes at 95% CL QBHs with $n = 6$ for $M_\text{th} \leq 8.7$ TeV.

10.4 High-mass eμ searches at the LHC at $\sqrt{s} = 8$ and 13 TeV

A comparison between the $\sqrt{s} = 8$ TeV results reported in this thesis and (partly) in Ref. [30], that are based on a dataset corresponding to an integrated luminosity of 19.7 fb^{-1}, and the abovementioned $\sqrt{s} = 13$ TeV LHC results (Refs. [32, 285]) with higher centre-of-mass energy but smaller integrated luminosity of 2.7 fb^{-1} (CMS 13 TeV) and 3.2 fb^{-1} (ATLAS 13 TeV) is instructive. In the case of the QBH signal, the $\sqrt{s} = 13$ TeV results supersede those obtained at $\sqrt{s} = 8$ TeV; for $n = 6$ extra dimensions the limits on the threshold mass M_th read 4.5 TeV (CMS 13 TeV), 4.5 TeV (ATLAS 13 TeV), and 3.63 TeV (CMS 8 TeV) at 95% CL. The underlying reason is once more the absence of potentially small coupling parameters in the signal cross section, because of which the lower bounds on the signal mass fall into the multi-TeV region. The parton luminosity for the production of a heavy particle with a mass of 3 TeV in quark/antiquark annihilation increases by about a factor of 20, when increasing the pp centre-of-mass energy from 8 TeV to 13 TeV [126], more than compensating for the smaller integrated luminosities used in the $\sqrt{s} = 13$ TeV searches. The corresponding enhancement of the quark/antiquark parton luminosity at a mass of 1 TeV is only a factor of three. Therefore, the outcome of the comparison between the published 8 TeV and 13 TeV searches in the case of the RPV $\tilde{\nu}_\tau$ signal depends on the size of the participating Yukawa couplings.

The publications by the CMS and ATLAS collaborations on high-mass eμ searches use the RPV $\tilde{\nu}_\tau$ model with non-zero production coupling λ'_{311} and $\text{d}\overline{\text{d}}$ initial state as a proxy for models involving a scalar narrow resonance. For small values of the couplings $\lambda'_{311} = \lambda_{312} = \lambda_{321} = 0.01$, the search presented in this work yields a lower bound on the $\tilde{\nu}_\tau$ mass of 1.28 TeV at 95% CL, whereas the corresponding result obtained by the CMS collaboration at $\sqrt{s} = 13$ TeV reads 1.0 TeV. When the coupling values are increased, the signal cross sections rise, as do the lower bounds on the $\tilde{\nu}_\tau$ mass. For the Yukawa couplings $\lambda'_{311} = 0.11$ and $\lambda_{312} = \lambda_{321} = 0.07$, both the 8 TeV CMS search and the 13 TeV ATLAS search obtain a lower bound on the $\tilde{\nu}_\tau$ mass of 2.3 TeV at 95% CL. At a mass of 2 TeV, the ratio of the quark/antiquark parton luminosities for $\sqrt{s} = 13$ TeV and $\sqrt{s} = 8$ TeV approximately corresponds to the ratio of the integrated luminosities used in the 8 TeV CMS and 13 TeV ATLAS searches [126]. If the couplings are increased further, the searches at higher pp centre-of-mass energy yield the stronger bounds on the $\tilde{\nu}_\tau$ mass. In summary, the 8 TeV searches with high integrated luminosity have the edge over the 13 TeV updates with data recorded in 2015 for coupling values $\lambda'_{311} = \lambda_{312} = \lambda_{321} \lesssim 0.1$, whereas the latter yield the more restrictive bounds for larger coupling values.

Although the choice of the $\text{d}\overline{\text{d}}$ production mode within the wider class of RPV $\tilde{\nu}_\tau$ models (λ'_{3jk} models) yields the largest signal cross section, the indirect bounds from low-energy experiments are particularly restrictive in this case as documented in Tab. 10.2. In all other λ'_{3jk} models discussed in Sec. 10.2.2, the signal cross section is smaller than in the λ'_{311} case for a fixed value of the production coupling, because of smaller parton luminosities of the associated initial states. The lower bounds on $M_{\tilde{\nu}_\tau}$ for the other λ'_{3jk} signal models take on smaller values than those reported for the λ'_{311} model in Tab. 10.1. This enhances the reach of the 8 TeV searches with high integrated luminosity compared to their 13 TeV counterparts with lower integrated luminosity.

Part III

A search for decays of heavy resonances into a $\mu\tau$ pair in pp collisions at $\sqrt{s} = 8$ TeV

Chapter 11

From the eμ search to a search for resonances decaying to $\mu\tau_{\mathrm{e}}$

In the search for new physics discussed above, models with charged lepton flavour violating interactions between the first and the second generation have been examined. In the following, the search in eμ final states is extended to cover cLFV interactions involving charged leptons of the second and third generation, muons and τ leptons, using the decay of the τ lepton into an electron and neutrinos, $\tau^- \to \mathrm{e}^- \nu_\tau \bar{\nu}_e$. The resulting search for high-mass $\mu\tau$ pairs is referred to either as *the $\mu\tau$ search* or as *the $\mu\tau_{\mathrm{e}}$ search* depending on the context; the first term puts emphasis on the type of cLFV interaction under study, whereas the second term highlights the experimental final state. When comparing the $\mu\tau_{\mathrm{e}}$ search to the eμ search, it ought to be kept in mind that the branching fraction of the considered τ decay is given by $\mathcal{B}(\tau^- \to \mathrm{e}^- \nu_\tau \bar{\nu}_e) = 17.83 \pm 0.04\%$ [5] and that only this fraction of the (hypothetical) $\mu\tau$ signal events is utilized. However, it will be shown that the search is very competitive when compared to other existing searches. In contrast to the eμ search with its inclusive event selection, the $\mu\tau$ search is designed with the resonant production of the $\mu\tau$ pair in mind. Again, an RPV SUSY model with $\tilde{\nu}_\tau$ LSP is used as a proxy for the wider class of BSM models involving heavy resonances that decay into a $\mu\tau$ pair. As pointed out in Sec. 1.1, the RPV $\tilde{\nu}_\tau$ model considered in the search for eμ resonances can be modified to lead to the resonant production of a prompt $\mu\tau$ pair by assuming the couplings λ_{312} and λ_{321} to be zero and the coupling λ_{323} to be non-zero. in the following, $\mathrm{d}\bar{\mathrm{d}}$ annihilation via the coupling λ'_{311} is assumed to be the only resonant production mode of the $\tilde{\nu}_\tau$ LSP at hadron colliders and all other couplings λ'_{ijk} are assumed to vanish.

The presentation of the $\mu\tau$ search is organized as follows: First, the reconstruction of τ lepton candidates with leptonic decays at high τ p_{T} is reviewed based on MC simulated signal samples. In this context it will be shown that key elements of the eμ resonance search can be adopted with small modifications when the search for $\mu\tau$ resonances is restricted to the leptonic decay mode of the τ to an electron and neutrinos. Afterwards, the event selection is discussed and the signal efficiency and mass resolution are determined analogous to the eμ resonance search. Finally, the statistical analysis of the experimental findings is presented. The results are interpreted in terms of the RPV $\tilde{\nu}_\tau$ model and put into context with other searches for new physics in $\mu\tau$ final states at hadron colliders and lower-energy facilities. The presentation of the $\mu\tau$ search concludes with a reinterpretation of the $\mu\tau$ resonance search in terms of a two-Higgs-doublet model with cLFV decay of a heavy Higgs boson. This model introduces a different kind of production mode of the heavy scalar resonance, the gluon-gluon fusion via a top-quark loop.

The presentation of the $\mu\tau_{\mathrm{e}}$ search is more compact than the detailed account on the eμ search because the two analyses share many features, as described in the following.

11.1 Kinematics of scalar $\mu\tau$ resonances with leptonic τ decay

In this section, the kinematics of the $\mu\tau_\mathrm{e}$ final state are studied based on simulated RPV $\tilde{\nu}_\tau$ signal samples. These studies justify the choice of the selection cuts and the key observable of the search, the *collinear mass* of the $\mu\tau_\mathrm{e}$ pair, $M_{\mu\tau}^{\mathrm{coll}}$.

11.1.1 Simulation of signal samples for the $\mu\tau$ resonance search

As in the search for eμ resonances, the `CALCHEP` event generator (v. 3.4.1) is utilized to generate the resonant $\tilde{\nu}_\tau$ production and its LFV decay to the prompt lepton pair in the final state with the generator settings summarized in Sec. 5.1.1. The PDF set CTEQ6L is used. In contrast to the eμ search, `PYTHIA` 8 (v. 8.185) [287] with the underlying event tune 4C [288] is employed for hadronization and τ decays rather than `PYTHIA` 6. Information on the τ lepton decay models implemented in `PYTHIA` 8 is given in Ref. [289]. The signal simulation starts from the LHE event files produced with `CALCHEP` that are then forwarded to a full simulation of the CMS detector based on `GEANT4` within the CMSSW software framework. In the simulated signal samples, the passage of the τ lepton through the inner tracking detectors before its decay, its energy depositions and the curvature of its trajectory in the magnetic field are included by invoking `GEANT4`. More details on the simulated $\mu\tau$ signal samples, including the signal model parameters, are given in App. C.2.

11.1.2 Leptonic decays of τ leptons with high p_T

As a preparation of the discussion of the signal acceptance and efficiency to follow in Sec. 11.3.1, the lepton kinematics in the $\mu\tau_\mathrm{e}$ final state are briefly reviewed. The muon kinematics correspond to those in the eμ resonance search described above. The η distribution of the electrons from τ decays is presented in Fig. 11.1. For resonance masses above 200 GeV, that are considered in the following, the geometric acceptance of the non-prompt electrons, defined as the fraction of electrons that fall within the boundary of the silicon strip tracker at $|\eta| = 2.5$, remains similar to that of the non-prompt muons. The transverse momentum distribution of the electrons from τ decays however is significantly shifted towards lower p_T compared to that of the τ leptons as shown in Fig. 11.2 (left). The signal selection efficiency would benefit from a threshold on the transverse momentum of the electron that is significantly lower than the E_T requirement in the eμ resonance search of 35 GeV, in particular for resonance masses between 200 GeV and 500 GeV. However, this would also result in larger backgrounds and require the analysis to be split into a search in the mass range between 200 GeV and 500 GeV, and a high mass search with different electron selections. In order to minimize the effort in converting the search for eμ resonances in final states with an electron and a muon into the search for $\mu\tau_\mathrm{e}$ resonances, the HEEP electron selection, that is employed in the eμ search, is retained and the cut on the electron E_T is set to 30 GeV.

The p_T of the sum of the neutrino momenta from the τ decay (the source of *true* missing transverse energy in the $\mu\tau_\mathrm{e}$ signal events) that is depicted in Fig. 11.2 (right) exhibits a broad distribution with a maximum well above zero. The missing transverse energy is required to exceed 25 GeV in the event selection.

Collinear approximation of highly boosted leptonic τ decays

Searches for objects decaying to high-mass ditau pairs, such as $\mathrm{Z}' \to \tau^+\tau^-$, suffer from the impossibility to reconstruct or at least deduce the full four-momentum of the decay products because the produced neutrinos escape undetected along the momentum vectors of both tau leptons in the final state. In these searches, spectra of the total transverse mass $M_\mathrm{T}^{\mathrm{tot}}$ [290] or other effective mass variables [291] are investigated for contributions from BSM physics. In searches for high-mass $\mu\tau$ resonances only one of the promptly produced final state leptons decays within the detector, leading to one or more neutrinos. For the search region covered in this analysis,

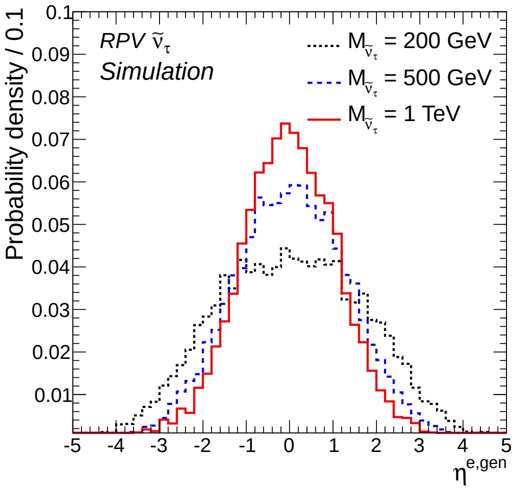

Figure 11.1: The η distributions of electrons from the leptonic τ decays obtained from simulated signal samples with $M_{\tilde{\nu}_\tau} = 200$ GeV, $M_{\tilde{\nu}_\tau} = 500$ GeV, and $M_{\tilde{\nu}_\tau} = 1$ TeV at generator level.

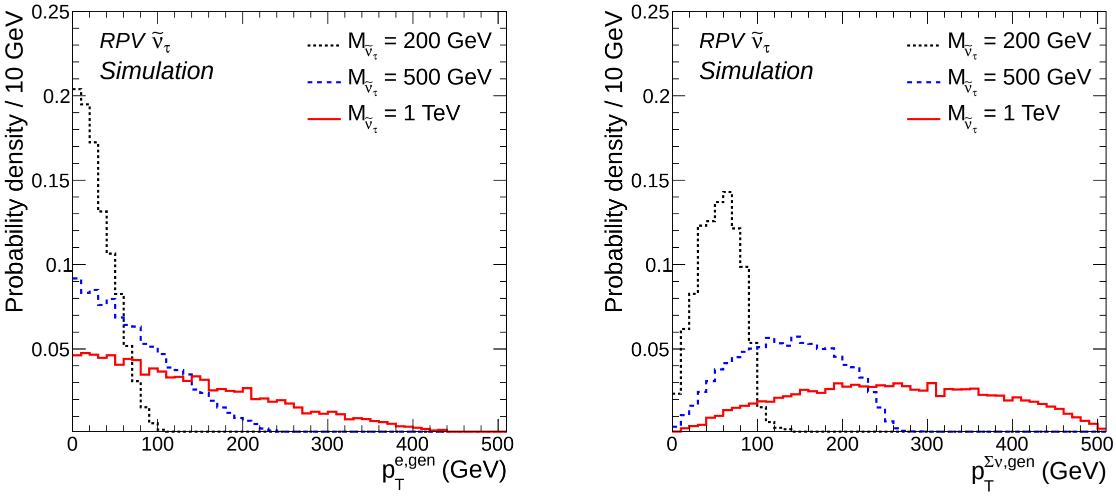

(a) Transverse momentum distribution of generated electrons from τ decays.

(b) Distribution of the transverse momentum obtained from the vector sum of the two neutrino momenta from the τ decay.

Figure 11.2: The p_T distributions of the electron and the sum of the two neutrino momenta from the τ decay obtained from simulated signal samples with $M_{\tilde{\nu}_\tau} = 200$ GeV, $M_{\tilde{\nu}_\tau} = 500$ GeV, and $M_{\tilde{\nu}_\tau} = 1$ TeV at generator level. The muon and electron in the $\mu\tau_e$ final state are required to fall into the geometrical acceptance of the muon system and the tracker, respectively.

$M_{\tilde{\nu}_\tau} \geq 200$ GeV, decays of τ leptons produced at the Jacobian edge come with a relativistic boost of $\gamma = E_\tau/m_\tau \gtrsim 50$ along the axis of the τ lepton's momentum. In these strongly boosted decays, the decay products are collimated and the direction of the momenta of neutrinos from the τ decay can be approximated by that of the momentum of the visible decay products. Furthermore, the neutrinos from the τ decay are the only source of $\not{E}_T$ at parton level. It is therefore possible to infer the full four-momentum of the τ lepton by reconstructing the visible decay products, the missing transverse momentum $\vec{\not{E}}_T$, and using the *collinear approximation* of the boosted τ decay. Before reviewing the accuracy of the collinear approximation, the details of the implementation

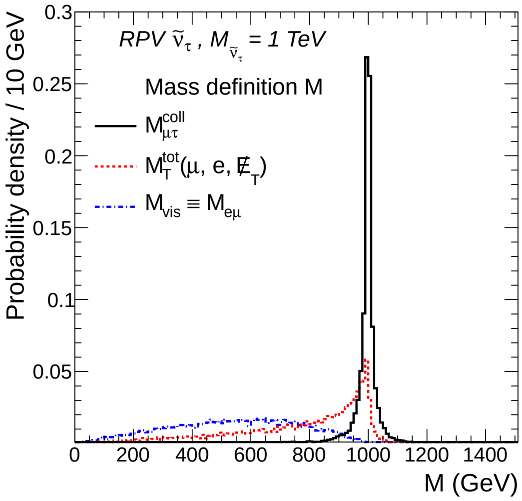

Figure 11.3: Comparison of distributions of different mass observables M at parton level for a simulated $\tilde{\nu}_\tau \rightarrow \mu\tau_{\mathrm{e}}$ signal sample with $M_{\tilde{\nu}_\tau} = 1$ TeV. The visible mass M_{vis}, defined as the mass of the eμ pair, the total transverse mass $M_{\mathrm{T}}^{\mathrm{tot}}$, and the $\mu\tau$ mass resulting from the collinear approximation of the leptonic τ decay $M_{\mu\tau}^{\mathrm{coll}}$ are introduced in the text.

are given for the τ decay mode of interest, namely $\tau^- \rightarrow \mathrm{e}^-\overline{\nu}_{\mathrm{e}}\nu_\tau$. This decay is abbreviated to τ_{e} in the following. The four-momentum of the τ lepton is defined by the mass of the τ lepton m_τ, the amplitude of its transverse momentum p_{T}^{τ}, and the directional quantities η^{τ} and ϕ^{τ}. The two parameters defined in the plane perpendicular to the beam axis, p_{T}^{τ} and ϕ^{τ}, are determined from the vector sum of the electron's transverse momentum $\vec{p}_{\mathrm{T}}^{\,e}$ and the missing transverse momentum as $\vec{p}_{\mathrm{T}}^{\,\tau} = \vec{p}_{\mathrm{T}}^{\,e} + \vec{\not{E}}_{\mathrm{T}}$. The pseudorapidity of the τ candidate is approximated using the directional information with respect to the beam axis of the electron, i.e. $\eta^{\tau} \equiv \eta^{e}$. The accuracy in the determination of the mass of the $\mu\tau$ pair that can be obtained using this approximation is studied on the simulated $\tilde{\nu}_\tau$ signal samples at generator level. The true mass $M_{\mu\tau}^{\mathrm{gen}}$ is compared to the mass $M_{\mu\tau}^{\mathrm{coll}}$ that results from the collinear approximation applied to the generated electron and neutrinos from the τ decay. The approximation introduces no substantial bias in the mass determination and the RMS of the relative difference between the two masses is only 1.3% at $M_{\tilde{\nu}_\tau} = 200$ GeV and below 0.5% for $M_{\tilde{\nu}_\tau} \gtrsim 800$ GeV. As will be shown in Sec. 11.3.2, this inaccuracy introduced by the approximation at generator level is subleading to the detector resolution in the reconstructed $\mu\tau$ mass. The comparison of mass distributions obtained from simulated signal events with $M_{\tilde{\nu}_\tau} = 1$ TeV for different definitions of the mass observable in Fig. 11.3 shows how the collinear approximation of the τ restores the resonance peak, and results in a signal shape that is better localized around $M_{\tilde{\nu}_\tau}$ than the distribution of the total transverse mass $M_{\mathrm{T}}^{\mathrm{tot}} = \sqrt{M_{\mathrm{T}}^2(\mu,\mathrm{e}) + M_{\mathrm{T}}^2(\mu,\not{E}_{\mathrm{T}}) + M_{\mathrm{T}}^2(\mathrm{e},\not{E}_{\mathrm{T}})}$.

These initial considerations suffice to outline a strategy of how to extend the search for eμ resonances to a search of $\mu\tau_{\mathrm{e}}$ resonances in events with an electron and a muon. The muon selection does not require modification. Starting from the electron selection, τ lepton candidates are formed by asking for significant $\not{E}_{\mathrm{T}}$ in the event that is roughly aligned with the electron in ϕ, and combining the electron and $\not{E}_{\mathrm{T}}$ via the collinear approximation. Additional cuts are then applied to the $\mu\tau_{\mathrm{e}}$ system and vetoes against additional objects in the event are required. The modelling of the background is migrated from the eμ resonance search with little additional effort. However, additional systematic uncertainties have to be considered because the usage of $\not{E}_{\mathrm{T}}$ in the analysis requires a description of the entire event and in particular the evaluation of uncertainties associated with the jet energy scale and resolution. Due to the accuracy of the collinear approximation at high p_{T}^{τ}, the modelling of the resonance signal shape and the statistical interpretation can be carried out in a similar fashion as described in detail in the eμ search.

Reconstruction of electrons from boosted τ decays

It remains to be shown whether the set of electron identification criteria described in Sec. 4.3, which defines the HEEP electron selection and is optimized for promptly produced electrons, is suitable for the selection of non-prompt electrons from τ decays. It is first checked that the reconstruction efficiency of GSF tracks for generated electrons in the acceptance does not differ from that of promptly produced electrons using the simulated signal samples. The identification efficiency of electrons from τ decays, defined as the ratio of events that pass the full electron selection to those with a GSF electron candidate that passes the E_{T} and η requirements and that can be matched to a generated electron within a cone of size $\Delta R = 0.1$, is shown in Fig 11.4 (left). For electron transverse momenta only slightly above the selection cut of 30 GeV, the electron identification efficiency drops as the τ p_{T} rises to values well above the electron p_{T}. This can be explained as a result of kinks in the trajectory formed by the two charged particles in the τ decay, the τ lepton itself and the electron from its decay, that lead to larger transverse impact parameters $|\mathrm{d}_{xy}|$ of the electron track compared to prompt electrons. Since the cut values on $|\mathrm{d}_{xy}|$ differ between 0.02 cm for electrons in the barrel and 0.05 cm for those in the endcaps, electrons from τ decays are effected differently by this cut in these two regions of the detector. This is reflected by the difference of the electron identification efficiencies of electrons from τ decays (taken from the $\mu\tau$ RPV $\tilde{\nu}_{\tau}$ signal simulation) and of promptly produced electrons (taken from the eμ RPV $\tilde{\nu}_{\tau}$ signal simulation) in Fig. 11.4 (right), which is negative for electrons with $p_{\mathrm{T}}^{\mathrm{gen}} \lesssim 500$ GeV in the barrel but compatible with zero over the entire probed p_{T} range for electrons in the endcaps.

In conclusion, the $\mu\tau_{\mathrm{e}}$ resonance search could benefit from a re-optimization of the transverse impact parameter cut for electrons in the barrel region. However, this would necessitate several changes to the analysis, in particular a re-evaluation of the jet-to-electron misidentification rate. Given that the electron identification efficiency is only impaired at low electron p_{T}, and that the loss in efficiency does not exceed $\mathcal{O}(10\%)$ in this region, the HEEP electron selection can be employed without spoiling the sensitivity of the $\mu\tau_{\mathrm{e}}$ analysis.

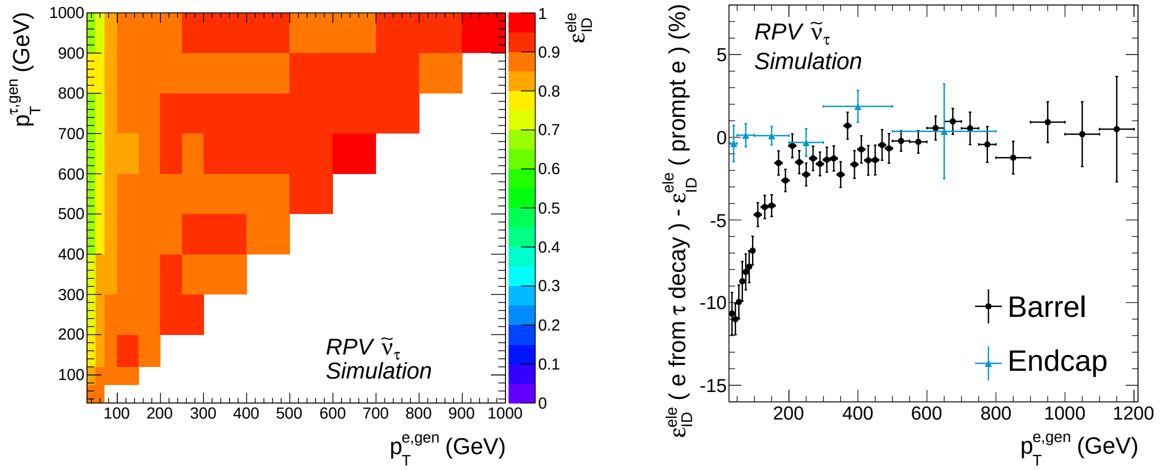

(a) The electron identification efficiency of GSF electron candidates from $\tau^{-} \to \mathrm{e}^{-}\overline{\nu}_{\mathrm{e}}\nu_{\tau}$ decays as a function of the generated τ p_{T} and electron p_{T}.

(b) Difference between the electron identification efficiency of GSF electron candidates from $\tau^{-} \to \mathrm{e}^{-}\overline{\nu}_{\mathrm{e}}\nu_{\tau}$ decays and that of promptly produced electrons.

Figure 11.4: The electron identification efficiency of GSF electron candidates from $\tau^{-} \to e^{-}\overline{\nu}_{e}\nu_{\tau}$ decays derived from simulated RPV $\tilde{\nu}_{\tau}$ signal samples.

11.2 Event selection and control distributions

The event selection is divided into two parts. First the $\mu\tau_\mathrm{e}$ pair is selected, then additional cuts are applied on the event topology to further suppress background. The selection criteria are given below in the form of bullet points referring back to the introductory chapter on physics object reconstruction, Sec. 3, and the event selection of the eμ search, Sec. 4.

Trigger

The HLT path `HLT_Mu22_Photon22` is used. It writes to the MuEG primary dataset and requires a global muon candidate with $p_\mathrm{T} > 22$ GeV and a cluster in the ECAL with $E_\mathrm{T} > 22$ GeV. No cuts on the isolation or the pseudorapidity are imposed on the trigger objects. Using this two-object trigger allows for reduced p_T thresholds at trigger level compared to the single-object triggers. Originally, this trigger path has been chosen in order to perform two searches, the presented $\mu\tau_\mathrm{e}$ search and a search for eτ_μ resonances, starting from the same primary dataset. However, the eτ_μ search has not been completed.

Selection of the $\mu\tau_\mathrm{e}$ pair

Details about the muon and electron identification criteria have been presented in Secs. 4.2 and 4.3. The terminology used to describe the $\not{E}_\mathrm{T}$ selection has been introduced in Sec. 3.4.3.

- Muon selection
  - $p_\mathrm{T}^\mu \geq 45$ GeV
  - $|\eta^\mu| \leq 2.4$
  - High-p_T muon selection
  - *Tune P* momentum assignment
- Electron selection
  - $E_\mathrm{T}^\mathrm{e} \geq 30$ GeV
  - $|\eta^\mathrm{e}| \leq 1.442$ (barrel) or $1.56 \leq |\eta^\mathrm{e}| \leq 2.5$ (endcap)
  - HEEP electron selection
- Missing transverse energy selection

  The missing transverse energy is obtained from the particle-flow (PF) description of the entire event. It is corrected for the difference between the muon momentum obtained from the global muon track, which is invoked in the PF algorithm, and the *Tune P* momentum assignment used in this analysis.
  - $\not{E}_\mathrm{T} \geq 25$ GeV
  - $\not{E}_\mathrm{T}$ event filters are applied
  - Jet energy and pileup corrections are applied to $\not{E}_\mathrm{T}$
  - $\not{E}_\mathrm{T}$ is corrected for the ϕ modulation
- τ_e selection

  τ_e candidates are formed from selected electrons and $\not{E}_\mathrm{T}$ using the collinear approximation described in Sec. 11.1.2.
  - $\Delta\phi(\mathrm{e}, \not{E}_\mathrm{T}) < 1.0$
  - $p_\mathrm{T}^\tau \geq 50$ GeV

Selection cuts on the event topology

After the selection of the $\mu\tau_{\mathrm{e}}$ pair, additional cuts are applied to the event topology in the following order.

1. $\Delta\phi(\mu, \tau_{\mathrm{e}}) \geq 2.5$
2. $p_{\mathrm{T}}^{\mu} \geq E_{\mathrm{T}}^{\mathrm{e}}$
3. Veto against b-tagged jets with $p_{\mathrm{T}}^{\mathrm{jet}} > 35$ GeV and $|\eta^{\mathrm{jet}}| < 2.4$
4. $M_{\mu,\not{E}_{\mathrm{T}}}^{\mathrm{coll}} \geq 100$ GeV
   The mass observable $M_{\mu,\not{E}_{\mathrm{T}}}^{\mathrm{coll}}$ is defined as $M_{\mu,\not{E}_{\mathrm{T}}}^{\mathrm{coll}} = [(p_{\mu} + p_{\Sigma\nu}^{\mathrm{coll}})^{\alpha}(p_{\mu} + p_{\Sigma\nu}^{\mathrm{coll}})_{\alpha}]^{1/2}$, where p_{μ} denotes the four-momentum of the muon and $p_{\Sigma\nu}^{\mathrm{coll}}$ denotes a (pseudo-)four-momentum representing the neutrinos from the τ decay in the collinear approximation. The latter is constructed by setting the associated transverse momentum equal to $\not{E}_{\mathrm{T}}$, using the ϕ coordinate of $\vec{\not{E}}_{\mathrm{T}}$ and the pseudorapidity of the electron, and assuming the mass $[(p_{\Sigma\nu}^{\mathrm{coll}})^{\alpha}(p_{\Sigma\nu}^{\mathrm{coll}})_{\alpha}]^{1/2}$ to be zero. The mass observable $M_{\mu,\not{E}_{\mathrm{T}}}^{\mathrm{coll}}$ allows for a better separation between the signal and background in this analysis than the more commonly used transverse mass $M_{\mathrm{T}}(\mu, \not{E}_{\mathrm{T}})$.

11.2.1 Background studies in control distributions

Study of the $\mathrm{t\bar{t}}$ background in control distributions with b-tagged jets

As pointed out in the context of the eμ resonance search, events containing an eμ pair and b-tagged jets constitute clean control samples of $\mathrm{t\bar{t}}$ events with an additional component of single-top production in the tW channel that accounts for about 7% of these events, according to simulations. In the $\mu\tau$ resonance search, such a control sample is selected by inverting the veto against b-tagged jets that is part of the event selection. After the selection of the $\mu\tau_{\mathrm{e}}$ pair, the thus defined top control sample consists of 4279 events. In Fig. 11.5 (left), the observed $M_{\mu\tau}^{\mathrm{coll}}$ distribution is compared to the sum of the simulated mass spectra of the $\mathrm{t\bar{t}}$ and single-top tW backgrounds, which yields a total of 4400 ± 480 (syst) expected events. The systematic uncertainties in the background expectation, that have not been introduced yet, are already included in the text and plots in this paragraph and will be discussed in detail in Sec. 12.2. The b-tagging efficiency in the simulation has been corrected to that measured in data by reweighting the events as described in Sec. 7.4. The reweighting of the top p_{T} in the simulated $\mathrm{t\bar{t}}$ background sample mentioned in Sec. 8.1.3 is not applied. The discrepancies between the $M_{\mu\tau}^{\mathrm{coll}}$ spectra obtained from data and simulation are covered within the statistical uncertainties over the entire mass range. At high $M_{\mu\tau}^{\mathrm{coll}}$, where the number of observed events per bin is low, the comparison between data and simulation is facilitated by the cumulative $M_{\mu\tau}^{\mathrm{coll}}$ distribution in Fig. 11.5 (right). No significant difference between data and expectation is observed in the shape of the two distributions or the overall event yield. In addition to the distribution in $M_{\mu\tau}^{\mathrm{coll}}$, the central observable in the $\mu\tau$ resonance search, the spectra of observables describing the muon and τ_{e} kinematics are investigated for discrepancies between data and simulation, such as the p_{T}^{τ} spectrum shown in Fig. 11.6 (left). No indications for a gross mis-modelling of these distributions by the simulation are found.

After these initial tests of the simulation at the level of the $\mu\tau_{\mathrm{e}}$ pair selection, the distributions of the observables associated with the cuts on the event topology are investigated cut stage by cut stage in Figs. 11.6 (right), 11.7 (left), and 11.7 (right). The observed spectra are described well by the simulation in all three cases. Among the events in the top control sample with a selected $\mu\tau_{\mathrm{e}}$ pair, 44% pass the cut $\Delta\phi(\mu, \tau) \geq 2.5$, and 64% of the remaining events feature a ratio of $p_{\mathrm{T}}^{\mu}/E_{\mathrm{T}}^{\mathrm{e}}$ above one. Of the remaining events, 97% feature $M_{\mu,\not{E}_{\mathrm{T}}}^{\mathrm{coll}}$ in excess of 100 GeV.

After the full event selection 1161 events remain. Their $M_{\mu\tau}^{\mathrm{coll}}$ distribution is presented in Fig. 11.8 together with the corresponding cumulative distribution. The most prominent discrepancy between data and expectation is found in the number of events above $M_{\mu\tau}^{\mathrm{coll}} = 800$ GeV. The event

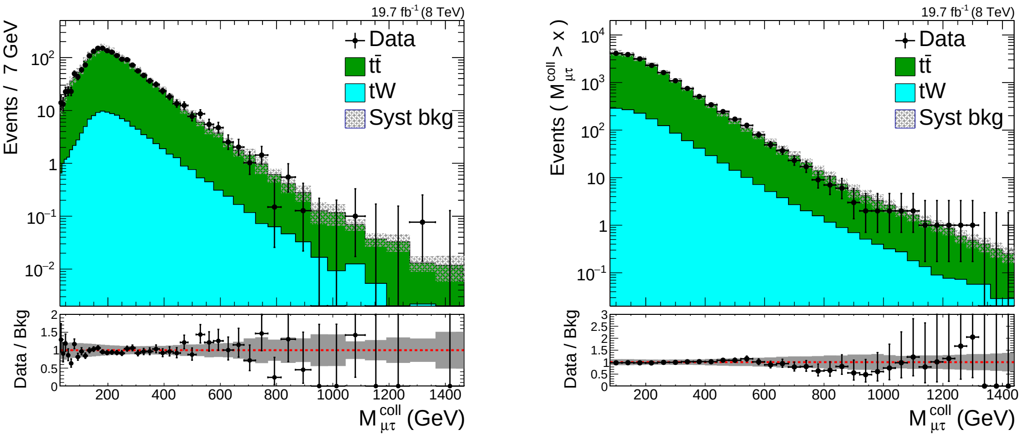

(a) The $M_{\mu\tau}^{\mathrm{coll}}$ distribution binned according to the detector resolution.

(b) The cumulative $M_{\mu\tau}^{\mathrm{coll}}$ distribution.

Figure 11.5: The $M_{\mu\tau}^{\mathrm{coll}}$ *distribution of events containing a b-tagged jet after the selection of a* $\mu\tau_{\mathrm{e}}$ *pair. The observed spectra are compared to the sum of the simulated mass spectra of the* $t\bar{t}$ *and single-top* tW *backgrounds. The shaded band in the ratio plot represents the systematic uncertainty in the background estimate.*

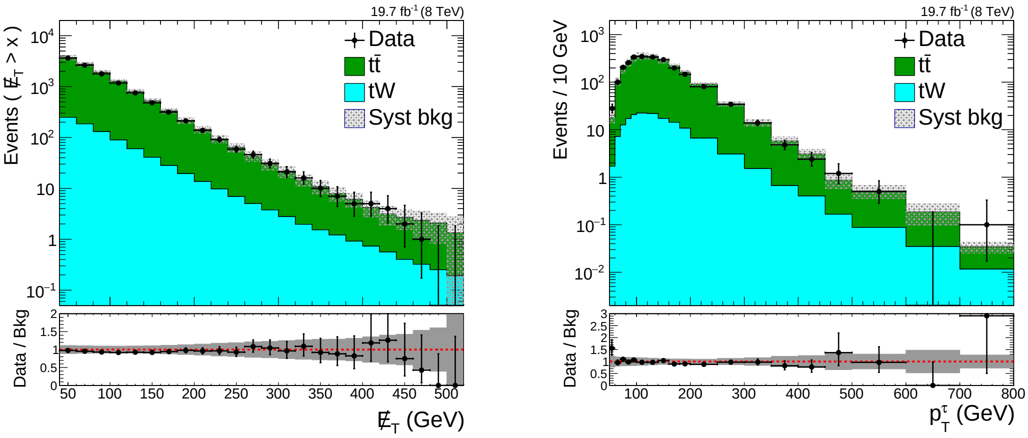

(a) The cumulative $\not{E}_{\mathrm{T}}$ distribution.

(b) The p_{T}^{τ} distribution.

Figure 11.6: The cumulative $\not{E}_{\mathrm{T}}$ *distribution and the* p_{T}^{τ} *distribution of events containing a b-tagged jet after the selection of a* $\mu\tau_{\mathrm{e}}$ *pair. The observed spectra are compared to the sum of the simulated spectra of the* $t\bar{t}$ *and single-top* tW *backgrounds.*

yield obtained from the background simulation is 6.9 ± 2.3 (syst), and three events are observed in data. Given that these numbers agree within the 2σ-level when considering the statistical uncertainty only, and that the agreement between data and simulation is even better at lower masses, this test in the top control region supports the usage of the simulation for the $\mathrm{t\bar{t}}$ and single-top tW backgrounds in the analysis.

Study of backgrounds at low $M_{\mu\tau}^{\mathrm{coll}}$

Searches for $\mu\tau$ resonances with resonance masses below 200 GeV have been carried out by the CMS collaboration, probing the data for signs of LFV Higgs decays [26]. No significant excess is observed. The $\mu\tau$ search presented in this work therefore targets the signal mass range $M_{\mathrm{res}} \geq 200$ GeV. The sample of events passing the event selection with $M_{\mu\tau}^{\mathrm{coll}} < 200\ \mathrm{GeV} - 3\,\sigma_M$,

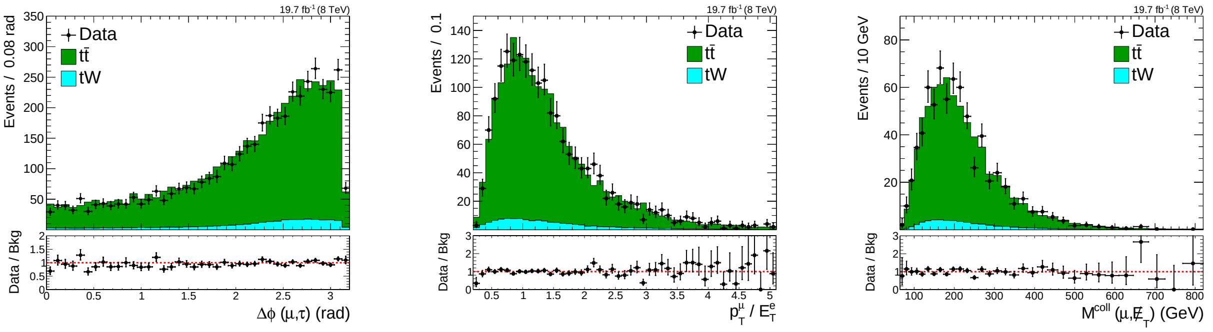

(a) The $\Delta\phi(\mu, \tau_{\mathrm{e}})$ distribution after the selection of a $\mu\tau_{\mathrm{e}}$ pair.

(b) The distribution of the ratio of muon p_{T} to electron E_{T} after the cut on $\Delta\phi(\mu, \tau_{\mathrm{e}})$.

(c) The $M^{\mathrm{coll}}_{\mu,\not{E}_{\mathrm{T}}}$ distribution after the cut on the ratio of muon p_{T} to electron E_{T}.

Figure 11.7: The distribution of $\Delta\phi(\mu, \tau_{\mathrm{e}})$, the ratio of muon p_{T} to electron E_{T}, and the $M^{\mathrm{coll}}_{\mu,\not{E}_{\mathrm{T}}}$ distribution of events containing a b-tagged jet. The observed spectra are compared to the sum of the simulated spectra of the $t\bar{t}$ and single-top tW backgrounds. The distributions are obtained at different stages of the event selection, that are specified in the individual captions.

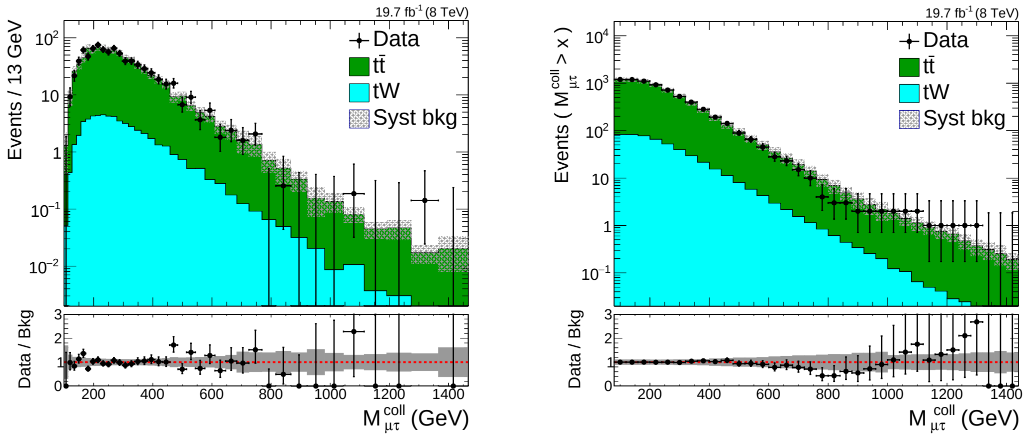

(a) The $M^{\mathrm{coll}}_{\mu\tau}$ distribution binned according to the detector resolution.

(b) The cumulative $M^{\mathrm{coll}}_{\mu\tau}$ distribution.

Figure 11.8: The $M^{\mathrm{coll}}_{\mu\tau}$ distribution of events in data containing a b-tagged jet after the full event selection. The observed spectra are compared to the sum of the simulated mass spectra of the $t\bar{t}$ and single-top tW backgrounds. The shaded band in the ratio plot represents the systematic uncertainty in the background estimate.

where σ_M denotes the $M^{\mathrm{coll}}_{\mu\tau}$ resolution, can be considered to be essentially free of contributions from signal events and can serve as a control region for the high-mass search. As will be shown in Sec. 11.3.2, the relative $M^{\mathrm{coll}}_{\mu\tau}$ resolution for a resonance mass of 200 GeV is about 8%, and the low-mass control region is therefore defined by the cut $M^{\mathrm{coll}}_{\mu\tau} < 150$ GeV. At lower masses, the Drell-Yan production of τ pairs is enhanced relative to other background processes, and the normalization of the corresponding simulated background sample can thus be tested in the low-mass control region. Figure 11.9 shows the distribution of the number of selected particle-flow jets and that of the number of b-tagged jets obtained from events in the low-mass control region that pass the $\mu\tau_{\mathrm{e}}$ pair selection, as well as the cuts on $\Delta\phi(\mu, \tau)$ and on the muon p_{T} to electron E_{T} ratio. In both distributions, data and simulation agree within the uncertainties. The leading background in the subset of events without selected jets is the Drell-Yan production of τ pairs, followed by the diboson WW background and the estimate of the W + jet and QCD multijet

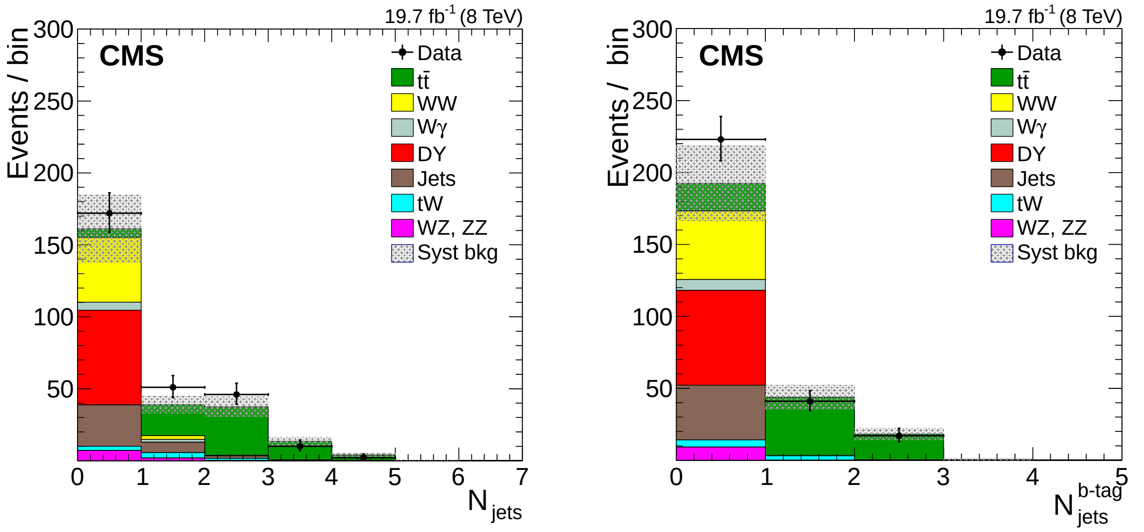

(a) The distribution of the number of selected particle-flow jets with $p_{\mathrm{T}}^{\mathrm{jet}} > 35$ GeV.

(b) The distribution of the number of selected particle-flow jets with a b-tag and $p_{\mathrm{T}}^{\mathrm{jet}} > 35$ GeV.

Figure 11.9: The distributions of the number of jets (left) and the number of b-tagged jets (right) obtained from events in the low-mass control region ($M_{\mu\tau}^{\mathrm{coll}} < 150$ GeV) that pass the $\mu\tau_{\mathrm{e}}$ pair selection, as well as the cuts on $\Delta\phi(\mu,\tau)$ and on the muon p_{T} to electron E_{T} ratio.

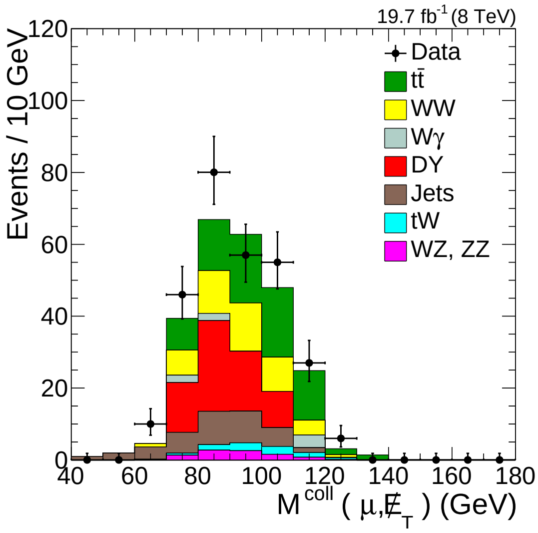

Figure 11.10: The $M_{\mu,\not{E}_{\mathrm{T}}}^{\mathrm{coll}}$ distribution obtained from events in the low-mass control region ($M_{\mu\tau}^{\mathrm{coll}} < 150$ GeV) that pass the $\mu\tau_{\mathrm{e}}$ pair selection, as well as the cuts on $\Delta\phi(\mu,\tau)$ and on the muon p_{T} to electron E_{T} ratio. Only the statistical uncertainties are shown.

background. The systematic uncertainty of about 15% in the expected event yield in the $N_{\mathrm{jet}} = 0$ bin arises mainly from the sizeable statistical uncertainty in the simulated Drell-Yan background and the uncertainty in the misidentification rate, that contribute uncertainties of 11% and 5%, respectively. The $M_{\mu,\not{E}_{\mathrm{T}}}^{\mathrm{coll}}$ distribution of the same subset of events in the low-mass control region is depicted in Fig. 11.10. Due to the small remaining number of selected events in the Drell-Yan background sample, the systematic uncertainties cannot be evaluated reliably and are therefore omitted in Fig. 11.10. The background estimate provides a satisfactory representation of the data within the statistical uncertainties.

11.3 Signal properties

11.3.1 Signal efficiency of the event selection

The signal efficiency evaluated at several stages of the event selection is presented in Figs. 11.11 and 11.12 as a function of the τ sneutrino mass. The overall fraction of resonantly produced $\mu\tau$ pairs that pass the event selection is shown in Fig. 11.11 (right). It is given by the product of the branching fraction $\mathcal{B}(\tau^- \to \mathrm{e}^-\overline{\nu}_\mathrm{e}\nu_\tau)$; the acceptance of the visible decay products, muon and electron; and the efficiency of the selection cuts. It exhibits a steep rise with the resonance mass from 2.3% at $M_{\tilde{\nu}_\tau} = 200$ GeV to 9.5% at about $M_{\tilde{\nu}_\tau} = 1$ TeV, and eventually reaches just below 11% at $M_{\tilde{\nu}_\tau} = 2.6$ TeV. The turn-on of the full selection efficiency extends over a mass range of several hundred GeV, that is much wider than in the eμ resonance search (Fig. 5.6). This behaviour is already present in the signal acceptance of the visible decay products in Fig. 11.11 (left), where the acceptance is defined by the cuts on pseudorapidity and transverse momentum of the muon and electron at generator level. It is a result of the three-body decay of the τ lepton, in which the τ momentum is shared among the decay products. The selection efficiencies for all consecutive steps of the event selection, defined relative to the set of events passing the previous cuts, are presented in Fig. 11.12. The fraction of eμ pairs in the acceptance that pass the lepton reconstruction and identification criteria as well as the trigger requirement reaches a plateau of about 70% at $M_{\tilde{\nu}_\tau} \approx 400$ GeV. All additional cuts reach values above 95% at high resonance masses but exhibit different turn-on curves. The reconstruction efficiency of the τ lepton using the collinear approximation rises steeply below $M_{\tilde{\nu}_\tau} = 500$ GeV mainly because it includes the $\not{E}_\mathrm{T}$ cut that introduces an inefficiency at low resonance mass. Over the entire resonance mass range probed, the requirement in $|\Delta\phi|$ between the muon and the τ candidate is over 90% efficient and its efficiency rises further as the relativistic boost of the $\tilde{\nu}_\tau$ in the transverse plane decreases at high $M_{\tilde{\nu}_\tau}$. All other selection efficiencies lie above 95% for signal masses above 200 GeV. The only cut that comes with a decreasing efficiency at higher $M_{\tilde{\nu}_\tau}$ is the veto of b-tagged jets, which is not directly linked to the $\tilde{\nu}_\tau$ production and decay kinematics. This decrease is due to the increase of the fraction of signal events that include light jets (u, d, s, g) with high p_T for rising $\sqrt{\hat{s}}$, and the increase in the b-tag misidentification rate of light jets for high jet p_T.

11.3.2 Collinear mass resolution

To the end of parameterizing the $M_{\mu\tau}^\mathrm{coll}$ distribution of the signal as a function of the resonance mass, the signal resolution is studied on selected $\mu\tau_\mathrm{e}$ events from simulated signal samples. Double-sided Crystal ball fits and constrained Gaussian fits are applied to the distributions of the relative residual $R_\mathrm{res}^\mathrm{coll} = (M_{\mu\tau}^\mathrm{coll,\,reco} - M_{\mu\tau}^\mathrm{gen})/M_{\mu\tau}^\mathrm{gen}$ obtained for different choices of $M_{\tilde{\nu}_\tau}$, as described in the context of the eμ search in Sec. 5.4. The fit results for $M_{\tilde{\nu}_\tau} = 0.2,\ 0.5$ and 2 TeV are presented in Fig. 11.13. The Gaussian model describes the distribution better than in the case of the eμ resonance (Fig. 5.9), and is only marginally improved by the CB model.

Figure 11.14 (left) displays the Gaussian core resolution of the $\mu\tau_\mathrm{e}$ mass as a function of the resonance mass. In contrast to the $M_{\mathrm{e}\mu}$ resolution in Fig. 5.10, the resolution of $M_{\mu\tau}^\mathrm{coll}$ does not rise monotonously with the resonance mass, but exhibits a minimum of 5.8% at around $M_{\tilde{\nu}_\tau} = 500$ GeV. Towards lower values of the resonance mass, the resolution is impaired by the missing transverse energy resolution at low $\not{E}_\mathrm{T}$, that is affected by the underlying event and pileup interactions. It reaches 8.3% at $M_{\tilde{\nu}_\tau} = 0.2$ TeV. Above $M_{\tilde{\nu}_\tau} = 500$ GeV, the $M_{\mu\tau}^\mathrm{coll}$ resolution rises because the muon transverse momentum resolution worsens, which influences both reconstructed leptons in the final state: the muon p_T measurement is affected directly, and the muon $\vec{p}_\mathrm{T}$ enters the $\vec{\not{E}}_\mathrm{T}$ calculation and thus the transverse momentum assigned to the τ_e candidate via the collinear approximation. As a result, the relative $M_{\mu\tau}^\mathrm{coll}$ resolution at $M_{\tilde{\nu}_\tau} = 1.7$ TeV is similar to that at $M_{\tilde{\nu}_\tau} = 0.2$ TeV. Care has to be taken to correct the default PF $\not{E}_\mathrm{T}$ that uses the muon p_T from the global muon fit to the *Tune P* p_T assignment. As illustrated in Fig. 11.14 (right) by the

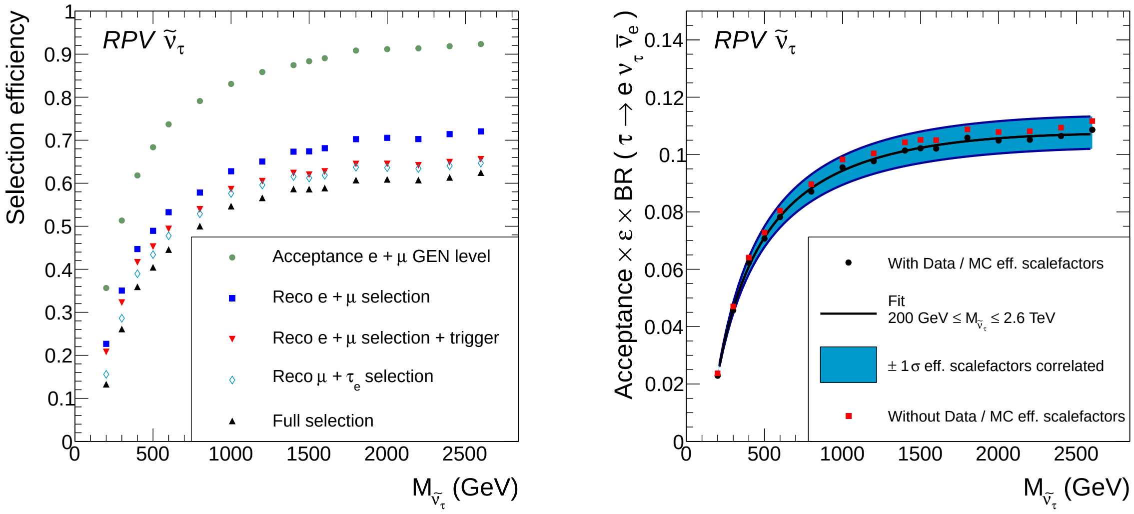

(a) Evolution of the RPV $\tilde{\nu}_\tau$ selection efficiency from the signal acceptance to the efficiency after the full event selection as a function of signal mass $M_{\tilde{\nu}_\tau}$ based on simulated signal samples. All efficiencies shown are defined as the fraction of events passing the indicated selection requirements relative to the total number of simulated $\tilde{\nu}_\tau \to \mu\tau_{\mathrm{e}}$ events in the corresponding MC sample. The acceptance of the generated eμ pair (green dots) is defined by the p_{T} and η cuts on the generated leptons after final state radiation.

(b) The product of signal acceptance, efficiency, and branching fraction $\mathcal{B}(\tau^- \to \mathrm{e}^-\overline{\nu}_{\mathrm{e}}\nu_\tau)$ for the RPV $\tilde{\nu}_\tau$ signal. The uncertainty in the efficiency is obtained by treating the uncertainties in the data-to-simulation scale factors of the individual efficiencies as fully correlated. For comparison, the full selection efficiency obtained from the simulation (red squares) without data-driven corrections to the efficiencies is shown. The solid black curve is the result of the fit that is one input to the parameterization of the signal.

Figure 11.11: Signal acceptance and selection efficiencies of the $\mu\tau_{\mathrm{e}}$ selection for the RPV $\tilde{\nu}_\tau$ model as a function of signal mass $M_{\tilde{\nu}_\tau}$.

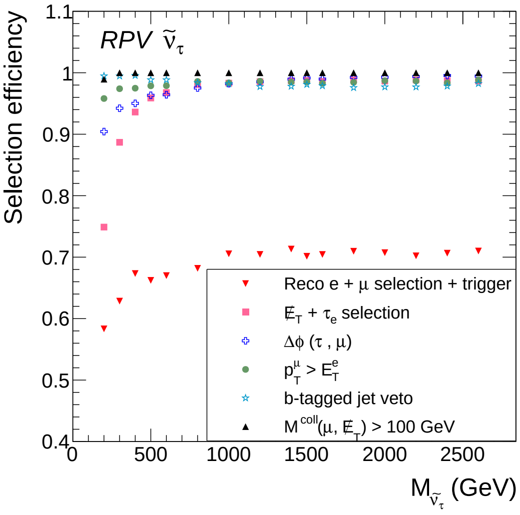

Figure 11.12: The efficiencies of various selection requirements as a function of the signal mass $M_{\tilde{\nu}_\tau}$. The efficiency of the eμ pair selection, that includes the trigger requirement, is defined with respect to the number of simulated signal events with an electron and a muon that pass the acceptance requirements at generator level. All other efficiencies are evaluated with respect to the events satisfying all previous cuts in the order indicated in the legend.

comparison between the RMS of the $R_{\text{res}}^{\text{coll}}$ distributions obtained with and without this correction, the usage of the default PF $\not{E}_{\mathrm{T}}$ widens the tails of the resonance peak in $M_{\mu\tau}^{\text{coll}}$ for large resonance masses and correspondingly high muon p_{T}.

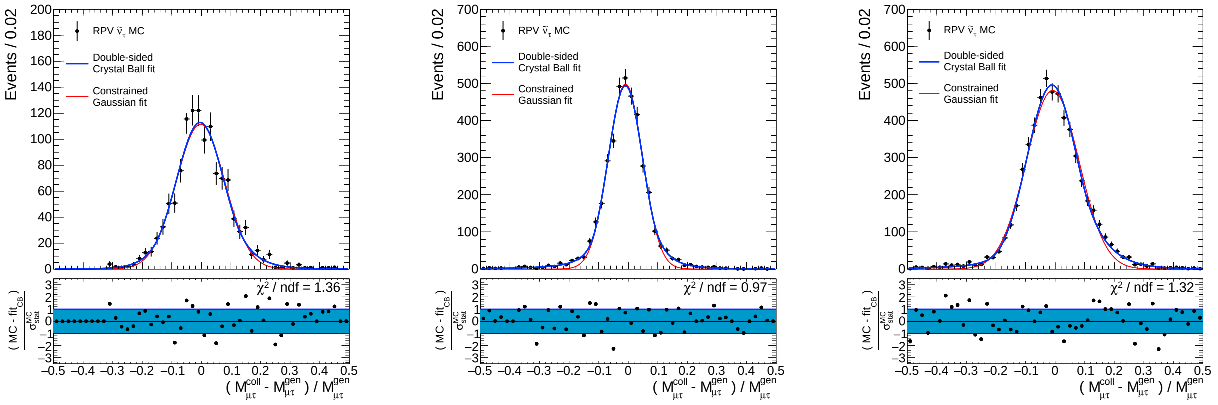

(a) $R_{\text{res}}^{\text{coll}}$ for $M_{\tilde{\nu}_\tau} = 200$ GeV. (b) $R_{\text{res}}^{\text{coll}}$ for $M_{\tilde{\nu}_\tau} = 500$ GeV. (c) $R_{\text{res}}^{\text{coll}}$ for $M_{\tilde{\nu}_\tau} = 2$ TeV.

Figure 11.13: Distributions of the relative residual $R_{\text{res}}^{\text{coll}}$ obtained from events passing the event selection in simulated signal samples for different $M_{\tilde{\nu}_\tau}$. Two different fits are applied to the simulated data, a double-sided CB fit and a Gaussian fit with restricted fit range. The uncertainty bars represent the statistical uncertainty in the number of simulated events, which are taken into account in the fits. Since the signal efficiency of the event selection is significantly lower for $M_{\tilde{\nu}_\tau} = 200$ GeV than for the other two considered resonance masses, less signal events enter the corresponding distribution.

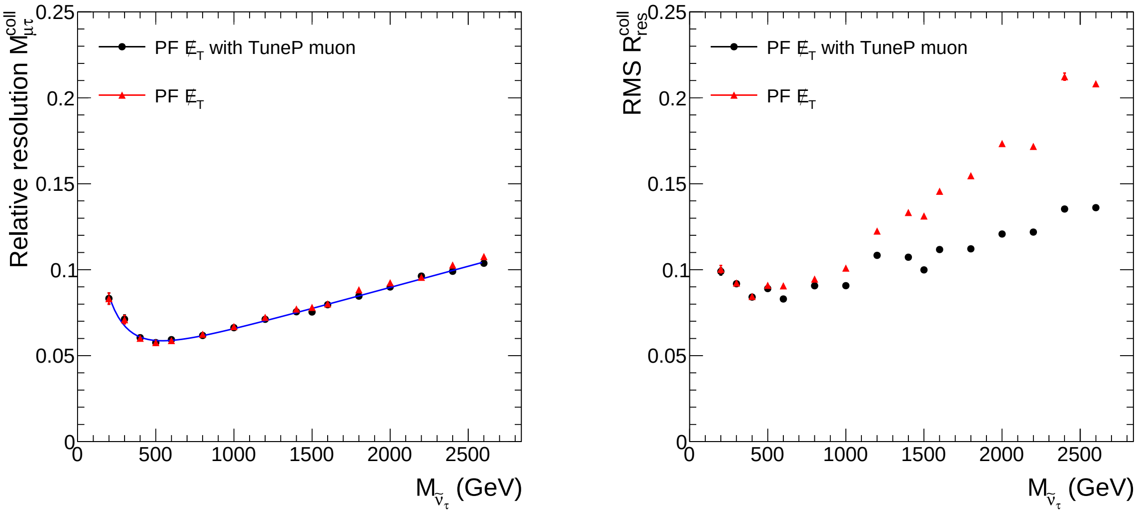

(a) The standard deviation obtained from constrained Gaussian fits to the $R_{\text{res}}^{\text{coll}}$ distribution evaluated as a function of $M_{\tilde{\nu}_\tau}$.

(b) The RMS of the $R_{\text{res}}^{\text{coll}}$ distribution evaluated as a function of $M_{\tilde{\nu}_\tau}$.

Figure 11.14: Comparison of two different measures of the $M_{\mu\tau}^{\text{coll}}$ resolution evaluated from simulated signal samples. The graphs are shown for two different muon p_{T} assignments used in the calculation of the PF $\not{E}_{\mathrm{T}}$; the first one obtained from the Tune P algorithm and the second one obtained from the standard global muon reconstruction.

Chapter 12

Comparing observation and expectation for selected $\mu\tau_{\mathrm{e}}$ events

12.1 Description of the selected event sample

12.1.1 Cutflow $\mu\tau$ selection

Apart from the changes concerning the trigger requirement and a slight reduction of the electron E_{T} cut from 35 GeV to 30 GeV, the selections of muons and electrons in the $\mu\tau$ resonance search are the same as in the eμ resonance search. Since the background estimation, the resulting background composition, and the level of agreement between background estimate and data have been discussed in detail in the context of the eμ resonance search, the preselection of eμ pairs serves as a starting point for this overview of the individual stages of the $\mu\tau_{\mathrm{e}}$ event selection. In the following paragraph, all distributions of observables to which selection cuts are applied are shown and the impact of the individual cuts on the background expectation is briefly discussed. The efficiencies of the selection cuts for the individual background processes and the total background expectation are summarized in Tab. 12.1. The systematic uncertainties assigned to the background yields given in the text, tables and figures in this paragraph will be discussed in detail in Sec. 12.2. As in the notation used in the presentation of the eμ search, the label *Jets* in the figures and tables refers to the data-driven background estimate of the W + jet and QCD multijet processes.

First, the initial steps of the τ_{e} selection that involve the missing transverse energy are explained. After selecting events that fulfill the trigger requirement, contain at least one isolated muon and one isolated electron and pass all $\not\!\!E_{\mathrm{T}}$ event filters listed in Sec. 3.4.3, 35470 events are observed in data. The $\not\!\!E_{\mathrm{T}}$ event filters remove 249 of the events with a selected eμ pair, corresponding to a rejection probability of seven per mille. The CSC beam halo filter is the reason for rejecting the event in 130 of the 249 cases. The $\not\!\!E_{\mathrm{T}}$ distribution of the selected 35470 events is shown in Fig. 12.1 (left). The highest missing transverse energy observed has a value of 554 GeV. In the tail of the distribution above 400 GeV, 12 events are found in data matching the expectation of 15 ± 3.6 (syst) events. As pointed out in Sec. 11.1.2, a significant fraction of signal events feature a missing transverse energy below 50 GeV for resonance masses below 500 GeV. The low $\not\!\!E_{\mathrm{T}}$ cut at 25 GeV yields a signal efficiency above 90% for a resonance mass of 300 GeV while only about 50% of the Drell-Yan background events pass this requirement.

According to the simulation, the subsequent cut on $\Delta\phi(e, \not\!\!E_{\mathrm{T}})$ rejects about 75% of the total background, as can be seen in Fig. 12.1 (middle). The cut is particularly efficient at rejecting W + jet events, in which the most typical event topology involves a W decaying into a muon and corresponding neutrino that results in missing transverse energy, and a recoiling jet that is misidentified as an electron. Only 15% of the events in the data-driven W + jet and QCD multijet background estimate pass the $\Delta\phi(e, \not\!\!E_{\mathrm{T}})$ requirement. It only rejects about a third of $\mathrm{Z}/\gamma \rightarrow \tau_{\mathrm{e}}\tau_{\mu}$ background events because the τ leptons are typically boosted in these events and the neutrinos from the τ decays tend to fall into the direction of the produced charged leptons. The signal efficiency of the $\Delta\phi(e, \not\!\!E_{\mathrm{T}})$ cut is 95% for a resonance mass of 200 GeV and it rises

Table 12.1: The efficiency of each cut in the event selection of the $\mu\tau_{\mathrm{e}}$ search for the total background estimate and the individual background processes in percent. The efficiency of the $\not\!\!E_{\mathrm{T}}$ cut is defined relative to the number of events passing the selection of an eμ pair, including the trigger requirement. The efficiencies of the subsequent cuts are defined relative to the number of events passing all previous requirements. The last row gives the total selection efficiency for events with an eμ pair. The efficiencies are evaluated at an accuracy of two significant digits.

	Selection cut	Cut efficiency (%) total background	Cut efficiency individual background processes (%)							
			$\mathrm{t\bar{t}}$	WW	tW	Jets	DY	WZ	ZZ	Wγ
A)	$\not\!\!E_{\mathrm{T}} \geq 25$ GeV	85	90	79	89	69	52	79	39	71
B)	$\Delta\phi(\mathrm{e}, \not\!\!E_{\mathrm{T}}) < 1.0$	28	28	20	26	15	67	26	34	24
C)	$p_{\mathrm{T}}^{\tau} \geq 50$ GeV	100	100	100	100	93	100	100	100	100
D)	$\Delta\phi(\mu, \tau) \geq 2.5$	47	45	74	51	68	33	51	55	47
E)	$p_{\mathrm{T}}^{\mu} \geq E_{\mathrm{T}}^{\mathrm{e}}$	70	65	84	70	91	92	74	69	86
F)	b-jet veto	56	36	100	57	100	100	99	98	100
G)	$M_{\mu,\not E_{\mathrm{T}}}^{\mathrm{coll}} \geq 100$ GeV	89	98	88	97	70	63	91	81	79
	All cuts	3.8	2.6	8.6	4.4	4.3	6.7	7.0	3.9	5.3

further towards higher masses.

After requiring the electron E_{T} and missing transverse energy to be larger than 30 GeV and 25 GeV, respectively, and selecting events in which these two object are close in ϕ, the p_{T} cut at 50 GeV on the τ_{e} candidate obtained from the collinear approximation rejects only few events. The tau p_{T} distribution after the selection of the $\mu\tau_{\mathrm{e}}$ pair (after cut C in Tab. 12.1) is depicted in Fig. 12.1 (right). The τ_{e} candidate with the highest observed transverse momentum reaches $p_{\mathrm{T}}^{\tau} = 1006$ GeV and is built from an electron with $E_{\mathrm{T}}^{\mathrm{e}} = 675$ GeV and missing transverse energy of $\not\!\!E_{\mathrm{T}} = 356$ GeV. The observed event counts after the selection of the $\mu\tau_{\mathrm{e}}$ pair in four bins of $M_{\mu\tau}^{\mathrm{coll}}$ and in total are compared to the background expectation in Tab. 12.2 that also includes a breakdown of the background composition. Within the uncertainties the number of selected events in data and the background expectation are compatible at this stage of the event selection. The selection of the τ_{e} candidate has reduced the number of expected events by more than a factor four compared to the number of initially selected events containing an eμ pair.

The distributions of observables on which the additional selection cuts are applied after the $\mu\tau_{\mathrm{e}}$ pair has been selected are shown in Fig. 12.2 as obtained at the stage of the event selection before the respective cut. Requiring the muon and the τ_{e} candidate to be separated in the transverse plane by $\Delta\phi(\mu, \tau) > 2.5$ removes about half of the remaining background events and is particularly efficient against the Drell-Yan background, of which 67% are rejected. Since the muon p_{T} requirement is more restrictive than the cut on the electron E_{T}, the cut on the ratio of $p_{\mathrm{T}}^{\mu}/E_{\mathrm{T}}^{\mathrm{e}} > 1$ removes only 30% of the total background. The veto against b-tagged jets mainly rejects $\mathrm{t\bar{t}}$ and single-top tW events with cut efficiencies of 36% and 57%, respectively, while leaving the remaining backgrounds almost unaffected. After this cut, $\mathrm{t\bar{t}}$ events remain the leading background component but contribute less than 50% to the total number of expected events. The final selection requirement on the collinear mass of the muon and the missing transverse energy,

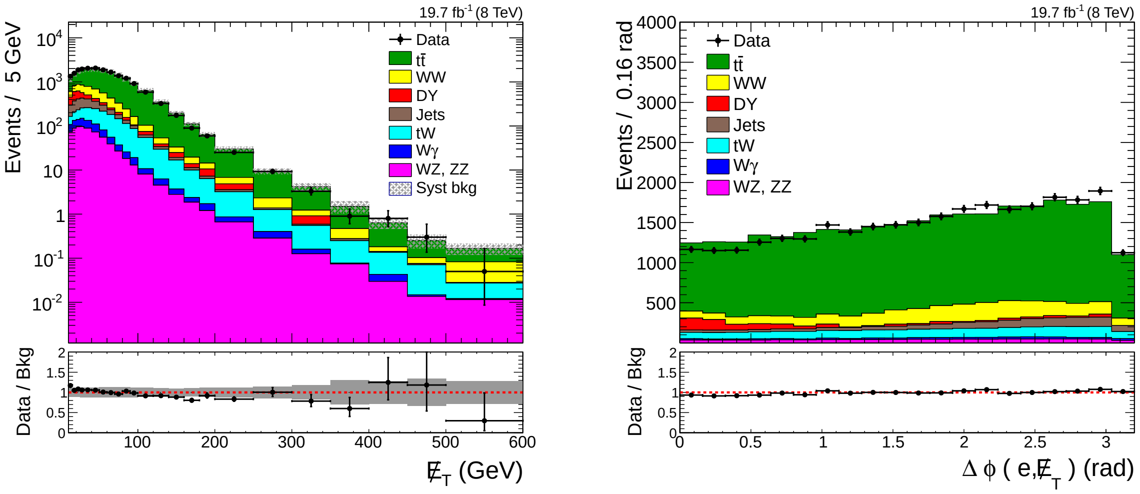

(a) The $\not{E}_\mathrm{T}$ distribution of selected events after the initial selection of an eμ pair.

(b) The $\Delta\phi(e, \not{E}_\mathrm{T})$ distribution after the selection cut on $\not{E}_\mathrm{T}$ at 25 GeV (cut stage A in Tab. 12.1).

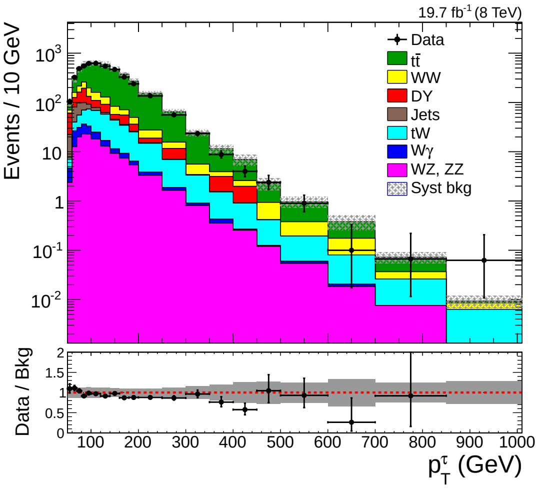

(c) The p_T^τ distribution after the selection of a $\mu\tau_\mathrm{e}$ pair (cut stage C in Tab. 12.1).

Figure 12.1: Distributions of observables related to the selection of a $\mu\tau_\mathrm{e}$ pair obtained at different stages of the event selection, that are given in the captions of the individual figures.

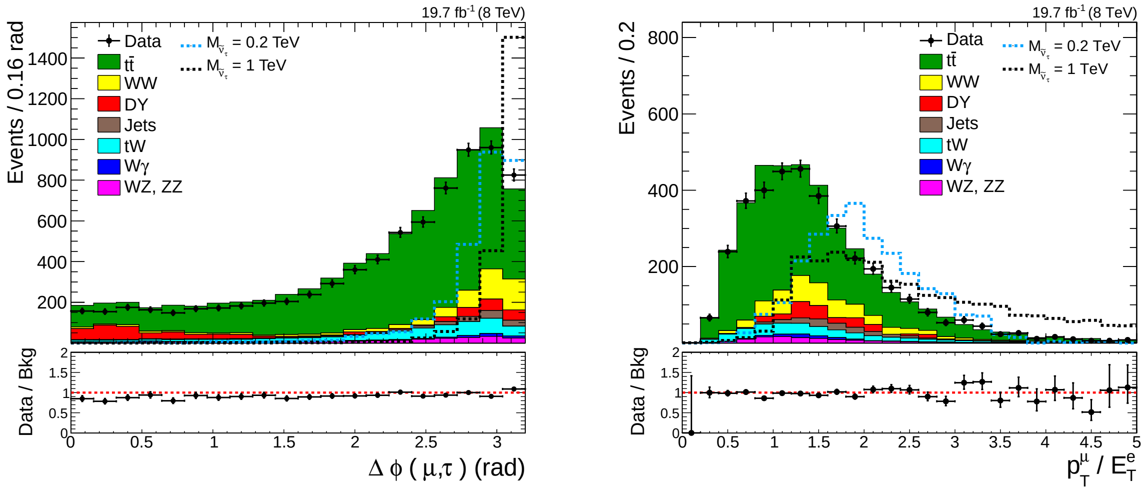

(a) The $\Delta\phi(\mu,\tau_\mathrm{e})$ distribution of selected events after the selection of a $\mu\tau_\mathrm{e}$ pair (cut stage C in Tab. 12.1).

(b) The ratio of selected muon p_T to electron E_T of events passing the $\Delta\phi(\mu,\tau_\mathrm{e})$ cut (cut stage D in Tab. 12.1).

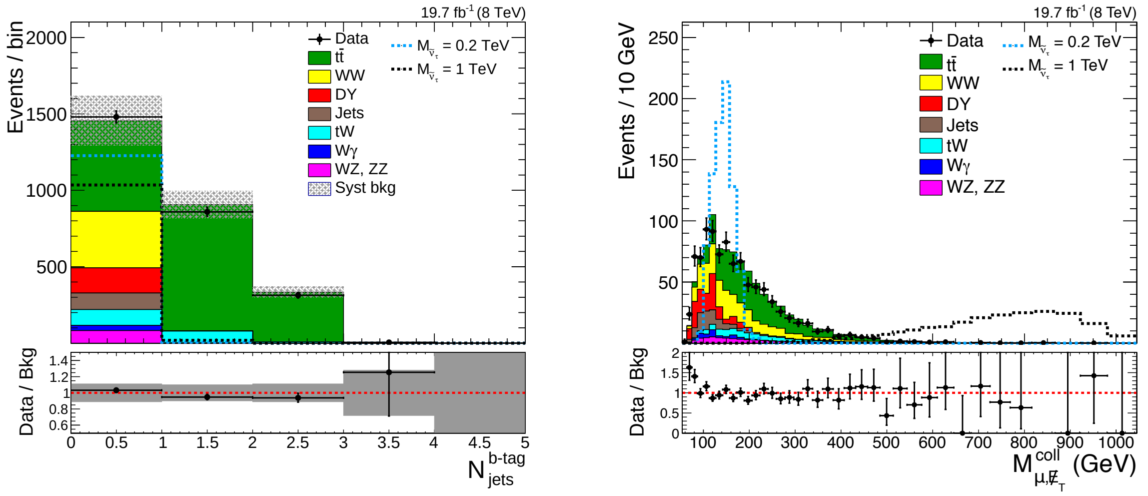

(c) The distribution of the number of b-tagged jets in events passing the cut on $p_\mathrm{T}^{\mu}/E_\mathrm{T}^{\mathrm{e}}$ (cut stage E in Tab. 12.1).

(d) The distribution of the collinear mass of the selected muon and $\vec{\not\!\!E}_\mathrm{T}$ in events passing the veto against b-tagged jets (cut stage F in Tab. 12.1).

Figure 12.2: Distributions of observables on which selection cuts are applied after the selection of the $\mu\tau_\mathrm{e}$ pair obtained at different stages of the event selection, that are given in the captions of the individual plots.

Table 12.2: The total expected and observed event yields after selection of the $\mu\tau_{\mathrm{e}}$ pair (after cut C in Tab. 12.1) and the corresponding number of events in four bins of $M_{\mu\tau}^{\mathrm{coll}}$. Systematic uncertainties in the background estimates include the statistical uncertainty arising from limited numbers of simulated events. It is added to the other uncertainties in quadrature. Due to correlations between the uncertainties in the individual backgrounds, their quadratic sum is smaller than the uncertainty in the total background estimate.

Sample	Total event yield	$M_{\mu\tau}^{\mathrm{coll}}$ ranges in units of GeV			
		< 200	200–500	500–1000	> 1000
$\mathrm{t\bar{t}}$	5985 ± 737	2648 ± 448	3146 ± 337	187 ± 29	3.6 ± 1.2
WW	598 ± 60	258 ± 37	306 ± 30	32 ± 4.1	1.5 ± 0.36
tW	540 ± 40	215 ± 17	302 ± 24	22 ± 2.2	0.62 ± 0.09
Jets	174 ± 52	122 ± 37	48 ± 15	3.1 ± 1	0.16 ± 0.09
DY	541 ± 99	491 ± 93	45 ± 17	4.9 ± 5.5	< 0.1
WZ	193 ± 15	87 ± 8.1	94 ± 7.8	11 ± 1.1	0.61 ± 0.11
ZZ	28 ± 2.9	16 ± 1.9	11 ± 1.1	0.85 ± 0.11	< 0.1
$\mathrm{W}\gamma$	104 ± 53	72 ± 37	30 ± 16	1.6 ± 1.1	< 0.1
Total bkg	8161 ± 847	3908 ± 510	3982 ± 388	264 ± 35	6.5 ± 1.3
Data	7651	3694	3680	268	9

$M_{\mu,\not{E}_{\mathrm{T}}}^{\mathrm{coll}} \geq 100$ GeV, only removes 11% of the total expected event yield but about one third of the Drell-Yan background. According to the background estimate, 96.2% of the background events passing the initial eμ selection are rejected in the course of the subsequent event selection. The corresponding reduction of the event count observed in data amounts to 96.4%.

The observed and expected event yields after the full event selection are presented in Tab. 12.3 together with the systematic uncertainty in the background estimate. Of the 1275 observed events 131 contain an eμ ($\tau_{\mathrm{e}}\mu$) pair in which the leptons carry the same electric charge in agreement with the background prediction of 113 ± 16 (syst) events. The leading backgrounds are $\mathrm{t\bar{t}}$ production that accounts for 46% of the total background estimate and WW production with 24%, followed by single-top tW production and the Drell-Yan background that contribute about 8%, each. Before turning to the observable of interest $M_{\mu\tau}^{\mathrm{coll}}$, the agreement between the background estimate and the data is checked in distributions of observables that separate the $\mathrm{t\bar{t}}$ process from other backgrounds but do not separate background and signal well, and would only deviate significantly from the background only hypothesis in case of a very large number of signal events. The distribution of the number of selected jets depicted in Fig. 12.3 (left) provides a handle to test the $\mathrm{t\bar{t}}$ component of the background composition. For $N_{\mathrm{jets}} \geq 1$, the $\mathrm{t\bar{t}}$ process is expected to dominate, and requiring at least two jets results in a $\mathrm{t\bar{t}}$ sample of high purity. The agreement between the background expectation and the data in these bins provides an additional check of the leading background process. The signal distributions in the plot for $M_{\tilde{\nu}_\tau} = 200$ GeV and $M_{\tilde{\nu}_\tau} = 1$ TeV explain why no veto against jets in the event is applied: Even for the smallest signal mass considered the fraction of events with at least one selected jet is 12%, and this fraction increases with resonance mass, or

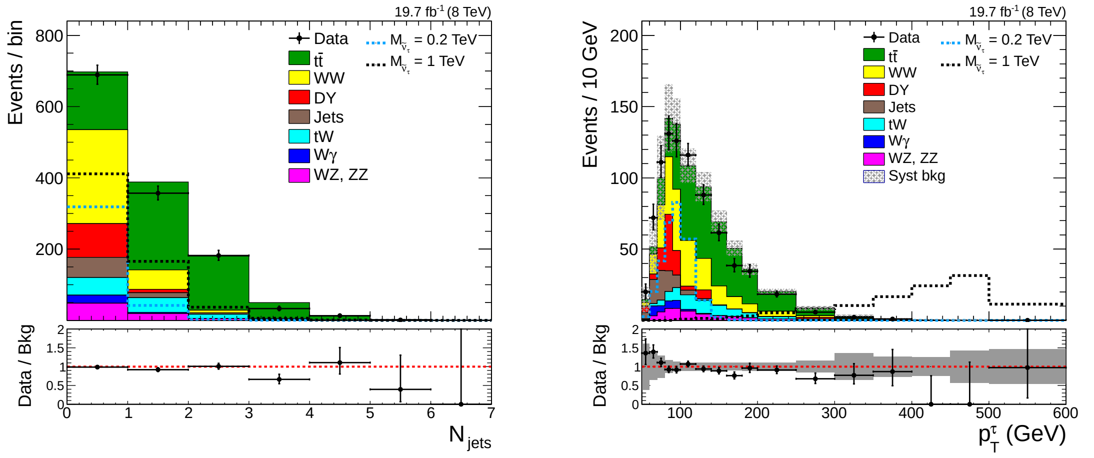

(a) The distribution of the number of selected jets obtained from events passing the full event selection.

(b) The p_T^τ distribution of events passing the full event selection.

Figure 12.3: The N_{jets} and p_T^τ distributions of events passing the full event selection.

Table 12.3: The total expected and observed event yields after the full event selection and the corresponding number of events in four bins of $M_{\mu\tau}^{\text{coll}}$. Systematic uncertainties in the background estimates include the statistical uncertainty arising from limited numbers of simulated events. It is added to the other uncertainties in quadrature.

Sample	Total event yield	$M_{\mu\tau}^{\text{coll}}$ ranges in units of GeV			
		< 200	200–500	500–1000	> 1000
tt̄	620 ± 82	103 ± 22	475 ± 63	40 ± 6.3	1.4 ± 0.64
WW	326 ± 29	87 ± 8.6	213 ± 21	26 ± 3.5	1.3 ± 0.34
tW	104 ± 8.4	19 ± 1.7	77 ± 6.7	7.5 ± 0.8	0.21 ± 0.05
Jets	76 ± 23	44 ± 13	30 ± 9.2	0.95 ± 0.32	< 0.1
DY	104 ± 27	70 ± 21	29 ± 13	4.9 ± 5.5	< 0.1
WZ	65 ± 5	15 ± 1.3	43 ± 3.6	7.1 ± 0.75	0.38 ± 0.09
ZZ	8.3 ± 0.71	2.6 ± 0.23	5.1 ± 0.49	0.51 ± 0.07	< 0.1
Wγ	33 ± 17	17 ± 9.2	15 ± 8.1	0.94 ± 0.89	< 0.1
Total bkg	1337 ± 124	358 ± 41	887 ± 90	88 ± 12	3.4 ± 0.8
Data	1275	359	837	76	3

$\sqrt{\hat{s}}$. The p_T^τ distribution of events passing the event selection is given in Fig. 12.3 (right). Within the uncertainties the background expectation and the data agree. A slight deficit with respect to the background expectation is observed for $p_T^\tau \geq 200$ GeV, where 142 events pass the selection in data and the background estimate yields 170 ± 20 (syst) events. One event with $p_T^\tau \geq 500$ GeV is observed at $p_{\mathrm{T}}^{\tau} = 576$ GeV, matching the expectation of 1.6 ± 0.7 (syst) events in this region. In summary, there is no indication of a significant deviation from the expectation in the tail of the p_{T}^{τ} distribution.

12.1.2 $M_{\mu\tau}^{\mathrm{coll}}$ spectrum of events passing the event selection

The overall agreement between the background expectation and the observation in several-hundred-GeV-wide slices of the $M_{\mu\tau}^{\mathrm{coll}}$ distribution is documented in Tab. 12.3. The $M_{\mu\tau}^{\mathrm{coll}}$ spectrum of events passing the event selection is shown in Fig. 12.5 with a binning according to the $M_{\mu\tau}^{\mathrm{coll}}$ resolution. In addition to the expectation from SM processes, two possible signal contributions are stacked on top of the background in the figure for the signal parameters $M_{\tilde{\nu}_\tau} = 200$ GeV and $\lambda'_{311} = \lambda_{323} = 0.015$; and $M_{\tilde{\nu}_\tau} = 1$ TeV and $\lambda'_{311} = \lambda_{323} = 0.04$, respectively. As can be seen in the ratio plot, the data agrees better with the background only hypothesis than with the sum of background and signal for these signal contributions. The corresponding cumulative distribution is presented in Fig. 12.6. Neither the spectrum binned according to the detector resolution nor the integral of the events in the high-mass tail exhibit a significant excess when taking the uncertainties into account.

The most striking feature of the $M_{\mu\tau}^{\mathrm{coll}}$ distribution is a single observed event with a mass of the $\mu\tau_{\mathrm{e}}$ pair of $1679 \pm 220\,(\delta p_{\mathrm{T}}^{\mu})$ GeV[1]. The corresponding event displays in the transverse plane r-ϕ and in the ρ-z plane are shown in Fig. 12.4.

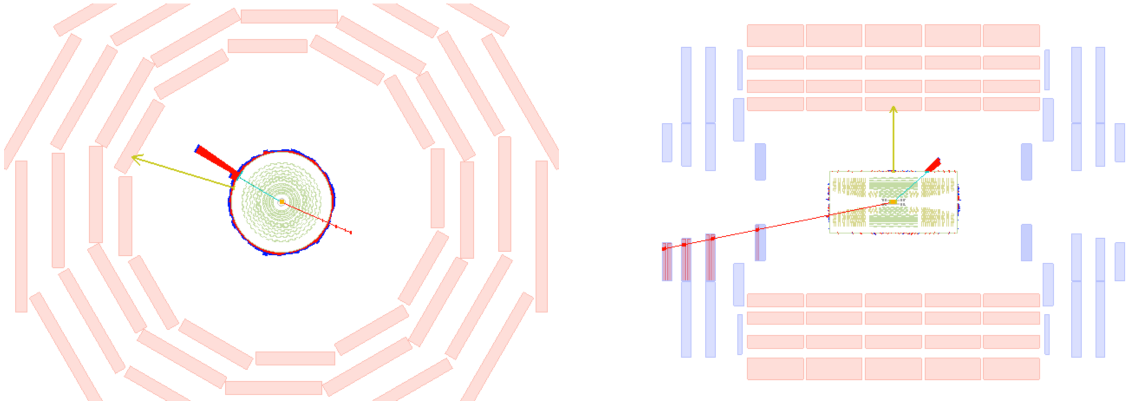

(a) View of the $M_{\mu\tau}^{\mathrm{coll}} = 1679$ GeV event in the transverse plane.

(b) View of the $M_{\mu\tau}^{\mathrm{coll}} = 1679$ GeV event in the ρ-z plane.

Figure 12.4: Event displays of the event with the highest collinear $\mu\tau_{\mathrm{e}}$ mass that passes the event selection. The muon track is shown in red, the red calorimeter towers represent clusters of calorimeter cells in the ECAL that together with the blue track in the inner tracking detectors are reconstructed as an electron. The arrow points into the direction of the missing transverse energy.

In the transverse plane, the event topology meets the requirements of a signal event. The missing transverse energy falls into the direction of the reconstructed electron with a distance in azimuthal angle of $\Delta\phi(\mathrm{e}, \not{E}_{\mathrm{T}}) = 0.27$. The τ_{e} candidate resulting from the collinear approximation has a transverse momentum of $p_{\mathrm{T}}^{\tau} = 313 \pm 40\,(\delta p_{\mathrm{T}}^{\mu})$ GeV to which both the electron with $E_{\mathrm{T}}^{\mathrm{e}} = 110$ GeV and the missing transverse energy of $\not{E}_{\mathrm{T}} = 206 \pm 40\,(\delta p_{\mathrm{T}}^{\mu})$ GeV contribute significantly. The muon with $p_{\mathrm{T}}^{\mu} = 316 \pm 40\,(\delta p_{\mathrm{T}}^{\mu})$ GeV is separated from the τ_{e} candidate in azimuth by $\Delta\phi(\mu, \tau_{\mathrm{e}}) = 3.07$. Apart from the electron and the muon no further high-p_{T} objects are reconstructed, and the highest p_{T} recorded among the additional jet candidates is below 30 GeV.

---

[1] The uncertainty that is assigned to the measured $M_{\mu\tau}^{\mathrm{coll}}$ value is obtained by propagating the uncertainty in the muon p_{T} from the muon track fit ($\delta p_{\mathrm{T}}^{\mu}/p_{\mathrm{T}}^{\mu} \approx 13\%$) to the missing transverse energy and thereby to the τ_{e} candidate. This uncertainty is specific for this event and denoted by the symbol $(\delta p_{\mathrm{T}}^{\mu})$ in this paragraph.

As depicted in the ρ-z view of the event, the muon lies close to the edge of the geometrical acceptance of the muon system with pseudorapidity of $\eta^{\mu} = -2.30$. The total muon momentum is $\mathrm{p}^{\mu} = 1589 \pm 210\,(\delta p_{\mathrm{T}}^{\mu})$ GeV and the momentum of the τ_{e} candidate is $\mathrm{p}^{\tau} = 475 \pm 60\,(\delta p_{\mathrm{T}}^{\mu})$ GeV. According to simulations, events with such a small $\mathrm{p}^{\tau}/\mathrm{p}^{\mu}$ ratio of 0.3 or below account for 2% of the total background yield after event selection, and 1% of signal events with $M_{\tilde{\nu}_{\tau}} = 1.6$ TeV.

In order to put the impact of this single high-mass event on the results into perspective, it is noted that the $M_{\mu\tau}^{\mathrm{coll}}$ resolution at $M_{\mu\tau}^{\mathrm{coll}} = 1.6$ TeV is 8%, and 1 event is observed above $M_{\mu\tau}^{\mathrm{coll}} = 1.2$ TeV, where 0.9 ± 0.2 (syst) background events are expected.

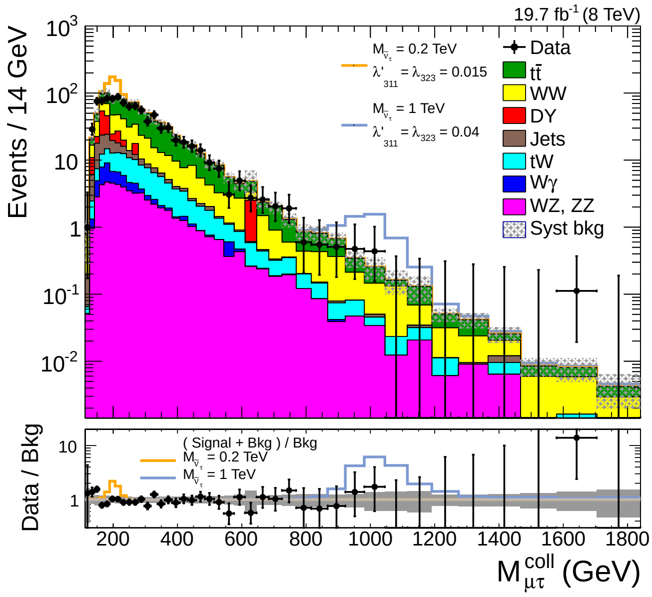

Figure 12.5: The $M_{\mu\tau}^{\mathrm{coll}}$ distribution of events passing the full event selection binned according to the mass resolution. The impact of possible signal contributions is illustrated by peaks of two simulated RPV $\tilde{\nu}_\tau$ signal samples with the parameters indicated in the legend. These signal contributions are added on top of the background expectation in the upper plot. In the lower ratio plot, the black dots with vertical uncertainty bars indicate the data to background ratio and its statistical uncertainty. The orange and blue lines in the ratio plot represent the ratio of the sum of signal and background contributions to the background contribution only.

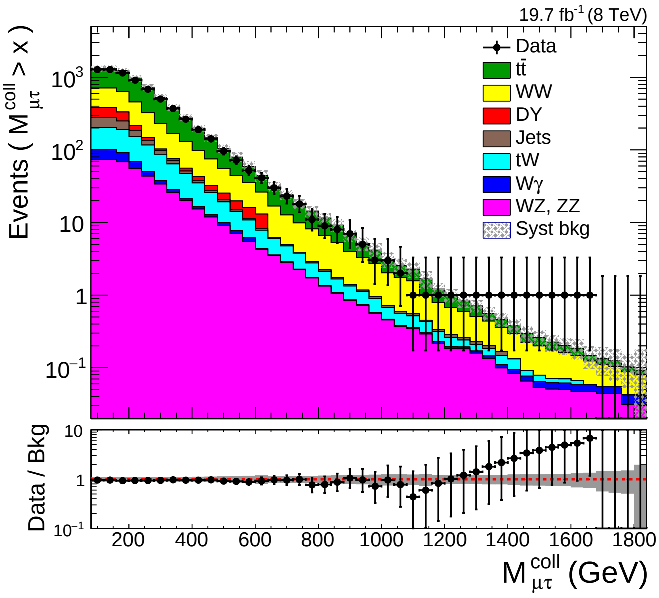

Figure 12.6: The cumulative $M_{\mu\tau}^{\mathrm{coll}}$ distribution of events passing the full event selection. The vertical uncertainty bars on the data points in black indicate the statistical uncertainty and the systematic uncertainty in the background expectation is given by the shaded band.

12.2 Systematic uncertainties

12.2.1 Systematic uncertainties in the background estimate

As described in the search for eμ resonances, the uncertainties in the background can be divided into two categories; one comprises uncertainties that vary significantly as a function of $M_{\mu\tau}^{\mathrm{coll}}$ (shape uncertainties) and the other comprises systematic uncertainties that do not change with $M_{\mu\tau}^{\mathrm{coll}}$ or can be assumed to be flat over the entire mass range without significantly changing the results (scaling uncertainties).

In the following all quantities that are varied within their uncertainties in order to determine the uncertainty estimate on the background yield in the $\mu\tau$ resonance search are listed. The uncertainties that are also relevant in the eμ resonance search are evaluated as explained in Sec. 8. The treatment of the uncertainties in the jet energy scale and resolution, the unclustered energy, and the b-tagging efficiency are described below. The missing transverse energy is recalculated in the evaluation of the uncertainties that affect it, such as the energy/momentum scales of the involved physics objects and the corresponding resolutions, according to the formula

$$\vec{E\!\!\!/}_{\mathrm{T}}^{\pm} = \vec{E\!\!\!/}_{\mathrm{T}} + \vec{p}_{\mathrm{T,\,X}} - \vec{p}_{\mathrm{T,\,X}}^{\,\pm} \ , \tag{12.1}$$

where $\vec{p}_{\mathrm{T,\,X}}$ denotes the transverse momentum vector of the object X and $\vec{p}_{\mathrm{T,\,X}}^{\,\pm}$ is the vector resulting after the shift by $\pm 1\sigma$ in the uncertainty under study.

- *Uncertainties associated with charged leptons*
  - Muon p_{T} scale
  - Muon p_{T} resolution
  - Electron energy scale
- *Uncertainties associated with jets and unclustered energy*

  As mentioned in the context of the $E\!\!\!/_{\mathrm{T}}$ corrections in Sec. 3.4.3, the treatment of PF jets with $p_{\mathrm{T}} \geq 10$ GeV (clustered energy) differs from that of PF jets with smaller p_{T} values (unclustered energy). This distinction is adopted in the treatment of the systematic uncertainties in $E\!\!\!/_{\mathrm{T}}$.

  - Jet energy scale

    Uncertainties associated with the JEC described in Sec. 3.4.2 are provided by the JetMET group as a function of jet p_{T} and η. The individual sources of uncertainty and their combination are outlined in Ref. [155]. The combination of individual sources of uncertainty referred to as *Total* in this reference is used to obtain the (relative) 1σ variations in the JEC, σ_{JEC}, with typical values of 1-3%. This uncertainty is applied to the p_{T} values of all PF jets in a given event according to the formula:

    $$p_{\mathrm{T,\,jet}}^{\pm} = \left[\,1 \pm \sigma_{\mathrm{JEC}}(p_{\mathrm{T,\,jet}},\, \eta_{\mathrm{jet}})\,\right] \times p_{\mathrm{T,\,jet}} \ . \tag{12.2}$$

    The uncertainty in the JEC is propagated to $\vec{E\!\!\!/}_{\mathrm{T}}$ by summing the variations in the jet transverse momentum vectors of all jets with $p_{\mathrm{T}} \geq 10$ GeV in a fully correlated way:

    $$\vec{E\!\!\!/}_{\mathrm{T,\,JEC}}^{\pm} = \vec{E\!\!\!/}_{\mathrm{T}} \mp \sum_{\substack{i\,\in\,\mathrm{jets} \\ p_{\mathrm{T}}\geq 10\ \mathrm{GeV}}} \sigma_{\mathrm{JEC}}(p_{\mathrm{T,\,i}},\, \eta_{\mathrm{i}}) \times \vec{p}_{\mathrm{T,\,i}} \ . \tag{12.3}$$

  - Jet energy resolution

    The uncertainty in the jet energy resolution is only included via its impact on $\vec{E\!\!\!/}_{\mathrm{T}}$. The variation in $\vec{E\!\!\!/}_{\mathrm{T}}$ is obtained from the $E\!\!\!/_{\mathrm{T}}$ uncertainty tool developed in the JetMET group [292].

  - Unclustered energy

    An uncertainty of 10% is applied to the transverse momenta of PF objects other than leptons, photons, or PF jets with $p_{\mathrm{T}} \geq 10$ GeV.

  - B-tagging efficiency

    Uncertainties in the data-to-simulation scale factors for the b-tagging efficiency introduced in Eqn. 7.1 are provided by the BTV group [257].

- *Uncertainties in background yields obtained from simulations*
  - Efficiency of the eμ pair selection
  - Luminosity
  - PDF uncertainty
  - Inclusive background cross sections
  - $\mathrm{t\bar{t}}$ process: top-p_{T} reweighting
  - WW process: Variation of renormalization and factorization scales
- *Uncertainties in background contributions obtained from data*
  - W + jet and QCD multijet processes: Jet-to-electron mis-identification rate

The background uncertainties are evaluated at each stage of the event selection for the $\not\!\!E_{\mathrm{T}}$, p_{T}^{τ}, and $M_{\mu\tau}^{\mathrm{coll}}$ distributions. The following presentation of the uncertainties is restricted to the $M_{\mu\tau}^{\mathrm{coll}}$ distribution and two stages of the event selection: the initial selection of a $\mu\tau_{\mathrm{e}}$ pair (Tab. 12.5) and the full event selection (Tab. 12.4). The uncertainties in the event yield in three mass bins are given. These mass bins are centered at $M_{\mu\tau}^{\mathrm{coll}} = 200$ GeV, $M_{\mu\tau}^{\mathrm{coll}} = 500$ GeV and $M_{\mu\tau}^{\mathrm{coll}} = 1$ TeV, respectively, and have a width of $\pm 3\,\sigma_M$, where σ_M is the $M_{\mu\tau}^{\mathrm{coll}}$ mass resolution evaluated at the center of the bin. For the sake of readability of the tables, asymmetric uncertainties in the event yield are symmetrized; the relative uncertainties in the event yield N reported in the tables are calculated as $\sigma_N = |\,N(\sigma_X^{\mathrm{up}}) - N(\sigma_X^{\mathrm{down}})\,|\,/\,(2\,N)$.

12.2.2 Systematic uncertainties in the signal contribution

The uncertainties in the signal contribution are treated in a similar way as in the eμ search by separating them into an uncertainty in the total number of expected signal events and an uncertainty in the signal pdf. Only the uncertainties in the product of acceptance and efficiency and on the luminosity are included as uncertainties related to the signal normalization in the statistical interpretation of the experimental findings. The PDF and scale uncertainties that affect the inclusive signal cross section are not included in the calculation of the observed significances and cross section limits.

The total uncertainty in $A \times \varepsilon$ is obtained as a function of the signal mass $M_{\tilde{\nu}_\tau}$ by treating the dominant contributions from individual sources of uncertainty as uncorrelated and adding them in quadrature. The result is depicted in Fig. 12.7. At high signal masses, the uncertainty in the efficiency of the visible decay products, namely the muon and electron, dominate, whereas all considered sources of systematic uncertainty are of similar importance at $M_{\tilde{\nu}_\tau} = 200$ GeV. The impact of the electron energy scale uncertainty at low signal masses is due to the shape of the E_{T} distribution of the electron from the τ decay with its maximum close to the cut value, see Fig. 11.2. The muon momentum scale uncertainty has an effect on both the muon p_{T} distribution and the $\not\!\!E_{\mathrm{T}}$ distribution, and impacts the fraction of signal events that pass the $\not\!\!E_{\mathrm{T}}$ requirement. The total systematic uncertainty in the product of signal acceptance and efficiency ranges from 3.8% at $M_{\tilde{\nu}_\tau} = 200$ GeV to about 5.5% for signal masses above $M_{\tilde{\nu}_\tau} = 600$ GeV. The uncertainty in the luminosity of 2.6% is the other uncertainty affecting the expected number of signal events that is taken into account. The shape uncertainty in the signal pdf is estimated by assigning a systematic uncertainty of 30% in the collinear mass resolution obtained from simulated signal samples.

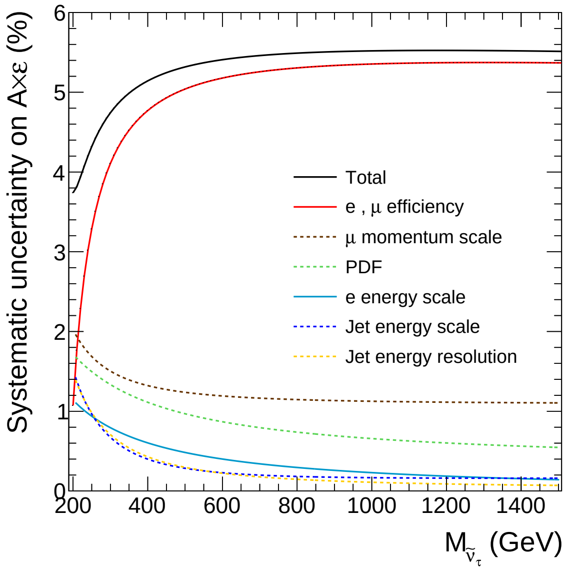

Figure 12.7: Individual uncertainties in the product of acceptance and efficiency and the resulting total uncertainty obtained by summing them in quadrature. The size of the individual uncertainties is reflected in the order in which they appear in the legend.

Table 12.4: The relative systematic uncertainties in the background yield after the full event selection in the mass bins 150 *GeV* $\leq M_{\mu\tau}^{\text{coll}} \leq$ 250 *GeV*, 410 *GeV* $\leq M_{\mu\tau}^{\text{coll}} \leq$ 590 *GeV*, *and* 800 *GeV* $\leq M_{\mu\tau}^{\text{coll}} \leq$ 1200 *GeV*.

Source of systematic uncertainty	Relative systematic uncertainty (%) on N_{bkg} in $M_{\mu\tau}^{\text{coll}} \pm 3\sigma_M$		
	200 GeV	500 GeV	1 TeV
Muon p_{T} resolution	0.2	0.5	0.3
Jet energy scale	1	1	0.3
Jet energy resolution	1	0.3	1
Unclustered energy	0.3	0.5	1
B-tagging efficiency	1	2	1
WW ren., fac. scales	1	1	3
$\mathrm{t\bar{t}}$ top-p_{T}	6	1	7
Muon p_{T} scale	0.3	2	5
Electron energy scale	0.5	0.9	0.8
PDF	5	6	9
Luminosity	2	3	3
$A \times \varepsilon$	5	5	5
Electron mis-id. rate	3	0.5	0.2
Cross sections			
$\mathrm{t\bar{t}}$	2	3	2
Wγ	2	0.4	< 0.1
DY	1	< 0.1	< 0.1
Total	10	10	15

Table 12.5: The relative systematic uncertainties in the background yield after the selection of a $\mu\tau_{\text{e}}$ *pair in the mass bins* 150 *GeV* $\leq M_{\mu\tau}^{\text{coll}} \leq$ 250 *GeV*, 410 *GeV* $\leq M_{\mu\tau}^{\text{coll}} \leq$ 590 *GeV*, *and* 800 *GeV* $\leq M_{\mu\tau}^{\text{coll}} \leq$ 1200 *GeV*.

Source of systematic uncertainty	Relative systematic uncertainty (%) on N_{bkg} in $M_{\mu\tau}^{\text{coll}} \pm 3\sigma_M$		
	200 GeV	500 GeV	1 TeV
Muon p_{T} resolution	0.1	0.2	0.7
Jet energy scale	1	1	4
Jet energy resolution	0.2	0.4	0.8
Unclustered energy	0.7	0.7	0.2
B-tagging efficiency	-	-	-
WW ren., fac. scales	0.3	0.5	1
$\mathrm{t\bar{t}}$ top-p_{T}	8	4	13
Muon p_{T} scale	0.5	2	7
Electron energy scale	< 0.1	0.3	0.5
PDF	5	6	9
Luminosity	3	3	3
$A \times \varepsilon$	5	5	5
Electron mis-id. rate	0.7	0.3	0.6
Cross sections			
$\mathrm{t\bar{t}}$	4	4	3
Wγ	0.7	0.2	0.2
DY	0.3	< 0.1	< 0.1
Total	12	10	19

Chapter 13

Statistical analysis and physics interpretation of the $\mu\tau_{\mathrm{e}}$ search

13.1 Implications of the $\mu\tau_{\mathrm{e}}$ resonance search for the RPV $\tilde{\nu}_\tau$ model

The statistical interpretation of the $\mu\tau$ collinear mass spectrum depicted in Fig. 12.5 in terms of a resonant signal contribution on top of the background expectation is carried out using the methods and tools described in Sec. 10.1. In particular, software tools developed within the CMS collaboration in the context of searches for the SM Higgs boson are again utilized for the evaluation of significances and exclusion limits on cross sections.

The signal efficiency and Gaussian pdf to model the signal shape that enter the binned likelihood function are obtained for all tested signal mass hypotheses from the parameterizations of the efficiency and detector resolution described in Secs. 11.3.1 and 11.3.2, respectively. The background model is obtained directly from the simulated background samples as a histogram with a binning smaller than the detector resolution. The search region from which events are included in the likelihood function is chosen as defined in Eqn. 10.3.

The presentation of the statistical interpretation of the findings in the $\mu\tau$ collinear mass spectrum is structured as follows: First, the local significance of observed excesses above the background expectation is quantified in Sec. 13.1.1. Then, upper bounds on the product of signal cross section and branching fraction for narrow $\mu\tau$ resonances are derived in Sec. 13.1.2. Finally, these bounds are translated into exclusion boundaries in the parameter space of the RPV $\tilde{\nu}_\tau$ signal model and compared to those obtained from other searches at high-energy colliders and indirect bounds from low-energy experiments.

13.1.1 Local significance of excesses

The significance calculation of excesses above the background expectation is based on the profile likelihood test statistic q_0 and the approximation of its pdf under the background-only hypothesis as a half chi-square distribution for one degree of freedom (Sec. 10.1.3). The local significance of observed upward deviations from the background as a function of the signal mass hypothesis $M_{\tilde{\nu}_\tau}$ is depicted in Fig. 13.1. With a z-score of 1.6σ, the most significant excess is found between $M_{\tilde{\nu}_\tau} = 1.6$ TeV and $M_{\tilde{\nu}_\tau} = 1.7$ TeV. It is associated with the single observed event at $M_{\mu\tau}^{\mathrm{coll}} = 1679$ GeV. All the other observed upward deviations have significances below 1σ. With no significant excess above the background observed, exclusion limits are set as discussed next.

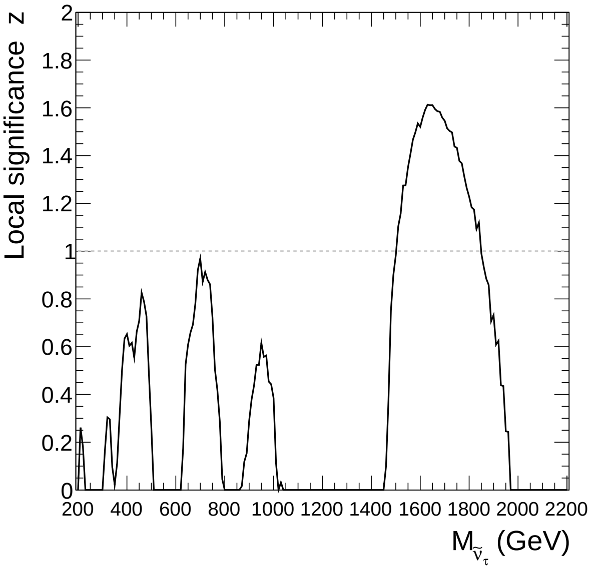

Figure 13.1: The significance, or z-score, of excesses over the background expectation observed in data as a function of the $\mu\tau$ resonance mass hypothesis. These are the local significance values that are not corrected for the look-elsewhere effect.

13.1.2 Exclusion limits

Cross section limits

The 95% CL upper limits on the product of signal cross section and branching fraction of the decay into the $\mu\tau$ final state[1] for narrow resonances are presented in Fig. 13.2 as a function of the signal mass hypothesis $M_{\tilde{\nu}_\tau}$. In the shown mass region from $M_{\tilde{\nu}_\tau} = 200$ GeV to $M_{\tilde{\nu}_\tau} = 2.2$ TeV, the median expected cross section limit at 95% CL ranges from 129 fb to 1.5 fb, while the corresponding observed limit decreases from 105 fb to 1.5 fb. A summary of the observed and expected limits at several mass points is given together with the total signal selection efficiency and the signal acceptance in Tab. F.1 in App. F.

The RPV $\tilde{\nu}_\tau$ signal with $\mu\tau$ decay is excluded at 95% CL below $M_{\tilde{\nu}_\tau} = 370$ GeV for RPV couplings $\lambda'_{311} = \lambda_{323} = 0.01$. The observed lower bound on the resonance mass increases for couplings $\lambda'_{311} = \lambda_{323} = 0.1$ to $M_{\tilde{\nu}_\tau} = 1.73$ TeV. Further observed mass limits and the corresponding expected bounds are given in Tab. 13.1.

Before taking the interpretation of the results further, the impact of both the systematic uncertainties and the simplification of choosing a Gaussian pdf to model the collinear mass distribution of the signal on the observed cross section limit is evaluated. The observed limit calculated without taking systematic uncertainties into account is compared to the full calculation in Fig. 13.3. For the smallest probed signal masses, the background expectation is sizeable and the systematic uncertainties on the background yield are in excess of 10%. In this region the impact of the systematic uncertainties on the extracted lower bound on the signal mass is relevant. For example, the limit on the RPV $\mu\tau$ resonance model with couplings $\lambda'_{311} = \lambda_{323} = 0.01$ calculated without systematic uncertainties is $M_{\tilde{\nu}_\tau} = 440$ GeV, and thus 70 GeV above the result including systematic uncertainties. For the signal with couplings $\lambda'_{311} = \lambda_{323} = 0.02$, the difference between the two mass limits is reduced to 30 GeV, and for $\lambda'_{311} = \lambda_{323} = 0.05$ the mass limit reads $M_{\tilde{\nu}_\tau} = 1.42$ TeV in both cases.

The bias introduced in the determination of the cross section limits by using a Gaussian pdf to

---

[1] For clarity it is emphasized that this is the branching fraction of the resonance decay into a $\mu\tau$ pair without the subsequent leptonic decay of the τ lepton into an electron and neutrinos.

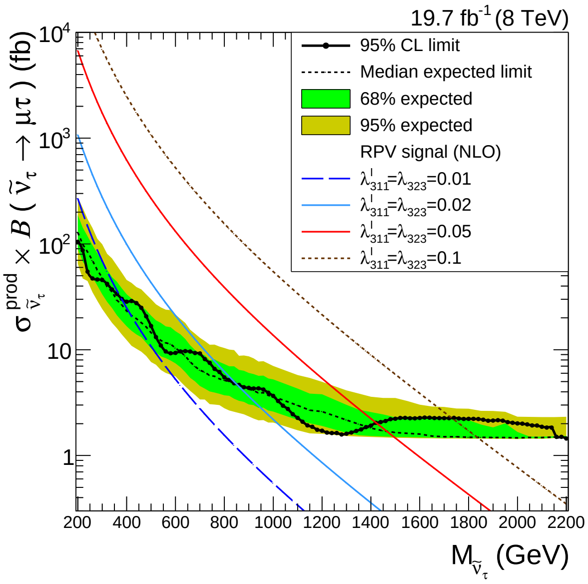

Figure 13.2: The observed and expected 95% CL exclusion limits on the product of $\tilde{\nu}_\tau$ production cross section and the branching fraction of its decay into the $\mu\tau$ final state as a function of the signal mass hypothesis. Curves representing the signal cross section evaluated at NLO in pQCD are shown for RPV couplings ranging from $\lambda'_{311} = \lambda_{323} = 0.01$ to $\lambda'_{311} = \lambda_{323} = 0.1$.

Table 13.1: The 95% CL lower limits on $M_{\tilde{\nu}_\tau}$ for four choices of the RPV couplings λ'_{311} and λ_{323}. The median expected limit is shown together with the boundaries of the corresponding 1σ uncertainty band. The chosen RPV coupling values are the same as in Fig. 13.2.

RPV coupling strength	95% CL lower limits on $M_{\tilde{\nu}_\tau}$ (GeV)			
$\lambda'_{311} = \lambda_{323}$	Observed	Median expected	$+1\sigma$	-1σ
0.01	370	410	510	310
0.02	850	850	950	760
0.05	1420	1470	1490	1360
0.1	1730	1840	1840	1740

model the collinear mass distribution of the signal rather than simulating a sufficient number of signal events for each mass hypothesis is estimated by comparing the cross section limits presented above to those obtained with the fully simulated $M^{\mathrm{coll}}_{\mu\tau}$ distribution for mass points for which the simulated signal samples are available. The relative difference between the two lies within ±3% for the 13 mass points probed in the range from $M_{\tilde{\nu}_\tau} = 200$ GeV to $M_{\tilde{\nu}_\tau} = 2.2$ TeV, which is small compared to the uncertainty in the expected limit in Fig. 13.2.

Exclusion boundaries in the parameter space of the RPV $\tilde{\nu}_\tau$ model

Using the narrow width approximation formula of the RPV signal cross section, the cross section limit is translated into exclusion bounds in the $(M_{\tilde{\nu}_\tau}, \lambda'_{311})$ plane of the parameter space of the RPV model for fixed values of the coupling responsible for the $\tilde{\nu}_\tau$ decay into a $\mu\tau$ pair, $\lambda^{\mathrm{fix}}_{323}$. As

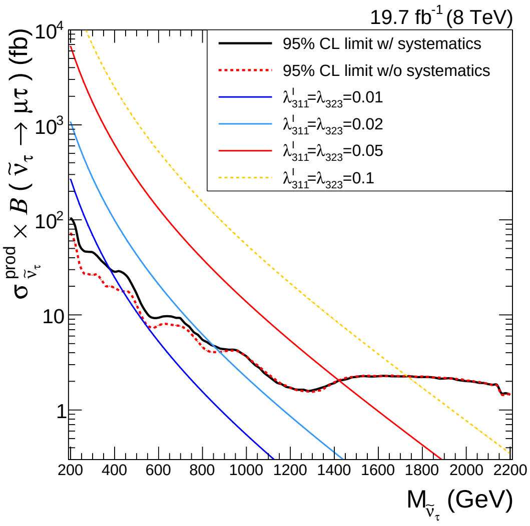

Figure 13.3: The observed 95% CL exclusion limits on the product of $\tilde{\nu}_\tau$ production cross section and the branching fraction of its decay into the $\mu\tau$ final state calculated with (black solid line) and without (red dashed line) the systematic uncertainties in the background and signal contributions. Curves representing the signal cross section evaluated at NLO in pQCD are shown for RPV couplings ranging from $\lambda'_{311} = \lambda_{323} = 0.01$ to $\lambda'_{311} = \lambda_{323} = 0.1$.

discussed in Sec. 1.1.4, the signal cross section can be factorized in the narrow width approximation as

$$\sigma \cdot \mathcal{B} \quad = \quad k(M_{\tilde{\nu}_\tau}) \frac{\left(\lambda'_{311}\right)^2 \left(\lambda^{\mathrm{fix}}_{323}\right)^2}{\left(3\left(\lambda'_{311}\right)^2 + \left(\lambda^{\mathrm{fix}}_{323}\right)^2\right)} \tag{13.1}$$

$$\underset{\lambda'_{311} \gg \lambda^{\mathrm{fix}}_{323}}{\rightarrow} \quad k(M_{\tilde{\nu}_\tau}) \left(\lambda^{\mathrm{fix}}_{323}\right)^2 / \, 3 \equiv \; \sigma \cdot \mathcal{B}_{\mathrm{max}} \left(M_{\tilde{\nu}_\tau}, \lambda^{\mathrm{fix}}_{323}\right). \tag{13.2}$$

If the observed cross section limit $\sigma \cdot \mathcal{B}_{\mathrm{obs}}$ lies above the cross section $\sigma \cdot \mathcal{B}_{\mathrm{max}}$ for a given parameter pair $(M_{\tilde{\nu}_\tau}, \lambda^{\mathrm{fix}}_{323})$, no limit on λ'_{311} can be set for that point in parameter space. Otherwise, the observed limit on λ'_{311} is given by

$$\lambda'_{311} = \sqrt{\frac{\sigma \cdot \mathcal{B}_{\mathrm{obs}} \left(\lambda^{\mathrm{fix}}_{323}\right)^2}{k(M_{\tilde{\nu}_\tau}) \left(\lambda^{\mathrm{fix}}_{323}\right)^2 - 3\sigma \cdot \mathcal{B}_{\mathrm{obs}}}}\,. \tag{13.3}$$

The resulting 95% CL exclusion boundaries in the $(M_{\tilde{\nu}_\tau}, \lambda'_{311})$ plane are shown in Fig. 13.4 with a comparison to the corresponding limits from CMS dijet searches that have been discussed in Sec. 10.2.2. The recast of the dijet searches in terms of the $\mu\tau$ RPV $\tilde{\nu}_\tau$ model is carried out in analogy to the procedure that is detailed in the context of the eμ search. After accounting for the signal acceptance, the observed 95% CL limits on the product of signal cross section and branching fraction $\sigma \cdot \mathcal{B}^{\mathrm{dijet}}_{\mathrm{obs}}$ from the dijet searches can be transformed into bounds on the Yukawa coupling λ'_{311} according to

$$\lambda'_{311} = \sqrt{\left(\frac{\sigma \cdot \mathcal{B}^{\mathrm{dijet}}_{\mathrm{obs}}}{3k(M_{\tilde{\nu}_\tau})} \left(\lambda^{\mathrm{fix}}_{323}\right)^2 + \left(\frac{\sigma \cdot \mathcal{B}^{\mathrm{dijet}}_{\mathrm{obs}}}{2k(M_{\tilde{\nu}_\tau})}\right)^2\right)^{\frac{1}{2}} + \frac{\sigma \cdot \mathcal{B}^{\mathrm{dijet}}_{\mathrm{obs}}}{2k(M_{\tilde{\nu}_\tau})}}\,. \tag{13.4}$$

The comparison of the limit boundaries obtained in the $\mu\tau$ search and from the reinterpretation of the dijet search in Fig. 13.4 exemplifies the importance of dilepton resonance searches with their

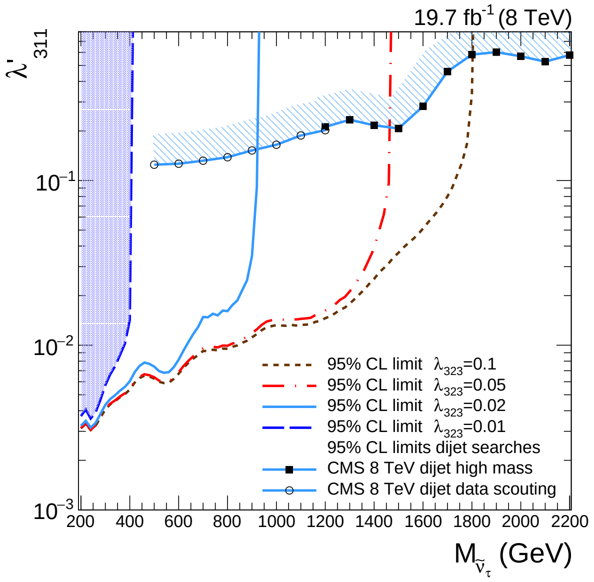

Figure 13.4: The 95% observed limit boundaries in the $(M_{\tilde{\nu}_\tau}, \lambda'_{311})$ *plane of the RPV model for four fixed values of the third parameter* λ_{323}*: 0.01, 0.02, 0.05 and 0.1. The regions of parameter space above the curves are excluded at a confidence level exceeding 95%. The results obtained from the analysis of the* $\mu\tau$ *final state are represented by the curves without markers. For* $\lambda_{323} = 0.02$*, these results are compared to the excluded regions obtained from the reinterpretation of the CMS dijet resonance searches at high dijet masses [95]* ($M_{\tilde{\nu}_\tau} \geq 1200$ *GeV) and at lower masses using the data scouting technique [282]* (500 *GeV* $\leq M_{\tilde{\nu}_\tau} \leq 1200$ *GeV). The bounds from dijet resonance searches are shown as curves with markers.*

relatively small background contamination in the LHC environment. While the dijet search does not constrain the RPV $\tilde{\nu}_\tau$ model for resonance masses below 500 GeV or couplings below $\lambda' \sim 0.1$, couplings of the size $\lambda'_{311} = \lambda_{323} \sim 0.01$ are probed in the $\mu\tau$ search for $M_{\tilde{\nu}_\tau} \lesssim 500$ GeV. As the $\tilde{\nu}_\tau$ production coupling λ'_{311} rises relative to λ_{323} and the $\tilde{\nu}_\tau$ mass increases, the regions of parameter space that are excluded by both searches overlap before the sensitivity of the $\mu\tau$ search vanishes and the dijet search provides the only bounds at $\lambda'_{311} \gg \lambda_{323}$.

As discussed already in the context of the eμ resonance search, bounds on models of new physics with charged lepton flavour violation at the TeV scale from low-energy experiments constitute a strong competition for the direct searches at the LHC. In the case of the RPV $\tilde{\nu}_\tau$ model with decay into a $\mu\tau$ pair, the most stringent of these exclusion limits stem from a search for the decay $\tau \to \mu\eta$ by the BELLE collaboration [70, 72] that has been introduced in Sec. 1.1.5:

$$|\lambda'_{311}\lambda_{323}| < 2.0 \cdot 10^{-3} \left(M_{\tilde{\nu}_\tau}/\mathrm{TeV}\right)^2 \ \ (90\%\ \mathrm{CL})\ . \tag{13.5}$$

To the end of comparing with this bound, the observed cross section limit from the $\mu\tau$ resonance search is recalculated at 90% CL. The results are presented side by side the 95% CL bounds in Tab. F.1 in App. F. From these numbers, limits on the product of the two RPV couplings of

$$|\lambda'_{311}\lambda_{323}| < 5.5 \cdot 10^{-4} \ \ (90\%\ \mathrm{CL}) \tag{13.6}$$

$$|\lambda'_{311}\lambda_{323}| < 6.7 \cdot 10^{-4} \ \ (95\%\ \mathrm{CL}) \tag{13.7}$$

are obtained for $M_{\tilde{\nu}_\tau} = 1$ TeV under the assumption $\lambda'_{311} = \lambda_{323}$. In contrast to the e$\mu$ search, where the indirect bounds on the RPV $\tilde{\nu}_\tau$ model are not surpassed, the bounds from low-energy experiments can be improved in the $\mu\tau$ resonance search.

The results are further compared to the direct search for $\mu\tau$ resonances by the ATLAS collaboration in the $\mu\tau_{\mathrm{had}}$ channel in pp collisions at the LHC at $\sqrt{s} = 8$ TeV [31]. In the ATLAS search, the same RPV signal model is used and the limits on the product of $\tilde{\nu}_\tau$ production cross section and its branching fraction into the $\mu\tau$ final state are set at 95% CL. The analysis is carried out for signal masses $M_{\tilde{\nu}_\tau} \geq 0.5$ TeV and the cross section bounds are documented in a plot from which the following numbers have been obtained: At $M_{\tilde{\nu}_\tau} = 0.5$ TeV, the observed exclusion limit on $\sigma \cdot \mathcal{B}(\tilde{\nu}_\tau \to \mu\tau)$ obtained in the ATLAS search is 60 fb (17 fb in the CMS $\mu\tau_{\mathrm{e}}$ analysis), at $M_{\tilde{\nu}_\tau} = 1$ TeV it is 9 fb (3.7 fb in the CMS $\mu\tau_{\mathrm{e}}$ analysis) and the expected limit is 5 fb, and at $M_{\tilde{\nu}_\tau} = 2$ TeV both the observed and expected limit read 2 fb (2.0 fb in the CMS $\mu\tau_{\mathrm{e}}$ analysis). At signal masses below $\mathcal{O}(1$ TeV), the ATLAS search in the $\mu\tau_{\mathrm{had}}$ channel comes with a much larger background than the search in the $\mu\tau_{\mathrm{e}}$ channel presented in this work, mainly because of a larger contribution from W + jet events. In the ATLAS search, 4200 ± 400 events are expected for dilepton masses $M(\mu, \tau_{\mathrm{had}}) > 200$ GeV [31], while 980 ± 90 events are expected in the $\mu\tau_{\mathrm{e}}$ analysis for $M^{\mathrm{coll}}_{\mu\tau} > 200$ GeV. Further differences between the two analyses include different mass resolutions, selection efficiencies, and a different approach to the statistical analysis [2]. For a signal mass of 2 TeV the observed limits in the two searches coincide because no events are observed at such high masses in either analysis, the background expectation has dropped to negligible levels, and the total signal selection efficiencies for $\mu\tau$ pairs (including the branching fraction of the τ lepton into the final state under investigation) are similar (ATLAS: $A \times \epsilon \times \mathcal{B} = 10\%$ [31], this work: $A \times \epsilon \times \mathcal{B}(\tau^- \to \mathrm{e}^-\nu_\tau\bar{\nu}_e) = 10.5\%$, Fig. 11.11).

In Fig. 13.5, the exclusion contours in the $(\lambda'_{311}, \lambda_{323})$ parameter plane of the RPV $\tilde{\nu}_\tau$ model derived from the $\mu\tau_{\mathrm{e}}$ search are compared to those obtained from the other searches mentioned above for a resonance mass of 1 TeV. This search extends the existing bounds in the region where the RPV coupling necessary for the production of the τ sneutrino, λ'_{311}, and that responsible for the decay to a $\mu\tau$ pair, λ_{323}, are of similar size.

---

[2] ATLAS uses a single-bin counting limit in a signal region around the resonance mass according to Ref. [293].

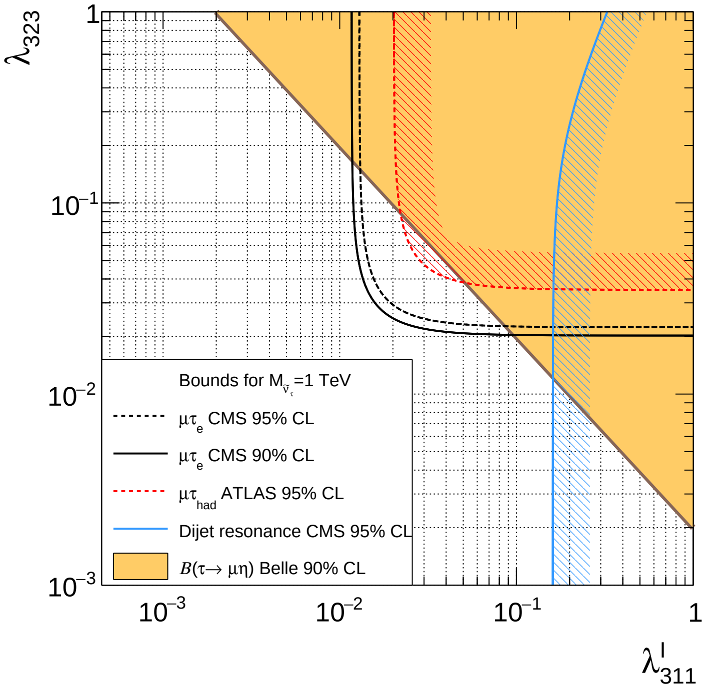

Figure 13.5: The limit boundaries in the $(\lambda'_{311}, \lambda_{323})$ RPV coupling plane for $M_{\tilde{\nu}_\tau} = 1$ TeV obtained in this work compared to the ATLAS search for $\mu\tau$ resonances [31], the CMS dijet resonance search using the data scouting technique [282], and a search for the decay $\tau \to \mu\eta$ by the BELLE collaboration [70, 72]. The limits of the CMS dijet search and the ATLAS search in the $\mu\tau$ final state are calculated at 95% CL whereas those by the BELLE collaboration are calculated at 90% CL. In order to allow for a comparison in both cases, the exclusion boundaries obtained from the $\mu\tau$ analysis in this work at 95% CL and 90% CL are shown.

13.2 Recasting the $\mu\tau$ search in the context of 2HDMs

The interpretation of the search for $\mu\tau$ resonances in terms of the RPV $\tilde{\nu}_\tau$ model is only one of several options of exploiting the potential for constraining BSM physics contained in the cross section bounds in Fig. 13.2. Although the signal selection efficiency has been calculated for a scalar resonance produced in a $\mathrm{d}\overline{\mathrm{d}}$ initial state, the cross section limits can be used to obtain an estimate of the bounds on signal models with a different production mechanism when corrected for the ratio of the two different signal acceptances. The acceptance in the $\mu\tau$ resonance search is defined in the following as the fraction of simulated $\mu\tau_\mathrm{e}$ signal events passing the selection cuts on the muon, the τ lepton and the electron from the τ decay (see Sec. 11.2). All cuts are applied at parton level. This definition comprises the p_T and η cuts on the leptons, the cut on $\Delta\phi(\mu,\tau)$, and the requirement $p_\mathrm{T}^\mu \geq p_\mathrm{T}^\mathrm{e}$.

In the following, a reinterpretation of the $\mu\tau$ resonance cross section bounds in terms of a signal model with a heavy Higgs boson H^0 is presented. In order to allow for such reinterpretations, detailed information on the cross section limits, signal efficiencies, and acceptances is given in Tab. F.1 in App. F.

13.2.1 A 2HDM with lepton flavour violation

It has been pointed out in the literature (see for example Refs. [294, 295]) that an observed excess above the background expectation in searches for the LFV Higgs decay $h^0(125\ \mathrm{GeV}) \rightarrow \mu\tau$ by both the CMS (2.4σ) [26] and ATLAS collaborations [27] may find an explanation in models with two Higgs doublets (2HDMs). In the following, selected features of 2HDMs are discussed based on Ref. [294], that inspired this reinterpretation of the $\tilde{\nu}_\tau$ cross section limits and contains the description of the model under study [3], with the purpose of introducing the model parameters and formulae that are most important in the context of this analysis. A more complete introduction of the used 2HDM is presented in App. F.2 including the exact definition of all model parameters, a justification for the chosen values of the parameters in the Higgs potential, and consistency checks of the chosen region in parameter space. More detailed information about 2HDMs is contained (for example) in the articles Refs. [296, 297].

The two Higgs doublets Φ_1 and Φ_2 can be expressed in the so-called Higgs basis, in which only one of them has a vacuum expectation value, $v = 246$ GeV, as

$$\Phi_1 = \begin{pmatrix} G^+ \\ \frac{1}{\sqrt{2}}\left(v + h_1^0 + iG^0\right) \end{pmatrix} \qquad \text{and} \qquad \Phi_2 = \begin{pmatrix} H^+ \\ \frac{1}{\sqrt{2}}\left(h_2^0 + ih_3^0\right) \end{pmatrix} , \tag{13.8}$$

with the Goldstone bosons G^+ and G^0, the charged Higgs boson H^+, and the three neutral Higgs bosons h_1^0, h_2^0, h_3^0. Assuming CP conservation, the neutral Higgs bosons come with definite CP parity: there is one CP-odd scalar $A^0 = h_3^0$, accompanied by two CP-even Higgs fields, h_1^0 and h_2^0. A mixing of the latter results in the mass eigenstates h^0 and H^0

$$\begin{pmatrix} h^0 \\ H^0 \end{pmatrix} = \begin{pmatrix} \cos\alpha & \sin\alpha \\ -\sin\alpha & \cos\alpha \end{pmatrix} \begin{pmatrix} h_1^0 \\ h_2^0 \end{pmatrix} , \tag{13.9}$$

with the mixing angle α and the mass relation $M_{h^0} \leq M_{H^0}$. The light Higgs boson h^0 is identified with the SM Higgs-like particle discovered by the ATLAS and CMS collaboration in 2012 [36, 37], whose mass is measured to be $M_{h^0} = 125.09 \pm 0.21\ (\mathrm{stat}) \pm 0.11\ (\mathrm{syst})$ GeV [298].

---

[3] There is one difference in the choice of the key model parameters: While Ref. [294] assumes $M_{H^0} = M_{A^0} = M_{H^+}$, the relation between the Higgs masses chosen in this work is $M_{A^0} = M_{H^+} = M_{H^0} + 80$ GeV for reasons discussed below. This in turn leads to a different choice of the Higgs potential parameters λ_2 and λ_3.

In the most general types of 2HDMs, the Yukawa matrices describing the couplings of the Higgs fields to fermions can include lepton flavour violating elements, allowing for the production of $\mu\tau$ resonances at the LHC in the processes $\mathrm{pp} \to h^0,\ H^0,\ A^0 \to \mu^\pm\tau^\mp$. Here, the focus will be put on the production of a heavy neutral Higgs boson H^0 via gluon-gluon fusion and its subsequent decay into a $\mu\tau$ pair. For the production of a neutral, CP-even Higgs boson in pp collisions, only the couplings to quarks are considered:

$$\mathcal{L} \supset -y^{ij}_{u,h^0}\bar{u}^i_L u^j_R h^0 - y^{ij}_{u,H^0}\bar{u}^i_L u^j_R H^0 - y^{ij}_{d,h^0}\bar{d}^i_L d^j_R h^0 - y^{ij}_{d,H^0}\bar{d}^i_L d^j_R H^0 + \text{h.c.}\ , \tag{13.10}$$

with generation indices i, j, the Yukawa couplings of the light Higgs boson y_{u,h^0} and y_{d,h^0} to the up-type and down-type quarks, respectively, and the corresponding Yukawa couplings of the heavy Higgs boson y_{u,H^0} and y_{d,H^0}. The structures of the Yukawa couplings to up-type quarks are given by (see App. F.2):

$$y^{ij}_{u,h^0} = \frac{m_{u_i}}{v}\delta^{ij}\cos\alpha + \frac{\eta^{ij}_{u,2}}{\sqrt{2}}\sin\alpha\ , \tag{13.11}$$

$$y^{ij}_{u,H^0} = -\frac{m_{u_i}}{v}\delta^{ij}\sin\alpha + \frac{\eta^{ij}_{u,2}}{\sqrt{2}}\cos\alpha\ , \tag{13.12}$$

where $\eta^{ij}_{u,2}$ denotes the elements of the coupling matrix that connects the quark weak isospin doublet, the up-type quark weak isospin singlet, and the Higgs doublet field Φ_2: $\mathcal{L} \supset -i\,\bar{Q}^0_L\sigma_2\Phi^*_2\eta_{u,2}U^0_R$ (an exact definition of $\eta_{u,2}$ including the differentiation between the weak eigenstates and the mass eigenstates of the quarks is given in App. F.2). In the alignment limit $\sin\alpha \to 0$, the SM couplings of the light Higgs boson are recovered. To simplify the discussion, the parameter space of type III 2HDMs is significantly reduced by only allowing a sizeable value of $\eta^{tt}_{u,2}$ and assuming all other couplings $\eta^{ij}_{u,2}$ and $\eta^{ij}_{d,2}$ to be negligible. As suggested in Ref. [294], the H^0 production cross section is approximated by replacing the top Yukawa coupling in the SM Higgs production cross section formula by y^{tt}_{u,H^0}, resulting in the relation

$$\sigma\left(\mathrm{pp} \to H^0\right) \approx \left(\sin\alpha - \eta^{tt}_{u,2}\cos\alpha\frac{v}{\sqrt{2}m_t}\right)^2 \times \sigma_{gg}\left(\mathrm{pp} \to h^0\right)\Big|^{\mathrm{SM}}_{M_{h^0}=M_{H^0}}\ , \tag{13.13}$$

where $\sigma_{gg}\left(\mathrm{pp} \to h^0\right)\Big|^{\mathrm{SM}}_{M_{h^0}=M_{H^0}}$ indicates the SM Higgs production cross section via gluon-gluon fusion at the LHC evaluated at the mass of the heavy Higgs boson.[4]

The decays of the CP-even Higgs bosons to the $\mu\tau$ final state are considered next. The interaction of charged leptons with the Higgs bosons is given by the Lagrangian (see App. F.2)

$$\mathcal{L}_\ell = -\bar{\ell}^i_L\ell^j_R\left[h^0\left(\frac{m_{\ell_i}}{v}\delta^{ij}\cos\alpha + \frac{\eta^{ij}_{\ell,2}}{\sqrt{2}}\sin\alpha\right) + H^0\left(-\frac{m_{\ell_i}}{v}\delta^{ij}\sin\alpha + \frac{\eta^{ij}_{\ell,2}}{\sqrt{2}}\cos\alpha\right)\right] + \text{h.c.}\ , \tag{13.14}$$

with generation indices i, j. All elements $\eta^{ij}_{\ell,2}$ are set to zero in the following, except for those leading to decays into a $\mu\tau$ pair, $\eta^{\mu\tau}_{\ell,2}$ and $\eta^{\tau\mu}_{\ell,2}$. The parameter space is further simplified by assuming $|\eta^{\mu\tau}_{\ell,2}| = |\eta^{\tau\mu}_{\ell,2}|$, as demanded by CP conservation [300]. The decay widths of the Higgs bosons' decays to the $\mu\tau$ final state are then given by [294]:

$$\Gamma\left(H^0 \to \mu\tau\right) \equiv \Gamma\left(H^0 \to \mu^+\tau^-\right) + \Gamma\left(H^0 \to \mu^-\tau^+\right) = \frac{1}{16\pi}M_{H^0}\cos^2\alpha \cdot 2\,|\eta^{\mu\tau}_{\ell,2}|^2 \tag{13.15}$$

$$\Gamma\left(h^0 \to \mu\tau\right) \equiv \Gamma\left(h^0 \to \mu^+\tau^-\right) + \Gamma\left(h^0 \to \mu^-\tau^+\right) = \frac{1}{16\pi}M_{h^0}\sin^2\alpha \cdot 2\,|\eta^{\mu\tau}_{\ell,2}|^2\ . \tag{13.16}$$

---

[4] Caveats of this approach are pointed out in Ref. [299].

While small values of the mixing angle α suppress the LFV decay of the light Higgs boson h^0, they enhance the decay to a $\mu\tau$ pair of the heavy Higgs boson H^0. According to Ref. [294], the CMS search for the process pp $\to h^0(125\text{ GeV}) \to \mu\tau$ constrains the parameter product $\sin\alpha \cdot |\eta^{\mu\tau}_{\ell,2}|$ to values below $0.005/\sqrt{2}$ at 95% CL.

13.2.2 Recasting the $\mu\tau$ resonance cross section limits

With the fundamentals of a 2HDM signal for the process pp $\to H^0 \to \mu\tau$ introduced, the choice of the key model parameters and the reinterpretation of the cross section bounds in Fig. 13.2 is discussed next.

In order to allow for a large decay width of the heavy Higgs boson H^0 to a $\mu\tau$ pair, the mixing angle is assumed to be small, $\sin\alpha = 0.01$. According to Eqn. 13.13, the absolute value of the parameter $\eta^{tt}_{u,2}$ then has to be sizeable to obtain a production cross section of the heavy Higgs boson that would allow for its observation at the LHC. For a value of $\eta^{tt}_{u,2} = 0.2$, the H^0 production cross section is only about 4% of the SM Higgs production cross section via gluon-gluon fusion at the LHC evaluated at M_{H^0}. The SM Higgs production cross sections in pp collisions at $\sqrt{s} = 8$ TeV are given in Ref. [144] for various masses, where the gluon fusion cross section is evaluated at NNLO in pQCD with next-to-next-to leading log (NNLL) QCD and NLO EWK corrections applied.

The choices for the relation between the Higgs boson masses M_{H^0}, M_{A^0}, M_{H^+}, and the values of the parameters in the 2HDM Higgs potential $V(\Phi_1, \Phi_2)$ differ from those in Ref. [294]. In order to separate the two peaks in the $M^{\rm coll}_{\mu\tau}$ spectrum that are caused by the processes pp $\to H^0 \to \mu^\pm\tau^\mp$ and pp $\to A^0 \to \mu^\pm\tau^\mp$, the mass relation $M_{A^0} = M_{H^+} = M_{H^0} + 80$ GeV is assumed. This choice ensures that the two peaks are separated by at least three times the invariant mass resolution, expressed in Gaussian standard deviations, in the entire mass range considered for the heavy neutral CP-even Higgs, $M_{H^0} \in [200\text{ GeV}, 500\text{ GeV}]$. Thus, there is no significant overlap between the two $M^{\rm coll}_{\mu\tau}$ distributions and the assumption of a narrow resonance signal in the derivation of the cross section limits in Fig. 13.2 holds. As described in App F.2.2, the mass splitting between the heavy CP-even and CP-odd neutral Higgs bosons has consequences for two of the seven parameters λ_{1-7} in the Higgs potential and leads to the choice $\lambda_2 = \lambda_3 = 2,\ \lambda_7 = 0$ that ensures vacuum stability.

With the 2HDM signal model defined, the reinterpretation of the $\mu\tau$ narrow resonance cross section bounds in Fig. 13.2 is described next. First, it is shown that a simple rescaling of the limits by the ratio of the acceptances obtained for the two signal models, $A_{\tilde{\nu}_\tau}/A_{H^0}$, is a good approximation of the bound obtained when reiterating the entire analysis starting from a complete description of the new signal process pp $\to H^0 \to \mu\tau$ with a full detector simulation. The process to be simulated is depicted in Fig. 13.6. LHE files with parton level events from this process are obtained by using the SM implementation provided in the MadGraph5_aMC@NLO (v. 2.4.2) event generator [301]. In a first step, the gluon fusion Higgs production with subsequent decay into a pair of τ leptons is generated, with the SM Higgs boson mass evaluated at the desired value of M_{H^0}. The exact value of the Higgs boson decay width that is used in the event generation is not of interest for this study, as long as it leads to a narrow resonance, which is the case for the values of the coupling parameters considered in the following (see App. F.2.2). Therefore, it is fixed at $\Gamma_{h^0} = 6.4$ MeV, the default value provided for the SM Higgs boson in the utilized SM implementation. In a second step, one of the two final state τ leptons is chosen randomly and replaced by a muon of the corresponding electric charge. The momentum of the originally generated τ lepton is passed on to the muon, whereas mass and energy of the muon are adapted. For the three signal masses 200 GeV, 350 GeV, and 500 GeV, the resulting events are passed through the entire chain of software tools for parton showering, hadronization and detector simulation that has been described in Sec. 11.1.1. In particular, the *FullSim* detector simulation is used for these signal samples. They are used to reiterate the entire analysis and obtain the

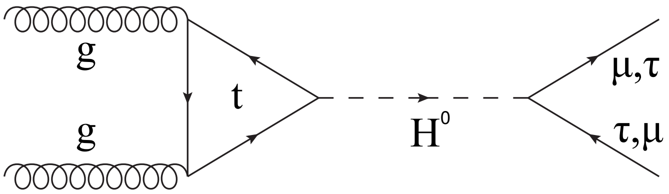

Figure 13.6: The production of a heavy Higgs boson H^0 via gluon fusion and a top-quark loop, and its subsequent LFV decay into a $\mu\tau$ pair.

resulting cross section limits. These can then be used to test the accuracy of a simple rescaling of the $\tilde{\nu}_\tau$ cross section bounds by the acceptance ratio of the two signals for these three signal masses. For all other mass hypotheses, the LHE events are hadronised with PYTHIA 8 (v. 8.185) [287], that also provides the τ decays and the *FastSim* detector simulation is employed. This kind of signal production suffices to determine the signal acceptance A_{H^0}. Each sample consists of 5000 generated events in which the decay of the τ lepton is forced to decay into an electron and neutrinos.

The key numbers for the reinterpretation are summarized in Tab. F.2 in App. F.2.3 and a summary for the signal mass points for which *FullSim* H^0 samples have been produced is given in Tab. 13.2. For the three signal masses considered therein, the acceptances of the H^0 and $\tilde{\nu}_\tau$ signals differ by 13% to 15%. The different signal acceptances are a result of the different production mechanisms of the H^0 and $\tilde{\nu}_\tau$ resonances via gluon-gluon fusion with a heavy quark loop and via $\mathrm{d}\overline{\mathrm{d}}$ annihilation, respectively. The differences in the full selection efficiency range from 12% to 23%. Most of this discrepancy is due to the change in acceptance. Therefore the most important difference between the two resonance signals for the purpose of extracting the cross section limit is accounted for by rescaling the $\tilde{\nu}_\tau$ bound with the ratio of the signal acceptances. For a resonance mass of 500 GeV, the observed 95% CL cross section bound for the $\tilde{\nu}_\tau$ signal is 16.8 fb, and the limit obtained from repeating the entire analysis with the heavy Higgs signal is 20.3 fb. This relative difference of about 17% is reduced to 7% when correcting the result for the $\tilde{\nu}_\tau$ signal with the ratio of the two signal acceptances. It can be decreased further to about 1% by rescaling with the ratio of the full selection efficiencies instead, but this approach does require a full detector simulation, which is part of the CMSSW software framework and is not available to scientists outside of the CMS collaboration. This remaining discrepancy of 1% lies within the inaccuracy introduced by choosing a Gaussian pdf to describe the resonance shape of the $\tilde{\nu}_\tau$ signal in the limit setting, as described in Sec. 13.1.2 (for the heavy Higgs signal, the shape is taken directly from the simulated samples).

For the signal masses $M_{\mathrm{res}} = 200$ GeV and $M_{\mathrm{res}} = 350$ GeV, the accuracy of the estimate of the H^0 cross section limit obtained by rescaling the $\tilde{\nu}_\tau$ limits according to the different acceptances is about 6% and 4%, respectively. In summary, an estimate of the observed cross section limit for the process $\mathrm{pp} \to H^0 \to \mu\tau$ with an accuracy better than 10% can be obtained by rescaling the cross section limit for the RPV $\tilde{\nu}_\tau$ model with the ratio of the two signal acceptances $A_{\tilde{\nu}_\tau}/A_{H^0}$.

The 95% CL H^0 cross section bounds resulting from this procedure are presented in Fig. 13.7 for signal mass hypotheses from 200 GeV to 500 GeV. The observed bounds on the product of the heavy Higgs production cross section and the branching fraction of its decay into a $\mu\tau$ pair range from 119 fb at $M_{H^0} = 200$ GeV to 18.9 fb at $M_{H^0} = 500$ GeV. For comparison, the SM Higgs production cross sections via gluon fusion for these two Higgs masses are $7080^{+6.0\%}_{-6.8\%}\,(\mathrm{scales})^{+7.4\%}_{-7.7\%}\,(\mathrm{PDF})$ fb and $1280^{+5.8\%}_{-5.1\%}\,(\mathrm{scales})^{+9.1\%}_{-8.5\%}\,(\mathrm{PDF})$ fb, respectively, as stated in Ref. [144]. According to Eqn. 13.13, the excluded region in the parameter space of the heavy Higgs model is therefore restricted to parameter points with sizeable values of the top quark Yukawa coupling to the second Higgs doublet Φ_2, $|\eta^{tt}_{u,2}| \gtrsim 0.13$, in the alignment limit $\sin\alpha \to 0$. This holds true even if the heavy Higgs boson decays exclusively into the $\mu\tau$ final state. The discussion of the exclusion boundaries in the 2HDM parameter space follows in the next paragraph.

Table 13.2: The key values for the comparison between the cross section bounds obtained by running the full analysis with the heavy Higgs signal and by rescaling the results for the $\tilde{\nu}_\tau$ signal. The acceptance (A) and full selection efficiency ($A\varepsilon$) are defined on the samples of produced $\mu\tau_\mathrm{e}$ events, i.e. the branching fraction of the leptonic τ decay is not included in these numbers. The last three columns contain the observed limits at 95% CL on the product of resonance production cross section and branching fraction into a $\mu\tau$ pair, $\mathcal{B}$. Among these three columns, the first contains the cross section limit obtained by running the full analysis with the heavy Higgs signal simulation, and the other two columns give the limits obtained by rescaling the $\tilde{\nu}_\tau$ cross section bounds with the indicated efficiency ratios.

M_res (GeV)	H^0		$\tilde{\nu}_\tau$		$\frac{(A\varepsilon)_{\tilde{\nu}_\tau}}{(A\varepsilon)_{H^0}}$	$\frac{A_{\tilde{\nu}_\tau}}{A_{H^0}}$	95% CL cross section limit (fb)		
	A	$A\varepsilon$	A	$A\varepsilon$			$(\sigma \times \mathcal{B})^\mathrm{obs}_{H^0}$	$(\sigma \times \mathcal{B})^\mathrm{obs}_{\tilde{\nu}_\tau} \times$	
	in %		in %					$(A\varepsilon)_{\tilde{\nu}_\tau}/(A\varepsilon)_{H^0}$	$A_{\tilde{\nu}_\tau}/A_{H^0}$
200	24.0	11.4	27.3	12.9	1.12	1.14	112	118	119
350	42.8	24.7	49.2	30.5	1.23	1.15	42.8	44.3	41.3
500	54.2	33.0	61.0	39.9	1.21	1.13	20.3	20.2	18.9

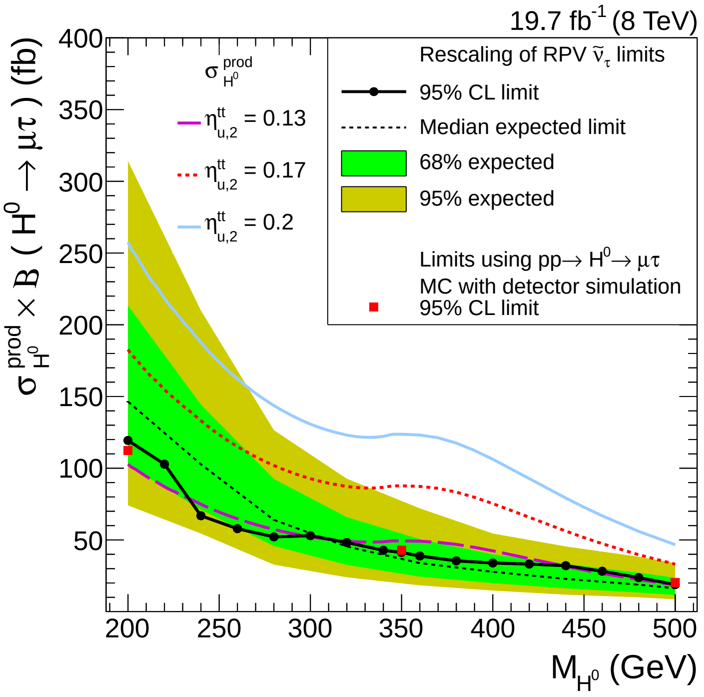

Figure 13.7: The 95% CL limits on the product of cross section and branching ratio for the process $pp \to H^0 \to \mu\tau$. The black solid curve represents the observed limit obtained from a rescaling of the RPV $\tilde{\nu}_\tau$ cross section limit in Fig. 13.2 with the ratio of the acceptances of the two signals $A_{\tilde{\nu}_\tau}/A_{H^0}$. The red dots show the observed cross section limit obtained when re-running the limit calculation from scratch with input from fully simulated $pp \to H^0 \to \mu\tau$ samples. The heavy Higgs production cross section (Eqn. 13.13) is shown for three different values of $\eta^{tt}_{u,2}$ and $\sin\alpha = 0.01$.

13.2.3 Bounds in 2HDM parameter space

In order to derive the exclusion boundaries in the parameter space of the heavy Higgs signal model, the dependence of the branching fraction of the H^0 decay into the $\mu\tau$ final state on the model parameters has to be studied. The `2HDMC` (v. 1.7.0) program [300] is utilized to calculate the H^0 decay widths. In addition to the direct heavy Higgs decays into fermion and boson pairs, it also includes decay channels that involve loops, such as $H^0 \to gg,\ \gamma\gamma,\ Z\gamma$. As explained in detail in App. F.2.2, the number of free parameters has been reduced to three by imposing conditions that relate the masses of the physical Higgs states and fixing the remaining free parameters in the Higgs potential. These remaining three parameters are the sine of the mixing angle, $\sin\alpha$, and the non-negligible Yukawa couplings to the second Higgs doublet Φ_2, $\eta^{tt}_{u,2}$, and $\eta^{\mu\tau}_{\ell,2} = \eta^{\tau\mu}_{\ell,2}$. The dependence of the total decay width Γ_{H^0} on these parameters is summarized in App. F.2.2.

For the choice of parameters $\sin\alpha = 0.01$, $\eta^{tt}_{u,2} = 0.2$, and $\eta^{\mu\tau}_{\ell,2} = \eta^{\tau\mu}_{\ell,2} = 0.1$, the branching fractions of the dominant H^0 decay modes are depicted in Fig. 13.8 (left). Below the mass threshold for top-pair production the branching fraction of the decay into the $\mu\tau$ final state exceeds 95%. This is due to the suppression of the decays into diboson final states - the corresponding branching fractions scale with $\sin^2\alpha \equiv 10^{-4}$. Above the $\mathrm{t\bar{t}}$ threshold, the branching fraction of the decay into the $\mathrm{t\bar{t}}$ final state exhibits a steep turn-on that levels out towards higher masses and surpasses the branching fraction of the $\mu\tau$ decay at $M_{H^0} \approx 400$ GeV. At $M_{H^0} = 500$ GeV, the top-pair channel is the dominant decay mode with a branching fraction of over 60%.

Since the branching fractions into the difermion final states scale with the square of the respective Yukawa couplings this picture changes significantly when the $\mu\tau$ Yukawa coupling $\eta^{\mu\tau}_{\ell,2}$ is decreased relative to $\eta^{tt}_{u,2}$. This is exemplified in Fig. 13.8 (right) for the parameters $\sin\alpha = 0.01$, $\eta^{tt}_{u,2} = 0.2$, and $\eta^{\mu\tau}_{\ell,2} = \eta^{\tau\mu}_{\ell,2} = 0.01$. At $M_{H^0} = 200$ GeV, the heavy Higgs decay into a $\mu\tau$ pair is dominant with a branching fraction of 80%. Towards the top-pair production threshold, this branching fraction falls to about 20%, and once the threshold is reached it exhibits a steep drop. Between about 280 GeV and 350 GeV the H^0 decay to a pair of light Higgs bosons is the dominant decay channel for this choice of the Yukawa couplings. More generally, the $H^0h^0h^0$ coupling in-

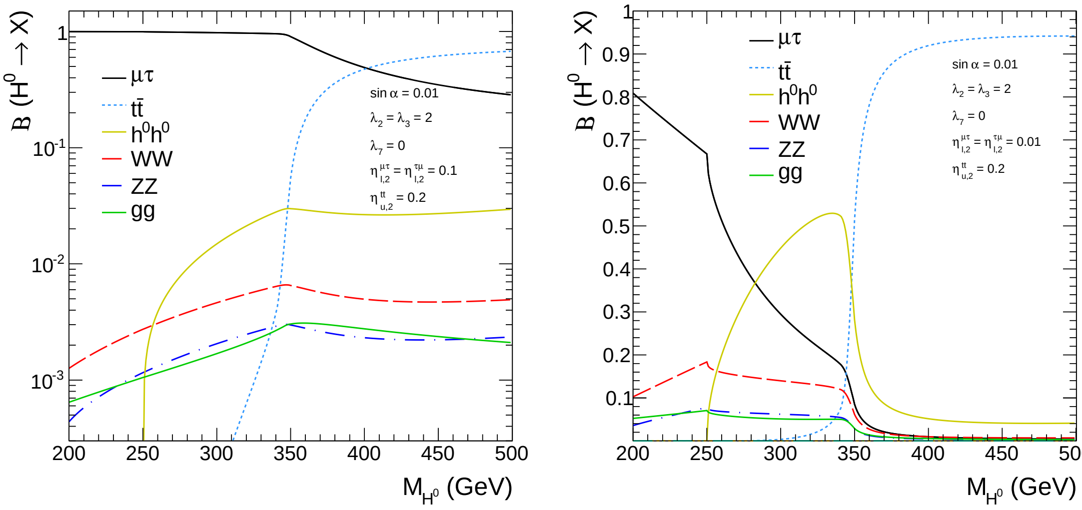

(a) Branching fractions of the H^0 decay modes for $\eta^{\mu\tau}_{\ell,2} = \eta^{\tau\mu}_{\ell,2} = 0.1$ and $\eta^{tt}_{u,2} = 0.2$.

(b) Branching fractions of the H^0 decay modes for $\eta^{\mu\tau}_{\ell,2} = \eta^{\tau\mu}_{\ell,2} = 0.01$ and $\eta^{tt}_{u,2} = 0.2$.

Figure 13.8: Branching fractions of the leading H^0 decay modes obtained with the `2HDMC` *program [300] for two different choices of the parameters $\eta^{\mu\tau}_{\ell,2} = \eta^{\tau\mu}_{\ell,2}$ and $\eta^{tt}_{u,2}$. In both cases, the alignment limit is considered by fixing the sine of the mixing angle at $\sin\alpha = 0.01$.*

troduces a dependence of the branching fraction of the decay into the $\mu\tau$ final state on the choice of the Higgs potential parameters λ_3 and λ_7 in the mass range $2M_{h^0} \lesssim M_{H^0} \lesssim 2m_t$ when small values of the $\mu\tau$ Yukawa coupling $\eta^{\mu\tau}_{\ell,2} \sim \sin\alpha$ are considered. The dependence of the decay width $\Gamma_{H^0 \to h^0 h^0}$ on the λ parameters in the Higgs potential is given in Ref. [294].

In order to arrive at a large enough production cross section of the heavy Higgs boson, the Yukawa coupling of the top quark must be of the order $\eta^{tt}_{u,2} \gtrsim 0.13$, as mentioned above. Taking into account the bound on the parameter product $\sin\alpha \cdot |\eta^{\mu\tau}_{\ell,2}|$ from the CMS search for $\mu\tau$ decays of the light Higgs boson, this means that the $\mathrm{t\bar{t}}$ final state will account for a significant part of the H^0 decay width for masses $M_{H^0} \gg 2m_{\mathrm{t}}$, favouring the search for the heavy Higgs boson in resonant $\mathrm{t\bar{t}}$ production. Therefore, the mass range is restricted to $M_{H^0} \leq 500$ GeV in this interpretation of the search for $\mu\tau$ resonances.

The 95% CL exclusion bounds in the parameter space of the studied 2HDM are presented as contours in the $(M_{H^0}, |\eta^{\mu\tau}_{\ell,2}| = |\eta^{\tau\mu}_{\ell,2}|)$ plane for several values of the Yukawa coupling $\eta^{tt}_{u,2}$ and $\sin\alpha = 0.01$ in Fig. 13.9. They are obtained in two steps. First the excluded branching fraction $\mathcal{B}^{\mathrm{excl}}_{H^0\to\mu\tau}$ is determined by comparing the observed cross section bounds in Fig. 13.7 at a given mass to the corresponding heavy Higgs production cross section from Eqn. 13.13. Then, the excluded Yukawa coupling is obtained using the formula for the decay width of the heavy Higgs decay into a $\mu\tau$ pair in Eqn. 13.15 as

$$|\eta^{\mu\tau}_{\ell,2}|^{\mathrm{excl}} = \sqrt{\frac{8\pi\Gamma^{\not{\mu\tau}}_{H^0}\mathcal{B}^{\mathrm{excl}}_{H^0\to\mu\tau}}{M_{H^0}\cos^2\alpha\left(1-\mathcal{B}^{\mathrm{excl}}_{H^0\to\mu\tau}\right)}}\,, \tag{13.17}$$

where $\Gamma^{\not{\mu\tau}}_{H^0}$ denotes the sum over all H^0 decay widths excluding the $\mu\tau$ decay width, which depends on $\eta^{\mu\tau}_{\ell,2}$. All decay widths in $\Gamma^{\not{\mu\tau}}_{H^0}$ are again evaluated using the `2HDMC` code.

The 95% CL exclusion boundaries in the $(M_{H^0}, |\eta^{\mu\tau}_{\ell,2}| = |\eta^{\tau\mu}_{\ell,2}|)$ plane in Fig. 13.9 for $\eta^{tt}_{u,2} = 0.13$ exhibits a very different shape compared to those for $\eta^{tt}_{u,2} = 0.2$ and $\eta^{tt}_{u,2} = 0.3$. The reason is that for this smallest choice of the top-quark Yukawa coupling the observed cross section limit is close to the heavy Higgs production cross section over the entire range of probed signal masses. For $\eta^{tt}_{u,2} = 0.13$ and $M_{H^0} = 200$ GeV, the H^0 production cross section is 103 fb while the 95% CL cross section bound is 120 fb. Since even the production cross section is not excluded at the required confidence level no limit can be set on the Yukawa coupling $\eta^{\mu\tau}_{\ell,2}$, which only affects the decay of the heavy Higgs boson but not its production at the LHC. When the observed cross section limit lies below the corresponding H^0 production cross section, as is the case for $M_{H^0} = 240$ GeV, an observed 95% CL bound on the branching fraction of the decay into a $\mu\tau$ pair can be set, and the resulting limit on $|\eta^{\mu\tau}_{\ell,2}|$ is as small as 0.02; all other allowed decay channels at this Higgs mass are strongly suppressed by the assumption $\sin\alpha = 0.01$. The exclusion contour for $\eta^{tt}_{u,2} = 0.13$ in Fig. 13.9 is very sensitive to fluctuations within the uncertainties on the cross section limit because the H^0 production cross section lies within the 1σ-band around the median expected limit in Fig. 13.7 for this choice of the top quark Yukawa coupling. This is not the case for the two other exclusion boundaries for $\eta^{tt}_{u,2} = 0.2$ and $\eta^{tt}_{u,2} = 0.3$. Here, the bound on $|\eta^{\mu\tau}_{\ell,2}|$ weakens slowly with increasing M_{H^0} due to the rising branching fractions of the diboson final states, see Fig. 13.8 (right). When the light Higgs pair production threshold is reached, the exclusion boundary of the $\mu\tau$ Yukawa coupling starts to rise, and once the top-pair production threshold is passed and the decay into the $\mathrm{t\bar{t}}$ final state sets in, the excluded value of $|\eta^{\mu\tau}_{\ell,2}|$ increases significantly. At $M_{H^0} = 350$ GeV, the 95% CL limits on the $\mu\tau$ Yukawa coupling to the Higgs doublet Φ_2 read $|\eta^{\mu\tau}_{\ell,2}| = 2.3 \cdot 10^{-2}$ and $|\eta^{\mu\tau}_{\ell,2}| = 1.8 \cdot 10^{-2}$, for $\eta^{tt}_{u,2} = 0.2$ and $\eta^{tt}_{u,2} = 0.3$, respectively, and $\sin\alpha = 0.01$. Coupling values in the per mille range are excluded if M_{H^0} is below 250 GeV. In particular, the bound on $|\eta^{\mu\tau}_{\ell,2}|$ in this mass region falls below the Cheng-Sher-type ansatz [302] for the FCNC-inducing Yukawa couplings, $|\eta^{\mu\tau}_{\ell,2}| = \sqrt{2m_\mu m_\tau}/v$, when $\eta^{tt}_{u,2} = \sqrt{2}m_t/v$ is assumed. These bounds are more restrictive than the corresponding signal-mass-independent limit of $|\eta^{\mu\tau}_{\ell,2}| \leq 0.5/\sqrt{2}$ resulting from the search for the decay of the light Higgs boson h^0 into a

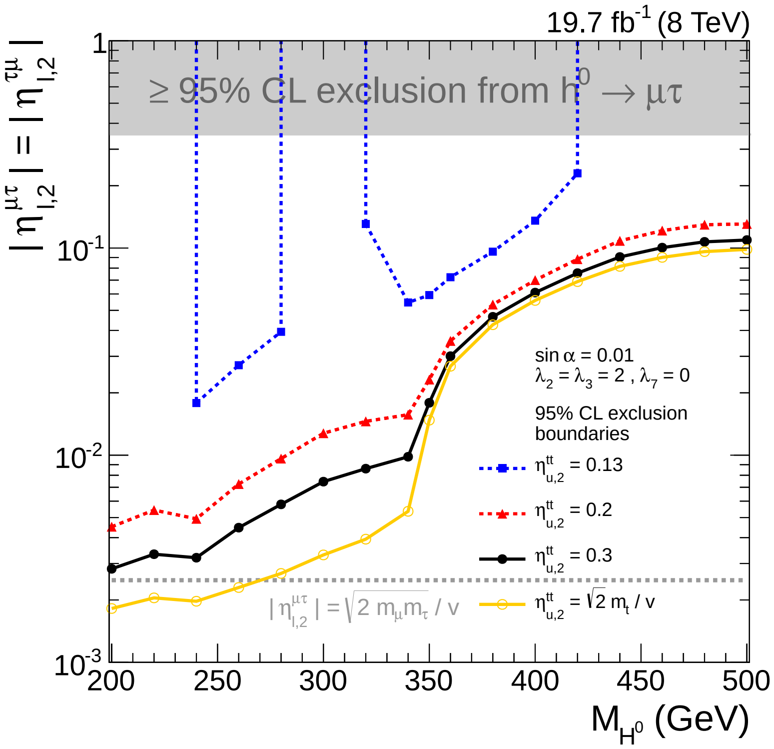

Figure 13.9: The 95% *CL exclusion boundaries in the* $(M_{H^0}, \eta^{\mu\tau}_{\ell,2})$ *plane of the 2HDM parameter space for three values of the parameter* $\eta^{tt}_{u,2}$*. It is assumed that* $\eta^{\mu\tau}_{\ell,2} = \eta^{\tau\mu}_{\ell,2}$ *and* $\sin\alpha = 0.01$*. The areas above the curves are excluded. The gray shaded area represents the bound on the product of* $\sin\alpha$ *and the LFV Yukawa coupling* $\eta^{\mu\tau}_{\ell,2}$ *from the* 8 *TeV CMS search for the decay* $h^0(125\ \mathrm{GeV}) \to \mu\tau$ *derived in Ref. [294].*

$\mu\tau$ pair.

In summary, stringent bounds on 2HDMs with cLFV between the second and third generation can be obtained from the presented search for narrow $\mu\tau$ resonances in the alignment limit assuming a sizeable Yukawa coupling of the top quark to the Higgs doublet Φ_2. In particular, the cross section limits in Fig. 13.7 cover the mass range for heavy neutral Higgs bosons between 200 GeV and the top-pair production threshold. Thereby, they close a gap between the searches for Higgs decays to a $\mu\tau$ pair around 125 GeV by the CMS and ATLAS collaborations [26, 27] and searches for high-mass $\mu\tau$ resonances above 400 GeV by the ATLAS collaboration [31, 63] carried out with data from Run I at the LHC.

Conclusion

In this thesis, two searches for physics beyond the Standard Model of particles physics (BSM physics) are described that look for signs of heavy states mediating charged lepton flavour violating (cLFV) interactions between the first and second generation ($\mathrm{e} \leftrightarrow \mu$) and the second and third generation ($\mu \leftrightarrow \tau$), respectively. The analyses use data samples of proton-proton (pp) collisions at $\sqrt{s} = 8$ TeV recorded with the CMS detector at the LHC that correspond to an integrated luminosity of 19.7 fb^{-1}. Both searches are performed in experimental final states including an electron/muon pair, i.e. in the $\mu\tau$ analyses the leptonic decay of the τ lepton $\tau^{-} \rightarrow \mathrm{e}^{-}\nu_{\tau}\bar{\nu}_{e}$ is considered. The $\mathrm{e}\mu$ and $\mu\tau_{\mathrm{e}}$ dilepton mass spectra are examined for contributions from BSM physics, in particular narrow peaks and excesses over the Standard Model expectation in the high-mass tails of the distributions. No evidence for BSM physics is found and upper bounds on signal cross sections are obtained at 95% confidence level (CL) and 90% CL for various BSM signal models that share the common experimental signature of a pronounced peak in the analyzed dilepton mass spectra. The tested signal models involve different types of heavy resonances or quantum black holes (QBHs) that mediate cLFV interactions. The cross section limits for these models are then translated into bounds on the corresponding model parameters.

In the $\mathrm{e}\mu$ search, limits are set on the resonant production of a tau sneutrino ($\tilde{\nu}_{\tau}$) lightest supersymmetric particle in R-parity violating (RPV) Supersymmetry (SUSY) and on the production of quantum black holes that decay into the $\mathrm{e}\mu$ final state. The lower exclusion bounds on the threshold mass M_{th} for QBH production at 95% CL range from 1.99 TeV ($n = 0$) to 3.63 TeV ($n = 6$), depending on the assumed number of extra dimensions n. Published in the journal paper Ref. [30] (and previously in Ref. [38]) by the CMS collaboration, this has been the first search for QBHs decaying into the $\mathrm{e}\mu$ final state at a high-energy collider. This type of search has since been repeated by the CMS collaboration in Ref. [285] and introduced by the ATLAS collaboration in Ref. [32], in both cases using data samples of pp collisions at $\sqrt{s} = 13$ TeV recorded in the initial stages of Run 2 of the LHC after its first long shutdown that allowed for upgrades, additional tests, and ultimately running at a higher centre-of-mass energy as of 2015. The 13 TeV searches yield more stringent mass bounds on QBHs. In the case of the resonant production of a $\tilde{\nu}_{\tau}$ in RPV SUSY via coupling to the $\mathrm{d}\bar{\mathrm{d}}$ initial state, the $\mathrm{e}\mu$ search presented in this work yields the strongest bounds obtained by direct searches at high-energy colliders for coupling values $\lambda'_{311} = \lambda_{312} = \lambda_{321} \lesssim 0.1$. For the coupling values $\lambda'_{311} = \lambda_{312} = \lambda_{321} = 0.1$, a lower bound on the $\tilde{\nu}_{\tau}$ mass of 2.42 TeV is obtained at 95% CL and the limit for $\lambda'_{311} = \lambda_{312} = \lambda_{321} = 0.01$ reads 1.28 TeV. The RPV $\tilde{\nu}_{\tau}$ search is extended to cover other initial states than the baseline choice $\mathrm{d}\bar{\mathrm{d}}$ and thus probes all 18 products of RPV Yukawa couplings of the forms $|\lambda'_{3jk}\,\lambda_{312}|$ and $|\lambda'_{3jk}\,\lambda_{321}|$. The bounds on the couplings products range from $|\lambda'_{311}\,\lambda_{312}| < 4.1 \times 10^{-5}$ ($\tilde{\nu}_{\tau}$ production via $\mathrm{d}\bar{\mathrm{d}}$) to $|\lambda'_{333}\,\lambda_{312}| < 5.9 \times 10^{-3}$ ($\tilde{\nu}_{\tau}$ production via $\mathrm{b}\bar{\mathrm{b}}$) at 90% CL, assuming $M_{\tilde{\nu}_{\tau}} = 1$ TeV and $\lambda'_{3jk} = \lambda_{312} = \lambda_{321}$. Presented in this form, the bounds can readily be compared to results from lower-energy experiments. The extension of the physics interpretation of the $\mathrm{e}\mu$ resonance search via a simple reinterpretation of the results obtained for the $\mathrm{d}\bar{\mathrm{d}}$ initial state is an example of how different BSM models can be tested with a single search at the LHC due to the various partonic initial states it provides.

The constraints from different indirect searches for cLFV at lower-energy facilities are very constrictive for BSM models involving resonant production of an $\mathrm{e}\mu$ pair in quark/antiquark annihilation at the LHC. A comparison of the bounds obtained for the different $\tilde{\nu}_{\tau}$ models with limits by various indirect searches for cLFV at lower energy facilities reveals that the presented search for eμ resonances is most competitive when considering the non-zero production coupling λ'_{313}. In the corresponding model, the $\tilde{\nu}_\tau$ is produced in $\mathrm{b\overline{d}}$ annihilation rather than $\mathrm{d\overline{d}}$ annihilation, which has been the choice in the RPV $\tilde{\nu}_\tau$ models tested in publications by experiments at the Tevatron [59, 60] and the LHC [30–32, 285].

Two considerations ought to be kept in mind when assessing the value of searches for eμ resonances at high-energy colliders in the light of the restrictive constraints from indirect searches for cLFV between the first and second generation at dedicated lower-energy experiments. First, the resonant production of the eμ pair via direct couplings to the proton constituents, that has been chosen as the signal model in terms of which the experimental findings are interpreted in this thesis, is not the only production mode covered by the presented search. If a heavy particle that decays to an eμ pair were produced in association with another particle or in a longer decay chain, the signature in the detector still were a peak in the eμ mass spectrum. The strong indirect constraints on resonant eμ production at the LHC thus suggest an inclusive event selection that covers many possible signal event topologies with a peak in the eμ mass spectrum. Such an approach has been chosen in this thesis. Secondly, searches for cLFV at the LHC provide information complementary to that from indirect searches.

In the $\mu\tau$ search, the stringent bounds that constrain cLFV between leptons of the first and second generation do not apply, motivating the presented extension of the eμ search to a search for heavy resonances that decay to the $\mu\tau_\mathrm{e}$ final state. In the RPV $\tilde{\nu}_\tau$ model with non-zero Yukawa couplings λ'_{311} and λ_{323}, the observed lower bounds on $M_{\tilde{\nu}_\tau}$ at 95% CL read 370 GeV and 1730 GeV for coupling values of $\lambda'_{311} = \lambda_{323} = 0.01$ and $\lambda'_{311} = \lambda_{323} = 0.1$, respectively. The bounds of the $\mu\tau$ resonance search are found to be more restrictive than those obtained by the ATLAS collaboration in pp collisions at $\sqrt{s} = 8$ TeV based on a data sample of similar integrated luminosity [31]. They are also competitive against the exclusion limits inferred from searches for cLFV in τ decays at B factories [72] and improve them in parts of the RPV $\tilde{\nu}_\tau$ model's parameter space. Finally, the interpretation of the $\mu\tau$ resonance search in terms of the production of a heavy Higgs boson in a 2HDM with cLFV relates this work to searches for extensions of the SM Higgs sector and makes a case for covering the intermediate mass region $M_{h^0} \lesssim M \lesssim 2\,m_\mathrm{t}$ in searches for heavy dilepton resonances.

In conclusion, the subject of this thesis is the direct search for various heavy states that mediate cLFV interactions at the LHC. At the time of their first publication, most of the presented searches have yielded the highest sensitivity to the BSM physics under study obtained at high-energy colliders. Analyses based on the first round of data from Run 2 of the LHC recorded in 2015 have improved the presented results only for signals with particles with masses above about 2 TeV. In the future, analyses of the full datasets recorded by the CMS and ATLAS collaborations in 2015 and 2016 should either reveal evidence for a signal or push the bounds on the model parameters further. However, even when datasets corresponding to integrated luminosities of several 100 fb^{-1} will eventually be accumulated by CMS and ATLAS, indirect constraints will remain a serious challenge in the case of searches for cLFV between leptons of the first and second generation at the LHC. The next generation of experiments that probe μ-e conversion [303, 304] are underway and are expected to improve the sensitivity of concluded experiments by orders of magnitude. This should motivate experimenters at the LHC to focus on searches for resonant production of $\mu\tau$ and eτ pairs rather than on searches for eμ resonances.

Appendix

Appendix A

Lagrangian from the trilinear RPV terms of the superpotential

The R-parity violating trilinear terms of the superpotential in SUSY with baryon triality symmetry B_3 read:

$$W_{LLE} = \frac{1}{2}\lambda_{ijk} L_i L_j \bar{E}_k = \epsilon_{ab}\,\frac{1}{2}\lambda_{ijk} L_i^a L_j^b \bar{E}_k = \frac{1}{2}\lambda_{ijk}\left(N_i E_j - E_i N_j\right)\bar{E}_k \tag{A.1}$$

$$W_{LQD} = \lambda'_{ijk} L_i Q_j \bar{D}_k = \epsilon_{ab}\,\lambda'_{ijk} L_i^a Q_j^{xb} \bar{D}_{kx} = \lambda'_{ijk}\left(N_i D_j^x - E_i U_j^x\right)\bar{D}_{kx}\ . \tag{A.2}$$

$SU(2)_L$ gauge invariance is enforced by the antisymmetric tensor ϵ_{ab} with $a, b \in \{1,2\}$ denoting the weak isospin indices of the $SU(2)_L$ doublet superfields and leads to a total of only 9 independent couplings λ_{ijk} [51]:

$$\lambda_{ijk}\epsilon_{ab} L_i^a L_j^b \bar{E}_k = -\lambda_{ijk}\epsilon_{ba} L_i^a L_j^b \bar{E}_k \underset{i\leftrightarrow j}{=} -\lambda_{jik}\epsilon_{ba} L_j^a L_i^b \bar{E}_k = -\lambda_{jik}\epsilon_{ba} L_i^b L_j^a \bar{E}_k \Rightarrow \boxed{\lambda_{ijk} = -\lambda_{jik}}\ . \tag{A.3}$$

From the superpotential W in Equations A.1 and A.2, the Yukawa terms in the Lagrangian are obtained [51, 305] by first replacing the superfields with the corresponding scalars ($W \rightarrow W(\phi)$):

$$W_{LLE} = \frac{1}{2}\lambda_{ijk}\left(N_i E_j - E_i N_j\right)\bar{E}_k \Rightarrow W_{LLE}(\phi) = \frac{1}{2}\lambda_{ijk}\left(\tilde{\nu}_{iL}\tilde{l}_{jL} - \tilde{l}_{iL}\tilde{\nu}_{jL}\right)\tilde{l}^c_{kR} \tag{A.4}$$

$$W_{LQD} = \lambda'_{ijk}\left(N_i D_j^x - E_i U_j^x\right)\bar{D}_{kx} \Rightarrow W_{LQD}(\phi) = \lambda'_{ijk}\left(\tilde{\nu}_{iL}\tilde{d}^x_{jL} - \tilde{l}_{iL}\tilde{u}^x_{jL}\right)\tilde{d}^c_{kxR}\ , \tag{A.5}$$

and then computing the derivatives with respect to all possible combinations of scalar fields:

$$\mathcal{L}_{LLE\ (LQD)} = -\frac{1}{2}\sum_{\alpha,\beta}\frac{\partial^2 W_{LLE\ (LQD)}(\phi)}{\partial\phi_\alpha\partial\phi_\beta}\bar{\psi}_{\alpha R}\psi_{\beta L} - \frac{1}{2}\sum_{\alpha,\beta}\frac{\partial^2 W^*_{LLE\ (LQD)}(\phi)}{\partial\phi^*_\alpha\partial\phi^*_\beta}\bar{\psi}_{\alpha L}\psi_{\beta R}\ . \tag{A.6}$$

The LQD term in the superpotential leads to the following interactions involving sneutrinos in the Lagrangian using Dirac spinors:

$$\mathcal{L}_{LQD} \supset -\lambda'_{ijk}\left(\tilde{\nu}_{iL}\bar{d}_{kR}d_{jL} + \bar{d}_{jR}d_{kL}\tilde{\nu}^*_{iL}\right)\ , \tag{A.7}$$

and the LLE term yields:

$$\mathcal{L}_{LLE} \supset -\frac{1}{2}\lambda_{ijk}\left(\tilde{\nu}_{iL}\bar{l}_{kR}l_{jL} - \tilde{\nu}_{jL}\bar{l}_{kR}l_{iL} + \bar{l}_{jR}l_{kL}\tilde{\nu}^*_{iL} - \bar{l}_{iR}l_{kL}\tilde{\nu}^*_{jL}\right)\ . \tag{A.8}$$

Appendix B

Datasets

Table B.1: The datasets used in the $e\mu$ resonance search (SingleMu, top) and $\mu\tau_e$ resonance search (MuEG, bottom). The sample names in the CMS data aggregation system (DAS) [170] are given in the second column. The values for the integrated luminosity are calculated with only those runs in which all CMS subdetectors have been fully operational as input (golden json).

Primary dataset	Sample name	Run range	$L_{\text{int}}^{\text{an}}$ (fb^{-1})
Single-muon triggers	SingleMu/Run2012A-22Jan2013-v1/AOD	190456-193621	0.9
	SingleMu/Run2012B-22Jan2013-v1/AOD	193833-196531	4.4
	SingleMu/Run2012C-22Jan2013-v1/AOD	198022-203742	7.1
	SingleMu/Run2012D-22Jan2013-v1/AOD	203777-208686	7.4
Muon + Electron/Photon cross-triggers	MuEG/Run2012A-22Jan2013-v1/AOD	190456-193621	0.9
	MuEG/Run2012B-22Jan2013-v1/AOD	193833-196531	4.4
	MuEG/Run2012C-22Jan2013-v1/AOD	198022-203742	7.1
	MuEG/Run2012D-22Jan2013-v1/AOD	203777-208686	7.4

Appendix C

List of simulated event samples

C.1 Signal simulation eμ resonance search

QBH signal samples

The parameter points of the QBH signal model for which signal samples have been produced are listed in Tab. C.1. All samples are based on events generated with `CALCHEP` and use `PYTHIA` 6 for parton showering and hadronization and are processed through the full `GEANT4`-based simulation of the CMS detector (FullSim).

RPV $\tilde{\nu}_\tau$ signal samples

The parameter points of the RPV $\tilde{\nu}_\tau$ model in the eμ resonance search (non-zero $\tilde{\nu}_\tau$ production coupling λ'_{311} with $\mathrm{d}\overline{\mathrm{d}}$ initial state) for which signal samples have been produced are listed in Tabs. C.2 and C.3. All samples are based on events generated with `CALCHEP` and use `PYTHIA` 6 for parton showering and hadronization and are processed through the full `GEANT4`-based simulation of the CMS detector (FullSim).

Two different muon misalignment scenarios are used in the simulation of RPV $\tilde{\nu}_\tau$ signal events, referred to as the baseline and the corrected baseline misalignment scenarios. Both are based on an alignment obtained from cosmic ray muon data collected during the *Cosmic Run At Four Tesla* (CRAFT) [214]. The *baseline* muon alignment scenario (the so-called 2012 STARTUP muon misalignment) has been used for the simulation of the signal samples that are summarized in Tab. C.2. These samples have been processed centrally in the Summer12 CMS production campaign. It was realized after completion of the samples that the position of the muon barrel system had been shifted unintentionally with respect to the inner tracking system by 0.2 cm in the configuration of the detector simulation. This shift is reversed in the *corrected* muon misalignment scenario (the so-called C1 muon misalignment) that has been used to produced the signal samples in Tab. C.3.

The RPV eμ resonance signal samples in Tab. C.2, that use the baseline muon misalignment, are used to obtain the signal selection efficiency in Fig. 5.6. A re-evaluation of the selection efficiency with the samples in Tab. C.3, that use the corrected muon alignment, yields deviations from the former result below 1.5%, well within the assigned systematic uncertainties.

The samples in Tab. C.3 are used to determine the eμ mass resolution in Fig. 5.10 and Eqn. 5.8. The simulated samples in Tab. C.2 are not used for the resolution study because they are affected by the unintended 0.2 cm shift of the barrel muon system that leads to a large bias in the p_T resolution of muons with $p_\mathrm{T} \sim \mathcal{O}(\mathrm{TeV})$.

C.2 Signal simulation $\mu\tau_{\mathrm{e}}$ resonance search

RPV $\tilde{\nu}_\tau$ signal samples

The simulated signal samples for the RPV $\tilde{\nu}_\tau$ model in the $\mu\tau_{\mathrm{e}}$ search are listed in Tab. C.4. The event generation is carried out with `CALCHEP`. Two versions of simulated samples have been produced starting from the same generated parton-level events. The first version, that is only used for cross-checks in the $\mu\tau_{\mathrm{e}}$ analysis, has been processed in one of the official CMS production campaigns; the samples are listed in the CMS data aggregation system (DAS) [170] under the sample name `RPVresonantToMuTau_M-scan_TuneZ2star_8TeV-calchep-pythia6`. `PYTHIA` 6 is employed for showering and hadronization, `Tauola` [306] is utilized for the decay of the τ lepton, and the baseline muon misalignment scenario is used in this official production. The τ lepton is allowed to decay via all its decay channels in these samples. The second version, the one used to obtain the signal efficiencies and mass resolution in Sec. 11.3, has been produced privately by the author. It employs `PYTHIA` 8 for both hadronization and τ decay and uses the corrected (C1) muon misalignment scenario. In these samples, the τ lepton is forced to decay leptonically into an electron and neutrinos. It is therefore necessary to include the branching fraction $\mathcal{B}(\tau^- \to \mathrm{e}^- \overline{\nu}_{\mathrm{e}}\, \nu_\tau)$ as an additional factor when scaling the event yields obtained from these samples, $N_{sig} = \sigma \times \mathcal{B}(\tilde{\nu}_\tau \to \mu\tau) \times \mathcal{B}(\tau^- \to \mathrm{e}^- \overline{\nu}_{\mathrm{e}}\, \nu_\tau) \times (A \times \epsilon)_{\mathrm{MC}} \times L_{\mathrm{int}}$.

C.3 Background simulation

The simulated background samples, that are used in the eμ and $\mu\tau_{\mathrm{e}}$ resonance searches, are listed in Tabs. C.5, C.6, and C.7. The samples that are used in the background estimation are presented in Tabs. C.5 and C.6 whereas the samples in Tab. C.7 are used for auxiliary studies and cross-checks.

Table C.1: Summary of simulated QBH signal samples with $n = 0$ extra dimensions (left) and $n \geq 1$ (right) extra dimensions. The samples for $n = 0$ have been produced in one of the official CMS production campaigns and are listed in the CMS data aggregation system (DAS) [170] under the sample names `QBHToemu_CI_CalcHEP_8TeV` *and* `QBHtoEMu_M-*_CI_CalcHEP_8TeV-pythia6`*, whereas those for $n \geq 1$ have been produced privately by Emmanuel Olaiya. The cross sections are evaluated at LO in pQCD using the event generator* `CALCHEP` *with the PDF set CTEQ6L and include the branching fraction into the desired $\mathrm{e}^{\pm}\mu^{\mp}$ final state. The samples for $n = 0$ contain 25000 generated events each and those for $n \geq 1$ contain 20000 events.*

n	M_{th} (TeV)	$\sigma \times \mathcal{B}(\mathrm{QBH} \to \mathrm{e}^{\pm}\mu^{\mp})$ (pb)
0	0.5	1.5
	0.6	0.59
	0.7	0.26
	0.8	0.12
	0.9	6.3×10^{-2}
	1	3.4×10^{-2}
	1.1	1.9×10^{-2}
	1.2	1.1×10^{-2}
	1.3	6.4×10^{-3}
	1.4	3.9×10^{-3}
	1.5	2.4×10^{-3}
	1.6	1.5×10^{-3}
	1.7	9.2×10^{-4}
	1.8	5.9×10^{-4}
	1.9	3.8×10^{-4}
	2	2.5×10^{-4}
	2.2	1.1×10^{-4}
	2.4	4.6×10^{-5}
	2.6	2.0×10^{-5}
	2.8	9.1×10^{-6}
	3	4.1×10^{-6}
1	0.5	28.9
	1	0.82
	1.5	6.3×10^{-2}
	2	6.9×10^{-3}
	2.5	9.0×10^{-4}
	3	1.2×10^{-4}
	3.5	1.6×10^{-5}
	4	1.9×10^{-6}
	4.5	2.0×10^{-7}
2	0.5	97.0
	1	29.0
	1.5	0.23
	2	2.6×10^{-2}
	2.5	3.4×10^{-3}
	3	4.6×10^{-4}
	3.5	6.1×10^{-5}
	4	7.5×10^{-6}
	4.5	7.7×10^{-7}
3	0.5	196
	1	6.0
	1.5	0.48
	2	5.4×10^{-2}
	2.5	7.1×10^{-3}
	3	9.9×10^{-4}
	3.5	1.3×10^{-4}
	4	1.6×10^{-5}
	4.5	1.7×10^{-6}
6	0.5	600
	1	19.0
	1.5	1.5
	2	0.17
	2.5	2.3×10^{-2}
	3	3.2×10^{-3}
	3.5	4.3×10^{-4}
	4	5.3×10^{-5}
	4.5	5.4×10^{-6}

Table C.2: Summary of simulated RPV $\tilde{\nu}_\tau$ signal samples for the eμ resonance search that have been produced in one of the official CMS production campaigns and are listed in the CMS data aggregation system (DAS) [170] under the sample name `RPVresonantToEMu_M-scan_TuneZ2star_8TeV-calchep-pythia6`*. The baseline muon misalignment scenario has been used in the production. The cross section in the fourth column is taken from the event generator* `CALCHEP` *using the PDF set CTEQ6L and includes the branching fraction into the desired* $\mathrm{e}^{\pm}\mu^{\mp}$ *final state. The NLO QCD k-factor,* σ_{NLO}/σ_{LO}*, is calculated as described in Sec. 1.1.2, based on Ref. [57]. Each sample contains 10000 generated events.*

λ'_{311}	$\lambda_{312} = \lambda_{321}$	$M_{\tilde{\nu}_\tau}$ (GeV)	$\sigma \times \mathcal{B}(\tilde{\nu}_\tau \to \mathrm{e}^{\pm}\mu^{\mp})$ (pb)	NLO (pQCD) k-factor
0.01	0.01	100	2.71	1.34
		200	3.06×10^{-1}	1.38
		300	8.30×10^{-2}	1.39
		400	2.90×10^{-2}	1.39
		500	1.25×10^{-2}	1.38
		600	6.19×10^{-3}	1.37
		700	3.31×10^{-3}	1.35
		800	1.90×10^{-3}	1.33
		900	1.12×10^{-3}	1.31
		1000	6.87×10^{-4}	1.29
		1100	4.33×10^{-4}	1.27
		1200	2.77×10^{-4}	1.25
		1300	1.80×10^{-4}	1.23
		1400	1.19×10^{-4}	1.21
		1500	7.9×10^{-5}	1.19
		1600	5.3×10^{-5}	1.18
		1700	3.6×10^{-5}	1.16
		1800	2.4×10^{-5}	1.14
		1900	1.6×10^{-5}	1.13
		2000	1.1×10^{-5}	1.12
0.05	0.05	500	3.15×10^{-1}	1.38
		1000	1.72×10^{-2}	1.29
		1500	1.99×10^{-3}	1.19
		2000	2.80×10^{-4}	1.12
0.1	0.1	2200	5.24×10^{-4}	1.09
		2400	2.41×10^{-4}	1.08
		2600	1.11×10^{-4}	1.07

Table C.3: Summary of simulated RPV $\tilde{\nu}_\tau$ signal samples for the $e\mu$ resonance search that have been produced privately by the author with the corrected (C1) muon alignment. In these samples, the $\tilde{\nu}_\tau$ is produced in the $d\bar{d}$ initial state via the corresponding non-zero coupling λ'_{311}. The cross section in the fourth column is taken from the event generator `CALCHEP` *using the PDF set CTEQ6L and includes the branching fraction into the desired $\mathrm{e}^{\pm}\mu^{\mp}$ final state. The NLO QCD k-factor, σ_{NLO}/σ_{LO}, is calculated as described in Sec. 1.1.2, based on Ref. [57]. Each sample contains 10000 generated events.*

λ'_{311}	$\lambda_{312} = \lambda_{321}$	$M_{\tilde{\nu}_\tau}$ (GeV)	$\sigma \times \mathcal{B}(\tilde{\nu}_\tau \to \mathrm{e}^{\pm}\mu^{\mp})$ (pb)	NLO (pQCD) k-factor
0.01	0.01	200	3.06×10^{-1}	1.38
		500	1.25×10^{-2}	1.38
		800	1.90×10^{-3}	1.33
		1000	6.87×10^{-4}	1.29
		1500	7.9×10^{-5}	1.19
		2000	1.1×10^{-5}	1.12
0.5	0.5	2600	4.8×10^{-3}	1.07
		3000	1.7×10^{-3}	1.07

Table C.4: Summary of simulated RPV $\tilde{\nu}_\tau$ *signal samples used in the* $\mu\tau_{\mathrm{e}}$ *resonance search. The cross section in the fourth column is taken from the event generator* `CALCHEP` *using the PDF set CTEQ6L and includes the branching fraction into the desired* $\mu^{\pm}\tau^{\mp}$ *final state (without the branching fraction* $\tau^- \to e^- \bar{\nu}_e \nu_\tau$*). The NLO QCD k-factor,* σ_{NLO}/σ_{LO}*, is calculated as described in Sec. 1.1.2, based on Ref. [57]. Each sample contains 10000 generated events.*

λ'_{311}	λ_{323}	$M_{\tilde{\nu}_\tau}$ (GeV)	$\sigma \times \mathcal{B}(\tilde{\nu}_\tau \to \mu\tau)$ (pb)	NLO (pQCD) k-factor
0.01	0.01	200	0.19	1.38
		500	8.0×10^{-3}	1.38
		1000	4.3×10^{-4}	1.29
0.05	0.05	100	43.6	1.34
		200	4.9	1.38
		300	1.2	1.39
		400	0.45	1.39
		500	0.20	1.38
		600	9.7×10^{-2}	1.37
		700	5.2×10^{-2}	1.35
		800	3.0×10^{-2}	1.33
		900	1.8×10^{-2}	1.31
		1000	1.1×10^{-2}	1.29
		1100	6.8×10^{-3}	1.27
		1200	4.3×10^{-3}	1.25
		1300	2.8×10^{-3}	1.23
		1400	1.9×10^{-3}	1.21
		1500	1.2×10^{-3}	1.19
		1600	8.3×10^{-4}	1.18
		1700	5.6×10^{-4}	1.16
		1800	3.8×10^{-4}	1.14
		1900	2.6×10^{-4}	1.13
		2000	1.7×10^{-4}	1.12
0.1	0.1	2200	3.3×10^{-4}	1.09
		2400	1.5×10^{-4}	1.08
		2600	6.9×10^{-5}	1.07

Table C.5: Information about the simulated background samples from official production within the CMS collaboration that enter the background estimates in the eμ and $\mu\tau$ resonance searches. The sample names in the third column correspond to the trunk of the name in the CMS data aggregation system (DAS) [170]. The cross section in the fourth column is that used for the scaling of the event yield, i.e. it contains branching fractions if primary particles in the final state decay further and efficiencies of applied acceptance cuts. Several cross sections have been obtained at NLO accuracy in pQCD with MCFM [244] and are documented in Ref. [245]. More information about the samples and cross sections listed here is presented in Sec. 6.

Process (final state)	GEN cuts	Sample name in DAS	Generator	$\sigma(\times\text{BR})$ (pb)	PDF set
$t\bar{t}$	-	TT_CT10_TuneZ2star_8TeV-powheg-tauola	`POWHEG`	245.8 (NNLO, Czakon et al. [222])	CT10
$t\bar{t}$	700 GeV $< M_{t\bar{t}} <$ 1 TeV	TT_Mtt-700to1000_CT10_TuneZ2star_8TeV-powheg-tauola	`POWHEG`	15.6×1.16 (scaled to NNLO)	CT10
$t\bar{t}$	$M_{t\bar{t}} >$ 1 TeV	TT_Mtt-1000toInf_CT10_TuneZ2star_8TeV-powheg-tauola	`POWHEG`	2.95×1.16 (scaled to NNLO)	CT10
$\mathrm{W^+W^-} \rightarrow 2\ell 2\nu$	-	WWJetTo2L2Nu_8TeV-powheg-pythia6	`POWHEG`	5.88 (NLO, MCFM)	CT10
$\mathrm{WZ} \rightarrow 3\ell\nu$	$M_{\ell\ell}(Z/\gamma^*) >$ 12 GeV	WZJetsTo3LNu_TuneZ2_8TeV-madgraph-tauola	`MadGraph`	1.09 (NLO, MCFM)	CTEQ6L1
$\mathrm{ZZ} \rightarrow 4\ell$	$M_{\ell\ell}(Z/\gamma^*) >$ 12 GeV	ZZJetsTo4L_TuneZ2star_8TeV-madgraph-tauola	`MadGraph`	0.18 (NLO, MCFM)	CTEQ6L1
$\mathrm{Z}/\gamma^* \rightarrow 2\ell$	$M_{\ell\ell}(Z/\gamma^*) >$ 50 GeV	DYJetsToLL_M-50_TuneZ2Star_8TeV-madgraph-tarball	`MadGraph`	3530 (NNLO, FEWZ [249])	CTEQ6L1
$\mathrm{tW} \rightarrow 2\ell 2\nu b$	-	TToDilepton_tW-channel-DR_8TeV-powheg-tauola	`POWHEG`	1.17 (approx. NNLO [258])	CTEQ6M
$\bar{\mathrm{t}}\mathrm{W} \rightarrow 2\ell 2\nu\bar{b}$	-	TBarToDilepton_tW-channel-DR_8TeV-powheg-tauola	`POWHEG`	1.17 (approx. NNLO [258])	CTEQ6M
$\mathrm{W}\gamma \rightarrow \ell\nu\gamma$	$p_T^\gamma >$ 5 GeV	WGToLNuG_TuneZ2star_8TeV-madgraph-tauola	`MadGraph`	462 (LO)	CTEQ6L1
$\mathrm{W}\gamma \rightarrow \ell\nu\gamma$	30 GeV $< p_T^\gamma <$ 50 GeV, $\lvert\eta^\gamma\rvert < 3.5$	WGToLNuG_PtG-30-50_8TeV-madgraph	`MadGraph`	20.4 (LO)	CTEQ6L1
$\mathrm{W}\gamma \rightarrow \ell\nu\gamma$	50 GeV $< p_T^\gamma <$ 130 GeV, $\lvert\eta^\gamma\rvert < 3.5$	WGToLNuG_PtG-50-130_8TeV-madgraph	`MadGraph`	3.3 (LO)	CTEQ6L1
$\mathrm{W}\gamma \rightarrow \ell\nu\gamma$	$p_T^\gamma >$ 130 GeV, $\lvert\eta^\gamma\rvert < 3.5$	WGToLNuG_PtG-130_8TeV-madgraph-pythia6_tauola	`MadGraph`	0.26 (LO)	CTEQ6L1

Table C.6: Information about the simulated background samples from private production that are part of the background estimate (high-mass $M_{e\mu}$ tails) for the $t\bar{t}$ and WW processes in the $e\mu$ and $\mu\tau_{\mathrm{e}}$ resonance searches. The corrected (C1) muon alignment is used in the production of these samples. Information about the combination with the corresponding bulk samples in Tab. C.5 is given in Secs. 6.1.1 and 6.1.2.

Process	GEN cuts	Generator	$\sigma(\times\mathcal{B})$ (pb)	PDF set
$t\bar{t} \rightarrow e^{\pm}\mu^{\mp}2\nu b\bar{b}$	$M_{e\mu} > 600$ GeV	`POWHEG`	$4.3 \times 10^{-3} \times 1.16$ (scaled to NNLO)	CT10
$\mathrm{W}^{+}\mathrm{W}^{-} \rightarrow e^{+}\mu^{-}2\nu$	$M_{e\mu} > 600$ GeV	`POWHEG`	$1.6 \times 10^{-3} \times 1.07$ (scaled to NLO MCFM)	CT10
$\mathrm{W}^{+}\mathrm{W}^{-} \rightarrow \mu^{+}e^{-}2\nu$	$M_{e\mu} > 600$ GeV	`POWHEG`	$1.6 \times 10^{-3} \times 1.07$ (scaled to NLO MCFM)	CT10

Table C.7: Information about the simulated background samples from official production within the CMS collaboration that do not enter the background estimates in the $e\mu$ and $\mu\tau$ resonance searches but are used for auxiliary studies. The sample names in the third column correspond to the trunk of the name in the CMS data aggregation system (DAS) [170]. The cross section in the fourth column is that used for the scaling of the event yield, i.e. it contains branching fractions if primary particles in the final state decay further and efficiencies of applied acceptance cuts. Several cross sections have been obtained at NLO accuracy in pQCD with MCFM [244] and are documented in Ref. [245].

Process (final state)	GEN cuts	Sample name in DAS	Generator	$\sigma(\times\mathcal{B})$ (pb)
$\mathrm{W} \to \ell\nu$	-	WJetsToLNu_TuneZ2Star_8TeV-madgraph-tarball	`MadGraph`	30400×1.21 (NNLO, FEWZ)
$\mathrm{W} \to \ell\nu$	$50\ \mathrm{GeV} \leq p_{\mathrm{T,W}} < 70\ \mathrm{GeV}$	WJetsToLNu_PtW-50To70_TuneZ2star_8TeV-madgraph	`MadGraph`	811×1.21 (scaled to NNLO)
$\mathrm{W} \to \ell\nu$	$70\ \mathrm{GeV} \leq p_{\mathrm{T,W}} < 100\ \mathrm{GeV}$	WJetsToLNu_PtW-70To100_TuneZ2star_8TeV-madgraph	`MadGraph`	429×1.21 (scaled to NNLO)
$\mathrm{W} \to \ell\nu$	$p_{\mathrm{T,W}} \geq 100\ \mathrm{GeV}$	WJetsToLNu_PtW-100_TuneZ2star_8TeV-madgraph	`MadGraph`	229×1.21 (scaled to NNLO)
QCD multijet μ enriched	$\hat{p}_{\mathrm{T}} > 20\ \mathrm{GeV}\ ,\ p_{\mathrm{T}}^{\mu} > 15\ \mathrm{GeV}$	QCD_Pt_20_MuEnrichedPt_15_TuneZ2star_8TeV_pythia6	`PYTHIA 6`	1.3×10^5 (LO) $\times 1.3$
$\mathrm{W}^+\mathrm{W}^- \to 2\ell 2\nu$	-	WWJetsTo2L2Nu_TuneZ2star_8TeV-madgraph-tauola	`MadGraph`	5.88 (NLO, MCFM)
$\mathrm{W}^-\mathrm{W}^-\, q_{\mathrm{u}}\, q_{\mathrm{u}}$	-	WmWmqq_8TeV-madgraph	`MadGraph`	0.089 (LO)
$\mathrm{W}^+\mathrm{W}^+\, q_{\mathrm{d}}\, q_{\mathrm{d}}$	-	WpWpqq_8TeV-madgraph	`MadGraph`	0.25 (LO)
WW multiparton scattering	-	WW_DoubleScattering_8TeV-pythia8	`PYTHIA 8`	0.59 (LO)
$\mathrm{Z}/\gamma^*\gamma \to 2\ell\gamma$	$M_{\ell\ell} > 10\ \mathrm{GeV}\ ,\ p_{\mathrm{T}}^{\gamma} > 5\ \mathrm{GeV}$	ZGToLLG_8TeV-madgraph	`MadGraph`	156 (NLO, MCFM)
Single t s-channel	-	TToLeptons_s-channel_8TeV-powheg-tauola	`POWHEG`	0.91 (NLO)
Single $\bar{\mathrm{t}}$ s-channel	-	TBarToLeptons_s-channel_8TeV-powheg-tauola	`POWHEG`	0.51 (NLO)
Single t t-channel	-	TToLeptons_t-channel_8TeV-powheg-tauola	`POWHEG`	15.2 (NLO)
Single $\bar{\mathrm{t}}$ t-channel	-	TBarToLeptons_t-channel_8TeV-powheg-tauola	`POWHEG`	8.1 (NLO)

Appendix D

Determination of the muon p_T resolution using cosmic ray muons

Table D.1: The datasets used in the muon p_T resolution study with cosmic ray muons. The sample names in the CMS data aggregation system (DAS) [170] are given in the first column. The second column contains the total number of recorded events in the samples. The number of events passing the data quality cuts (DT system and inner tracking system fully operational) are given in columns three and four, separated by two operation modes of the tracker front-end electronics; the peak and deconvolution modes [219].

Sample name	Events in sample	Events after DQ cuts	
		Peak	*Deconvolution*
/Cosmics/Commissioning12-CosmicSP-26Mar2013-v1 /RAW-RECO	272 372	62 114	715
/Cosmics/Run2012A-CosmicSP-22Jan2013-v1/RAW-RECO	216 642	96 567	28 575
/Cosmics/Run2012B-CosmicSP-22Jan2013-v1/RAW-RECO	372 256	74 289	88 074
/Cosmics/Run2012C-CosmicSP-22Jan2013-v1/RAW-RECO	424 235	31 524	68 056
/Cosmics/Run2012D-CosmicSP-22Jan2013-v1/RAW-RECO	432 569	0	0
Total	1 718 074	264 494	185 420

Table D.2: DAS names of the simulated samples of cosmic ray events.

Sample name
/TKCosmics_p10/Summer12-CosmicSuperPointing-COSMC_53_PEAC_cosmics-v1/GEN-SIM-RAW-RECO
/TKCosmics_p100/Summer12-CosmicSuperPointing-COSMC_53_PEAC_cosmics-v1/GEN-SIM-RAW-RECO
/TKCosmics_p500/Summer12-CosmicSuperPointing-COSMC_53_PEAC_cosmics-v1/GEN-SIM-RAW-RECO
/TKCosmics_p10/Summer12-CosmicSuperPointing-COSMC_53_DECC_cosmics-v1/GEN-SIM-RAW-RECO
/TKCosmics_p100/Summer12-CosmicSuperPointing-COSMC_53_DECC_cosmics-v1/GEN-SIM-RAW-RECO
/TKCosmics_p500/Summer12-CosmicSuperPointing-COSMC_53_DECC_cosmics-v1/GEN-SIM-RAW-RECO

Appendix E

Detailed information eμ resonance search

E.1 Pseudorapidity distributions of leptons in same-sign eμ events

Figure. E.1 shows the pseudorapidity distributions of electrons (left) and muons (right) in same-sign eμ events (e$^{\pm}\mu^{\pm}$). The correction of the normalization of the t$\bar{\text{t}}$ background simulation by a factor two that is explained in Sec. 9.1.2 has been applied. The observed difference in the shape of the two pseudorapidity distributions is mainly caused by the W + jet process which is part of the data-driven jet background estimate.

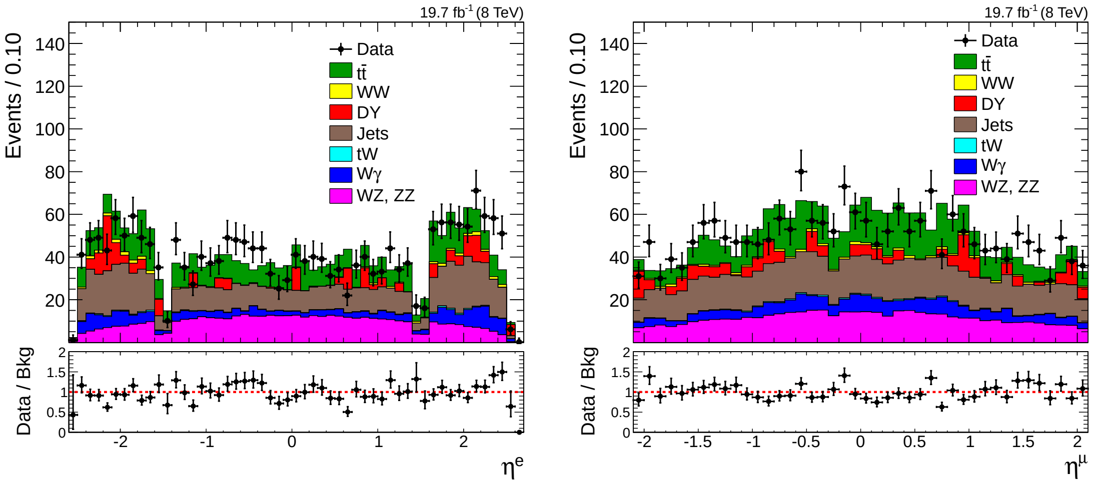

(a) The electron η distribution.

(b) The muon η distribution.

Figure E.1: The pseudorapidity distributions of electrons (left) and muons (right) in selected eμ pairs in which the two leptons carry the same electric charge.

E.2 Jet p_{T} and $\not{E}_{\mathrm{T}}$ in selected eμ events

Figure. E.2 illustrates the impact of the top-p_{T} reweighting, introduced in the context of the description of systematic uncertainties in the $\mathrm{t\bar{t}}$ simulation in Sec. 8.1.3, on the simulated $\not{E}_{\mathrm{T}}$ distribution of events that pass the eμ selection. The agreement between data and expectation improves after the correction is applied. The slope in the $\not{E}_{\mathrm{T}}$ dependence of the ratio between data and background expectation is reduced.

The p_{T} spectra of all jets in eμ events passing the jet selection and of the subset of b-tagged jets are shown in Fig. E.3. In both cases, the top-p_{T} reweighting has been applied to the $\mathrm{t\bar{t}}$ simulation.

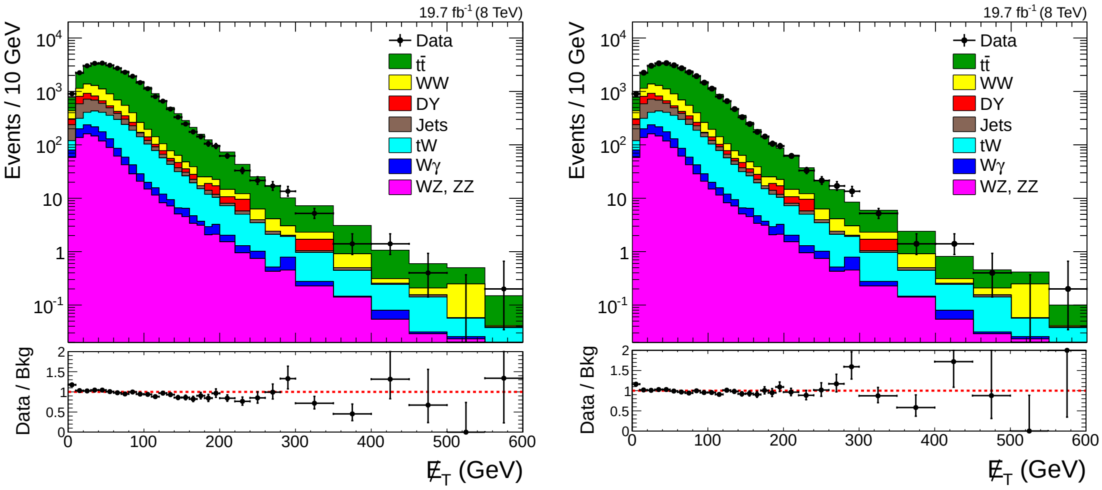

(a) $\not{E}_{\mathrm{T}}$ distribution as obtained from simulation.

(b) $\not{E}_{\mathrm{T}}$ distribution after applying the top-p_{T} reweighting to the $\mathrm{t\bar{t}}$ simulation.

Figure E.2: The $\not{E}_{\mathrm{T}}$ distribution in selected eμ events as obtained when using the $t\bar{t}$ simulation without correction (left) and after applying the top-p_{T} reweighting (right).

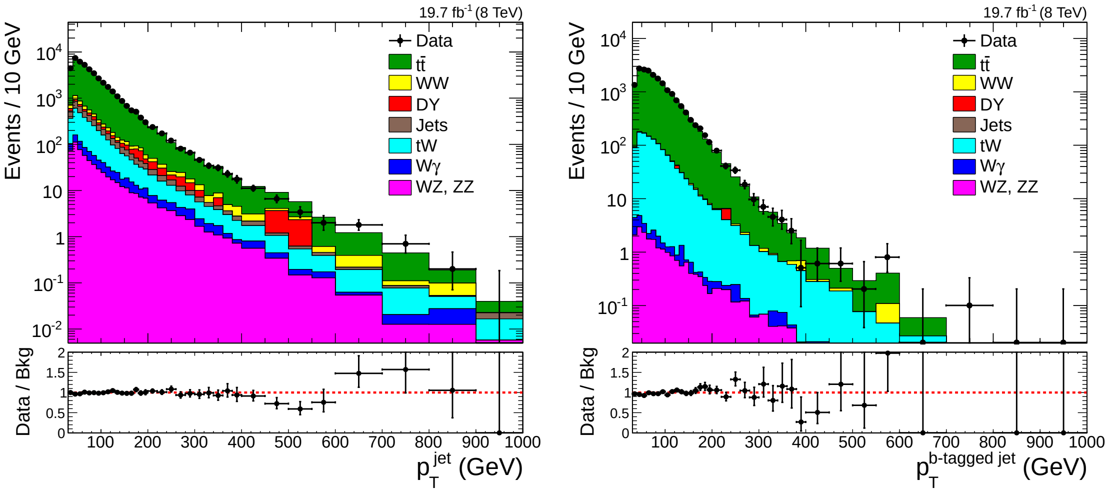

(a) The jet p_{T} distribution.

(b) The p_{T} distribution of b-tagged jets.

Figure E.3: The p_{T} spectra of all jets passing the jet selection in eμ events (left) and of all selected jets with a b-tag. The top-p_{T} reweighting has been applied to the $t\bar{t}$ simulation in both cases.

E.3 Details invariant mass distribution

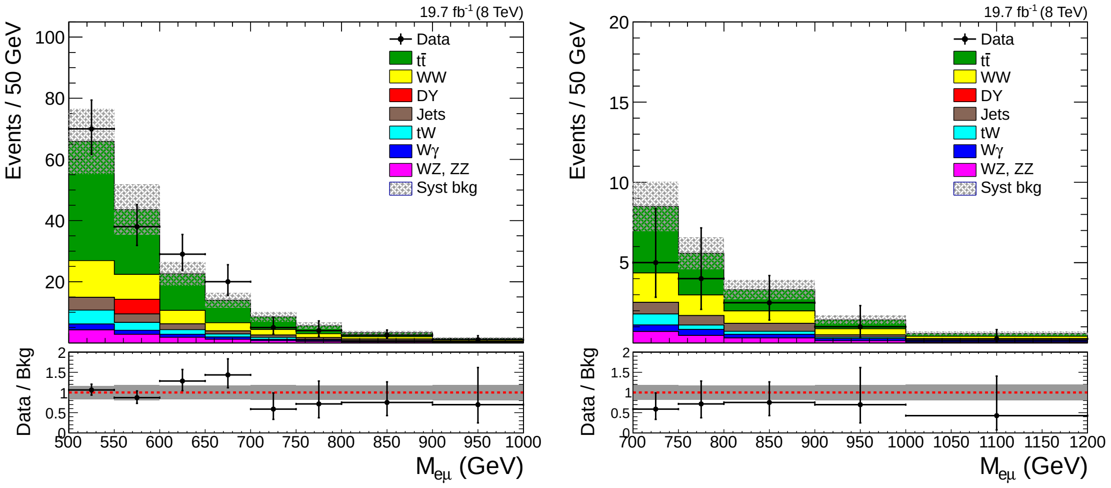

(a) $M_{e\mu}$ spectrum of selected eμ events with 500 GeV $\leq M_{e\mu} \leq$ 1 TeV.

(b) $M_{e\mu}$ spectrum of selected eμ events with 700 GeV $\leq M_{e\mu} \leq$ 1.2 TeV.

Figure E.4: The $M_{e\mu}$ *distributions of selected* eμ *events in the ranges* 500 *GeV* $\leq M_{e\mu} \leq$ 1 *TeV (left) and* 700 *GeV* $\leq M_{e\mu} \leq$ 1.2 *TeV (right). The grey bands in the spectra and the ratio plots indicate the systematic uncertainty in the background prediction for each bin.*

E.4 Muon identitifcation variables of muons with $p_{\mathrm{T}}^{\mu} > 200$ GeV

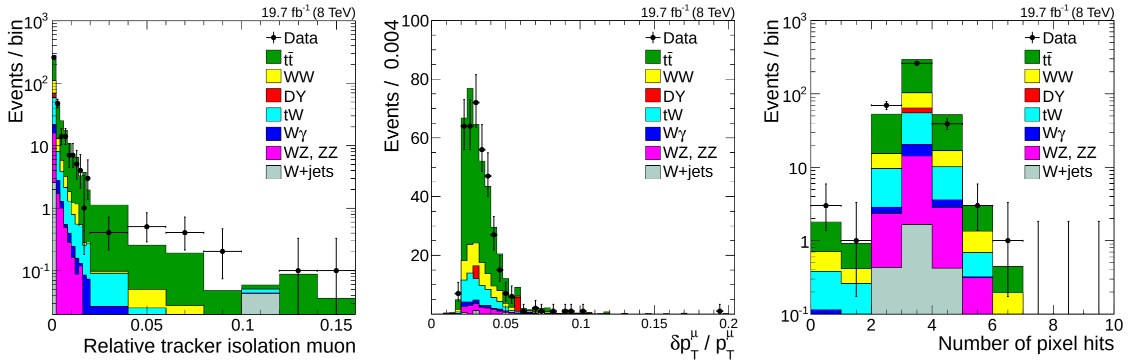

(a) The relative tracker isolation I_{rel}^{μ}.

(b) The relative uncertainty in the p_{T} measurement from the fit of the muon track.

(c) The number of hits in the pixel detector associated with the muon track.

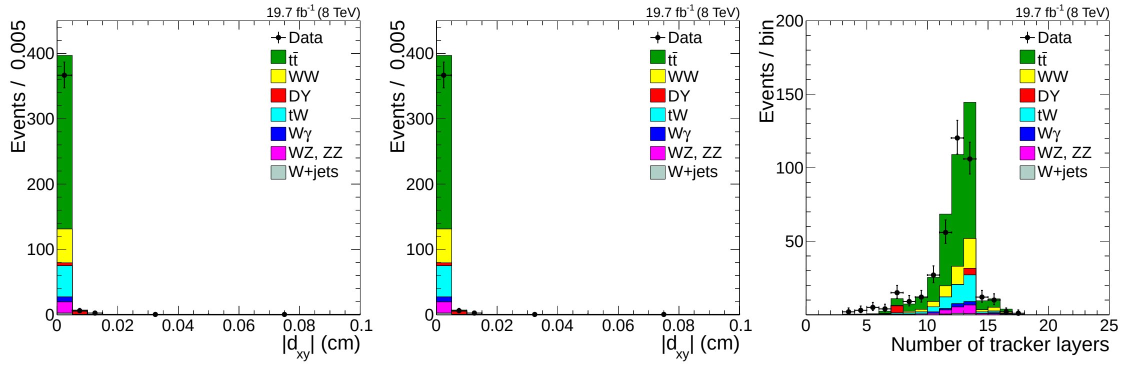

(d) The transverse impact parameter $|\mathrm{d}_{\mathrm{xy}}|$ of the muon track relative to the primary vertex.

(e) The longitudinal impact parameter $|\mathrm{d}_{\mathrm{z}}|$ of the muon track relative to the primary vertex.

(f) The number of tracker layers with hits associated with the muon track.

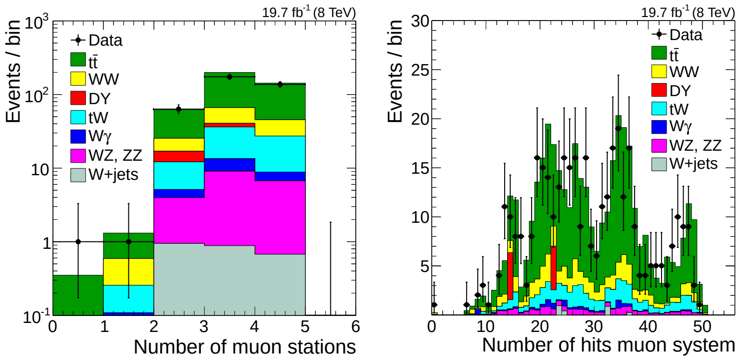

(g) The number of muon stations with track segments that are matched to the muon track.

(h) The number of hits in the muon system associated with the muon track.

Figure E.5: Distributions of muon identification variables of muons in $e\mu$ events with transverse momenta above 200 GeV. These are the $N-1$ distributions, i.e. all cuts of the muon selection are applied apart from that on the plotted variable.

E.5 Details high-$M_{e\mu}$ events

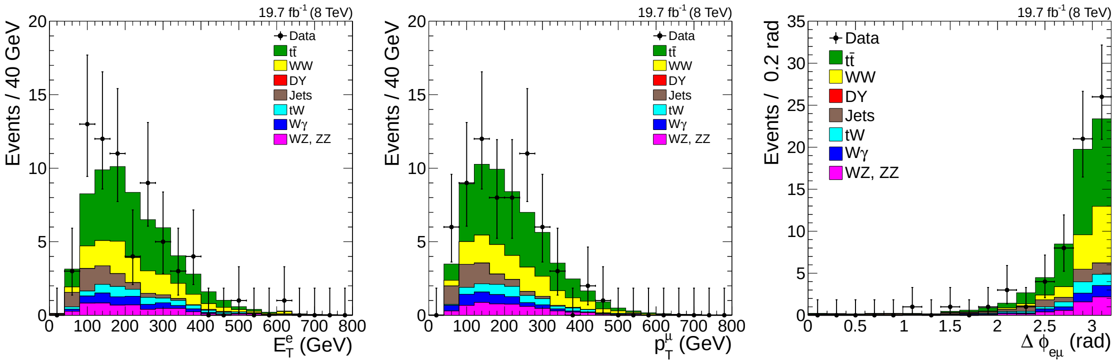

(a) The electron E_T distribution. (b) The muon p_T distribution. (c) The absolute value of the difference in azimuthal angle of the leptons $\Delta\phi_{e\mu}$.

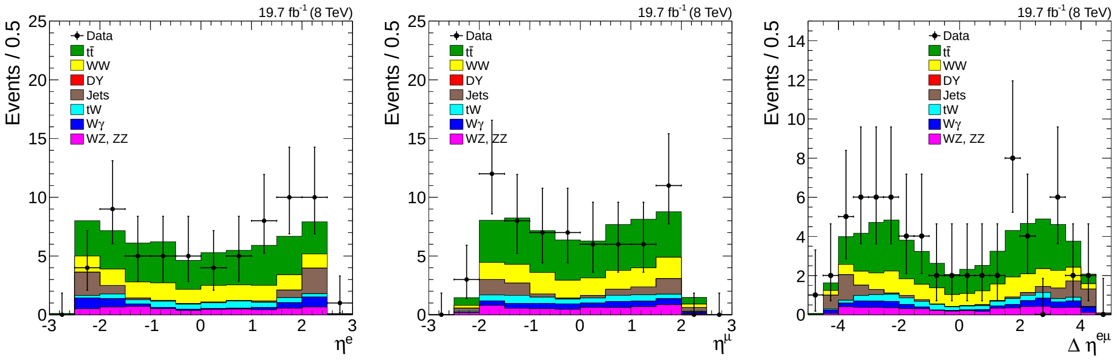

(d) The electron η distribution. (e) The muon η distribution. (f) The $\Delta\eta^{e\mu}$ distribution.

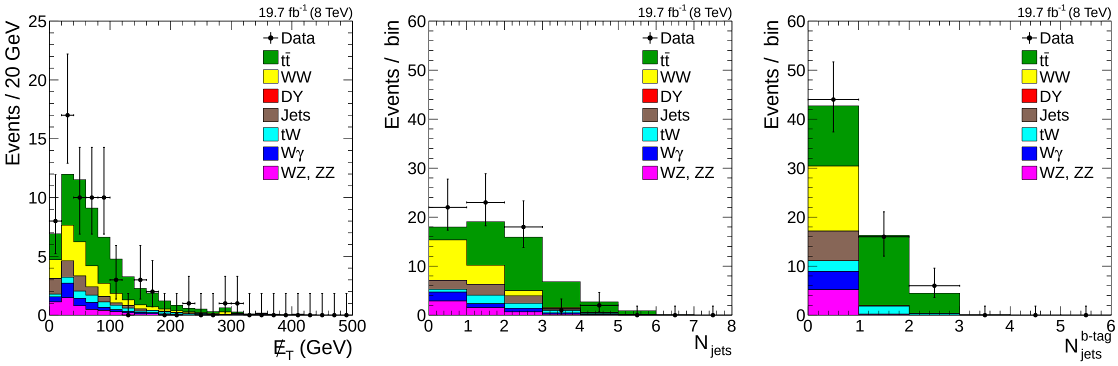

(g) The missing transverse energy $\not{E}_T$. (h) The number of selected jets. (i) The number of selected jets with a b-tag.

Figure E.6: Distributions of variables describing the lepton kinematics and event topology in the 66 events observed in data with eμ pairs that satisfy $M_{e\mu} \geq 600$ GeV.

E.6 Summary of cross section limits for the RPV $\tilde{\nu}_\tau$ signal

Table E.1: The upper limits on the product of the $\tilde{\nu}_\tau$ production cross section and the branching fraction of its decay into an $e\mu$ pair for various masses. In addition to the observed cross section limit at 95% CL, the median expected limit at 95% CL is given together with the corresponding boundaries of the 1σ uncertainty band. The observed limit at 90% CL is also presented because it is used as input to the calculation of the 90% CL bounds in RPV parameter space in Sec. 10.2.2 that are compared to bounds from indirect searches in the literature which are available at this confidence level. The full signal selection efficiency and acceptance are included in columns 7 and 8 to allow for a reinterpretation of the cross section limits in terms of other signal models with slightly different kinematics.

	Upper limits on $\sigma \times \mathcal{B}(\tilde{\nu}_\tau \to \mathrm{e}\mu)$ (fb)						
$M_{\tilde{\nu}_\tau}$ (GeV)	**95% CL**				90% CL	Efficiency (%)	Acceptance (%)
	Observed	**Expected**	**$+1\sigma$**	**-1σ**	Observed	$A \times \varepsilon$	A
200	13	9	13	6.5	11	42	58.6
202	10	8.8	12	6.3	8.2	42.2	58.9
204	9.2	8.6	12	6.3	7.6	42.5	59.2
206	8.9	9.3	12	6.4	7.5	42.7	59.5
208	8.5	8.2	12	5.9	7	43	59.8
210	9.1	8.4	12	6.1	7.8	43.2	60
212	9.7	8.4	12	6.1	8.2	43.4	60.3
214	12	8	11	5.9	10	43.6	60.6
216	11	8.2	12	5.9	9.2	43.9	60.9
218	10	8.4	12	5.8	8.7	44.1	61.1
220	9.3	7.9	11	5.8	8	44.3	61.4
222	8.7	8.1	11	5.6	7.4	44.5	61.6
224	7.6	7.3	10	5.4	6.3	44.7	61.9
226	7.1	7.5	11	5.5	5.7	44.9	62.1
228	7.2	7.3	9.9	5.4	6	45.1	62.4
230	7.1	7.5	10	5.5	5.8	45.3	62.6
232	6.9	7.6	10	5.5	5.8	45.5	62.9
234	6.4	7.5	10	5.4	5.3	45.7	63.1
236	6	7.4	10	5.3	5	45.9	63.3
238	5.8	7	10	5.1	4.8	46.1	63.6
240	6	7.1	9.9	5	4.7	46.3	63.8
242	6.2	6.8	10	4.9	5.1	46.5	64
244	7.3	6.6	9.5	4.8	6.2	46.7	64.3
246	7.7	6.7	9.1	4.7	6.5	46.9	64.5
248	7.3	6.5	9.4	4.7	6.3	47	64.7

$M_{\tilde{\nu}_\tau}$ (GeV)	Upper limits on $\sigma \times \mathcal{B}(\tilde{\nu}_\tau \to \mathrm{e}\mu)$ (fb)						
	95% CL				90% CL	Efficiency (%)	Acceptance (%)
	Observed	**Expected**	**$+1\sigma$**	**-1σ**	Observed	$A \times \varepsilon$	A
250	5.8	6.6	8.9	4.8	4.8	47.2	64.9
252	5.2	6.6	9.3	4.6	4.3	47.4	65.1
254	5.3	6.5	9	4.7	4.3	47.6	65.3
256	5.2	6.2	8.9	4.5	4.3	47.7	65.5
258	6.3	6.2	8.7	4.4	5.1	47.9	65.7
260	6.3	6.3	8.7	4.6	5.3	48.1	65.9
262	6	6	8.5	4.2	5	48.2	66.1
264	5.9	5.9	8.4	4.3	5	48.4	66.3
266	6	6	8.7	4.4	4.9	48.5	66.5
268	5.5	5.9	8.3	4.2	4.6	48.7	66.7
270	6.2	5.5	7.9	4	5.4	48.8	66.9
272	7.4	5.7	8.1	4.1	6.4	49	67.1
274	9.2	5.4	7.7	3.9	8.3	49.1	67.3
276	10	5.4	7.7	3.9	9.3	49.3	67.5
278	11	5.3	7.4	3.8	9.5	49.4	67.7
280	9.9	5.2	7.1	3.8	8.8	49.6	67.8
282	8.5	5.2	7.1	3.7	7.6	49.7	68
284	8	5.1	7	3.7	6.9	49.9	68.2
286	6.6	5.1	7	3.7	5.8	50	68.4
288	5.6	4.8	6.8	3.5	4.7	50.2	68.5
290	5	4.8	6.9	3.6	4.3	50.3	68.7
292	4.1	4.9	7.1	3.4	3.3	50.4	68.9
294	3.7	4.8	7	3.5	3	50.6	69.1
296	3.3	4.8	6.6	3.4	2.6	50.7	69.2
298	3	4.7	6.7	3.4	2.3	50.8	69.4
300	2.8	4.5	6.3	3.3	2.2	50.9	69.5
305	2.5	4.7	6.6	3.3	2	51.3	69.9
310	3.1	4.4	6.1	3	2.5	51.6	70.3
315	4.7	4.5	6.4	3.2	3.9	51.9	70.7
320	5.2	4.1	5.8	2.9	4.4	52.2	71.1
325	5.2	4.1	5.8	3	4.2	52.4	71.4
330	3.1	4	5.7	2.7	2.5	52.7	71.8
335	1.9	3.9	5.4	2.8	1.5	53	72.1
340	1.8	3.7	5.4	2.7	1.4	53.2	72.4
345	2.9	3.8	5.3	2.7	2.2	53.5	72.8
350	5.1	3.5	5	2.5	4.4	53.7	73.1
355	6.2	3.5	4.9	2.5	5.3	54	73.4
360	5.5	3.2	4.7	2.3	4.8	54.2	73.7
365	4.7	3.3	4.6	2.3	4	54.4	74
370	4.3	3	4.4	2.2	3.7	54.7	74.3
375	4.3	3	4.4	2.2	3.7	54.9	74.5
380	4.3	2.9	4.1	2.1	3.7	55.1	74.8
385	3.9	3	4.3	2.1	3.4	55.3	75.1
390	3.3	2.8	3.8	2	2.7	55.5	75.4
395	3.7	2.8	3.9	2	3	55.7	75.6
400	3.4	2.6	3.7	1.9	2.9	55.9	75.9
410	3.2	2.5	3.5	1.8	2.7	56.3	76.3
420	2.5	2.4	3.3	1.7	2.1	56.6	76.8
430	2.1	2.2	3.2	1.6	1.6	56.9	77.3
440	1.9	2.1	3	1.5	1.6	57.3	77.7
450	1.9	2	2.9	1.4	1.6	57.6	78.1
460	2	2	2.9	1.4	1.6	57.9	78.5
470	2.9	1.9	2.7	1.3	2.6	58.2	78.9
480	3.2	1.8	2.6	1.3	2.8	58.4	79.3
490	3	1.7	2.5	1.3	2.6	58.7	79.6
500	2.2	1.6	2.4	1.2	2	58.9	80
510	1.8	1.6	2.2	1.1	1.5	59.2	80.3
520	1.8	1.5	2.1	1.1	1.5	59.4	80.6
530	1.8	1.4	2	1	1.6	59.6	80.9
540	1.9	1.3	1.9	0.97	1.6	59.9	81.2
550	1.8	1.3	1.8	0.91	1.5	60.1	81.5
560	1.5	1.2	1.8	0.86	1.3	60.3	81.8
570	1.1	1.2	1.7	0.88	0.91	60.4	82
580	0.89	1.2	1.7	0.85	0.7	60.6	82.3
590	0.82	1.2	1.7	0.85	0.65	60.8	82.6

	Upper limits on $\sigma \times \mathcal{B}(\tilde{\nu}_\tau \to \mathrm{e}\mu)$ (fb)						
$M_{\tilde{\nu}_\tau}$ (GeV)	**95% CL**				90% CL	Efficiency (%)	Acceptance (%)
	Observed	**Expected**	$+1\sigma$	-1σ	Observed	$A \times \varepsilon$	A
600	1	1.2	1.7	0.82	0.87	61	82.8
610	1.3	1.1	1.5	0.76	1.1	61.1	83
620	1.5	1	1.5	0.72	1.3	61.3	83.3
630	1.6	1	1.4	0.71	1.3	61.5	83.5
640	1.4	0.95	1.4	0.67	1.2	61.6	83.7
660	1.7	0.91	1.3	0.66	1.5	61.9	84.1
680	1.3	0.84	1.2	0.6	1.1	62.1	84.5
700	0.71	0.77	1.1	0.55	0.57	62.4	84.9
720	0.49	0.7	1	0.5	0.4	62.6	85.2
740	0.42	0.7	0.97	0.49	0.33	62.8	85.6
760	0.41	0.65	0.94	0.46	0.32	63	85.9
780	0.51	0.61	0.86	0.43	0.41	63.2	86.2
800	0.58	0.57	0.81	0.39	0.48	63.4	86.5
820	0.57	0.55	0.77	0.38	0.46	63.6	86.7
840	0.54	0.52	0.75	0.37	0.44	63.7	87
860	0.49	0.5	0.72	0.36	0.4	63.9	87.2
880	0.4	0.48	0.7	0.36	0.31	64	87.5
900	0.33	0.46	0.66	0.33	0.26	64.1	87.7
920	0.36	0.44	0.6	0.32	0.28	64.3	87.9
940	0.42	0.42	0.58	0.31	0.34	64.4	88.1
960	0.44	0.39	0.54	0.29	0.36	64.5	88.3
980	0.44	0.39	0.54	0.29	0.36	64.6	88.5
1000	0.44	0.37	0.52	0.28	0.36	64.7	88.7
1020	0.4	0.36	0.52	0.27	0.31	64.7	88.8
1040	0.35	0.36	0.51	0.27	0.27	64.8	89
1060	0.33	0.35	0.49	0.25	0.27	64.9	89.2
1080	0.31	0.34	0.47	0.26	0.25	65	89.3
1100	0.28	0.34	0.46	0.25	0.22	65	89.4
1120	0.25	0.33	0.46	0.24	0.19	65.1	89.6
1140	0.24	0.32	0.44	0.24	0.18	65.2	89.7
1160	0.24	0.32	0.44	0.24	0.18	65.2	89.8
1180	0.24	0.31	0.42	0.24	0.18	65.3	90
1200	0.24	0.3	0.41	0.24	0.18	65.3	90.1
1250	0.24	0.29	0.39	0.24	0.18	65.4	90.4
1300	0.24	0.26	0.36	0.24	0.18	65.5	90.6
1350	0.24	0.24	0.35	0.23	0.18	65.6	90.8
1400	0.24	0.24	0.34	0.23	0.18	65.6	91.1
1450	0.24	0.24	0.34	0.23	0.18	65.6	91.2
1500	0.23	0.24	0.33	0.23	0.18	65.7	91.4
1550	0.23	0.24	0.3	0.23	0.18	65.7	91.6
1600	0.24	0.24	0.28	0.23	0.18	65.7	91.7
1650	0.24	0.24	0.27	0.23	0.18	65.6	91.9
1700	0.23	0.24	0.25	0.23	0.18	65.6	92
1750	0.23	0.24	0.24	0.23	0.18	65.6	92.1
1800	0.23	0.23	0.24	0.23	0.18	65.6	92.2
1850	0.24	0.24	0.24	0.23	0.18	65.5	92.3
1900	0.23	0.24	0.24	0.23	0.18	65.5	92.4
1950	0.23	0.23	0.24	0.23	0.18	65.4	92.4
2000	0.24	0.23	0.24	0.23	0.18	65.4	92.5
2000	0.24	0.23	0.24	0.23	0.18	65.4	92.5

E.7 Note concerning the limits on RPV parameters from searches for LFV meson decays

The bounds in the parameter space of different RPV $\tilde{\nu}_\tau$ models derived from limits on rare kaon and b-meson decays, that are presented in Tab. 10.2, are obtained as follows:

A non-zero value of the coupling product $|\lambda'_{312}\lambda_{312}|$ leads to the rare kaon decay $\mathrm{K}^0_\mathrm{L} \to \mathrm{e}^\pm\mu^\mp$. The most sensitive search for such decays is reported in Ref. [20] and yields a bound of

$$\mathcal{B}(\mathrm{K}^0_\mathrm{L} \to \mathrm{e}^\pm\mu^\mp) < 4.7 \times 10^{-12} \tag{E.1}$$

at 90% CL. The bound on the RPV coupling product has first been derived in Ref. [307] and has been updated to the current experimental bound in Ref. [51]. Both references use the same definition of the RPV part of the superpotential as this work, Eqn. 1.2. However, they assume that there is only one product of (independent) RPV couplings contributing to the kaon decay. In the $\tilde{\nu}_\tau$ model considered in this work, there are two such coupling products, namely $|\lambda'_{312}\lambda_{312}|$ and $|\lambda'_{312}\lambda_{321}|$, that are assumed to be equal. Therefore, the bound $|\lambda'_{312}\lambda_{312}| < 6 \times 10^{-7}(M_{\tilde{\nu}_\tau}/\mathrm{TeV})^2$ from Ref. [51] is divided by a factor $\sqrt{2}$ in Tab. 10.2.

The most stringent experimental bounds on the branching fraction of the decays $\mathrm{B}^0_\mathrm{d} \to \mathrm{e}^\pm\mu^\mp$ and $\mathrm{B}^0_\mathrm{s} \to \mathrm{e}^\pm\mu^\mp$ have been set by the LHCb collaboration [21] and read at 90% CL:

$$\begin{aligned} \mathcal{B}(\mathrm{B}^0_\mathrm{d} \to \mathrm{e}^\pm\mu^\mp) &< 2.8 \times 10^{-9} \;, && \text{(E.2)} \\ \mathcal{B}(\mathrm{B}^0_\mathrm{s} \to \mathrm{e}^\pm\mu^\mp) &< 1.1 \times 10^{-8} \;. && \text{(E.3)} \end{aligned}$$

The general formula for the contribution of trilinear RPV coupling products to the decay widths of these processes is given in Ref. [308]. The calculation in this reference starts from a definition of the RPV superpotential that includes an additional factor 1/2 in the definition of the λ couplings compared to Eqn. 1.2. After accounting for this difference in the definition of the model parameters, the relation between the branching fractions and the RPV couplings in the $\tilde{\nu}_\tau$ model under study is given by:

$$|\lambda'_{3k3}\lambda_{312}| = \left(\mathcal{B}\left(\mathrm{B}^0_{\mathrm{q}_k} \to \mathrm{e}^\pm\mu^\mp\right)\frac{\Gamma\left(\mathrm{B}^0_{\mathrm{q}_k}\right)/\mathrm{GeV}}{2 \times 2.93 \times 10^{-14}}\right)^{\frac{1}{2}}\left(\frac{M_{\tilde{\nu}_\tau}}{1\ \mathrm{TeV}}\right)^2 \;, \quad \text{with } k \in \{1,2\}\ ;\ \mathrm{q}_k \in \{\mathrm{d},\mathrm{s}\} \tag{E.4}$$

$$\Rightarrow \quad |\lambda'_{313}\lambda_{312}| \approx 2.72\sqrt{\mathcal{B}\left(\mathrm{B}^0_\mathrm{d} \to \mathrm{e}^\pm\mu^\mp\right)}\left(\frac{M_{\tilde{\nu}_\tau}}{1\ \mathrm{TeV}}\right)^2 \underset{\text{(E.2)}}{<} 1.4 \times 10^{-4}\left(\frac{M_{\tilde{\nu}_\tau}}{1\ \mathrm{TeV}}\right)^2 \;, \tag{E.5}$$

$$|\lambda'_{323}\lambda_{312}| \approx 2.73\sqrt{\mathcal{B}\left(\mathrm{B}^0_\mathrm{s} \to \mathrm{e}^\pm\mu^\mp\right)}\left(\frac{M_{\tilde{\nu}_\tau}}{1\ \mathrm{TeV}}\right)^2 \underset{\text{(E.3)}}{<} 2.9 \times 10^{-4}\left(\frac{M_{\tilde{\nu}_\tau}}{1\ \mathrm{TeV}}\right)^2 \;. \tag{E.6}$$

Before the publiaction of the LHCb bounds, the strongest limit on the branching fraction of these b-meson decays had been provided by the CDF collaboration [284]. These bounds read at 90% CL:

$$\begin{aligned} \mathcal{B}(\mathrm{B}^0_\mathrm{d} \to \mathrm{e}^\pm\mu^\mp) &< 6.4 \times 10^{-8} \;, && \text{(E.7)} \\ \mathcal{B}(\mathrm{B}^0_\mathrm{s} \to \mathrm{e}^\pm\mu^\mp) &< 2.0 \times 10^{-7} \;. && \text{(E.8)} \end{aligned}$$

The resulting bounds on the RPV coupling products included in Tab. 10.2 are:

$$|\lambda'_{313}\lambda_{312}| < 6.9 \times 10^{-4}\left(\frac{M_{\tilde{\nu}_\tau}}{1\ \mathrm{TeV}}\right)^2 \;, \tag{E.9}$$

$$|\lambda'_{323}\lambda_{312}| < 1.2 \times 10^{-3}\left(\frac{M_{\tilde{\nu}_\tau}}{1\ \mathrm{TeV}}\right)^2 \;. \tag{E.10}$$

Appendix F

Detailed information $\mu\tau$ resonance search

F.1 Summary of cross section limits for the RPV $\tilde{\nu}_{\tau}$ signal

Table F.1: The upper limits on the product of the $\tilde{\nu}_\tau$ production cross section and the branching fraction of its decay into a $\mu\tau$ pair for various masses. In addition to the observed cross section limit at 95% CL, the median expected limit at 95% CL is given together with the corresponding boundaries of the 1σ uncertainty band. The observed limit at 90% CL is also presented because it is used as input to the calculation of the 90% CL bounds in RPV parameter space in Sec. 13.1.2 that are compared to bounds from indirect searches in the literature which are available at this confidence level. The full signal selection efficiency and acceptance are included to allow for a reinterpretation of the cross section limits in terms of other signal models with slightly different kinematics. The definitions of the signal efficiency and the acceptance include the branching fraction of the leptonic τ decay to an electron and neutrinos, $\mathcal{B}_{\tau_e}$. The acceptance is defined as the fraction of simulated signal events passing the selection cuts on the muon, the τ lepton and the electron from the τ decay (see Sec. 11.2), applied at parton level. This definition comprises the p_T and η cuts on the leptons, the cut on $\Delta\phi(\mu,\tau)$, and the requirement $p_T^\mu \geq p_T^e$.

	Upper limits on $\sigma \times \mathcal{B}(\tilde{\nu}_\tau \to \mu\tau)$ (fb)						
$M_{\tilde{\nu}_\tau}$ (GeV)	**95% CL**				90% CL	Efficiency (%)	Acceptance (%)
	Observed	**Expected**	$+1\sigma$	-1σ	Observed	$A \times \varepsilon \times \mathcal{B}_{\tau_e}$	$A \times \mathcal{B}_{\tau_e}$
200	105	129	187	90	84	2.3	4.9
220	87	99	143	68	73	2.9	5.6
240	55	84	118	58	44	3.4	6.2
260	47	70	97	48	37	3.8	6.8
280	46	57	82	40	38	4.2	7.3
300	46	48	68	33	38	4.6	7.8
320	42	40	57	28	35	5.0	8.2
340	37	35	49	25	31	5.3	8.6
350	36	-	-	-	-	5.4	8.8
360	34	29	44	21	28	5.6	9.0
380	30	27	38	19	26	5.8	9.3
400	28	23	33	17	24	6.1	9.6
420	29	21	31	15	24	6.3	9.9
440	28	20	29	14	23	6.5	10.2
460	25	18	26	13	21	6.7	10.4
480	21	16	24	12	18	6.9	10.7
500	17	15	21	10	14	7.1	10.9
520	13	13	19	9.5	11	7.3	11.1
540	11	12	18	8.7	8.7	7.4	11.3
560	9.6	12	17	8.3	7.8	7.6	11.5
580	9.3	11	16	7.9	7.5	7.7	11.6
600	9.3	10	15	7.4	7.5	7.8	11.8
620	9.6	9.6	14	6.8	7.7	8.0	12.0
640	9.7	8.7	13	6.1	8.3	8.1	12.1
660	9.6	7.7	11	5.4	8.1	8.2	12.3
680	9.3	6.9	9.9σ	5.0σ	7.9	8.3	12.4
700	9.2	6.4	9.2	4.5	7.9	8.4	12.5
720	8.2	6.1	8.9	4.3	7.0	8.5	12.6
740	7.5	5.7	7.9	4.0	6.4	8.6	12.8
760	6.6	5.6	8.1	3.9	5.5	8.7	12.9
780	6.2	5.3	7.7	3.8	5.0	8.7	13.0
800	5.5	5.1	7.3	3.7	4.4	8.8	13.1
820	5.2	5.0	7.0	3.7	4.2	8.9	13.2
860	4.6	4.6	6.4	3.3	3.7	9.0	13.4
900	4.4	4.2	6.0	3.0	3.6	9.2	13.5
940	4.3	3.9	5.7	2.8	3.5	9.3	13.7
1000	3.7	3.6	5.2	2.6	3.0	9.4	13.9
1100	2.3	3.0	4.3	2.2	1.7	9.7	14.2
1200	1.7	2.6	3.8	1.9	1.3	9.8	14.4
1300	1.6	2.2	3.0	1.6	1.2	10.0	14.7
1400	1.9	1.8	2.6	1.5	1.5	10.1	14.8
1500	2.2	1.6	2.3	1.5	1.8	10.2	15.0
1600	2.3	1.6	2.3	1.5	1.8	10.3	15.1
1700	2.3	1.5	2.2	1.5	1.8	10.4	15.3
1800	2.2	1.5	2.2	1.5	1.8	10.5	15.4
1900	2.1	1.5	1.8	1.5	1.7	10.5	15.5
2000	2.0	1.5	1.7	1.4	1.6	10.6	15.5

F.2 Reinterpretation of the $\mu\tau$ resonance search in terms of the heavy Higgs boson signal

F.2.1 Short introduction to 2HDMs

This introduction is primarily based on Refs. [294, 297, 300]. Consider two complex scalar $SU(2)_L$ doublet fields Φ_1 and Φ_2 with hypercharge $Y = 1$ and component representation

$$\Phi_i(x) = \begin{pmatrix} \Phi_i^+(x) \\ \\ \Phi_i^0(x) \end{pmatrix} \tag{F.1}$$

that are related by a global $U(2)$ symmetry under which the doublet fields transform as

$$\Phi_a(x) \to U_{ab}\Phi_b(x) \ , \ \Phi_a^\dagger(x) \to \Phi_b^\dagger(x) U_{ba}^\dagger \ . \tag{F.2}$$

The Higgs potential and physical Higgs states

The most general renormalizable and gauge invariant Higgs potential with two Higgs doublet fields is given by [297]:

$$\begin{aligned} V(\Phi_1,\Phi_2) &= \mu_1^2\Phi_1^\dagger\Phi_1 + \mu_2^2\Phi_2^\dagger\Phi_2 + \left(\mu_3^2\Phi_1^\dagger\Phi_2 + h.c.\right) + \lambda_1\left(\Phi_1^\dagger\Phi_1\right)^2 + \lambda_2\left(\Phi_2^\dagger\Phi_2\right)^2 \\ &+ \lambda_3\left(\Phi_1^\dagger\Phi_1\right)\left(\Phi_2^\dagger\Phi_2\right) + \lambda_4\left(\Phi_1^\dagger\Phi_2\right)\left(\Phi_2^\dagger\Phi_1\right) \\ &+ \left[\left(\lambda_5\Phi_1^\dagger\Phi_2 + \lambda_6\Phi_1^\dagger\Phi_1 + \lambda_7\Phi_2^\dagger\Phi_2\right)\left(\Phi_1^\dagger\Phi_2\right) + h.c.\right] \ , \end{aligned} \tag{F.3}$$

with six real parameters μ_1^2, μ_2^2, λ_{1-4} and four parameters that are complex in the most general case μ_3^2, λ_{5-7}. The imaginary parts of the latter introduce CP-violating effects which are not the subject of this analysis. All parameters are therefore assumed to be real. Note that while the functional form of the potential $V(\Phi_1, \Phi_2)$ is fixed, different conventions are used in the literature for the parameters, e.g. additional minus signs and factors two. In particular, the potential given above is the same as in Ref. [294] but differs from Ref. [300] that is used for consistency checks of the analyzed 2HDM parameter space below.

This most general Higgs potential is invariant under $U(2)$ transformations (Eqn. F.2). Therefore, the parameters in the potential can only acquire physical meaning after a specific choice of the fields Φ_1 and Φ_2, or choice of basis, is introduced. A choice of basis is defined by fixing the vacuum expectation values of the Higgs doublet fields after EWSB, v_1 and v_2, that satisfy the relation $(v_1^2 + v_2^2)^{1/2} = v = (\sqrt{2}G_F)^{-1/2} \approx 246$ GeV. This corresponds to a choice of the parameter $\tan\beta$ when a generic basis is expresses as [300]

$$\langle\Phi_1\rangle = \frac{v}{\sqrt{2}}\begin{pmatrix} 0 \\ \\ \cos\beta \end{pmatrix} \ , \ \langle\Phi_2\rangle = \frac{v}{\sqrt{2}}\begin{pmatrix} 0 \\ \\ \sin\beta \end{pmatrix} \ . \tag{F.4}$$

In this work, the so-called Higgs basis, or Georgi basis, is chosen, in which only Φ_1 acquires a non-zero vacuum expectation value after EWSB and $\tan\beta = 0$. Note that in a general 2HDM $\tan\beta$ is not a parameter with physical meaning because the different bases are equivalent. In order to achieve EWSB, the number of parameters in the Higgs potential, Eqn. F.3, is reduced from 10 to 8 by two minimization conditions [300].

The relation between the 8 remaining model parameters and the Higgs masses is discussed next. In the Higgs basis, the two Higgs doublet fields are given by

$$\Phi_1 = \begin{pmatrix} G^+ \\ \\ \frac{1}{\sqrt{2}}\left(v + h_1^0 + iG^0\right) \end{pmatrix} \qquad \text{and} \qquad \Phi_2 = \begin{pmatrix} H^+ \\ \\ \frac{1}{\sqrt{2}}\left(h_2^0 + ih_3^0\right) \end{pmatrix} \ . \tag{F.5}$$

Of the 8 degrees of freedom, three make up the Goldstone bosons G^0 and G^+ that provide the longitudinal components of the W and Z bosons, and five lead to physical Higgs states: two CP-even scalars h_1^0 and h_2^0, one CP-odd scalar h_3^0 that is commonly denoted A^0, and the charged Higgs boson H^+. Since the CP-conserving 2HDM is considered here, only the two CP-even scalars mix to form the two mass eigenstates h^0 and H^0, whose masses satisfy the convention $M_{H^0} \geq M_{h^0}$. These mass eigenstates are related to the initial scalars h_1^0 and h_2^0 by the mixing angle α via

$$\begin{pmatrix} h^0 \\ H^0 \end{pmatrix} = \begin{pmatrix} \cos\alpha & \sin\alpha \\ -\sin\alpha & \cos\alpha \end{pmatrix} \begin{pmatrix} h_1^0 \\ h_2^0 \end{pmatrix} . \tag{F.6}$$

Combining Eqns. F.6 and F.5 yields

$$\Phi_1 = \begin{pmatrix} G^+ \\ \frac{1}{\sqrt{2}}\left(v + \cos\alpha\ h^0 - \sin\alpha\ H^0 + iG^0\right) \end{pmatrix} , \ \Phi_2 = \begin{pmatrix} H^+ \\ \frac{1}{\sqrt{2}}\left(\sin\alpha\ h^0 + \cos\alpha\ H^0 + ih_3^0\right) \end{pmatrix} . \tag{F.7}$$

After these considerations, first conclusions concerning the couplings of the light and heavy Higgs bosons, h^0 and H^0, can be drawn. The couplings of the Higgs bosons to the massive gauge boson are fixed by EWSB and only involve the Higgs doublet field Φ_1. They scale with $\cos\alpha$ in the case of h^0 and $\sin\alpha$ for H^0.

The Yukawa sector

The most general structure of the Yukawa matrices of the two Higgs doublets allows for flavor-changing-neutral-currents (FCNCs) at tree-level. However, tree-level FCNCs are absent if a given fermion couples only to one Higgs doublet, as stated by the Weinberg-Glashow theorem [309]. A basis fulfilling this condition exists in so-called type I and type II 2HDM models. In this work, the general case that allows for couplings of a given fermion to both Higgs doublets, frequently referred to as type III [1], is considered.

In type III 2HDMs, the Lagrangian density describing the coupling of Higgs doublet fields to quarks can be written in a compact fashion as [297]:

$$-\mathcal{L}_{\text{Yukawa}}^{\text{quarks}} = \bar{Q}_L^0 \tilde{\Phi}_1 \eta_{u,1}^0 U_R^0 + \bar{Q}_L^0 \Phi_1 \eta_{d,1}^0 D_R^0 + \bar{Q}_L^0 \tilde{\Phi}_2 \eta_{u,2}^0 U_R^0 + \bar{Q}_L^0 \Phi_2 \eta_{d,2}^0 D_R^0 + h.c. \ , \tag{F.8}$$

with $\tilde{\Phi}_i \equiv i\sigma_2 \Phi_i^*$, the quark weak isospin doublet Q_L^0 and weak isospin singlets U_R^0 and D_R^0 denote the interaction basis states. The individual Yukawa couplings are elements $(\eta_{q,a}^0)^{ij}$ with $i, j \in \{1, 2, 3\}$ of the matrices in flavor space $\eta_{q,a}^0$ with $q \in \{u, d\}$ and $a \in \{1, 2\}$. On the two linear combinations of the Yukawa matrices

$$\kappa_q^0 \equiv \cos\beta\ \eta_{q,1}^0 + \sin\beta\ \eta_{q,2}^0 \tag{F.9}$$

$$\rho_q^0 \equiv -\sin\beta\ \eta_{q,1}^0 + \cos\beta\ \eta_{q,2}^0 \ , \tag{F.10}$$

a rotation in flavor space is performed that diagonalizes the two matrices κ_d and κ_u [297]:

$$\kappa_q^{ij} = \left(V_{q,L} \kappa_q^0 V_{q,R}^\dagger\right)^{ij} = \delta^{ij} \sqrt{2} \frac{m_{q_i}}{v} \ . \tag{F.11}$$

The unitary matrices $V_{q,L}$ satisfy $K_{CKM} = V_{u,L} V_{d,L}^\dagger$ with the Cabibbo-Kobayashi-Maskawa matrix K_{CKM}. The matrices $\eta_{q,a}^0$ and ρ_q^0 are related to their counterparts $\eta_{q,a}$ and ρ_q by the same rotation.

---

[1] The term type III 2HDM is also used with a different meaning, as for example in Ref. [300].

The corresponding terms for the leptonic sector with the coupling matrices of the charged leptons $\eta_{\ell,1}$ and $\eta_{\ell,2}$ are

$$-\mathcal{L}^{\text{leptons}}_{\text{Yukawa}} = \bar{L}_L \Phi_1 \eta_{\ell,1} \ell_R + \bar{L}_L \Phi_2 \eta_{\ell,2} \ell_R + h.c. \;, \tag{F.12}$$

with the lepton weak isospin doublet L_L and the charged lepton weak isospin singlet ℓ_R.

After considering the basis-independent case, the Yukawa terms in the Lagrangian describing the interactions between the physical Higgs fields and the fermions are now expressed in the Higgs basis that is used in Sec. 13.2. In the Higgs basis, v_2 vanishes such that $\tan\beta = 0$, and only the couplings of the Higgs doublet Φ_1 to fermions contributes to the fermion masses (Eqn. F.9). The terms in the Lagrangian Eqn. F.8 that describe interactions between the neutral Higgs bosons and the quark mass eigenstates can be expressed as:

$$\begin{aligned} \mathcal{L}^{\text{quarks}}_{\text{Yukawa}} \supset & - y^{ij}_{u,h^0} \bar{u}^i_L u^j_R h^0 - y^{ij}_{u,H^0} \bar{u}^i_L u^j_R H^0 - y^{ij}_{d,h^0} \bar{d}^i_L d^j_R h^0 - y^{ij}_{d,H^0} \bar{d}^i_L d^j_R H^0 + \text{h.c.} \\ & + i \frac{\eta^{ij}_{u,2}}{\sqrt{2}} \bar{u}^i_L u^j_R A^0 - i \frac{\eta^{ij}_{d,2}}{\sqrt{2}} \bar{d}^i_L d^j_R A^0 + \text{h.c.} \;, \end{aligned} \tag{F.13}$$

with generation indices i, j, the Yukawa couplings of the light Higgs boson y_{u,h^0} and y_{d,h^0} to the up-type and down-type quarks, respectively, and the corresponding Yukawa couplings of the heavy Higgs boson y_{u,H^0} and y_{d,H^0}. The structures of these Yukawa couplings are given by:

$$y^{ij}_{q,h^0} = \frac{m_{q_i}}{v} \delta^{ij} \cos\alpha + \frac{\eta^{ij}_{q,2}}{\sqrt{2}} \sin\alpha \tag{F.14}$$

$$y^{ij}_{q,H^0} = -\frac{m_{q_i}}{v} \delta^{ij} \sin\alpha + \frac{\eta^{ij}_{q,2}}{\sqrt{2}} \cos\alpha \;. \tag{F.15}$$

The terms in the Lagrangian that correspond to the vertices connecting the neutral Higgs bosons and charged leptons read

$$\begin{aligned} \mathcal{L}^{\text{leptons}}_{\text{Yukawa}} \supset & - y^{ij}_{\ell,h^0} \bar{\ell}^i_L \ell^j_R h^0 - y^{ij}_{\ell,H^0} \bar{\ell}^i_L \ell^j_R H^0 + \text{h.c.} \\ & - i \frac{\eta^{ij}_{\ell,2}}{\sqrt{2}} \bar{\ell}^i_L \ell^j_R A^0 + \text{h.c.} \;, \end{aligned} \tag{F.16}$$

with the Yukawa couplings

$$y^{ij}_{\ell,h^0} = \frac{m_{\ell_i}}{v} \delta^{ij} \cos\alpha + \frac{\eta^{ij}_{\ell,2}}{\sqrt{2}} \sin\alpha \tag{F.17}$$

$$y^{ij}_{\ell,H^0} = -\frac{m_{\ell_i}}{v} \delta^{ij} \sin\alpha + \frac{\eta^{ij}_{\ell,2}}{\sqrt{2}} \cos\alpha \;. \tag{F.18}$$

In the alignment limit $\sin\alpha \to 0$ the light Higgs boson h^0 has the same couplings as the SM Higgs boson. In the CP-conserving case that is considered here, the three matrices that induce FCNC at tree-level, i.e. $\eta_{u,2}$, $\eta_{d,2}$, and $\eta_{\ell,2}$, are real and symmetric [300]. Therefore, they introduce another 18 independent, real parameters to the model.

F.2.2 Complete definition of the analyzed 2HDM

A given CP-conserving type-III 2HDM is described by fixing 8 parameters in the Higgs potential and 18 additional Yukawa couplings, 9 of which induce FCNC at tree level. Rather than fixing the parameters μ_3^2 and λ_{1-7} in the Higgs potential, it can be convenient to choose the physical Higgs masses and the mixing angle $\sin\alpha$. The set of parameters used in the following and in Sec. 13.2 as the starting point to define the 2HDM under study is

$$M_{h^0},\ M_{H^0},\ M_{A^0},\ M_{H^+},\ \sin\alpha,\ \lambda_2,\ \lambda_3,\ \lambda_7\ . \tag{F.19}$$

The light CP-even Higgs boson h^0 is identified with the scalar particle discovered by the ATLAS and CMS collaborations in 2012 [36,37], such that $M_{h^0} = 125.1$ GeV. The masses of the charged Higgs bosons and the CP-odd neutral Higgs boson, that are not of primary interest in this study, are set equal. They are further assumed to be 80 GeV heavier than the heavy CP-even neutral Higgs boson H^0. This choice is arbitrary from the point of view of model-building but reasonable when considering the search strategy and experimental constraints: The aim of the analysis in Sec. 13.2 is to re-interpret a search for a narrow resonance that is isolated in the reconstructed mass spectrum of final state particles and whose mass distribution can be approximated by a single Gaussian. In this recast of cross section limits, the narrow resonance is identified with H^0 and the process depicted in Fig. 13.6 is considered. According to the 2HDM Lagrangian density in Eqns. F.13 and F.16, the CP-even Higgs boson H^0 can be replaced by the CP-odd A^0 in this interaction, yielding a second resonance at M_{A^0}. Therefore, M_{H^0} has to be well-separated from M_{A^0} for the re-interpretation of the narrow resonance cross section limits. The chosen criterion to quantify a sufficient separation is $M_{A^0} \gtrsim M_{H^0} + 3\sigma_M$, with σ_M denoting the detector mass resolution evaluated at M_{H^0}. The mass range considered here for M_{H^0} is $M_{H^0} \in [200\text{ GeV}, 500\text{ GeV}]$. According to Fig. 11.14, the $M_{\mu\tau}^{\text{coll}}$ mass resolution at 500 GeV is about 28 GeV and the choice $M_{A^0} = M_{H^0} + 80$ GeV provides the desired mass separation for all considered values of M_{H^0}. After these simplifications of the parameter space, the only remaining variable mass parameter is M_{H^0}.

The next parameter is the sine of the mixing angle, $\sin\alpha$. It is set to the small value $\sin\alpha = 0.01$ to ensure that the light Higgs couples very similar to the SM Higgs boson, and to suppress the H^0 decay modes into two vector bosons and two light Higgses that scale with $\mathcal{O}(\sin^2\alpha)$.

Since the parameters in the Higgs potential λ_2, λ_3, and λ_7 do not enter directly in the process under study, their values are chosen such that the resulting Higgs potential is stable, perturbativity of the couplings is ensured, and tree-level unitarity of the S-matrix holds. Using the 2HDMC (v. 1.7.0) program [300] these conditions are found to be fulfilled for $\lambda_2 = \lambda_3 = 2$ and $\lambda_7 = 0$. The checks carried out with 2HDMC are explained below in Sec. F.2.2.

Finally, the free Yukawa couplings have to be specified. The production of the heavy Higgs boson H^0 is mediated by the coupling $\eta_{u,2}^{33}$ and the decay into a $\mu\tau$ pair is allowed by a finite value of $\eta_{\ell,2}^{23} = \eta_{\ell,2}^{32}$. All other Yukawa couplings $\eta_{u,2}^{ij}, \eta_{d,2}^{ij}$, and $\eta_{\ell,2}^{ij}$ are assumed to be zero. In Sec. 13.2 the more intuitive naming convention $\eta_{u,2}^{tt} \equiv \eta_{u,2}^{33}$, $\eta_{\ell,2}^{\mu\tau} \equiv \eta_{\ell,2}^{23}$ is used for the finite couplings.

In summary, the chosen parameter (sub-)space that is studied in Sec. 13.2 contains three independent parameters

$$M_{H^0} \quad , \quad \eta_{u,2}^{tt} \quad , \quad \eta_{\ell,2}^{\mu\tau} = \eta_{\ell,2}^{\tau\mu}\ , \tag{F.20}$$

and the set of dependent or fixed parameters

$$\begin{aligned} M_{A^0} = M_{H^+} &= M_{H^0} + 80\text{ GeV} \quad , \quad M_{h^0} = 125.1\text{ GeV} \quad , \\ \lambda_2 = \lambda_3 &= 2 \quad , \quad \lambda_7 = 0 \quad , \quad \sin\alpha = 0.01 \quad . \end{aligned} \tag{F.21}$$

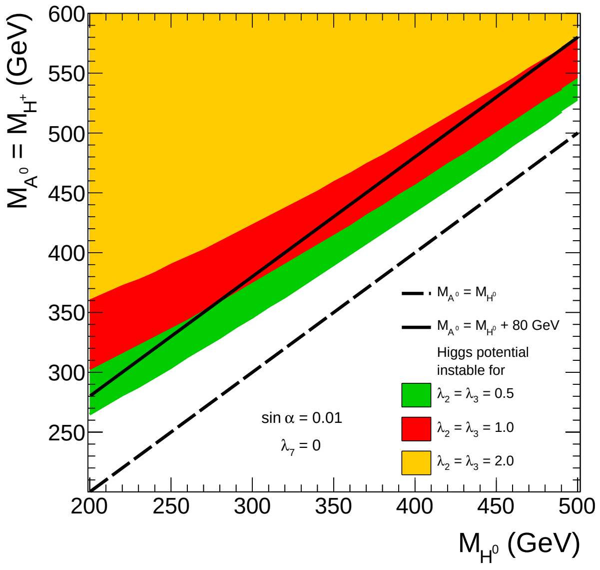

Figure F.1: Regions in the $(M_{H^0}, M_{A^0} = M_{H^+})$ parameter plane that involve an instable Higgs potential for different choices of the couplings $\lambda_2 = \lambda_3$, indicated by colored areas. The Higgs potential stability is checked with the 2HDMC *code [300]. The choice for the CP-odd Higgs mass $M_{A^0} = M_{H^0} + 80$ GeV that is used in the recast of the $\mu\tau$ cross section limits is indicated by the solid black line.*

Consistency checks in the chosen region of parameter space

A choice of the three Higgs masses M_{h^0}, $M_{A^0} = M_{H^+}$, and the mixing angle $\sin\alpha$ corresponds to a choice of four parameters in the Higgs potential. According to Ref. [294] that utilizes the definition of the mixing angle given in Eqn. F.6, the following relations are obtained:

$$\lambda_1 = \frac{M_{H^0}^2 + M_{h^0}^2 - \cos 2\alpha (M_{H^0}^2 - M_{h^0}^2)}{4v^2} \tag{F.22}$$

$$\lambda_4 = \frac{M_{H^0}^2 + M_{h^0}^2 - 2M_{A^0}^2 + \cos 2\alpha (M_{H^0}^2 - M_{h^0}^2)}{2v^2} \quad , \quad \lambda_5 = \frac{\lambda_4}{2} \tag{F.23}$$

$$\lambda_6 = -\sin 2\alpha \frac{M_{H^0}^2 - M_{h^0}^2}{2v^2} \ . \tag{F.24}$$

The parameter λ_6 is negative for positive $\sin\alpha$ and $M_{H^0} > M_{h^0}$. Furthermore the parameter λ_4 and thereby λ_5 are negative in the alignment limit, where $\cos 2\alpha \approx 1$, for $M_{A^0} > M_{H^0}$. With the choice $M_{A^0} = M_{H^0} + 80$ GeV justified above, sizeable negative quartic couplings arise in the Higgs potential and pose a threat to the vacuum stability of the signal model. With the assumption $\lambda_7 = 0$, positive values of the couplings λ_2, λ_3 can stabilize the vacuum. The 2HDMC (v. 1.7.0) code [300] is used to check the three requirements vacuum stability, tree-level unitarity, and coupling perturbativity. The resulting unallowed regions in the $(M_{H^0}, M_{A^0} = M_{H^+})$ parameter plane are shown as colored areas in Fig. F.1 for different choices of the parameters λ_2, λ_3. The plot shows that the assumption $M_{A^0} = M_{H^0} + 80$ GeV is viable for $\lambda_2 = \lambda_3 = 2$ in the entire mass range considered for the heavy Higgs, $M_{H^0} \in [200 \text{ GeV}, 500 \text{ GeV}]$. The differences in the definitions of parameters in this work and in the 2HDMC code are accounted for [2].

---

[2] In order to carry out the tests with 2HDMC, the parameters in Eqn. F.19 are translated into the parameter set $\{\lambda_{1-7}, M_{H^+}\}$. The 2HDM in the 2HDMC code is then initialized with the corresponding parameter set where $\lambda_1^{\text{2HDMC}} = 2\lambda_1$, $\lambda_2^{\text{2HDMC}} = 2\lambda_2$, and $\lambda_5^{\text{2HDMC}} = 2\lambda_5$, using the function `set_param_higgs`.

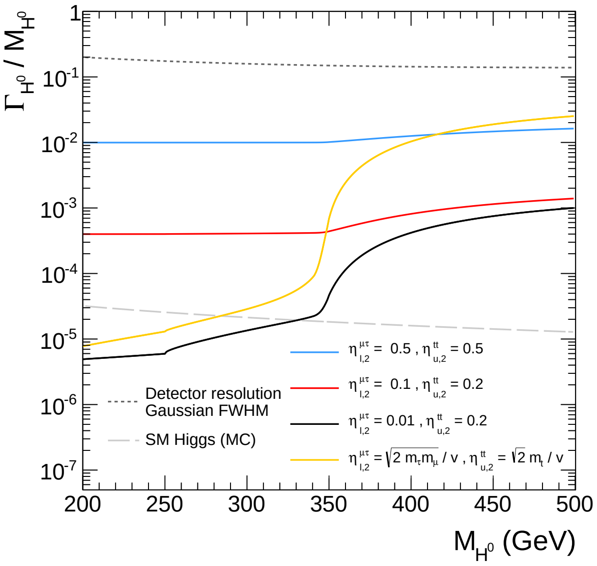

Figure F.2: The relative decay width of the heavy Higgs boson H^0 *as a function of* M_{H^0} *for various choices of the Yukawa couplings* $\eta^{tt}_{u,2}$ *and* $\eta^{\mu\tau}_{\ell,2} = \eta^{\tau\mu}_{\ell,2}$*. For comparison, the Higgs decay width of* 6.4 *MeV used in the generation of the MC signal samples (App. F.2.3) and the* $M^{\text{coll}}_{\mu\tau}$ *detector resolution (Sec. 11.3.2) expressed as the FWHM of the corresponding Gaussian are shown.*

Heavy Higgs decay width Γ_{H^0}

The 2HDMC code is also utilized to calculate the decay width of the heavy Higgs boson H^0. The relative decay width is evaluated as a function of M_{H^0} in Fig. F.2 for the parameters in Eqn. F.21 and different choices of the Yukawa couplings $\eta^{tt}_{u,2}$ and $\eta^{\mu\tau}_{\ell,2} = \eta^{\tau\mu}_{\ell,2}$. For all presented choices of the Yukawa couplings and in the entire mass range, the relative decay width does not exceed $2-3\%$ and is at least a factor four smaller than the detector resolution expressed as the full width at half maximum (FWHM) of the corresponding Gaussian. It is considered safe to use the fixed narrow width of 6.4 MeV set in the SM Higgs implementation in MadGraph5_aMC@NLO (v. 2.4.2) because the H^0 resonance shape is predominantly determined by the detector resolution.

F.2.3 Details on the Higgs boson signal simulation

Table F.2: The key values for the comparison between the cross section bounds obtained by running the full analysis with the heavy Higgs signal and by rescaling the results for the $\tilde{\nu}_\tau$ signal: The acceptance (A) and full selection efficiency (Aε) are defined on the set of produced $\mu\tau_\mathrm{e}$ events, i.e. the branching fraction of the leptonic τ decay is not included in these numbers. They are given for both signals together with the corresponding ratios. The shown uncertainties on the acceptances and selection efficiencies obtained from the simulated heavy Higgs samples are the binomial statistical uncertainties on these numbers resulting from the limited amount of produced signal events. The second column indicates whether the FullSim or FastSim detector simulation has been used in the production. The last three columns contain the 95% CL observed limits on the product of resonance production cross section and branching fraction into a $\mu\tau$ pair, $\mathcal{B}$. Among these three columns, the first contains the cross section limit obtained by running the full analysis with the heavy Higgs signal simulation, the second contains the bound for the $\tilde{\nu}_\tau$ signal rescaled with the ratio of the full selection efficiencies of the two signals, and the third gives the bound for the $\tilde{\nu}_\tau$ signal rescaled with the ratio of the signal acceptances.

M_res (GeV)	Detector Sim.	H^0		$\tilde{\nu}_\tau$		$\frac{(A\varepsilon)_{\tilde{\nu}_\tau}}{(A\varepsilon)_{H^0}}$	$\frac{A_{\tilde{\nu}_\tau}}{A_{H^0}}$	95% CL cross section limit (fb)		
		A	$A\varepsilon$	A	$A\varepsilon$			$(\sigma\times\mathcal{B})^\mathrm{obs}_{H^0}$	$(\sigma\times\mathcal{B})^\mathrm{obs}_{\tilde{\nu}_\tau}\times$	
		(%)		(%)					$(A\varepsilon)_{\tilde{\nu}_\tau}/(A\varepsilon)_{H^0}$	$A_{\tilde{\nu}_\tau}/A_{H^0}$
200	FULL	24.0 ± 0.6	11.4 ± 0.5	27.3	12.9	1.12	1.14	112	118	119
	FAST	24.0 ± 0.6	13.1 ± 0.5	27.3	12.9	0.98	1.14	-	103	119
220	FAST	26.4 ± 0.6	15.6 ± 0.5	31.2	16.0	1.03	1.18	-	89.2	103
240	FAST	28.5 ± 0.6	17.7 ± 0.5	34.8	18.9	1.07	1.22	-	58.5	66.9
260	FAST	31.0 ± 0.7	19.6 ± 0.6	38.0	21.5	1.10	1.23	-	51.8	57.9
280	FAST	36.1 ± 0.7	23.6 ± 0.6	40.9	23.8	1.01	1.13	-	46.6	52.2
300	FAST	37.5 ± 0.7	24.3 ± 0.6	43.5	25.9	1.07	1.16	-	48.7	53.0
320	FAST	40.0 ± 0.7	27.0 ± 0.6	45.9	27.9	1.03	1.15	-	43.2	48.2
340	FAST	41.8 ± 0.7	27.2 ± 0.6	48.1	29.6	1.09	1.15	-	40.5	42.8
350	FULL	42.8 ± 0.7	24.7 ± 0.6	49.2	30.5	1.23	1.15	42.8	44.3	41.3
360	FAST	43.6 ± 0.7	29.6 ± 0.6	50.2	31.3	1.06	1.15	-	35.6	38.8
380	FAST	44.5 ± 0.7	29.6 ± 0.6	52.1	32.8	1.11	1.17	-	33.5	35.4
400	FAST	45.1 ± 0.7	31.5 ± 0.7	53.9	34.2	1.09	1.19	-	30.9	33.9
420	FAST	48.3 ± 0.7	33.1 ± 0.7	55.5	35.5	1.07	1.15	-	31.0	33.2
440	FAST	49.1 ± 0.7	33.5 ± 0.7	57.0	36.7	1.10	1.16	-	30.3	32.1
460	FAST	51.7 ± 0.7	35.6 ± 0.7	58.4	37.8	1.06	1.13	-	26.4	28.2
480	FAST	52.1 ± 0.7	35.3 ± 0.7	59.8	38.9	1.10	1.15	-	22.8	23.7
500	FULL	54.2 ± 0.7	33.0 ± 0.7	61.0	39.9	1.21	1.13	20.3	20.2	18.9

Bibliography

[1] Super-Kamiokande Collaboration, "Evidence for oscillation of atmospheric neutrinos", *Phys. Rev. Lett.* **81** (1998) 1562, `arXiv:hep-ex/9807003`. `doi:10.1103/PhysRevLett.81.1562`.

[2] KamLAND Collaboration, "First results from KamLAND: Evidence for reactor anti-neutrino disappearance", *Phys. Rev. Lett.* **90** (2003) 021802, `arXiv:hep-ex/0212021`. `doi:10.1103/PhysRevLett.90.021802`.

[3] SNO Collaboration, "Direct evidence for neutrino flavor transformation from neutral current interactions in the Sudbury Neutrino Observatory", *Phys. Rev. Lett.* **89** (2002) 011301, `arXiv:nucl-ex/0204008`. `doi:10.1103/PhysRevLett.89.011301`.

[4] A. Yu. Smirnov, "Solar neutrinos: Oscillations or No-oscillations?", `arXiv:1609.02386`.

[5] Particle Data Group, K.A. Olive, et al., "Review of Particle Physics", *Chin. Phys. C* **38** (2014) 090001. `doi:10.1088/1674-1137/38/9/090001`.

[6] CMS Collaboration, "The CMS experiment at the CERN LHC", *JINST* **3** (2008) S08004. `doi:10.1088/1748-0221/3/08/S08004`.

[7] L. Evans and P. Bryant, "LHC Machine", *JINST* **3** (2008) S08001. `doi:10.1088/1748-0221/3/08/S08001`.

[8] M. Raidal et al., "Flavour physics of leptons and dipole moments", *Eur. Phys. J. C* **57** (2008) 13, `arXiv:0801.1826`. `doi:10.1140/epjc/s10052-008-0715-2`.

[9] A. de Gouvêa and P. Vogel, "Lepton Flavor and Number Conservation, and Physics Beyond the Standard Model", *Prog. Part. Nucl. Phys.* **71** (2013) 75, `arXiv:1303.4097`. `doi:10.1016/j.ppnp.2013.03.006`.

[10] Y. Kuno and Y. Okada, "Muon decay and physics beyond the standard model", *Rev. Mod. Phys.* **73** (2001) 151, `arXiv:hep-ph/9909265`. `doi:10.1103/RevModPhys.73.151`.

[11] R. H. Bernstein and P. S. Cooper, "Charged Lepton Flavor Violation: An experimenter's guide", *Phys. Rept.* **532** (2013) 27, `arXiv:1307.5787`. `doi:10.1016/j.physrep.2013.07.002`.

[12] S. Mihara et al., "Charged Lepton Flavor-Violation Experiments", *Annual Review of Nuclear and Particle Science* **63** (2013) 531, `arXiv:http://dx.doi.org/10.1146/annurev-nucl-102912-144530`. `doi:10.1146/annurev-nucl-102912-144530`.

[13] T. Mori on behalf of the MEG Collaboration, "Final results of the MEG experiment", *Nuovo Cim.* **39C** (2016) 325, `arXiv:1606.08168`. `doi:10.1393/ncc/i2016-16325-7`.

[14] SINDRUM Collaboration, "Search for the Decay $\mu^+ \to \mathrm{e}^+\mathrm{e}^+\mathrm{e}^-$", *Nucl. Phys. B* **299** (1988) 1. `doi:10.1016/0550-3213(88)90462-2`.

[15] BABAR Collaboration, "Searches for Lepton Flavor Violation in the Decays $\tau^{\pm} \to \mathrm{e}^{\pm}\gamma$ and $\tau^{\pm} \to \mu^{\pm}\gamma$", *Phys. Rev. Lett.* **104** (2010) 021802, `arXiv:0908.2381`. `doi:10.1103/PhysRevLett.104.021802`.

[16] BABAR Collaboration, "Limits on τ lepton-flavor violating decays into three charged leptons", *Phys. Rev. D* **81** (2010) 111101. `doi:10.1103/PhysRevD.81.111101`.

[17] Belle Collaboration, "New search for $\tau \to \mu\gamma$ and $\tau \to \mathrm{e}\gamma$ decays at Belle", *Phys. Lett. B* **666** (2008) 16, `arXiv:0705.0650`. `doi:10.1016/j.physletb.2008.06.056`.

[18] K. Hayasaka et al., "Search for lepton-flavor-violating τ decays into three leptons with 719 Million produced $\tau^{+}\tau^{-}$ pairs", *Phys. Lett. B* **687** (2010) 139, `arXiv:1001.3221`. `doi:10.1016/j.physletb.2010.03.037`.

[19] SINDRUM II Collaboration, "A search for $\mu - \mathrm{e}$ conversion in muonic gold", *Eur. Phys. J. C* **47** (2006) 337. `doi:10.1140/epjc/s2006-02582-x`.

[20] BNL E871 Collaboration, "New Limit on Muon and Electron Lepton Number Violation from $\mathrm{K}^0_{\mathrm{L}} \to \mu^{\pm}\mathrm{e}^{\mp}$ Decay", *Phys. Rev. Lett.* **81** (1998) 5734. `doi:10.1103/PhysRevLett.81.5734`.

[21] LHCb Collaboration, "Search for the Lepton-Flavor-Violating Decays $B^0_s \to e^{\pm}\mu^{\mp}$ and $B^0 \to e^{\pm}\mu^{\mp}$", *Phys. Rev. Lett.* **111** (2013) 141801. `doi:10.1103/PhysRevLett.111.141801`.

[22] ATLAS Collaboration, "Search for the lepton flavor violating decay $\mathrm{Z} \to \mathrm{e}\mu$ in pp collisions at $\sqrt{s} = 8$ TeV with the ATLAS detector", *Phys. Rev. D* **90** (2014) 072010, `arXiv:1408.5774`. `doi:10.1103/PhysRevD.90.072010`.

[23] CMS collaboration Collaboration, "Search for Lepton Flavor Violation in Z decays in pp collisions at $\sqrt{s} = 8$ TeV", CMS Physics Analysis Summary CMS-PAS-EXO-13-005, 2015.

[24] S. L. Glashow, J. Iliopoulos, and L. Maiani, "Weak Interactions with Lepton-Hadron Symmetry", *Phys. Rev. D* **2** (1970) 1285. `doi:10.1103/PhysRevD.2.1285`.

[25] J. I. Illana and T. Riemann, "Charged lepton flavor violation from massive neutrinos in Z decays", *Phys. Rev. D* **63** (2001) 053004, `arXiv:hep-ph/0010193`. `doi:10.1103/PhysRevD.63.053004`.

[26] CMS Collaboration, "Search for Lepton-Flavour-Violating Decays of the Higgs Boson", *Phys. Lett. B* **749** (2015) 337, `arXiv:1502.07400`. `doi:10.1016/j.physletb.2015.07.053`.

[27] ATLAS Collaboration, "Search for lepton-flavour-violating $H \to \mu\tau$ decays of the Higgs boson with the ATLAS detector", *JHEP* **11** (2015) 211, `arXiv:1508.03372`. `doi:10.1007/JHEP11(2015)211`.

[28] ATLAS Collaboration, "Search for lepton-flavour-violating decays of the Higgs and Z bosons with the ATLAS detector", *Eur. Phys. J. C* **77** (2017) 70, `arXiv:1604.07730`. `doi:10.1140/epjc/s10052-017-4624-0`.

[29] CMS Collaboration, "Search for lepton flavour violating decays of the Higgs boson to $\mathrm{e}\tau$ and $\mathrm{e}\mu$ in proton-proton collisions at $\sqrt{s} = 8$ TeV", *Phys. Lett. B* (2016) `arXiv:1607.03561`. `doi:10.1016/j.physletb.2016.09.062`.

[30] CMS Collaboration, "Search for lepton flavour violating decays of heavy resonances and quantum black holes to an $\mathrm{e}\mu$ pair in proton-proton collisions at $\sqrt{s} = 8$ TeV", *Eur. Phys. J. C* **76** (2016) 317, `arXiv:1604.05239`. `doi:10.1140/epjc/s10052-016-4149-y`.

[31] ATLAS Collaboration, "Search for a Heavy Neutral Particle Decaying to $e\mu$, $e\tau$, or $\mu\tau$ in pp Collisions at $\sqrt{s} = 8$ TeV with the ATLAS Detector", *Phys. Rev. Lett.* **115** (2015) 031801, `arXiv:1503.04430`. `doi:10.1103/PhysRevLett.115.031801`.

[32] ATLAS Collaboration, "Search for new phenomena in different-flavour high-mass dilepton final states in pp collisions at $\sqrt{s} = 13$ TeV with the ATLAS detector", *Eur. Phys. J. C* **76** (2016) 541, `arXiv:1607.08079`. `doi:10.1140/epjc/s10052-016-4385-1`.

[33] LHCb Collaboration, "Search for the lepton flavour violating decay $\tau^- \to \mu^-\mu^+\mu^-$", *JHEP* **02** (2015) 121, `arXiv:1409.8548`. `doi:10.1007/JHEP02(2015)121`.

[34] ATLAS Collaboration, "Probing lepton flavour violation via neutrinoless $\tau \to 3\mu$ decays with the ATLAS detector", *Eur. Phys. J. C* **76** (2016) 232, `arXiv:1601.03567`. `doi:10.1140/epjc/s10052-016-4041-9`.

[35] ATLAS Collaboration, "The ATLAS Experiment at the CERN Large Hadron Collider", *JINST* **3** (2008) S08003. `doi:10.1088/1748-0221/3/08/S08003`.

[36] CMS Collaboration, "Observation of a new boson at a mass of 125 GeV with the CMS experiment at the LHC", *Phys. Lett. B* **716** (2012) 30, `arXiv:1207.7235`. `doi:10.1016/j.physletb.2012.08.021`.

[37] ATLAS Collaboration, "Observation of a new particle in the search for the Standard Model Higgs boson with the ATLAS detector at the LHC", *Phys. Lett. B* **716** (2012) 1, `arXiv:1207.7214`. `doi:10.1016/j.physletb.2012.08.020`.

[38] CMS Collaboration, "Search for Lepton Flavour Violating Decays of Heavy Resonances and Quantum Black Holes to electron/muon Pairs in pp Collisions at a centre of mass energy of 8 TeV", CMS Physics Analysis Summary CMS-PAS-EXO-13-002, 2015.

[39] A. Güth et al., "Search for Lepton Flavour Violating Decays of Heavy States to eμ Pairs in pp Collisions at $\sqrt{s} = 8$ TeV", CMS Analysis Note AN-2013/422, 2015.

[40] S. P. Martin, "A Supersymmetry primer", *Adv. Ser. Direct. High Energy Phys.* **18** (1998) 1, `arXiv:hep-ph/9709356`. `doi:10.1142/9789812839657_0001, 10.1142/9789814307505_0001`.

[41] M. Drees, R. Godbole, and P. Roy, "Theory and phenomenology of sparticles: An account of four-dimensional N=1 supersymmetry in high energy physics". World Scientific Publishing, 2004.

[42] I. J. R. Aitchison, "Supersymmetry in Particle Physics. An Elementary Introduction". Cambridge University Press, 2007.

[43] N. Sakai, "Naturalness in supersymmetric GUTS", *Z. Phys. C* **11** (1981) 153. `doi:10.1007/BF01573998`.

[44] E. Witten, "Dynamical Breaking of Supersymmetry", *Nucl. Phys. B* **188** (1981) 513. `doi:10.1016/0550-3213(81)90006-7`.

[45] M. Veltman, "The Infrared - Ultraviolet Connection", *Acta Phys. Polon. B* **12** (1981) 437.

[46] R. K. Kaul and P. Majumdar, "Cancellation of Quadratically Divergent Mass Corrections in Globally Supersymmetric Spontaneously Broken Gauge Theories", *Nucl. Phys. B* **199** (1982) 36. `doi:10.1016/0550-3213(82)90565-X`.

[47] S. Dimopoulos, S. Raby, and F. Wilczek, "Supersymmetry and the Scale of Unification", *Phys. Rev. D* **24** (1981) 1681. `doi:10.1103/PhysRevD.24.1681`.

[48] L. E. Ibanez and G. G. Ross, “Low-Energy Predictions in Supersymmetric Grand Unified Theories”, *Phys. Lett. B* **105** (1981) 439. `doi:10.1016/0370-2693(81)91200-4`.

[49] W. J. Marciano and G. Senjanović, “Predictions of Supersymmetric Grand Unified Theories”, *Phys. Rev. D* **25** (1982) 3092. `doi:10.1103/PhysRevD.25.3092`.

[50] G. Jungman, M. Kamionkowski, and K. Griest, “Supersymmetric dark matter”, *Phys. Rept.* **267** (1996) 195, `arXiv:hep-ph/9506380`. `doi:10.1016/0370-1573(95)00058-5`.

[51] R. Barbier et al., “R-parity violating supersymmetry”, *Phys. Rept.* **420** (2005) 1, `arXiv:hep-ph/0406039`. `doi:10.1016/j.physrep.2005.08.006`.

[52] G. R. Farrar and P. Fayet, “Phenomenology of the Production, Decay, and Detection of New Hadronic States Associated with Supersymmetry”, *Phys. Lett. B* **76** (1978) 575. `doi:10.1016/0370-2693(78)90858-4`.

[53] S. Dimopoulos, S. Raby, and F. Wilczek, “Proton Decay in Supersymmetric Models”, *Phys. Lett. B* **112** (1982) 133. `doi:10.1016/0370-2693(82)90313-6`.

[54] H. K. Dreiner, C. Luhn, and M. Thormeier, “What is the discrete gauge symmetry of the minimal supersymmetric standard model?”, *Phys. Rev. D* **73** (2006) 075007, `arXiv:hep-ph/0512163`. `doi:10.1103/PhysRevD.73.075007`.

[55] L. E. Ibanez and G. Ross, “Discrete gauge symmetries and the origin of baryon and lepton number conservation in supersymmetric versions of the standard model”, *Nucl. Phys. B* **368** (1992) 3. `doi:10.1016/0550-3213(92)90195-H`.

[56] M. Bernhardt, S. Das, H. Dreiner et al., “Sneutrino as Lightest Supersymmetric Particle in B_3 mSUGRA Models and Signals at the LHC”, *Phys. Rev. D* **79** (2009) 035003, `arXiv:0810.3423`. `doi:10.1103/PhysRevD.79.035003`.

[57] H. K. Dreiner, S. Grab, M. Krämer et al., “Supersymmetric NLO QCD corrections to resonant slepton production and signals at the Fermilab Tevatron and the CERN LHC”, *Phys. Rev. D* **75** (2007) 035003, `arXiv:hep-ph/0611195`. `doi:10.1103/PhysRevD.75.035003`.

[58] J. Pumplin, D. Stump, J. Huston et al., “New generation of parton distributions with uncertainties from global QCD analysis”, *JHEP* **0207** (2002) 012, `arXiv:hep-ph/0201195`. `doi:10.1088/1126-6708/2002/07/012`.

[59] CDF Collaboration, “Search for R-parity Violating Decays of τ sneutrinos to $e\mu$, $\mu\tau$, and $e\tau$ Pairs in $\mathrm{p\overline{p}}$ Collisions at $\sqrt{s} = 1.96$ TeV”, *Phys. Rev. Lett.* **105** (2010) 191801, `arXiv:1004.3042`. `doi:10.1103/PhysRevLett.105.191801`.

[60] D0 Collaboration, “Search for sneutrino production in $e\mu$ final states in 5.3 fb^{-1} of $\mathrm{p\overline{p}}$ collisions at $\sqrt{s} = 1.96$ TeV”, *Phys. Rev. Lett.* **105** (2010) 191802, `arXiv:1007.4835`. `doi:10.1103/PhysRevLett.105.191802`.

[61] ATLAS Collaboration, “Search for a heavy particle decaying into an electron and a muon with the ATLAS detector in $\sqrt{s} = 7$ TeV pp collisions at the LHC”, *Phys. Rev. Lett.* **106** (2011) 251801, `arXiv:1103.5559`. `doi:10.1103/PhysRevLett.106.251801`.

[62] ATLAS Collaboration, “Search for a heavy neutral particle decaying into an electron and a muon using 1 fb^{-1} of ATLAS data”, *Eur. Phys. J. C* **71** (2011) 1809, `arXiv:1109.3089`. `doi:10.1140/epjc/s10052-011-1809-9`.

[63] ATLAS Collaboration, “Search for a heavy narrow resonance decaying to $e\mu$, $e\tau$, or $\mu\tau$ with the ATLAS detector in $\sqrt{s} = 7$ TeV pp collisions at the LHC”, *Phys. Lett. B* **723** (2013) 15, `arXiv:1212.1272`. `doi:10.1016/j.physletb.2013.04.035`.

[64] A. Faessler et al., “Exotic $\mu^- - e^-$ conversion in nuclei and R-parity violating supersymmetry”, *Nucl. Phys. B* **587** (2000) 25, `arXiv:hep-ph/9904335`. `doi:10.1016/S0550-3213(00)00446-6`.

[65] J. Sato and M. Yamanaka, “A way to crosscheck $\mu - e$ conversion in the case of no signals of $\mu \to e\gamma$ and $\mu \to 3e$”, *Phys. Rev. D* **91** (2015) 055018, `arXiv:1409.1697`. `doi:10.1103/PhysRevD.91.055018`.

[66] T. S. Kosmas, S. Kovalenko, and I. Schmidt, “b-quark mediated neutrinoless μ^- – e$^-$ conversion in presence of R-parity violation”, *Phys. Lett. B* **519** (2001) 78, `arXiv:hep-ph/0107292`. `doi:10.1016/S0370-2693(01)01096-6`.

[67] G. W.-S. Hou, “Possible resonances in μ^+e$^-$ $\to$ μ^-e$^+$ collisions”, *Nucl. Phys. Proc. Suppl.* **51A** (1996) 40, `arXiv:hep-ph/9605204`. `doi:10.1016/0920-5632(96)00414-8`.

[68] J. E. Kim, P. Ko, and D.-G. Lee, “More on R-parity- and lepton-family-number-violating couplings from muon(ium) conversion, and τ and π^0 decays”, *Phys. Rev. D* **56** (1997) 100, `arXiv:hep-ph/9701381`. `doi:10.1103/PhysRevD.56.100`.

[69] L. Willmann et al., “New bounds from searching for muonium to antimuonium conversion”, *Phys. Rev. Lett.* **82** (1999) 49, `arXiv:hep-ex/9807011`. `doi:10.1103/PhysRevLett.82.49`.

[70] K. Hayasaka, “Recent Tau Decay Results at B Factories: Lepton Flavor Violating Tau Decays”, `arXiv:1010.3746`.

[71] BABAR Collaboration, “Search for Lepton Flavor Violating Decays $\tau^\pm \to \ell^\pm\pi^0$, $\ell^\pm\eta$, $\ell^\pm\eta'$”, *Phys. Rev. Lett.* **98** (2007) 061803, `arXiv:hep-ex/0610067`. `doi:10.1103/PhysRevLett.98.061803`.

[72] Belle Collaboration, “Search for lepton flavor violating τ^- decays into $\ell^-\eta$, $\ell^-\eta'$ and $\ell^-\pi^0$”, *Phys. Lett. B* **648** (2007) 341, `arXiv:hep-ex/0703009`. `doi:10.1016/j.physletb.2007.03.027`.

[73] Particle Data Group, R.M. Barnett, et al., “Review of Particle Physics”, *Phys. Rev.* **D54** (1996) 1.

[74] T. Banks and W. Fischler, “A Model for high-energy scattering in quantum gravity”, `arXiv:hep-th/9906038`.

[75] S. Dimopoulos and G. L. Landsberg, “Black holes at the LHC”, *Phys. Rev. Lett.* **87** (2001) 161602, `arXiv:hep-ph/0106295`. `doi:10.1103/PhysRevLett.87.161602`.

[76] S. B. Giddings and S. D. Thomas, “High-energy colliders as black hole factories: The End of short distance physics”, *Phys. Rev. D* **65** (2002) 056010, `arXiv:hep-ph/0106219`. `doi:10.1103/PhysRevD.65.056010`.

[77] P. Meade and L. Randall, “Black Holes and Quantum Gravity at the LHC”, *JHEP* **0805** (2008) 003, `arXiv:0708.3017`. `doi:10.1088/1126-6708/2008/05/003`.

[78] G. L. Landsberg, “Black Holes at Future Colliders and Beyond”, *J. Phys. G* **32** (2006) R337, `arXiv:hep-ph/0607297`. `doi:10.1088/0954-3899/32/9/R02`.

[79] X. Calmet, S. D. Hsu, and D. Reeb, “Quantum gravity at a TeV and the renormalization of Newton’s constant”, *Phys. Rev. D* **77** (2008) 125015, `arXiv:0803.1836`. `doi:10.1103/PhysRevD.77.125015`.

[80] L. Randall and R. Sundrum, "Large Mass Hierarchy from a Small Extra Dimension", *Phys. Rev. Lett.* **83** (1999) 3370, `arXiv:hep-ph/9905221`. `doi:10.1103/PhysRevLett.83.3370`.

[81] L. Randall and R. Sundrum, "An Alternative to Compactification", *Phys. Rev. Lett.* **83** (1999) 4690, `arXiv:hep-th/9906064`. `doi:10.1103/PhysRevLett.83.4690`.

[82] N. Arkani-Hamed, S. Dimopoulos, and G. Dvali, "The Hierarchy problem and new dimensions at a millimeter", *Phys. Lett. B* **429** (1998) 263, `arXiv:hep-ph/9803315`. `doi:10.1016/S0370-2693(98)00466-3`.

[83] N. Arkani-Hamed, S. Dimopoulos, and G. Dvali, "Phenomenology, astrophysics, and cosmology of theories with submillimeter dimensions and TeV scale quantum gravity", *Phys. Rev. D* **59** (1999) 086004, `arXiv:hep-ph/9807344`. `doi:10.1103/PhysRevD.59.086004`.

[84] X. Calmet and N. Gausmann, "Non-thermal quantum black holes with quantized masses", *International Journal of Modern Physics* **28** (2013) `arXiv:1209.4618`. `doi:10.1142/S0217751X13500450`.

[85] X. Calmet, W. Gong, and S. D. Hsu, "Colorful quantum black holes at the LHC", *Phys. Lett. B* **668** (2008) 20, `arXiv:0806.4605`. `doi:10.1016/j.physletb.2008.08.011`.

[86] D. M. Gingrich, "Quantum black holes with charge, colour, and spin at the LHC", *J. Phys. G* **37** (2010) 105008, `arXiv:0912.0826`. `doi:10.1088/0954-3899/37/10/105008`.

[87] CMS Collaboration, "Search for microscopic black holes in pp collisions at $\sqrt{s} = 7$ TeV", *JHEP* **1204** (2012) 061, `arXiv:1202.6396`. `doi:10.1007/JHEP04(2012)061`.

[88] CMS Collaboration, "Search for microscopic black holes in pp collisions at $\sqrt{s} = 8$ TeV", *JHEP* **1307** (2013) 178, `arXiv:1303.5338`. `doi:10.1007/JHEP07(2013)178`.

[89] ATLAS Collaboration, "Search for microscopic black holes in a like-sign dimuon final state using large track multiplicity with the ATLAS detector", *Phys. Rev. D* **88** (2013) 072001, `arXiv:1308.4075`. `doi:10.1103/PhysRevD.88.072001`.

[90] ATLAS Collaboration, "Search for microscopic black holes and string balls in final states with leptons and jets with the ATLAS detector at $\sqrt{s} = 8$ TeV", *JHEP* **1408** (2014) 103, `arXiv:1405.4254`. `doi:10.1007/JHEP08(2014)103`.

[91] E.G. Adelberger et al., "Torsion balance experiments: A low-energy frontier of particle physics", *Prog. Part. Nucl. Phys.* **62** (2009) 102. `doi:10.1016/j.ppnp.2008.08.002`.

[92] Particle Data Group, J. Beringer, et al., "Review of Particle Physics", *Phys. Rev. D* **86** (2012) 010001. `doi:10.1103/PhysRevD.86.010001`.

[93] A. Belyaev and X. Calmet, "Quantum Black Holes and their Lepton Signatures at the LHC with CalCHEP", *JHEP* **08** (2015) 139, `arXiv:1412.2661`. `doi:10.1007/JHEP08(2015)139`.

[94] CMS Collaboration, "Search for microscopic black holes in pp collisions at $\sqrt{s} = 8$ TeV", *JHEP* **07** (2013) 178, `arXiv:1303.5338`. `doi:10.1007/JHEP07(2013)178`.

[95] CMS Collaboration, "Search for resonances and quantum black holes using dijet mass spectra in proton-proton collisions at $\sqrt{s} = 8$ TeV", *Phys. Rev. D* **91** (2015) 052009, `arXiv:1501.04198`. `doi:10.1103/PhysRevD.91.052009`.

[96] CMS Collaboration, “Search for narrow resonances decaying to dijets in proton-proton collisions at $\sqrt{s} = 13$ TeV”, *Phys. Rev. Lett.* **116** (2016) 071801, `arXiv:1512.01224`. `doi:10.1103/PhysRevLett.116.071801`.

[97] ATLAS Collaboration, “Search for new phenomena in the dijet mass distribution using pp collision data at $\sqrt{s} = 8$ TeV with the ATLAS detector”, *Phys. Rev. D* **91** (2015) 052007, `arXiv:1407.1376`. `doi:10.1103/PhysRevD.91.052007`.

[98] ATLAS Collaboration, “Search for new phenomena in dijet mass and angular distributions from pp collisions at $\sqrt{s} = 13$ TeV with the ATLAS detector”, *Phys. Lett. B* **754** (2016) 302, `arXiv:1512.01530`. `doi:10.1016/j.physletb.2016.01.032`.

[99] ATLAS Collaboration, “Search for new phenomena in photon+jet events collected in proton–proton collisions at $\sqrt{s} = 8$ TeV with the ATLAS detector”, *Phys. Lett. B* **728** (2014) 562, `arXiv:1309.3230`. `doi:10.1016/j.physletb.2013.12.029`.

[100] ATLAS Collaboration, “Search for new phenomena with photon+jet events in proton-proton collisions at $\sqrt{s} = 13$ TeV with the ATLAS detector”, *JHEP* **03** (2016) 041, `arXiv:1512.05910`. `doi:10.1007/JHEP03(2016)041`.

[101] ATLAS Collaboration, “Search for Quantum Black-Hole Production in High-Invariant-Mass Lepton+Jet Final States Using Proton-Proton Collisions at $\sqrt{s} = 8$ TeV and the ATLAS Detector”, *Phys. Rev. Lett.* **112** (2014) 091804, `arXiv:1311.2006`. `doi:10.1103/PhysRevLett.112.091804`.

[102] ATLAS Collaboration, “Search for high-mass dilepton resonances in pp collisions at $\sqrt{s} = 8$ TeV with the ATLAS detector”, *Phys. Rev. D* **90** (2014) 052005, `arXiv:1405.4123`. `doi:10.1103/PhysRevD.90.052005`.

[103] ALICE Collaboration, “The ALICE experiment at the CERN LHC”, *JINST* **3** (2008) S08002. `doi:10.1088/1748-0221/3/08/S08002`.

[104] LHCb Collaboration, “The LHCb Detector at the LHC”, *JINST* **3** (2008) S08005. `doi:10.1088/1748-0221/3/08/S08005`.

[105] O. S. Brüning et al., “LHC Design Report Vol. 1: The LHC Main Ring”, TDR CERN-2004-003-V-1, CERN-2004-003, 2004.

[106] O. S. Brüning et al., “LHC Design Report Vol. 2: The LHC infrastructure and general services”, TDR CERN-2004-003-V-2, CERN-2004-003, 2004.

[107] M. Benedikt et al., “LHC Design Report. Vol. 3: The LHC injector chain”, TDR CERN-2004-003-V-3, CERN-2004-003, 2004.

[108] M. Lamont and O. Johnson, “LHC beam and luminosity lifetimes revisited”, CERN Accelerator Note CERN-ACC-2014-0255, 2014.

[109] M. Lamont, “Status of the LHC”, *J. Phys. Conf. Ser.* **455** (2013) 012001. `doi:10.1088/1742-6596/455/1/012001`.

[110] R. Bailey, “An Application for Research: the Large Hadron Collider”, in *Proceedings, CAS - CERN Accelerator School: Ion Sources, Senec, Slovakia, May 29-June 8, 2012*, p. 565. 2013. `arXiv:1404.0966`.

[111] CERN, “LHC Accelerator Performance and Statistics”. `https://acc-stats.web.cern.ch/acc-stats/#lhc/`, 2017.

[112] CMS Collaboration, “CMS Luminosity - Public Results”. `https://twiki.cern.ch/twiki/bin/view/CMSPublic/LumiPublicResults#2012_Proton_Proton_Collisions`, 2017.

[113] R. K. Ellis, W. J. Stirling, and B. R. Webber, “QCD and collider physics”, volume 8 of *Camb. Monogr. Part. Phys. Nucl. Phys. Cosmol.* Cambridge University Press, 1996.

[114] A. R. Baden, “Jets and kinematics in hadronic collisions”, *Int. J. Mod. Phys. A* **13** (1998) 1817. `doi:10.1142/S0217751X98000809`.

[115] D. Green, “High P_{T} Physics at Hadron Colliders”, volume 22 of *Camb. Monogr. Part. Phys. Nucl. Phys. Cosmol.* Cambridge University Press, 2005.

[116] M. Perelstein, “Introduction to Collider Physics”, in *Physics of the large and the small, TASI 09, proceedings of the Theoretical Advanced Study Institute in Elementary Particle Physics, Boulder, Colorado, USA, 1-26 June 2009*, p. 421. 2011. `arXiv:1002.0274`.

[117] Particle Data Group, C. Patrignani, et al., “Review of Particle Physics”, *Chin. Phys. C* **40** (2016) 100001. `doi:10.1088/1674-1137/40/10/100001`.

[118] R. K. Ellis et al., “Perturbation Theory and the Parton Model in QCD”, *Nucl. Phys. B* **152** (1979) 285. `doi:10.1016/0550-3213(79)90105-6`.

[119] J. C. Collins, D. E. Soper, and G. F. Sterman, “Factorization of Hard Processes in QCD”, *Adv. Ser. Direct. High Energy Phys.* **5** (1989) 1, `arXiv:hep-ph/0409313`. `doi:10.1142/9789814503266_0001`.

[120] G. Altarelli and G. Parisi, “Asymptotic Freedom in Parton Language”, *Nucl. Phys. B* **126** (1977) 298. `doi:10.1016/0550-3213(77)90384-4`.

[121] V. N. Gribov and L. N. Lipatov, “Deep inelastic e p scattering in perturbation theory”, *Sov. J. Nucl. Phys.* **15** (1972) 438.

[122] Y. L. Dokshitzer, “Calculation of structure functions of deep-inelastic scattering and e^+e^- annihilation by perturbation theory in quantum chromodynamics”, *Sov. Phys. JETP* **46** (1977) 641.

[123] A. Manohar et al., “How bright is the proton? A precise determination of the photon parton distribution function”, *Phys. Rev. Lett.* **117** (2016), no. 24, 242002, `arXiv:1607.04266`. `doi:10.1103/PhysRevLett.117.242002`.

[124] M. L. Mangano et al., “Physics at a 100 TeV pp collider: Standard Model processes”, `arXiv:1607.01831`.

[125] A. D. Martin, W. J. Stirling, R. S. Thorne et al., “Parton distributions for the LHC”, *Eur. Phys. J. C* **63** (2009) 189, `arXiv:0901.0002`. `doi:10.1140/epjc/s10052-009-1072-5`.

[126] W.J. Stirling, “Parton luminosity and cross section plots”. `http://www.hep.ph.ic.ac.uk/~wstirlin/plots/plots.html`, 2017.

[127] TOTEM Collaboration, “Luminosity-Independent Measurement of the Proton-Proton Total Cross Section at $\sqrt{s} = 8$ TeV”, *Phys. Rev. Lett.* **111** (2013) 012001. `doi:10.1103/PhysRevLett.111.012001`.

[128] TOTEM Collaboration, “The TOTEM experiment at the CERN Large Hadron Collider”, *JINST* **3** (2008) S08007. `doi:10.1088/1748-0221/3/08/S08007`.

[129] CMS and TOTEM collaborations, “Measurement of pseudorapidity distributions of charged particles in proton-proton collisions at $\sqrt{s} = 8$ TeV by the CMS and TOTEM experiments”, *Eur. Phys. J. C* **74** (2014) 3053, `arXiv:1405.0722`. `doi:10.1140/epjc/s10052-014-3053-6`.

[130] CMS Collaboration, “Transverse-momentum and pseudorapidity distributions of charged hadrons in pp collisions at $\sqrt{s} = 7$ TeV”, *Phys. Rev. Lett.* **105** (2010) 022002, `arXiv:1005.3299`. `doi:10.1103/PhysRevLett.105.022002`.

[131] D. Green, ed., “At the Leading Edge - The ATLAS and CMS LHC Experiments”. World Scientific Publishing, 2010.

[132] LHC Higgs Cross Section Working Group Collaboration, “Handbook of LHC Higgs Cross Sections: 2. Differential Distributions”, `arXiv:1201.3084`. `doi:10.5170/CERN-2012-002`.

[133] CMS Collaboration, “Search for the standard model Higgs boson produced through vector boson fusion and decaying to $b\bar{b}$”, *Phys. Rev. D* **92** (2015) 032008, `arXiv:1506.01010`. `doi:10.1103/PhysRevD.92.032008`.

[134] CMS Collaboration, “The CMS magnet project : Technical Design Report”, TDR CERN-LHCC-97-010, CMS-TDR-1, 1997.

[135] CMS Collaboration, “Precise Mapping of the Magnetic Field in the CMS Barrel Yoke using Cosmic Rays”, *JINST* **5** (2010) T03021, `arXiv:0910.5530`. `doi:10.1088/1748-0221/5/03/T03021`.

[136] V. I. Klyukhin et al., “Measurement of the CMS Magnetic Field”, *IEEE Trans. Appl. Supercond.* **18** (2008) 395, `arXiv:1110.0306`. `doi:10.1109/TASC.2008.921242`.

[137] V. I. Klyukhin et al., “Measuring the Magnetic Flux Density in the CMS Steel Yoke”, *J. Supercond. Nov. Magn.* **23** (2013) 1307, `arXiv:1212.1657`. `doi:10.1007/s10948-012-1967-5`.

[138] CMS Collaboration, “The CMS tracker system project : Technical Design Report”, TDR CERN-LHCC-98-006, CMS-TDR-5, 1998.

[139] CMS Collaboration, “The CMS tracker : addendum to the Technical Design Report”, TDR CERN-LHCC-2000-016, CMS-TDR-5-add-1, 2000.

[140] CMS Collaboration, “Description and performance of track and primary-vertex reconstruction with the CMS tracker”, *JINST* **9** (2014) P10009, `arXiv:1405.6569`. `doi:10.1088/1748-0221/9/10/P10009`.

[141] L. Rolandi, W. Riegler, and W. Blum, “Particle Detection with Drift Chambers”. Particle Acceleration and Detection. Springer, 2008.

[142] CMS Collaboration, “The CMS electromagnetic calorimeter project : Technical Design Report”, TDR CERN-LHCC-97-33, CMS-TDR-4, 1997.

[143] CMS Collaboration, “Addendum to the CMS ECAL technical design report: Changes to the CMS ECAL electronics”, TDR CERN-LHCC-2002-027, CMS-TDR-4-add-1, 2002.

[144] LHC Higgs Cross Section Working Group Collaboration, “Handbook of LHC Higgs Cross Sections: 3. Higgs Properties”, `arXiv:1307.1347`. `doi:10.5170/CERN-2013-004`.

[145] A. A. Annenkov, M. V. Korzhik, and P. Lecoq, “Lead tungstate scintillation material”, *Nucl. Instrum. Meth. A* **490** (2002) 30. `doi:10.1016/S0168-9002(02)00916-6`.

[146] CMS Collaboration, “Energy Calibration and Resolution of the CMS Electromagnetic Calorimeter in pp Collisions at $\sqrt{s} = 7$ TeV”, *JINST* **8** (2013) P09009, `arXiv:1306.2016`. `doi:10.1088/1748-0221/8/09/P09009`.

[147] P. Baillon et al., “Performance of the Cooling System of CMS ECAL”, in *Astroparticle, Particle and Space Physics, Detectors and Medical Physics Applications, proceedings of the 8th Conference Villa Olmo, Como, Italy, 6-11 October 2003*, p. 203. 2004.

[148] CMS Collaboration, “Radiation hardness qualification of $PbWO_4$ scintillation crystals for the CMS Electromagnetic Calorimeter”, *JINST* **5** (2010) P03010, `arXiv:0912.4300`. `doi:10.1088/1748-0221/5/03/P03010`.

[149] CMS Collaboration, “Performance and Operation of the CMS Electromagnetic Calorimeter”, *JINST* **5** (2010) T03010, `arXiv:0910.3423`. `doi:10.1088/1748-0221/5/03/T03010`.

[150] P. Adzic et al., “Energy resolution of the barrel of the CMS electromagnetic calorimeter”, *JINST* **2** (2007) P04004. `doi:10.1088/1748-0221/2/04/P04004`.

[151] CMS Collaboration, “Performance of Electron Reconstruction and Selection with the CMS Detector in Proton-Proton Collisions at $\sqrt{s} = 8$ TeV”, *JINST* **10** (2015) P06005, `arXiv:1502.02701`. `doi:10.1088/1748-0221/10/06/P06005`.

[152] CMS Collaboration, “CMS Physics : Technical Design Report Volume 1: Detector Performance and Software”, TDR CERN-LHCC-2006-001, CMS-TDR-8-1, 2006.

[153] CMS Collaboration, “The CMS hadron calorimeter project : Technical Design Report”, TDR CERN-LHCC-97-031, CMS-TDR-2, 1997.

[154] CMS HCAL Collaboration, G. Baiatian et al., “Design, Performance, and Calibration of CMS Hadron-Barrel Calorimeter Wedges”, CMS Note CERN-CMS-NOTE-2006-138, 2007.

[155] CMS Collaboration, “Jet energy scale and resolution in the CMS experiment in pp collisions at 8 TeV”, *JINST* **12** (2017) P02014, `arXiv:1607.03663`. `doi:10.1088/1748-0221/12/02/P02014`.

[156] CMS Collaboration, “The Muon Project. Technical Design Report”, TDR CERN-LHCC-97-032, CMS-TDR-3, 1997.

[157] M. S. Kim, “CMS reconstruction improvement for the muon tracking by the RPC chambers”, *JINST* **8** (2013) T03001, `arXiv:1209.2646`. `doi:10.1088/1748-0221/8/03/T03001`.

[158] CMS Collaboration, “CMS, The TriDAS project: Technical Design Report, Volume 1: The Trigger Systems”, TDR CERN-LHCC-2000-038, CMS-TDR-6-1, 2000.

[159] CMS Collaboration, “CMS, The TriDAS Project: Technical Design Report, Volume 2: Data Acquisition and High-Level Trigger”, TDR CERN-LHCC-2002-026, CMS-TDR-6, 2002.

[160] CMS Collaboration, “The CMS trigger system”, *JINST* **12** (2017) P01020, `arXiv:1609.02366`. `doi:10.1088/1748-0221/12/01/P01020`.

[161] G. Bauer et al., “Operational experience with the CMS data acquisition system”, *J. Phys. Conf. Ser.* **396** (2012) 012007. `doi:10.1088/1742-6596/396/1/012007`.

[162] I. Bird, “Computing for the Large Hadron Collider”, *Ann. Rev. Nucl. Part. Sci.* **61** (2011) 99. `doi:10.1146/annurev-nucl-102010-130059`.

[163] CMS Collaboration, “CMS Offline Software”. `https://github.com/cms-sw/cmssw`, 2017.

[164] CMS Offline Group, “CMSSW Application Framework”. `https://twiki.cern.ch/twiki/bin/view/CMSPublic/WorkBookCMSSWFramework`, 2017.

[165] GEANT4 Collaboration, “GEANT4: A Simulation toolkit”, *Nucl. Instrum. Meth. A* **506** (2003) 250. `doi:10.1016/S0168-9002(03)01368-8`.

[166] CMS Collaboration, S. Sekmen, “Recent Developments in CMS Fast Simulation”, in *Proceedings, 38th International Conference on High Energy Physics (ICHEP 2016): Chicago, IL, USA, August 3-10, 2016*. 2017. `arXiv:1701.03850`.

[167] S. Abdullin et al., “The fast simulation of the CMS detector at LHC”, *J. Phys. Conf. Ser.* **331** (2011) 032049. `doi:10.1088/1742-6596/331/3/032049`.

[168] CMS Collaboration, “Public CMS Data Quality Information”. `https://twiki.cern.ch/twiki/bin/view/CMSPublic/DataQuality#2012_Proton_Proton_Collisions`, 2017.

[169] CMS Collaboration, “LHC and CMS Records Online in 2012 - Protons”. `http://cmsyear.web.cern.ch/cmsyear/cmswbm/servlet/YearlyReport?YEAR=2012&TYPE=1`, 2017.

[170] CMS Collaboration, “CMS Data Aggregation System (DAS)”. `https://cmsweb.cern.ch/das`, 2017.

[171] R. Mankel, “A Concurrent track evolution algorithm for pattern recognition in the HERA-B main tracking system”, *Nucl. Instrum. Meth. A* **395** (1997) 169. `doi:10.1016/S0168-9002(97)00705-5`.

[172] R. Frühwirth, “Application of Kalman filtering to track and vertex fitting”, *Nucl. Instrum. Meth. A* **262** (1987) 444. `doi:10.1016/0168-9002(87)90887-4`.

[173] CMS Collaboration, “Performance of CMS muon reconstruction in pp collision events at $\sqrt{s} = 7$ TeV”, *JINST* **7** (2012) P10002, `arXiv:1206.4071`. `doi:10.1088/1748-0221/7/10/P10002`.

[174] Particle Data Group, K.A. Olive, et al., “Atomic and nuclear properties of iron”. `http://pdg.lbl.gov/2014/AtomicNuclearProperties/HTML/iron_Fe.html`, 2014.

[175] W. Adam et al., “Reconstruction of electrons with the Gaussian-sum filter in the CMS tracker at the LHC”, *Journal of Physics G Nuclear Physics* **31** (2005) N9. `doi:10.1088/0954-3899/31/9/N01`.

[176] R. Frühwirth et al., “Data Analysis Techniques for High-Energy Physics”, volume 11 of *Camb. Monogr. Part. Phys. Nucl. Phys. Cosmol.* Cambridge University Press, 2000.

[177] S. Baffioni et al., “Electron reconstruction in CMS”, *Eur. Phys. J. C* **49** (2007) 1099. `doi:10.1140/epjc/s10052-006-0175-5`.

[178] H. Bethe and W. Heitler, “On the Stopping of Fast Particles and on the Creation of Positive Electrons”, *Proceedings of the Royal Society of London Series A* **146** (1934) 83. `doi:10.1098/rspa.1934.0140`.

[179] R. Frühwirth, “A Gaussian-mixture approximation of the Bethe-Heitler model of electron energy loss by bremsstrahlung”, *Computer Physics Communications* **154** (2003) 131. `doi:10.1016/S0010-4655(03)00292-3`.

[180] CMS Collaboration, “Particle-Flow Event Reconstruction in CMS and Performance for Jets, Taus, and MET”, CMS Physics Analysis Summary CMS-PAS-PFT-09-001, 2009.

[181] CMS Collaboration, “Commissioning of the Particle-flow Event Reconstruction with the first LHC collisions recorded in the CMS detector”, CMS Physics Analysis Summary CMS-PAS-PFT-10-001, 2010.

[182] M. Cacciari, G. P. Salam, and G. Soyez, "The Anti-k_t jet clustering algorithm", *JHEP* **04** (2008) 063, `arXiv:0802.1189`. `doi:10.1088/1126-6708/2008/04/063`.

[183] CMS Collaboration, "Determination of Jet Energy Calibration and Transverse Momentum Resolution in CMS", *JINST* **6** (2011) P11002, `arXiv:1107.4277`. `doi:10.1088/1748-0221/6/11/P11002`.

[184] CMS Collaboration, "Jet Performance in pp Collisions at 7 TeV", CMS Physics Analysis Summary CMS-PAS-JME-10-003, 2010.

[185] CMS Collaboration, "Identification of b-quark jets with the CMS experiment", *JINST* **8** (2013) P04013, `arXiv:1211.4462`. `doi:10.1088/1748-0221/8/04/P04013`.

[186] CMS Collaboration, "Performance of b tagging at $\sqrt{s} = 8$ TeV in multijet, ttbar and boosted topology events", CMS Physics Analysis Summary CMS-PAS-BTV-13-001, 2013.

[187] R. Fruhwirth, W. Waltenberger, and P. Vanlaer, "Adaptive vertex fitting", *J. Phys.* **G34** (2007) N343. `doi:10.1088/0954-3899/34/12/N01`.

[188] CMS Collaboration, "Performance of the CMS missing transverse momentum reconstruction in pp data at $\sqrt{s} = 8$ TeV", *JINST* **10** (2015) P02006, `arXiv:1411.0511`. `doi:10.1088/1748-0221/10/02/P02006`.

[189] CMS JetMET group, "MET Optional Filters". `https://twiki.cern.ch/twiki/bin/view/CMS/MissingETOptionalFilters`, 2017.

[190] CMS Collaboration, "Search for Displaced Supersymmetry in events with an electron and a muon with large impact parameters", *Phys. Rev. Lett.* **114** (2015) 061801, `arXiv:1409.4789`. `doi:10.1103/PhysRevLett.114.061801`.

[191] CMS Collaboration, "Search for displaced leptons in the e-mu channel", CMS Physics Analysis Summary CMS-PAS-EXO-16-022, 2016.

[192] CMS Collaboration, "Search for physics beyond the standard model in dilepton mass spectra in proton-proton collisions at $\sqrt{s} = 8$ TeV", *JHEP* **1504** (2015) 025, `arXiv:1412.6302`. `doi:10.1007/JHEP04(2015)025`.

[193] CMS Collaboration, "A search for a doubly-charged Higgs boson in pp collisions at $\sqrt{s} = 7$ TeV", *Eur. Phys. J. C* **72** (2012) 2189, `arXiv:1207.2666`. `doi:10.1140/epjc/s10052-012-2189-5`.

[194] A. G. Akeroyd, M. Aoki, and H. Sugiyama, "Probing Majorana Phases and Neutrino Mass Spectrum in the Higgs Triplet Model at the CERN LHC", *Phys. Rev. D* **77** (2008) 075010, `arXiv:0712.4019`. `doi:10.1103/PhysRevD.77.075010`.

[195] CMS Collaboration, "Measurements of Inclusive W and Z Cross Sections in pp Collisions at $\sqrt{s} = 7$ TeV", *JHEP* **01** (2011) 080, `arXiv:1012.2466`. `doi:10.1007/JHEP01(2011)080`.

[196] CMS Collaboration, "Measurement of inclusive W and Z boson production cross sections in pp collisions at $\sqrt{s} = 8$ TeV", *Phys. Rev. Lett.* **112** (2014) 191802, `arXiv:1402.0923`. `doi:10.1103/PhysRevLett.112.191802`.

[197] M. Cacciari and G. P. Salam, "Pileup subtraction using jet areas", *Phys. Lett. B* **659** (2008) 119, `arXiv:0707.1378`. `doi:10.1016/j.physletb.2007.09.077`.

[198] S. Harper et al., "HEEP Electron ID and isolation". `https://twiki.cern.ch/twiki/bin/view/CMS/HEEPElectronID`, 2017.

[199] CMS Collaboration, “Measurement of the muon stopping power in lead tungstate”, *JINST* **5** (2010) P03007, `arXiv:0911.5397`. `doi:10.1088/1748-0221/5/03/P03007`.

[200] P. D. Group, K.A. Olive, et al., “Atomic and nuclear properties of lead tungstate”. `http://pdg.lbl.gov/2014/AtomicNuclearProperties/HTML/lead_tungstate.html`, 2014.

[201] CMS Collaboration, “Single Muon efficiencies in 2012 Data”, Detector Performance Note CMS-DP-2013-009, CERN-CMS-DP-2013-009, 2013.

[202] CMS Muon POG, “Reference muon id and isolation efficiencies”. https://twiki.cern.ch/twiki/bin/view/CMS/MuonReferenceEffs, 2017.

[203] A. Belyaev, N. D. Christensen, and A. Pukhov, “CalcHEP 3.4 for collider physics within and beyond the Standard Model”, *Comput. Phys. Commun.* **184** (2013) 1729, `arXiv:1207.6082`. `doi:10.1016/j.cpc.2013.01.014`.

[204] J. Alwall et al., “A Standard format for Les Houches event files”, *Comput. Phys. Commun.* **176** (2007) 300, `arXiv:hep-ph/0609017`. `doi:10.1016/j.cpc.2006.11.010`.

[205] M. Bondarenko et al., “High Energy Physics Model Database : Towards decoding of the underlying theory (within Les Houches 2011: Physics at TeV Colliders New Physics Working Group Report)”. 2012. `arXiv:1203.1488`.

[206] G. Corcella et al., “HERWIG 6: An Event generator for hadron emission reactions with interfering gluons (including supersymmetric processes)”, *JHEP* **01** (2001) 010, `arXiv:hep-ph/0011363`. `doi:10.1088/1126-6708/2001/01/010`.

[207] S. Moretti et al., “Implementation of supersymmetric processes in the HERWIG event generator”, *JHEP* **04** (2002) 028, `arXiv:hep-ph/0204123`. `doi:10.1088/1126-6708/2002/04/028`.

[208] C. F. Uhlemann and N. Kauer, “Narrow-width approximation accuracy”, *Nucl. Phys. B* **814** (2009) 195, `arXiv:0807.4112`. `doi:10.1016/j.nuclphysb.2009.01.022`.

[209] D. Berdine, N. Kauer, and D. Rainwater, “Breakdown of the Narrow Width Approximation for New Physics”, *Phys. Rev. Lett.* **99** (2007) 111601, `arXiv:hep-ph/0703058`. `doi:10.1103/PhysRevLett.99.111601`.

[210] E. Accomando et al., “Z’ at the LHC: Interference and Finite Width Effects in Drell-Yan”, *JHEP* **10** (2013) 153, `arXiv:1304.6700`. `doi:10.1007/JHEP10(2013)153`.

[211] T. Sjöstrand, S. Mrenna, and P. Skands, “PYTHIA 6.4 physics and manual”, *JHEP* **05** (2006) 026, `arXiv:hep-ph/0603175`. `doi:10.1088/1126-6708/2006/05/026`.

[212] R. Field, “Early LHC Underlying Event Data - Findings and Surprises”, in *Hadron collider physics. Proceedings, 22nd Conference, HCP 2010, Toronto, Canada, August 23-27, 2010.* 2010. `arXiv:1010.3558`.

[213] W. Verkerke, “Statistical software for the LHC”, in *Statistical issues for LHC physics. Proceedings, Workshop, PHYSTAT-LHC, Geneva, Switzerland, June 27-29, 2007*, p. 169. 2007.

[214] CMS Collaboration, “Commissioning of the CMS Experiment and the Cosmic Run at Four Tesla”, *JINST* **5** (2010) T03001, `arXiv:0911.4845`. `doi:10.1088/1748-0221/5/03/T03001`.

[215] CMS Collaboration, “Performance of CMS muon reconstruction in cosmic-ray events”, *JINST* **5** (2010) T03022, `arXiv:0911.4994`. `doi:10.1088/1748-0221/5/03/T03022`.

[216] J. M. Tucker, “High transverse momentum muon reconstruction, a search for narrow dimuon resonances, and statistical techniques for LHC analyses”. PhD thesis, University of California, Los Angeles, 2011.

[217] T. Hebbeker and P. Biallass, “Parametrization of the Cosmic Muon Flux for the Generator CMSCGEN”. 2009. `arXiv:0907.5514`.

[218] L. Sonnenschein, “CMS: Cosmic muons in simulation and measured data”, *Proceedings, 24th International Symposium on Lepton-Photon Interactions at High Energy (LP09), Conf. Proc.* **C0908171** (2010) 454. `doi:10.3204/DESY-PROC-2010-04/P19`.

[219] M. Raymond et al., “The CMS tracker APV25 0.25 μm CMOS readout chip”, in *proceedings of the 6th Workshop on Electronics for LHC Experiments, Krakow, Poland, 11-15 Sep 2000*, p. 130. 2000. doi:10.5170/CERN-2000-010.130.

[220] CMS Collaboration, “Measurement of the charge ratio of atmospheric muons with the CMS detector”, *Phys. Lett. B* **692** (2010) 83, `arXiv:1005.5332`. `doi:10.1016/j.physletb.2010.07.033`.

[221] F.-P. Schilling, “Top Quark Physics at the LHC: A Review of the First Two Years”, *Int. J. Mod. Phys. A* **27** (2012) 1230016, `arXiv:1206.4484`. `doi:10.1142/S0217751X12300165`.

[222] M. Czakon, P. Fiedler, and A. Mitov, “Total Top-Quark Pair-Production Cross Section at Hadron Colliders Through $O(\alpha_S^4)$”, *Phys. Rev. Lett.* **110** (2013) 252004, `arXiv:1303.6254`. `doi:10.1103/PhysRevLett.110.252004`.

[223] M. Cacciari et al., “Top-pair production at hadron colliders with next-to-next-to-leading logarithmic soft-gluon resummation”, *Physics Letters B* **710** (2012) 612, `arXiv:1111.5869`. `doi:10.1016/j.physletb.2012.03.013`.

[224] M. Czakon and A. Mitov, “Top++: A Program for the Calculation of the Top-Pair Cross-Section at Hadron Colliders”, *Comput. Phys. Commun.* **185** (2014) 2930, `arXiv:1112.5675`. `doi:10.1016/j.cpc.2014.06.021`.

[225] A. Buckley et al., “LHAPDF6: parton density access in the LHC precision era”, *Eur. Phys. J. C* **75** (2015) 132, `arXiv:1412.7420`. `doi:10.1140/epjc/s10052-015-3318-8`.

[226] W. Hollik and M. Kollár, “NLO QED contributions to top-pair production at hadron colliders”, *Phys. Rev.* **D77** (2008) 014008, `arXiv:0708.1697`. `doi:10.1103/PhysRevD.77.014008`.

[227] W. Bernreuther, M. Fücker, and Z.-G. Si, “Weak interaction corrections to hadronic top quark pair production”, *Phys. Rev. D* **74** (2006) 113005, `arXiv:hep-ph/0610334`. `doi:10.1103/PhysRevD.74.113005`.

[228] J. H. Kühn, A. Scharf, and P. Uwer, “Electroweak effects in top-quark pair production at hadron colliders”, *Eur. Phys. J. C* **51** (2007) 37, `arXiv:hep-ph/0610335`. `doi:10.1140/epjc/s10052-007-0275-x`.

[229] J. H. Kühn, A. Scharf, and P. Uwer, “Weak Interactions in Top-Quark Pair Production at Hadron Colliders: An Update”, *Phys. Rev. D* **91** (2015), no. 1, 014020, `arXiv:1305.5773`. `doi:10.1103/PhysRevD.91.014020`.

[230] P. Nason, “A new method for combining NLO QCD with shower Monte Carlo algorithms”, *JHEP* **11** (2004) 040, `arXiv:hep-ph/0409146`. `doi:10.1088/1126-6708/2004/11/040`.

[231] S. Frixione, P. Nason, and C. Oleari, "Matching NLO QCD computations with Parton Shower simulations: the POWHEG method", *JHEP* **11** (2007) 070, `arXiv:0709.2092`. `doi:10.1088/1126-6708/2007/11/070`.

[232] S. Alioli et al., "A general framework for implementing NLO calculations in shower Monte Carlo programs: the POWHEG BOX", *JHEP* **1006** (2010) 043, `arXiv:1002.2581`. `doi:10.1007/JHEP06(2010)043`.

[233] S. Frixione, P. Nason, and G. Ridolfi, "A Positive-weight next-to-leading-order Monte Carlo for heavy flavour hadroproduction", *JHEP* **09** (2007) 126, `arXiv:0707.3088`. `doi:10.1088/1126-6708/2007/09/126`.

[234] H.-L. Lai et al., "New parton distributions for collider physics", *Phys. Rev. D* **82** (2010) 074024, `arXiv:1007.2241`. `doi:10.1103/PhysRevD.82.074024`.

[235] N. Kidonakis, "Top Quark Production", in *Proceedings, Helmholtz International Summer School on Physics of Heavy Quarks and Hadrons (HQ 2013): JINR, Dubna, Russia, July 15-28, 2013*, p. 139. 2014. `arXiv:1311.0283`. doi:10.3204/DESY-PROC-2013-03/Kidonakis.

[236] E. Re, "Single-top Wt-channel production matched with parton showers using the POWHEG method", *Eur. Phys. J. C* **71** (2011) 1547, `arXiv:1009.2450`. `doi:10.1140/epjc/s10052-011-1547-z`.

[237] C. D. White et al., "Isolating Wt production at the LHC", *JHEP* **11** (2009) 074, `arXiv:0908.0631`. `doi:10.1088/1126-6708/2009/11/074`.

[238] S. Frixione et al., "Single-top hadroproduction in association with a W boson", *JHEP* **07** (2008) 029, `arXiv:0805.3067`. `doi:10.1088/1126-6708/2008/07/029`.

[239] M. Grazzini et al., "W^+W^- production at the LHC: fiducial cross sections and distributions in NNLO QCD", *JHEP* **08** (2016) 140, `arXiv:1605.02716`. `doi:10.1007/JHEP08(2016)140`.

[240] T. Gehrmann et al., "W^+W^- Production at Hadron Colliders in Next to Next to Leading Order QCD", *Phys. Rev. Lett.* **113** (2014) 212001, `arXiv:1408.5243`. `doi:10.1103/PhysRevLett.113.212001`.

[241] C. Kao and D. A. Dicus, "Production of W^+W^- from gluon fusion", *Phys. Rev. D* **43** (1991) 1555. `doi:10.1103/PhysRevD.43.1555`.

[242] J. M. Campbell, R. K. Ellis, and C. Williams, "Vector boson pair production at the LHC", *JHEP* **07** (2011) 018, `arXiv:1105.0020`. `doi:10.1007/JHEP07(2011)018`.

[243] J. M. Campbell and R. K. Ellis, "An Update on vector boson pair production at hadron colliders", *Phys. Rev.* **D60** (1999) 113006, `arXiv:hep-ph/9905386`. `doi:10.1103/PhysRevD.60.113006`.

[244] J. M. Campbell and R. K. Ellis, "MCFM for the Tevatron and the LHC", *Nucl. Phys. Proc. Suppl.* **205-206** (2010) 10, `arXiv:1007.3492`. `doi:10.1016/j.nuclphysbps.2010.08.011`.

[245] P. Lenzi et al., "Standard Model Cross Sections for CMS at 8 TeV". `https://twiki.cern.ch/twiki/bin/viewauth/CMS/StandardModelCrossSectionsat8TeV`, 2017.

[246] A. Bierweiler et al., "Electroweak corrections to W-boson pair production at the LHC", *JHEP* **11** (2012) 093, `arXiv:1208.3147`. `doi:10.1007/JHEP11(2012)093`.

[247] M. Billoni et al., "Next-to-leading order electroweak corrections to pp $\to$ W^+W^- $\to$ 4 leptons at the LHC in double-pole approximation", *JHEP* **12** (2013) 043, `arXiv:1310.1564`. `doi:10.1007/JHEP12(2013)043`.

[248] T. Melia et al., "W^+W^-, WZ and ZZ production in the POWHEG BOX", *JHEP* **11** (2011) 078, `arXiv:1107.5051`. `doi:10.1007/JHEP11(2011)078`.

[249] K. Melnikov and F. Petriello, "Electroweak gauge boson production at hadron colliders through $\mathcal{O}(\alpha_S^2)$", *Phys. Rev. D* **74** (2006) 114017, `arXiv:hep-ph/0609070`. `doi:10.1103/PhysRevD.74.114017`.

[250] Y. Li and F. Petriello, "Combining QCD and electroweak corrections to dilepton production in the framework of the FEWZ simulation code", *Phys. Rev. D* **86** (2012) 094034, `arXiv:1208.5967`. `doi:10.1103/PhysRevD.86.094034`.

[251] B. Clerbaux et al., "Update of the $Z' \to$ ee analysis with Jan 22 re-recoed data", CMS Analysis Note AN-2013/359, 2012.

[252] CMS Collaboration, "CMS Luminosity Based on Pixel Cluster Counting - Summer 2013 Update", CMS Physics Analysis Summary CMS-PAS-LUM-13-001, 2013.

[253] TOTEM Collaboration, "Luminosity-independent measurements of total, elastic and inelastic cross-sections at $\sqrt{s} = 7$ TeV", *Europhys. Lett.* **101** (2013) 21004. `doi:10.1209/0295-5075/101/21004`.

[254] CMS Collaboration, "Measurement of the inelastic proton-proton cross section at $\sqrt{s} = 7$ TeV", *Phys. Lett. B* **722** (2013) 5, `arXiv:1210.6718`. `doi:10.1016/j.physletb.2013.03.024`.

[255] CMS collaboration Collaboration, "Measurement of the inelastic pp cross section at $\sqrt{s} = 7$ TeV", CMS Physics Analysis Summary CMS-PAS-QCD-11-002, CERN, 2011.

[256] CMS Collaboration, "Search for physics beyond the standard model in final states with a lepton and missing transverse energy in proton-proton collisions at $\sqrt{s} = 8$ TeV", *Phys. Rev. D* **91** (2015) 092005, `arXiv:1408.2745`. `doi:10.1103/PhysRevD.91.092005`.

[257] CMS BTV group, "Usage of b tag objects for 8 TeV data with the 53X Re-reco". `https://twiki.cern.ch/twiki/bin/viewauth/CMS/BtagRecommendation53XReReco`, 2017.

[258] N. Kidonakis, "Differential and total cross sections for top pair and single top production", in *proceedings of the 20th International Workshop on Deep-Inelastic Scattering and Related Subjects (DIS 2012): Bonn, Germany, March 26-30, 2012*, p. 831. 2012. `arXiv:1205.3453`. doi : 10.3204/DESY-PROC-2012-02/251.

[259] CMS Muon POG, "Reference muon momentum scale and resolution". `https://twiki.cern.ch/twiki/bin/viewauth/CMS/MuonReferenceResolution`, 2017.

[260] CMS Collaboration, "Measurement of differential top-quark pair production cross sections in pp colisions at $\sqrt{s} = 7$ TeV", *Eur. Phys. J. C* **73** (2013) 2339, `arXiv:1211.2220`. `doi:10.1140/epjc/s10052-013-2339-4`.

[261] CMS Collaboration, "Measurement of the differential cross section for top quark pair production in pp collisions at $\sqrt{s} = 8$ TeV", *Eur. Phys. J. C* **75** (2015) 542, `arXiv:1505.04480`. `doi:10.1140/epjc/s10052-015-3709-x`.

[262] M. Goerner et al., "Pt(top-quark) based reweighting of ttbar MC". `https://twiki.cern.ch/twiki/bin/viewauth/CMS/TopPtReweighting`, 2017.

[263] N. Kidonakis, "NNLL threshold resummation for top-pair and single-top production", *Phys. Part. Nucl.* **45** (2014), no. 4, 714–722, `arXiv:1210.7813`. `doi:10.1134/S1063779614040091`.

[264] N. Kidonakis, "NNNLO soft-gluon corrections for the top-quark p_T and rapidity distributions", *Phys. Rev. D* **91** (2015) 031501, `arXiv:1411.2633`. `doi:10.1103/PhysRevD.91.031501`.

[265] M. Czakon, D. Heymes, and A. Mitov, "High-precision differential predictions for top-quark pairs at the LHC", *Phys. Rev. Lett.* **116** (2016) 082003, `arXiv:1511.00549`. `doi:10.1103/PhysRevLett.116.082003`.

[266] M. Aldaya et al., "NNLO+NNLL top-quark-pair cross sections". `https://twiki.cern.ch/twiki/bin/view/LHCPhysics/TtbarNNLO`, 2017.

[267] S. Alekhin et al., "The PDF4LHC Working Group Interim Report", `arXiv:1101.0536`.

[268] M. Botje, J. Butterworth, A. Cooper-Sarkar et al., "The PDF4LHC Working Group interim recommendations". 2011. `arXiv:1101.0538`.

[269] H.-L. Lai et al., "New parton distributions for collider physics", *Phys. Rev. D* **82** (2010) 074024, `arXiv:1007.2241`. `doi:10.1103/PhysRevD.82.074024`.

[270] R. D. Ball et al., "Parton distributions with LHC data", *Nucl. Phys. B* **867** (2013) 244, `arXiv:1207.1303`. `doi:10.1016/j.nuclphysb.2012.10.003`.

[271] A. Apyan et al., "Measurement of inclusive W and Z boson cross section in pp collisions at $\sqrt{s} = 8$ TeV", cms analysis note.

[272] G. Schott, "RooStats for Searches", in *Proceedings, PHYSTAT 2011 Workshop on Statistical Issues Related to Discovery Claims in Search Experiments and Unfolding, CERN,Geneva, Switzerland 17-20 January 2011*, p. 199. 2011. `arXiv:1203.1547`. doi : 10.5170/CERN-2011-006.199.

[273] ATLAS and CMS Collaborations, and the LHC Higgs Combination Group, "Procedure for the LHC Higgs boson search combination in Summer 2011", CMS Note and ATLAS Physics Publication: CMS-NOTE-2011-005, ATL-PHYS-PUB-2011-11, 2011.

[274] G. Cowan, "Statistical Data Analysis". Oxford University Press, 1998.

[275] G. Cowan et al., "Asymptotic formulae for likelihood-based tests of new physics", *Eur. Phys. J. C* **71** (2011) 1554, `arXiv:1007.1727`. [Erratum: Eur. Phys. J.C73,2501(2013)]. `doi:10.1140/epjc/s10052-011-1554-0, 10.1140/epjc/s10052-013-2501-z`.

[276] N. Metropolis et al., "Equation of state calculations by fast computing machines", *J. Chem. Phys.* **21** (1953) 1087. `doi:10.1063/1.1699114`.

[277] W. K. Hastings, "Monte Carlo Sampling Methods Using Markov Chains and Their Applications", *Biometrika* **57** (1970) 97. `doi:10.1093/biomet/57.1.97`.

[278] J. S. Conway, "Incorporating Nuisance Parameters in Likelihoods for Multisource Spectra", in *Proceedings, PHYSTAT 2011 Workshop on Statistical Issues Related to Discovery Claims in Search Experiments and Unfolding, CERN,Geneva, Switzerland 17-20 January 2011*, p. 115. 2011. `arXiv:1103.0354`. doi : 10.5170/CERN-2011-006.115.

[279] K. Cranmer, "Practical Statistics for the LHC", in *Proceedings, 2011 European School of High-Energy Physics (ESHEP 2011): Cheile Gradistei, Romania, September 7-20, 2011*, p. 267. 2015. `arXiv:1503.07622`. doi : 10.5170/CERN-2015-001.247, 10.5170/CERN-2014-003.267.

[280] E. Gross and O. Vitells, “Trial factors or the look elsewhere effect in high energy physics”, *Eur. Phys. J. C* **70** (2010) 525, `arXiv:1005.1891`. `doi:10.1140/epjc/s10052-010-1470-8`.

[281] A. Wald, “Tests of Statistical Hypotheses Concerning Several Parameters When the Number of Observations is Large ”, *Transactions of the American Mathematical Society* **54** (1943) 426. `doi:10.1090/S0002-9947-1943-0012401-3`.

[282] CMS Collaboration, “Search for narrow resonances in dijet final states at $\sqrt{s} = 8$ TeV with the novel CMS technique of data scouting”, *Phys. Rev. Lett.* **117** (2016) 031802, `arXiv:1604.08907`. `doi:10.1103/PhysRevLett.117.031802`.

[283] K. Cheung, W.-Y. Keung, and P.-Y. Tseng, “Lepton-Flavor-violating Z′ using the electron-muon channel at the LHC”, *Phys. Rev. D* **94** (2016) 075006, `arXiv:1606.06696`. `doi:10.1103/PhysRevD.94.075006`.

[284] CDF Collaboration, “Search for the Decays $B^0_{(s)} \to e^+\mu^-$ and $B^0_{(s)} \to e^+e^-$ in CDF Run II”, *Phys. Rev. Lett.* **102** (2009) 201801, `arXiv:0901.3803`. `doi:10.1103/PhysRevLett.102.201801`.

[285] CMS Collaboration, “Search for high-mass resonances and quantum black holes in the $e\mu$ final state in proton-proton collisions at $\sqrt{s} = 13$ TeV”, CMS Physics Analysis Summary CMS-PAS-EXO-16-001, 2016.

[286] ATLAS Collaboration, “Search for New Phenomena in Dijet Events with the ATLAS Detector at $\sqrt{s}$=13 TeV with 2015 and 2016 data”, ATLAS Note ATLAS-CONF-2016-069, 2016.

[287] T. Sjostrand, S. Mrenna, and P. Z. Skands, “A Brief Introduction to PYTHIA 8.1”, *Comput. Phys. Commun.* **178** (2008) 852, `arXiv:0710.3820`. `doi:10.1016/j.cpc.2008.01.036`.

[288] R. Corke and T. Sjostrand, “Interleaved Parton Showers and Tuning Prospects”, *JHEP* **03** (2011) 032, `arXiv:1011.1759`. `doi:10.1007/JHEP03(2011)032`.

[289] P. Ilten, “Tau Decays in Pythia 8”, *Nucl. Phys. Proc. Suppl.* **253-255** (2014) 77, `arXiv:1211.6730`. `doi:10.1016/j.nuclphysbps.2014.09.019`.

[290] ATLAS Collaboration, “A search for high-mass resonances decaying to $\tau^+\tau^-$ in pp collisions at $\sqrt{s} = 8$ TeV with the ATLAS detector”, *JHEP* **07** (2015) 157, `arXiv:1502.07177`. `doi:10.1007/JHEP07(2015)157`.

[291] CMS Collaboration, “Search for high-mass resonances and large extra dimensions with tau-lepton pairs decaying into final states with an electron and a muon at $\sqrt{s} = 8$ TeV”, CMS Physics Analysis Summary CMS-PAS-EXO-12-046, 2015.

[292] CMS JetMET group, “Official Prescription for calculating corrections and uncertainties on Missing Transverse Energy (MET)”. `https://twiki.cern.ch/twiki/bin/viewauth/CMS/MissingETUncertaintyPrescription`, 2017.

[293] ATLAS Collaboration, “Search for a Heavy Neutral Particle Decaying to eμ, eτ, or $\mu\tau$ in pp Collisions at $\sqrt{s} = 8$ TeV with the ATLAS Detector, Auxiliary Material”. `https://atlas.web.cern.ch/Atlas/GROUPS/PHYSICS/PAPERS/SUSY-2013-06`, 2017.

[294] M. Buschmann et al., “New Signatures of Flavor Violating Higgs Couplings”, *JHEP* **06** (2016) 149, `arXiv:1601.02616`. `doi:10.1007/JHEP06(2016)149`.

[295] M. Sher and K. Thrasher, “Flavor Changing Leptonic Decays of Heavy Higgs Bosons”, *Phys. Rev. D* **93** (2016) 055021, `arXiv:1601.03973`. `doi:10.1103/PhysRevD.93.055021`.

[296] G. C. Branco et al., “Theory and phenomenology of two-Higgs-doublet models”, *Phys. Rept.* **516** (2012) 1, `arXiv:1106.0034`. `doi:10.1016/j.physrep.2012.02.002`.

[297] S. Davidson and H. E. Haber, “Basis-independent methods for the two-Higgs-doublet model”, *Phys. Rev. D* **72** (2005) 035004, `arXiv:hep-ph/0504050`. [Erratum: Phys. Rev.D72,099902(2005)]. `doi:10.1103/PhysRevD.72.099902, 10.1103/PhysRevD.72.035004`.

[298] ATLAS, CMS Collaboration, “Combined Measurement of the Higgs Boson Mass in pp Collisions at $\sqrt{s} = 7$ and 8 TeV with the ATLAS and CMS Experiments”, *Phys. Rev. Lett.* **114** (2015) 191803, `arXiv:1503.07589`. `doi:10.1103/PhysRevLett.114.191803`.

[299] R. Harlander et al., “Interim recommendations for the evaluation of Higgs production cross sections and branching ratios at the LHC in the Two-Higgs-Doublet Model”, `arXiv:1312.5571`.

[300] D. Eriksson, J. Rathsman, and O. Stål, “2HDMC: Two-Higgs-Doublet Model Calculator Physics and Manual”, *Comput. Phys. Commun.* **181** (2010) 189, `arXiv:0902.0851`. `doi:10.1016/j.cpc.2009.09.011`.

[301] J. Alwall et al., “The automated computation of tree-level and next-to-leading order differential cross sections, and their matching to parton shower simulations”, *JHEP* **07** (2014) 079, `arXiv:1405.0301`. `doi:10.1007/JHEP07(2014)079`.

[302] T. P. Cheng and M. Sher, “Mass-matrix ansatz and flavor nonconservation in models with multiple Higgs doublets”, *Phys. Rev. D* **35** (1987) 3484. `doi:10.1103/PhysRevD.35.3484`.

[303] Mu2e Collaboration, “Mu2e Technical Design Report”, `arXiv:1501.05241`.

[304] COMET Collaboration, R. Akhmetshin et al., “COMET Phase-I Technical Design Report”, TDR COMET-TDR-2016-v2, 2016.

[305] I. J. Aitchison, “Supersymmetry and the MSSM: An Elementary introduction”. 2005. `arXiv:hep-ph/0505105`.

[306] Z. Was, “TAUOLA the library for τ lepton decay, and KKMC / KORALB / KORALZ /... status report”, *Nucl. Phys. Proc. Suppl.* **98** (2001) 96, `arXiv:hep-ph/0011305`. `doi:10.1016/S0920-5632(01)01200-2`.

[307] D. Choudhury and P. Roy, “New constraints on lepton nonconserving R-parity violating couplings”, *Phys. Lett. B* **378** (1996) 153, `arXiv:hep-ph/9603363`. `doi:10.1016/0370-2693(96)00444-3`.

[308] J.-H. Jang, J. K. Kim, and J. S. Lee, “Constraints on the R-parity and lepton-flavor-violating couplings from B^0 decays to two charged leptons”, *Phys. Rev. D* **55** (1997) 7296, `arXiv:hep-ph/9701283`. `doi:10.1103/PhysRevD.55.7296`.

[309] S. L. Glashow and S. Weinberg, “Natural conservation laws for neutral currents”, *Phys. Rev. D* **15** (1977) 1958. `doi:10.1103/PhysRevD.15.1958`.